

# WOFEX 2019

proceedings of the 17<sup>th</sup> annual workshop

Faculty of Electrical Engineering and Computer Science,  
VŠB – Technical University of Ostrava

ISBN 978-80-248-4333-9



# WOFEX 2019 *wofex*

<http://wofex.vsb.cz/2019/>

17<sup>th</sup> annual workshop,  
Ostrava, 10<sup>th</sup> September 2019  
Proceedings of papers

*Organized by*

VŠB – Technical University of Ostrava  
Faculty of Electrical Engineering and Computer Science

WOFEX 2019

© Michal Krátký, Jiří Dvorský, Pavel Moravec, editors

ISBN 978-80-248-4333-9

This work is subject to copyright. All rights reserved. Reproduction or publication of this material, even partial, is allowed only with the editors' permission.

Page count: 535  
Impression: 200  
Edition: 1<sup>st</sup>  
First published: 2019

This proceedings was typeset by pdfL<sup>A</sup>T<sub>E</sub>X.

Published by Faculty of Electrical Engineering and Computer Science, VŠB – Technical University of Ostrava

# Preface

The workshop WOFEX 2019 (PhD workshop of Faculty of Electrical Engineering and Computer Science) was held on September 10<sup>th</sup> September 2019 at the VŠB – Technical University of Ostrava. The workshop offers an opportunity for students to meet and share their research experiences, to discover commonalities in research and studentship, and to foster a collaborative environment for joint problem solving. PhD students are encouraged to attend in order to ensure a broad, unconfined discussion. In that view, this workshop is intended for students and researchers of this faculty offering opportunities to meet new colleagues.

This book of proceedings includes 84 papers of faculty PhD students and 3 papers of external authors. The proceedings of WOFEX 2019 are also available at the web site <http://wofex.vsb.cz/2019/>. I would like to thank the authors and the Organizing Committee from Department of Computer Science, namely Jiří Dvorský and Pavel Moravec, for their arduous editing work.

September 2019

Michal Krátký  
Program Committee Chair  
WOFEX 2019



# Organization

## Program Committee

Chair:

Michal Krátký (VŠB – Technical University of Ostrava)

Members:

Pavel Brandštetter (VŠB – Technical University of Ostrava)

Radim Briš (VŠB – Technical University of Ostrava)

Zdeněk Dostál (VŠB – Technical University of Ostrava)

Petr Chlebiš (VŠB – Technical University of Ostrava)

Jiří Luňáček (VŠB – Technical University of Ostrava)

Stanislav Rusek (VŠB – Technical University of Ostrava)

Václav Snášel (VŠB – Technical University of Ostrava)

Vladimír Vašínek (VŠB – Technical University of Ostrava)

## Organizing Committee

Jiří Dvorský (VŠB – Technical University of Ostrava)

Pavel Moravec (VŠB – Technical University of Ostrava)

Hana Dluhošová (VŠB – Technical University of Ostrava)

## Technical Program Committee

Marek Dvorský (VŠB – Technical University of Ostrava)

Igor Hlubina (VŠB – Technical University of Ostrava)

Stanislav Kocman (VŠB – Technical University of Ostrava)

Ludvík Koval (VŠB – Technical University of Ostrava)

Pavel Moravec (VŠB – Technical University of Ostrava)

Tadeusz Sikora (VŠB – Technical University of Ostrava)

Libor Štěpanec (VŠB – Technical University of Ostrava)

Oldřich Vlach (VŠB – Technical University of Ostrava)

*Workshop Location:*

Campus of VŠB – Technical University of Ostrava

17. listopadu 15, 708 33 Ostrava–Poruba, Czech Republic

10<sup>th</sup> September 2019

<http://wofex.vsb.cz/2019/>



# Table of Contents

## Study Programme P2649 Electrical Engineering

### Electrical Power Engineering (3907V001)

Modelling of large light sources radiation to the upper hemisphere – obtrusive light . . . . .	1
<i>Petr Běčák, Tomáš Novák, and Karel Sokanský</i>	
Off-Grid System as Part of Warning Traffic System . . . . .	7
<i>Vojtěch Blažek and Stanislav Mišák</i>	
Power load shifting model based on power quality parameters short-term forecasting . . . . .	14
<i>Ibrahim S. Jahan and Stanislav Mišák</i>	
Fault distance measuring using fault module and protection relay . . . . .	20
<i>Michal Kotulla and Radomír Goňo</i>	
Current Transformer – Protection Relay Protection Circuit Error Investigation . . . . .	26
<i>David Lazecký</i>	
Energy Harvesting as an Energy Supply for Road Signalling . . . . .	33
<i>Michal Petružela</i>	
An Estimation of the Appliance Start-up Impact on the THDV and Pst Values in Off-grid Environment . . . . .	41
<i>Jan Vysocký and Stanislav Mišák</i>	

### Electrical Machines, Apparatus and Drives (2642V004)

Implementation of Induction Motor Speed Estimator Using Feedforward Neural Network . . . . .	48
<i>Jakub Bača and Daniel Kouřil</i>	
Online Stator Resistance Estimation By Using Particle Swarm Optimization Algorithm For Induction Motor Drives . . . . .	54
<i>Sang Dang Ho</i>	
An ARM-based Embedded Microcontroller System Development Platform	60
<i>Daniel Kouřil and Jakub Bača</i>	
Investigation of a Damaged Filter-compensation Unit . . . . .	66
<i>Stanislav Nowak and Stanislav Kocman</i>	

Influence of Anisotropy Metal Sheets on the Nominal Values Induction Machine . . . . .	72
<i>Pavel Pečínka, Stanislav Kocman, and Vladana Pečínková</i>	

A Fault Tolerant Control Method Against the Failure of a Current Sensor in Induction Motor Drive . . . . .	78
<i>Cuong Dinh Tran</i>	

## **Electronics (2612V015)**

Detonation Combustion and its Influences on Exhaust Emission Formation . . . . .	84
<i>Tomáš Harach</i>	

The Software Analysis of Electronic Diesel Control Systems . . . . .	90
<i>Tomáš Klein</i>	

Energy management architecture of experimental electric vehicle . . . . .	96
<i>Martin Kořený</i>	

Safety Braking System by Wire . . . . .	102
<i>Samuel Przewczek</i>	

Frequency Applicability of the TMS320F28335 DSC Built in A/D Converter . . . . .	108
<i>Jan Strossa and Vladislav Damec</i>	

## **Technical Cybernetics (2612V045)**

Development of Power Quality analyser in BROADBAND <sup>LIGHT</sup> grid . . . . .	114
<i>Jan Baroš and Radek Martinek</i>	

Data Compression in WSNs using Wavelet Transformation . . . . .	120
<i>Monika Borová and Michal Prauzek</i>	

Multichannel System for Non-Invasive Fetal ECG and Adult ECG Monitoring Based on Commercially Available Biosignal Amplifier and Virtual Instrumentation . . . . .	126
<i>Jindřich Brablík and Radek Martinek</i>	

Concept of low-power smart sensor system for Industry 4.0 based on industrial buses . . . . .	132
<i>Radek Byrtus</i>	

Visible Light Communication system based on SDR and LabVIEW . . . . .	138
<i>Lukáš Danys and Radek Martinek</i>	

Battery Electric Vehicle Range Estimation . . . . .	144
<i>Jan Dedek and Jan Žídek</i>	

Boundary value problem solving with additional optimization procedure . . . . .	150
<i>Tomáš Dočekal</i>	



Concept of testbed for measuring of diagnostic data . . . . .	156
<i>Jakub Dohmal</i>	
Analysis of the image quality of a radiographic cassette in dependence on X-ray irradiation . . . . .	162
<i>Klára Fiedorová and Martin Augustynek</i>	
Simulation Framework for Weather Forecasting Simulation Based on Historical Solar Irradiance Data . . . . .	168
<i>Karolína Gaiová and Michal Prauzek</i>	
Data processing using PLC and MCU based on IoT . . . . .	174
<i>Antonín Gavlas</i>	
Connecting demonstration stand for the education purposes to the university network . . . . .	180
<i>Matěj Golembiovský</i>	
A Hardware Communication Interface by NXP FlexIO Module . . . . .	186
<i>Libor Chrástecský, Jaromír Konečný, Martin Stankuš, and Michal Prauzek</i>	
Hybrid Methods for Processing of Fetal Electrocardiogram . . . . .	192
<i>René Jaroš and Radek Martinek</i>	
Fetal Cardiac Activity Monitoring: An Overview . . . . .	198
<i>Radana Kahánková and Radek Martinek</i>	
Evaluation of different methods used for recognition of lens types . . . . .	204
<i>Pavel Kodytek</i>	
Acoustic Sensor for Multi-Area Application . . . . .	210
<i>Jakub Kolařík and Radek Martinek</i>	
Numerical SW Tools for Solutions of Optimal Control Problems . . . . .	216
<i>Filip Krupa</i>	
Model of Retinal Vasculature from Images Taken by RetCam 3 with Using the Morphological Operation Methods . . . . .	222
<i>Alice Křesťanová and Marek Penhaker</i>	
Biological Signal Processing Using MATLAB Modular Processing System: An Overview . . . . .	228
<i>Martina Ládrová and Radek Martinek</i>	
The Control Design with REXYGEN in Industrial and Educational Applications . . . . .	233
<i>Jakub Němčík</i>	
Statistical analysis of electrogastrographic signals before and after food intake . . . . .	239
<i>David Oczka and Martina Litschmannová</i>	

Simulation of ultrasonic wave with 2 MHz frequency using convective wave equation . . . . .	243
<i>Tomáš Ondraczka</i>	
Design of a Bioimpedance Measurement Device Based on AD5933 Impedance Converter . . . . .	249
<i>Martin Schmidt and Marek Penhaker</i>	
Development and design of module for signal modulation . . . . .	255
<i>Miroslav Schneider</i>	
Smart sensors and technology of project Broadband <sup>LIGHT</sup> for “Smart City” concept . . . . .	261
<i>Lukáš Šoustek</i>	
Wireless Measurement of Environmental Quantities by use of IQRFTechnology . . . . .	267
<i>Jan Velička, Martin Pieš, Radovan Hájovský, and Štěpán Ožana</i>	
Embedded systems powered by piezoelectric transducers . . . . .	273
<i>Martin Vításek, Michal Prauzek, and Jaromír Konečný</i>	
Application of Transformation Methods on Pathological ECG Records . . .	279
<i>Jaroslav Vondrák and Marek Penhaker</i>	

## **Study Programme P1807 Computer Science, Communication Technology and Applied Mathematics**

### **Informatics (1801V001)**

Similarity comparison of LZ78, LZW and Fuzzy methods with different approaches of generating data . . . . .	285
<i>Martin Bielik and Jan Platoš</i>	
Knowledge Base for the TIL-Script Inference Machine; Polymorphic Deduction System . . . . .	291
<i>Michal Fait</i>	
Distributed Processing in Dynamically Growing Networks . . . . .	298
<i>Tomáš Janečko</i>	
Natural Gas Consumption Forecasting . . . . .	304
<i>Vojtěch Kotík and Jan Platoš</i>	
Co-authorship Network Dataset – StanBerk . . . . .	310
<i>Jakub Plesník and Miloš Kudělka</i>	
Swarm Malware . . . . .	316
<i>Lukáš Révay</i>	

Intelligent Malware . . . . .	322
<i>Lubomír Sikora</i>	
Skeleton Action Recognition Based on Singular Value Decomposition . . . .	328
<i>Radek Šimkanič</i>	
Text Topic Detection Based on Topic Modeling and Feature Selection . . .	334
<i>Yujia Sun and Jan Platoš</i>	
Crowdsourcing-enhanced N-grams Algorithm for Text Document Classification . . . . .	340
<i>Petr Šaloun, David Andrešič, and Barbora Cigánková</i>	
On the Particle Swarm Optimization Control . . . . .	345
<i>Lukáš Tomaszek</i>	
Comparison of range query performance for UB-tree and R-tree . . . . .	351
<i>Lukáš Zátoupek and Michal Krátký</i>	

## **Computational and Applied Mathematics (1103V036)**

Mountain pass algorithm for boundary value problems with p-Laplacian .	357
<i>Michaela Bailová</i>	
Modeling hydro-mechanical processes in fractured porous media . . . . .	363
<i>Michal Béréš and Radim Blaheta</i>	
Acceleration of adaptive MCMC methods in Bayesian inversion using surrogate models . . . . .	369
<i>Šimona Domesová</i>	
Parallel methods for solving the parabolic problem . . . . .	375
<i>Ladislav Foltyn</i>	
Estimating Parameters of Gaussian Mixtures using Variational Bayesian Approach . . . . .	381
<i>Petra Kozielová</i>	
PCDeflation: A High-performance Deflation Preconditioner in PETSc . . .	387
<i>Jakub Kružík and David Horák</i>	
Quaternions and dynamics of particles . . . . .	393
<i>Ondřej Markovič</i>	
An Optimization Approach to Solving the Kohn-Sham Equation . . . . .	397
<i>Martin Mrovec</i>	
Duality Based Solver for the Navier-Stokes Problem . . . . .	403
<i>Jan Pacholek</i>	
Fitting of potential energy surfaces using neural networks . . . . .	407
<i>Stanislav Paláček</i>	

Proof of Concept: Balancing Predictive Relevance of Biochemical Activities Employing SVM Classification and Platt's Calibration . . . . .	413
<i>Marek Pecha</i>	
Coupling Parareal and Schwarz method . . . . .	419
<i>Ivo Peterek</i>	
Use of generalized truncation for computer search for $(k, g)$ -graphs . . . . .	425
<i>Tom Raiman</i>	
Modelling of transient piezoelectricity – acoustic problem . . . . .	431
<i>Erika Straková and Dalibor Lukáš</i>	
High-order boundary element method . . . . .	436
<i>David Ulčák</i>	
Dealing with the variable selection problem in the analysis of mixed data . . . . .	442
<i>Adéla Vrtková</i>	
On Almost Regular Graphs and on Social Networks . . . . .	447
<i>Jakub Závada</i>	

## Communication Technology (2601V018)

VoIP simulation network by applying stochastic process methods . . . . .	452
<i>Ladislav Beháň</i>	
Development of LoRaWAN backend web application . . . . .	458
<i>Jakub Jalowiczor and Miroslav Vozňák</i>	
Influence of dry ice on a modulated optical beam on the basis of SDR for an FSO system . . . . .	464
<i>Jan Látal, Jakub Kolář, Jan Vitásek, and Lukáš Hájek</i>	
Micro-bending sensor made from polydimethylsiloxane . . . . .	470
<i>Martin Novák</i>	
Non-invasive heart rate sensor for magnetically interfered environments . . . . .	476
<i>Stanislav Žabka</i>	

## Study Programme P1701 Physics

### 1702V001 Applied Physics

Study of neutron-rich nuclei within the Skyrme-Hartree-Fock Model and the Algebraic Collective Model . . . . .	482
<i>Mojgan Abolghasem and Petr Alexa</i>	
Bloch surface waves as a tool for refractive index sensing . . . . .	488
<i>M. Gryga, D. Ciprian and P. Hlubina</i>	
Observation of Magnetic Domains using the Magnetic Force Microscopy . . . . .	494
<i>Dmitry Markov, Jana Trojčková, and Ondřej Životský</i>	

## **External Authors**

Vision Control of Industrial Processes .....	500
<i>Lukasz Miszuda</i>	
Assessment of the Effectiveness and Accuracy of Object Detection on the Example of a Power Line Insulator Detection System .....	506
<i>Jakub Osuchowski</i>	
Artificial Intelligence in the field of expressing human emotions – overview of available frameworks .....	512
<i>Agnieszka Rozanska</i>	

## **Author Index**



# Modelling of large light sources radiation to the upper hemisphere – obtrusive light

Petr Běčák, Tomáš Novák, and Karel Sokanský

Department of Electrical Power Engineering, FEECS,  
VŠB – Technical University of Ostrava, 17. listopadu 15,  
708 33 Ostrava – Poruba, Czech Republic  
petr.becak@vsb.cz

**Abstract.** The article describes one possible way of conducting evaluation of lighting system in aspect of influence of emitted luminous flux on outdoor environment in upper hemisphere using software goniophotometer. It is focused on modelling, evaluation and limitations of obtrusive light on practical/everyday examples and applications. Nowadays information and discussions stimulated research to find “simple” model of radiation of luminous flux to the upper hemisphere. It means that the model will evaluate luminous flux (direct and reflected) not only generally, but to the affected directions too. Therefore the goal of modelling is to quantify several sources of disturbing light. First, the original HPS lighting system of public lighting then the replacement of this system by LED lighting system. Furthermore, the proportion of obtrusive light from windows, billboards and car headlamps should be quantified.

**Keywords:** software goniophotometer, obtrusive light, public lighting, billboards, windows, headlamps, luminous flux, radiation, upper hemisphere

## 1 Introduction

Recently there has been a lot of media coverage related to obtrusive light viewed not only from quantitative and qualitative points of view. The above mentioned information usually come from astronomers, doctors and biologists recommendations who do not have any feedback on quantification of luminous flux outdoors. Information presented in such a way often give the impression that outdoor lighting (mainly public lighting) is an unwanted phenomena which causes many lifestyle diseases. De-facto people usually disapprove with outdoor lighting at night ignoring its main purpose - which is a transfer of information to the brain in the best possible quality and highest possible speed, so that safety of people in a given illuminated area is ensured by visual perception.

## 2 Modelling of obtrusive light using a software goniophotometer

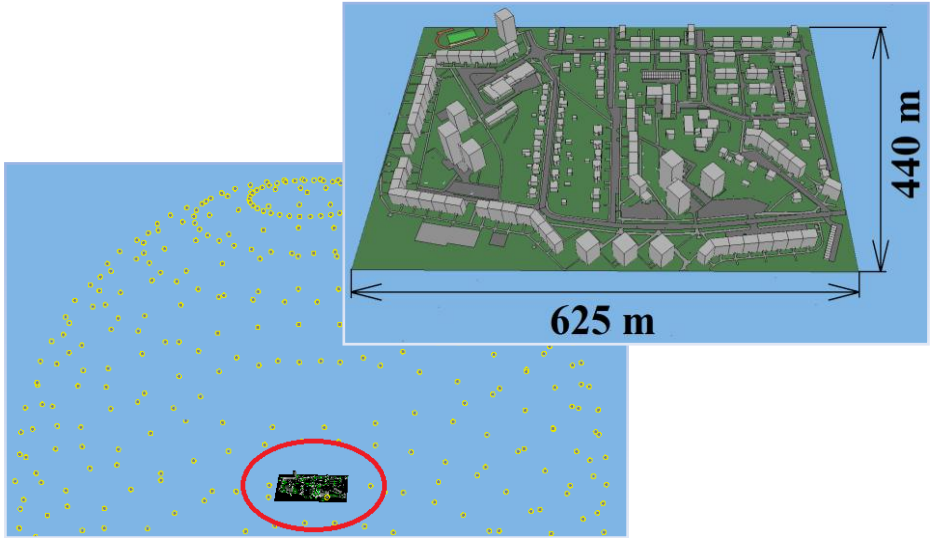
This part of the article is description of the software goniophotometer possibilities. It will show modelling of the luminous flux in upper hemisphere generated by outdoor light sources. The model was prepared because of necessity to predict behaviour of lighting systems from the point of view obtrusive light. Until this time it was possible to do only some partial short or long term measurements mentioned above.

The Kolarikovo housing estate located in Frydek-Mistek was deliberately chosen for modeling because there is a large amount of lighting system with high-pressure sodium lamps in the shape of a sphere, which radiate a large proportion of their luminous flux into the upper half-space. Therefore, we can say that this housing estate is a very bad example, because it contains a large number of unsuitable luminaires contributing significantly to the amount of disturbing light and the associated increased sky brightness. Obtrusive light cannot be completely prevented, but its effects can be greatly reduced by effective lighting. Only luminaires and lighting systems that do not directly radiate into the upper half-space should be installed. Obtrusive light is not caused only by public lighting, but also by architectural lighting of buildings, illuminated signs (billboards), lighting of sports facilities and parking lots. It is also the light that escapes from interiors of high-rise buildings and residential buildings, as well as the light from car headlights. In general, all artificial lighting, not just public lighting, is a negative phenomenon and nowadays is a "thorn in astronomers and environmentalists side,.". Therefore, it is necessary to verify all sources of obtrusive light and point out the fact that its magnitude is not caused only by public lighting. [1]

## 3 Function of the software goniophotometer

Software enable to insert calculation grid in sphere shape. Each calculated point describe normal illuminance in direction to the middle of sphere. This system duplicate function of the real goniophotometer. Principal of the goniophotometer is in possibility to measure luminous intensity in different levels and in different angles. It can be to interpret by sphere with calculation grid. The software goniophotometer duplicates this function only with difference, that is possible insert LDT file of luminaire or city LDT file with unbounded size. New possibility is option to choose density of calculation grid in angle step according standard used levels for luminaire measurement in  $C$ ,  $\gamma$  planes. For correct calculation it is necessary to take each object as simple point source. It means that object has insignificant dimensions against distance of point which is calculated. In praxis is this ratio requested higher than 5 so as light source was taken as simple point source. [2] Figure 1 shows situation of simple point source (model of blocks of flats) regarding to calculation grid of the software goniophotometer. When the longest distance of model is 625 m, then diameter of calculation points is 5000 m. The distance is longer than requirement and that it is why the calculation fulfill needed condition.





**Fig. 1.** Model of blocks of flats placed under the software goniophotometer.

Software is working on basis of inverse square law. It means that each calculation point of the grid represented normal illuminance and after it is converted to luminous intensity in solved direction. Output is final luminous intensity distribution for whole calculated lighting system, which is possible exported to the LDT file. All calculations were done with maintenance factor 1. It represent the worst case of the obtrusive light level.

#### 4 The district with blocks of flats Kolarikovo description


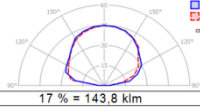
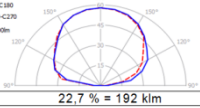

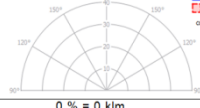
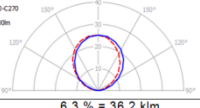

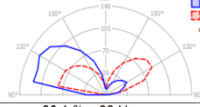
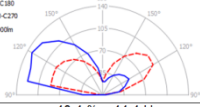

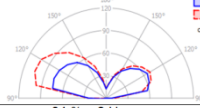
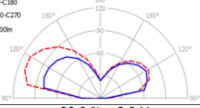

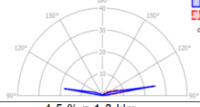
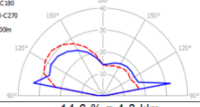
Basis for model is part of town Frydek-Mistek with roads and build up area. The district is placed on GPS coordinates  $49^{\circ}40'30.4''N$   $18^{\circ}20'03.6''E$ . Build up area is generally formed by blocks of flats and family houses. All surfaces like roads, houses and green spaces are described by their average reflectivity. It means 30 % for buildings, 20 % for footpaths and 10 % for roads, parking places and grass).

The HPS lighting system was inserted into the model by means of individual LDT file of the luminaire on the given position based on the dwg file, by means of which we also inserted buildings, roads, grassed areas, etc. The model features 192 luminaires, 94 of which are ball-shaped luminaires that radiate 50 % of the luminous flux into the upper half-space. The next step was to replace this outdated system of public lighting for a modern LED. [3] The replacement was based on the luminous flux into the lower half-space of the original lighting system. There are 141 luminaires in this newly created system, that do not emit any amount of luminous flux into the upper half-space. Other sources of obtrusive light entering the calculation are windows and billboards. These models were created on the basis of luminance analysis of several

samples and LDT file were created using the band-factor method with respect to the cosine radiation characteristic. 217 windows were placed randomly on the building's facades. The same was done for billboards. As there are no illuminated billboards in the housing estate, 10 billboards respecting the brightness of  $20 \text{ cd}\cdot\text{m}^{-2}$  and 10 billboards with a brightness of  $50 \text{ cd}\cdot\text{m}^{-2}$  were inserted. As the last source of disturbing light there are cars that respect low beams. The radiation characteristics of the two headlamps were measured on a photometric bench and then recalculated together to allow the insertion of one LDT file defining 1 car. Even this recalculation, or merging of multiple LDT files, can be done by a software goniophotometer. 20 merged headlamps were placed randomly on roads across the entire housing estate model.

Obrusive light represents a total luminous flux that spreads to the upper half-space and therefore increases sky brightness. It is formed by direct (ULOR) and reflected (DLOR) luminous flux from the terrain and particular objects. The most important thing is the evaluation of the luminous flux that is distributed directly to the upper half-space by ULR.

**Table 1.** Parameters of obtrusive light sources in the model and their distribution curves

Source of obtrusive light	System power (kW)	System luminous flux (klm)	ULOR (klm)	DLOR (klm)	ULOR + DLOR (klm)	ULOR + DLOR (%)	Luminous intensity distribution included only direct luminous flux to the upper hemisphere	Luminous intensity distribution included direct and reflected luminous flux to the upper hemisphere
	16,8	846	143,8	48,2	192	22,7	 17 % = 143,8 klm	 22,7 % = 192 klm
	5,5	575	0	36,2	36,2	6,3	 0 % = 0 klm	 6,3 % = 36,2 klm
	-	102,4	39	5,4	44,4	43,4	 38,1 % = 39 klm	 43,4 % = 44,4 klm
	-	5,86	2	0,3	2,3	38,6	 34 % = 2 klm	 38,6 % = 2,3 klm
	-	29,4	1,3	3	4,3	14,6	 4,5 % = 1,3 klm	 14,6 % = 4,3 klm
<b>Total values</b>	-	<b>1558,7</b>	<b>186,1</b>	<b>93,1</b>	<b>279,2</b>	<b>17,9</b>		

From the table it is apparent that by use of the LED lighting system we limit the input to 1/3 of the original lighting system with HPS. This results in a reduction in the

overall luminous flux of the lighting system from 846 klm to 575 klm. If we look at the amount of luminous flux to the upper half-space, there is more than fivefold decrease from 192 klm to 36,2 klm. Importantly, in LED lighting systems, the luminous flux into the upper half-space only gets as a reflection of the road, grassy areas and building facades, as shown in Table 1, where we see the distribution curves of all sources of obtrusive light in the housing estate model. If we compare the LED system with the billboards system, it is clear that 20 billboards emit more disturbing light than 141 public lighting fixtures, specifically billboards emit 44,4 klm. We must not forget the radiation from windows and cars. 217 windows emit 2,3 klm and 20 cars 4,3 klm. All the radiation characteristics of the above-mentioned obtrusive light sources are shown in the following table. There is also quantified both direct and total luminous flux of lighting systems in both percent and luminous flux (klm).

## 5 Conclusion

From the above we can conclude that the luminous flux emitted to the upper half-space is not only from the lighting fixtures but also from other more or less important light sources. This article presents a relatively easy to use tool using which it is possible to quantify obtrusive light based on light-technical calculations. It is not only the calculation of the total luminous flux, but also the directional characteristics of entire cities (or lighting systems), which can be presented, for example, in the LDT file and then used, in addition to the aforementioned quantification, to calculate the flux spread in the atmosphere.

## 6 Acknowledgment

Work is partially supported by Grants SGS SP2019/143 - BroadbandLIGHT - Public Lighting in SMART City and VI20172019071 - Analysis of Visibility of Transport Infrastructure for Safety Increasing during Night, Sunrise and Sunset.

## 7 References

- [1] Becak, P., Novak, T., Baleja, R., Sokansky, K.: Radiation of the Luminous Flux into the Upper Half-Space in Wils - Building Design. Proceedings of 7th Lighting Conference of the Visegrad Countries, LUMEN V4 2018, Grand HotelTrebic Czech Republic, ISBN: 978-153867923-4
- [2] Becak, P., Novak, T., Baleja, R., Sokansky, K.: Testing of the software goniophotometer in Wils - Building design computational programme. 19th International Scientific Conference on Electric Power Engineering, EPE 2018, DOI: 10.1109/EPE.2018.8395994
- [3] Becak, P., Wlosokova, J., Novak, T., Sokansky, K.: Vyzářování světelného toku do horního poloprostoru z reálného modelu části města. 2018, Kurz osvětlovací techniky XXXIV, Kouty nad Desnou, ISBN 978-80-248-4221-9

## **8 Publications**

Novak, T., Gasparovsky, D., Becak, P., Sokansky, K.: Modelling of large light sources radiation to the upper hemisphere - obtrusive light. The 29th Session of the CIE Washington D.C., USA, June 14 – 22, 2019, DOI: 10.25039/x46.2019.PO171

# Off-Grid System as Part of Warning Traffic System

Vojtěch Blažek and Stanislav Mišák

Department of Electrical Power Engineering, FEECS,  
VŠB – Technical University of Ostrava, 17. listopadu 15,  
708 33 Ostrava – Poruba, Czech Republic  
vojtech.blazek@vsb.cz

**Abstract.** The paper describes the development of a small off-grid system as a smart crash barrier and shows the concept where the new version will go. The main function of this system is to make the road section with limited sight distance on the road more transparent. The result of our research is a system based on the off-grid platform that is meant to work anywhere on the road in the Czech Republic. This off-grid system is modular, and its components are the solar controller, photovoltaic panel, Arduino, laser rangefinder, LED strip and accumulation in the form of batteries. This paper describes the development path of smart crash barrier and his early prototypes based on piezoelectric element and wind turbine.

**Keywords:** Autonomous Warning Traffic System, Off-Grid, Smart Crash Barrier, Dangerous road sections, Micro Grid, Smart Grids, Energy Harvesting

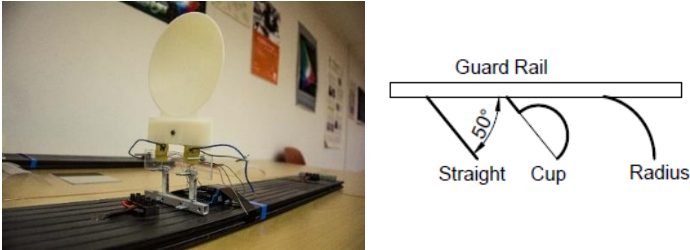
## 1 Introduction

This paper is based on an already published article that was published at the conference 20th International Scientific Conference on Electric Power Engineering. Paper name is Off-Grid System for Warning or Signaling Lighting of Dangerous Sections of Roads. In this paper, we will describe the past and possible future development of the smart crash barrier.

Many accidents happen on-road sections with limited sight distance. Based on this and own experiences from driving on Czech roads we came up with the idea to create a system that improves road safety and is energetically self-sufficient. First, we investigated the idea to utilize energy harvesting as an energy source for the system [1][2]. There are many methods of energy harvesting like piezoelectric, electromagnetic, thermoelectric etc. We were inspired by [3],[4] to utilize ANSYS Workbench during the development stage of the system's power source based on piezoelectric element and wind turbine. In the development, we realized a few prototypes. Every prototypes was tested in the VSB campus.

## 2 Prototypes

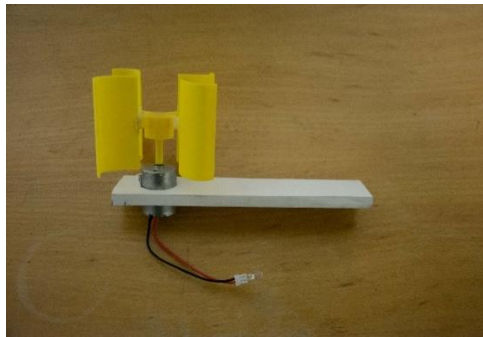
Fig. 1 shows first prototype and another tested shapes where are used in development. This prototype based on piezoelectric element as a power source.



**Fig. 1.** First prototype based on piezoelectric element and tested shapes

The prototype works on a base mechanical movement of wind flap who transformed into bending of piezoelectric element that generates electric energy to LED. The wind creates a passing car to caught by the wind flap.

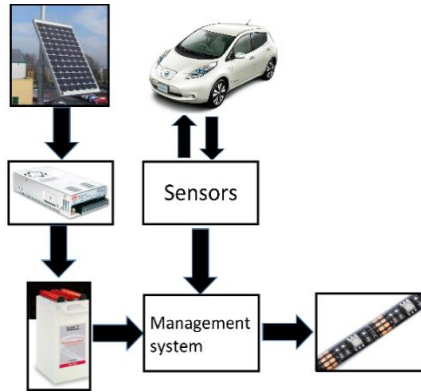
There was a problem with this prototype that energy from piezoelectric element was not always enough to light up the LEDs. The piezo prototype did not have satisfactory results and development is taking a new direction.



**Fig. 2.** Prototyp with wind turbine

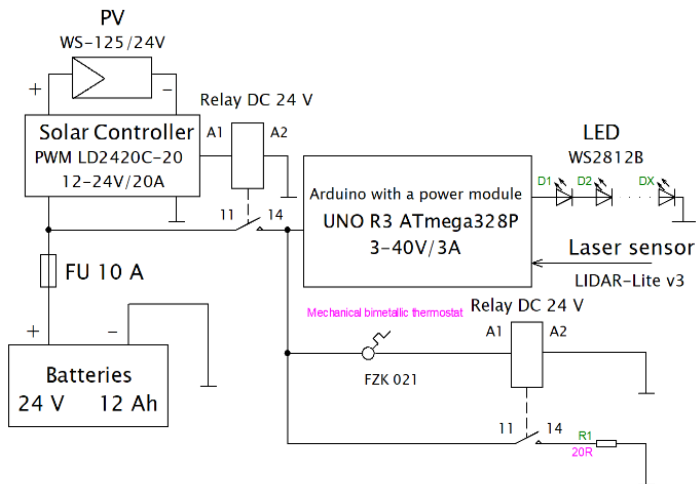
Next prototype based on small wind turbine as a power source show on Fig 2. Similarly, like in the previous concept with piezoelectric element also here energy of car passing by is captured in this case by the wind turbine. The oncoming wind moves wind turbine blades attached to the axis connected with the rotor of the dynamo, this causes rotation of axis and rotor and thus the generation of electric energy. This voltage is DC so there is no need for the rectifier and is possible to connect LED directly to the dynamo.

After testing we have a similar result like with piezo prototype. So, we had to redirect our research to a different concept. The concept of the system that gets its power for signalization from photovoltaic panel and batteries shows in Fig.3 and Fig.4.



**Fig. 3.** Block diagram of the Off-Grid system like Smart crash barrier

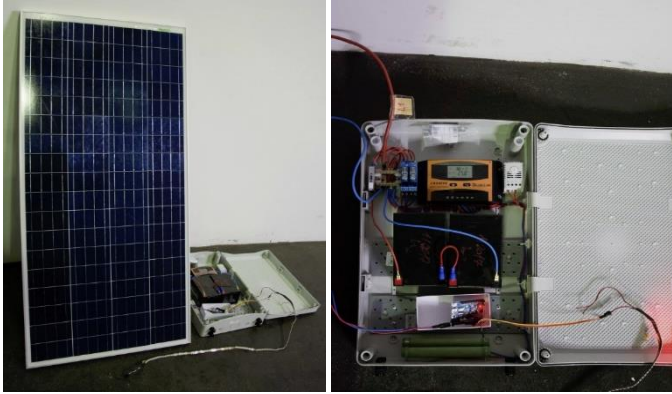
### 3 Off-Grid as Smart Crash Barrier



**Fig. 4.** Electric schematic of the system

The smart crash barrier is powered by lead-acid batteries of total capacity 12 Ah. These accumulator batteries are recharged by the photovoltaic solar regulator. This is the same concept as small off-grid houses. One photovoltaic panel 125 Wp is connected to this regulator and is mounted on a structure next to the guard rail. As a device for vehicle detection, we chose laser sensor LIDAR (Light detection and ranging). LIDAR is placed on the guard rail and work in the following manner – by shooting a laser at an

object and then measuring the time it takes for that light to return to the sensor. Lidar sends information to microcontroller Arduino UNO. Arduino will evaluate this information and turns on the LEDs. Arduino UNO is fully compatible with original Arduino. This microcontroller is based on ATmega328 with in-circuit system programming, 16 MHz crystal, 6 analog inputs, 16 digital input/outputs and USB connectivity. The control program for Arduino was written in C++ programming language in Express if IoT Development Framework with standard libraries. Fig 5. shows what the system looked like during development.



**Fig. 5.** Photos from the development

The current testing version of the system is powered by valve regulated lead-acid battery (VRLA). This battery composes of 4 cells that are connected in series. Each cell has 6 V and capacity 12 Ah. The total capacity of the battery is 250 Wh of usable energy but capacity can be increased. During the development we used long-term experience with development off-grid system [5],[6],[7].

## 4 Development of a New Concept

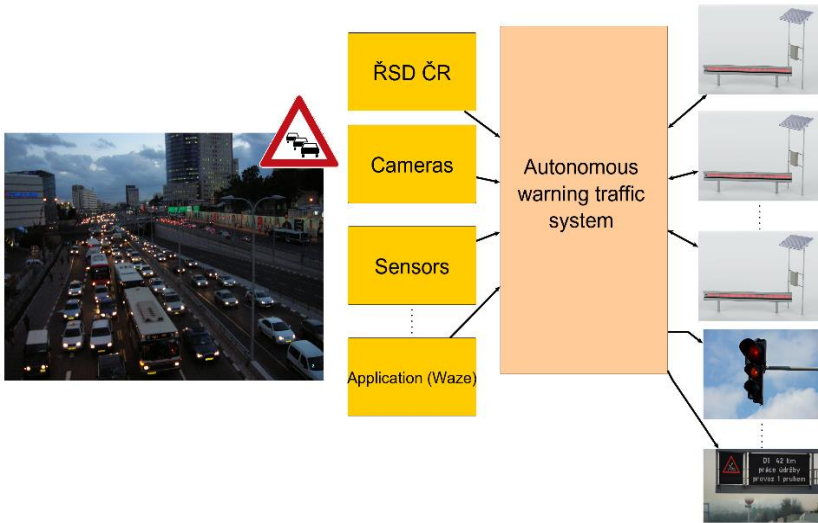
The smart crash barrier is adapted for possible scalability. This means, for example, we can add sensors or another new device. I am currently considering improvements to the existing concept. One way is to both sides communicate with the smart crash barrier in real-time by a user or traffic system. The smart crash barrier has own autonomous system but sometimes we need to show new information in real-time like road closed. This communication generally could more improve traffic flow, traffic data collection or safety on roads.

Communication between user or warning traffic system and smart crash barrier could work via the global Internet of Things (IoT) network like LoRa Technology. LoRa abbreviation for Long-Range Technology. LoRa can communicate with a limited number of backward messages in the 868 MHz frequency band. This technology enables devices to communicate inexpensively, safely and over long distances with mini-



mal power consumption. LoRa used mainly for sensors in towns, car parks, and businesses. LoRa allows the deployment of individual broadcasters even in local locations, thereby reinforcing their signal and providing coverage where needed [8].

In the future warning traffic system should be autonomous and responsive. The system would evaluate, based on the input, the best possible solution for the traffic situation. Inputs data for this system come from cameras, motion sensors, an application like Waze, etc. A smart crash barrier could be part of that system with real-time communication.



**Fig. 6.** New concept

Fig. 6 shows the concept of a possible future development. Nowadays smart crash barrier without real-time communication testing in village Suche Lazce and new feature is in development. In Fig.7 you can see how current version smart crash barrier look.



**Fig. 7.** Current version smart crash barrier located in Suche Lazce

## 5 Discussion and Conclusions

Early prototypes were based on the idea of energy harvesting of wind flow caused by a vehicle passing by and usage of this energy to supply the whole system. After tests and analyzing with the result that there isn't enough energy for reliable operation of the system. The current testing prototype is based on Off-Grid system. The current system is high modularity, low price, and accessibility of parts. We can easily modify the system by adding more batteries, connecting different photovoltaic panel or RGB LED strip.

Next version is in development. Last planned thing is the incorporation of the IoT into the system. IoT should be used to process information and control traffic with real-time communication, which leads with the aim to further improve traffic fluency. Also, it is planned to increase energy capacity by adding more batteries.

## Acknowledgment

This paper was supported by the following projects: LO1404: Sustainable Fig. 2. Shapes of tested wind flaps development of ENET Centre; SP2019/159 and SP2019/28 Students Grant Competition and TACR TH02020191 and TACR TH777911, Czech Republic and the Project LTI17023 "Energy Research and Development Information Centre of the Czech Republic" funded by Ministry of Education, Youth and Sports of the Czech Republic, program INTER-EXCELLENCE, subprogram INTER-INFORM and project TN01000007 National Centre for Energy

## References

1. Wei, C., Jing, X., "A comprehensive review on vibration energy harvesting: Modelling and realization," *Renew. Sustain. Energy Rev.*, vol. 74, no. December 2016, pp. 1–18, 2017.
2. Khaligh, A., Zeng, P., Cong Zheng, "Kinetic Energy Harvesting Using Piezoelectric and Electromagnetic Technologies - State of the Art", *IEEE Trans. Ind. Electron.*, vol. 57, no. 3, pp. 850-860, Mar. 2010.
3. Kacor, P., Misak, S., and Prokop, L., Optimization and redesign of vertical axis wind turbine for generator of independent source of energy, *Annals of DAAAM for 2010 & Proceedings of the 21st International DAAAM Symposium*, 20-23rd October 2010, Zadar, Croatia, ISSN 1726-9679, ISBN 978-3-901509-73-5, Katalinic, B. (Ed.), pp. 1053-1054, Published by DAAAM International Vienna, Vienna, 2010.
4. Kacor, P., Misak, S., Prokop, L., Modification of construction design of vertical axis wind turbine *Annals of DAAAM and Proceedings of the International DAAAM Symposium*, pp. 723-724, 2011.
5. Mišák, S., Stuchlý, J., Platoš, J., Krömer, P.: A heuristic approach to active demand side management in off-grid systems operated in a smart-grid environment. *Energy and buildings*, vol. 96, pp. 274-284 (2015).
6. Mišák, S., Stuchlý, J., Vramba, J., Prokop, L., Uher, M., Power Quality Analysis in Off-Grid Power Platform

7. Vantuch, T., Mišák, S., Jeżowicz, T., Buriánek, T., Snášel, V., The power quality forecasting model for off-grid system supported by multiobjective optimization. In: IEEE Transactions on Industrial Electronics, vol. 64, no. 12, pp. 9507-9516 (2017).
8. Bor, M., Vidler, J., Roedig, U., (2016). LoRa for the Internet of Things. EWSN. 361-366.

## Publications

Petruzela, M., Blazek, V., Vysocky, J., Prokop, L., Seidl, D.: Energy Harvesting from Discontinuous Flow, 2019 20<sup>th</sup> International Scientific Conference on Electric Power Engineering (EPE), Kouty nad Desnou, Czech Republic, DOI: 10.1109/EPE.2019.8777989

Blažek, V., Petruzela, M., Vysocky, J., Prokop, L., Misak, S., Seidl, D.: Off-Grid System for Warning or Signalling Lighting of Dangerous Sections of Roads, 2019 20<sup>th</sup> International Scientific Conference on Electric Power Engineering (EPE), Kouty nad Desnou, Czech Republic, DOI: 10.1109/EPE.2019.8778091

Vysocky, J., Blažek, V., Petruzela, M., Misak, S., Prokop, L.,: New User-Friendly Software Application to Simulate and Visualize The Distribution System Operation, 2019 20<sup>th</sup> International Scientific Conference on Electric Power Engineering (EPE), Kouty nad Desnou, Czech Republic, DOI: 10.1109/EPE.2019.8778180

Petruzela, M., Blazek, V., Vysocky, J. Analysis of appliance impact on total harmonic distortion in off-grid system, (2020) 2019 5<sup>th</sup> International Conference on Advanced Engineering Theory and Applications (AETA), vol. 554, pp. 844-849, Ostrava, Czech Republic, DOI: 10.1007/978-3-030-14907-9\_81.

# Power load shifting model based on power quality parameters short-term forecasting

Ibrahim S. Jahan and Stanislav Mišák

ENET Centre, VŠB – Technical University of Ostrava,  
17. listopadu 15, 708 33 Ostrava – Poruba, Czech Republic  
jahan\_nw@yahoo.com, stanislav.misak@vsb.cz

**Abstract.** This study focuses on power load shifting as parts of my thesis. The main goal of my thesis is to design a smart control system, which I plan to do in two main sections. The first section is about designing forecasting models, and the second section concentrates on designing an optimization model for power load shifting. This article contributes to the second section of my thesis. Accurate and reliable smart power control system is a vital task as it may greatly influence the operation and management of electrical power generation systems. In off-grid platforms, smart control systems are needed to keep the consumed power equal to generated power as well as to maintain the power quality at standard levels of power quality parameters. Many models of smart power system have been designed. Still, the controlling of power from generation to consumers in optimal way remains an open issue. In this article, I will explain steps of designing an intelligent approach for shifting electrical load using data taken from an off-grid platform. The planned approach will build on following steps—the first step is the designing of system for power quality parameters forecasting (Frequency, voltage, THDV, THDC and Flicker), in the second step according to results of these models load will shift to run in switch time.

**Keywords:** power quality parameters, power load shifting, renewable energy, smart grid.

## 1 Introduction

The goal of power systems is to supply electrical power to customers at standard levels of power quality. Because many modern devices and factories are sensitive to the power supply designed for some standard power supply, the supply of electrical power of standard power quality should allow sensitive modern devices to work efficiently. To design smart control systems usually three parameters are needed, which should be forecasted in advance, i.e. power demand, power quality parameters, and generation power. Next, the main task is to decide which device should run, so that the consumed power meets the generated power. In some cases in the process of power failure isolation, some unfailed parts will lose power. So, a smart control model for

reconfiguring distribution power systems for reconnecting the power for these parts in a short time is required and considered a challenge [1].

## 2 Related Works

There are many studies which designed smart control systems using various and different models. Belkacemi and Feliachi have designed a multi agent system (MAS) for reconfiguration and restoration of distribution power system. The designed model was built using an artificial immune system. The proposed system was tested and the experimental results proved the ability and efficiency of the proposed method for reconfiguration power system [2]. Duan et al. designed a model for the reconfiguration of power system using a genetic algorithm (GA). The simulation results of the proposed system showed that the GA can deal with reconfiguration of distributed system, and it can be used to set a switch process program. And the results were promising to reduce the power loss as well increase the reliability of the power system [3]. Reinforcement Learning (RL) technique has been applied by Vlachogiannis and Hatziaargyriou to control a power distribution grid (DG). RL algorithm was used to choose the best branch which will flow the power, which will help in minimizing the power loss. The system was able to control and set DG better than other approaches when comparing the performance [4]. Solanki et al. applied and proposed a MAS for the restoration of power distribution system after an electrical defect. The system was tested under three different cases, which confirmed that the MAS are suitable for resetting power distribution system after electrical default [1]. Amanulla et al. used a Binary particle swarm optimization (BPSO) algorithm to find a better configuration of the switches in the distribution power grid, in each cycle of learning the algorithm the reliability and the power loss are calculated. The model was successful having been evaluated and tested using 32 bus and 123 bus distribution system [5]. Fathabadi applied Dynamic Fuzzy C-means (DFCM) clustering with 3-layers artificial neural network (ANN) for optimal reconfiguration of power distribution system. The proposed approach implemented on IEEE 33 and IEEE 69 bus. The simulation results proved that the designed system needed a shorter computation time, had a simple design, and higher accuracy when compared with other traditional models [6]. Nagata and Sasaki applied a multi agent model for the restoration of power distribution system after an electrical failure. The experiment proved that the designed system can set the switches of the distribution system using local information, and it can be applied for complex and wide-range power network [7]. Saraiva and Asada designed a multi agent model for reconfiguration of the topology of the power distribution network. The model was tested under two systems- 11-Bus and 16-Bus. The results demonstrated the validity of the system, which gave good quality reconfiguration of the distribution network [8]. Teaching learning based optimization algorithm has been applied to determine the best reconfiguration of the distribution generation (DG), which will help in improving the voltage profile, voltage stability, and minimizing the power loss, by Mohanty and Tripathy. The type was evaluated using two radial distribution system 33 bus and 6 bus, the effectiveness of the system was good when compared with the results for the same tested system [9]. Gupta et al. designed a model for the reconfiguration of a radial distribution system in fuzzy framework using a genetic algorithm. The designed

model was tested for 70 and 136 bus distribution power system. The experiment results were compared with results of other methods which proved the validity of the system [10]. Automatic reconfiguration of shipboard power distribution system using Q-learning was applied by Das et al. The results demonstrated the validity of the designed system to find an optimal configuration of power system [11]. Distribution power system reconfiguration using a mathematical mode with consideration of some factors as load balancing, switching cost, and line loss minimization. This model has been investigated by Hyder et al. The system was tested under three distribution system- 32, 70, 135 bus [12]. Reddy et al. designed a system for the optimal reconfiguration of power system using a whale optimization algorithm. The mode is estimated under different numbers of test bus and as well the results of proposed system outperformed the results of other models when comparing the results [13]. Candelo-Becerra et al. investigated three methods to find the optimal reconfiguration of renewable power distribution system- the harmony search (HS), bat-inspired (BA), and cuckoo search (CS) techniques. The performance of three models was tested using radial distribution network with 33 nodes. In BA and HS better results than CS [14]. For reducing the electrical power losses Sedighzadeh et al. designed a model to reach an optimal solution for the reconfiguration of power system using an improved binary particle swarm optimization (IBPSO) algorithm. The proposed system was tested using 16, and 33 bus. The validity of the designed system was proved when compared with the results of others [15]. Kumar and Naveen applied a catfish particle swarm optimization (PSO) to solve the feeder power network. The system was tested for 33 and 16 bus power network. The article as well concluded that the proposed mode is a suitable method for distribution grid restoration [16]. Applying Fuzzy multi-objective technique for the purpose of minimizing the active power loss and power system reliability has been designed by Syahputra et al. The constructed system was tested for 70 nodes distribution generation. The results showed that the system reduced the loss active power by 37.92% [17]. Despite the reported improvements, reliable load forecasting still remains a challenge, in particular in the off-grid power systems. This article proposes an intelligent approach to power load forecasting in off-grid platforms by means of selected input variables, and describes the model construction.

### **3 Experiment process**

#### **3.1 Data set**

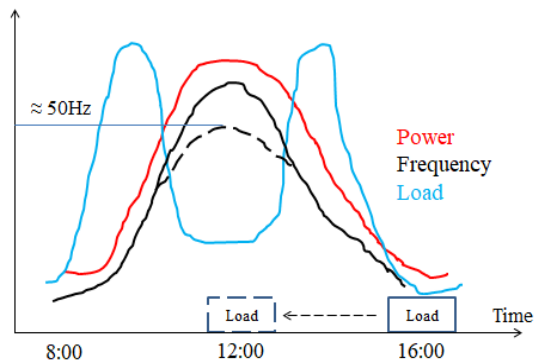
The data set used in this article was taken from the off-grid platform constructed at the Faculty of Electrical Engineering and Computer Science at VSB-Technical University of Ostrava, the Czech Republic. This data set contains meteorology data, power quality parameters (as voltage frequency, flicker, and so on) and in the same time step home appliances (when running = 1, off = 0). The home appliances as TV, AC heating, lights, and fridge.

In our experiment, I will use weather conditions as temperature, humidity, wind speed, and pressure, with home appliances. These are used as input variables, while power quality parameters will be used as the output of forecasting system.

### 3.2 Experiment Setup

The experiments are still in the progress. The main goal of these experiments is to building a smart control system which will consist of two main stages- the first one is designing a forecasting model to predict few minutes ahead of power quality parameters, and in the second one build an optimization model- use short-term predicted values of power parameters from step one to shift the load to run in suitable time, this process will help towards correcting the power quality.

As can be seen in figure 1, and figure 2, the use of home appliances may be moved which will correct the frequency to nominal value [EN 50160] as much as possible. More details about the planned system as following-



**Fig. 1.** Curves show moving the load to correct the Frequency

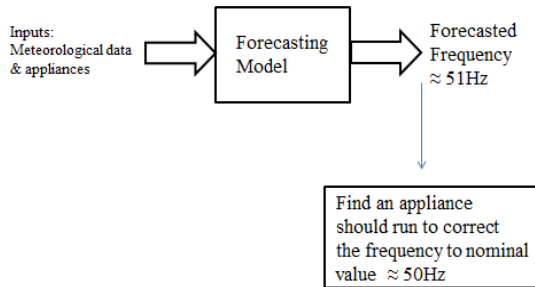
Step one- designing five forecasting systems for predict power quality parameters: voltage forecasting, frequency forecasting, THDV forecasting, THDC forecasting, and Flicker forecasting. The inputs of forecasting system will be weather conditions as temperature, wind speed, humidity, and pressure, additional home appliances either on or off. And the output of the system will be one of power quality parameters. One example of forecasting model as in neural network and decision tree [18].

Step two- Moving the load to turn on in a switch time according to the forecasted values of the power quality parameters from step one. The moving schedule of home appliances will keep quality of the power and optimizing following the power to the devices.

## 4 Conclusion

Accurate smart control models are important for the operation and control of power systems as they ensure the supply of accurate and reliable electricity to users.

Smart control systems of the power utility- aim to balance the consumed power and generated power as well as to maintain power quality parameters at standard levels as much as possible.



**Fig.2.** The basic principle of how to correct the frequency in power system

Despite a number of previous studies focused on the design of various types of smart control systems, the challenge remains to design and apply efficient control systems in real time. In this study, I explained a design a smart control system using data set taken from off-grid platform in VSB-TUO. This study contributes as a second part of my study. The planed system is still in the progress that constructed in two steps- forecasting system which will forecast power quality parameters in the second step use the forecasted values from step one to moving the load which will keep the power with good quality.

## Acknowledgements

This work was conducted in the framework of the project LO1404 TUCENET – Sustainable Development of Centre ENET, and the project CZ.1.05/2.1.00/19.0389.CZ.1.05/2.1.00/19.0389- Research Infrastructure Development of the CENET.

## References

1. Solanki JM, Khushalani S, Schulz NN. A multi-agent solution to distribution systems restoration. IEEE Transactions on Power systems. 2007 Aug;22 (3):1026-34.



2. Belkacemi R, Feliachi A. Multi-agent design for power distribution system reconfiguration based on the artificial immune system algorithm. InCircuits and Systems (ISCAS), Proceedings of 2010 IEEE International Symposium on 2010 May 30 (pp. 3461-3464). IEEE.
3. Duan DL, Ling XD, Wu XY, Zhong B. Reconfiguration of distribution network for loss reduction and reliability improvement based on an enhanced genetic algorithm. International Journal of Electrical Power & Energy Systems. 2015 Jan 1;64:88-95.
4. Vlachogiannis JG, Hatziaargyriou N. Reinforcement learning (RL) to optimal reconfiguration of radial distribution system (RDS). InHellenic Conference on Artificial Intelligence 2004 May 5 (pp. 439-446). Springer, Berlin, Heidelberg.
5. Amanulla B, Chakrabarti S, Singh SN. Reconfiguration of power distribution systems considering reliability and power loss. IEEE transactions on power delivery. 2012 Apr;27(2):918-26.
6. Fathabadi H. Power distribution network reconfiguration for power loss minimization using novel dynamic fuzzy c-means (dFCM) clustering based ANN approach. International Journal of Electrical Power & Energy Systems. 2016 Jun 1;78:96-107.
7. Nagata T, Sasaki H. A multi-agent approach to power system restoration. IEEE transactions on power systems. 2002 May;17(2):457-62.
8. de Oliveira Saraiva F, Asada EN. Multi-agent systems applied to topological reconfiguration of smart power distribution systems. InNeural Networks (IJCNN), 2014 International Joint Conference on 2014 Jul 6 (pp. 2812-2819). IEEE.
9. Mohanty B, Tripathy S. A teaching learning based optimization technique for optimal location and size of DG in distribution network. Journal of Electrical Systems and Information Technology. 2016 May 1;3(1):33-44.
10. Gupta, N., A. Swarnkar, K. R. Niazi, and R. C. Bansal. "Multi-objective reconfiguration of distribution systems using adaptive genetic algorithm in fuzzy framework." IET generation, transmission & distribution 4, no. 12 (2010): 1288-1298.
11. Das, S., Bose, S., Pal, S., Schulz, N.N., Scoglio, C.M. and Natarajan, B., 2013. Dynamic reconfiguration of shipboard power systems using reinforcement learning. IEEE Transactions on Power Systems, 28(2), pp.669-676.
12. Hyder, M.M. and Mahata, K., 2016. Reconfiguration of distribution system using a binary programming model. AIMS ENERGY, 4(3), pp.461-480.
13. Reddy, P.D.P., Reddy, V.V. and Manohar, T.G., 2017. Whale optimization algorithm for optimal sizing of renewable resources for loss reduction in distribution systems. Renewables: Wind, Water, and Solar, 4(1), p.3.
14. Candelo-Becerra, J.E., Hernandez-Riao, H.E. and Santander-Mercado, A.R., 2015. Comparison of multiobjective harmony search, cuckoo search and bat-inspired algorithms for renewable distributed generation placement. Tecno Lgicas, 18(35), pp.105-116.
15. Sedighzadeh, M., Dakhem, M., Sarvi, M. and Kordkheili, H.H., 2014. Optimal reconfiguration and capacitor placement for power loss reduction of distribution system using improved binary particle swarm optimization. International Journal of Energy and Environmental Engineering, 5(1), p.3.
16. Kumar, K.S. and Naveen, S., 2014. Power system reconfiguration and loss minimization for a distribution systems using Catfish PSO algorithm. Frontiers in Energy, 8(4), pp.434-442.
17. Syahputra, R., Robandi, I. and Ashari, M., 2012, May. Reconfiguration of distribution network with DG using fuzzy multi-objective method. In Innovation Management and Technology Research (ICIMTR), 2012 International Conference on (pp. 316-321). IEEE.
18. Jahan, Ibrahim S., Michal Prilepok, Stanislav Misak, and Vaclav Snael. "Intelligent system for power load forecasting in off-grid platform." In 2018 19th International Scientific Conference on Electric Power Engineering (EPE), pp. 1-5. IEEE, 2018.

# Fault distance measuring using fault module and protection relay

Michal Kotulla and Radomír Goňo

Department of Electrical Power Engineering, FEECS,  
VŠB – Technical University of Ostrava, 17. listopadu 15,  
708 33 Ostrava – Poruba, Czech Republic  
michal.kotulla.st@vsb.cz

**Abstract.** This article is focused on measuring of fault distance with feeder protection relay REF630 from ABB and its function fault locator. This function provides impedance-based fault location. For measuring was used laboratory at Faculty of Electrical Engineering and Computer Science where is laboratory stand with inbuilt REF630 and fault module and where is also available transmission network module. Fault distance was measured for two fault types. Parameters of typical 11 kV distribution network was set up in protection relay by ABB software PCM600. In case of phase-to-phase fault measured distance corresponded with parameters of model. However, in case of phase-to-earth fault measured fault distance was more than two times lower than our model. Measurement was repeated with parameters of zero sequence reactance equal to positive sequence reactance. Next results corresponded to our model parameters. All results confirmed assumption that higher fault resistance causes lower accuracy of calculated fault distance.

**Keywords :** fault locator, REF 630, short circuit, fault distance, fault resistance

## 1 Introduction

Protection systems are installed to clear faults, like short circuits, because shortcircuit currents can damage the cables, lines, busbars, and transformers. The voltage and current transformers provide measured values of the actual voltage and current to the protective relay. The relay processes the data and determines, based on its settings, whether or not it needs to operate a circuit breaker in order to isolate faulted sections or components. Nowadays computerized relays are taking over as they have many advantages: computerized relays can perform a self-diagnosis, they can record events and disturbances in a database, and they can be integrated in the communication, measurement, and control environment of modern substations [1].

Protection must be selective and discriminative in its operation – it should select and disconnect the minimum amount of equipment necessary to isolate the fault, thereby minimizing disruption to the wider network. In order to accomplish this,

individual protections are applied to different items of equipment such as busbars, lines, transformers or connections, etc.

There are three main techniques for short circuit fault detection:

Current

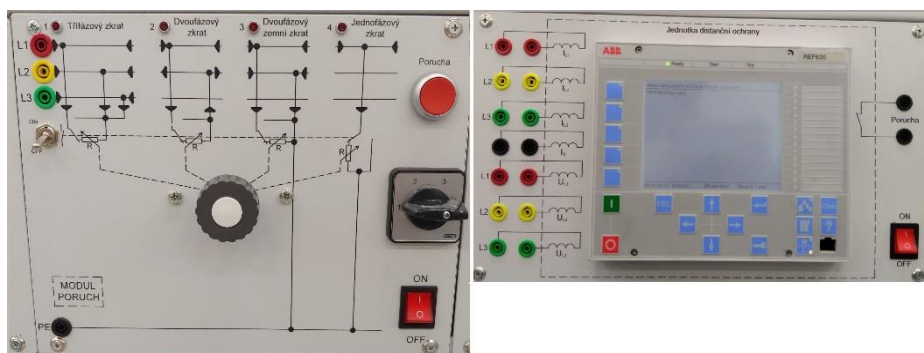
Impedance (distance)

Differential (unit) protection

Generally, for an overhead line, its impedance can be considered proportional to its length, and hence measuring the impedance can be used to measure the distance. A distance relay is set to measure a specific impedance, termed its reach, and will then operate for faults up to that reach. In order to do this, it must measure the voltage and current flowing at the relaying point in order to establish if the calculated impedance to the fault is within its reach setting [2].

## 2 Function of fault locator and fault module

Article deals with measuring fault distance with fault locator (FLOC) when malfunction occur in distribution network. The measuring took place in laboratory at VŠB-TUO, where is placed fault module and feeder protection relay REF630, which is built into laboratory stand (Figure 1). This module can simulate three-phase short circuit, phase-to-phase short circuit, phase-to-phase earth fault and phase-to-earth fault in distribution networks (more information about malfunction in distribution networks can be found in [3]).



**Fig. 1.** Fault module and protection relay REF630

The FLOC uses measured fundamental frequency, current and voltage phasors from local substation for distance calculation. All three currents and phase-to-earth voltages, which are measured, are needed for full operation of FLOC.

The fault distance calculation consists of two steps. The fault type identification is compulsory for correct operation of the fault locator function. It is because only one of the impedance measuring elements, that is, fault loop, gives the correct result for a specific fault type. After the first step, the fault distance is calculated.

The FLOC employs independent algorithms for each fault type in order to achieve optimal result of fault distance. The result of the fault distance calculation is the ohmic fault loop impedance value [4]:

$$Z_{FLOOP} = R_{FLOOP} + jX_{FLOOP} + R_F \quad \square\square\square$$

Each fault type has different fault loop for calculation of fault loop impedance. For example, on Figure 2 is shown fault loop for phase-to-phase fault.

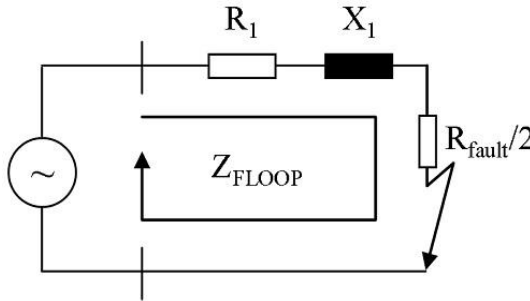


Fig. 2. Fault loop impedance for phase-to-phase fault [4].

### 3 Fault distance measuring

Measuring was taking place in laboratory at VŠB-TUO, but first it was necessary to configurate and set up parameters of FLOC function block in PCM600.

Line parameters in FLOC function block include positive sequence impedance and zero sequence impedance. Positive sequence was obtained from datasheet for typical 11 kV conductors (flat tower configuration assumed). Zero sequence impedance was need as well, because phase-to-earth fault was measured. The zero sequence impedance was calculated according to equations from technical manual of REF630. Line parameters are shown in Table 1.

Table 1. Line parameters

Line parameter	Value	Unit
$R_1$	0.532	ohm/pu
$X_1$	0.373	ohm/pu
$R_0$	0.680	ohm/pu
$X_0$	1.670	ohm/pu
Line Length	70	pu

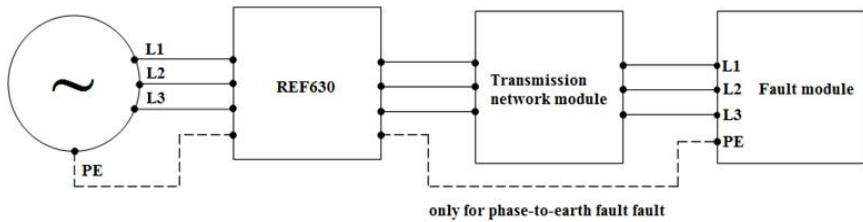
Simulated fault distance was set up with distribution network simulator. It's parameters with determine fault distance are shown in Table 2.

**Table 2.** Parameters of transmission network simulator

Parameter	Value	Unit
$R_1$	19.3	$\Omega$
$X_1$	13.5	$\Omega$
Fault distance	36.22	km

Fault module is used to simulate phase-to-phase fault and phase-to-earth fault. It is also possible to change fault resistance. Fault resistance was set up from 0  $\Omega$  to 115  $\Omega$  to see how it will affect calculation of fault distance.

First measured fault was phase-to-phase fault and the fault distance should be 36.22 km. The connection diagram is shown in Figure 3.



**Fig. 3.** Connection diagram for measuring of fault distance

Table 3. shows that changing fault resistance has influence on fault distance. Higher the fault resistance is the result is more likely to be inaccurate, because if the resistive part of fault loop impedance is much larger than the reactive part the accuracy deteriorates.

**Table 3.** Fault distance values for phase-to-phase fault

Parameters	Phase-to-phase fault							
	$R_f$ ( $\Omega$ )	0	15	35	55	75	95	115
Fault distance (km)	36.22	36.10	35.55	34.99	34.40	34.14	33.84	

Measuring of phase-to-earth fault has the same range of fault resistivity and fault distance should be the same as for phase-to-phase fault. However, values in Table 4. are completely different. It has the same pattern as the phase-to-phase fault that with increasing fault resistance the accuracy decreases, but the value of the fault distance at 0  $\Omega$  is 16.71 km, which is more than half of the simulated fault distance.

**Table 4.** Fault distance values for phase-to-earth fault

Parameters	Phase-to-earth fault						
$R_f (\Omega)$	0	15	35	55	75	95	115
Fault distance (km)	16.71	16.61	15.93	15.45	15.31	15.55	14.90

Because fault distance for phase-to-phase fault at  $0 \Omega$  was correct. The positive sequence impedance was kept the same, but zero sequence was changed. Zero sequence reactance was set up to the same value as the positive sequence reactance. The fault reactance XFLOOP will consist only of positive sequence impedance because calculation for earth return path reactance is  $X_N = X_0 - X_1$ . The fault resistance should have major influence on the fault distance, when the earth return path reactance is neglect. Results from another measuring of phase-to-earth fault are shown in Table 5.

**Table 5.** Second results for phase-to-earth fault

Parameters	Phase-to-earth fault						
$R_f (\Omega)$	0	15	35	55	75	95	115
Fault distance (km)	33.76	35.58	34.74	33.42	32.81	32.24	30.68

It is evident that the major effect on the fault distance has the zero sequence impedance for the phase-to-earth fault. The zero sequence reactance which was calculated according by the REF630 technical manual was main factor why the fault distance values were so inaccurate. After neglected the earth return path reactance, the fault distance value at  $0 \Omega$  of the fault resistance is very close to simulated distance. The fault resistance increase caused inaccuracy in calculation. The fault resistance also created bigger fault in calculation than for the phase-to-phase fault.

## 4 Conclusion

Fault localization is complicated task. Many factors can deteriorate the accuracy of the fault distance calculation. One of the most important factor is fault resistance. If the fault resistance is small, it is more likely that the calculated fault distance will be accurate. The accuracy depends on ratio of resistive and reactive part of the fault loop impedance. The fault resistance causes bigger inaccuracy in calculation of the fault distance for the phase-to-earth fault than for the phase-to-phase fault (see Table 6.). Big issue is also determination of zero sequence reactance, because wrong value will cause incorrect result (see Table 5).

**Table 6.** Comparison of fault distance results

Parameters	Phase-to-phase fault						
	$R_f (\Omega)$	0	15	35	55	75	95
Fault distance (km)	36.22	36.10	35.55	34.99	34.40	34.14	33.84
	Phase-to-earth fault						
Fault distance (km)	33.76	35.58	34.74	33.42	32.81	32.24	30.68

## 5 Acknowledgment

This research was partially supported by the SGS grant from VSB - Technical University of Ostrava (No. SP2019/20) and by the project TUCENET (No. LO1404).

## 6 References

1. Ito, H. Switching Equipment, Springer 2019
2. Krieg, T., Finn, J. Substations, Springer 2019
3. IEC 60909-0, Short-circuit currents in three-phase a.c. systems - Calculation of currents
4. ABB s.r.o.: Technical Manual 630 series. ABB s.r.o. 2012. ID: 1MRS756508
5. Novosel, Damir, Hart, David G., Saha, Murari Mohan, Gress, Solweig Optimal fault location for transmission systems (1994) ABB Review, (8), pp. 20-27.
6. Das, R., Sachdev, M.S., Sidhu, T.S. A fault locator for radial subtransmission and distribution lines (2000) Proceedings of the IEEE Power Engineering Society Transmission and Distribution.
7. Johns, A.T., Jamali, S. Accurate fault location technique for power transmission lines (1990) IEE Proceedings C: Generation Transmission and Distribution, 137 (6), pp. 395-402.
8. M. Kotulla, R. Goño, M. Vrzala, "Measuring of fault distance using the fault locator function of protection relay", 2019, 20th International Scientific Conference on Electric Power Engineering, EPE 2019

## 7 Publications

M. Kotulla, R. Goño, M. Vrzala, "Measuring of fault distance using the fault locator function of protection relay", 2019, 20th International Scientific Conference on Electric Power Engineering, EPE 2019

# Current Transformer – Protection Relay Protection Circuit Error Investigation

David Lazecký

Department of Electrical Power Engineering, FEECS,  
VŠB – Technical University of Ostrava, 17. listopadu 15,  
708 33 Ostrava – Poruba, Czech Republic  
david.lazecky.st@vsb.cz

**Abstract.** The paper describes current results of student's research in the field of current transformers (CTs) and protection relays. All measured devices are described, and the results are presented and discussed in the paper. The results will be the subject of further research.

**Keywords:** Current transformer, electrical networks, error evaluation, protection core, protection relay

## 1 Introduction

Instrument transformers are essential parts of many metering, control and protection systems. The instrument transformer quality directly affects the accuracy and performance of these systems since they can be as accurate as the provided network information. Two basic functions are provided by the transformers: change of magnitude (but not the nature) of primary to secondary values; and insulation between primary and secondary circuit. The majority of currently used instrument transformers is still based on magnetic core design, although newly designed instrument sensors are available on the market. [1, 2, 3]

The requirements for instrument transformers are specified in (national) technical standards. The predecessor for currently valid standard is IEC 60044. For current transformers, IEC 60185 (and IEC 185) are even older. Currently valid standard family is IEC 61869. [8]

Protection relay overcurrent protection function is the second part of the protection circuit. Tripping algorithm for overcurrent and fault current values is based on an old mechanical design, but the recording and representation of measured values are dependent on the manufacturer of a relay. [8]

## 2 Current Transformer

Current transformer (CT) is a device used for continuous interpretation of primary-side current in values that metering devices connected to secondary-side of the CT



can handle. It is designed to be connected in the primary circuit; the most common connection is in series. Typical values of secondary-side currents are 1 A and 5 A (nominal value), while the primary current is a subject of design need. In power electrical CTs, there are two types of cores, one for measurement and the other for protection. The protection core requirements are described below in accordance with technical standards specifications. As in any real device, there are factors affecting CT performance and output values. In case of CTs (and proper installation), they are connected with an iron core, precisely its design. [1, 2, 3, 8]

## 2.1 Protection Core Specification

For protection purposes, the CT core has to be designed to operate under various network disturbances (over currents and fault currents). The values of normal operation are not so important. Therefore only ratio error and phase displacement at rated primary current are specified, and composite error at rated accuracy limit of the primary current is introduced. The performance above the accuracy limit is not guaranteed. The accuracy classes and error values are depicted in the following table.

**Table 1.** Accuracy requirements for CT protection core [5]

Accur. class	Current error ( $\pm\%$ ) at $I_n$	Angle error ( $\pm$ minutes) at $I_n$	Total error ( $\pm\%$ ) at accuracy limit
5P	1	60	5
10P	3	-	10

## 2.2 Tested Current Transformers

The current transformers for the measurement were obtained from one of the Czech electrical distribution companies. According to the provided information, the measured CTs were installed and run under common operating conditions in the past.

All CTs are oil-insulated type for outdoor usage with three cores, one measurement core and two protection cores. Both CTs are designed for up to 123 kV voltage level. The table below specifies the unit values most important for the measurement. The rest of the CTs' specification is not listed due to its insignificance. Both CTs were configured for 600 A primary current.

**Table 2.** Measured CTs significant values [8]

Mfg.	Model	Mfg. year	$I_{PRI}$ (A)	Measured core		
				$I_{SEC}$ (A)	Accur. Class	Load (VA)
ABB	IMB 123	1997	150-300- <u>600</u>	1	5P10	30
PFIFNER	JOF 123	1994	150-300- <u>600</u>	1	5P10	30

### 3 Protection Relay

Protection relay is a device used in electrical systems for controlling a certain part of a system, and based on input values, it generates a signal to affect the protected object. A protection relay acquires signals from instrument transformers and has to take action and prevent damage in the occurrence of a failure.

One of the important functions of protection relays is overcurrent protection. State-of-art digital relays are equipped with fault recorder that provides information for a fault investigation (when set properly).

#### 3.1 Tested relays

All measured relays were adapted for the Russian market, but no difference was found for the measured functions in the provided documentation. The relays are products of well-known manufacturers, and they are available also for the European market.

**Table 3.** Tested protection relays

<b>Mfg.</b>	<b>Model line</b>	<b>Model</b>	<b>Full model No</b>
Merlin Gerin	Sepam	S40	MDS-40R
Siemens	SIPROTEC	7SJ62	7SJ6215-6EB22-3FG1/FF
Alstom	MiCOM	P14DZ	P14DZ26A7C6500A
		P543	P54391KA7M5750M

## 4 Results

The measurement of CTs was realized in the Centre for Research and Utilization of Renewable Energy (CVVOZEPowerLab), Brno University of Technology, Czech Republic via an open access policy. In addition, the cooperation and technical support from the owner of the CTs were provided too.

The tested relays and testing equipment were provided by Tomsk Polytechnic University, Russia, where the measurement was realized.

#### 4.1 Current Transformers

Measured values were gathered using LabView software and saved in a proprietary format as files with \*.lvm extension. The time sampling rate is 0.02 ms for all measurements. For values used as a source signal for protection relays, the source switch-on time is 100 ms.

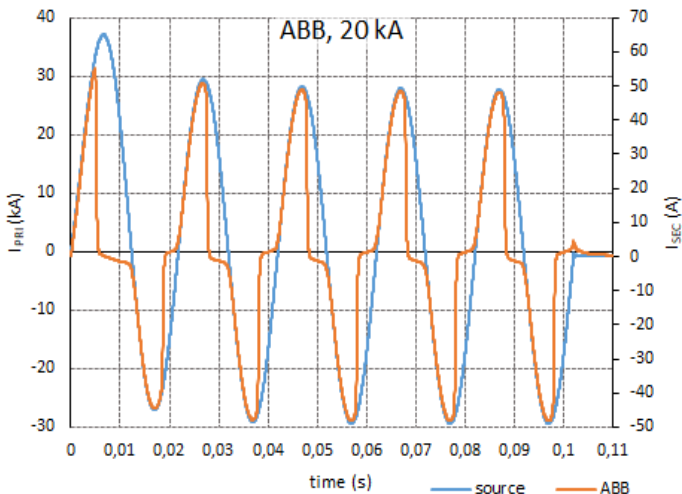


Fig. 1. The highest recorded currents, ABB CT

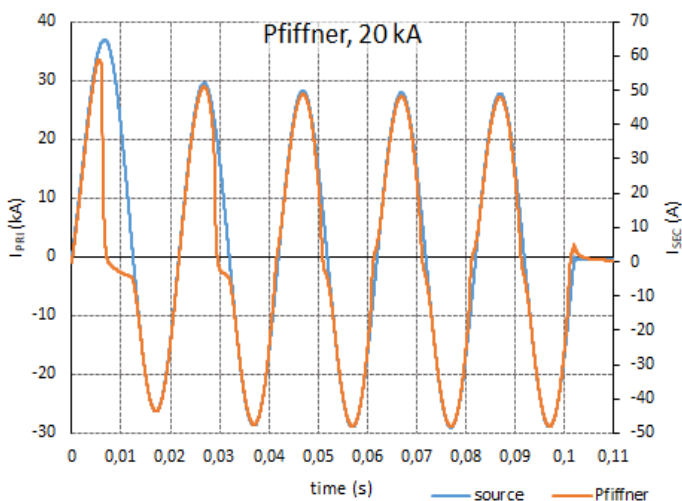


Fig. 2. The highest recorded currents, Pfiffner CT

The highest recorded currents figures show the saturation limits for both CTs. From the lower figure, it could be seen that the Pfiffner CT has a higher limit than the ABB CT.

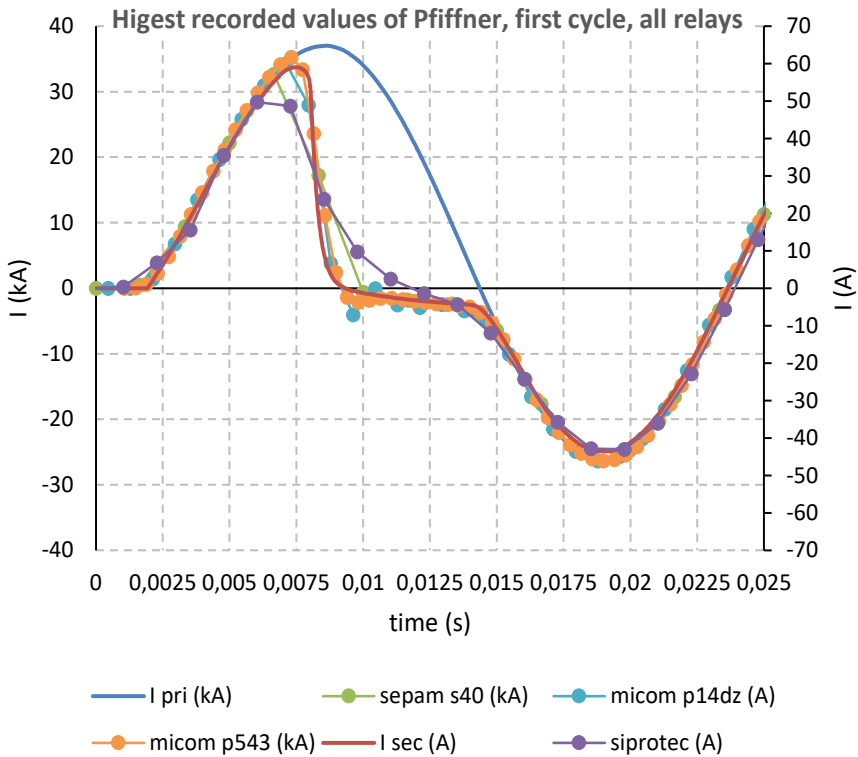
#### 4.2 Protection Relays

All relays were tested using the same source signal device (Retom-51). All output datasets were transferred to table processor SW (Excel 2013). All matching curves were adjusted to the beginning of the first cycle and displayed. The following table displays the signals' specifications.

**Table 4.** Measured signals' specification

Relay	Samples per cycle	No. of samples	Total record length
	(-)	(-)	(s)
Source signal	1000	15000	0,3
Sepam S40	12	3000	4,99833
Siprotec 7SJ62	16	982	1,22625
MiCOM P14DZ	25	1752	1,50709
MiCOM P543	48	3600	1,50098

The following plot depicts the highest recorded current values of the Pfiffner CT signal in detail for the first cycle, which is the most interesting one.



**Fig. 3.** The highest recorded fault-current values of the Pfiffner CT, first cycle detail, all relays

## 5 Conclusion

The result of the evaluation of two older current transformers obtained from one of the Czech distribution electrical grid operators are presented in [8], and they are used for further work with protection relays and their fault recording function.

The protection relays part shows, depending on the relay, slightly biased records of the measured fault-current wave. As could be seen from the last plot, even only twelve samples per cycle are enough for representation of the original current although some fast transient events might not be recorded and therefore those might be missed. As discussed with colleagues whose research is more connected with protection relays, some problems might be also caused by an aliasing filters in relays which are not very well described in the relays' manuals (if the connection diagram is presented) – Siprotec values are a quite clear example.

In general, all recordings are usable for the original fault-current estimation and reconstruction by using only simple mathematical methods even though only some manufacturers provide sufficient information describing the internal connection of protection relay.

Further research should be continued.

### Acknowledgements.

This research was partially supported by the SGS grant from VSB - Technical University of Ostrava (No. SP2019/20) and by the project TUCENET (No. LO1404).

Part of this research work has been carried out with the support of CVVOZEPowerLab Research Infrastructure (project No. LM2015092).

Part of this research work has been carried out in laboratories of Tomsk Polytechnic University, Russia.

### References

1. Gill, P. *Electrical Power Equipment Maintenance and Testing*, 2nd ed. Boca Raton: CRC Press, 2009.
2. Elmore, W. *Protective Relaying Theory and Applications*, 2nd ed. New York: Marcel Dekker, 2004.
3. Bayliss, C., Hardy, B. *Transmission and Distribution Electrical Engineering*, 4th ed. Oxford: Elsevier, 2012.
4. *IEC 60044: Instrument Transformers* (family of standards)
5. *IEC 61869-2: Instrument transformers - Part 2: Additional requirements for current transformers*
6. Mathews, P. *Protective Current Transformers and Circuits*. London: Chapman & Hall, 1955.
7. Král, J., Vaněk, J. *Elektromagnetické přístroje*, Brno: VUT, 1984.
8. Lazecky, D., Kral, V., Rusek, S., Hytka, Z. Error Ratio Evaluation of Protection Core of Selected Older Distribution Current Transformers, *Proceedings of the 2019 20<sup>th</sup> International Scientific Conference on Electric Power Engineering, EPE 2019*, Kouty nad Desnou, Czech Republic.
9. Upper, D. *The unsuccessful self-treatment of a case of "writer's block"*. Journal of Applied Behavior Analysis, 1974, vol: 7, n: 3: 497.

## Publications

Lazecky, D., Kral, V., Rusek, S., Gono, R. Software solution design for application of reliability centered maintenance in preventive maintenance plan, *Proceedings of the 2017 18<sup>th</sup> International Scientific Conference on Electric Power Engineering, EPE 2017*, Kouty nad Desnou, Czech Republic. ISBN: 978-150906405-2, DOI: 10.1109/EPE.2017.7967354

Lazecky, D. Analysis of the Failure Rate of MV Circuit Breakers, *Proceedings of the 15<sup>th</sup> Annual Workshop WOFEX 2017*, Ostrava, Czech Republic. FEECS, VŠB - Technical University of Ostrava ISBN: 978-80-248-4056-7

Lazecky, D. Comparison of Maintenance Strategies among Selected Electrical Companies, *Proceedings of the 14<sup>th</sup> Workshop ELNET 2017*, Ostrava, Czech Republic. FEECS, VŠB -Technical University of Ostrava ISBN: 978-80-248-4154-0

Lazecky, D. Possibilities of Optimizing Maintenance Strategies Applicable on Electrical Network in the Czech Republic, *Proceedings of the 16<sup>th</sup> Annual Workshop WOFEX 2018*, Ostrava, Czech Republic. FEECS, VŠB -Technical University of Ostrava ISBN: 978-80-248-4206-6

Lazecky, D., Kral, V., Rusek, S., Hytka, Z. Error Ratio Evaluation of Protection Core of Selected Older Distribution Current Transformers, *Proceedings of the 2019 20<sup>th</sup> International Scientific Conference on Electric Power Engineering, EPE 2019*, Kouty nad Desnou, Czech Republic. ISBN: 978-1-7281-1333-3

# Energy Harvesting as an Energy Supply for Road Signalling

Michal Petružela

Department of Electrical Power Engineering, FEECS,  
VŠB – Technical University of Ostrava, 17. listopadu 15,  
708 33 Ostrava – Poruba, Czech Republic  
michal.petruzela@vsb.cz

**Abstract.** This paper deals with harvesting energy of airflow created by vehicle passing by crash barrier and use of this energy for light signalization. Two-way fluid-structure interaction in ANSYS was used to analyse airflow and to design shape of a wind flap harnessing this airflow. Wind flap is mechanical extension of piezoelectric element (piezoelement). According to the analysis results the best shape of wind flap was selected. Few of best shapes were experimentally tested to verify analyses. Next step was design of electronics that accumulates enough of electric energy to power light signalling device (in our case LED) for a short time.

**Keywords:** Energy harvesting, two-way FSI, airflow, piezoelectric element

## 1 Introduction

Road traffic safety was always important and nowadays with increasing traffic density it is increasing concern to the authorities and road users. It is endless effort to decrease amount of traffic accidents or at least its severity.

According to statistics, the accident ratio in the Czech Republic is decreasing [0]. Nevertheless, there are still many of car accidents, especially on the roads with limited sight distance. This paper presents possible solution for the road safety on such road sections. At the moment our solution is applicable only to the sections with crash barriers.

Idea is based on energy harvesting as an energy source for system [2],[3]. There are many energy harvesting methods – piezoelectric, electromagnetic, thermoelectric etc. Piezoelectric method was selected because it is the one of the most common methods.

Airflow created by a car passing by crash barrier is pulse energy source that could be harvested and used for signalization to the road user on oncoming lane for example via LED. Shape of wind flap was designed in order to capture as much energy as possible from the wind gust.

Airflow moves wind flap located in the groove (channel) of the guard rail. One side of the piezoelement is attached to the wind flap, other side of the piezoelement is attached to the mount on the guard rail. So a motion of the wind flap causes deformation of the piezoelement and thus generation of electric energy [2].

Guard rail profile and results of airflow analysis in ANSYS determine shape of wind flap. Articles [4],[5] were inspiration to utilize ANSYS. Wind flap height is limited by profile of guard rail. Length is given by how much of wind flap is sticking out of guard rail. Wind flap thickness comes from the need for lightweight but stiff enough wind flap to minimize energy wasted on its deformation. Also there is need for faster swinging flap because piezoelement is more effective at higher frequencies [2],[3],[6]. Different shapes were analysed in ANSYS from simple straight plate over bend plates to the shape of cup. Generated energy of analysed shapes was compared.. And most suitable shape was selected for further use.

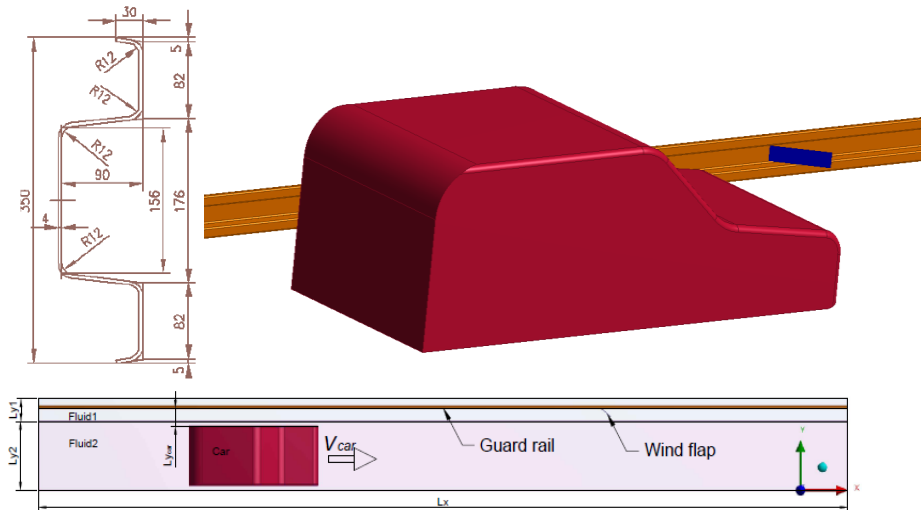
According theory there is direct relationship between a stress applied on the piezoelement and generated electric charge [2]. Electric charge generated by one compression of the piezoelement is around 0.5 mJ. It is a very small amount of energy and to light up even a low power LED (2 mA, 1.8 V) a few compressions is needed and luminous intensity of this LED is roughly 1.5 mcd. Such intensity is just enough for small light source, but not enough for signalization in an environment with higher light pollution. This leads to need to use higher luminous intensity LED at least around 1 cd, power of such LED is 270 mW at 1.8 V and 150 mA. Experimentally was found that if the stress is applied on piezoelement in a way that causes its bending instead of compression it generates more electric charge. To bend the piezoelement smaller amount of stress is required than for the compression. This fact comes handy for intended application, because there is a little amount of mechanical energy in an oscillations of wind flap.

Even if energy harnessed by wind flap is used for piezoelement bending, amount of generated electric energy is small [2],[6] and first have to be accumulated for example into capacitor before releasing it to the LED and for this purpose was electronic circuit created.

## 2 Analysis description

Fig. 1(a) shows profile of guard rail type NH4 which is commonly used in the Czech Republic. Fig. 1(b,c) shows top and isometric view of analysis setup. Isometric view shows moment in analysis when car is close to the wind flap for the sake of detail. Analysis itself is composed of two fluid domains one stationary is named Fluid1. Guard rail and wind flap are the located in Fluid1 domain. Other one named Fluid2 is moving and contains car. Both fluid domains have same length  $L_x = 26$  m and both are 1.7 m tall,  $L_{y1} = 0.7$  m is width of Fluid1 and  $L_{y2} = 2.1$  m is width of Fluid2. Dimension  $L_{y\text{car}} = 0.6$  m describes how far the car from the guard rail is. Bottom face of each fluid domain represent road and is set as a wall.





**Fig. 1.** (a) Guard rail profile, (b) 3D model in Ansys, (c) top view of analysis

Common faces of both domains are set as interface. All remaining faces of both domains are set as opening with relative pressure 0 Pa, to allow air freely flow in and out through this faces. Both fluid domains are set as the air at 25°C. Guard rail surface is defined as a wall inside Fluid1. Two-way fluid-structure interaction was utilised, so transient structural analysis required to define materials of solid bodies. Material of car is steel, wind flap and piezoelement are from custom materials. Wind flap's material had properties that roughly represents 3D print. Length of piezoelement is 40 mm. Car movement is also defined here and it's speed is set to 10 m/s along the x-axis. Selected speed comes from proposed use of this device for example close to the 90 degree curves where we can expect that the speed of car is around the set value. Last but not least, all faces of car and wind flap are set as fluid solid interface. This interface is necessary for data exchange between solver of transient structural and CFX.

### 3 Analysis results

Three different shapes (straight plate, bent plate, cup) of wind flap were analysed. To get comparable results it was decided that the angle between straight plate and guard rail is fixed at 50° even if the generated torque was greater as angle was closer to the 90°. Reason for this decision was simple, to limit how big part of wind flap is sticking out to the road. Same reason is a limit 135 mm of the distance between the two endpoints of wind flap. Also height of all shapes is limited to 120 mm because of guard rail's profile. Straight plate is used as initial shape with which are other shapes compared. It has only one dimension that was changed and it is length. For bent plate it is bend angle, radius and angle between plate and guard rail. Bent plate dimensions

are set the way so the end of bent plate is at the same location as is the end of straight plate.

Torque, force and movement of flap assembly and piezoelement were analysed and used to calculate energy. Fig. 2 shows total energy generated over time, moment when car reached wind flap is marked by yellow dashed line. Equation for energy of torque is:

$$E = \int_{\varphi_1}^{\varphi_2} T \cdot d\varphi \quad (1)$$

Where  $E$  is energy in J,  $T$  is torque in Nm and  $\varphi_1$  and  $\varphi_2$  angular are angular positions of body in radians. To calculate generated energy we used following equation:

$$E = \sum_{t=1} T_t \cdot (\varphi_t - \varphi_{t-1}) \quad (2)$$

Where  $t$  is time step,  $\varphi_t$  and  $\varphi_{t-1}$  are angular positions of assembly in radians while affected by torque  $T$  in Nm.

Results in Table 1 and Fig. 2 show that the most energy is generated by bent plate shaped wind flap. There are few explanations why wind flap in shape of a cup didn't generate the most energy. Mass of the cup shaped wind flap is greater than other flaps and our case is discontinuous airflow where steady state isn't reached and start-up of heavier flap is slower. Also shape of cup is more dependent on direction of incoming wind.

Fig. 3 shows wind velocity distribution along the guard rail and car. Wind velocity in and near groove of guard rail is very low – mostly under 1.25 m/s and highest wind speed is under guard rail. Wind speed under rail ranges from 3.75 to speed over 5 m/s. Equation (3) for energy of wind [7]:

$$E = \frac{1}{2} \cdot m \cdot v^2 = \frac{1}{2} \cdot (A \cdot v \cdot t \cdot \rho) \cdot v^2 = \frac{1}{2} \cdot A \cdot \rho \cdot t \cdot v^3 \quad (3)$$

Where  $\rho$  is air density in kg/m<sup>3</sup> and  $A \cdot v \cdot t$  is volume of wind passing through area  $A$  perpendicular to the flow in m<sup>3</sup>. Then  $A \cdot v \cdot t \cdot \rho$  is mass  $m$  of wind. Therefore the energy in wind is proportional to the cube of wind speed. All this tells us that placing the wind flap under the guard rail would lead to approximately tenfold increase of energy generation. But placing wind flap under guard rail have a few cons, increased risk of wind flap damage and more difficult mounting.

TABLE I. CALCULATED ENERGY OF ANALYSED WIND FLAPS

	Total energy (J)	Difference from straight (%)
Straight	4.12e-4	-
Bent	4.56e-4	10.8
Cup	3.14e-4	-23.7

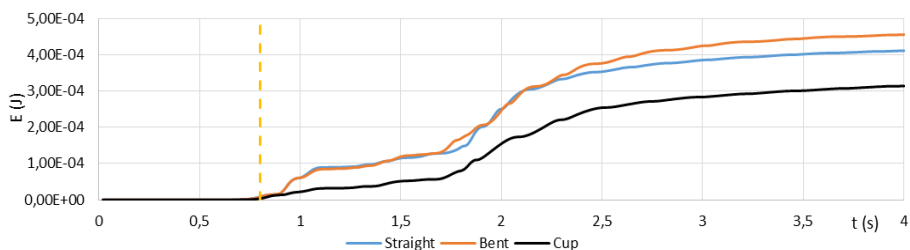


Fig. 2. Energy generated over time

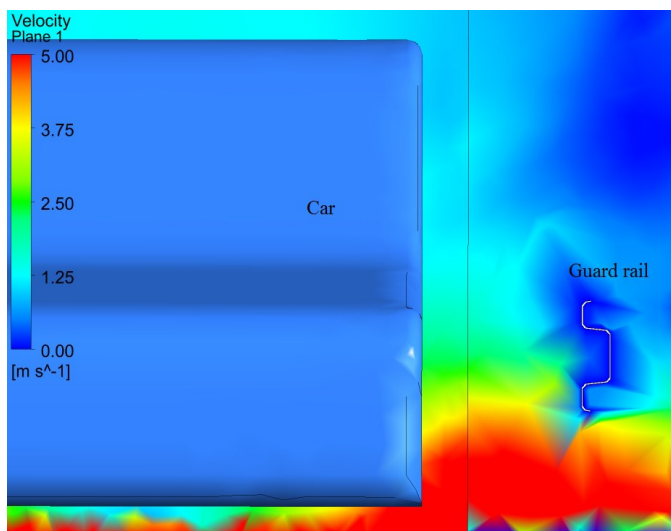


Fig. 3. Front view – wind velocity along car and guard rail

## 4 Design of electronics

Piezoelement is able to generate voltage up to hundreds of volts, but it has relatively high internal resistance which was  $130\text{ k}\Omega$  in our case. With this value of internal resistance even the small current caused high voltage drop. So it is better to use LEDs with higher operating voltage and connect them in parallel. It wasn't possible to connect LED directly because piezoelement generated about  $26\text{ V}$  which gives short circuit current  $0.2\text{ mA}$ . This current isn't enough to power low power LED. This led to need of electronic circuit that accumulates and releases energy to LED.

Realized electronic circuit is depicted in Fig. 4 was built on FET operational amplifier LTC1540 with very low standby power consumption. Quiescent current of LTC1540 is only  $0.3\text{ }\mu\text{A}$  [8]. Other components of circuit are two electrolytic capacitors, full wave rectifier (to increase efficiency of charging because voltage generated by piezoelement is AC) and transistor (as a switch). Energy is accumulated into capaci-

tors C1 and C2 until voltage reaches threshold set by voltage divider R2 and R3, then transistor Q1 switches and releases energy into terminal X2 where is LED connected.

Real condition testing showed that even use of the very low power consumption LTC1540 is not enough to allow capacitor to reach sufficient charge. Due to voltage growth, the more is capacitor charged the less efficient charging is. Also problem is self-discharge (due to internal resistance) of the capacitor in tens of seconds.

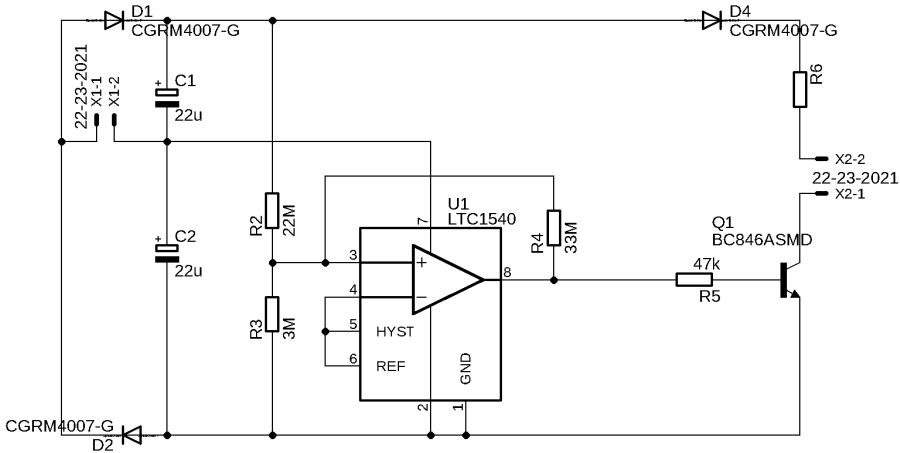


Fig. 4. Electric scheme of designed circuit

## 5 Conclusion

Different shapes of wind flap were analysed, total energy generated over time period 4 seconds was calculated and compared in Table 1. Most energy generated was by bent plate in  $60^\circ$  with radius 100 mm, forming  $32^\circ$  with guard rail. Poor result of the cup shaped wind flap is explained by its wind flow direction dependency.

Electronic circuit was designed to accumulate energy generated by piezoelement, because energy of parameters 26 V and 0.2 mA isn't enough to power even the low power LED. This relatively simple circuit based on operational amplifier LTC1540 uses electrolytic capacitors for energy accumulation. Later was found that even with circuit it wasn't operating sufficiently due to very low efficiency of piezoelement. Piezoelement's efficiency is units of % in an ideal conditions (frequency of oscillations), in our case it isn't met. And due to capacitor self-discharge. Means to overcome these disadvantages will be researched in future. For example replace wind flap and piezoelement by different widely used energy harvesting method which is electromagnetic.

**Acknowledgements.** This paper was supported by the following projects: LO1404: Sustainable development of ENET Centre; SP2019/159 and SP2019/28 Students Grant Competition and TACR TH02020191 and TACR TH777911, Czech Republic

and the Project LTI17023 "Energy Research and Development Information Centre of the Czech Republic" funded by Ministry of Education, Youth and Sports of the Czech Republic, program INTER-EXCELLENCE, subprogram INTER-INFORM and project TN777901 National Centre of Energy.

## References

1. Kuzel, T., Zly, J.: Dopravní nehodovost na území moravskoslezského kraje za rok 2018 [online]. In: 2019 [cit. 2019-03-01]. Online: <https://www.policie.cz/clanek/dopravni-nehodovost-v-roce-2018.aspx>
2. Wei, C., Jing, X.: A comprehensive review on vibration energy harvesting: Modelling and realization, *Renew. Sustain. Energy Rev.*, vol. 74, no. December 2016, pp. 1–18, 2017.
3. Khaligh, A., Zeng, P., Zheng, C.: Kinetic Energy Harvesting Using Piezoelectric and Electromagnetic Technologies - State of the Art, *IEEE Trans. Ind. Electron.*, vol. 57, no. 3, pp. 850-860, March 2010.
4. Kacor, P., Misak, S., Prokop L.: Modification of construction design of vertical axis wind turbine, *Annals of DAAAM & Proceedings of the 22nd International DAAAM Symposium*, vol. 22, no. 1, pp. 723-724, Vienna, Austria, 2011.
5. Kacor, P., Misak, S., Prokop L.: "Optimization and redesign of vertical axis wind turbine for generator of independent source of energy," *Annals of DAAAM for 2010 & Proceedings of the 21st International DAAAM Symposium*, vol. 21, no. 1, pp. 1053-1054, Vienna, Austria, 2010.
6. Rubes, O., Hadas, Z.: Design and Simulation of Bistable Piezoceramic Cantilever for Energy Harvesting from Slow Swinging Movement, 2018 IEEE 18th International Power Electronics and Motion Control Conference (PEMC), pp. 663-668, Budapest, August 2018 doi: 10.1109/EPEPMC.2018.8521846
7. Grogg, K.: *Harvesting the Wind: The physics of Wind Turbines*, Digital Commons@Carleton College, Northfield, 2005.
8. Analog devices, Nanopower Comparator with Reference, LTC1540 data sheet, 1997 (Revised 2017)

## Publications

Petruzela, M., Blazek, V., Vysocky, J., Prokop, L., Seidl, D.: Energy Harvesting from Discontinuous Flow, 2019 20<sup>th</sup> International Scientific Conference on Electric Power Engineering (EPE), Kouty nad Desnou, Czech Republic, DOI: 10.1109/EPE.2019.8777989

Blažek, V., Petruzela, M., Vysocky, J., Prokop, L., Misak, S., Seidl, D.: Off-Grid System for Warning or Signalling Lighting of Dangerous Sections of Roads, 2019 20<sup>th</sup> International Scientific Conference on Electric Power Engineering (EPE), Kouty nad Desnou, Czech Republic, DOI: 10.1109/EPE.2019.8778091

Vysocky, J., Blažek, V., Petruzela, M., Misak, S., Prokop, L.: New User-Friendly Software Application to Simulate and Visualize The Distribution System Operation, 2019 20<sup>th</sup> International Scientific Conference on Electric Power Engineering (EPE), Kouty nad Desnou, Czech Republic, DOI: 10.1109/EPE.2019.8778180

Petruzela, M., Blazek, V., Vysocky, J. Analysis of appliance impact on total harmonic distortion in off-grid system, (2020) 2019 5<sup>th</sup> International Conference on Advanced Engineering Theory and Applications (AETA), vol. 554, pp. 844-849, Ostrava, Czech Republic, DOI: 10.1007/978-3-030-14907-9\_81.

# An Estimation of the Appliance Start-up Impact on the THDV and Pst Values in Off-grid Environment

Jan Vysocký and Stanislav Mišák

Department of Electrical Power Engineering, FEECS,  
VŠB – Technical University of Ostrava, 17. listopadu 15,  
708 33 Ostrava – Poruba, Czech Republic  
jan.vysocky@vsb.cz

**Abstract.** Powering various houses or factories with off-grid electrical systems is now possible thanks to modern electrical systems, and many people and companies want to use this option in their buildings. Thanks to control systems using algorithms based on a variety of intelligent data analysis methods, real-time optimization, and predictive models, the off-grid electrical systems can deliver electrical power continuously and with high quality. These modern control systems make the process of producing and consuming electrical power more efficient. These systems thus help reduce greenhouse and harmful gas emissions and improve the quality of the environment. For the correct design of the control algorithm, we need to know the influence of individual devices connected to the off-grid system on this system, as well as the operation patterns of individual devices. This paper presents an analysis of the various appliances impact on the off-grid electrical system; in particular, this paper presents how different electrical appliances affect the value of the total harmonic distortion of voltage, and the short-term flicker perceptibility during their start-up in the off-grid electrical system. The results of this analysis were used to improve the control capabilities of the algorithm used to control the off-grid electrical system located at VSB – Technical University of Ostrava.

**Keywords:** Off-grid electrical system, Total harmonic distortion, Short-term flicker perceptibility, Power quality

## 1 Introduction

Various off-grid electrical systems are developed by various research teams and commercial companies, and one off-grid electrical systems is long-term developed by our research team at VSB – Technical University of Ostrava. Our goal is to create an off-grid system which would be a fully autonomous energy platform and which all the electrical energy supplied to connected appliances would be obtained through renewable energy sources (RES).

Our off-grid electrical system is powered by two photovoltaic power plants and one wind power plant. The local wind power and local solar irradiation changes over time, so the power output of our power plants varies over time. Fluctuating power

supply to the off-grid system leads to fluctuations in the power sources' short-circuit power. In the off-grid system, the short-circuit power drop results in deterioration of the values of electrical power quality (PQ) parameters [1], [2].

The aim of our recent measurements and analyzes is to determine which appliances significantly affect the values of the total harmonic distortion of voltage (THDV) and the short-term flicker perceptibility (Pst) in the off-grid system. This knowledge is important for us because it would help us to take procurations to prevent PQ parameter values from deteriorating when the appliances are connected. Many appliances require high values of PQ parameters and the occurrence of bad PQ could lead to poor operation of these PQ-high-sensitive appliances. This concept was proposed and designed in a study by Misak [3]. This concept was described as Active Demand Side Management (ADSM). ADSM includes a power quality forecasting module designed by Vantuch et al. [4].

## 2 Experiment Description

In the experiment, we used ten various usual appliances (see Table 1) to create 120 combinations of three. In any part of the measurement, there were three appliances turned on because only one running appliance is uncommon in a house. Every combination was switched on at a defined time. We focused on processes that take place during the start-up of individual appliances. Appliances were supplied by off-grid system battery energy storage (BES) without connection to the external grid and RESs. During the first minute after the appliances started, we measured the values of THDV and Pst. When the one measuring interval had ended, BES was charged from

**Table 1.** Operation parameters of the appliances used during experiment (PF = Power factor, avg = average, C = Continuous, S = Switch, N = Neither continuous nor switch)

Appliance	Load (W)			PF	Characteristic	Power supply (C / S)
	avg	min	max	avg		
Mower	538	532	549	0,52	Inductive	C
Drill	157	150	167	0,49	Inductive	C
Kettle	619	617	628	1,00	Resistive	C + S
Fridge	208	196	220	0,72	Inductive	C
Switched mode	410	410	420	0,78	Capacitive	C + S
Microwave	203	77	1348	0,84	Inductive	N
AC heating	880	853	910	0,91	Inductive	C
Boiler	307	306	347	0,99	Resistive	C
TV	44	43	51	0,60	Capacitive	C + S
Lights	156	153	165	0,84	Capacitive	C + S

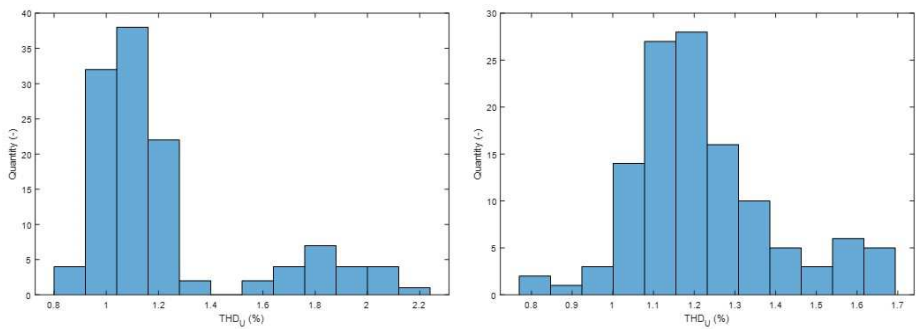


the external grid. THDV and Pst values were measured by the power analyzer KMB SMC 144. We measured all appliance combinations with two different state of charge (SoC) of BES: fully and half charged. The BES consist of 40 NiCd batteries KPL 375 FERAK (individual batteries are connected in series). The capacity of each battery is 375 Ah and its nominal voltage is 1.2 V. Off-grid AC part is powered by the hybrid inverter Conext XW + 8545. Its nominal power is 6.8 kW.

### 3 Results of Experiment

#### 3.1 Total Harmonic Distortion of Voltage

Fig. 1 show THDV values of each appliance combination measured during appliance start-up with the half (left chart) and fully (right chart) charged batteries.



**Fig. 1.** Histogram of measured THDV values distribution

Fig. 2 and Fig. 3 show the data series of THDV values for individual appliances for SoC 100% and 50%. These data series were created by assigning individual measured THDV values to the three appliances which were part of the individual combinations started at individual measured intervals. Each appliance was started-up in 36 intervals of total 120 intervals of the entire measurement, so the data series of each appliance contains 36 values.

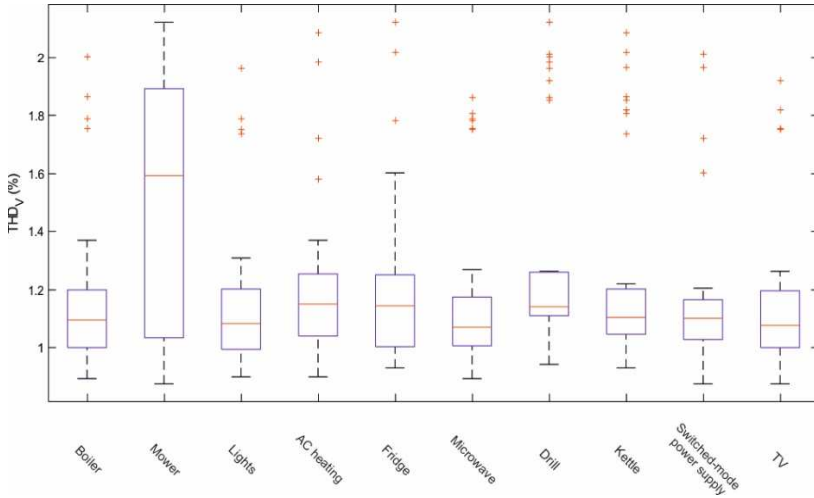


Fig. 2. Box plot for all used appliances – impact of appliance operation on THDV, SoC 100%

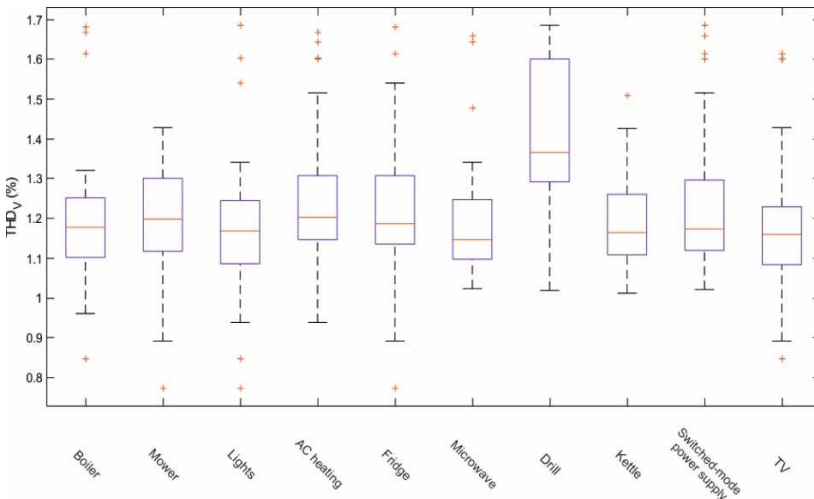
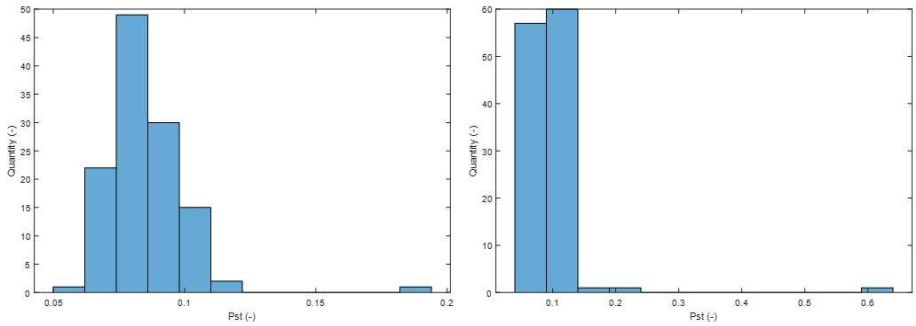


Fig. 3. Box plot for all used appliances – impact of appliance operation on THDV, SoC 50%

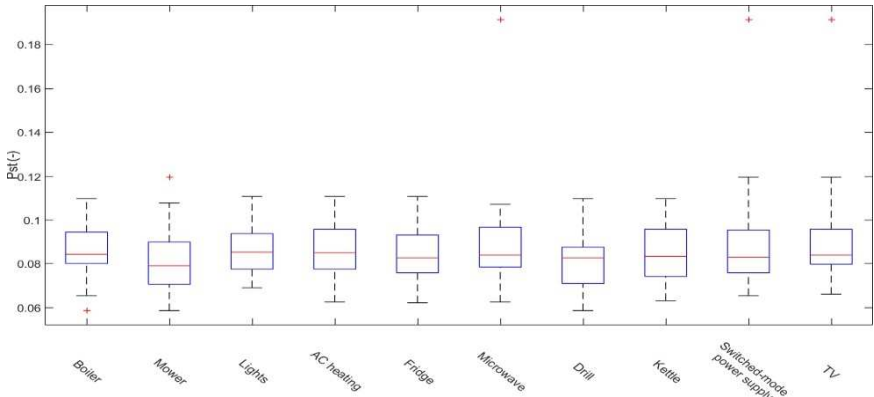
### 3.2 Short-term Flicker Perceptibility

Fig. 4 show Pst values of each appliance combination measured during appliance start-up with the half (left chart) and fully (right chart) charged batteries.

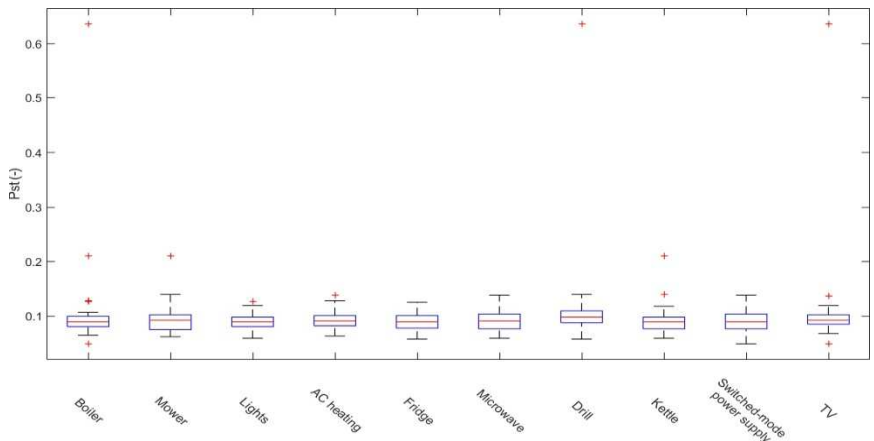


**Fig. 4.** Histogram of measured Pst values distribution

Fig. 5 and Fig. 6 show the data series of Pst values for individual appliances for SoC 100% and 50%. These data series were created analogously like the data series presented in Fig. 2 and Fig. 3.



**Fig. 5.** Box plot for all used appliances – impact of appliance operation on Pst, SoC 100%



**Fig. 6.** Box plot for all used appliances – impact of appliance operation on Pst, SoC 50%

## 4 Discussion and Conclusions

Our research team performed an experiment to investigate the effect of starting ten appliances on THDV and Pst values in an off-grid electrical system.

A statistical analysis of the data describing appliance start-up impact on THDV value for SoC 100% showed that the start-up of most combinations containing the mower caused a significantly higher THDV value than the start-up of combinations which did not contain the mower. Based on this finding, we conclude that when the SoC is 100%, the mower start-up causes an increase in THDV value. A statistical analysis of the data describing appliance start-up impact on THDV value for SoC 50% showed that the start-up of most combinations containing the drill caused a significantly higher THDV value than the start-up of combinations which did not contain the drill. Based on this finding, we conclude that when the SoC is 50%, the drill start-up causes an increase in THDV value. Comparing the THDV measurements for SoC 100% and SoC 50%, we find that the average impact of the average appliance on THDV value is the same for both SoCs.

A statistical analysis of the data describing appliance start-up impact on Pst value for both SoCs showed that the start-up of any appliance used in the experiment does not significantly affect the Pst value. Analysis of Pst data for SoC 100% measurement data showed that the highest average Pst value was measured for combinations which contained the TV. However, the difference between the average Pst values of the appliance causing the highest Pst value and the appliance causing the lowest Pst value was only 0.007, so, the differences in the measured Pst values are not statically significant. Analysis of Pst data for SoC 50% measurement data showed that the highest average Pst value was measured for combinations containing the drill. The average Pst value for combinations containing the drill was 0.113, and compared to the appliance with the second-highest average Pst value, the Pst for the drill was 0.005 higher, so we can say that the start-up of the drill causes a higher Pst value than the start-up of other appliances. Comparing the Pst data for SoC 100% and SoC 50%, we find that for the start-up of any appliance used in the measurement, the Pst values for SoC 50% are higher than the Pst values for SoC 100%.

The longer-time measurement within a shorter time-scale will be our future work. This measurement should give us more precise values for further processing.

## Acknowledgment

This paper was supported by the following projects: LO1404: Sustainable Fig. 2. Shapes of tested wind flaps development of ENET Centre; SP2019/159 and SP2019/28 Students Grant Competition and TACR TH02020191 and TACR TH777911, Czech Republic and the Project LTI17023 "Energy Research and Development Information Centre of the Czech Republic" funded by Ministry of Education, Youth and Sports of the Czech Republic, program INTER-EXCELLENCE, subprogram INTER-INFORM and project TN01000007 National Centre for Energy.

## References

1. Eckbert, D., Larsson-Edefors, P.: Interconnect-driven short-circuit power modeling. In: Digital Systems Design. Euromicro Symposium, pp. 414-421. IEEE (2001).
2. Saradarzadeh, M., Farhangi, S., Schanen, J.-L., Jeanin, P.-O., Frey, D., Combination of power flow controller and short-circuit limiter in distribution electrical network using a cascaded h-bridge distribution static synchronous series compensator. In: IET Generation, Transmission & Distribution, vol. 6, no. 11, pp. 1121-1131, IET Digital Library (2012)
3. Mišák, S., Stuchlý, J., Platoš, J., Krömer, P.: A heuristic approach to active demand side management in off-grid systems operated in a smart-grid environment. Energy and buildings, vol. 96, pp. 274-284 (2015).
4. Vantuch, T., Mišák, S., Ježowicz, T., Buriánek, T., Snašel, V., The power quality forecasting model for off-grid system supported by multiobjective optimization. In: IEEE Transactions on Industrial Electronics, vol. 64, no. 12, pp. 9507-9516 (2017).

## Our publications

Petruzela, M., Blazek, V., Vysocky, J., Prokop, L., Seidl, D.: Energy Harvesting from Discontinuous Flow, 2019 20<sup>th</sup> International Scientific Conference on Electric Power Engineering (EPE), Kouty nad Desnou, Czech Republic, DOI: 10.1109/EPE.2019.8777989

Blažek, V., Petruzela, M., Vysocky, J., Prokop, L., Misak, S., Seidl, D.: Off-Grid System for Warning or Signalling Lighting of Dangerous Sections of Roads, 2019 20<sup>th</sup> International Scientific Conference on Electric Power Engineering (EPE), Kouty nad Desnou, Czech Republic, DOI: 10.1109/EPE.2019.8778091

Vysocky, J., Blažek, V., Petruzela, M., Misak, S., Prokop, L.,: New User-Friendly Software Application to Simulate and Visualize The Distribution System Operation, 2019 20<sup>th</sup> International Scientific Conference on Electric Power Engineering (EPE), Kouty nad Desnou, Czech Republic, DOI: 10.1109/EPE.2019.8778180

Petruzela, M., Blazek, V., Vysocky, J. Analysis of appliance impact on total harmonic distortion in off-grid system, (2020) 2019 5<sup>th</sup> International Conference on Advanced Engineering Theory and Applications (AETA), vol. 554, pp. 844-849, Ostrava, Czech Republic, DOI: 10.1007/978-3-030-14907-9\_81.

# Implementation of Induction Motor Speed Estimator Using Feedforward Neural Network

Jakub Bača and Daniel Kouřil

Department of Electronics, FEECS,  
VŠB – Technical University of Ostrava, 17. listopadu 15,  
708 33 Ostrava – Poruba, Czech Republic  
{jakub.baca, daniel.kouril}@vsb.cz

**Abstract.** Sensorless control still ranks among the leading points of interest in the research field of electric drives. The objective is the elimination of a mechanical speed sensor, which results in a highly reliable, robust and low-cost electric drive. There have been many methods proposed to achieve this task that utilize different computational algorithms. One of the possibilities is the application of Artificial Neural Networks (ANN), which belong to the domain of soft computing. Here, we briefly present the laboratory implementation of a vector-controlled induction motor drive utilizing a purely neural speed estimator. The advantage of this approach is that we do not need to know the parameters of the induction motor. A data acquisition system was developed to enable the collection of training data and a feedforward neural network with a single hidden layer was trained to work as a speed estimator. Experimental results shown such an estimator is feasible.

**Keywords:** Induction motor, Sensorless control, Speed estimation, Neural network.

## 1 Introduction

Induction motor is the most common type of electric motor employed in industry due to its low maintenance requirements, reliability, simple construction and relatively low cost. This is especially true in the case of the squirrel-cage induction motor, as there are no brushes or slip rings which would wear out. For demanding electrically driven systems, where very high dynamic and the accuracy of regulated quantities are essential, the vector control or direct torque control is applied to control the speed of an induction motor.

The aim of vector control and direct torque control is to achieve AC drive characteristics comparable to DC drives. This means these methods are supposed to allow the independent control of the torque and excitation (magnetic flux) of electric machine [1, 2]. The required course of the actual speed is then achieved by controlling these two quantities.

There are two major problems concerning the speed estimation – measurement of quantities and system modeling. Most of sensorless algorithms benefit in some way

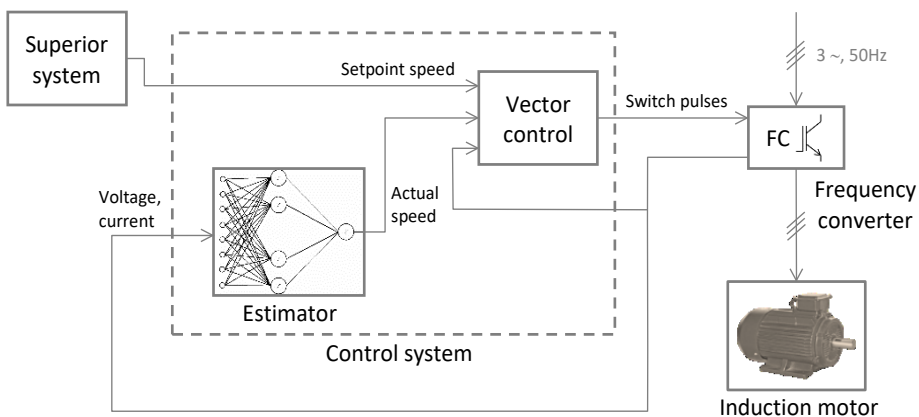
from the knowledge of the mathematical model of an electric motor [3]. The model comprises of equations, describing the relationship between input and output quantities, and parameters of these equations, whose values map the general model to a particular system. But even the best models or estimation algorithms known would be useless without accurate enough inputs, therefore, measuring as well as modeling is important. If a model is known, then the speed of an induction motor can be determined from measured stator voltages and currents.

In connection with induction motors, many papers presenting different applications of artificial neural networks have been published (e.g. [4, 5, 6, 7, 8]). The presented approach to speed estimation is based on a feedforward neural network that acts as a model of induction motor. The network is offline-trained, which means that a set of training patterns need to be available before it can be trained and applied to a particular drive and later the network is not being adapted during operation.

The network was trained and tested in Matlab using the Neural Network Toolbox. Then an implementation of the network was created that can be used within the vector control structure in our control system. It is a control system with the TMS320F28335 digital signal controller from Texas Instruments. The same control system was also used to collect training data. The implementation of the control algorithm was developed in the C language.

## 2 Control Structure

The conception of the implemented control structure is shown in **Fig. 1**. In the case of the experimental application, the superior system was an application created using the LabVIEW development environment that allows the user to operate the control system, and thus the whole electric drive. The key element of the structure is the vector control that ensures the actual speed follows the setpoint speed given by the superior system. The output from the vector control is six signals that determine switching of transistors in the frequency converter powering the induction motor with three-phase voltage.



**Fig. 1.** Simplified block diagram of the sensorless control structure

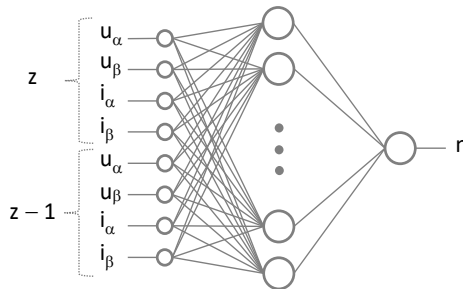
The last element, which is the scope of this paper, is the estimator that provides the actual (estimated) rotation speed of the induction motor. The estimation algorithm receives the actual stator voltage and current of the motor on its input and calculates the speed of the motor. More precisely, the input values are four – two voltages  $u_\alpha, u_\beta$  and two currents  $i_\alpha, i_\beta$ . The indexes  $\alpha$  and  $\beta$  refer to the stator (or stationary) reference frame. The current is obtained by transformation of phase currents  $i_a$  and  $i_b$  from the three-phase coordinates ABC. The voltage is not measured directly, it is estimated by making use of DC link voltage  $u_d$ . It follows that three quantities in total are necessary to be measured: DC link voltage and two phase currents.

### 3 Network Structure

There is no general way to design a neural network for a specific application. Most of the rules available are usually rules of thumb rather than theoretically derivable principles. Without any prior experiences with the application, the only way is the method of trial and error. Knowledge of the mathematical model is beneficial for the design.

The network structure presented in this paper was already being explored at our department in the past. In terms of network structure, we followed suit of the previous work to see if the new implementation would perform better with more accurate training data and higher sampling frequency.

The structure of the network can be seen in **Fig. 2**. It is a fully connected feedforward neural network with eight inputs, a single hidden layer and one output. The number of hidden neurons is twenty-two, therefore the network is marked as 8-22-1. The expressions  $z$  and  $z - 1$  denote that two consecutive sets of samples are passed to the network's input. The output is the estimated rotor speed of an induction motor.



**Fig. 2.** Network structure (8-22-1)

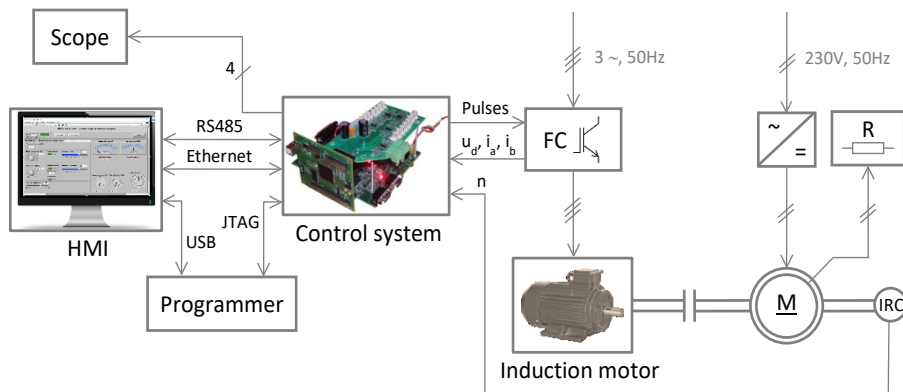
### 4 Experimental Results

The trained network which seemed to be the best was implemented in the control system. The used control system was developed at the Department of Electronics, at the Technical University of Ostrava and was designed for control applications in the field of electric drives and power electronics [9, 10]. The cornerstone of this control system



is the TMS320F28335 Digital Signal Controller (DSC) from Texas Instruments, which belongs to the C2000 family of microcontrollers. It is a floating-point controller that has been developed for use in embedded real-time systems, including electric drives.

Measurements were carried out at a laboratory workplace whose block diagram is in **Fig. 3**. The laboratory drive comprised of an induction motor, a loading mechanism (separately excited DC motor), an indirect frequency converter with DC link and the control system. Rated parameters of the induction motor are summarized in this listing: *Power 2.2 kW; Rotor speed 1425 min<sup>-1</sup>; Torque 14.7 Nm; Stator voltage 400Y/230Δ V; Stator current 4.8 A; Frequency 50 Hz*. The DC link voltage was set to  $U_{DC} = 200$  V.

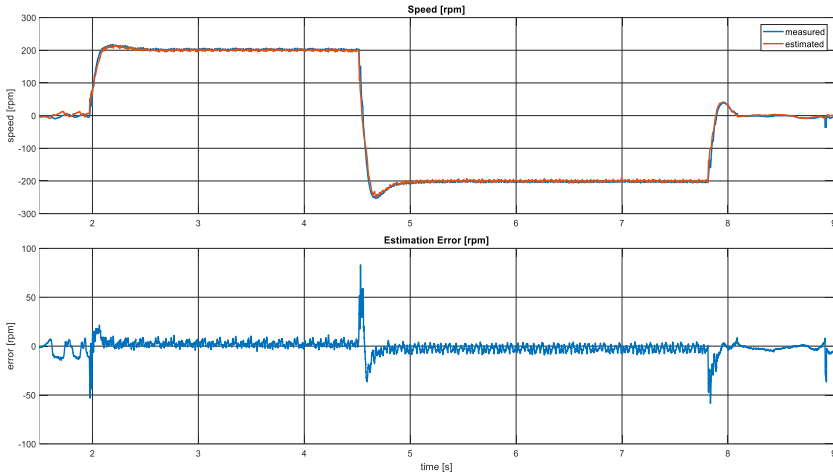


**Fig. 3.** Block diagram of the laboratory stand

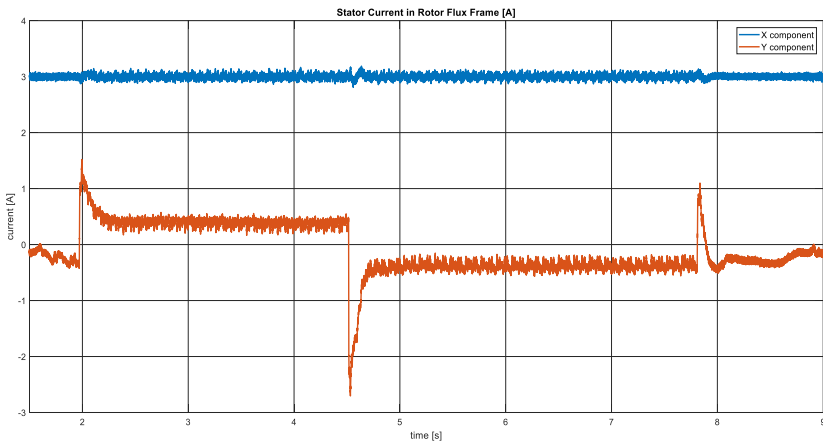
First, it was necessary to measure training patterns that comprised of stator voltage, current and actual speed. The measurement was being performed for 30 seconds for different speeds and loads, a collection of 600,000 patterns was gathered. The network was trained on a set of about 50 000 patterns that were selected randomly, the remaining patterns were used for testing and evaluating of the generalization. The training algorithm used was the Lavenberg-Marquardt backpropagation algorithm, the training was terminated in the 245<sup>th</sup> epoch and resulted in the mean squared error 0.722 rpm.

Graphs in **Fig. 4** and **Fig. 5** below display start-up, steady state, reversal and stop where the induction motor was not loaded and the speed command had a rectangular shape. The estimation error was obtained by subtracting the ANN-estimated speed from the speed measured by an incremental encoder. In steady states, if the zero speeds are omitted, the estimation error was within the range from  $-8$  to  $9$  rpm, given that we can say the steady state error was approx. 5 %. For transients, very high peaks can be observed in the course of the error, the peaks were the higher the higher steps of the speed command. Elimination of these peaks is probably the matter of training patterns selection and stator voltage estimation.

The real error is higher than the error reached through training. Moreover, speed fluctuations occur. At this point, it is important to note that the network operated in a closed loop during operation, which means the ANN output served as the input for the speed controller and rotor flux evaluation unit. The accuracy of the rotor flux calculation strongly influences the performance of vector control.



**Fig. 4.** Courses of measured and estimated speed –  $\pm 200$  rpm, no load



**Fig. 5.** Courses of stator current –  $\pm 200$  rpm, no load

## 5 Conclusion

A laboratory implementation of a sensorless induction motor drive utilizing ANN-based speed estimator has been developed. Improvements could be achieved by further experimenting with the network structure and selection of training patterns.

In the subsequent work, we attempt to prove that this type of estimator is capable of higher performance for different loads in both steady states and transients. Then we proceed with applications of neural networks as part of MRAS (Model Reference Adaptive System) speed observers.

## Acknowledgement

This paper was supported by the project No. IRP/2018/227 funded by the Ministry of Education, Youth and Sports and by the project No. SP2019/113 funded by the Student Grant Competition of VSB – Technical University of Ostrava.

## References

1. VAS, Peter. Artificial-intelligence-based electrical machines and drives: application of fuzzy, neural, fuzzy-neural, and genetic-algorithm-based techniques. New York: Oxford University Press, c1999. ISBN 019859397X.
2. LEONHARD, Werner. *Control of electrical drives*. 3rd ed. New York: Springer, c2001. ISBN 3-540-41820-2.
3. HOLTZ, J. Sensorless control of induction motor drives. *Proceedings of the IEEE*. 2002, **90**(8), 1359-1394. DOI: 10.1109/JPROC.2002.800726. ISSN 0018-9219.
4. WANG, Jinjiang, Peilun FU, Laibin ZHANG, Robert X. GAO a Rui ZHAO. Multi-level information fusion for induction motor fault diagnosis. *IEEE/ASME Transactions on Mechatronics*. , 1-1. DOI: 10.1109/TMECH.2019.2928967. ISSN 1083-4435.
5. YANG, Xuebo a Xiaolong ZHENG. Gradient Descent Algorithm-Based Adaptive NN Control Design for an Induction Motor. *IEEE Transactions on Systems, Man, and Cybernetics: Systems*. , 1-8. DOI: 10.1109/TSMC.2019.2894661. ISSN 2168-2216.
6. QUINTERO-MANRIQUEZ, Eduardo, Edgar N. SANCHEZ, Ronald G. HARLEY, Sufeí LI a Ramon A. FELIX. Neural Inverse Optimal Control Implementation for Induction Motors via Rapid Control Prototyping. *IEEE Transactions on Power Electronics*. 2019, **34**(6), 5981-5992. DOI: 10.1109/TPEL.2018.2870159. ISSN 0885-8993.
7. VENKADESAN, A., HIMAVATHI, S., MUTHURAMALINGAM, A. Novel SNC-NN-MRAS based speed estimator for sensor-less vector controlled IM drives. World Academy of Science, Engineering and Technology. 2011, 51, 1211-1216. Available from: <https://waset.org/publications/15677>
8. REDDY, Sama Vijay Bharath Simha, Bhavnesh KUMAR a D. SWAROOP. Investigations on Training Algorithms for Neural Networks Based Flux Estimator Used in Speed Estimation of Induction Motor. In: *2019 6th International Conference on Signal Processing and Integrated Networks (SPIN)*. IEEE, 2019, 2019, s. 1090-1094. DOI: 10.1109/SPIN.2019.8711623. ISBN 978-1-7281-1380-7.
9. HAVEL, Ales, Martin SOBEK a Petr CHAMRAD. Control methods of modern systems utilizing accumulation of electrical energy. In: *2017 18th International Scientific Conference on Electric Power Engineering (EPE)*. IEEE, 2017, 2017, s. 1-6. DOI: 10.1109/EPE.2017.7967338. ISBN 978-1-5090-6406-9.
10. HAVEL, Ales, Martin SOBEK a Petr PALACKY. The measuring and control center for accumulation systems of electrical energy. *Electrical Engineering*. 2017, **99**(4), 1295-1303. DOI: 10.1007/s00202-017-0619-y. ISSN 0948-7921.

# Online Stator Resistance Estimation By Using Particle Swarm Optimization Algorithm For Induction Motor Drives

Sang Dang Ho

Faculty of Electrical and Electronics Engineering,  
Ton Duc Thang University, Ho Chi Minh City, Vietnam,  
Faculty of Electrical Engineering and Computer Science,  
VŠB – Technical University of Ostrava, 17. listopadu 15,  
708 33 Ostrava – Poruba, Czech Republic  
hodangsang@tdtu.edu.vn

**Abstract.** This paper presents a new method of online estimation of induction motor stator resistance for the Rotor flux oriented control (RFOC) scheme by using the Particle Swarm Optimization (PSO) algorithm. The stator resistance determination is accomplished by capturing the error between the measured and estimated stator current and applying the PSO algorithm. The proposed method is implemented in Matlab/Simulink environment, as well as is compared with the conventional Proportional Integral (PI) estimator to show the effectiveness.

**Keywords:** induction motor, rotor flux oriented control, particle swarm optimization, proportional integral.

## 1 Introduction

Recently years, the most popular AC machines are IM due to their reliability, ruggedness, and relatively low cost. Besides that, the most common control scheme for high performances of IM is rotor flux oriented control (RFOC). Nevertheless, the RFOC depends on the correct information of the IM parameters, such as stator and rotor resistance, which vary with working conditions of the IM. The mismatch between the actual and estimated values will lead to unsatisfied operation condition and hence, to poor dynamic performance. Therefore, the determination of stator resistance is essential; as a consequence, numerous online schemes for stator resistance estimation have been proposed in the recent past [1]-[4]. One example of resistance estimation reported in [1], which applied the Model Reference Adaptive System (MRAS), and others used Artificial Intelligence techniques [2], [3], and [4] used the closed-loop stator flux estimator technique to tuning stator resistance.

In this study, online stator resistance estimation by using PSO algorithms is proposed. At first, the conventional PI-based mechanism (PI-M) for stator resistance estimation is presented [1], and the next section describes the method of stator resistance estimation using PSO algorithm mechanism (PSO-M). Finally, the suggested process is simulated in Matlab/Simulink environment to show the significant achievement compare with conventional PI-M.

## 2 PI-based mechanism stator resistance estimation

Fig.1 describes the structure of the PI-M for IM. In this scheme, two independent observers are used to estimate the rotor flux of IM: voltage-model and current-model.

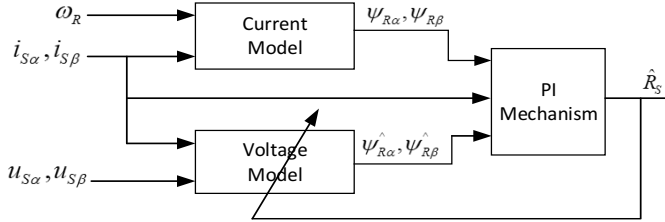


Fig. 1. Structure of PI-based stator resistance estimator

In the voltage-model, the stator voltage  $[u_{S\alpha}, u_{S\beta}]$  and current  $[i_{S\alpha}, i_{S\beta}]$  are measured for obtaining rotor flux vector components  $[\psi_{R\alpha}, \psi_{R\beta}]$ . In the current-model, these components  $[\hat{\psi}_{R\alpha}, \hat{\psi}_{R\beta}]$  are also calculated from the measured values of stator current and rotor speed ( $\omega_R$ ). The PI-M operates in the stationary reference frame  $[\alpha, \beta]$  and it is described with the following equations [1]:

$$\psi_{R\alpha} = \frac{L_R}{L_m} \int (u_{S\alpha} - \hat{R}_S i_{S\alpha}) dt - \sigma L_S i_{S\alpha} \quad (1)$$

$$\psi_{R\beta} = \frac{L_R}{L_m} \int (u_{S\beta} - \hat{R}_S i_{S\beta}) dt - \sigma L_S i_{S\beta}$$

$$\hat{\psi}_{R\alpha} = \int \left( \frac{L_m}{T_R} i_{S\alpha} - \frac{1}{T_R} \hat{\psi}_{R\alpha} - \omega_R \hat{\psi}_{R\beta} \right) dt \quad (2)$$

$$\hat{\psi}_{R\beta} = \int \left( \frac{L_m}{T_R} i_{S\beta} - \frac{1}{T_R} \hat{\psi}_{R\beta} + \omega_R \hat{\psi}_{R\alpha} \right) dt$$

The adaptive signal, derived from the error between two models ( $\xi_{RS}$ ), is utilized to estimate stator resistance ( $\hat{R}_S$ ) by PI-M as follows:

$$\xi_{RS} = (\psi_{R\alpha} - \hat{\psi}_{R\alpha}) i_{S\alpha} + (\psi_{R\beta} - \hat{\psi}_{R\beta}) i_{S\beta} \quad (3)$$

$$\hat{R}_S = K_P \xi_{RS} + K_I \int_0^t \xi_{RS} dt$$

## 3 Proposed PSO-based mechanism stator resistance estimation

Particle swarm optimization (PSO) was first proposed by Russell Eberhart and James Kennedy (1995) [5, 6]. PSO is an evolutionary computation technique motivated by the simulation of social behaviors. Among particles “flying” through a multidimensional

search space, each particle is representing a single solution of all search dimensions. PSO has two primary operators: updating new solutions via velocity and via position. The advantage of the PSO over the other optimization algorithms is its relative simplicity and stable convergence with good computational efficiency. The modified velocity and position of each particle can be determined by (4) and (5) [6]. This process is iteratively implemented until the minimum error is achieved.

$$V_i^{(t+1)} = wV_i^{(t)} + C_1 \text{Rand}_1 (P_{best,i} - X_i^{(t)}) + C_2 \text{Rand}_2 (G_{best} - X_i^{(t)}) \quad (4)$$

$$X_i^{(t+1)} = X_i^{(t)} + V_i^{(t+1)} \quad (5)$$

where:  $w$  -inertia weigh;  $V_i^{(t)}$  - current velocity of particle  $i$  at iteration  $t$ ;  $V_i^{(t+1)}$  - new velocity of particle  $i$  at iteration  $(t+1)$ ;  $C_1$  - adjustable cognitive acceleration constants (self-confidence);  $C_2$  - adjustable social acceleration constant (swarm confidence);  $\text{Rand}_{1,2}$  - random number between 0 and 1;  $X_i^{(t)}$  - current position of particle  $i$  at iteration  $t$ ;  $P_{best,i}$  - the personal best of particle  $i$ ;  $G_{best}$  - the global best of the population;  $X_i^{(t+1)}$  - denotes the position of particle  $i$  at the next iteration  $(t+1)$ . This process is iteratively implemented until the minimum error is achieved.

In this paper, the PSO-M is proposed to replace the PI-M for stator resistance estimation, whose structure is showed in Fig. 2. In this scheme, the PSO-M procedures is described by the following equations.

The Eq. (1) and (2) from section 2, can also be rewritten as:

$$\sigma L_S \frac{di_{S\alpha}}{dt} = u_{S\alpha} - \hat{R}_S i_{S\alpha} - \frac{L_m}{L_R T_R} (L_m i_{S\alpha} - \hat{\psi}_{R\alpha} - \hat{\omega}_R T_R \hat{\psi}_{R\beta}) \quad (6)$$

$$\sigma L_S \frac{di_{S\beta}}{dt} = u_{S\beta} - \hat{R}_S i_{S\beta} - \frac{L_m}{L_R T_R} (L_m i_{S\alpha} - \hat{\psi}_{R\beta} + \hat{\omega}_R T_R \hat{\psi}_{R\alpha}) \quad (7)$$

Using the discrete form of (6)

$$\hat{i}_{S\alpha}(k) = W_1 \hat{\psi}_{R\alpha}(k-1) + W_2 \hat{\psi}_{R\beta}(k-1) + W_3 u_{S\alpha}(k-1) + W_4 \hat{i}_{S\alpha}(k-1) \quad (8)$$

Where:  $W_1 = [T_S / (\sigma L_S)] [L_m / (L_R T_R)]$ ;  $W_2 = [T_S / (\sigma L_S)] [(L_m / L_R) \hat{\omega}_R]$ ;  $W_3 = T_S / (\sigma L_S)$ ;

$$W_4 = [1 - (T_S / \sigma L_S) \hat{R}_S - (T_S / \sigma L_S) (L_m^2 / (L_R T_R))].$$

The Eq. (8) expresses the estimation of stator current, which is variable with stator resistance ( $R_S$ ). Weights  $W_1$ ,  $W_2$ ,  $W_3$  are directly calculated from the motor speed ( $\omega_R$ ), motor parameters, and sampling time ( $T_S$ ). It is considered that motor parameters are constant except stator resistance ( $R_S$ ). The error function ( $E_\alpha$ ) is given:

$$E_\alpha = \frac{1}{2} \varepsilon_\alpha^2 = \frac{1}{2} (i_{S\alpha}(k) - \hat{i}_{S\alpha}(k))^2 \quad (9)$$

Similarly, using the discrete form of Eq. (7)

$$\hat{i}_{S\beta}(k) = W_1 \hat{\psi}_{R\beta}(k-1) - W_2 \hat{\psi}_{R\alpha}(k-1) + W_3 u_{S\beta}(k-1) + W_4 \hat{i}_{S\beta}(k-1) \quad (10)$$

$$E_\beta = \frac{1}{2} \varepsilon_\beta^2 = \frac{1}{2} (i_{S\beta}(k) - \hat{i}_{S\beta}(k))^2 \quad (11)$$

With the proposed PSO algorithm, the  $R_S$  value of  $W_4$  weight will be searched so that the minimum objective function  $F$  is minimized:

$$F = E_\alpha + E_\beta \quad (12)$$

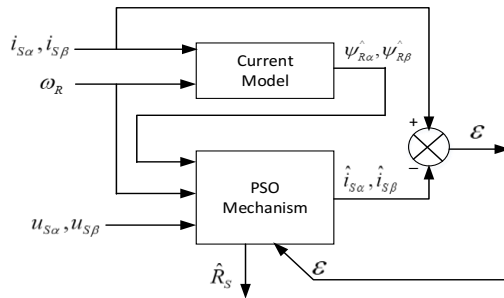


Fig. 2. Structure of PSO-based stator resistance estimator.

### 4 Simulation and Result

The designed control algorithms were simulated in the RFOC control structure of the IM drive using Matlab/Simulink, and the two structure of estimator PI-M and PSO-M are examined sequentially. The parameters of IM are given in Table 1. The simulation results (from Fig. 5 to Fig. 7) are obtained with the ratio of variation of stator resistance is illustrated in Fig. 3 and reference of speed and load torque as Fig. 4.

Table 1. PARAMETERS OF INDUCTION MOTOR

Parameter	Value
Rated Power ( $P_n$ )	3.3 (kW)
Rated Voltage ( $V_n$ )	380 (V)
Stator resistance ( $R_S$ )	4.179 ( $\Omega$ )
Stator inductance ( $L_S$ )	0.209 (H)
Rotor time constant ( $T_R = L_R/R_R$ )	0.0987 (H/ $\Omega$ )
Mutual inductance ( $L_m$ )	0.192 (H)
Number of poles	4
Moment of inertia	0.047 kgm <sup>2</sup>

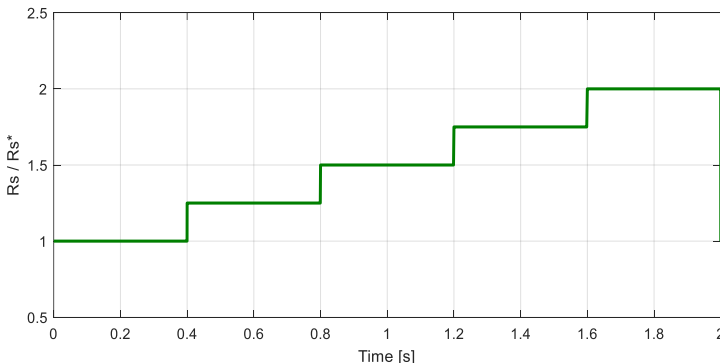


Fig. 3. The variation ratio between changed and reference stator resistance

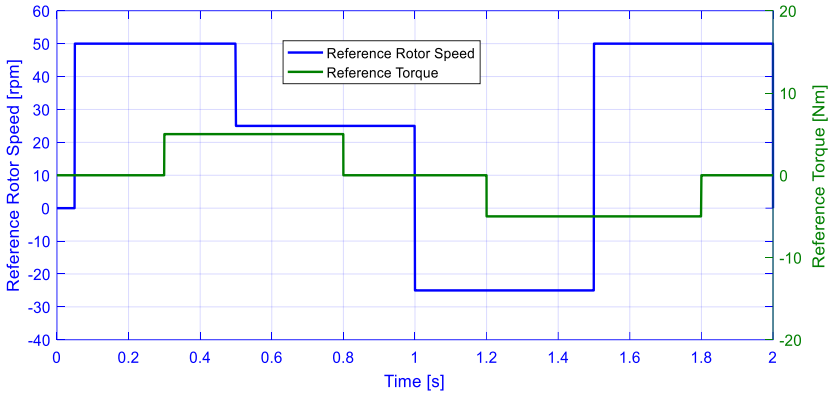


Fig. 4. Reference of speed and load torque.

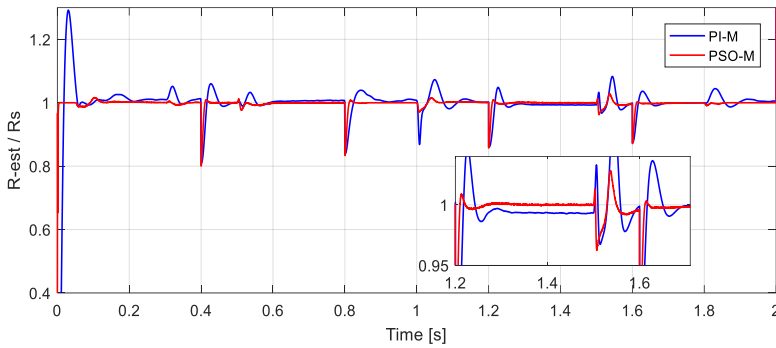


Fig. 5. PI-M (blue) and PSO-M (red) estimator: the ratio between estimated and known value of stator resistance

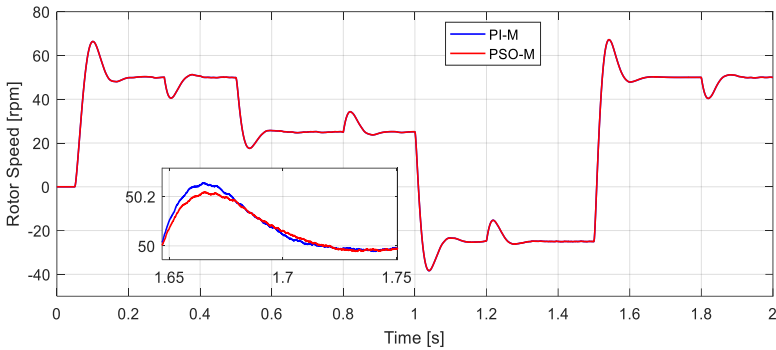
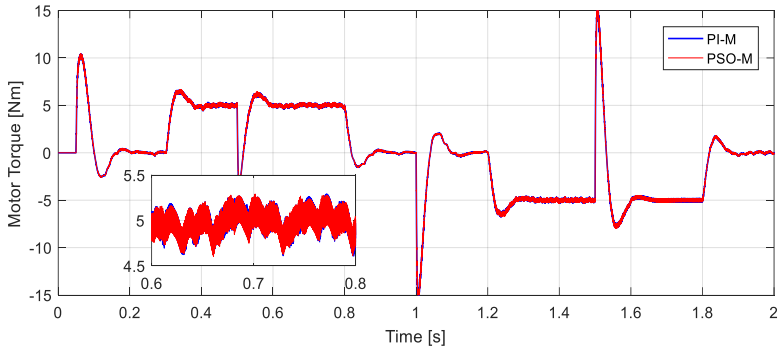


Fig. 6. PI-M and PSO-M: Rotor speed responding

To exam the effectiveness of the proposed method, the simulation is implemented with a ratio of stator resistance variation from 1 to 2 times as Fig. 3. From Fig. 5, it can be seen that that estimated value of the proposed estimator can track the actual value of the stator resistance quickly and stable, and the PSO-M scheme gives estimated stator resistance more accurately than PI-M as well. Fig. 6 and Fig. 7 show the motor speed and torque respond of both schemes are almost equal, but the overshoot of speed with PSO-M is less than PI-M.





**Fig. 7.** PI-M and PSO-M: motor torque

## 5 Conclusion

In this study, a new method of online estimation of the stator resistor of induction motor for RFOC scheme by using the PSO algorithm is presented. It has been demonstrated that the proposed estimator can identify changes in stator resistance and can converge to the steady-state value of the resistance. The proposed technique also shows higher accuracy compared with the conventional PI mechanism ones.

## Acknowledgment

In the paper, there are the results of Project reg. No. SP2019/113 - Student Grant Competition of VSB-Technical University of Ostrava, Research and development of modern control methods in the field of electrical controlled drives, 2019.

## References

1. Vasic, V., Vukosavic, S. N., & Levi, E.: A stator resistance estimation scheme for speed sensorless rotor flux oriented induction motor drives. *IEEE transactions on Energy Conversion*, 18(4), 476-483 (2003).
2. Karanayil, B., Rahman, M. F., & Grantham, C.: Online stator and rotor resistance estimation scheme using artificial neural networks for vector controlled speed sensorless induction motor drive. *IEEE transactions on Industrial Electronics*, 54(1), 167-176 (2007).
3. H. H. Vo, P. Brandstetter, C. S. T Dong, T. C. Tran: Speed Estimators Using Stator Resistance Adaption for Sensorless Induction Motor Drive. *Advances In Electrical And Electronic Engineering*, p.p 267-273 (2016), DOI: 10.15598/aece.v14i3.1732.
4. Mitronikas, E. D., Safacas, A. N., & Tatakis, E. C.: A new stator resistance tuning method for stator-flux-oriented vector-controlled induction motor drive. *IEEE Transactions on Industrial Electronics*, 48(6), 1148-1157 (2001).
5. Kennedy, J., Eberhart, R.: Particle swarm optimization. In: *Proceedings of the IEEE International Conference on Neural Networks*, pp. 1942–1948 (1995).
6. Shi, Y., Eberhart, R.: A modified particle swarm optimizer. In: *Proceedings of the IEEE International Conference on Evolutionary Computation*, pp. 69–73 (1998).

# An ARM-based Embedded Microcontroller System Development Platform

Daniel Kouřil and Jakub Bača

Department of Electronics, FEECS,  
VŠB – Technical University of Ostrava, 17. listopadu 15,  
708 33 Ostrava – Poruba, Czech Republic  
{daniel.kouril, jakub.baca}@vsb.cz

**Abstract.** This article describes the hardware co-design of a new Embedded Microcontroller system based on the NXP Kinetis series microcontroller, the K64F family. It is a development board that should be used to develop new applications based on an ARM core microcontroller, especially focused on Power Electronics, as a control system unit, at the Department of Electronics. At the same time, it serves as a modern work and study aid for teaching a subject focused on microprocessor technology and an Embedded system for automotive applications.

**Keywords:** A/D converters, Communication interfaces, D/A converters, Development board, Embedded Microcontroller Systems and applications, Ethernet, Hardware/Software co – design

## 1 Introduction

We can observe a pretty rapid progression in the field of Microelectronics technology over recent years. Especially for Microprocessors and Microcontrollers the innovations and progress are fast and the existing solutions are often replaced by new ones. Older families of a Microcontrollers (MCUs) and a Digital Signal Processors (DSPs) are pushed out by new, more powerful, floating-point Microcontrollers. Manufacturers development support is also often terminated.

The current trend in an Embedded Microcontroller Systems is the application of an ARM core-based Microcontroller with real-time operating system support, such like a MbedOS or a FreeRTOS, which can provide industry-leading computing power, special peripherals, and relatively low cost and speed. Manufacturers frequently trying to overtake each other to provide user-friendliness Integrated Development Environment (IDE), with various useful toolbox configurations that make software co-design easier.

The aim was to developed a new concept of a development platform hardware / software co-design, in particular to innovate existing Microcontroller Systems equipment used for teaching subjects at the Department of Electronics, so that students could work with modern MCU systems that are used in the industry. It also brings some innovations for teaching an Embedded System for an automotive electronic application.

## 2 The NXP Kinetis MK64F Microcontroller

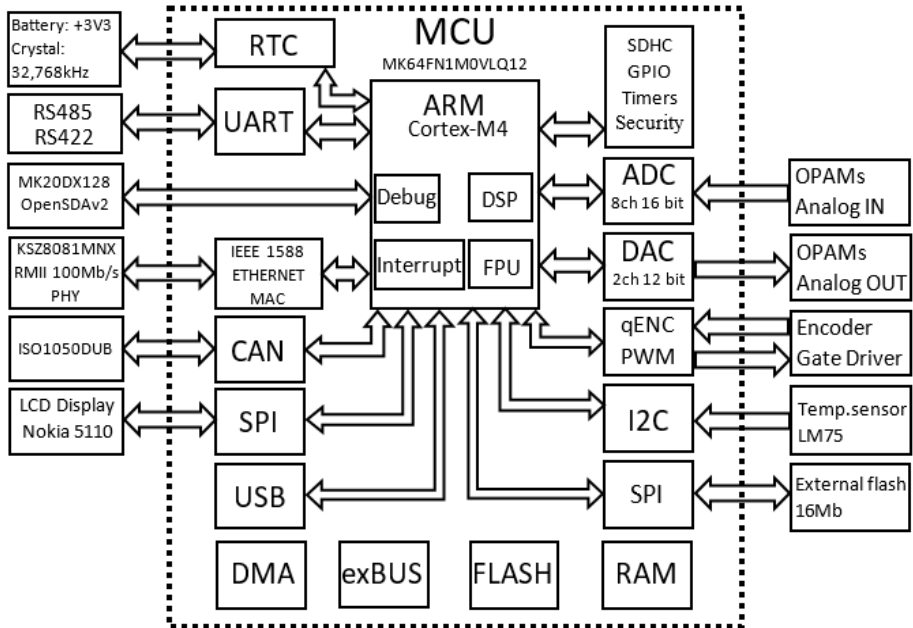


Fig. 1. The MK64F development board topology block diagram

The NXP MK64F microcontroller was selected for a new concept of a development platform. The K6x series of microcontrollers are very powerful and very energy efficient. Thanks to smart integration on the chip, it significantly reduces the overall Bill of Materials. [1]

The entire order offers a scalable portfolio with varying levels of integration, offering a rich package of control, analog and communications peripherals to meet a wide range of requirements. It is used in the field of IoT, medical purpose monitoring, industrial control and an automation. [1]

An integrated A/D converter supports up to 4pairs of differential inputs and up to 8 single-ended inputs with maximal 16-bit resolution mode. It further allows selectable external or internal voltage reference source, Self-Calibration function, hardware triggering and asynchronous clock source. [1], [2]

The DAC converter module is 12-bit, includes an internal reference source with reference voltage selection and a boosted analog output, and is capable of controlling external loads without an additional operating network. It is also capable of synchronizing with PWM modules. [1], [2]

Noteworthy also an Open SDAv2 feature on board, which is an open - standard for serial and debug adapter. It allows debugging communication between a USB host and an embedded target processor. It based on MK20DX128 microcontroller. Figure 1 shows the topology of the proposed development board.

### 3 The topology of an Embedded Microcontroller System Development board

Kinetis K64 Arm Cortex –M4 Development Board is a new development board for teaching subjects focused on Microprocessor technology at the Department of Electronics. The development kit based on NXP MK64FN1MOVLQ12 microcontroller.

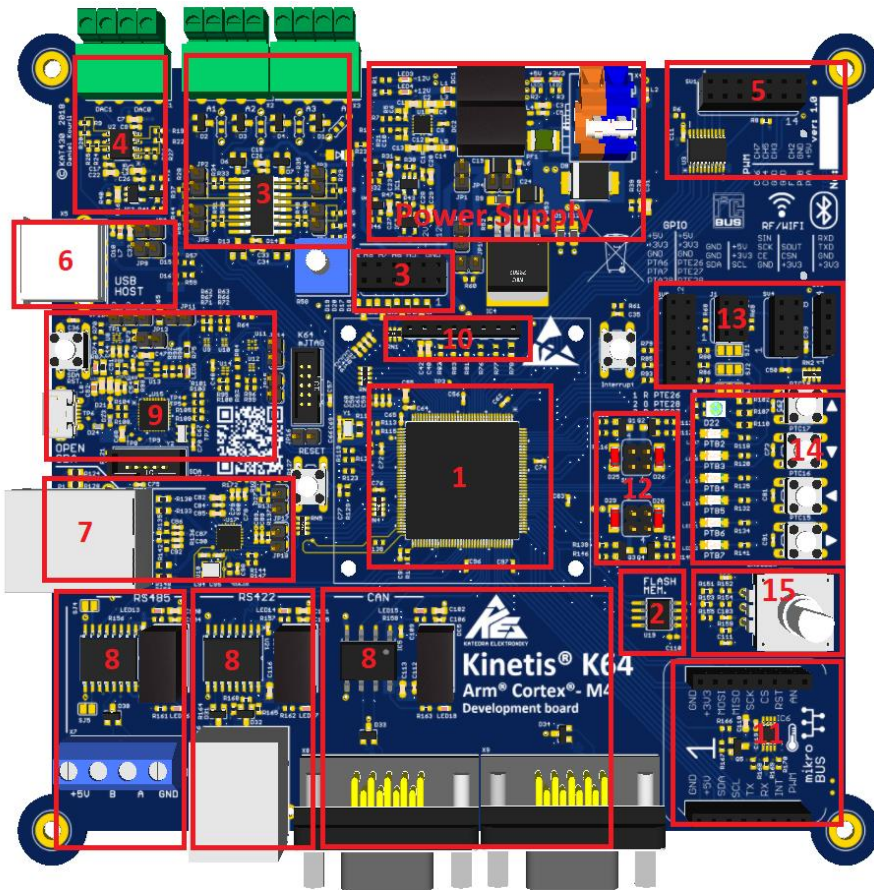


Fig. 2. Hardware topology of an Embedded Microcontroller System Development board

**Core & Memory:**

1. An ARM Cortex M-4, 120 MHz, 1MB Flash, 256KB RAM,
2. An external Flash 16 Mb thru SPI

**A/D converter:**

3. ADC: Internal 16bit ADC converter; 4 channels connected thru OPAMS networks;4 channels connected to Pin Header

**D/A converter:**

DAC: 2 channels 12 bit DAC outputs connect thru OPAMS networks.

PWM modulator: 6 channels FlexTimerPWM/MotorControl modulators, 2 channels FlexTimer PWM/quadrature decoder

**Communication interfaces:**

USB (host/device) allows fed the board

ETHERNET RMII to 100Mb/s, (KSZ8081RNACA PHY module)

Support industrial communication standards with galvanic isolation such as UART/RS485, UART/RS422 and CAN.

Debug: OpenSDAv2, SWD/JTAG

**An external modules extension:**

LCD Nokia 5110 Display

MikroBUS standard support

4. 2x GPIO open collector (5V)

2x GPIO open collector (3,3V)

5. 6x GPIO; 1xI2C; RF/WIFI support (NRF24L01, ESP8266 modules); Bluetooth (JY-MCU)

6. 6xLED;

1x RGB LED; 4x toggle switch;

2x interrupt switch

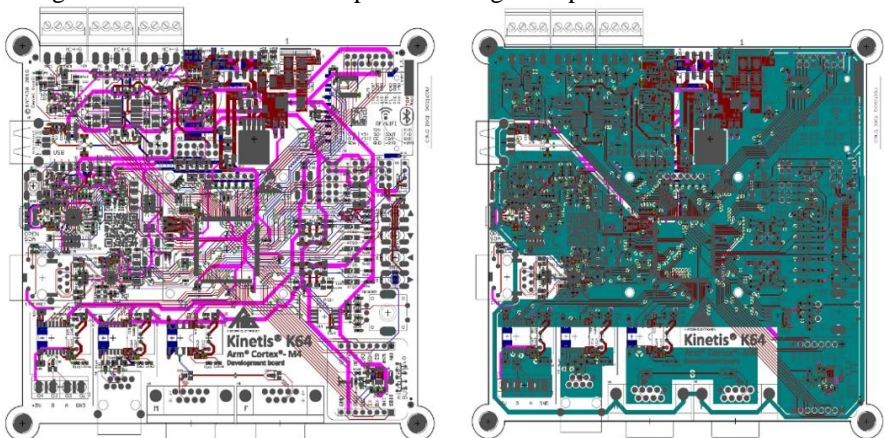
7. 1x rotary encoder with switch (24 pulses per rotation)

**Other features:**

- Digital I2C temperature sensor LM75
- SDHC slot
- RTC
- Potentiometer

## 4 Hardware co-design of an Embedded Microcontroller Development board

Hardware was designed like single 4 layers PCB, worth mentioning is the galvanic isolation of industrial communication standards such as RS485, RS422 and CAN bus. PCB is on an advanced level with a high degree of integration with SMD components. All design rules such as differential pairs and length adaptation are taken into account.



**Fig. 3.** Hardware co-design of Kinetis K64 Development board

## 5 Software development platform and support

The Kinetis Design Studio IDE is no longer being actively developed it was replaced by the MCUXpresso IDE for new designs with NXP Kinetis and LPC family microcontrollers. The new configuration module MCUXpresso can assign signals from the peripherals to the microcontroller's outlets using the *"Pins Tool"*, and set the system clocks with the *"Clocks Tool"*. You can then download and import the configuration into the project. The K6x family still have support from Processor Expert Software.

Processor Expert Software can be used to create, configure, optimize, migrate, and deliver software components that generate source code for our silicon. It is available as a plugin feature of the independent Eclipse-based IDE. Each component encapsulates a discrete set of functionality designed to accomplish the component's design objectives. It is a pretty useful tool for easier software co-design and teaching purpose.

## 6 Embedded Microcontroller Systems and applications

To demonstrate the application with the new development kit, a program for communication via CAN interface was created, such tasks can be applied, for example, in the course Microcomputers in the automotive industry for the newly established study program Automotive Electronic Systems.

```
Data1[8] = {0x48U, 0x6fU, 0x77U, 0x20U, 0x61U, 0x72U, 0x65U, 0x20U}; /*How are */
Data2[4] = {0x79U, 0x6fU, 0x75U, 0x3fU}; /*you?*/
```

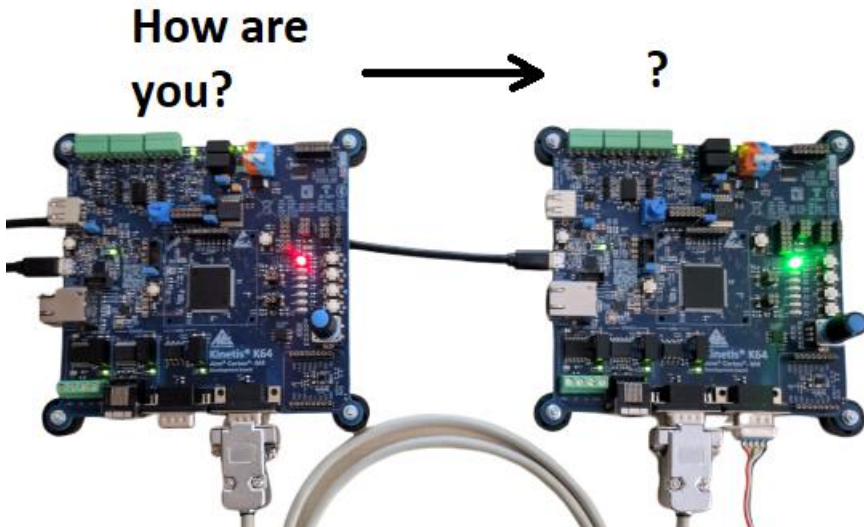


Fig. 4. The connection of two development boards thru CAN bus

Fig. 4 shows a simple example of connecting two development boards using a CAN bus. The development board (Red) asks the second one (Green) in two buffers *"How*



are you?" The development board receives the message and the communication is terminated. Data Frame of CAN bus communication is shown in Fig. 5.

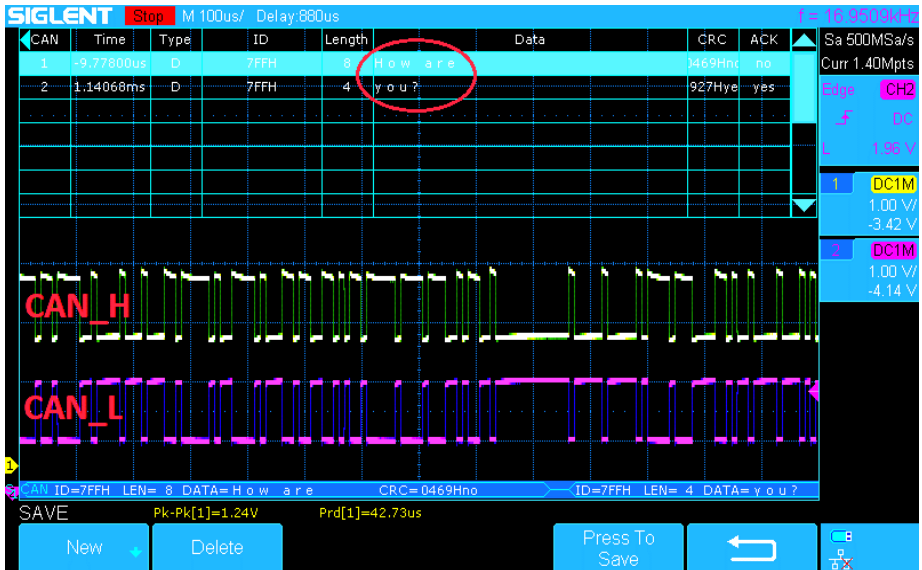


Fig. 5. CAN bus data frame communication example

## 7 Conclusion

The development kit brings new advanced application development solutions to the department of Electronics. Innovations of existing laboratory habitats, new automotive applications. It brings with it the modernization and improvement of the taught subjects, which leads to the improvement of students' knowledge of their better orientation in modern embedded systems based on the ARM cortex M4 microcontrollers.

## Acknowledgment

The results of this paper were supported by the projects Reg. No. 63/2019/RPP-TO-2 funded by the Institutional Development Project and SP2019/113 funded by the Student Grant Competition of VSB - Technical University of Ostrava.

## References

1. *K64 Sub- Family Reference Manual* [online]. NXP, 2017 [cit. 2019-07-16]. Available from: <https://www.nxp.com/webapp/spa/download/preDownload.jsp?render=true>
2. *Technical data: Kinetis K64F Sub-Family DataSheet* [online]. NXP, 2016 [cit. 2019-07-18]. Available form: <https://www.nxp.com/docs/en/datasheet/K64P144M120SF5.pdf>

# Investigation of a Damaged Filter-compensation Unit

Stanislav Nowak and Stanislav Kocman

Department of Electrical Engineering, FEECS,  
VŠB – Technical University of Ostrava, 17. listopadu 15,  
708 33 Ostrava – Poruba, Czech Republic  
{stanislav.nowak.st, stanislav.kocman}@vsb.cz

**Abstract.** Nowadays, almost 50% of steel is made from steel scrap by electric heating and melting, mostly in an arc furnace. The electric arc furnace with all its equipment is often a key unit in the entire steel manufacturing process. Therefore, all electric arc furnace equipment must be designed with respect to the requirement of high reliability for a long-term work under very hard conditions in the steel mill. The real failure of the medium voltage equipment will be described. The costs of repair reached the level of tens kEUR. The failure occurred at an unexpected moment and its causes were also unexpected.

**Keywords:** Electric arc furnace, Filter-compensation unit, Transformer, Capacitor, Melting process, Failure, Power factor, Reactive power.

## 1 Introduction

Many steel mills are equipped by electric arc furnaces. Their purpose is heating and melting the steel. In the electric steel mill (a kind of steel mill, based on the electric heating and melting), is AC electric arc furnace the main and the most important technological unit, in the other steel mills (working on the oxygen technology) there is usually used a special kind of electric arc furnace. This furnace is called ladle heating furnace (LHF), it is used for the precision heating and the other secondary treatment of the liquid steel. The melting process is based on the AC electric arc (3 arcs). The arcs always burn between the graphite electrodes and the melted or heated steel material. The electric consumption of arc furnaces varies from units of MW to hundreds of MW.

Electric current, drawn by the furnace from MV supply system, is strongly non-harmonic due to electrical properties of the electric arc. Volt-ampere characteristic of the arc is non-linear. Moreover, the burning of the arc is a volatile process difficult to control precisely. To increase the stability of the burning arcs a phase shift on the secondary site of the furnace transformer is required. The phase shift must be inductive, the right power factor of the furnace is recommended between  $\cos(\phi) = 0.75$  and  $\cos(\phi) = 0.80$ , maximum  $\cos(\phi) = 0.85$ . For example, at power factor  $\cos(\phi) = 0.78$  and the active power 24 MW, the reactive power consumed by the furnace oversteps 19 MVAR. It is necessary to



compensate the reactive power and also to reduce the level of harmonics content in the current drawn by the furnace [2].

## 2 Filter-compensating unit

To reduce the distortion of voltage on supplying grid a passive power medium voltage filter is used. A simple passive filter connected in parallel to the three-phase grid is a set of series resonant circuits. In Fig. 1 a simple configuration example of a real medium voltage power passive filter (in the next text filter-compensating unit - FCU) is shown. The FCU can also have a different configuration, it can be a more complex set of resonant circuits. It usually depends on the designer's experience. The fundamental function of the FCU is to compensate the reactive power generated by AC electric arc furnace and also to filter the voltage in supplying point by trapping the harmonics of currents through the tuned series resonant circuits. It limits their penetration into the power grid. All components of the FCU must be sufficiently dimensioned, which is a prerequisite for their reliable operation.

In some steel mills, the power supply concept does not allow the switch-off the FCU during breaks between the melts, so that the FCU is permanently switched on (under full voltage). At the start of every melting process, the furnace is switched on by the main furnace breaker, but the electric arcs are ignited later. It means the connecting the furnace transformer to full voltage under no-load mode. This switch-on is every time accompanied by a transient phenomenon when time courses of all primary currents in the first seconds are very non-harmonic. The causes of this phenomenon are well described in [3]. The worst moment to connect the transformer (with an iron core) to the alternating current is the moment when the instantaneous voltage value goes through zero. The capacitors that are sensitive to voltage and current overload (current  $\sim dU/dt$ ) are especially vulnerable.

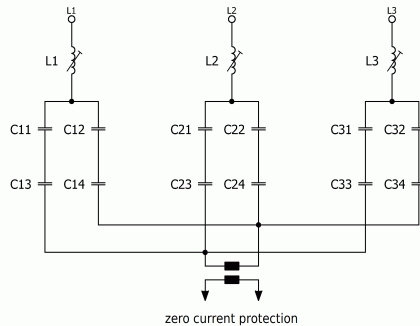
The passive FCU is equipped by a simple monitoring system based on the function of zero current protection unit. The capacitor section of the FCU is divided into two identical parts. Every part is a three-phase serial capacitor circuit connected in the star. The common point (centre of the star circuit) of the star is isolated. Between the common points of these two parts, there should be zero potential. In the case of damage of any capacitor, its star circuit is misbalanced. This damage generates non-zero potential between the centres of both stars which causes the current to flow between the centres. The protection unit detects the current between the centres and sends the switch-off signal to the FCU breaker.

## 3 Description of the electric arc furnace installation

In described equipment, the FCU is designed for power factor correction and also for 3-rd. harmonics filtration. The filter works on the medium voltage (MV) level - 22 kV/50 Hz grid. The grid is powered by high voltage (HV) transformer from

the public distribution grid on the high voltage level 110 kV. The apparent power of the HV transformer is 42 MVA. The HV transformer is exclusively dedicated to supplying the AC electric arc furnace in a steel plant. The voltages on the arcs are in the range of hundreds of volts, the currents are in the range from kA (low power heating) to tens of kA (fast heating). The apparent power of the furnace transformer is 30 MVA, primary voltage is 22 kV, secondary voltage 240 - 460 V. The furnace transformer is equipped with an on-load tap changer (13 positions). The usual furnace assembly [1] is shown in Fig. 2, where 1 - main disconnector, 2 - grid voltage measurement, 3 - furnace current measurement, 4 - main furnace breaker, 5 - additional reactor, 6 - shorting switch, 7 - furnace transformer, 8 - secondary voltage measurement, 9 - electrode current measurement, 10 - high current cable connection, 11 - heating part of the furnace.

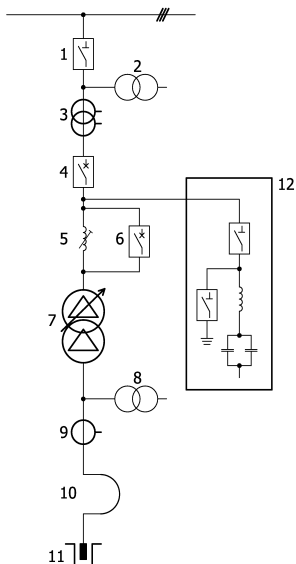
The investigated FCU is tuned on the third harmonic frequency, the circuit is gently subtuned. The FCU installed in 1990 worked without any problems until 2017. In 2017 it was decided to change the relatively old capacitors. This exchange was recommended because the electric parameters of capacitors get worse when they grow old, also the probability of their fault increases. The owner of the whole installation decided to exchange the all old capacitors in the FCU. The new capacitors with identical parameters were ordered. After the delivery the capacitors were installed, the whole FCU was completed and connected back to the system. The 27 years old reactors were still in good condition, and the decision was to do nothing with them.



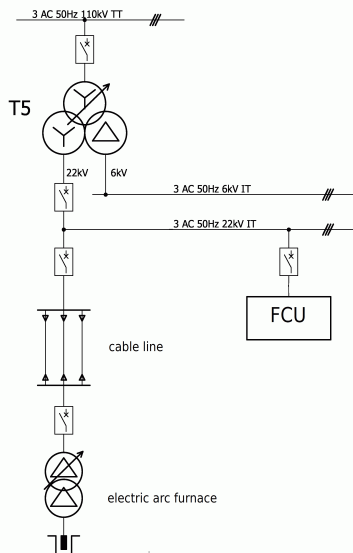
**Fig. 1.** Scheme of the investigated filter-compensating unit (FCU).

## 4 Failure investigation

In our case, the new capacitor was damaged after it was installed while replacing the old capacitors with new ones (as described above). The damage was detected by the filter protection unit, the filter was immediately switched-off, subsequently



**Fig. 2.** Usual furnace assembly [1].

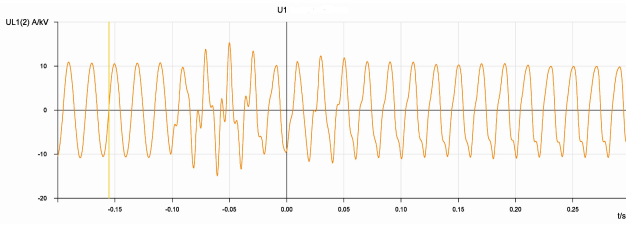


**Fig. 3.** Single line scheme of investigated installation.

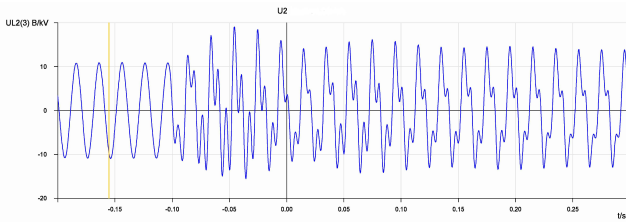
disconnected, and by measuring the capacitance of the capacitors, the damaged capacitor was identified. Subsequently, the defective capacitor was sent to a specialized test laboratory where the expected damage was verified. It was a breakdown of one of the capacitor roll. After an extensive debate among experts in this field, it was recommended to order new capacitors with higher voltage resistance parameters.

However, it was also decided to verify the level of the instantaneous voltage stress during operation. Therefore, the measurement of the instantaneous level of selected electrical values was carried out. The new capacitors were removed, and old undamaged capacitors were installed in their place. The FCU was put back into operation. Time courses of currents drawn by the furnace transformer as well as the time courses of the all three voltages on the capacitors  $C_{13}$ ,  $C_{23}$ , and  $C_{33}$  were measured and subsequently memorized. The memorized time courses were visually checked and evaluated. Time courses of measured values (critical parts) are shown from Fig. 4 to Fig. 9.

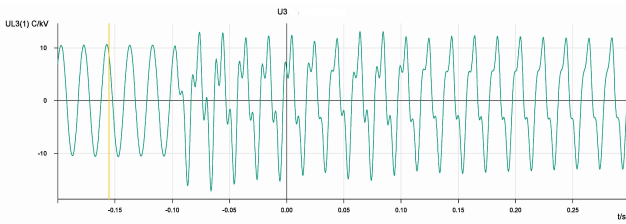
The results were somewhat surprising. It has been shown that the greatest risk to the capacitors does not occur during rapid heating (maximum power), but at the moment the furnace is switched on (the furnace transformer is in no-load mode). This is due to the transient phenomenon as described above. The currents of the individual phases have highly non-harmonic time courses, which are also very different. The measured time courses are shown in the following figures, the furnace breaker was switched on at the time  $t = -0.1$  s in relation to the time axis of the time courses.



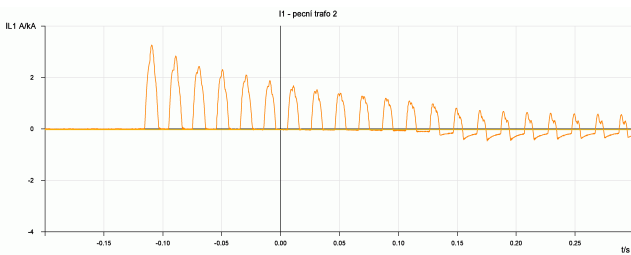
**Fig. 4.** Time course of the voltage on the capacitor  $C_{13}$ .



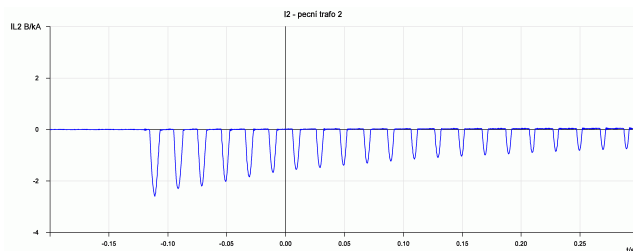
**Fig. 5.** Time course of the voltage on the capacitor  $C_{23}$ .



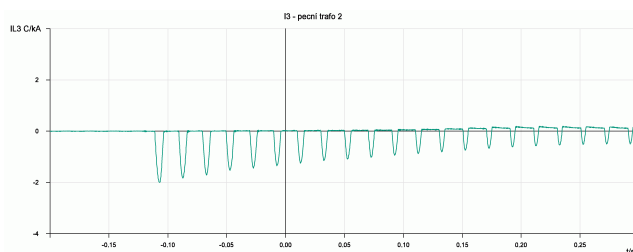
**Fig. 6.** Time course of the voltage on the capacitor  $C_{33}$ .



**Fig. 7.** Time course of the furnace current – phase 1.



**Fig. 8.** Time course of the furnace current – phase 2.



**Fig. 9.** Time course of the furnace current – phase 3.

## 5 Conclusion

The case has been described, where high-voltage power device (FCU) filtering harmful harmonics and compensating reactive power works correctly. However, this device is also connected while the arc furnace is disconnected from the power supply. Switching on the furnace without consuming electricity for the heating (furnace transformer being under no-load mode) is the critical moment when the device is most stressed. The measured voltages of the capacitors reach 190% of the normal operating values, and there is a real risk of damaging the capacitors. This case, unfortunately, confirms it. Therefore, equipment designers must not omit any, albeit seemingly insignificant, factor in its design.

**Acknowledgement** This work has been supported by Project SP2019/65 of the Student Grant System, VB - Technical University of Ostrava, Czech Republic.

## References

1. Kruczynin, A. M., Sawicki, A.: *Piece i urzadzenia lukowe* Politechnika Czestochowska. 2000, ISBN 83-7193-122-0
2. Hradilek, Z.; Laznickova, I.; Kral, V.: *Elektrotepelná technika*. CVUT v Praze. 2011, ISBN 978-80-01-04938-9
3. Novak, M., *Prechodovy dej pri zapnuti transformatoru*. Disertacni prace, TU v Liberci, Fakulta mechatroniky, 2003.

# Influence of Anisotropy Metal Sheets on the Nominal Values Induction Machine

Pavel Pečínka, Stanislav Kocman, and Vladana Pečínková

Department of Electrical Engineering, FEECS,  
VŠB – Technical University of Ostrava, 17. listopadu 15,  
708 33 Ostrava – Poruba, Czech Republic  
{pavel.pecinka.st, stanislav.kocman, vladana.pecinkova}@vsb.cz

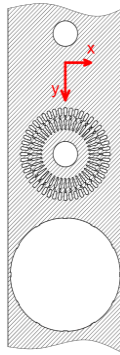
**Abstract.** The article deals with the influence of the anisotropy of electrotechnical sheets metal for rotating machine. Specifically, the article is investigated by influence, some nominal values. Using the Ansys Maxwell 2D simulation software, we attempted to describe behavior in different states, and we also propose a solution to this problem.

**Keywords:** anisotropy;  $BH$  curves; deformation of the rotating magnetic field; starting current, simulations

## 1 Introduction

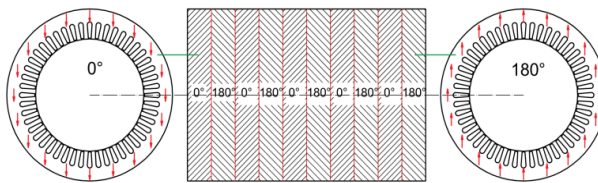
The design of the induction machine is very complicated by itself and only in the calculation that is theoretical, but in many parts, it is based on empirical relations and does not consider production problems. The influence on the behavior of the real machine has mechanical tolerances that can cause the air gap to be constant throughout the circumference. Unbalance of the overhangs or the winding itself, which may cause the asymmetry of the magnetic flux in the active part of the machine. Furthermore, the quality of the material or the surface of the housing, which degrades the heat transfer or the quality of the electromagnetic metal sheets. In rotating electrical machines, so-called non-oriented sheets are used, which are sheets having the same properties in all directions. These problems are also mentioned in [1] - [8]. References [1] - [8] summarize the existing knowledge concerning anisotropy. However, even the production of sheets themselves is burdened by production possibilities, so EN 10106: 2015 specifies tolerances of material properties [1] - [3]. With the increasing efficiency requirements, the choice of metal sheets used for the manufacture of rotary machines, primarily has been limited on M530-50A and M330-50A. The disadvantage is that metal sheet with a lower loss number suffers from a greater influence on partial directivity. This is also indicated by the greater deviation of directivity. To confirm this, we made measurements that confirmed this fact. In the result, this means that the sheet, which should have the same properties in all directions, does not have the same properties in all directions. The sheet for the construction of active parts is produced as a roll product. As

mentioned earlier, the sheet metal has a more dominant conductivity in one direction (axis) than in the second axis, see Fig.1.



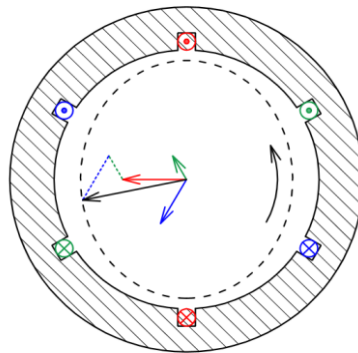
**Fig. 1.** Metal sheet production by progressive stamping tool.

The metal sheets are turn over for mechanical reasons by  $180^\circ$ . In this way the coaxiality of both the rotor and the stator packet is improved, see Fig. 2.



**Fig. 2.** Metal sheets folding.

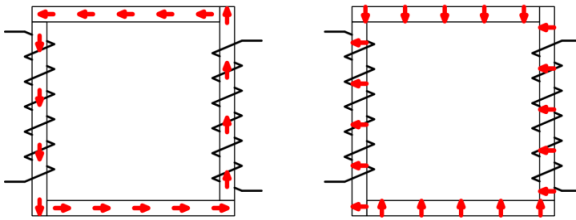
In this way, mechanical imperfections are suppressed, but the magnetic properties are still dominant in one direction. Specifically, in one direction, the metal sheet has a lesser magnetic resistance than in the axis of the other. The magnetic field vector will not write a circle with its end but see the ellipse. This is presented in Fig. 3.



**Fig. 3.** Vector of rotating magnetic field.

## 2 Measurement

Measurements are made in accordance with IEC 404-2 [1] - [3] and magnetic induction of 1,0 T and 1,5 T. The principle of measurement is to use the Epstein frame. According to the standard, the sheets are cut in the direction and perpendicular rolling in the same way they are also assembly to the Epstein frame. This mixed folding is denoted  $0^\circ / 90^\circ$ . For the experiment was selected the metal sheet M330-50A, which is more prone to partial directivity. The additional measurements were made again on the Epstein frame, but with the change that once the frame was assembly only of the strips in the direction of rolling (see in Fig. 4. a - we denote  $0^\circ$ ).



**Fig. 4.** a) Assembly of  $0^\circ$  b) Assembly of  $90^\circ$ .

The above measurements served to accurately determine the magnitude of the effect of the rotation. The reason is that in the direction of rolling the resistance gives the smallest magnetic resistance and in the vertical direction the magnetic circuit causes the greatest resistance. The evaluation of individual measurements is shown in Table 1.

**Table 1.** The results of measurements on Epstein frame with different configurations.

$\Delta P$ Losses as a function of sheet rotation [W/kg]					
B [T]	1. Mixed $0^\circ/90^\circ$	2. In direction of rolling $0^\circ$	3. Perpendicular on direction of rolling	Deviation acc. to EN 10106	Limitation acc. to EN 10106
1,5	4,38	4,15	4,6	5,14%	10%
1,0	1,97	1,85	2,1	6,33%	10%
Different versus $0/90^\circ$ at 1,5T:		-5,25%	5,02%		

For FEM simulations, it is necessary to obtain a specific  $BH$  characteristic,  $BH$  characteristics have been measured with the same sheet configurations. The results of the measurement of the individual  $BH$  characteristics for the above presented configurations are shown in Fig. 5. On the  $BH$  curves we can see the difference in curves, the red curve corresponds to the sheets that are in the rolling direction and the green in the direction perpendicular to the rolling. The  $BH$  characteristics table is below.



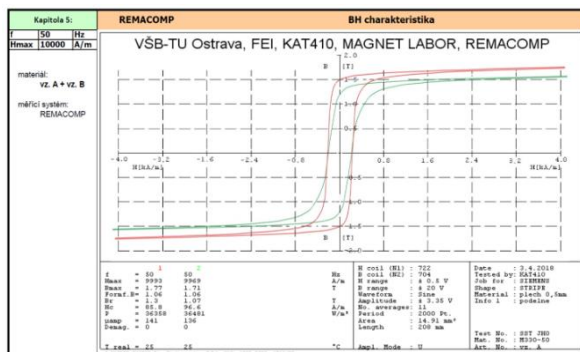


Fig. 5.  $BH$  curves for  $0^\circ$  and  $90^\circ$  metal sheet assembly.

### 3 FEM Simulation

The electromagnetic field in induction motor is described by the set of Maxwell's equations stated as:

$$\operatorname{div} \underline{B} = 0 \quad (1)$$

where  $\underline{B}$  is the magnetic flux density,

$$\operatorname{rot} \underline{E} = -\frac{\partial \underline{B}}{\partial t} \quad (2)$$

where  $\underline{E}$  is the electric field,

$$\operatorname{rot} \underline{H} = \underline{J} \quad (3)$$

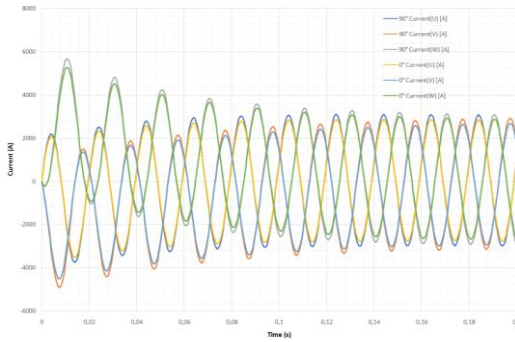
where  $\underline{H}$  is the magnetic field,  $\underline{J}$  is the current density.

$$\sigma \frac{\partial \underline{A}}{\partial t} + \operatorname{rot} \underline{H} - \sigma \underline{v} \times \underline{B} = \underline{J}_e \quad (4)$$

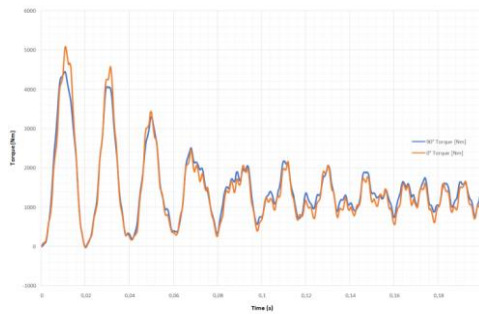
$$\operatorname{rot} \underline{A} = \underline{B} \quad (5)$$

where  $\underline{A}$  is the magnetic vector potential,  $\sigma$  is the electric conductivity,  $\underline{v}$  is the velocity of conductors,  $\underline{J}_e$  is the externally generated current density. A FEM model was created for a two - pole motor.

In the first case, the rotor and stator are rotated relative to each other by  $90^\circ$ , in the second case the rotor and stator are both in the direction of rolling and the third model is in the state when the sheets are perfectly oriented. The results of each simulation are listed in Fig. 6 and Fig. 7.

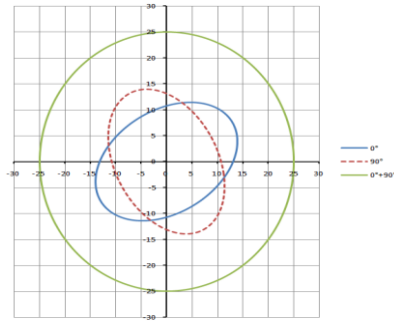


**Fig. 6.** The current waveforms in diametric and quadrature initial positions.



**Fig. 7.** The torque waveforms in diametric and quadrature initial positions.

Deviations may seem minimal, but it must be considered that they are deviations caused by tolerance standards and only with sheet properties. The possibility of reducing the influence of asymmetry of the non-oriented sheets is to gradually alternate the rotation of the sheet by  $90^\circ$ . Due to the fact that in one direction the metal sheet has less magnetic resistance, instead of a circular magnetic field, the field is elliptical. However if the sheets are rotated  $90^\circ$  instead of  $180^\circ$ , the sum of two elliptical fields is generated resulting in the required circular field as shown in Fig. 8.



**Fig. 8.** Sum of two different magnetic fields, which are rotated  $90^\circ$  each other.

## 4 Conclusion

The principle may seem simple, but it also carries certain constraints for the design of the machine, as the sheets are rotated only by  $90^\circ$ , and the rotor and sheet design must be mirrored in quarters. However if this problem is resolved, this design brings both advantages in stabilizing results and simplifying short circuit measurements. Then also by symmetry of the magnetic field of the machine. This reduces the occurrence of shaft voltages.

## 5 References

1. Cold rolled non-oriented electrical steel strip and sheet delivered in the fully processed state; EN 10106:2015. 1. Brussel: CEN-European committee for standartization, 2015.
2. CEI IEC 404-2: "Methods of measurement of the magnetic properties of electrical steel sheet and strip by means of an Epstein frame" 1. Geneve: International Standard CEI, 1996.
3. Beckley, P. "Electrical Steels for Rotating Machines": IEE Power and Energy Series, 37. 1. USA: Institution of Engineering and Technology, 2002. ISBN 978-0852969
4. Kocman, S., Pečínka P., Hrubý T.: "Induction motor modeling using COMSOL multiphysics. 17th International Scientific Conference on Electric Power Engineering (EPE) 2016"
5. Hamrit O., De La Barrière O., Lobue M., Mazaleyart F.: "Anisotropy of Losses in Non-Oriented Iron Silicon Sheets: Influence on Electrical Machine Applications," in IEEE Transactions on Magnetics, vol. 52, no. 2, pp. 1-7, Feb. 2016, Art no. 6300107. doi: 10.1109/TMAG.2015.2494856
6. Wolbank T. M., Machl J. L., Hauseh H. Macheiner P.: "Lamination material anisotropy and its influence on the operation of inverter-fed induction machines," in IEEE Transactions on Magnetics, vol. 39, no. 5, pp. 3283-3285, Sept. 2003. doi: 10.1109/TMAG.2003.816155
7. Soinski M., Bak Z., Bragiel P.: "Anisotropy of magnetic properties in thin electrical sheets," in IEEE Transactions on Magnetics, vol. 26, no. 6, pp. 3076-3079, Nov. 1990. doi: 10.1109/20.102894
8. Tamaki T., Fujisaki K., Wajima K., Fujiwara K.: "Comparison of Magnetic Field Analysis Methods Considering Magnetic Anisotropy," in IEEE Transactions on Magnetics, vol. 46, no. 2, pp. 187-190, Feb. 2010. doi: 10.1109/TMAG.2009.20335

# A Fault Tolerant Control Method Against the Failure of a Current Sensor in Induction Motor Drive

Cuong Dinh Tran

Faculty of Electrical and Electronics Engineering,  
Ton Duc Thang University, Ho Chi Minh City, Vietnam,  
Faculty of Electrical Engineering and Computer Science,  
VŠB – Technical University of Ostrava, 17. listopadu 15,  
708 33 Ostrava – Poruba, Czech Republic  
trandinhcuong@tdtu.edu.vn

**Abstract.** The paper describes a fault tolerant control (FTC) method based on the Kirchhoff's law against a current-sensor fault to maintain the stable operation of the induction motor (IM) drive. The control structure applying field oriented control (FOC) is presented briefly. The simulation in MATLAB/Simulink software has been implemented to demonstrate the effectiveness of the method.

**Keywords:** current sensor, detection step, induction motor, fault tolerant control, field oriented control.

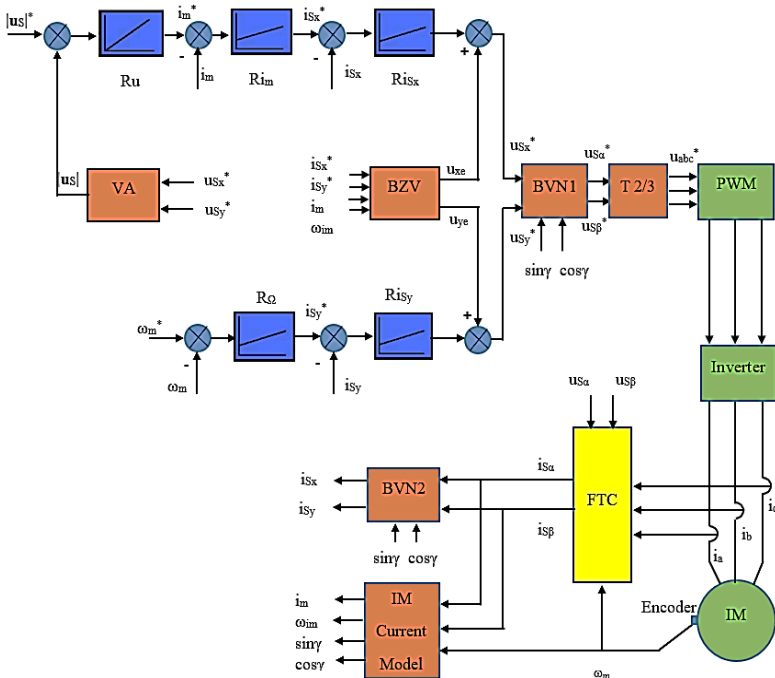
## 1 Introduction

The induction motor (IM) is one of the most popular machine types, which are applied widely in various industrial applications due to their simple structure, low cost, stable operation [1]. Nowadays, by the combination of a high-performance power converter and modern control techniques, the IM has excellent capabilities for the requirements of controlling speed and torque in the drive systems. In the operation of the IM drive, the reliability and stability are always the highest requirements in drive systems. However, during operating, unexpected problems of current sensors can deteriorate the performance of IM drive system, and the improper of feedback signals can lead to the incorrect control actions. Moreover, if the failure of the current sensor cannot be detected and isolated quickly, it can cause a breakdown of the drive system [2], [3]. Thus, the application of fault tolerant control (FTC) against the current sensor failure is necessary demand to keep the stable operation of IM drive systems.

In this article, we will present the fault tolerance algorithm based on Kirchhoff's law against a single failure of current sensors to keep the stable operation of IM drive. It uses the scheme of three stator current observers for the fault tolerant control unit. First of all, the fault detection is checked by comparing the sum of three measured phase currents equals zero or not, then the observed errors among three observers are used to determine the failure phase location [2], and finally a suitable configuration based on the healthy current sensors is suggested to implement the control task.

## 2 The Field Oriented Control Technique

The induction motor is controlled in a closed loop with the FOC scheme, as shown in Fig.1 .The first, the inputs include: stator currents, rotor speed measured from sensors, and voltages estimated from switching signals of inverter combining DC link voltage are transferred to FOC control loop. Next, the Clark’s formulas are used to transform quantities from three-phase [a, b, c] system to stationary  $[\alpha, \beta]$  system. The Park’s formulas are also applied to transform stator currents from stationary  $[\alpha, \beta]$  system to rotating  $[x, y]$  system. Then the control action can be performed in the control loop to achieve the control variables, and these variables will be transformed from rotating  $[x, y]$  system to stationary  $[\alpha, \beta]$  system by reverse Park transformation. Finally, the reverse Clark transformation is used to transform control variables from two-phase  $[\alpha, \beta]$  to three-phase [a, b, c] system. These reference variables are used to control the switching inverter by sine pulse width modulation method [4].



**Fig. 1.** The Scheme of FOC including FTC unit for induction motors

In FOC method, we can independently control the torque and the rotor flux variables as the same as the controllers of DC motors. Here, the stator current space vectors are divided into two perpendicular elements,  $i_{Sx}$  and  $i_{Sy}$  in the rotating  $[x,y]$  coordinate system, corresponding to the rotor flux space vector orientation to the x-axis as shown in Fig. 2. In this way, the component  $i_{Sx}$  is to maintain the identified amplitude of the rotor flux and the torque is controlled by adjusting the component  $i_{Sy}$ .

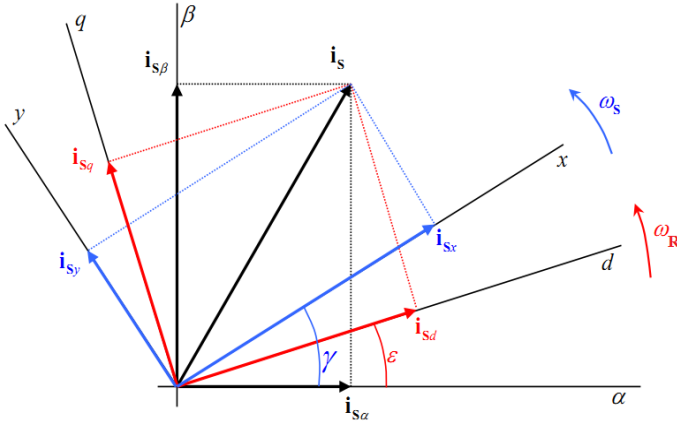


Fig. 2. The principle of FOC method

### 3 Fault tolerant control

In order to keep the stable operation of IM drive under the failure of one current sensor, the FTC unit will be added into the control loop as in Fig. 1. The inputs of FTC unit comprise the stator voltages  $[u_{s\alpha}, u_{s\beta}]$ , the stator currents  $[i_a, i_b, i_c]$  from current sensors, the rotor angular speed  $\omega_R$  calculated from a speed encoder  $\omega_m$  and the number of poles,  $2p$ . The outputs,  $i_{s\alpha}$ , and  $i_{s\beta}$  are results from calculation and comparing algorithms for controlling the IM drive. The FTC algorithm comprises three steps: fault detection, fault location, and reconfiguration steps.

**Fault detection step:** An error condition is detected by applied Kirchhoff's law that means the sum of three stator current must be zero at the same time, if not, there is a failure of one current sensor and the indication flag  $F$  will be set to high level.

**Fault location step:** Three observers will be used, each observer will receive two phase stator current inputs and calculate the other current as (1):

$$\begin{aligned}
 \text{Observer}_a : i_{a\_cal} &= -i_b - i_c \\
 \text{Observer}_b : i_{b\_cal} &= -i_c - i_a \\
 \text{Observer}_c : i_{c\_cal} &= -i_a - i_b
 \end{aligned} \tag{1}$$

In the stationary  $[\alpha, \beta]$  coordinate system, the measured stator currents  $[i_{s\alpha\_i}, i_{s\beta\_i}]$  of each observer can be obtained from  $(i_a, i_b, i_c)$  by Eq. (2). As a result, the currents  $[i_{s\alpha\_i}, i_{s\beta\_i}]$  of each observer are independent from the respective current sensors.

$$\begin{aligned}
 i_{s\alpha} &= \frac{2i_a - i_b - i_c}{3}; \\
 i_{s\beta} &= \frac{i_b - i_c}{\sqrt{3}}
 \end{aligned} \tag{2}$$

The estimated stator current is also calculated by the formulas (3), [5], [6].

$$\begin{aligned}\frac{di_s^S}{dt} &= A[\mathbf{u}_s^S - (R_s + j\frac{L_m^2}{L_R} p\omega_m)\mathbf{i}_s^S + (\frac{L_m R_R}{L_R} - jL_m p\omega_m)\mathbf{i}_R^S] \\ \frac{di_R^S}{dt} &= A[(\frac{1}{L_s}\mathbf{u}_s^S - (\frac{R_s}{L_s} + jp\omega_m)\mathbf{i}_s^S + (\frac{R_R}{L_m} - j\frac{L_R}{L_m} p\omega_m)\mathbf{i}_R^S]\end{aligned}\quad (3)$$

$$\text{where : } A = \frac{L_R}{L_s L_R - L_m^2}$$

Then the currents  $[i_{s\alpha_i}, i_{s\beta_i}]$  of each observer will be compared with the estimated stator current  $[i_{s\alpha}, i_{s\beta}]$  by (4):

$$e_{-i} = \left\| i_{s\alpha_{-i}} \times \hat{i}_{s\beta} - i_{s\beta_{-i}} \times \hat{i}_{s\alpha} \right\| \quad (4)$$

When the failure occurs at a specific current sensor, the error values of two other observers will increase strongly. Thus, combined with step one, the faulty sensor will be located at the minimum value among the three errors by the proposed algorithm below:

$$\begin{aligned}IF : (F_{e_{-i}} = \min\{e_{-i}\}), THEN : (F_{e_{-i}} = 1), ELSE : (F_{e_{-i}} = 0); \\ IF : (F = 1) \& (F_{e_{-i}} = 1), THEN : (F_i = 1), ELSE : (F_i = 0).\end{aligned}\quad (5)$$

Reconfiguration step: After the faulty current sensor is determined, the FTC will replace the stator currents  $[i_{s\alpha_m}, i_{s\beta_m}]$  of sensors by the stator currents  $[i_{s\alpha_i}, i_{s\beta_i}]$  of the relative observers. This FTC will maintain the stable operation of IM drive in the faulty sensor conditions.

## 4 Simulation results

The simulation will be implemented in MATLAB/SIMULINK with parameters of IM listed below:

$$P_n = 2.2 \text{ kW}, T_n = 14.8 \text{ Nm}, \omega_n = 1420 \text{ rpm}, p = 2.$$

$$I_{Sn} = 4.85 \text{ A}, I_{Sxn} = 3.96 \text{ A}, I_{Syn} = 5.6 \text{ A}.$$

$$U_{Sn} = 230/400 \text{ V}, \Psi_{Rn} = 0.757 \text{ Wb}.$$

$$R_s = 3.179 \text{ } \Omega, R_R = 2.118 \text{ } \Omega,$$

$$L_s = 0.209 \text{ H}, L_R = 0.209 \text{ H}, L_m = 0.192 \text{ H}, T_R = 0.0987 \text{ s}.$$

In this simulation, the IM has been operated at the normal speed ranges where the FOC method has been applied in the control scheme with three current sensors. A constant load torque of 5 N.m has been applied during the time of 0.2s. Fig.3 describes the characteristics of the speed of IM where the three-phase stator currents have been fully measured by healthy sensors. Fig.4 shows the performance of the controller with a current sensor fault occurring at the time of 1.0s without FTC. Fig.5 presents the functions of FTC to detect and locate the failure exactly. The method used the minimum error among the three comparators to locate the faulty phase. In this case, the current sensor of phase A is the faulty device. Additionally, the Fig.5 demonstrates the capability of the FTC to keep the stable operation of IM drive in this faulty situation.

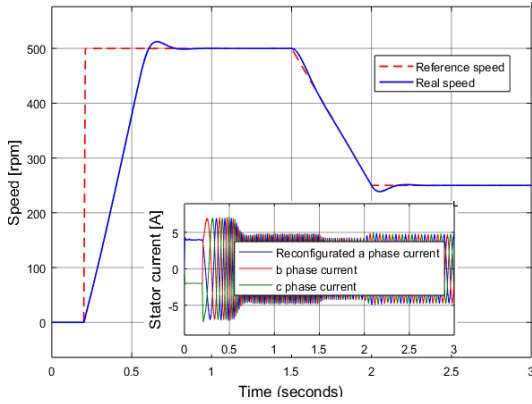


Fig. 3. Reference, real speed, and three phase currents in the healthy sensors – condition.

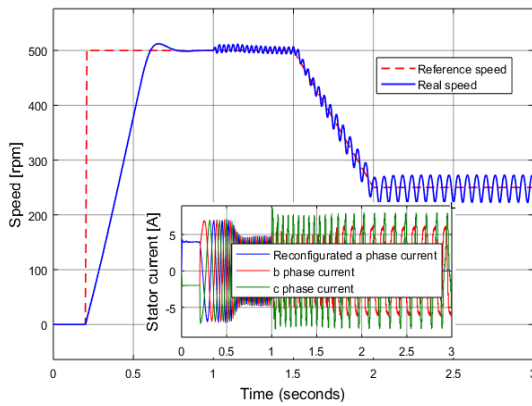


Fig. 4. Reference, real speed, and three phase currents with A phase current sensor fault without FTC.

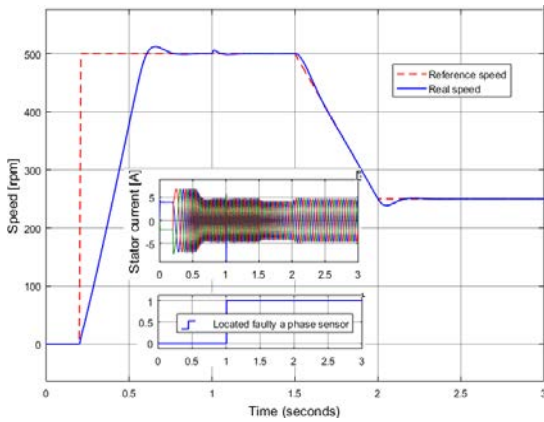


Fig. 5. Reference, real speed, three phase currents, and fault indication signal with A phase current sensor fault with FTC.



## 5 Conclusion

This paper presents a solution of fault tolerant control to deal with the abnormal condition of one phase current failure in IM's drives. This method consists of three steps: detection, location, and reconfiguration, where a model estimating the stator currents from the differential equation of the rotor currents and the stator currents has been applied to detect the location of the faulty phase sensor. The simulation results have demonstrated the effectiveness of the algorithm to maintain both speed and torque of IM drive systems in the case of occurring a single phase sensor fault.

## Acknowledgement

In the paper, there are the results of the Project reg. no. SP2019/113 - Student Grant Competition of VSB-Technical University of Ostrava, Research and development of modern control methods in the field of electrical controlled drives, 2019.

## References

1. Vas, P.: Sensorless vector and direct torque control. Oxford Univ. Press (1998).
2. Baghli, L., Poure, P., Rezzoug, A.: Sensor fault detection for fault tolerant vector controlled induction machine. In: Power Electronics and Applications, 2005 European Conference on (pp. 10-pp). IEEE (2005).
3. Yu, Y., Zhao, Y., Wang, B., Huang, X., Xu, D.: Current sensor fault diagnosis and tolerant control for VSI-based induction motor drives. *IEEE Transactions on Power Electronics*, 33(5), 4238-4248 (2018).
4. Brandstetter, P.: Electrical Drive III. Ostrava Univ (2014).
5. Tran, C. D., Brandstetter, P., Dinh, B. H., Ho, S. D., Nguyen, M. H. C.: Current-Sensorless Method for Speed Control of Induction Motor Based on Hysteresis Pulse Width Modulation Technique. *Journal of Advanced Engineering and Computation* 2, no. 4 (2018): 271-280.
6. Tran, C. D., Brandstetter, P., Ho, S. D., Tran, T. C., Nguyen, M. C. H., Phan, H. X., Dinh, B. H.: Improving Fault Tolerant Control to the one current sensor failures for induction motor drives. In: International Conference on Advanced Engineering Theory and Applications, pp. 789-798. Springer, Cham, 2018.

# Detonation Combustion and its Influences on Exhaust Emission Formation

Tomáš Harach

Department of Electronics, FEECS,  
VŠB – Technical University of Ostrava, 17. listopadu 15,  
708 33 Ostrava – Poruba, Czech Republic  
tomas.harach@vsb.cz

**Abstract.** This paper deals with the introduction to the influences of detonation combustion in gasoline engines on the produces exhaust emissions. It deals with the basic of common engine intake mixture and exhaust gases composition. The paper also describes an experiment that was conducted in order to measure engine emission compounds relation to the presence of detonation combustion.

**Keywords:** Detonation combustion · gasoline engine · emission analysis · engine performance.

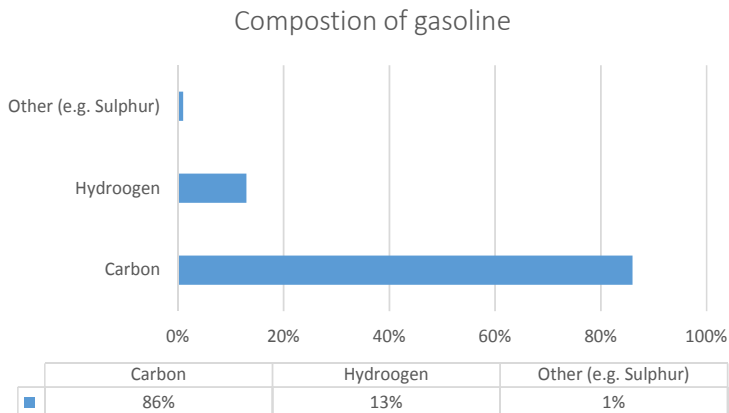
## 1 Introduction

Detonation combustion is an undesirable phenomenon occurring in petrol engines. For the even run of the engine and the longer life of its components, it is necessary to eliminate this phenomenon as much as possible. Prolonged exposure of engine components to detonation may result in mechanical crank failure, engine piston damage, cylinder head rupture etc. During detonation combustion a higher value of unburned hydrocarbons and carbon monoxide can be present, which is undesirable for modern power units. Formation of these substances is undesirable for the sake of global human health and the health of the environment.

In order to avoid detonations in the engine's combustion chamber, it is necessary to determine the correct moment of ignition of the fuel-air mixture by the spark plug. At the correct moment of ignition of the mixture, the force generated by the combustion of the mixture acting on the piston during the expansion stroke is transferred to the crank gear gradually. At that time, the crank mechanism of the engine is loaded in the right way and the mixture in the engine compartment is well burned.

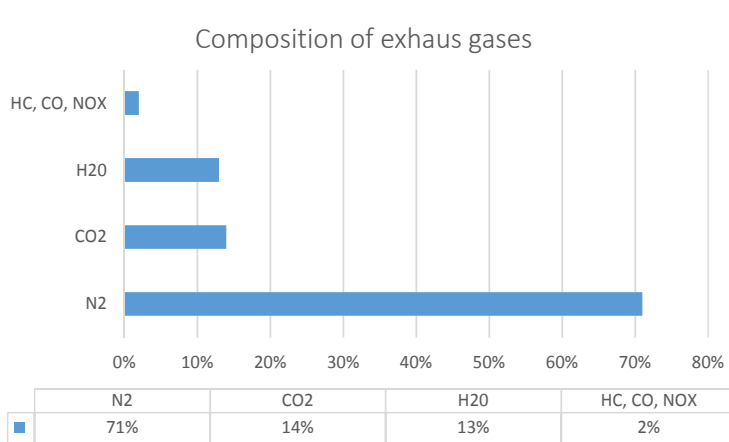
## 2 Engine Intake/Exhaust Composition Analysis

The process of burning the air/fuel mixture during combustion defines the composition of exhaust gases. There are many variables interfering with the fuel



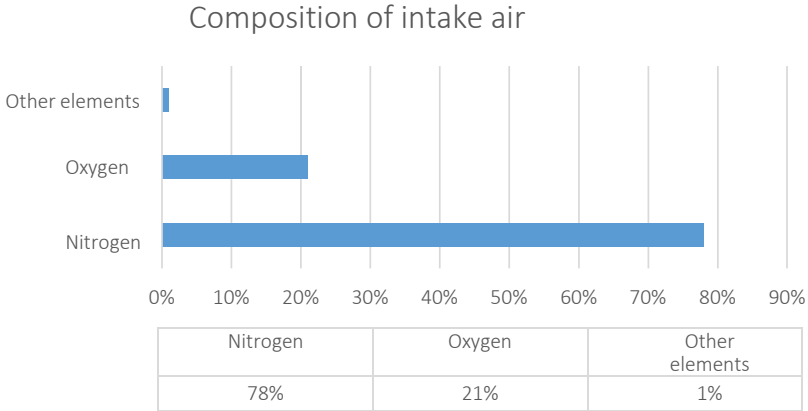
**Fig. 1.** Composition of diesel fuel [1] edited by the author.

combustion process. Characteristics of fuel spray, injection pressure, injection nozzle design, and injection schedule and the common deviations present in the engine management systems are some of the main variables that affect the formation of emission gases and particulate matter and many others.



**Fig. 2.** Composition of exhaust gases [1] edited by the author.

Other elements in diesel combustion engine emissions gases are Carbon Monoxide (CO), Sulphur Dioxide (SO<sub>2</sub>), Hydrocarbons (HC), Oxides of Nitrogen (NO<sub>x</sub>) and some particulate matter.



**Fig. 3.** Composition of intake air [1] edited by the author.

**Carbon dioxide  $\text{CO}_2$ .** This non-poisonous gas forms naturally by the combustion of hydrogen-based fuels. Increase of carbon dioxide in the earth's atmosphere leads to an increase in the volume of the greenhouse effect.

**Carbon monoxide  $\text{CO}$**  forms during oxygen deficiency, resulting in an incomplete combustion of carbon-based fuels. This gas is highly poisonous as it bonds itself to hemoglobin so that even small doses inhaled for a long period can be fatal.

**Hydrocarbons  $\text{HC}$**  include a large spectrum of different compounds which also form during an incomplete combustion of fuel. A bad condition of the engine mechanical components (e.g. worn-out piston rings causing compression deficit) has a high impact on the formation of hydrocarbons. Exhaust gases can contain 3 types of hydrocarbons:

1. saturated hydrocarbons have slightly narcotic impact and irritate skin,
2. unsaturated hydrocarbons irritate skin and have impact on the ozone hole and smog formation,
3. aromatic hydrocarbons are highly poisonous, have narcotic impact and cause cancer.

**Nitrogen oxides  $\text{NO}_x$  ( $\text{NO}_2$ ,  $\text{N}_2\text{O}$ ,  $\text{NO}$ ).** These are generated in presence of high pressure, high temperatures and excessive air combustion during the combustion process. Releasing of Nitrogen oxides to the atmosphere is prevented by exhaust gas recirculation (EGR) systems and selective catalytic reduction (SCR) systems. Nitric Oxide ( $\text{NO}$ ) Oxides to Nitrogen Oxide ( $\text{NO}_2$ ).  $\text{NO}_2$  irritates the skin and the lungs and creates smog particles.

**Carbon soot particles (Particulate matter)** are formed through a variety of causes. One of them being a lack of oxygen in the combustion process. Rich mixture areas can form in a combustion chamber as a result of oxygen deficiency, effectively not allowing for the fuel present in these areas to be burned efficiently.

The quantity of particles in exhaust gases is generally affected by the quality of the combustion process. The quality of combustion depends on fuel atomization, vaporization and dispersion into the combustion chamber.

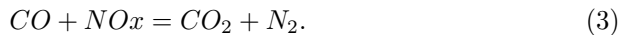
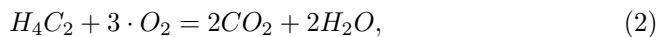
To limit the formation of carbon soot particles, engine parameters can be optimized. Designing optimal flow of gases in the inlet and outlet ports, higher fuel injection pressures, or the optimization of combustion chamber can improve the creation of soot particles significantly. Particulate filters must be implemented in the powertrain system if the new emissions regulations are to be fulfilled [1].

### Strategies for emission reduction in diesel engines [1]:

- emissions component performance monitoring (On Board Diagnostics),
- treatment of exhaust gases before they are released into the atmosphere,
- improvement and new technologies in engine management systems.

The composition of exhaust gases and particulate matter coming out of the combustion process can be affected in three ways. The first way of interfering with formation of exhaust elements is the formation and precision in air-fuel mixture creation, atomization of fuel while injecting into the cylinder, the general layout of fuel spray pattern, timing for injection period, beginning of injection and the character of entering air mass. The second way is, as mentioned before in reducing carbon soot particles, optimization of the engine combustion chamber, air and exhaust gases flow and overall improvements of engine components precision. The third way is to treat exhaust gases after they exit the combustion chamber with a catalytic converter, particulate filter, EGR system, SCR system and others [3].

## 2.1 Experimental Analysis



For subsequent measurements, a gasoline Hyundai 1.6 G4FC engine equipped with indirect MPI injection was used. This power unit was used to monitor the emissions generated by the combustion process. For the purposes of measuring exhaust emissions produced by the combustion process the catalytic converter had to be removed from the exhaust pipe of the measured engine unit.

Equation (1), Eq. (2) and Eq. (3) indicate the ideal decomposition of the individual gases using a 3-way oxidation catalytic converter. With ideal decomposition, only carbon dioxide ( $CO_2$ ), nitrogen ( $N_2$ ) values would be measured

downstream of the catalyst and the presence of water ( $\text{H}_2\text{O}$ ) would be recorded.

In real measurements, the presence of unburnt Hydrocarbons (HC) and Carbon Monoxide (CO) can be observed after the catalyst. In the case of the measurements mentioned in this work, the gas concentration will be higher due to the lack of catalyst.

To measure the emissions, the BOSCH BEA 050 Emission Analyzer was used. Three different measurement scenarios were conducted on the vehicle:

1. with knock sensor feedback and normal operating conditions,
2. with knock sensor feedback and increased intake air temperature,
3. with the knock sensor feedback disconnected and with increased intake air temperature disconnected.

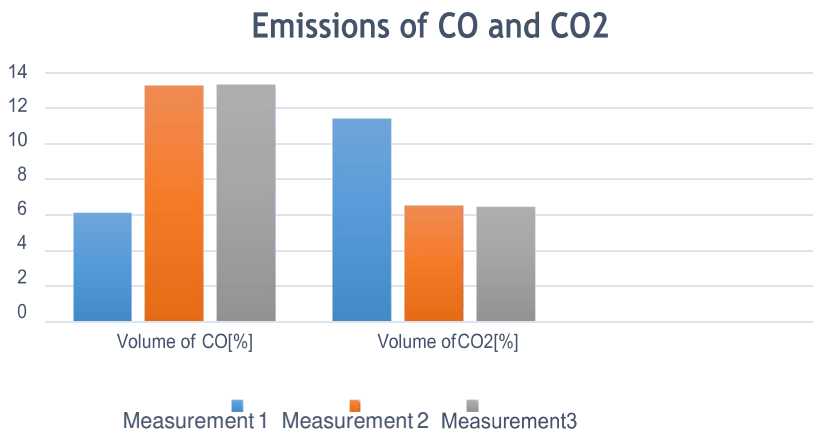
**Table 1.** Measured values of emission components during idle.

IDLE	RPM [ $\text{min}^{-1}$ ]	CO[%]	HC[ppm]	CO <sub>2</sub> [%]	O <sub>2</sub> [%]	Lambda [-]
Meas. 1	660	0.376	278	14.48	0.91	1.017
Meas. 2	660	0.445	284	14.4	0.951	1.016
Meas. 3	660	0.437	266	14.48	0.89	1.015
LOAD	RPM [ $\text{min}^{-1}$ ]	CO[%]	HC[ppm]	CO <sub>2</sub> [%]	O <sub>2</sub> [%]	Lambda [-]
Meas. 1	5210	6.076	115	11.41	0.17	0.84
Meas. 2	5180	13.23	183	6.49	0.08	0.65
Meas. 3	5190	13.3	209	6.44	0.07	0.647

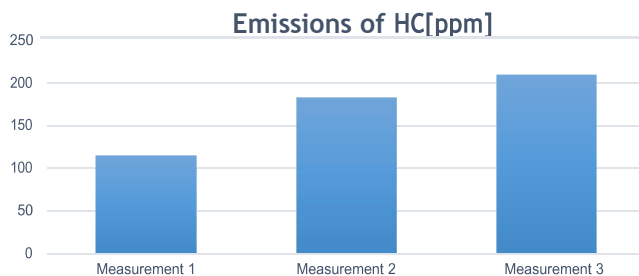
The presence of an increased amount of Hydrocarbons (HC) in measurements 2 and 3 indicates that there is imperfectly burned fuel in the exhaust gases. An incomplete fuel burn occurs during detonation combustion. This measurement confirms the deterioration of the combustion process itself due to the presence of detonation combustion.

Increased Carbon Monoxide (CO) values are due to unconverted Carbon Monoxide (CO) to Carbon Dioxide (CO<sub>2</sub>), which is partly attributable to the lack of a catalyst (normally CO should be less than 4 % vol., vehicles without a catalyst of less than 6 % vol.). In part, this can also be attributed to reduced oxygen (O<sub>2</sub>) presence. Measurements 2 and 3 with elevated intake air temperature show an increased amount of Carbon Monoxide (CO) compared to the measurement 1.

In measurements 2 and 3 (increased intake air temperature - in the range between 56-67C), there was a noticeable increase in Carbon Monoxide (CO) emissions, which, in addition to incomplete combustion of Hydrocarbons (HC), also shows a problem with the supply of oxygen when burning the mixture.



**Fig. 4.** The volume of exhaust gases during measurements.



**Fig. 5.** Measured volume of hydrocarbons.

## Acknowledgement

This paper presents the results from the project reg. no. SP2019/117 funded by the Student Grant Competition of VSB–Technical University of Ostrava. This research was supervised by Ing. Petr Simonik, Ph.D.

## References

1. Audi of America, Inc. : Motor vehicle exhaust emissions, Emission control and standards, 40 p., USA 2001.
2. Vlk, F. : Prislusenstvi vozidlovych motoru, Brno 2002, ISBN 80-238-8755-6.
3. Advanced Automotive Fault Diagnosis, 2nd Edition. USA 2004, Butterworth-Heinemann Ltd. 2006, 288 p., ISBN 0-7506-6991-8
4. RIBBENS, B., W.: Understanding Automotive Electronics, Sixth Edition, USA 2003, Elsevier Science, 480p., ISBN 0-7506-7599-3.

# The Software Analysis of Electronic Diesel Control Systems

Tomáš Klein

Department of Electronics, FEECS,  
VŠB – Technical University of Ostrava, 17. listopadu 15,  
708 33 Ostrava – Poruba, Czech Republic  
tomas.klein@vsb.cz

**Abstract.** This paper describes the analysis of the engine control unit software from Bosch EDC for the purposes of simulation of control algorithms in Matlab Simulink design. The analysis is performed by investigating original settings (fields of constants) of a specific vehicle. These simulations can then be compared with a real vehicle. Consequently, this algorithm can be used for a fully programmable controller platform supporting a model-based algorithms.

**Keywords:** Bosch EDC · OLS300 · control and regulation · Simulink · WinOLS.

## 1 Introduction

The control algorithms used in vehicle ECUs are the know-how of developers or suppliers of control units. With the help of software WinOLS with real time emulator OLS300 and reverse engineering methodology it is possible to understand how the algorithm works. Section 2 describes the program WinOLS, which is used for software analysis. Next section describes an analysis of engine control unit fields of constants as a reference for creating a model-based algorithm in Matlab Simulink.

## 2 Software WinOLS

WinOLS is an application, which is written specially for modifying the memory contents of ECUs (FLASH, micro FLASH, EEPROM). It facilitates the searching and finding of maps, which can then be named, changed and viewed in different ways. To change the data, different functions are available to edit the maps.



Switching of the view: 8bit, 16bit, 32bit, decimal, hexadecimal, binary.

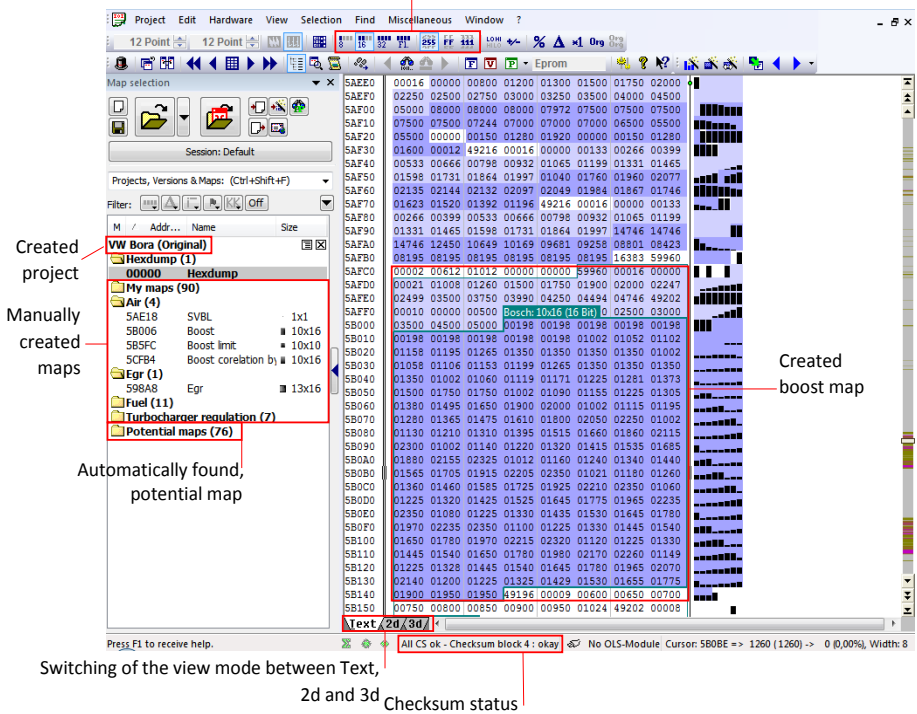


Fig. 1: WinOLS main screen.

## 2.1 Fields of Constant Search

After creating a new project, WinOLS will automatically start searching for potential maps. These maps can be edited into a more appropriate form - by naming, adding axes and units, or editing views.

WinOLS can not automatically identify the map. For easier and faster work it is necessary manually describe the desired maps and edit them into a preferable form. Another option is to import a Damos file, which comments on individual places of the fields of constant data area.

## 2.2 OLS300 Module

The OLS300 is an add-on module from EVC, which emulate the FLASH memory of the engine control unit. With software WinOLS, it is possible to change all parameters from the emulated memory in real time while the engine is running.

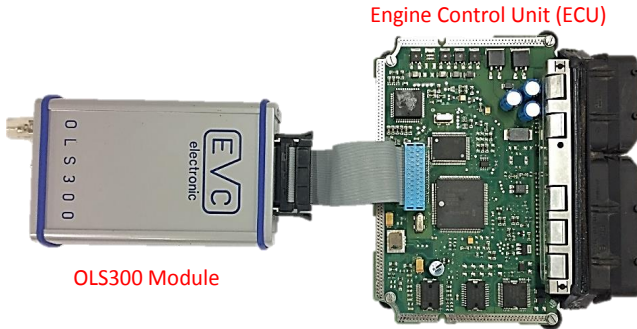


Fig. 2: ECU with connected OLS300 Module

Figure 2 shows the OLS300 emulator connected to the EDC15P+ ECU. The original FLASH memory has been removed and replaced with special OLS344 interface. Each control unit software contains several checksum points blocks. Checksum is additional information used to check data for errors. If you want to make changes in fields of constant while the engine is running, you need real time checksum correction. Otherwise, the microcontroller evaluates the error and engine stops.

### 3 Software Analysis of Electronic Diesel Control

Software for analysis was read from the vehicle containing the Bosch EDC15P+ control unit. The analysis was divided into 2 areas - fuel injection and turbocharger regulation.

#### 3.1 Fuel Injection

Table 1: Accelerator pedal map [mg/str].

%	Driver wish (Pedal position, Rpm) / mg/str							
	1	4	10	25	37	56	80	100
min-1								
0	18,70	41,90	46,00	54,00	61,70	68,90	70,00	70,00
399	7,70	27,88	33,34	41,20	49,50	62,70	70,00	70,00
609	0,00	19,62	25,80	34,70	43,60	59,10	70,00	70,00
693	0,00	16,00	22,70	32,00	41,40	57,60	70,00	70,00
798	0,00	11,40	19,00	28,20	37,60	56,30	70,00	70,00
903	0,00	6,60	14,50	24,60	33,90	54,70	70,00	70,00
1008	0,00	4,90	9,00	21,00	30,30	53,10	70,00	70,00
1113	0,00	3,80	7,00	18,35	27,20	51,32	69,00	70,00
1218	0,00	2,80	5,75	15,70	24,60	49,60	68,00	70,00
1491	0,00	1,50	3,50	11,50	20,66	45,60	66,00	70,00
1995	0,00	0,80	2,10	9,00	17,00	41,32	62,00	70,00
2499	0,00	0,70	2,00	7,50	15,00	38,32	59,50	70,00
3003	0,00	0,50	1,50	6,50	13,00	35,50	57,28	67,84
3990	0,00	0,00	1,00	4,99	10,90	31,88	52,78	64,40
4998	0,00	0,00	0,00	2,62	7,88	26,66	45,78	59,96
5355	0,00	0,00	0,00	0,50	1,10	20,50	29,50	45,46

The basic map is the required amount of fuel - the accelerator pedal map. The resulting value is very important for other control and regulation processes in the engine control unit (e.g. the required fuel injection length, the required boost pressure etc.). This map gives fuel injection amount [mg/str], which is further adjusted (limited) by a pair of restriction maps - torque limiter and smoke limiter (shown in Fig. 3).

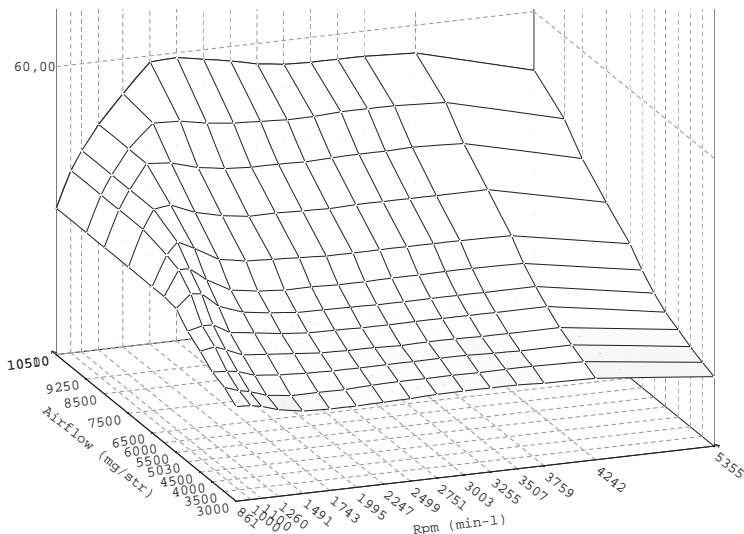


Fig. 3: Smoke limiter - 3D view.

Another very important fuel injection map is the start of fuel injection map (Tab. 2) and the fuel injection length map.

Table 2: Start of fuel injection map [°].

mg/str min-1	0,00	5,00	10,00	15,00	20,00	25,00	27,50	30,00	35,00	40,00	45,00	50,00
100	7,99	7,99	7,99	7,99	7,99	7,99	7,99	7,99	7,99	7,99	7,99	7,99
400	-1,01	-1,01	-1,01	0,49	3,00	7,22	11,11	15,00	15,00	15,00	15,00	15,00
800	-1,01	-1,01	-1,01	0,49	3,00	7,22	11,11	15,00	15,00	15,00	15,00	15,00
1000	-1,01	-1,01	-1,01	0,49	3,00	7,22	11,11	15,00	15,00	15,00	15,00	15,00
1250	0,49	0,49	0,49	0,49	3,00	7,22	11,11	15,00	15,00	15,00	15,00	15,00
1500	1,50	1,50	1,50	1,50	3,00	7,22	7,97	8,74	9,96	10,74	11,25	11,51
1750	3,00	3,00	3,00	3,00	4,95	7,22	7,99	8,77	9,96	10,74	11,25	11,51
2000	4,50	4,50	4,50	4,50	6,70	8,04	8,74	9,45	10,22	10,99	11,51	12,24
2250	5,72	5,72	5,72	6,49	8,06	9,05	9,77	10,50	11,23	12,00	12,49	13,01
2500	6,96	6,96	6,96	7,74	9,40	10,22	10,85	11,51	12,24	13,01	13,52	14,02
2750	8,25	8,25	8,25	9,02	10,43	11,37	12,05	12,73	13,48	14,25	14,77	15,28
3000	9,00	9,00	9,00	9,99	11,46	12,47	13,08	13,71	14,49	15,24	16,01	16,50
3500	10,76	10,76	10,76	12,00	13,45	14,60	15,17	15,70	16,74	17,51	18,26	19,52
4000	12,49	12,49	12,49	13,97	15,49	16,71	17,18	17,67	18,70	19,48	22,01	22,27
4250	13,48	13,48	13,48	14,88	16,38	17,70	18,19	18,68	19,69	20,46	23,51	23,51
5000	16,22	16,22	16,22	17,72	19,29	20,58	21,12	21,68	22,71	23,74	25,78	25,78

The start of fuel injection is given in degrees of camshaft rotation. The X-axis indicates the actual amount of fuel injected [mg/str], the Y-axis indicates the current engine speed [rpm]. The fuel injection length map determines how many degrees of camshaft rotation at a given speed is needed to inject the required amount of fuel.

### 3.2 Turbocharger Regulation

The basis for regulating the turbocharger is a map of the desired value of the intake air pressure (Tab. 3). The required boost pressure values are absolute, including atmospheric pressure. This reference setpoint is further limited by the boost limiters and corrections.

Table 3: Boost pressure map [mbar].

mg/str min-1	0,0		10,0		20,0		30,0		45,0		
		5,0	15,0	25,0	35,0	50,0					
0	198	198	198	198	198	198	198	198	198	198	
21	1002	1052	1102	1158	1195	1265	1350	1350	1350	1350	
1008	1002	1058	1106	1153	1199	1265	1350	1350	1350	1350	
1260	1002	1060	1119	1171	1225	1281	1373	1500	1750	1750	
1500	1002	1090	1155	1225	1305	1380	1495	1650	1900	2000	
1750	1002	1115	1195	1280	1365	1475	1610	1800	2050	2250	
1900	1002	1130	1210	1310	1395	1515	1660	1860	2115	2300	
2000	1002	1140	1220	1320	1415	1535	1685	1880	2155	2325	
2247	1012	1160	1240	1340	1440	1565	1705	1915	2205	2350	
2499	1021	1180	1260	1360	1460	1585	1725	1925	2210	2350	
3500	1060	1225	1320	1425	1525	1645	1775	1965	2235	2350	
3750	1080	1225	1330	1435	1530	1645	1780	1970	2235	2350	
3990	1100	1225	1330	1445	1540	1650	1780	1970	2215	2320	
4250	1120	1225	1330	1445	1540	1650	1780	1980	2170	2260	
4494	1149	1225	1328	1445	1540	1645	1780	1965	2070	2140	
4746	1200	1225	1325	1429	1530	1655	1775	1900	1950	1950	

Table 4: VTG setpoint map [%].

min-1 mg/str	N75 Duty cycle (Rpm, Amount of fuel) / %									
	760	780	1000	1150	1350	1500	1650	1743	1911	2058
0,0	25,0	25,0	25,0	25,0	28,0	34,0	37,0	39,0	41,5	43,5
5,0	25,0	25,0	25,0	25,0	28,0	34,0	37,0	39,0	41,5	43,5
10,0	25,0	25,0	25,0	25,0	28,0	34,0	37,0	39,0	41,5	43,5
15,0	20,0	20,0	20,0	20,0	28,0	37,3	40,7	42,7	46,0	48,4
20,0	20,0	20,0	20,0	20,0	28,0	40,3	43,2	45,2	48,5	50,9
25,0	20,0	20,0	20,0	20,0	28,0	42,3	45,4	47,2	50,5	53,1
30,0	20,0	20,0	20,0	20,0	31,0	44,3	47,6	49,6	52,4	54,9
35,0	20,0	20,0	20,0	20,0	35,0	45,6	49,6	53,3	54,3	56,8
40,0	20,0	20,0	20,0	20,0	38,0	47,0	52,1	59,0	60,8	61,3
45,0	20,0	20,0	20,0	20,0	40,0	47,0	52,8	59,3	62,0	63,8
50,0	20,0	20,0	20,0	20,0	40,0	47,0	54,0	57,4	61,8	66,1
55,0	20,0	20,0	20,0	20,0	40,0	47,0	54,9	56,8	60,7	66,0
58,0	20,0	20,0	20,0	20,0	40,0	48,0	54,9	56,9	61,7	65,0

Very important map for regulating VTG turbocharger is N75 position set-point. The map indicates the desired turbocharger blade geometry setting [%] for the given engine speed and the given fuel injection amount. Subsequently, an integrated PID controller intervenes in the boost pressure control, which compares the actual and desired intake air pressure measured by the MAP sensor on the engine intake manifold and adjusts the turbocharger geometry value based on the control deviation. PID regulator values are given in Tab. 5.

Table 5: PID regulator values for turbocharger regulation.

Amount of fuel [mg/str]	$K_p$	$\tau_i$	$\tau_d$
0,0	0,6020	0,0700	0,1040
5,0	0,5650	0,0700	0,1960
10,0	0,4080	0,1520	0,2135
15,0	0,3666	0,1872	0,2132
25,0	0,3130	0,2104	0,1867
30,0	0,3040	0,2232	0,1623
37,5	0,3040	0,2104	0,1196

## Acknowledgement

This paper presents the results of the project reg. no. SP2019/117 funded by the Student Grant Competition of VSB–Technical University of Ostrava. This research was supervised by Ing. Petr Simonik, Ph.D.

## References

1. BOSCH R. *Electronic Diesel Control EDC*. Bentley Publishers, 2003. ISBN 978-0-83-761088-7.
2. BOSCH R. *Diesel Fuel-Injection Systems Unit Injector System/Unit Pump System: Bosch Technical Instruction*. Bentley Publishers, 2000. ISBN 978-0-83-760615-6.
3. Volkswagen AG, Wolfsburg. *Electronic Diesel Control EDC16*.

# Energy management architecture of experimental electric vehicle

Martin Kořený

Department of Electronics, FEECS,  
VŠB – Technical University of Ostrava, 17. listopadu 15,  
708 33 Ostrava – Poruba, Czech Republic  
martin.koreny@vsb.cz

**Abstract.** This article describes energy management architecture of the university experimental electric vehicle named Democar. The vehicle implements several electrical and electromechanical systems with various power requirements like steering control, power train, battery management, braking system etc.

**Keywords:** electric vehicle, energy management, ECU, battery, system architecture.

## 1 Introduction

The electrical system of the Democar is divided into six subsystems as shown in Fig.1. with following purpose:

- Central Control Unit (CCU) - responsible for data harvesting and evaluation from all other units. It acts also as a gateway between remote control and vehicle private CAN. The vehicle is remotely operated via 16 channels remote control Jeti – Duplex DC-16 EX, 2.4GHz. Several values like vehicle speed (acceleration, braking), vehicle direction (turn, forwards, backwards) or headlights functionality is implemented to be controlled remotely.
- Energy Management Control Unit (EMCU) – due to the fact that the only energy source is battery energy the system manages energy transfers from and to the battery, realizes safety features related to the electrical shock, fail safe reactions when sudden power loss occurs and the vehicle instantly lose braking and steering capabilities, battery protection against dangerous states like over/under voltage, short circuit, high temperature etc.
- Steering Control Unit (SCU) - implements steer-by-air functionality over the remote control. The system consists of stepper motor with a linear mechanism which was after intensive testing due to its insufficient force needed to be supported by power steering which creates up to 80A current draw from the battery pack. Therefore, the battery pack has increased in capacity.

- Drive Control Unit (DCU) - management of four 3f synchronous motors with permanent magnets. The system can manage 2WD or 4WD. Two front motors are connected to front wheels over the gearbox, similarly for rear motors. The main challenge for the system is very precise synchronization with brake system because when intensive braking is requested motors has to not negatively influence braking.
- Brake Control Unit (BCU) - implements braking functionality and is tightly connected to the drive system. Brakes are on all wheels. The system consists of a hydraulic regulator which is another significant power requirement and is essential in case of power loss where in such a case safely stops the vehicle by accumulated hydraulic energy in the regulator.
- Light Control Unit (LCU) - implements body lighting functionality by utilizing LED headlights and rear lights. There are also small signal lights used to inform user visually of the vehicle status by color and/or state change.

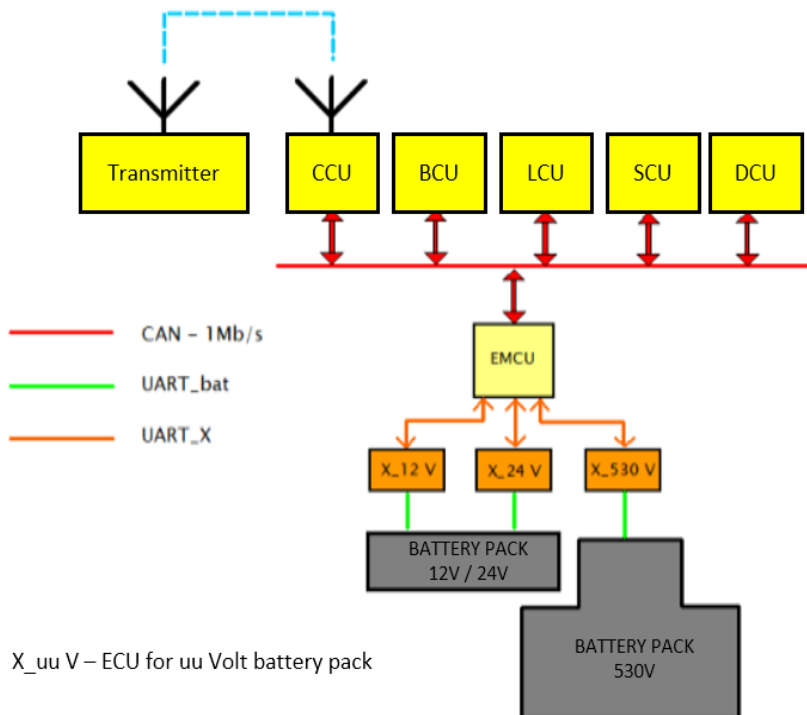
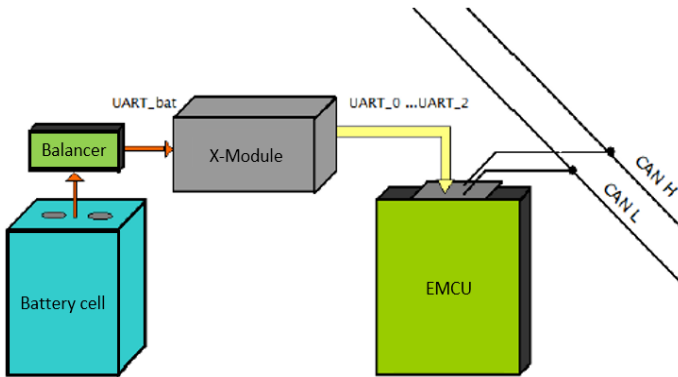


Fig. 1. Democar system architecture [2]

## 2 Energy management concept



**Fig. 2.** Energy management concept

In the Fig.2 is principal architecture of one three energy management blocks see Fig.4 used in Democar. As energy source there are exclusively installed LiFePo4 cells of nominal capacity 20Ah. Each cell has its own passive balancer see Fig.3 which communicates over UART with so called X-Module which acts as UART gateway able to communicate with max. 64 balancers. X-Module measures current by voltage drop on current shunt and further sends measured data over UART to EMCU for processing. Balancers and X-Module are off the shelf parts.

There are in total currently three battery packs used in Democar due to different power requirements:

- 12V pack for ECUs, body lighting, brake system and steering servo made of 4S4P (four in series and four in parallel) cells of total capacity 80Ah
- 24V pack for frequency drives logic and steering made of 8S2P cells of total capacity 40Ah
- 530V pack for powering the powertrain motors made of 156 cells connected in series

If the power is interrupted the vehicle is considered as uncontrollable and therefore very dangerous to its near surrounding. Those aspects were taken into the design consideration so the system secure the following features:

- Full control over energy from and to battery packs
- Adaptive charging
- Real time monitoring of battery values (SOC, temperature, cell voltage, total pack current, balancing current)
- Switching off at failure states like insufficient isolation value, overtemperature, overcurrent, short circuit etc.).



CCU basically controls EMCU only in case of power on/off states for the complete vehicle electrical system.

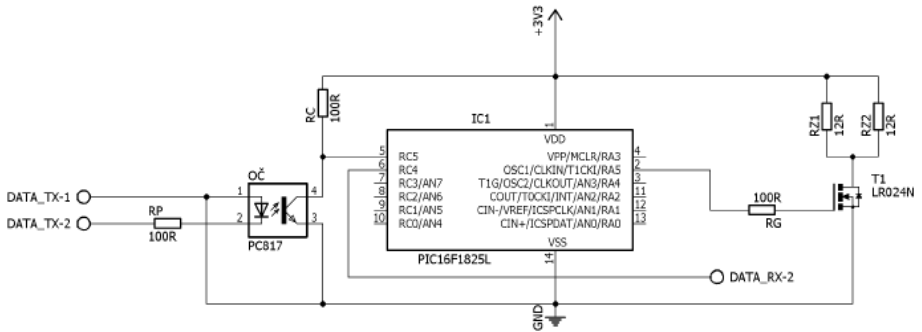


Fig. 3. Balancer schematic

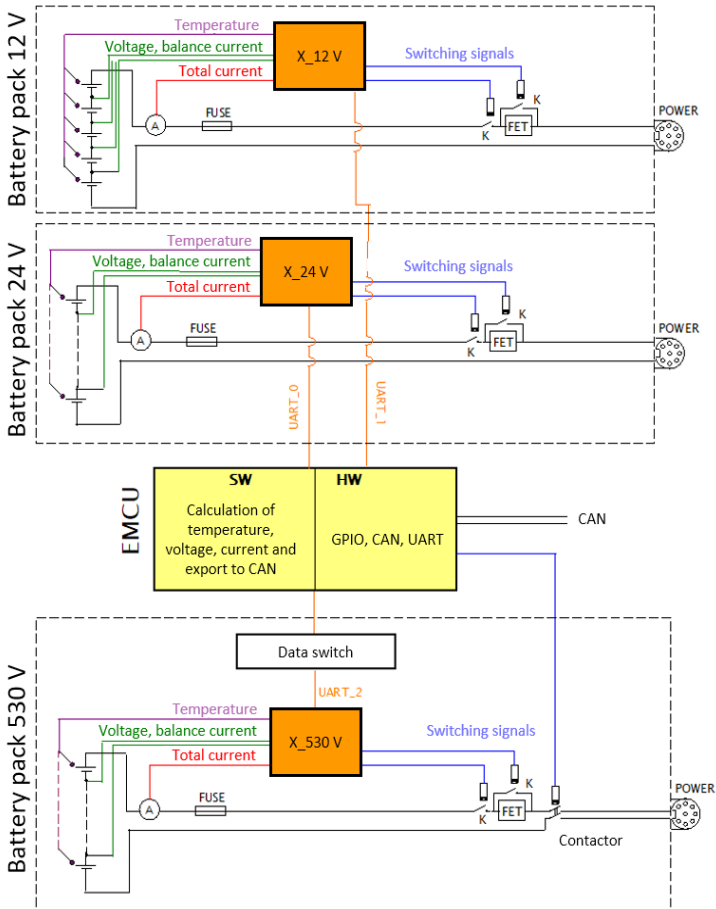


Fig. 4. Energy management architecture

All 3 packs have its own X-Module with switches to be able to quickly disconnect from the load in case of emergency and in case of charging current regulation.

Special care had been taken for 530V pack due to its direct connection to the DC circuit of the frequency drives. The DC circuit has very high capacity so to decrease inrush current resistor has to be switched on to the current path and this is driven by time relay.

### 3 EMCU Application software

Functional safety according to ISO 26262 was analyzed with safety cases varying from ASIL B to ASIL D. Therefore, ECU is equipped by two core automotive grade 32-bit microcontroller Qorivva MPC5643L which supports up to ASIL D applications. It has to be noted that current application SW was not developed according to A-spice and all ISO26262 standards, this will be the future focus. The IDE used for application software development is CodeWarrior with combination of MQX real time operating system.

The application starts by the initialization of all peripherals and creating two tasks. The TASK1 is responsible for data acquisition and the second for CAN communication. In the TASK1 there is a request generated for reading battery pack data from the UART\_x of one of the X-Module (see Fig.4). Until X-Module responds TASK1 is suspended and waits for data retrieval. When data are received data completeness check is performed, if the check is successful data are stored to the array and total pack voltage is calculated in 2 bytes format with a factor of 0.01.

Next step is to check each cell voltage for over/undervoltage of all cells in the pack. If the check fails corresponding flags are set.

Task1 continues to identify the maximal balancing current of all cells in the packs. The same in principle is check for maximal temperature.

When TASK1 has processed all values TASK2 is activated to assembly CAN message in the format visible in Tab1. The message structure is the same for all three packs. Data from each pack are identified by a unique ID. 530 V pack has ID 1500, 24 V pack has ID 1400 and 12 V pack has ID 1300. The message is sent over CAN bus to other ECUs.

ID	Upack Lo	Upack Hi	Cell max. temp	Max ballanc- ing current	Undervolt- age flag	Overvolt- age flag
1500	0x30	0xD9	0x19	0x00	0x00	0x00

**Tab. 1.** CAN message example

## 4 Conclusion

The energy management concept of the Democar was implemented and fully tested by simulating over/under voltage of the complete pack as well as individual cells. Charging current regulation is also working as intended. Thanks to the parametrization of the energy management unit all values can be easily customized for further experimental purposes. Future intention is to replace ECUs in the Democar by the powerful professional ECU solutions namely to comply ISO26262 requirement and to use benefits of e.g. faster FlexRay for implementing autonomous driving features. Of course, application software has to be developed and tested at the university. Experience from developing and implementing the current system will be very beneficial and gives a solid basis for enhancements and new features.

## 5 Acknowledgment

In the paper, there are the results of the project reg. no. SP2019/117 funded by the Student Grant Competition of VSB-Technical University of Ostrava. This research was supervised by Ing. Petr Šimoník, Ph.D.

## 6 References

1. JAROLIM, A.: Návrh a praktická realizace koncepce managementu napájení vozidla s elektrickým pohonem Democar. Ostrava, 2016, Diplomová práce. Vysoká škola báňská – Technická univerzita Ostrava. Vedoucí práce Ing. Petr Šimoník, Ph.D.
2. OBRUSNIK, S.: Návrh a realizace energy managementu demonstračního vozítka s elektrickým pohonem. Ostrava, 2018, Diplomová práce. Vysoká škola báňská – Technická univerzita Ostrava. Vedoucí práce Ing. Petr Šimoník, Ph.D.

# Safety Braking System by Wire

Samuel Przeczek

Department of Electronics, FEECS,  
VŠB – Technical University of Ostrava, 17. listopadu 15,  
708 33 Ostrava – Poruba, Czech Republic  
samuel.przeczek@vsb.cz

**Abstract.** This paper deals with the concept of the braking system by wire. It composes of three parts: an electro-hydraulic ABS unit with additional sensors and actuators controlled by a master control unit, an integrated emergency brake and the applied brake control algorithms. Implementation took place on a quad bike called "Democar". It is equipped with control units such as electric drive control unit, steering control unit, lighting control unit, energy management control unit, and central control unit. All of the control units communicate with each other via CAN bus. The emergency brake is used in the event of a power failure or failure of the service brake system.

**Keywords:** ABS, ABS/ASR/ESP module, application software, brake system, C/C++, CAN bus, control unit, electric vehicle, emergency brake, microcontroller, MQX.

## 1 Introduction

Two important concepts present the main role in the automotive industry: safety and reliability. This fact makes braking systems particularly important. In the case of brake failure, the car becomes more dangerous for the passengers in the vehicle but also for other road users. Therefore, it is important to diagnose faults that can be present within the system. The braking system provides a stopping force and blocks spontaneous movement of the vehicle. Brake systems principle is based on increasing the frictional force. The kinetic energy of the vehicle is converted to heat during braking and escapes into the surroundings.

The classic hydraulic brake system composes of the following components: a main brake cylinder, a vacuum booster, a buffer tank for brake fluid, and connecting piping. According to the law, it is mandatory that the hydraulic part is divided into two separate circuits. These circuits are continuously controlled through the brake pedal. A failure of one of the circuits will not cause a complete failure of the braking system. Some of the brake elements will remain pressurized and therefore functional.

## 2 The braking system of Democar

The Democar is an unmanned remotely controlled vehicle, brake pedal can't be used for braking. The braking system pressure is generated by the ABS / ASR / ESP hydraulic module. This module is controlled by the control unit. The control unit receives and processes commands from the RC transmitter, which are entered by the user. It also communicates with the other control units via CAN bus. The module also serves as an emergency brake which ensures stopping of the vehicle in case of an emergency.

## 3 Hydraulic Unit

The task of the hydraulic modulator (shown in Fig. 1) is to change the brake pressure which causes the brake force to change. The modulator is equipped with a pump which changes the brake pressure levels. A damping chamber is present in the system. Its purpose is to dampen pressure fluctuations in the brake circuit. The modulation of the braking effect occurs through the inlet and outlet valves for hydraulic circuits of each wheel [2]. The modulator is placed between the master cylinder and the individual brake cylinders. This modulator is an actuator that receives and executes commands from the controller. Communication with the other control units is performed via CAN bus. This bus is also used for the purposes of serial diagnostics. The power unit is divided into three branches: the power supply of the electric motor and the control unit, power supply for solenoid valves, and power supply which is activated through the switch box.

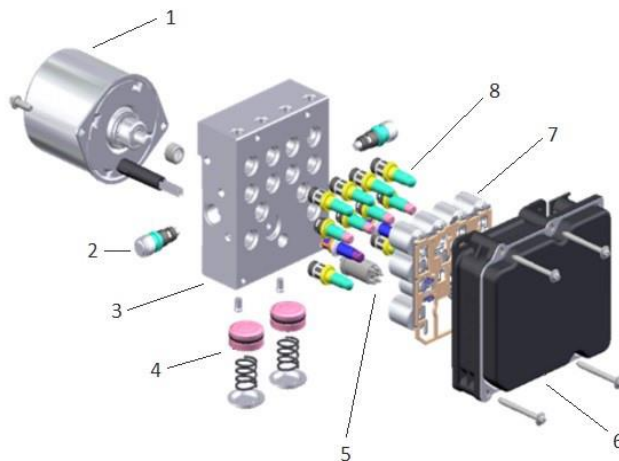


Fig. 1. Hydraulic Unit [2]

The modulator consists of the following components: 1 - motor 2 - pump (2pc), 3 - hydraulic valve block, 4 - accumulator (2pc), 5 - pressure sensor, 6 - control unit (ECU), 7 - coils (12pc), 8 - solenoid valve (12pc).

## 4 Application Software

The entire application software can be divided into six interdependent tasks. This is one primary (main task), which creates and runs the other ones. Listing each task:

- CAN 0 Rx (CANcontrol),
- CAN 0 Tx (CANcontrol),
- CAN 1 Rx (CANabs),
- CAN 1 Tx (CANabs),
- CHECK ABS.

The Main Task occurs after the power supply gets turned ON as the first initialization of CAN modules. In functions CAN Init 0 and CAN Init 1 the required parameters of the buses are set, communication mailboxes are created, and the operating function interrupt to receive data from the CAN buses is installed. The activation of the bus is executed in the last step. After this step, the activation of tasks, which serve for receiving and sending data via the CAN bus is performed. Each of the CAN modules has its own task to send and to receive data. These tasks also deal with functions for braking. The CHECK ABS task is responsible for checking the status of ABS / ASR / ESP module. All of these procedures are performed only once, at the startup.

The function of CAN 0 Rx task will be described now. Its purpose is to receive data on the bus CANcontrol. Task runs in a cyclic mode, in which it receives data. For receiving data, the library functions for MQX are utilized and the received data are stored in the variable and generate an event. As prevention for overwriting of the data, the event data is locked. The ID is checked and then further processed. The variable is then released and awaits new data. This task can receive data transmitted from the transmitter via the central control unit, steering control unit and drive control unit. Data received from the transmitter can request a start of the handbrake and a requirement to drive forward or backward. The requirement for driving forward or backwards is evaluated in the braking algorithm as a condition for determining whether to apply the brakes. By receiving data from the steering control unit, it can be determined only whether the module is working properly or whether it has encountered an error. In case of failure of this module, emergency stop is performed. Data about the status and motor speeds are received from the drive control unit. Again, when an error of the DCU is detected, the emergency stop is performed. The engine speed data is used as criteria for evaluating the intensity of braking.

Task CAN 1 Rx receives data from the ABS / ASR / ESP module on bus CANabs. These data are evaluated for communication properties to determine a faulty state of the module. This evaluation takes place in the task CHECK ABS. This evaluation is described below. The task CAN 0 Tx task sends data on bus CANcontrol. It checks the defined identifier information to determine whether the ABS / ASR / ESP module is working properly. The drive control unit also uses this information. This message is sent every second. This reporting format is standardized, and it is also used in drive control unit and steering control unit.

**Table 1.** The format of messages indicating the status of the BCU

ID 140								
Correct	B0	B1	B2	B3	B4	B5	B6	B7
	0	0	0	0	0	0	0	0
Fault	B0	B1	B2	B3	B4	B5	B6	B7
	0	0	0	120	0	0	0	0

The function of CHECK ABS task will be described now. This task uses data that are received on the bus CANabs by ABS / ASR / ESP module. One identifier is chosen to set a steady state of the module. The value of the zero byte is checked in the selected identifier. After checking the value of the variable in which this value is stored, the value is deleted, and control runs again. In case that no value that determines the proper function of ABS / ASR / ESP module is received, the bus CANcontrol sends information about these circumstances to the DCU. The drive control unit then turns off and the brake control unit activates the emergency brake.

**Table 2.** Message format used for ABS control

ID	B0	B1	B2	B3	B4	B5	B6	B7
497	11	255	255	255	255	255	255	255

Data Sending to the ABS / ASR / ESP module runs in task CAN 1 Tx task. This task is also carrying out braking algorithm. The pattern of the required messages for starting the pump and opening / closing of solenoid valves is formed first. The function is called to pressurize the emergency brake and is only performed during the first run. A recall of this function is possible if the pressure in the accumulator is not sufficient for an emergency stop. The condition for starting the parking brake is then checked. The start of the parking brake relies on two criteria. The vehicle must be stationary, and the user must enter this requirement on the corresponding lever on the RC transmitter. The main braking loop follows afterwards. This is based on two conditions. The system checks the status of the steering control unit and drive control unit, which both must be running without faults. Otherwise, the emergency brake is engaged, and the vehicle is stopped. The braking algorithm is divided into five parts. These parts represent the intensity of braking. Conditions for achieving certain intensities are indicated by two parameters: vehicle speed and the acceleration lever position of the RC transmitter. Braking intensity is divided into 5 levels and is shown in Table 3.

**Table 3.** Intensity of braking while driving forward/reverse

Lever position	Velocity	From 5 to 10 km/h	To 20 km/h	To 30 km/h
<b>Forward</b>				
200 - 1500		1	2	3
1501 - 3000		2	3	4
3001 - 3768		3	4	5

<b>Reverse</b>			
-200 – (-1500)	1	2	3
-1501 – (-3000)	2	3	4
-3001 – (-4007)	3	4	5

The speed data obtained from the DCU is sent as RPM, it has to be recalculated for conversion to kilometers / hour. This intensity adjusting braking system is implemented because it provides smooth braking force and reduces wear on brake accessories. The intensity settings are executed by sequentially arranged data messages that are sent to ABS / ASR / ESP module. Because this procedure is executed in the diagnostic mode of the module, it is necessary to activate the diagnostic mode before any braking sequence. This mode is active only for 5 seconds. If the unit is not in this diagnostic mode, the messages that are sent to it are not executed. A security delay occurs after every message before sending the next one. Removing these delays leads to unpredictable behavior of ABS / ASR / ESP module. The module receives messages but is not able to perform them in such a short period of time.

**Table 4.** Delays

<b>Intesity 1</b>	<b>Intesity 2</b>	<b>Intesity 3</b>	<b>Intesity 4</b>	<b>Intesity 5</b>
5315 ms	5290 ms	5265 ms	5240 ms	5215 ms

After sending the message to activate the diagnostic mode, follows the message to activate the pump, open the intake valves (HSV) and close the overflow valve (TCV). This operation lasts the same time for all of the braking intensity settings - 80 ms. Followed by the message only to close the overflow valve. The pump is then turned off and the intake valves remain open. The intensity of the braking force is modulated using the delay between commands. Delay times are given in Table 4. Application software solves the following situations: 5 levels of intensity braking, parking brake, receiving from the transmitter, receiving the status of the DCU and SCU, receiving the motor speed from the DCU, checking the condition of the ABS unit, sending to other units the BCU status information, pressuring the emergency brake.

## 5 Conclusion

At present, the results of this proposal are implemented on development demonstration vehicle, so called Democar. Further improvements and developments are under way. All applications are realized within the research activity in the branch of automotive electronics in the Department of Electronics.



## 6 References

1. PALACKY, P., D. SLIVKA, P. HUDECEK and M. SOBEK. Synerga of Control Units in Electric Vehicle. In: International Scientific Conference EPE. Kouty nad Desnou, 2011, vol. 12. ISBN 978-80-248-2393-5.
2. BOSCH, R. Safety, Comfort and Convenience Systems. Robert Bosch GmbH. 1998. ISBN 978-0-837-60473-2.
3. BRANDSTETTER, P., J. VANEK and T. VERNER. Electric vehicle energy consumption monitoring. In: Proceedings of the 2014 15th International Scientific Conference on Electric Power Engineering (EPE). Brno: IEEE, 2014, pp. 589–592. ISBN 978-1-4799-3807-0. DOI: 10.1109/EPE.2014.6839444.
4. VO, H. H., P. BRANDSTETTER, C. S. T. DONG, T. Q. THIEU and D. H. VO. An Implementation on MATLAB Software for Stability Analysis of Proportional Controllers in Linear Time Invariant Control Systems. In: New Advances in Information Systems and Technologies. Cham: Springer International Publishing, 2016, pp. 671–680. ISBN 978-3-319-31231-6. DOI: 10.1007/978-3-319-31232-3 63.
5. BRANDSTETTER P., DOBROVSKY M. and KUCHAR M. Implementation of Genetic Algorithm in Control Structure of Induction Motor AC Drive. Advances in Electrical and Computer Engineering, 2014, vol. 14, iss. 4, pp. 15–20. ISSN 1582-7445. DOI: 10.4316/AECE.2014.04003.

## Acknowledgment

This work was supported by the European Regional Development Fund in the Research Centre of Advanced Mechatronic Systems project, project number CZ.02.1.01/0.0/0.0/16 019/0000867 within the Operational Programme Research, Development and Education. This research is partially supported by Grant of SGS No. SP2018/167, Research and development of electronic vehicle systems with autonomous control II, VSB–Technical University of Ostrava, Czech Republic.

# Frequency Applicability of the TMS320F28335 DSC Built in A/D Converter

Jan Strossa and Vladislav Damec

Department of Electronics, FEECS,  
VŠB – Technical University of Ostrava, 17. listopadu 15,  
708 33 Ostrava – Poruba, Czech Republic  
[jan.strossa.st@vsb.cz](mailto:jan.strossa.st@vsb.cz)

**Abstract.** This article deals with the frequency usability of Analogue/digital converter built in the TMS320F28335 digital signal controller with references to converter properties and possibilities of processing the converted data by the DSP unit. The block diagram of the A/D built in converter is stated at first, then the features of its working modes are described, the results of experimental testing are presented next.

**Keywords:** A/D Converter, Frequency Applicability, Sampling Frequency, TMS320F28335

## 1 Introduce

Digital signal controllers perform an irreplaceability role at the area of all the electronic controlled devices and equipment at the present time. The cooperation of control units based on the digital processing with the analogue/digital converters, which enable to process the physically continuing measured values by the control algorithms applied on the digital structures hardware, is necessary.

The quality of measuring and converting of the analogues signals effects the limit of the regulation accuracy, because these measured signals are usually used as feedback values for the regulation algorithms. The sampling frequency of the conversion limits the time response of the regulation, that also means that the steepness of the feedback value, which the regulator is capable react on, is limited – there is a system step response limitation. As the sampling frequency limits the step response, the signal-to-noise ratio limits the accuracy of the regulation.

## 2 TMS320F28335 DSC built in A/D converter

### 2.1 Block diagram generally

Generally, different block structures of connecting the digital processing units and its peripherals – e.g. A/D converters, PWM outputs ect. – are in use. The

TMS320F28335, which this paper deals with, is a DSP based on the concept, where the internal central processing unit and its build in peripherals - including the A/D converter - are integrated in one common case.

TMS320F28335 contains 16-channel A/D converter, which is internally divided into A and B sections, each section has its own sample/hold memory, which is multiplexed between the section’s inputs. Outputs of the S/H circuits are multiplexed into 1-channel A/D module. It means generally, that the TMS320F28335 contains in fact only 1-channel A/D converter, which can successively convert up to 16 analogue inputs, where two ones of the conversion sequence can be sampled at the same moment.

The order of the sequence is not fixed by the hardware and it can be set by the user program in the registry map. The total amount of the conversions per one sequence is also set in registers, so not all of the 16 channel have to be converted.

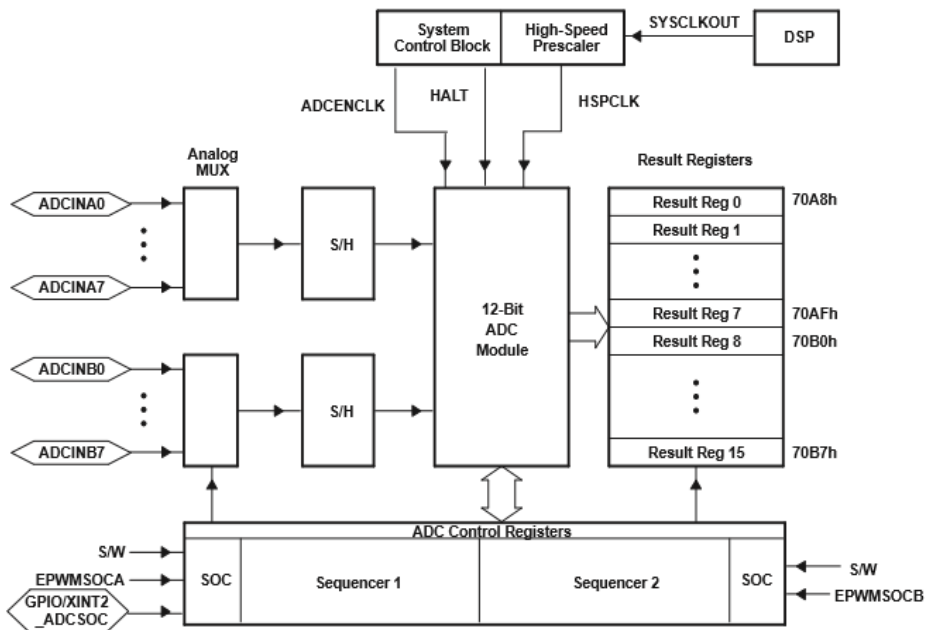


Fig. 1. Block Diagram of the ADC Module, taken from [1]

The built in A/D converter is synchronized by the internal clock, which can be set up to 150 MHz – according to the “Device clock Table” in [1]. The clock prescaler is placed between the system internal clock bus and the module of A/D conversion.

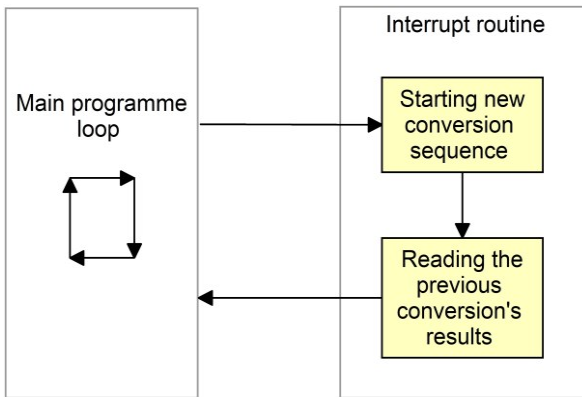
## 2.2 Cooperating of the converter with the CPU unit

The A/D converter processes the whole converse without using any part of the CPU core, this core can be used for applying some other software algorithms for dif-

ferent activities at the same time. But the CPU unit has to start separately every one sequence of the conversion.

The output of the A/D converter is connected to the system interrupt mask, the results of the conversion sequence are saved in the converter output mirrored registry.

The process of the input analogue values conversions can be started by the user program at once just at the moment, when reading the values is requested. It can be performed periodically as well - in that case the interrupt handling code of the finished conversion results reading contains also the start command of the new conversion sequence. The interrupt is called after the end of every conversion sequence then.



**Fig. 2.** Block diagram of program processing within CPU, when periodically A/D conversion is performed

### 2.3 Attainable sampling frequency

When the periodically starting of conversions is performed, as shown in Fig. 2, the sampling frequency is theoretically upper limited by the duration of taking one conversion sequence.

This time is affected by the internal clock bus frequency, which is used for synchronizing of the A/D converter, by the number of a converted input channels, by the sampling delay of sampling the signals to the sample/hold memories, and by the conversion duration of converting the sampled values to a digital form.

## 3 Obtained results

The possibilities of attainment the high sampling frequencies were inspected. The DSP TMS320F28335 with the internal clock configured to frequency 150 MHz, which was an input of the A/D converter clock prescaler, was used. The high speed part of the prescaler was set to 2 – prescaling ratio equalled 4, and the low speed part of the prescaler was set to 0 – prescaling ratio equalled 1, so the input synchronizing

frequency of the ADC module shown in Fig. 1 was 37,5 MHz, which is a quarter of the internal clock bus.

We set the sample store duration of sample/hold memories on 3 periods of the synchronizing clock. The following code of initial settings the registry was used:

```

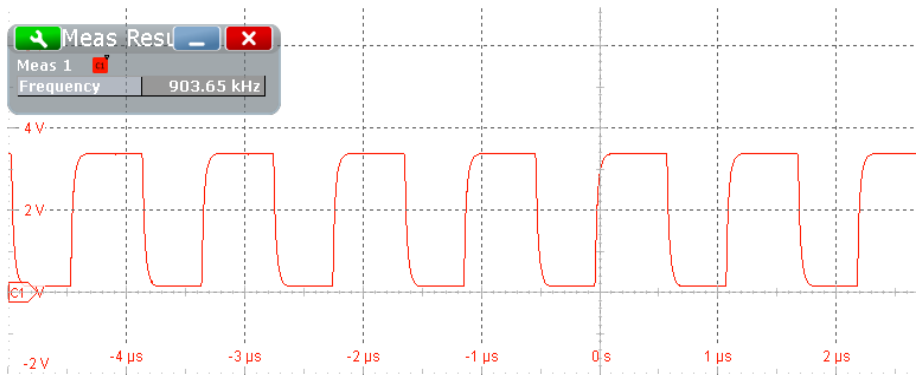
AdcRegs.ADCTRL3.bit.ADCCLKPS = 2;
AdcRegs.ADCTRL1.bit.CPS = 0;
AdcRegs.ADCTRL1.bit.ACQ_PS = 2;
    
```

It was ascertained, that using lower ratio of input clock prescaling or decreasing the time of storing the analogue values into the sample/hold memories notably decreases the signal-to-noise ratio, so the stated setting seems to define the upper sample frequency limits.

### 3.1 Amount of used analogue channels frequency impact

A code with a structure shown in Fig. 2 was created and a double toggling of a bit DSC output into an interrupt routine code to indicate starting and stopping the interrupt was inserted. This output was connected to the oscilloscope and its frequency equals the sampling frequency of A/D converter.

Then the number of converted/used analogues channels was changed and the impact of it on a sampling frequency was inspected.



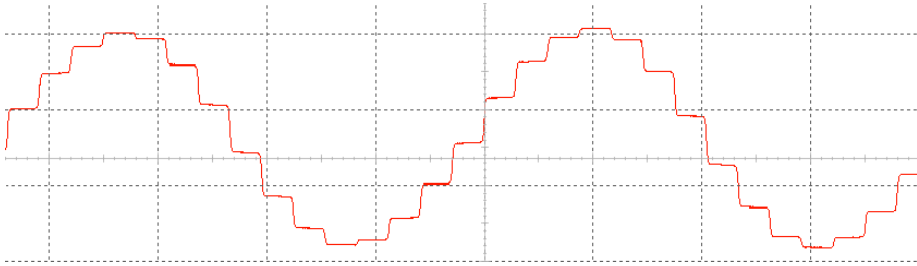
**Fig. 3.** Indication of an obtained sampling frequency, 1 channel is converted, conversions results are taken within the interrupt routine from 8 channels (no frequency impact)

The obtained sampling frequency for 1 channel used is approx. 904 kHz, as it is shown in Fig. 3.

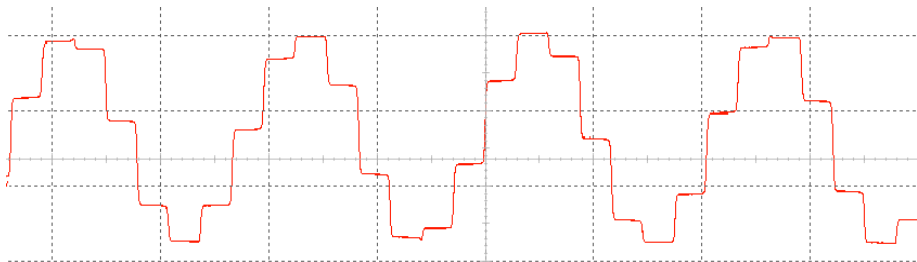
The obtained sampling frequencies in case of 8 and then for all channels enabled were obtained analogically – it is approx. 735 kHz for 8 channel used and 452 kHz for 16 channels used.

### 3.2 Obtained converted signals

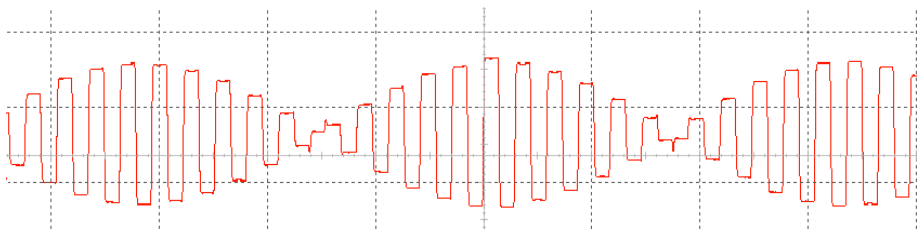
The following results of the converted input signals for 8 active channels were obtained, the converted values are displayed by reconstructions of the saved converted digital data. As an input signal, the sinus waveform was used in all cases.



**Fig. 4.** Reconstruction of the converted sinus 50 kHz waveform, 10 μs div



**Fig. 5.** Reconstruction of the converted sinus 100 kHz waveform, 10 μs div



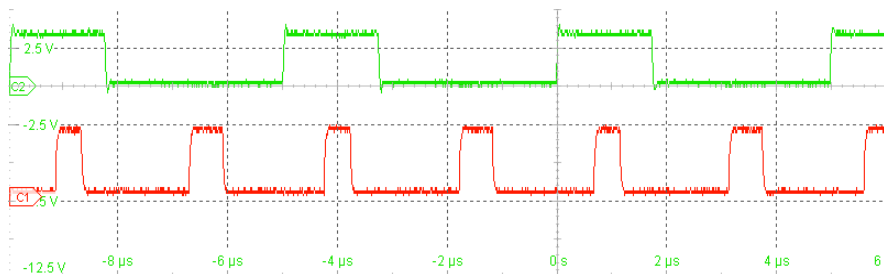
**Fig. 6.** Reconstruction of the converted sinus 350 kHz waveform – aliasing, 10 μs div

### 3.3 Possibilities of the obtained conversions results processing

The curve shown in Fig. 3 consists of two periodically repeating parts – higher voltage state, this time appears after the end of each conversion sequence and it includes the interrupt routine for taking the results of the conversions by a program running in the CPU. The second lower voltage part appears after the end of the interrupt routine and in this time the CPU works in the main loop or in the other parts of the code. In this part the CPU is able to process the regulation algorithms based on the converted values feedback.

The frequency possibilities of the converting were stated, but the frequency possibilities of all the DSP depends also on the CPU ability to process the measured values as fast, as the A/D converter can provide them.

The next result was obtained, when A/D converter was set to 8 channels conversions, and the calculating of the average values of the 3 of 8 measured inputs were required.



**Fig. 7.** Measured data processing timing indication - RED curve - interrupt routine, high state routine running; GREEN curve average values calculating, high state calculate in process

## 4 Conclusions

It was ascertained that if the calculations from some string of saved values between two interrupts within the main code loop are required, the sampling frequency has to be decreased down to approx. 184 kHz to be able to process the average calculations within one sampling period.

## 5 Acknowledgement

This paper was supported by the projects: Center for Intelligent Drives and Advanced Machine Control (CIDAM) project, Reg. No. TE02000103 funded by the Technology Agency of the Czech Republic and Project Reg. No. SP2019/117 funded by the Student Grant Competition of VSB – Technical University of Ostrava. This research was supervised by prof. Ing. Chlebiš Petr, CSc.

## 6 References

1. TMS320F28335, TMS320F28334, TMS320F28332 Digital Signal Controllers (DSCs). Analog, Embedded Processing, Semiconductor Company, Texas Instruments - TI.com [online]. 2019 [cit. 2019-07-12]. Available from: <http://www.ti.com/lit/ds/symlink/tms320f28335.pdf>

# Development of Power Quality analyser in BROADBAND<sup>LIGHT</sup> grid

Jan Baroš and Radek Martinek

Department of Cybernetics and Biomedical Engineering, FEECS,  
VŠB – Technical University of Ostrava, 17. listopadu 15,  
708 33 Ostrava – Poruba, Czech Republic  
{jan.baros, radek.martinek}@vsb.cz

**Abstract.** This article is about development of power quality analyser in SMART grid. The grid is situated on parking lot near faculty of electrotechnics and computer science in Technical University of Ostrava. Proposed system is based on virtual instrumentation. Testing is performed on two different technologies of public lights. Results shows that with change of sodium lights for LEDs, the power quality is significantly increased.

**Keywords:** LabVIEW, Power Quality, BROADBAND<sup>LIGHT</sup>, SMART grid, SMART parking lot, Virtual Instrumentation

## 1 Introduction about BROADBAND<sup>LIGHT</sup> testing polygon

In April 2018 our team has built its own testing polygon for various SMART technologies called BROADBAND<sup>LIGHT</sup> which focuses predominantly on SMART public lighting. BROADBAND<sup>LIGHT</sup> testing polygon is situated on the parking lot next to the faculty of electrical engineering and computer science of Technical University of Ostrava [1, 2, 3, 4]. It consists of 20 lamps on 10 poles with central management located in indoor laboratory. The purpose of this testing polygon is to test incorporation of SMART technologies into street lighting and future implementation of Visible Light Communication (VLC) technology, see [2]. In order to measure and analyse the power quality of our BROADBAND<sup>LIGHT</sup> testing polygon [1] the modular portable system had to be constructed. To achieve modularity, simple approach based on Virtual Instrumentation was chosen.

Similar approach was also chosen by Esim et. al. [8], where they used the NI USB-6211 for collecting data and LabVIEW to develop application. Designed system complied with EN 50160 and IEEE 1459 standards. Upadhyay N. et. al. [7] used ethernet chassis NI cDAQ-9178 combined with NI 9225 voltage module and NI 9227 current module. The measurement was made on single phase loads according to IEEE 1459 standard. Subtirelu et.al. [9] did only simulation approach of power quality analyser and they have not used real hardware. More robust approach in terms of precision using



NI cRIO platform was made by [6]. Theirs system was designed for testing frequency converters.

Our approach had to be taken differently. A number of experiments on compensation of higher harmonics by shunt active filters will be carried out [2, 4, 5]. These experiments will lead to lower harmonics distortion and significant increase in Power Quality of BROADBAND<sup>LIGHT</sup> grid. The main advantage of this approach is, that the system can be quickly dismantled and moved somewhere else without much effort. In order to achieve modularity, the Virtual Instrumentation (VI) approach was chosen. The main advantage of this approach is that the system's functionality can be rapidly changed into something else, because it is mainly defined by software and only marginally limited by used hardware. Simplified diagram of parking lot can be seen on **Fig. 1**.



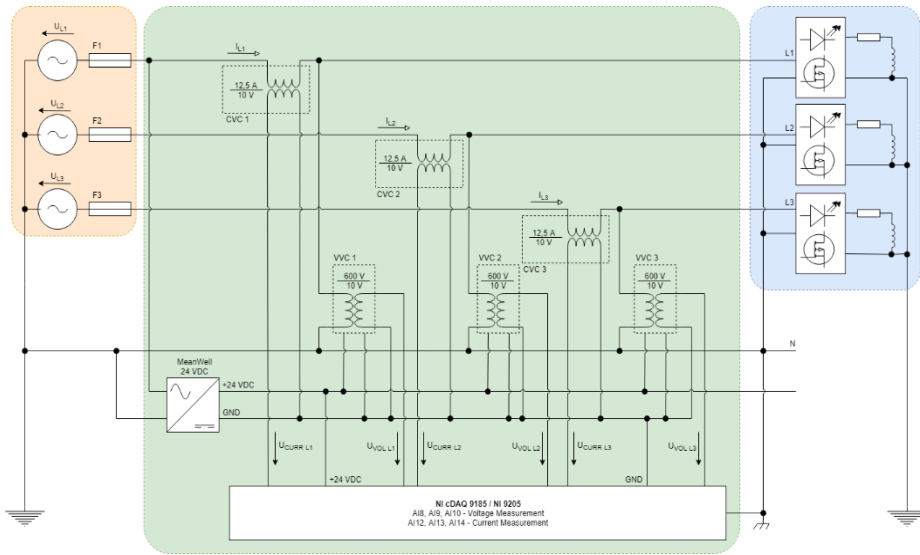
**Fig. 1.** Simplified diagram of SMART parking lot

## 2 Description of designed system

The whole system is situated in electricity substation in the basement of Faculty of electrical engineering and computer science. The system consists of NI 9185

measurement chassis with NI 9205 measurement card, power supply for active parts (chassis, measurement converters) and Wi-Fi router for the communication with laboratory.

The benefit of this system is the wireless communicating chassis NI 9185 equipped with NI 9205 which has sampling frequency of 250kS/s per channel. The measurements are carried out on totally six channels (3x voltage and 3x current), so the system can make measurements up to 41.6kS/s. The card uses RSE (Referenced Single Ended) wiring. The wiring can be seen on **Fig. 2**.



**Fig. 2.** The wiring of the system

Chassis is powered by the Meanwell power source with 24V output voltage. This source is also powering the active converters for transforming the voltage and current into lower measurable voltages. These converters conversion characteristic is very linear with maximal error of conversion up to 0.2%. Used converters are VVC-600/300, for voltage conversions, and CVC-25/12.5 for current conversions, both were made by the 32dev s.r.o.

Each converter has 2 adjustable ranges for input signal. These ranges are  $\pm 600\text{V}$ ,  $\pm 300\text{V}$  for voltage conversions, respectively  $\pm 25\text{A}$ ,  $\pm 12.5\text{A}$  for current conversions. Both ranges are down converted to working voltage in range of  $\pm 10\text{V}$ , which is acceptable for measuring card. Since the system is mainly designed for Power Quality measurements,  $\pm 600\text{V}$  and  $\pm 12.5\text{A}$  ranges for voltage/current are used. The converters are designed to withstand  $\pm 1\text{kV}$  and  $\pm 17\text{A}$  up to 10s.

The output voltage, due to the linearity of the converters, is only divided by a coefficient (1), (2). The shape of the signal remains the same as the input signal with minimal harmonic deformation. The frequency range of converters is up to 100kHz.

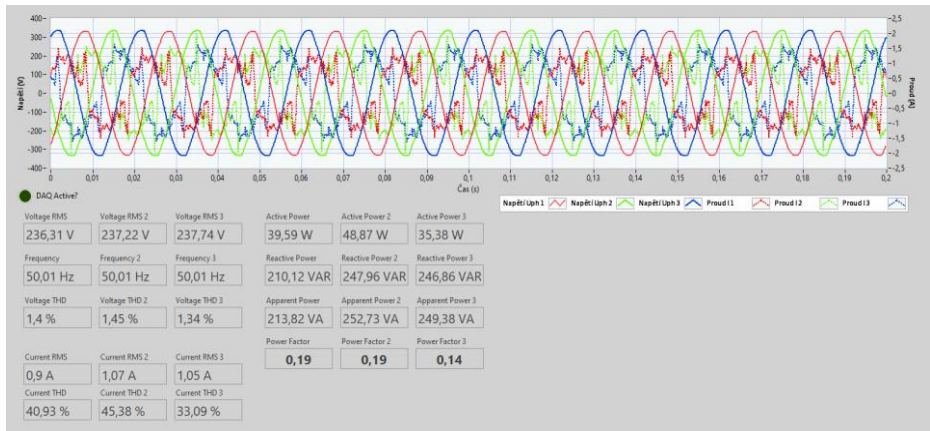
$$U_{VOL}(t) = \frac{U_{L1}(t)}{100} \tag{1}$$

$$U_{CURR}(t) = \frac{10 \cdot I_{L1}(t)}{12.5} \quad (2)$$

The connection with chassis is maintained through NI MAX and NI VISA. Because of the Virtual Instrumentation nature of the system, the functionality is realized through the application that is connected to the system. The benefit of this approach is that, the system can rapidly change its functionality into something else than Power Quality Analyser e.g. Frequency Analyser, Oscilloscope etc. The only limitation is the hardware specifications mentioned above.

The prototype application is written in the graphical programming language G in LabVIEW environment due to the reusability of the code. To comply with the EN 50160 and EN 61000-4 norms, the LabVIEW Electrical Power Toolkit was used for programming the Power Quality Analyser. To access data from the measurement card, the DAQmx library was used. The front panel of the application can be seen on **Fig. 3**.

According to the EN 50160 there must be 192 samples per period of the voltage sine signal. Typically, the frequency of the grid is 50Hz, so the minimal sampling frequency must be at least 9600S/s. The used sampling frequency of 41.6kS/s has a significant reserve to cover major frequency changes.



**Fig. 3.** Front panel of the application

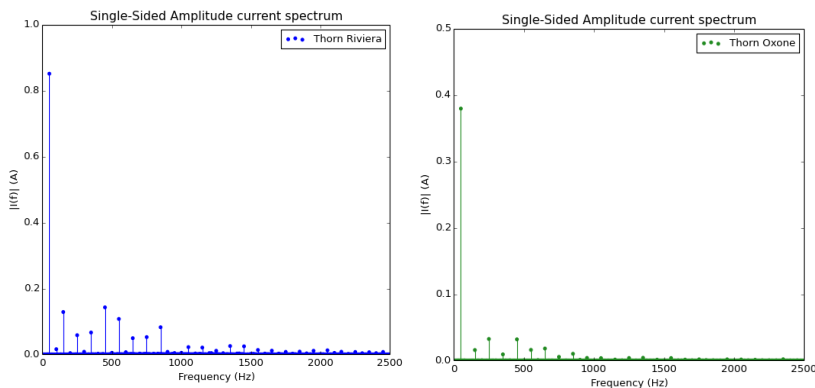
### 3 Proof of functionality

In order to prove the functionality of the system, a number of measurements were carried out. The subject of the measurement was to compare two technologies of public lighting. The first one was the sodium-based Thorn Riviera and the second one was the LED based Thorn Oxone. Monitored variables were voltage, current, frequency, THD of the voltage and current, active power, reactive power and power factor. Results of measurements can be seen on the **Table 1**.

**Table 1.** Basic quantities evaluation

Quantities / Lighting	Thorn Riviera	Thorn Oxone
Voltage RMS (V)	239,9 V	239,9 V
Current RMS (A)	0,91 A	0,40 A
Frequency (Hz)	50,01 Hz	50,01 Hz
Voltage THD (%)	2,27 %	2,23 %
Current THD (%)	32,92 %	14,43 %
Active Power (W)	201,61 W	87,93 W
Reactive Power (VAR)	69,44 VAR	37,17 VAR
Power Factor (-)	0,94	0,92

As expected, the LED lighting has almost 43% decrease in power consumption, also the reactive power decreased by 53%. The grid voltage variables have been the same for both measurements, so as expected the load doesn't change the frequency of the grid, or the voltage THD. However, the current variables are very different. The harmonic distortion with LED lighting decreased by 17%. This was caused by power converters in Thorn Oxone which were used instead of the bulb in Thorn Riviera. Measured current spectrums can be seen on **Fig. 4**.

**Fig. 4.** Amplitude current spectrum of Thorn Riviera and Thorn Oxone

## 4 Conclusion

As mentioned above, the designed systems functionality has been confirmed. In the current state the system can measure Power Quality according to standards EN 50160 and IEC 61000-4 up to 50th harmonic. Also, the system is communicating with other components (PC, server) wirelessly and is modular.

To prove functionality of the system two measurements were carried out on two public lighting lights. Two technologies were compared, sodium lights and LED lights. As expected, the transition from sodium to LEDs lights increased the Power Quality.

## 5 Acknowledgements

This article was supported by the Ministry of Education of the Czech Republic (Project No. SP2019/85 and SP2019/118). This work was supported by the European Regional Development Fund in the Research Centre of Advanced Mechatronic Systems project, project number CZ.02.1.01/0.0/0.0/16\_019/0000867 within the Operational Programme Research, Development and Education. This work was supported by the European Regional Development Fund in A Research Platform focused on Industry 4.0 and Robotics in Ostrava project, CZ.02.1.01/0.0/0.0/17\_049/0008425 within the Operational Programme Research, Development and Education.

## 6 References

1. Kuncicky R., J. Kolarik, L. Soustek, L. Kuncicky, and R. Martinek (2018, September). IoT Approach to Street Lighting Control Using MQTT Protocol. *In International Conference on Advanced Engineering Theory and Applications* (pp. 429-438). Springer, Cham.
2. Martinek R., L. Danys and R. Jaros (2019). Visible Light Communication System Based on Software Defined Radio: Performance Study of Intelligent Transportation and Indoor Applications. *Electronics*, 8(4), 433.
3. Martinek, R., J. Rzigdy, R. Jaros, P. Bilik and M. Ladrova (2019). Least Mean Squares and Recursive Least Squares Algorithms for Total Harmonic Distortion Reduction Using Shunt Active Power Filter Control. *Energies*, 12(8), 1545.
4. Martinek, R., J. Vanus, P. Bilik, T. Stratil and J. Zidek (2016). An efficient control method of shunt active power filter using adaline. *IFAC-PapersOnLine*, 49(25), 352-357.
5. Martinek R. and P. Bilik (2015, September). P.: New Strategies for Application of Recursive Least Square Algorithm in Active Power Filters. *In 8th International Scientific Symposium on Electrical Power Engineering (Elektroenergetika)*, Stara Lesna, Slovakia (pp. 344-347).
6. Horinek, M. and P. Bilik. "Power analyzer for converter testing based on cRIO hardware platform." *2010 International Conference on Applied Electronics* (2010): 1-4.
7. Upadhyay N., V.D. Juyal, A. Chakravorty, K.V. Singh and S. Singh (2018, February). Virtual Instrument for Power Quality Measurement. *In 2018 3rd International Conference on Internet of Things: Smart Innovation and Usages (IoT-SIU)* (pp. 1-6). IEEE.
8. Esim, J. and S.L. Oleagordia (2015). Research and Development of a Virtual Instrument for Measurement, Analysis and Monitoring of the Power Quality. *Journal of Fundamentals of Renewable Energy and Applications*. 05. 10.4172/2090-4541.1000185.
9. Subtirelu G.E., M. Dobriceanu and M. Linca (2017, March). Power quality analyzer. *In 2017 10th International Symposium on Advanced Topics in Electrical Engineering (ATEE)* (pp. 909-914). IEEE.

# Data Compression in WSNs using Wavelet Transformation

Monika Borová and Michal Prauzek

Department of Cybernetics and Biomedical Engineering, FEECS,  
VŠB – Technical University of Ostrava, 17. listopadu 15,  
708 33 Ostrava – Poruba, Czech Republic  
`monika.borova@vsb.cz`

**Abstract.** Data compression approach using Wavelet transform represents one of the options for edge computing. The main advantage of this approach is a reduction of transferred data amount which leads to lower energy demands for data transmission. Data are compressed in a microcontroller in environmental sensor and after transferred by communication interface.

For experiment purpose dataset with temperature and CO<sub>2</sub> concentration measurements was used. On this dataset wavelet transform was gradually applied with using four types of mother wavelet - Haar wavelet, Meyer wavelet, Symlet wavelet and Biorthogonal wavelet.

**Keywords:** Data compression, Wavelet transformation, Wireless sensor networks

## 1 Introduction

Environmental monitoring systems can be implemented as wireless sensor networks (WSN) collecting environmental parameters over time (see [2]). In such areas there are many research goals mainly aimed on functional optimization, energy harvesting and general WSN topology (more detailed in [3]). Nowadays, the InternetOfThings (IoT) domain offers many communication technologies applicable in low-power and low-cost environmental WSN. However, such communication interfaces are strictly limited by maximum amount of transmitted data.

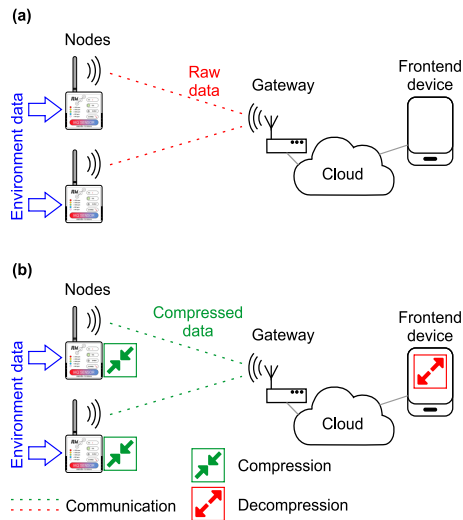
The data limitation issues of IoT communication interfaces can be solved by various edge computing techniques (see [1]). A principle of this feature is based on data processing methods implemented in a microcontroller in a sensor node therefore only compress data or extracted information are transferred by communication interface and stored to a cloud server. This approach leads to reduction of transmitted data amount which affect a total power consumption of environmental WSNs.

This research uses Wavelet transform as primary compression approach applicable in edge computing domain. Data are compressed after its collection directly in an environmental sensor node and then post-processed data are transmitted by IoT communication interface. This paper brings results from temperature and CO<sub>2</sub> concentration environmental parameters but this principle can be implemented for other environmental data.

## 2 Background

### 2.1 IoT sensor network

An IoT sensor network includes various number of sensor nodes which transferring parameters to central cloud. Fig. 1a shows the IoT environmental sensor network acquiring environmental data and it using IoT communication protocol (LoRaWAN, Sigfox, IQRF etc.) transferring data to cloud. In general, all IoT standards allows to transmit only limited amount of data during time period. Due to such limitation we are proposing edge computing compression method for IoT environmental sensor nodes based on wavelet transformation. This approach allows to compress data by node computational resources and transmit compressed data to gateway (see Fig. 1b). Transferred data are decompressed in the gateway and after that the data are stored to a cloud server.



**Fig. 1.** IoT sensor network. (a) Schematic with raw data transmission (b) Edge computing implemented in nodes and a cloud server.

### 2.2 Wavelet transform (WT)

The wavelet transform is a mathematical tool for analyzing of stationary signal and its decomposition into different scales with different levels. WT provides a local representation of signal compared with Fourier transform, because stores information about time and frequency of given signal (see [6]).

The wavelet transform of signal  $x(t)$ , which is defined in  $L^2(R)$  space, is given by the equation:

$$WT \{x(t)\} = \frac{1}{\sqrt{|a|}} \cdot \int_{-\infty}^{\infty} x(t) \cdot \overline{\psi\left(\frac{t-b}{a}\right)} dt \quad (1)$$

where  $\psi(t)$  is mother wavelet and  $a$  is dilation parameter –  $a \in \mathbb{R} \setminus \{0\}$ ,  $b$  is translation parameter, when  $b \in \mathbb{R}$ .

The selection of mother wavelet is one of the important thing, due to detecting and localizing various types of some abnormality or disturbances (see [4], [5]). The mother wavelet is composed of filter coefficients  $h(n)$ , which form scaling functions  $\phi(t)$  and  $g(n)$ , which is a parameter of orthonormal wavelet  $\psi(t)$ . The filter coefficients are computed according to the following equation:

$$\phi(t) = \sqrt{2} \sum_n h(n) \cdot \phi(2t - n) \quad (2)$$

$$\psi(t) = \sqrt{2} \sum_n g(n) \cdot \phi(2t - n) \quad (3)$$

In each step of decomposition the input signal is decomposed on two vectors –  $a_1(n)$  and  $d_1(n)$ , which are defined by:

$$a_1(n) = \sum_k h(k - 2n) \cdot a_0(k) \quad (4)$$

$$d_1(n) = \sum_k g(k - 2n) \cdot a_0(k) \quad (5)$$

The results of the decomposition are vectors  $a_m, d_m, d_{m-1}, \dots, d_1$ , forming a wavelet spectrum describing the time-frequency localization of the input signal. These vectors determine the overall trend of input data ( $a_m$ ) and additional information about subtleties ( $d_m$ )(see [5]).

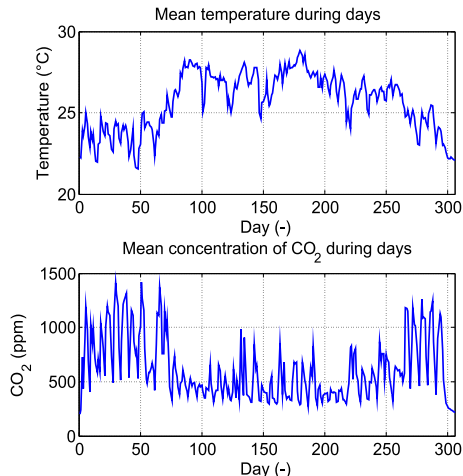
### 3 Experiments

For experiment purposes the dataset including temperature and CO<sub>2</sub> concentration measurements was used. A total of 306 days was used, giving data at 5 minute intervals – 288 records per day. Fig. 2 shows mean value of temperature/concentration CO<sub>2</sub> for each day ([7]).

The discrete wavelet transform (DWT) has been applied to these input data to compress the amount of data that will be further processed (transmission). For comparison, four different wavelet types were applied – Haar wavelet, Meyer wavelet, Symlet wavelet and Biorthogonal.

Using DWT, the input signal was divided into approximation and detail coefficients at three levels. The number of coefficients is always equal to half of the coefficients at the previous level. Due to the character of the signal, in which there are not many abrupt changes, it is possible to omit detailed coefficients and to reconstruct the signal only from approximation coefficients.





**Fig. 2.** Mean values of temperature and CO<sub>2</sub> concentration during the days

A relative error ( $\delta$ ) was determined between the original signal (original) and the signal reconstructed (approx) only from the approximation coefficients at each level according following equation:

$$\delta = \frac{\text{norm}(\text{original} - \text{approx})}{\text{norm}(\text{original})} \cdot 100 \quad (6)$$

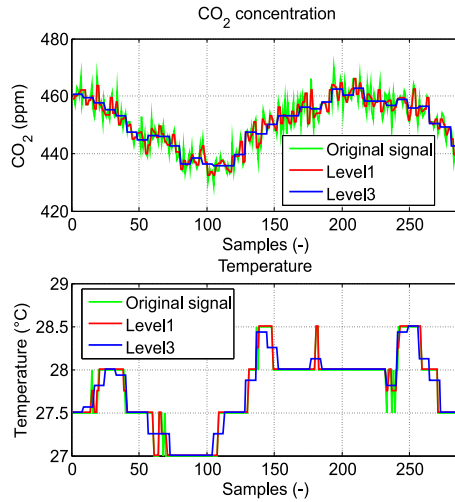
## 4 Testing and Results

### 4.1 Visual representation

One day in April was chosen for the visual presentation of the results. On the data of CO<sub>2</sub> concentration as well as on data about temperature, DWT was performed. Subsequently, signal was reconstructed only from approximation coefficients on level 1 and 3. For comparison, three selected mother wavelets were applied on input signal – Haar wavelet (Fig. 3), Meyer wavelet, Symlet and Biorthogonal.

### 4.2 Summary evaluation

The results for each configuration are shown at Fig. 4. The graph represents the relative errors ( $\delta$ ) of selected wavelets determined by the equation 6. Testing was performed in three different configuration. The first is the signal reconstruction only from approximation coefficients at the first level – the number of these values is exactly half of the original signal. Second and third configurations describe reconstructions from approximation coefficients at second and third levels. The number of coefficients in the third level is only 36.



**Fig. 3.** Original signal of one day and reconstruction from approximation coefficients at level 1 and 3 for Haar wavelet

With respect to the number of coefficients needed to reconstruct the signal, compression ratio of 2:1, 4:1 and 8:1 were determined. The same configurations and compression ratios are also used for temperature testing. As can be seen, using of Meyer wavelet achieves the lowest values of relative error compared to other types. Given the appropriate selection of the mother wavelet, it can be said that all selected wavelet types are suitable and show a great ratio between the compression level and the signal reconstruction.

## 5 Conclusion

Discrete Wavelet Transform was applied to a dataset containing information about temperature and CO<sub>2</sub> concentration. This data was collected throughout the year at the office at five minute intervals. The wavelet transform was gradually applied on this dataset using different types of mother wavelet – Haar wavelet, Meyer wavelet, Symlet wavelet and Biorthogonal wavelet.

Subsequently, the signal was reconstructed back to the original signal using only approximation coefficients at each level. The numbers of approximation coefficients are different in each levels – always half of the number from the previous level. The detailed coefficients are reset – this means that out the original 288 values, only 144 values are nonzero on first level of approximation, 72 values on second level and so on.

The Euclidean norm was determined to evaluate the results and then the relative error was calculated for each configuration and for each wavelet type. Based on the obtained results it is possible to claim that the best results were achieved using the Meyer wavelet. However, all selected wavelets achieved comparable results.

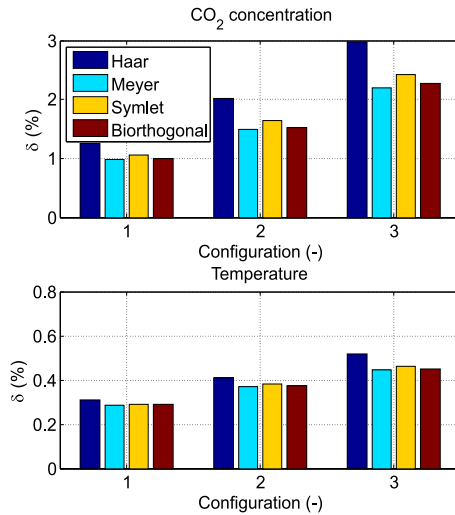


Fig. 4. Relative error for each configuration

## References

1. Li, J.R., Li, X.Y., Gao, Y.L., Gao, Y.Q., Fang, B.X.: Review on data forwarding model in internet of things. *Ruan Jian Xue Bao/Journal of Software* 29(1), 196–224 (2018)
2. Musilek, P., Prauzek, M., Krmer, P., Rodway, J., Barto, T.: Intelligent energy management for environmental monitoring systems. *Smart Sensors Networks: Communication Technologies and Intelligent Applications* pp. 67 – 94 (2017)
3. Prauzek, M., Konecny, J., Borova, M., Janosova, K., Hlavica, J., Musilek, P.: Energy harvesting sources, storage devices and system topologies for environmental wireless sensor networks: A review. *Sensors (Switzerland)* 18(8) (2018)
4. Safitri, I., Novamizanti, L., Yunawan, Y.: Dwt ss image watermarking with compressive sensing. In: *2018 3rd International Conference on Information Technology, Information System and Electrical Engineering (ICITISEE)*. pp. 335–339. IEEE (2018)
5. Santoso, S., Powers, E.J., Grady, W.M.: Electric power quality disturbance detection using wavelet transform analysis. In: *Proceedings of IEEE-SP International Symposium on Time-Frequency and Time-Scale Analysis*. pp. 166–169. IEEE (1994)
6. Santoso, S., Powers, E.J., Grady, W.M., Hofmann, P.: Power quality assessment via wavelet transform analysis. *IEEE transactions on Power Delivery* 11(2), 924–930 (1996)
7. Velicka, J., Pies, M., Hajovsky, R.: Monitoring of environmental variables in rooms of the department of cybernetics and biomedical engineering. In: *2018 IEEE 20th International Conference on e-Health Networking, Applications and Services, Healthcom 2018* (2018)

# Multichannel System for Non-Invasive Fetal ECG and Adult ECG Monitoring Based on Commercially Available Biosignal Amplifier and Virtual Instrumentation

Jindřich Brabлік and Radek Martinek

Department of Cybernetics and Biomedical Engineering, FEECS,  
VŠB – Technical University of Ostrava, 17. listopadu 15,  
708 33 Ostrava – Poruba, Czech Republic  
{jindrich.brabлік, radek.martinek}@vsb.cz

**Abstract.** This paper introduces a concise description of developed system for non-invasive fetal ECG and adult ECG monitoring based on commercially available biosignal amplifier and virtual instrumentation. Experiments including measurements of four different configurations of electrode placement for fetal electrocardiography on a subject at 34th week of pregnancy by means of developed monitoring system were presented. The experiments results with a selection of the best configuration in terms of the signal quality. Current use of developed system is described in the conclusion.

**Keywords:** Fetal electrocardiogram, NI-Fetal monitoring, Biosignal amplifier, Virtual instrumentation, LabVIEW

## 1 Introduction

Fetal Electrocardiography (fECG) is one of the most promising methods in terms of replacing conventional monitoring methods using CTG [7]. The fetal well-being is assessed based on the electric potentials sensed by means of electrodes placed on the maternal body (non-invasive method, NI-fECG) or directly on the fetal scalp (invasive fECG monitoring). The fetal heart rate is calculated from the detected RR intervals and thus this method is able to monitor fHR variability more accurately [5]. Moreover, both mother and fetus are not exposed to any kind of radiation. Uterine contractions can be also monitored by sensing the electrical activity on the maternal abdomen. This method is known as electrohysterography and it is potentially more accurate for uterine activity monitoring than intra-uterine pressure catheter [4] Therefore, NI-fECG is capable to fully replace the conventional monitoring by means of CTG [3].

Nevertheless, contrary to adults ECG research, the research community focused on fetal ECG signal processing suffers from lack of open access databases for the evaluation of the algorithms. Moreover, this method has not been standardized in terms of electrode placement, which varies according to the fetal position [8]. Therefore, each

of the available databases includes different data and it makes an objective evaluation nearly impossible.

In this paper, we introduce a system for non-invasive monitoring of fetal ECG and adult ECG designed around commercially available biosignal amplifier and virtual instrumentation. We propose the optimal system configuration to acquire high quality NI-fECG recordings. This is a vital condition for the fECG extraction algorithms to perform well. We also provide the evaluation of various measurement deployments. Based on that, we suggest the optimal electrode placement in accordance with the system configuration in terms of its clinical feasibility and the quality of the output signals.

## 2 Measurement system

As a measurement system we used 2.0 generation g.USBamp biosignal amplifier from g.tec medical engineering company, designed mainly for investigation of brain, heart and muscle activity. System features 16 DC-coupled simultaneously sampled analog input channels with 24-bit resolution, sampling frequency up to 38.4 kHz,  $\pm 250$  mV and biosignal pre-amplifier. Channels are clustered into four groups per four channels with separate ground and reference inputs, which allows measurement of up to four subjects at the same time. As a preprocessing, internal digital bandpass and notch filters as well as bipolar derivation can be applied to each measured channel. For advanced timing synchronization with external events, digital triggering inputs and outputs can be used. Input channels are designed to be compatible with both passive and active electrodes. System offers easy configuration, setup and high-speed online data processing for SIMULINK and LabVIEW as well as driver package/API for other programming languages.

For our research we developed a custom application (Fig.1) in LabVIEW development environment (using the provided LabVIEW API) that allows complex configuration of g.USBamp system, data logging to .tdms files and basic signal processing ( real-time peak detection and heart rate calculation). Custom cables and connectors were created to comfortably connect electrodes to the system. Based on brief experimentation we employed following configuration when conducting measurements. Measurements with this configuration provided the highest quality signals where noise and movement artefacts were significantly suppressed.

- **Sample rate** 600 Sa/s
- **Ground and reference** inputs for all groups **interconnected** to single potential.
- **Bandpass** 8<sup>th</sup> order Butterworth approximation filter with  $f_L = 0,5$  Hz and  $f_H = 60$  Hz.
- **Notch** 4<sup>th</sup> order Butterworth approximation filter with  $f_L = 48$  Hz and  $f_H = 52$  Hz
- **Bipolar derivation** between sensing electrodes (Fig. 1 white) and selected reference sensing electrode (Fig. 1 blue).

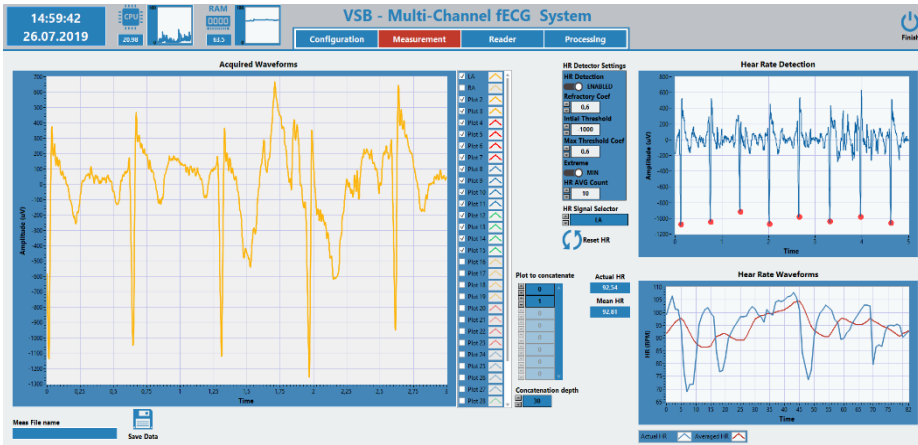


Fig. 1. Measurement tab of custom LabVIEW application for multichannel monitoring system.

### 3 Experiments

There are significant differences in electrode deployment among the databases, different researchers and also the commercially available devices, as illustrated in Fig. 2. While the positioning of the measurement electrodes does only influence the magnitude or polarity of the signal, the placement of common reference electrode (blue) and the active ground (black) causes significant changes in the recorded signals since it may help in minimizing both the polarization potential and the maternal component. As first step in our research we used the developed monitoring system to conduct a comparative measurements with configurations illustrated in Fig. 2. Our goal was to select a configuration that provides the best results from the perspective of noise suppression, artefact suppression and the fetal to maternal amplitude ratio. Selected configuration was then employed for all measurements that followed.

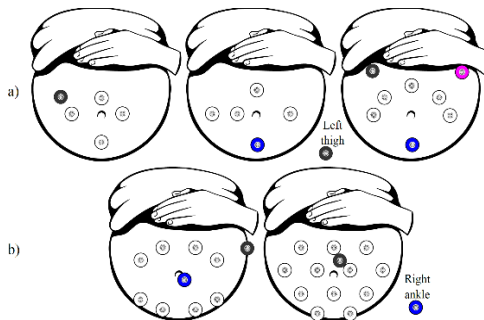
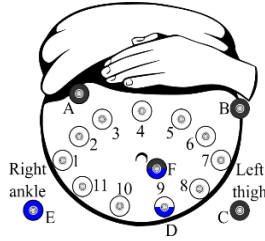


Fig. 2. Examples of the deployment of the measurement electrodes (abdominal – white, and chest– purple), common reference (blue), and the active ground (black): a) from left: commercially available device MONICA AN24, positioning used in publicly available databases ADFECGDB and NIFEADB; b) from left: Vullings [10] and Taylor [9].

To ensure feasibility and reproducibility of the experiments and to cover most of the available electrode placements, as depicted in Fig. 1, we designed the universal measurement deployment, see fig. 2. The design included total of 16 electrodes that were positioned on the body of the pregnant woman – 14 on the abdomen, one on the right ankle, and one on the left thigh. The switch between the individual configurations was performed by changing the inputs of the system. It is important to note that we omitted some of the electrodes that were redundant (i.e. the recordings included almost identical signals). This lowered the number of electrodes in some of the configurations, such as the one used in Taylor [9].



**Fig. 3.** Measurement deployment. Sensing electrodes (white 1 – 11), ground reference (black A, C, F), and common reference electrode (blue D, E, F).ac

Four different configurations of the measurement system were tested:

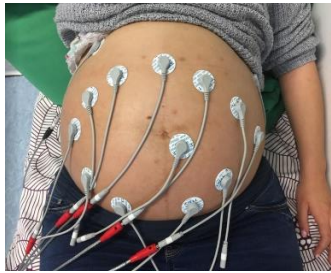
1. **Jejewski.** This configuration was used in the ADFECGDB database [6]. It includes 4 SEs (1, 2, 4, and 7), the GND (C) placed on the left thigh and the reference (D) on the bottom of the abdomen.
2. **Behar.** This configuration was used in the NIFEADB database [1]. It includes 4 SEs (1, 3, 4, 5, and 7), the GND (A) placed on the left thigh and the reference (D) on the bottom of the abdomen.
3. **Vullings.** The configuration introduced in the investigation [10] includes 8 SEs (2, 3, 5, 6, 8, 9, 10, and 11), the GND (B) placed on the left waist, and the reference (F) is placed adjacent to the navel.
4. **Taylor.** This configuration of Taylor [9] includes 11 sensing electrodes(1 – 11); the GND (F) is placed adjacent to the navel and the common reference (E) on the right ankle.

Table 1 summarizes the above mentioned configurations and links them to the design of the general measurement deployment introduced in fig. 2.

**Table 1.** Configurations tested

Configuration Name	Sensing electrodes	Ground reference	Reference
Jejewski	1, 2, 4, 7	C	D
Behar	1, 3, 4, 5, 7	A	D
Vullings	2, 3, 5, 6, 8 – 11	B	F
Taylor	1 – 11	F	E

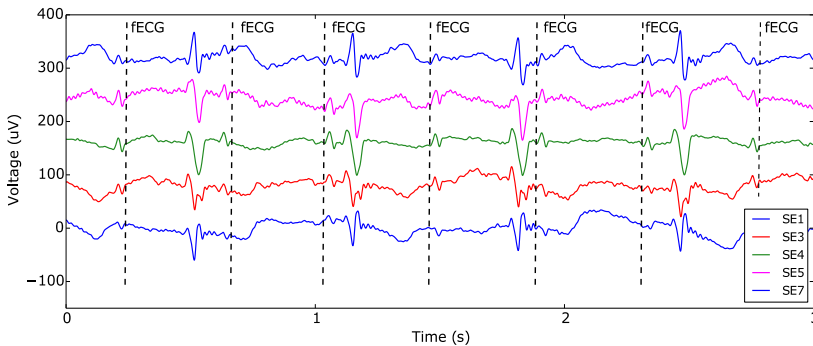
The experiments included measurements on a real subject in 34<sup>th</sup> week of pregnancy. The total of 14 electrodes were positioned on the abdomen in the way to cover most of the commonly used electrode deployment as shown in fig. 3.



**Fig. 4.** Measurement deployment in real subject at 34<sup>th</sup> week of pregnancy.

## 4 Results

The best results were acquired from Behar configuration (see fig. 5) where the measured signals were of high quality, contained least noise, motion artefacts and fetus-maternal amplitude ratio reached the lowest value. On contrary the worst results were acquired from Vullings and Taylor configuration where the fetus-maternal amplitude ratio reached high value. Results from conducted experiments are summarized in table 2.



**Fig. 5.** Results acquired from Behar configuration.

**Table 2.** Summary of results from conducted experiments.

Configuration Name	Best quality signal SE	m:f ratio	mQRS
Jezewski	3, 4	Low	Positive
Behar	2, 3, 4	Low	Negative/biphasic
Vullings	5, 6	High	Positive
Taylor	2, 3, 9, 7	High	biphasic



## 5 Conclusion

This article describes a developed system for non-invasive fetal and adult ECG monitoring. Also an experiment in the form of a comparative measurements were conducted to select optimal electrode placement configuration used by other researchers. The results showed that the electrode placement herein denoted as *Behar* is the most suitable in terms of the signal quality. Moreover, the placement of the sensing electrodes is convenient, because it offers a space for the placement of the conventional CTG probes if needed.

Developed system is now being used for comparison of fetal heart rate curves obtained by commercial CTG device and Non-Invasive fECG monitoring system and for testing of fetal ECG extraction algorithms. System was also used to obtain reference ECG signal on adult subjects for comparison of systems for monitoring heart activity based on different principles (optical, acoustic) and techniques.

### REFERENCES

1. Behar, J. A., Bonnemains, L., Shulgin, V., Oster, J., Ostras, O., & Lakhno, I. (2019). Non-invasive fetal electrocardiography for the detection of fetal arrhythmias. *Prenatal diagnosis*, 39(3), 178-187.
2. Carrera, J. M. (2003). The technological development of fetal surveillance: a long history. In *Controversies in Perinatal Medicine* (pp. 22-39). CRC Press.
3. Graatsma, E. M. (2010). *Monitoring of fetal heart rate and uterine activity* (Doctoral dissertation, Utrecht University).
4. Jacod, B. C., Graatsma, E. M., Van Hagen, E., & Visser, G. H. (2010). A validation of electrohysterography for uterine activity monitoring during labour. *The Journal of Maternal-Fetal & Neonatal Medicine*, 23(1), 17-22.
5. Jezewski, J., Wrobel, J., Matonia, A., Horoba, K., Martinek, R., Kupka, T., & Jezewski, M. (2017). Is abdominal fetal electrocardiography an alternative to doppler ultrasound for FHR variability evaluation?. *Frontiers in physiology*, 8, 305.
6. Jezewski, J., Matonia, A., Kupka, T., Roj, D., and Czabanski, R. "Determination of fetal heart rate from abdominal signals: evaluation of beat-to-beat accuracy in relation to the direct fetal electrocardiogram," *Biomedizinische Technik/Biomed. Eng.*, vol. 57, no. 5, pp. 383- 394, 2012.
7. Reinhard, J., Hayes-Gill, B. R., Yi, Q., Hatzmann, H., & Schiermeier, S. (2010). Comparison of non-invasive fetal electrocardiogram to Doppler cardiocogram during the 1st stage of labor. *Journal of perinatal medicine*, 38(2), 179-185.
8. Rooijackers, M. J., Song, S., Rabotti, C., Oei, S. G., Bergmans, J. W., Cantatore, E., & Mischi, M. (2014). Influence of electrode placement on signal quality for ambulatory pregnancy monitoring. *Computational and mathematical methods in medicine*, 2014.
9. Taylor, M. J., Smith, M. J., Thomas, M., Green, A. R., Cheng, F., Oseku-Afful, S., ... & Gardiner, H. M. (2003). Non-invasive fetal electrocardiography in singleton and multiple pregnancies. *BJOG: An International Journal of Obstetrics & Gynaecology*, 110(7), 668-678.
10. Vullings, R. (2010). Non-invasive fetal electrocardiogram: analysis and interpretation. Eindhoven: Technische Universiteit Eindhoven. 2010. 225 p.

# Concept of low-power smart sensor system for Industry 4.0 based on industrial buses

Radek Byrtus

Department of Cybernetics and Biomedical Engineering, FEECS,  
VŠB – Technical University of Ostrava, 17. listopadu 15,  
708 33 Ostrava – Poruba, Czech Republic  
byr0034@vsb.cz

**Abstract.** This paper describes concept the low-power sensor system, which is based on industrial buses. In fact, this is necessary for implementing standards of incoming Industry 4.0 revolution. Sensor nodes of sensor system must be self-sufficient, durable, low-power and meet the challenges of new standards in industry such as remote controlling, self-diagnosis, IIoT, and others. Main application of this sensor system is in condition monitoring based on vibration and sound measurement. This long-term data can be further processed, for example, in cloud systems for predictive maintenance purposes by using data processing and analytical methods.

## Keywords:

Low-power, industrial buses, CAN, MCU, Industry 4.0, accelerometer, microphone, condition monitoring, industry, sensors

## 1 Introduction

Current state in the industry usually end with a preventive replacement of a particular defective piece of machine based on replacement interval. However, it often happens that only preventive replacement is insufficient[1]. Machines and their parts tend to deteriorate and then it is necessary to stop the machine or line and repair the defective part. Such unexpected downtime costs extra money.

These days, the world must face the new challenges posed by the new Industry 4.0 trend. The main changes that this standard brings include, for example Industrial Internet of Things (IIoT), remote management and control, predictive maintenance, cyber-physical systems, digital twin, artificial intelligence, machine-to-machine communication and others [1], [2]. These changes need to be satisfied with new innovative ideas and products that meet these new requirements which Industry 4.0 brings to maintain a competitive environment. Some of the companies already started with their own solutions mainly for rotating machines. It means for example *SIPLUS CMS* system from SIEMENS. The idea described in this article looks primarily at creating a small, portable, inexpensive and widely usable sensor system for condition monitoring.

Machine condition monitoring can be made in several ways. We rank especially the determination of the condition by the measurement of vibrations and acoustic emissions together with the measurement of temperature or electric energy quality and current spectral analysis in time domain[4].

## 2 Design

The main idea of this concept is therefore also implementation of the latest trends that Industry 4.0 brings. The goal is to make each device self-sufficient, self-monitored and self-diagnostics. It must also be able to communicate via a selected industrial communication bus and thus transfer data to a collection point (collector) or through a gateway to a cloud system. There is also the possibility to use the computational potential of the MCU itself for data preprocessing and application of basic analytical methods.

As mentioned earlier, sensor system device is folded for condition monitoring. For this reason, we need an MCU that is both sufficient in performance and at the appropriate SPI bus speed for timing and data retrieval from microphone. Here are some of the criteria by which the selection was made:

- **Power consumption**

Power consumption must be very low due to the demand for self-sufficiency or limited access to power supply.<sup>1</sup>

- **RTOS support**

Industrial buses requires real-time platform to implement. As another benefit, we can mention the higher possibilities of program code management such as priorities, threads, and more. The disadvantage, however, is the greater amount of overhead.

- **Support and 3th party development kits**

The team of developers is very limited and therefore the extension of the target platform, its support and thus the size of the community is a great added value. Implementation of the program code and solution must also take place on a development kit, which will significantly speed up the development of whole device. This also applies to integration of industrial bus.

Manufacturer	Model	Power consumption (mA)	RTOS support	Support	Interfaces	IB shield
NPX	MKL28Z512VLL7	13,6; 9,0; ~1,0	yes, FreeRTOS	good	3x IIC, 3x SPI, I2S	no
NPX	MKL25Z128VLLK4	6,4; 3,1; ~0,8	yes, FreeRTOS	good	2x IIC, 2x SPI	no
Microchip	ATSAMC21E17A	~5,1; 1,3; 0,04	unknown	very good	4x IIC, 4x SPI, CAN	no
STM	STM32F103RB	~40,0; 9,1 ~0,02	yes, FreeRTOS	very good	2x IIC, 2x SPI, CAN	yes

Fig. 1: Comparison of MCU candidates

Microchip, STMicroelectronics and NXP (Freescale) MCUs were included in the selection. In the table 1 we can see a comparison of the selected MCUs

<sup>1</sup> Consumption in table: 1st - running mode; 2nd - idle mode; 3th - sleep mode

and their properties, which are crucial for the concept of the sensory system. The MCU from the portfolio of STMicroelectronics was chosen mainly to support RTOS and 3th party development kits with industrial bus interfaces. This means that development will be greatly accelerated thanks to the provided program libraries and examples. The disadvantages of this MCU include higher consumption than the competition. However, the value of power consumption is given as maximum at 105°C.

## 2.1 Sensor system platform

The PCB size with the MCU selected is large. If there are sensors (temperature, vibration, etc.) together with the MCU on this PCB, the measured values can be greatly distorted. For this reason, it is necessary to come up with a solution of separate sensors from the main PCB. By processing smaller PCBs with specific sensors and much smaller MCUs, we can largely solve this problem. However, the problem now arises with linking these smaller sensory PCBs to the main PCB of the sensing system node. The solution is in the use of the bus. The simplest solution would be to use the IIC bus, but the problem is that the devices will be deployed in an industrial environment where interference is generated. In addition, the IIC bus is not well resistant to parasitic capacity, which can degrade the transmission. This is why the MCU with CAN bus support has been chosen and is now widely used not only in the automotive industry. The CAN bus is resistant to interference, provides sufficient transmission speed and longer wires can be used to connect individual sensors to the main node. Regardless of the selected bus, it is also necessary to use two additional wires to supply smaller MCUs with sensors.

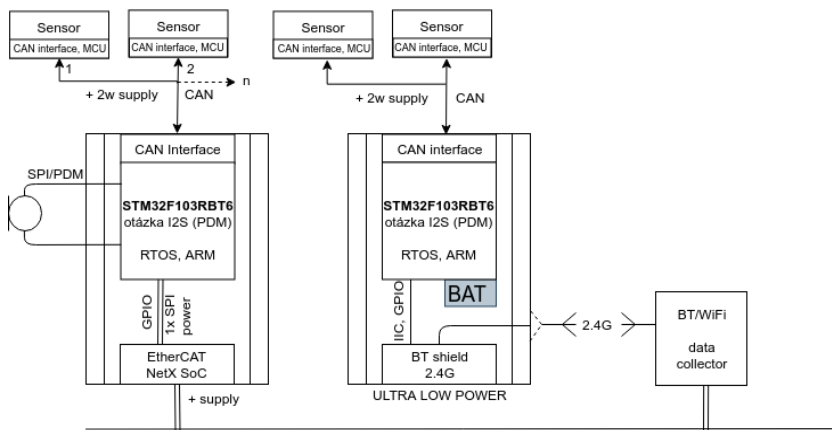


Fig. 2: Planned concept of sensor system nodes

Picture no. 2 describes concept of sensor system. At the bottom we can see chosen industrial bus to which either the sensor system node or the wireless

collection point is connected. Thus, the node itself consists of a selected big 32-bit MCU that is used to collect data from smaller 8-bit MCUs with sensors as well as data preprocessing. The microphone cannot be connected to a small 8-bit MCU not only because of insufficient CAN bus transfer rate, but also 8-bit MCU miss needed interface speed, so it is necessary to connect it to the 32-bit MCU of node. Connection to the industrial bus is provided by 3th party chip, which is to the MCU connected via SPI bus. One of the industrial bus chips is NetX from Hilscher company<sup>2</sup>.

## 2.2 Sensors

An important part are sensors, which must meet the selected purpose, ie measuring vibration, magnetic field, temperature and more. These were chosen again from STM company portfolio due to broad support. In the table below you can find several selected sensors for testing:

Sensor STM ID	Value	Interface	Properties
MP34DT05TR-A	Digital microphone, acoustic emissions	SPI (PDM)	Omnidirectional, 64dB S-t-N ratio
IIS2MDC	3-axis digital magnetic sensor	IIC, SPI	+/- 50 gauss, up to 150Hz
IIS328DQTR	3-axis digital accelerometer	IIC, SPI	Linear, +/- 8g, up to 1kHz
ISM330DLCTR	Digital 3D accelerometer and gyroscope	IIC, SPI	+/- 8g, up to +/- 2000 dps, SMART
MP34DT06J	Digital microphone, acoustic emissions	SPI (PDM)	Omnidirectional, 64dB S-t-N ratio, cap.
HTS221	Relative humidity and temperature	IIC, SPI	0% - 100%, -40°C to +120°C, 12Hz

Fig. 3: Sensors chosen for testing

Sensors with communication bus SPI or IIC are placed on PCB with smaller 8-bit MCU. Measured values include temperature, relative humidity, magnetic field sensor, and vibrations. All this data can be used to evaluate the condition of the machine monitored by the sensors. In the other hand, microphones requiring higher SPI bus speeds and higher MCU performance are connected to a large 32-bit MCU of node.

## 3 Methodology of data transfer

Measured values of the sensors are cyclicly read out by 8-bit or 32-bit MCU. In the case of an 8-bit MCU, the data must be transferred via the CAN bus to the 32-bit MCU. Here, the raw data can be preprocessed using statistical and analytical methods. Also, various warnings can be implemented on the MCU. Subsequently, both raw, preprocessed data and also warnings are sent from the nodes through the industrial bus to the collection point. The collection point can be represented by a local computing system with storage space and implied analytical methods for monitoring the condition of monitored equipment and thus provide data for predictive maintenance and an overview of the current

<sup>2</sup> <https://www.hilscher.com/netx/introduction/>

state of the system (lines, machines, etc.). Another option is to send data through the gateway to the cloud system (IBM Bluemix, Microsoft Azure, Mindshere, etc.), where the data will be processed again to provide information about the monitored system.

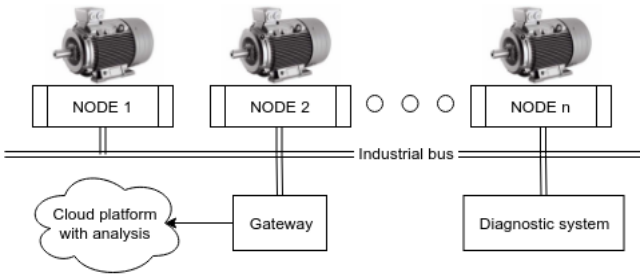


Fig. 4: Methodology of sensor system

### 3.1 Real-time system on MCU of node

Implementing program code on a 32-bit MCU also includes a real-time system (RTOS). RTOS is very useful in this case because of the possibility of splitting the program code into several threads and then assign these threads different priorities according to the importance of implemented code. Data read from a microphone or accelerometer are much more valuable than the actual temperature reading, so reading them is preferred. It is also important to computationally separate the reading of values from the sensors and the data preprocessing itself. If computationally demanding tasks are implemented, it may happen that data reading does not take place as often as it should. RTOS have also disadvantages - one of the biggest one is system overhead and also synchronization problems.

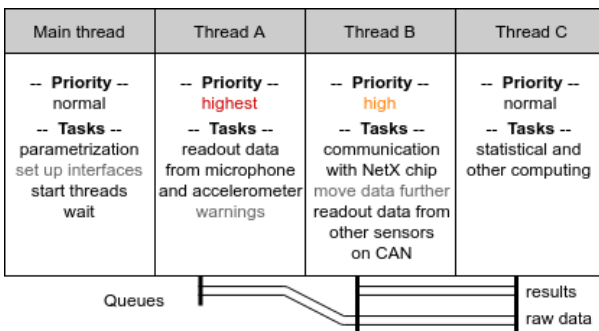


Fig. 5: Concept of multi-thread system

The implementation envisages a total of four threads. The thread with the highest priority handles the most critical part, which is reading data from the accelerometers and microphone, as well as evaluating alarm conditions. The data is further preprocessed and moved to the queue where it is available to the other two threads. A thread with a higher than normal priority takes care of forwarding data to the selected industrial bus. This thread also takes care of communication via CAN bus - data readout. Normal priority threads are two in total - the main thread and the compute thread. The compute thread is in run only if there is no need to do something more important. At that moment, it processes the data using the statistical apparatus and place the results to second queue for posting. The main thread starts first when the program starts. Parameterization of used interfaces, reading of information about connected sensors and its calibration are performed here.

## 4 Conclusion and future work

This paper describes a possible concept of a sensor system based on industrial buses. Nowadays, there are various solutions from reputable industry companies such is SIEMENS, but none of them are open-source and also these solutions are very expensive, single - purpose and fixed to company platform, so the goal of the idea described in this article is to come up with a new solution that is cheap, versatile and reliable, usable for an analytical system, where can be monitored condition of industrial equipment.

Center of mechatronics project is planned for four year by 2022, so work is in beginning and in these days the solver team is working on implementation of RTOS to the development kits and also on interfacing of the sensors. After processing a functional prototype of one node of the sensory system, the PCBs with MCU and chip for communication with industrial buses will be created.

There is also a lot of improvement ideas like self-sufficiency based on battery, wireless connection via IIOT and implementation supply by energy harvesting.

**Acknowledgement:** The following grant si acknowledged for the financial support provided for this research by project *Centrum výzkumu pokročilých mechatronických systémů CZ.02.1.01/0.0/0.0/16\_019/0000867*, VSB - Technical University of Ostrava.

## References

1. MAŘÍK, Vladimír. *Průmysl 4.0: výzva pro Českou republiku*. Praha: Management Press, 2016. ISBN 978-80-7261-440-0.
2. GILCHRIST, Alasdair. *Industry 4.0: the industrial internet of things*. New York, NY: Springer Science Business Media, 2016. ISBN 978-148-4220-467.
3. WANG, K. C. *Embedded and real-time operating systems*. Cham: Springer, 2017. ISBN 978-3-319-51516-8.
4. TŮMA Jiří *Diagnostika strojů*. Ostrava: VŠB - Technická univerzita Ostrava, 2009. ISBN 978-80-248-2116-0.

# Visible Light Communication system based on SDR and LabVIEW

Lukáš Danys and Radek Martinek

Department of Cybernetics and Biomedical Engineering, FEECS,  
VŠB – Technical University of Ostrava, 17. listopadu 15,  
708 33 Ostrava – Poruba, Czech Republic  
{lukas.danys, radek.martinek}@vsb.cz

**Abstract.** In this paper, the VLC communication system based on SDR is presented. The system itself is highly modular and based on LabVIEW software, modified software defined radios (SDR) and commercially available LED car tail-lights. This work explores testing platform and measurements of multistate QAM modulation formats impaired by fog. A reference laser is used for monitoring of fog density throughout the whole experimental phase.

**Keywords:** Visible Light Communication, Quadrature Amplitude Modulation, LabVIEW.

## 1 Introduction

Latterly, visible light communications resurfaced as an alternative to radio frequency technologies, such as Wi-Fi or Bluetooth. Communication bands of these technologies tend to be overfilled and often lack free channels. VLC is an optical wireless system operating in visible light spectrum (380 to 780 nm), which uses a light source operating in this band as transmitter and photodetector or CMOS camera as receiver. VLC is a capable technology, tested for short-range communications as well as long-range solutions. Appliances vary greatly — from vehicle-to-vehicle communications to vehicle-to-infrastructure communication or as an alternative to local area networks (LAN) called Li-Fi [1]. LED technology is backbone of this technology, as LEDs offer long lifespan, low power consumption, high tolerance to humidity, high efficiency and mainly fast switching capabilities and capability of operation in VLC spectrum. LED light sources can be used for communication while maintaining illumination capabilities.

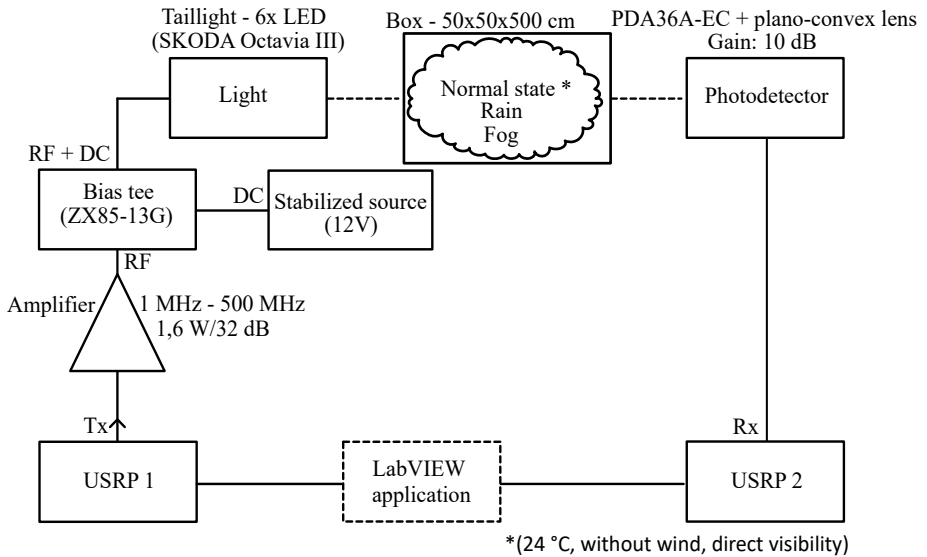
## 2 Methodics and results

### 2.1 Testing setup

Setup is based on LabVIEW application, which is used for input/output signal processing and measurement. Application output was fed into NI USRP (2921),



which is used as transmitting element. Signal is then amplified by 1.6W amplifier. Amplified signal then goes through bias tee into the transmitting light source. A modifiable plexiglass box with dimensions of 50x50x50cm is inserted between transmitter and receiver. This box can be used for testing of variable nature conditions such as rain, fog or thermal turbulence [2]. A Thorlabs photodetector is used as receiver. Receiver signal is processed by another NI USRP (also 2921), whose output is connected to the same computer running LabVIEW application. Signal is then processed and evaluated, measured parameters are saved to a file. Figure 1 shows used experimental setup.



**Fig. 1.** Testing setup design.

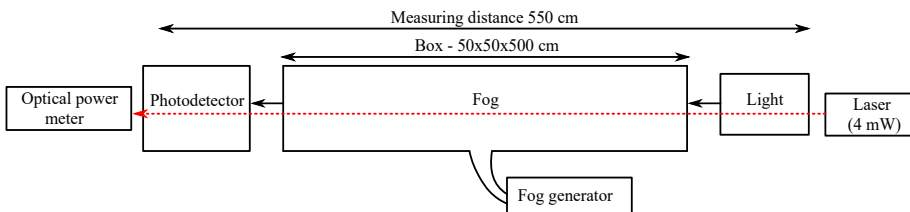
Used USRPs had to be modified with Ettus daughterboards, since the original TX/RX boards are operating in different band, than intended. Ettus LFRX/LFTX Daughterboards operate at 0-30 MHz. This band is approximately what was intended when designing whole system. To further improve received signal level, a planoconvex lens were mounted on receiving photodetector. Also connectors on Octavia tail-light had to be adjusted, since they are designed for car engine control unit. ZX85-12G+ bias tee from Mini-Circuits was used — it operates from 0.2 MHz to 12 GHz, its maximal throughput current is 0.4A and maximal input voltage 25 V. Following parameters can be configured in LabVIEW application:

- Carrier frequency: max 30 MHz
- Bandwidth
- Sample width
- Number of states: max 4096-QAM
- Message symbols

- Used TX filter
- TX gain
- RX gain
- TX USRP IP address
- RX USRP IP address

## 2.2 Impact of the fog on system performance

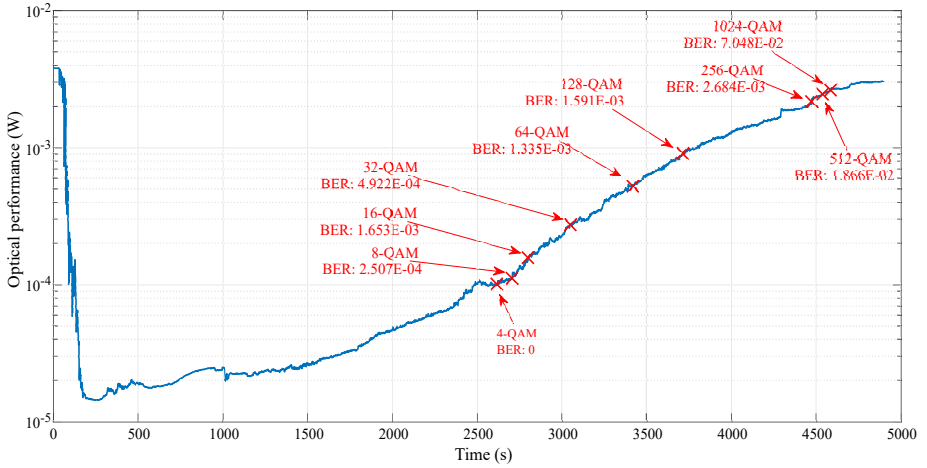
Measurements were carried out in sealed plastic box mentioned earlier. A fog machine was connected to bottom part, which served as a source of artificial fog. The main problem with this measurement was, that the conditions inside box varied across multiple measurements. For this reason, a 4 mW laser and optical power meter were added to our experiment. During measurements, optical power levels were gathered to use them as a reference values to approximately monitor fog density. Figure 2 describes the setup. The following configuration was used for testing:



**Fig. 2.** Testing setup for simulation of fog.

- Carrier frequency: 3 MHz
- Bandwidth: 1–4 MHz
- Modulation type: M-QAM
- TX/RX gain: 0 dB
- Message symbols: 10,000
- Tx filter: root raised cosine
- Sample width: 16-bit
- Receiver-transmitter distance: 550 cm
- Measured distance: 0–350 cm (step of 25 cm)
- Photodetector with planoconvex lens → more suitable for this scenario
- Measured parameters: BER, EVM

Higher modulation formats could not be measured until fog density dropped below certain level. When BER reached threshold of  $e^{-3}$ , measurements were carried out. All bandwidths had to be measured at once, since the fog dissipated quite quickly. Figure 3 describes a slow dissipation of fog inside box. Figure describes minimal optical power of laser needed to cross BER threshold for multiple multistate QAM modulations.



**Fig. 3.** Fog dissipation with BER thresholds for multiple QAM modulations.

Table 1 consists of measured optical power level thresholds for every bandwidth/QAM modulation scheme. It is visible that for higher modulation schemes a lot more power needs to be received, therefore the density of fog needs to be lower. The difference between the lowest and highest modulation format is considerable.

**Table 1.** Received optical power level thresholds for each modulation/channel width combination

M-QAM	Bandwidth			
	1 MHz	2 MHz	3 MHz	4 MHz
4-QAM	101 mW	95 mW	97 mW	93 mW
8-QAM	112 mW	135 mW	175 mW	189 mW
16-QAM	154 mW	205 mW	250 mW	276 mW
32-QAM	275 mW	308 mW	463 mW	550 mW
64-QAM	525 mW	780 mW	930 mW	951 mW
128-QAM	905 mW	1.095 mW	1.399 mW	1.550 mW
256-QAM	2.180 mW	2.394 mW	2.545 mW	2.585 mW
512-QAM	2.475 mW	2.522 mW	2.735 mW	2.930 mW
1024-QAM	2.640 mW	2.955 mW	3.120 mW	3.172 mW

Measured BER values are displayed on Figure 4. These values must be compared to Table 1, as it is necessary to reach certain fog density for each modulation. For example, at a least quarter of transmitted optical power had to be received for 128-QAM, 2MHz combination to work.

Fog has significant influence on VLC channel quality [3]. Figure 5 displays attenuation characteristics, which were measured with appropriate power levels. There is a significant degradation in signal quality. Possible solution lies in

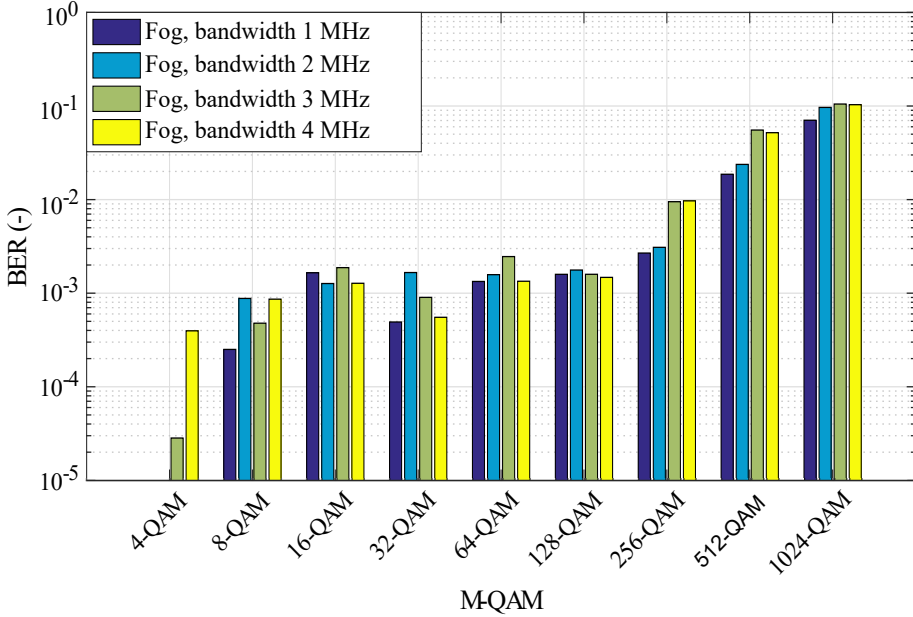


Fig. 4. Measured BER levels for different channel widths.

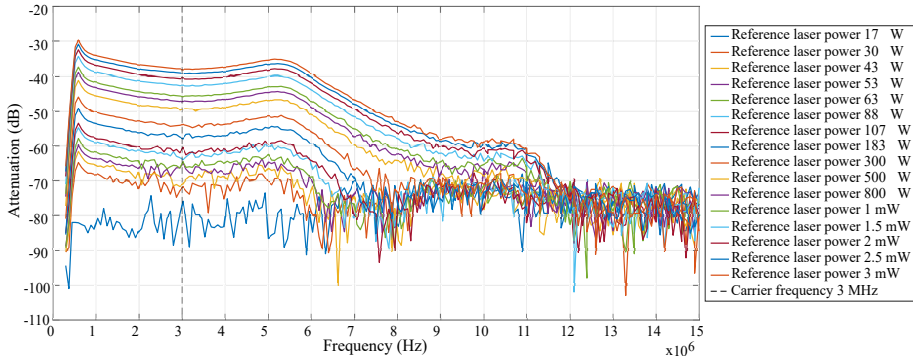


Fig. 5. Attenuation characteristics of laser powers levels for different frequencies.

adaptive modulation and equalization, which would compensate degradation by switching to lower M-QAM modulation scheme, which are more robust [4, 5].

### 3 Conclusion

In this paper, results of our research focused on VLC communication under different natural conditions were presented. Fog has the greatest impact and will be hard to overcome in the future. Adaptive modulation or possibly channel width in combination with equalization, seems to be the only way how to over-

come it. Our first LabVIEW prototype has multiple limiting factors, from lower performance of USRPs and non-linearity of amplifier to limiting factor of ethernet interface used between computer and USRP itself. However, most of these factors will be adjusted in future versions, as new parts were already ordered.

## Acknowledgment

This article was supported by the Ministry of Education of the Czech Republic (Project No. SP2019/85 and SP2019/118). This work was supported by the European Regional Development Fund in the Research Centre of Advanced Mechatronic Systems project, project number CZ.02.1.01/0.0/0.0/16\_019/0000867 within the Operational Programme Research, Development and Education. This work was supported by the European Regional Development Fund in A Research Platform focused on Industry 4.0 and Robotics in Ostrava project, CZ.02.1.01/0.0/0.0/17\_049/0008425 within the Operational Programme Research, Development and Education. This article was also a part of project VI20172019071.

## References

1. TSONEV, Dobroslav; VIDEV, Stefan; HAAS, Harald. Light fidelity (Li-Fi): towards all-optical networking. In: *Broadband Access Communication Technologies VIII*. 2014, vol. 9007, p. 900702.
2. MARTINEK, Radek; DANYS, Lukas; JAROS, Rene. Visible Light Communication System Based on Software Defined Radio: Performance Study of Intelligent Transportation and Indoor Applications. *Electronics*. 2019, vol. 8, no. 4, pp. 433.
3. LATAL, Jan; VITASEK, Jan; HAJEK, Lukas; VANDERKA, Ales; MARTINEK, Radek; VASINEK, Vladimir. Measurement of changes of polarization of optical beam affected by atmospheric effects. In: *2017 19th International Conference on Transparent Optical Networks (ICTON)*. 2017, pp. 1–5.
4. NEDOMA, Jan; MARTINEK, Radek; KOUDELKA, Petr; VANUS, Jan; KONECNY, Jaromir; FAJKUS, Marcel; KAHANKOVA, Radana. The effect of matched filtering with programmable root raised cosine filter on error vector magnitude of M-QAM broadband over visible light. In: *2017 40th International Conference on Telecommunications and Signal Processing (TSP)*. 2017, pp. 510–514.
5. MARTINEK, Radek; VANUS, Jan; KELNAR, Michal; BILIK, Petr; ZIDEK, Jan. Application of recursive least square algorithm to adaptive channel equalization. In: *XXI IMEKO World Congress "Measurement in Research and Industry"*. 2015, pp. 1–4.

# Battery Electric Vehicle Range Estimation

Jan Dedek and Jan Žídek

Department of Cybernetics and Biomedical Engineering, FEECS,  
VŠB – Technical University of Ostrava, 17. listopadu 15,  
708 33 Ostrava – Poruba, Czech Republic  
[jan.dedek@vsb.cz](mailto:jan.dedek@vsb.cz)

**Abstract.** The aim of this paper is to discover how the range calculation algorithms work in battery electric vehicles (BEV) and to suggest possibilities of improving the current state. In most contemporary BEVs are used inaccurate algorithms, that probably do not take into account the planned route, but only the consumption history of the last few tens of kilometers. This regression analysis does not reach the qualities to reliably predict the exact range. In this paper will be described the origin of the problem and motivation for its solution, then the specific methods that were created to identify the algorithms used by the most widespread cheap electric vehicles. The article will conclude the discussion and evaluate the results together with the direction of further research.

**Keywords:** Battery electric vehicle, Range anxiety, Range estimation, Nissan Leaf, Peugeot Ion.

## 1 Introduction

Range is the number of units of length, most often km that can be driven on the remaining battery energy. Due to the generally lower range of BEV compared to vehicles with an internal combustion engine (ICE), it is necessary to continuously monitor the range parameter.

Unfortunately, this very important parameter for BEV is not sophisticated in most electric vehicles, but it is an extrapolation based on regression analysis taking into account current consumption and remaining battery power. However, during the course of the route, most of the energy consumption varies greatly depending on many factors: Vehicle load, weather, driving style, aerodynamic drag (vehicle speed and wind speed and direction), but especially on the elevation profile of the route and use electric vehicle (EV) systems such as heating, ventilation or air conditioning (HVAC) Zhang et al., 2012; Badin et al., 2013; Barney et al., 2013; Neubauer et al., 2012. With such a number of variables and without knowing the route elevation profile to the destination, the roll-out value estimated by the regression analysis based extrapolation cannot be considered credible. This untrustworthiness of the most watched data in the BEV control causes distrust among the users in the BEV itself.

## 2 State of the art

Unfortunately, even battery-powered electric vehicles with a cost of over 45000 Euros today cannot adapt the declared value of the range to the actual route conditions to the destination. Algorithms for calculating roll-out value seem to be impossible (due to the protection of information in the automotive industry) to be validated as extrapolation of regression analysis taking into account recent driving style, HVAC system consumption, vehicle electronics consumption and modern BEV and battery temperature management (heating or cooling) see the equation 1. KW et al., 2016.

$$R = \frac{E_{bat}}{P_{engine} + P_{HVAC} + P_{ele} + P_{bat}}, \quad (1)$$

where  $R$  is in km,  $E_{bat}$  is the energy stored in the battery in kWh, and  $P$  is the power input of the BEV in kWh per km, ie:  $P_{engine}$  - engine,  $P_{HVAC}$  - comfort systems,  $P_{ele}$  - onboard electronics and  $P_{bat}$  - battery care systems.

As part of the testing for this paper, several experimental measurements have been made on several types of battery electric vehicles to confirm the above mentioned assumptions. On business trips with the BEVs tested, telemetry data was recorded, in particular regarding the displayed range at the beginning and end of the measured route. The selected test routes are shown in the table 1.

Table 1: Tested trips table

Vehicle	Distance	Range start	Range end	Error
Leaf 24 kWh	84 km	154 km	-1 km	-71 km
Kona 64 kWh	209 km	279 km	6 km	-64 km
Leaf 24 kWh	144 km	161 km	28 km	11 km
Leaf 24 kWh	100 km	117 km	66 km	49 km

The table 1 shows how inaccurate the BEV range is. In one case, the roll-out error was even 46 %, which led to a failure to reach the target and the necessary towing of the vehicle.

## 3 Material and metods

In order to carry out the algorithm identification, we created a dataset of BEV driving data, which consisted of more than 250 variables. The data for the experiments were measured by means of two most commonly used electromobiles: Nissan Leaf (24 kWh) and Peugeot IoN (16 kWh). In both vehicles, data was recorded on several trips varying in trip time and distance, elevation or speed. Further processing and algorithm tests were performed using MATLAB.

For the range estimation, two different algorithms were tested. The core of those algorithms is derived from equation 1. The first algorithm incorporates

the floating average in order to obtain more accurate estimation and thus the remaining range is calculated as follows:

$$R_a[k] = \frac{E_{bat}[k]}{\sum_{i=k-n}^k P[i]} \times 100, \quad (2)$$

where  $k$  is the iteration of the trip (in  $km$ ), the energy stored in the battery in  $kWh$ ,  $P$  is the power input of the BEV in  $kW$ ,  $n$  is the defined distance (e.g. last 30  $km$ ), and  $i$  is the iteration of the floating average.

The second algorithm defined by equation 3 extends the equation 2 as follows:

$$R_b[k] = R_b[0] - k + (R_a[k] - R_a[k - 1] + 1), \quad (3)$$

The estimated range is then smoothed by the weighted average of the current and previous range as follows:

$$R_{bavg}[k] = \frac{3 \times R_{bavg}[k - 1] + R_b[k]}{4}. \quad (4)$$

## 4 BEV energy consumption measurement and range estimation

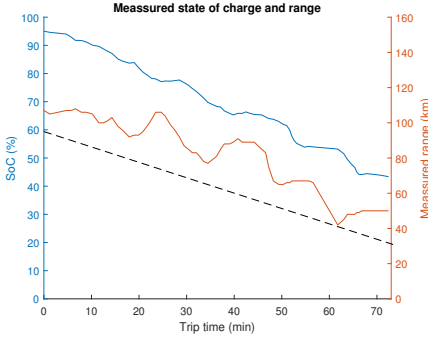
In this section, we introduce the results of the consumption measurement and range estimation using the proposed algorithms. We also provide a comparison of the estimation on the dataset from two different electric vehicles – Nissan Leaf and Peugeot Ion.

### 4.1 Nissan Leaf

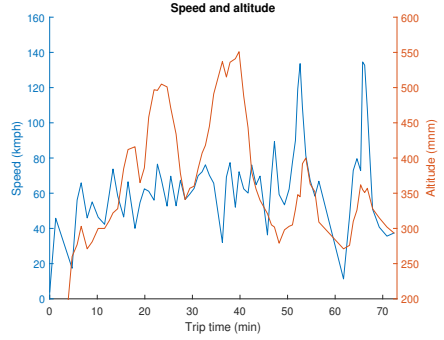
This vehicle logs 159 variables approximately every two seconds, giving tremendous possibilities for diagnostics. Unfortunately, one of the unregistered data important for further research is the range displayed on the vehicle (Human - Mashine Interface) HMI. This range was obtained using the timelapse sequence of the displayed data on the display using the camera during measured trip. The graph of the state of the charge and the displayed BEV range over time is shown in the figure 1a. Black dashed line indicate initial range.

In the figure 1a a disproportionately small range due to the standards for this BEV, which is due to the relatively aggressive highway driving preceding the measured one. That is why we can see a rather unusual phenomenon, when the range ascend instead of its logical descent, even in places where the terrain is rising at a considerable speed. The speed and altitude profile of the route is shown in the figure 1b. The above-mentioned phenomenon confirms the assumption that the calculation of the range of this vehicle is a variant of the floating average, i.e. the inclusion of the consumption of the last rides for the calculation of the current range. The comparison of the displayed range car and the calculated range using the equation 2 is shown in the figure 1c. The comparison of the

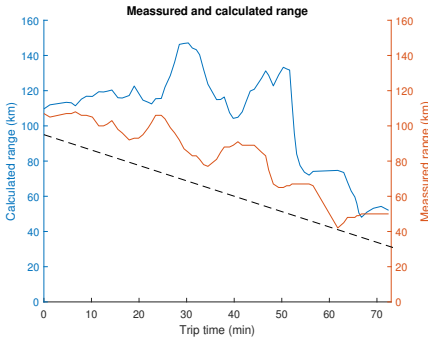




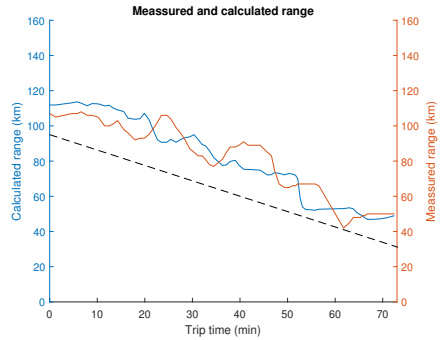
(a) Leaf: State of charge and range over trip time.



(b) Leaf: Speed and altitude over trip time.



(c) Leaf: Comparison of calculated and measured range over trip time.



(d) Leaf: Comparison of calculated and measured range over trip time.

Fig. 1: Processed data of Nissan Leaf

displayed range car and the calculated range using the equation 4 is shown in the figure 1d.

## 4.2 Peugeot IoN

This vehicle logs 127 variables in three datalogs. Every datalog have its own technique of logging, one log is made every second, one log every driven km. Peugeot IoN log displayed range - so there is no need of additional data acquisition. The graph of the state of the charge and the displayed BEV range over time is shown in the figure 2a.

Contrary of Nissan Leaf log in these graphs can be observed that well experienced driver lead this small and short range BEV through relatively long journey so the deviations is relatively small. The speed and altitude profile of the route is shown in the figure 2b. Speed is nearly constant whole journey, despite the fact that this vehicle absent cruise control. The speed and altitude profile of the route is shown in the figure 2b. The comparison of the displayed range car and

the calculated range using the equation 2 is shown in the figure 2c. The comparison of the displayed range car and the calculated range using the equation 4 is shown in the figure 2d.

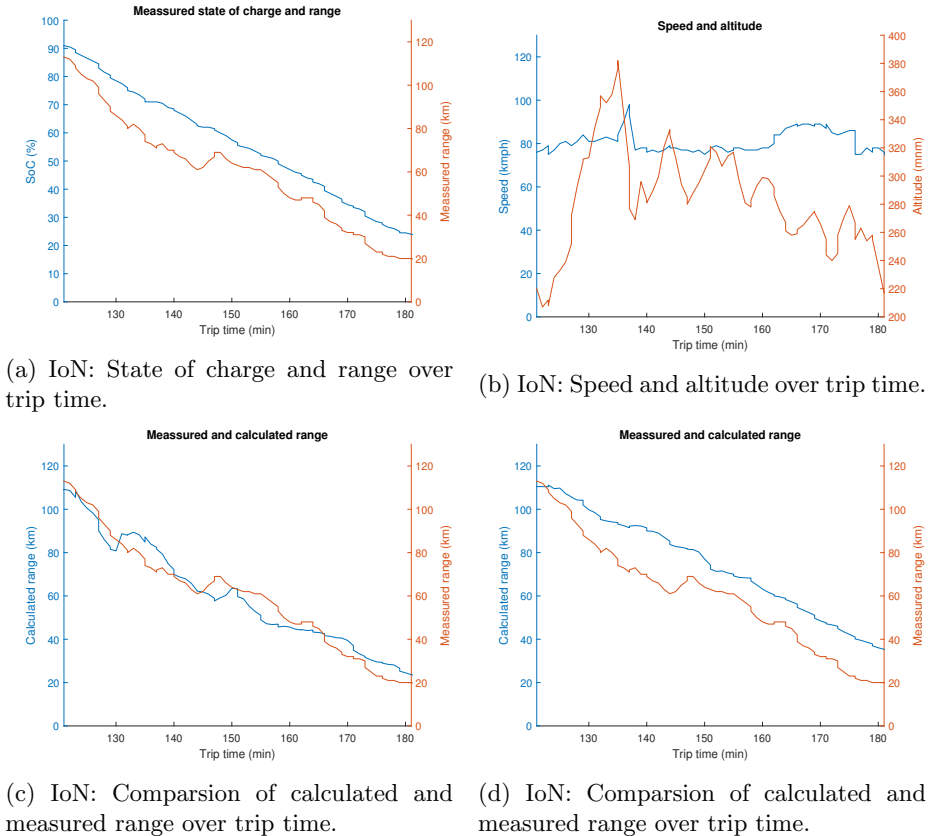


Fig. 2: Processed data of Peugeot IoN

## 5 Conclusion

The presented article outlines the issue of the BEV range parameter, the problems of most contemporary BEVs with the range parameter and two ways to calculate the range in their own way. Data from BEV paths were measured to identify the range calculation algorithm. This identification was only partially successful. The assumption of a simple floating average was not confirmed; on the contrary, the assumption was made that in any ride that was logged in, the range parameter was not developed as predicted and there were always deviations from the forecast. The magnitude of the deviations depended on the change

in driving style or terrain compared to the latest rides made. Further, the possibilities of improving the credibility of the range parameter were discussed by refining the estimate based on modern control theory. In the next research, Least mean squares (LMS), Model predictive control (MPC) and Adaptive neuro fuzzy inference system (ANFIS) algorithms will be tested to calculate range and to optimize energy flow in BEV.

## References

- BADIN, F.; BERR, F. Le; ...; CONDEMINÉ, E., 2013. Evaluation of EVs energy consumption influencing factors, driving conditions, auxiliaries use, drivers aggressiveness. In: *Evaluation of EVs energy consumption influencing factors, driving conditions, auxiliaries use, drivers aggressiveness. 2013 World Electric Vehicle Symposium and Exhibition (EVS27)*. IEEE. Available from DOI: 10.1109/evs.2013.6914723.
- BARNEY, Richard; CARLSON; LOHSE-BUSCH, Henning; DIEZ, Jeremy; GIBBS, Jerry, 2013. The Measured Impact of Vehicle Mass on Road Load Forces and Energy Consumption for a BEV, HEV, and ICE Vehicle. *SAE International Journal of Alternative Powertrains*. Vol. 2, no. 1, pp. 105–114. Available from DOI: 10.4271/2013-01-1457.
- KW, Chew; YR, Yong, 2016. Effectiveness Comparison of Range Estimator for Battery Electric Vehicles. *Advances in Automobile Engineering*. Vol. 05, no. 01. Available from DOI: 10.4172/2167-7670.1000128.
- NEUBAUER, Jeremy; BROOKER, Aaron; WOOD, Eric, 2012. Sensitivity of battery electric vehicle economics to drive patterns, vehicle range, and charge strategies. *Journal of Power Sources*. Vol. 209, pp. 269–277. ISSN 0378-7753. Available from DOI: <https://doi.org/10.1016/j.jpowsour.2012.02.107>.
- ZHANG, Y.; WANG, W.; KOBAYASHI, Y.; SHIRAI, K., 2012. Remaining driving range estimation of electric vehicle. In: *Remaining driving range estimation of electric vehicle. 2012 IEEE International Electric Vehicle Conference*. IEEE. Available from DOI: 10.1109/ievc.2012.6183172.

# Boundary value problem solving with additional optimization procedure

Tomáš Dočekal

Department of Cybernetics and Biomedical Engineering, FEECS,  
VŠB – Technical University of Ostrava, 17. listopadu 15,  
708 33 Ostrava – Poruba, Czech Republic  
tomas.docekal@vsb.cz

**Abstract.** This article deals with a control of nonlinear systems. The focus is on the reference state trajectories and appropriate feed forward control signal planning. This problem is called boundary value problem. One of the complicated parts when solving this problem is to specify the initial guess for state trajectories. The additional optimization procedure for dealing with this is described in this paper. There is an emphasis on universality of described boundary value problem solving process because application in connection with the various nonlinear systems.

**Keywords:** boundary value problem; optimization; inverted pendulum;

## 1 Introduction

The need to manage a system is very common nowadays. The increasing trend is related to the development of control systems performance and technical cybernetics, especially modern control theory [1], [2]. Due to these facts it is common to control more and more complex nonlinear systems. There are two basic tasks to deal with. The first one is stabilization in specific operating point. In this case, it is possible to linearize the controlled system and to use linear control methods. The second task is to move the system between different operating points. This task is more complicated, because it is necessary to work with nonlinear system. The more advance methods have to be used.

The complex problem of moving between operating points in state space is called trajectory tracking because of the need to specify the trajectory between these points. It is possible and useful to divide the problem into two parts – designing open-loop control with associated state trajectories and designing closed-loop controller for system stabilization along the trajectories. This paper is focused on the trajectory planning problem.

The problem is specified with state space description of controlled system and two operating points described by state space variables values in selected times. This problem can be also called two points boundary value problem (TPBvP). If there are the same number of state space equations and boundary conditions (equations specify-

ing both operating points), the problem is called boundary value problem (BvP). However, if there are more boundary conditions than equations describing the system dynamics, we are speaking about BvP with free parameters. The free parameters are generally referred to as  $\lambda$  and their number corresponds to the difference between number of boundary conditions and state space equations. They are used for parameterizing the control signal candidate function, which has to be specified.

The Matlab was used for its solving. This environment includes functions called *bvp4c* and others for solving the BvP [5]. The following parts deal with issues connected with using these functions, especially the need to enter the initial guess of the state trajectories and also parameters  $\lambda$  when solving BvP with free parameters.

## 2 Initial guess influence

Influence will be presented on simple example. System described by differential equation (1) will be used.

$$y'' + y^2 = 0 \quad (1)$$

There are two boundary conditions, (2) for  $t = 0$  and (3) for  $t = 4$ .

$$y(0) = 0 \quad (2)$$

$$y(4) = 1 \quad (3)$$

For the purpose of solving BvP it is necessary to rewrite the equation (1) to group of first order ODEs (4) and (5).

$$y_1' = y_2 \quad (4)$$

$$y_2' = -y_1^2 \quad (5)$$

Where  $y_1 = y$  and  $y_2 = y'$ .

It is necessary to specify initial guess for the shape of  $y_1$  and  $y_2$ . In this simple example the constant values are used despite the fact that it does not meet the boundary conditions (2) and (3). The initial guess is used for choosing which solution will be found by *bvp4c* function.

The differences of  $y_1$  and  $y_2$  resulting waveforms for initial guesses  $[1; -1]$  and  $[-1; 1]$  are shown in fig. 1.

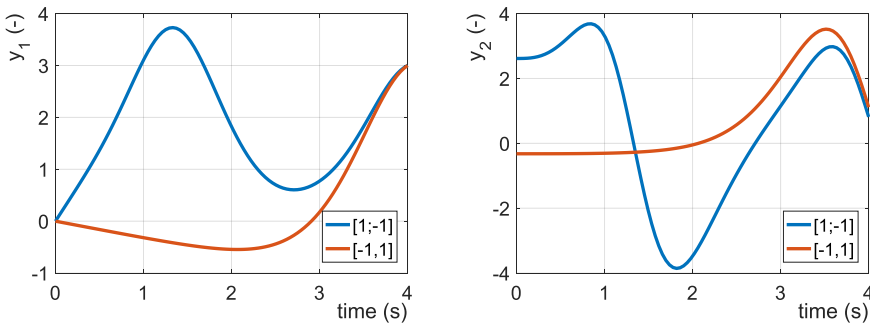


Fig. 1. Resulting waveforms of  $y_1$  (left) and  $y_2$  (right) for different initial guesses

### 3 BvP solving algorithm

Described algorithm was tested for planning inverted pendulum swing up control signal and state trajectories during its development. The description of inverted pendulum according to the [3] was used. The boundaries for swing up are  $[\pi, 0, 0, 0]$  for starting point and  $[0, 0, 0, 0]$  for ending point. Only state space equations for pendulum angle and angular speed were used. The reason is that control signal for this model is cart acceleration and the boundaries for cart position and speed can be fulfilled by choosing appropriate candidate function. This procedure will be described in next part.

#### 3.1 Candidate function

It is expectable that the motion of pendulum will be oscillating, so the sum of harmonic signals (6) was chosen as the candidate function with parameters  $\lambda$  as amplitudes of individual components. The period  $T$  of first harmonic is equivalent to length of transition between specified boundaries.

$$u(t) = \sum_{k=1}^3 \lambda_k \sin(kt\omega) \tag{6}$$

According to the specification of BvP with free parameters, it is possible to use two parameters  $\lambda$ , that means two harmonic components. The third is used to fulfill boundaries conditions for cart speed (7) and position (8). These values can be obtained by integration of control signal.

$$v(t) = \int u(t)dt = \sum_{k=1}^3 -\frac{\lambda_k \cos(kt\omega)}{k\omega} \tag{7}$$

$$s(t) = \int v(t)dt = \sum_{k=1}^3 -\frac{\lambda_k \sin(kt\omega)}{(k\omega)^2} \tag{8}$$

When checking the boundary values by substituting  $t = 0$  and  $t = T$ , the cart position (8) is zero due to  $\sin(k \cdot 2\pi)$  is zero for integer value  $k$ . However, the speed is defined for both points by (9) and it has to be zero.

$$v(0) = v(T) = -\frac{\lambda_1}{\omega} - \frac{\lambda_2}{2\omega} - \frac{\lambda_3}{3\omega} = 0 \quad (9)$$

Based on (9) it is possible to derive value of  $\lambda_3$  (10) to meet boundary conditions. The resulting candidate function with two parameters  $\lambda$  is equivalent to (11), which is derived from (6) and (10).

$$\lambda_3 = -3\lambda_1 - \frac{3}{2}\lambda_2 \quad (10)$$

$$u(t) = \left(-3\lambda_1 - \frac{3}{2}\lambda_2\right) \sin(3t\omega) + \sum_{k=1}^2 \lambda_k \sin(kt\omega) \quad (11)$$

### 3.2 Optimization procedure

The chapter 2 described the influence of initial guess using simple example. It is even greater when working with complex system. While solving BvP with free parameters, the initial guess for state trajectories and for parameters  $\lambda$  is required. The preparation of the first one depends on specific system. The trajectories should fulfill the boundary conditions. This procedure will be described later on the inverted pendulum system.

The second part of initial guess consists of parameters  $\lambda$  constant values. Their values can be determined in specific cases based on experimental measures or simulations; however there is usually no rule on how to choose them. The problem is that their values significantly affect the BvP results, which can be inappropriate for use with real system despite the fact that they fulfill the boundary conditions.

This problem was solved by using optimization procedure. It is possible to specify the cost function that the results will be heading towards specified properties. The cost function can also contains limitations of state values based on real system limitations. This approach is generally applicable to a wide range of systems. It repeats iteratively several steps:

- Select parameters  $\lambda$  values
- Calculate BvP for selected boundaries and system
- Calculate the cost function for BvP results
- Change the values of parameters  $\lambda$  to reduce the criterion

The function *fmincon* was used for this purpose in Matlab. The intention is to find a global minimum in the manner described in [4].

## 4 Experimental verification

The described algorithm for solving BvP with free parameters was tested for planning control signal and reference state trajectories for inverted pendulum swing-up, as was mentioned. This process of planning includes several steps, which will be described. Identification of inverted pendulum and state space model derivation will not be included, it can be found in [3].

First step before running the solving algorithm is preparation of state trajectories initial guess. As was mentioned before, only two state space variables will be included in BvP, therefore two waveforms are necessary – for pendulum arm angle and angular speed. The simulation in Simulink was prepared for this purpose. At the beginning of the simulation, the pendulum arm was placed near the top unstable equilibrium and the uncontrolled swing down was simulated. Because the settling in bottom equilibrium would last long time, the additional varying damping was included. The waveform of pendulum arm angle and angular speed are noted  $x_1(t)$  and  $x_2(t)$ , length of simulation is  $T$ . After reversing the flow of the time (12), the obtained swing down trajectory of pendulum arm angle can be used as the initial guess for BvP.

$$x_{1rev}(t) = x_1(T - t) \tag{12}$$

The trajectory for angular speed is also necessary; however it cannot be obtained in the same way as previous one. Equation (13) shows that reversing the flow of time leads to negative reverse waveform obtained from swing down simulation. The other way is to calculate derivation from the previous trajectory.

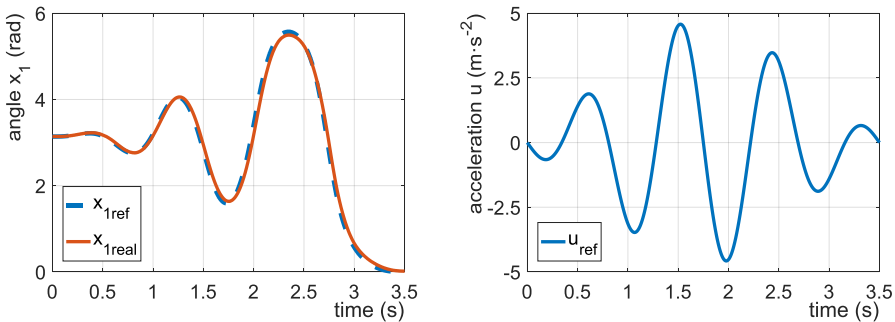
$$x_{2n}(t) = \frac{dx_{1n}(t)}{dt} = \frac{d[x_1(T-t)]}{dt} = x_2(T - t) \cdot (-1) = -x_2(T - t) \tag{13}$$

With initial guess prepared, the next step is running the solving algorithm. It is also necessary to specify the cost function (14). In this case, the sum of squares of difference between arm angle resulting and initial guess trajectory was used.

$$J = \sum_{i=0}^N (x_{1-init}[i] - x_{1-result}[i])^2 \tag{14}$$

where  $N$  is number of samples used for representing the trajectories.

The resulting control signal and state space trajectories were used for designing stabilizing feedback time varying LQR controller. This leads to use of two degrees of freedom control structure [6], [7]. The resulting control system was implemented in REXYGEN environment and tested in real time SIL simulation [3], [8] and then with real inverted pendulum. Figure 2 show the comparison of designed reference trajectory and the real one for inverted pendulum arm angle and designed reference control signal  $u(t)$ .



**Fig. 2.** Reference and real inverted pendulum arm angle swing up trajectory (left) and reference control signal for inverted pendulum swing up (right)



## 5 Conclusion

The trajectory planning problem can be solved by various methods. One of them is specifying it as BvP with or without free parameters. The influence of choosing the initial guess for state space variables and for parameters  $\lambda$  was described. The proposed solution consists in using the additional optimization procedure. It is responsible for choosing the initial  $\lambda$  values so that the selected cost function is minimized. This approach allows the user to limit state space variables due to real system limitations and also to modify the performance of resulting state trajectories and control signal.

The described method was tested for planning the trajectories and feed forward signal for inverted pendulum swing up. The results were used for designing stabilizing time varying LQR controller. The entire control system were implemented in REXYGEN environment and tested in SIL simulation and then with real inverted pendulum laboratory model.

Further work involves preparing set of parameterized candidate function and algorithm to choose appropriate one for controlled system, among other things. Another area of work is to modify the function for BvP solving.

## References

1. Kirk, Donald E. *Optimal control theory: an introduction*. Courier Corporation, 2012.
2. Tripathi, Saurabh Mani. *Modern control systems: an introduction*. Jones & Bartlett Publishers, 2008.
3. Ozana, Stepan, and Tomas Docekal. "Numerical methods for discretization of continuous nonlinear systems used in SIL/PIL/HIL simulations." *2019 22st International Conference on Process Control (PC)*. IEEE, 2019.
4. Ozana, Stepan, and Tomas Docekal. "PID controller design based on global optimization technique with additional constraints." *Journal of Electrical Engineering* 67.3 (2016): 160-168.
5. Shampine, Lawrence F., Jacek Kierzenka, and Mark W. Reichelt. "Solving boundary value problems for ordinary differential equations in MATLAB with bvp4c." *Tutorial notes 2000* (2000): 1-27.
6. Kevickzy, László, and Cs Bányász. *Two-degree-of-freedom control systems: The Youla parameterization approach*. Academic Press, 2015.
7. Araki, Mituhiko, and Hidefumi Taguchi. "Two-degree-of-freedom PID controllers." *International Journal of Control, Automation, and Systems* 1.4 (2003): 401-411.
8. Koziorek, Jiri, et al. "Modeling and simulations in control software design." *Analytic Methods in Systems and Software Testing* (2018): 287.

# Concept of testbed for measuring of diagnostic data

Jakub Dohnal

Department of Cybernetics and Biomedical Engineering, FEECS,  
VŠB – Technical University of Ostrava, 17. listopadu 15,  
708 33 Ostrava – Poruba, Czech Republic  
doh0028@vsb.cz

**Abstract.** The concept of a testing workplace was designed to create a system that will generate data for the cloud platform. Various data processing and analysis methods corresponding to predictive maintenance will be further applied to these data. The proposed solution deals with the problem of measurement of operating variables of a rotating machine. The aim is to construct a rotating machine equipped with a motor, shaft, brake, sensors and a data collecting device. The rotating machine will be equipped with an electrometer for electrical measurement and an electric brake for change of mechanical load. The rotating machine will allow adjustment of the shaft balance. This option can simulate states that correspond to situations where the rotating machine is not operating in the correct condition.

**Keywords:** Predictive maintenance, Industry 4.0, induction motor, FFT, PLC

## 1 Introduction

Nowadays in modern industrial companies there is pressure to reduce the operating cost of production lines. These production lines often consist of electric, pneumatic, or hydraulic motors with other mechanical parts like bearings, shafts, clutches. Unplanned machine shutdowns make many companies lose profits[4]. Proper operational variables measurement with analysis can provide data on which can be determined the need for predictive maintenance. This predictive maintenance can be planned when the production line will be inactive, which reduces the money loss due to unfunctional production line. Predictive maintenance is one of many technologies in Industry 4.0 and requires a long-time measurement of targeted machine to determine correct and fault states of machine[4].

## 2 Electric motor fault diagnosis

Combination of measurement with data processing provides rotating machines monitoring using spectral analysis of operational process parameters (e.g. electric current, vibration, temperature, etc.). Time domain analysis using characteristic val-

ues to determine changes by trend setting, spectrum analysis to determine trends of frequencies, amplitude and phase relations, as well as cepstrum analysis to detect periodical components of spectra are used as evaluation tools. In many situations, vibration monitoring methods were utilized for incipient fault detection. However, stator current monitoring was found to provide the same indication without requiring access to the motor.[2]

According to the root cause of faults, electric motor faults can be generally categorized into two groups: electrical faults and mechanical faults. Fig. 1 shows pie chart describing fault occurrence percentage. The pie chart indicates bearing faults and stator-related faults are the most common faults in electric motors.

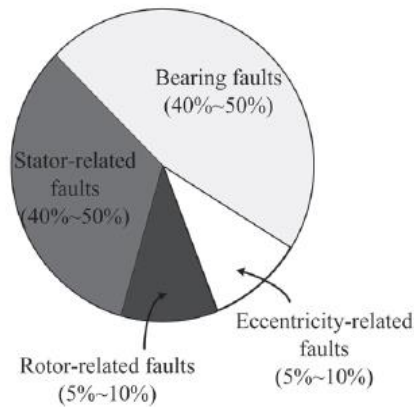


Fig. 1 – Electric motor fault occurrence rates [2]

## Measured variables for motor diagnosis

Sample rate for measurement should be high enough for further signal analysis. According to Nyquist theorem the sample rate should be at least two times bigger than the highest component of frequency spectrum[5].

### 2.1 Vibration measurement

Vibration measurement can determine mechanical state of the machine, typical state of bearings, shaft and stator[3]. There must be direct contact between motor and sensor to measure vibration, but there is another possible way, how to measure contactless. With microphones is measuring vibration via acoustic emission possible. When measuring vibration with acoustic emission, there is need for use of filters to filter ambient noises.

### 2.2 Electrical measurement

Electrical measurement can be made by measuring current and voltage of electrical motor. Current measurement can be made with measuring transformer or Hall sensor.

With these variables can be power, phase or advanced calculation like FFT and cepstrum made.

### 2.3 Other variables

There are more variables, vital to diagnose rotating device. Temperature of the motor is another factor, which can influence motor life span.

## 3 Data processing

Collected data can be further processed for thorough analysis. This analysis will help to determine state of the machine parts and from these data can decision-making algorithm provide feedback about predictive maintenance (change of bearings, repair of shaft, faulty stator coil, change of rotor etc.)

### 3.1 FFT

Fast Fourier transformation is possible to do with both vibration and electric current. For this method is necessary to implement these processing sections:

**1) Sampler:** Its purpose is to monitor a single-phase stator current. This is accomplished by removing the 50 Hz excitation component through low pass filtering, and sampling the resulting signal. The single-phase current is sensed by a current transformer or Hall sensor and sent to a 50 Hz notch filter where the fundamental component is reduced. The analog signal is then amplified, and low pass filtered. This is continued over a sampling period that is sufficient to achieve the required Fast Fourier Transformation.

**2) Preprocessor:** It converts the sampled signal to the frequency domain using an FFT algorithm. The generated spectrum includes only the magnitude information about each frequency component. Signal noise that is present in the calculated spectrum is reduced by averaging a predetermined number of generated spectra.

**3) Fault Detection Algorithm:** In order to reduce the large amount of spectral information to a usable level, an algorithm, in fact a frequency filter, eliminates those components that provide no useful failure information.

**4) Postprocessor:** Since a fault is not a spurious event but continues to degrade the motor, the postprocessor diagnostics the frequency components and then classifies them (for each specified fault).[1]

Processing sections 2 – 4 will be implemented in cloud platform.

## 4 Concept of testbed

Concept is based on Siemens products, which collects data from sensor modules and send them to cloud platform for further analysis.

### 4.1 Components for testbed

There are components used for data acquisition from sensors, control of load for motor, motor itself and others.

Fig. 2 shows electrical concept of testbed with power supply. Power supply of 24 V is used for powering PLC and all other modules. Power supply of symmetric 15 V is used for powering additional electronic for amplification and filtration of control for passive load (BLDC motor).

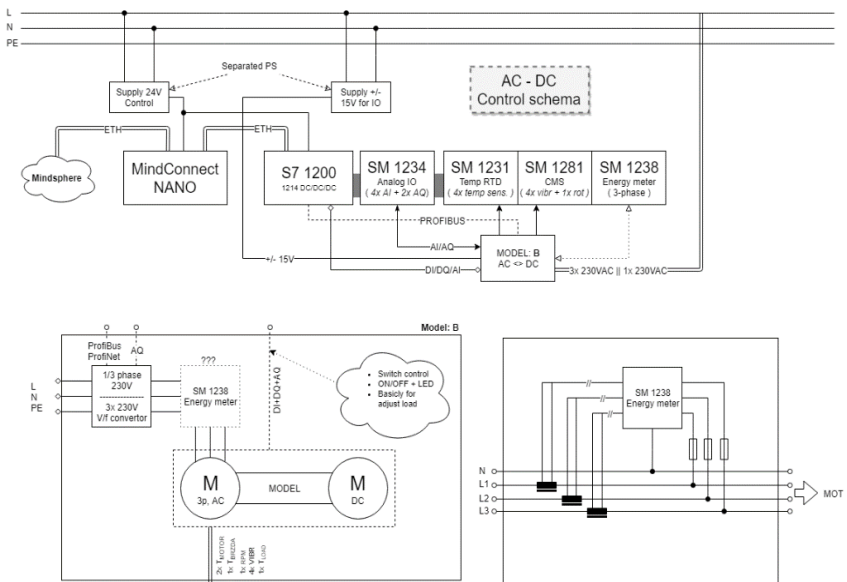


Fig. 2 – Electrical concept of testbed

In first step is 3 phase induction motor connected directly to power line, after first measurements is made, motor will be connected to frequency converter and comparison will be made.

Fig. 3 shows data and signal flows in testbed. Motor is measured for voltage, current and temperature, signals are connected to appropriate modules. Bearings are measured for vibration and temperature and there is possibility to change them from in good condition to in bad condition. Passive load (BLDC) is controlled via PLC with PWM signal and measured for wasted power on connected resistors (voltage and current, temperature). Mechanical eccentric part is possible to adjust manually and results in change of vibration, which furthermore influences supply current for induction motor.

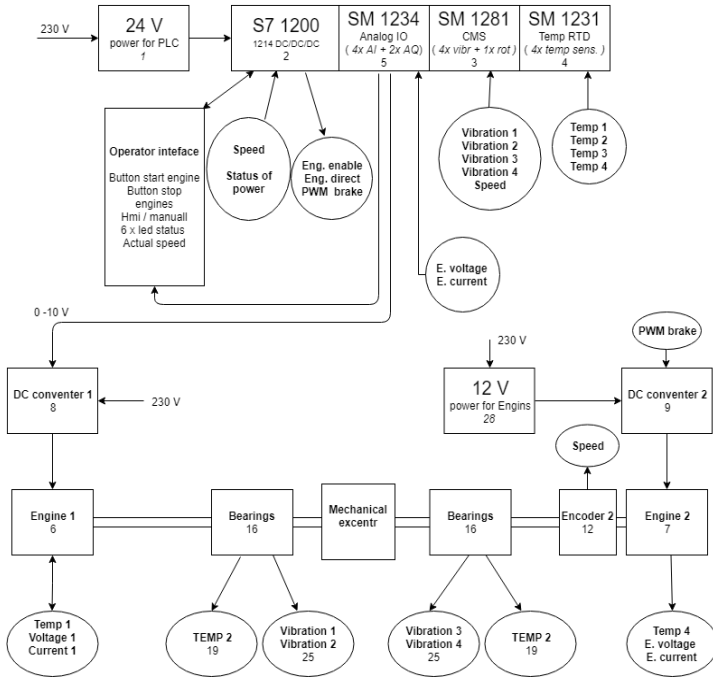


Fig. 3 – Data flow concept of testedbed

## 5 Conclusion

In this paper are described motor faults and their diagnosis, possible data processing and concept of testbed, which will generate data for this analysis. This analysis will be processed on PC and next on cloud platform. This testbed will serve as first step in real data analysis within Center of mechatronics project, which ends in 2022. Other goal of this project is to develop sensor system, which will be measuring data from sensors placed on machine and will alarm maintenance if some operating values will change from normal state. This sensor system will be tested on proposed testbed before it will be tested in real industrial operation.

Development of this testbed is still in progress, and there is a lot of possibilities to improve this testbed. Goal is to make testbed as modular as possible. This will lead to possibility of changing electric motor, electric break, bearings, or to addition of clutch and other mechanical parts like mechanical break.

## 6 Acknowledgement

The following grant is acknowledged for the financial support provided for this research by project: Centrum výzkumu pokročilých mechatronických systémů CZ.02.1.01/0.0/0.0/16\_019/0000867, VSB - Technical University of Ostrava.

## 7 References

1. Benbouzid, M. E. H., A review of induction motors signature analysis as a medium for faults detection, IEEE Transactions on Electron Devices, Vol. 47, No. 5, 984-993, 1998.
2. Lin, Fei & Chau, K.T. & C. Chan, C & Chunhua, Liu. (2013). Fault Diagnosis of Power Components in Electric Vehicles. Journal of Asian Electric Vehicles. 11. 1659-1666. 10.4130/jaev.11.1659.
3. Tůma Jiří, Diagnostika strojů. Ostrava: VŠB - Technická univerzita Ostrava, 2009. ISBN 978-80-248-2116-0.
4. Mařík, Vladimír. Průmysl 4.0: výzva pro Českou republiku. Praha: Management Press, 2016. ISBN 978-80-7261-440-0.
5. Nevřiva, Pavel. Úvod do analýzy signálů a soustav pro integrovanou výuku VUT a VŠB-TU. Ostrava: VŠB-Technická univerzita Ostrava, 2014. ISBN 978-80-248-3560-0.

# Analysis of the image quality of a radiographic cassette in dependence on X-ray irradiation

Klára Fiedorová and Martin Augustynek

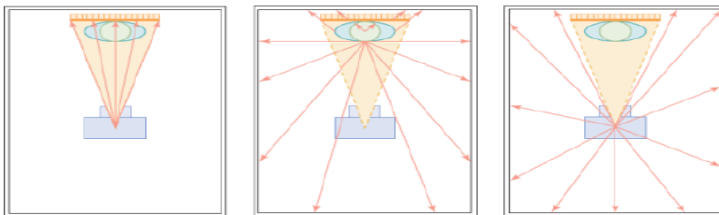
Department of Cybernetics and Biomedical Engineering, FEECS,  
VŠB – Technical University of Ostrava, 17. listopadu 15,  
708 33 Ostrava – Poruba, Czech Republic  
{klara.fiedorova, martin.augustynek}@vsb.cz

**Abstract.** The use of X-ray devices is nowadays a standard in imaging methods. Radiographic cassettes are used to create images that are stored in workplaces and affected by secondary radiation. Exposure to secondary radiation can damage the cassette and make it difficult to diagnose a health problem. The work deals with the analysis of the effect of secondary radiation on the radiographic cassette, which is produced by x-ray mobile device. The analysis is performed by the method of multiregional segmentation - OTSU, where the number of damaged pixels is determined. The result of this work is a predictive model, which should classify the level of deterioration of the image of skiagraphy.

**Keywords:** secondary radiation, skiagraphic cassette, OTSU.

## 1 Introduction

The primary beam breaks during X-ray examination and secondary radiation is produced. This radiation is a burden for the patient under investigation and for the x-ray cassettes stored in the examination room. Changes in the image that are caused by the exposure to secondary radiation will be reflected in the contrast in the image. The basic solve of the problem is the processing and editing of the images for quality information. The effect of secondary radiation decreases with increasing distance from the source. The generation of radiation load is shown in Figure 1. [1][2]



**Fig. 1.** Primary, scattered, leaking radiation



Image processing is an important process for obtaining important information. The basic image processing tools are adjusting the brightness, contrast or focus of the image. More advanced processing is used in specific radiological operations. Image segmentation algorithms are used. [3][4][5]

## 2 Experimental measurement

Measurements effect of secondary radiation on cassette was performed in The University Hospital in Ostrava. Phantom was used to replace the human body. Radiation exposure monitoring is provided by the DMC 3000 dosimeter. The X-ray source was provided by Siemens Mobile Mira. A piece of lead 1 mm thick sheet of 55 mm x 45 mm was used to investigate damage to the cassette.

### 2.1 Measurement conditions

The measurement was performed under constant conditions. The distance and other parameter settings were constant for each series of measurements. The phantom was on a stand at a height of 75cm and at 85cm from the X-ray device. The central beam generated by the mobile device is focused on the chest of the phantom.

The CR cassette with piece of lead and the dosimeter were placed perpendicular to the phantom and were placed 1m, 1.5m and 2m from the radiation source. The exposure values were: 77 kV and 11 mA. Ten same type of cassette were used.

## 3 Measurement results

Table 1 shows the measured dose values from the dosimeter and surface kerma (ionizing radiation energy).

**Table 1.** Measured values.

Distance (m)	Voltage (kV)	Exposition (mAs)	Spatial Kerma (cGy·cm <sup>2</sup> n)	Effective dose (mSv)
1	77	11	63.67	0.0010
1.5	77	11	63.73	0.0009
2	77	11	63.69	0.0005

## 4 Image processing

The obtained image on the memory film was latent, the conversion to digital form was performed by a red laser. Processing of image was performed using tool MATLAB. Areas of Interest (RoI) were extracted, removing unwanted portions of the main image. Removing portions produces an image of 1008 x 832 pixels. [6][7][8]

### 4.1 Image Segmentation

The obtained images were processed by the multilevel Otsu method. Using this method, a multiregional segmentation model is created. The method works by determining the threshold value in the image, which is calculated from the variance value between classes. [3][4][5] A histogram has been created that plots pixel frequencies depending on the gray level. The histogram (Fig. 3) shows two peaks corresponding to the two object classes in the image and the threshold is determined there. The histogram is divided into regions, the number of which is given by the number of thresholds. Eight segmentation classes were used, where levels  $<5$  were the interest area with assigned value 1 corresponding to secondary radiation. Threshold levels  $\geq 5$  represented objects with an assigned value of 0 corresponding to the lead object (Fig. 2).



Fig. 2. Original image, multiregional segmentation output.

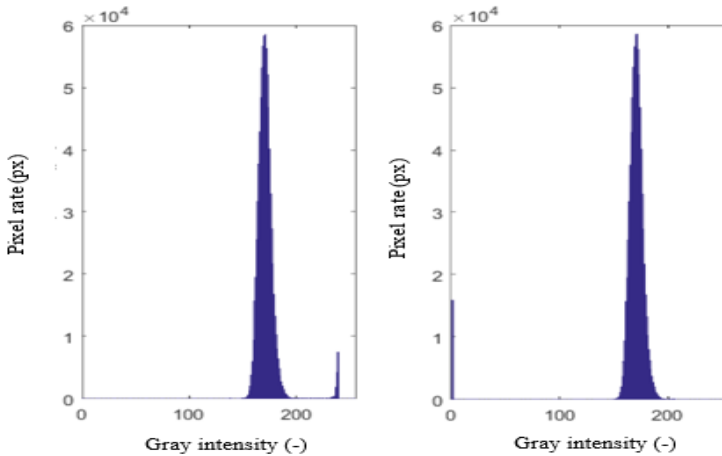
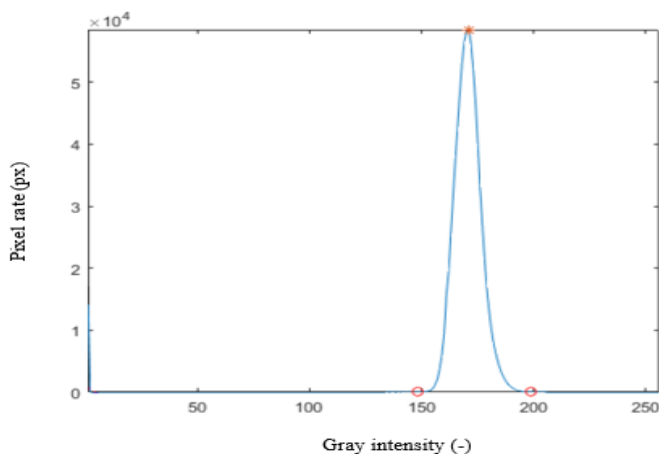


Fig.3. Histogram of the original image, histogram of the image after segmentation.

### 4.2 The band intensity

After segmentation, the histogram was fitted with a curve determined by the dominant peak. The curve used is characterized by two depressions for different levels intensity of secondary radiation (Fig. 4). Then, the pixels below the histogram were calculated. These pixels correspond to the secondary radiation. The table 2 shows a sample of the elements after extraction.



**Fig. 4** The curve showing the number of the pixels for single levels of gray.

**Table 2.** Elements after extraction.

Distance (m)	Number of pixels (px)	Maximum peak intensity (-)	Lower bandwidth limit (-)	The upper limit of the bandwidth (-)
1	823115	82	61	111
1.5	820991	135	112	160
2	823450	174	153	205

## 5 Data processing

Statistical analysis was performed within the number of pixels below the histogram curve and the percentage of pixels associated with secondary radiation was calculated. The assumption set in the introduction is confirmed that secondary beam pixels occupy the same pixel on the entire frame at all 10 images at all 3 distances. Furthermore, the maximum intensity values were subjected to statistical analysis. The intensity of the gray peak increases as the distance of the CR cassette from the source increases. As a result, it is confirmed that the radiation loses its intensity with increasing distance. Due to the calculated average intensity limit, it was possible to determine the average bandwidth for each distance.

Tables 3 and 4 contain calculated statistics indicators for the effective dose and subsequently for the kerma region. The effective dose was measured with 100% accuracy, except for 1.5 m with a small standard deviation. Surface kerma is independent of the distance of the CR cassette from the radiation source.

**Table 3.** Effective dose indicators.

	1 m	1.5 m	2 m
Number of measurements	10	10	10
Minimum	0.0010	0.0008	0.0005
Lower quartile	0.0010	0.0009	0.0005
Average value	0.0010	0.0009	0.0005
Median	0.0010	0.0010	0.0005
Upper quartile	0.0010	0.0010	0.0005
Maximum	0.0010	0.0010	0.0005
Variance	0	0	0
Std. deviation	0	0.0001	0

**Table 3.** Surface kerma indicators

	1 m	1.5 m	2 m
Number of measurements	10	10	10
Minimum	63.41	63.41	63.69
Lower quartile	63.55	63.71	63.76
Average value	63.579	63.695	63.806
Median	63.585	63.725	63.83
Upper quartile	63.62	63.73	63.85
Maximum	63.67	63.77	63.87
Variance	0.005	0.0105	0.0034
Std. deviation	0.0711	0.10255	0.0582

## 6 Conclusion

In hospitals, cassettes are often stored in an examination room where they are exposed to radiation and can be damaged. In this work we developed a method based on OTSU segmentation to find and separate the effect of secondary radiation on cassettes. The secondary radiation pattern may be determined by the intensity of the incident secondary radiation depending on the distance from the radiation source. The influence of said radiation on the quality of the analyzed image is evaluated by the: number of pixels below the histogram curve, maximum intensity, lower and upper band limits. The obtained information was used to create a predictive model. The model is used to evaluate the image quality depending on the distance from the radiation source.

## References

1. CHOY, Hak, et al. Radiation therapy systems that include primary radiation shielding, and modular secondary radiation shields. U.S. Patent Application No 14/688,751, 2016.
2. PISANO, S., et al. Single and double spin asymmetries for deeply virtual Compton scattering measured with CLAS and a longitudinally polarized proton target. *Physical Review D*, 2015, 91.5: 052014.
3. VALERI, Gianluca, et al. Open source software in a practical approach for post processing of radiologic images. *La radiologia medica*, 2015, 120.3: 309-323.
4. MAHMOOD, Nadeem, et al. Image segmentation methods and edge detection: an application to knee joint articular cartilage edge detection. *Journal of Theoretical and Applied Information Technology*, 2015, 71.1: 87-96
5. WILLIAM, Wasswa, et al. A review of applications of image analysis and machine learning techniques in automated diagnosis and classification of cervical cancer from pap-smear images. In: 2018 IST-Africa Week Conference (IST-Africa). IEEE, 2018. p. Page 1 of 11
6. PATIL, Prachi; PATIL, S. V.; CHAUDHARI, D. D. Research on conversion of DICOM multi-frame medical image in to multimedia format using MATLAB. *International Journal of Current Engineering and Technology*, 2015, 5: 156-160.
7. PAL, Sankar K., Ashish GHOSH a Malay K. KUNDU. *Soft computing for image processing*. New York: Physica-Verlag, 2000. ISBN 3790812684.
8. KUBICEK, J., Penhaker, M., Cerny, M., Augustynek, M., Korhelik, K., Vodakova, A., Oczka, D. Analysis and modeling of secondary X-ray effect on structure of skiagraphy images (2018) *BIODEVICES 2018 - 11th International Conference on Biomedical Electronics and Devices, Proceedings; Part of 11th International Joint Conference on Biomedical Engineering Systems and Technologies, BIOSTEC 2018*, 1, pp. 30-38.

# Simulation Framework for Weather Forecasting Simulation Based on Historical Solar Irradiance Data

Karolína Gaiová and Michal Prauzek

Department of Cybernetics and Biomedical Engineering, FEECS,  
VŠB – Technical University of Ostrava, 17. listopadu 15,  
708 33 Ostrava – Poruba, Czech Republic  
karolina.gaiova@vsb.cz

**Abstract.** This contribution solves the method for Environmental Wireless Sensor Network (EWSN) node management. The aim of this research contribution is find methods how to Maintain all systems features desirable for a power management and recharging from alternative sources. The research explores the possibilities of the weather forecasting and the resulting energy management. This paper offers a proposal of arrangements for weather prediction of solar irradiance based on historical data. The node is placed to an environment and it has to manage measurement and data transmission. The aim is to design simulations based on weather forecasts from obtained data.

**Keywords:** forecast, weather prediction, WSN, environment monitoring

## 1 Introduction

Weather forecasting is a part of science and technology, which is used to predict the conditions of the atmosphere for a certain location and time. Weather Prediction Techniques (Numerical, statistical, and more...) represent a significant part in the meteorological field as it presents for the time theories and software of the complex dynamical and physical processes required. That's a reason why forecasts can be less accurate as the difference between current time and specific time for which the forecast is being made increases [9].

There are many different methods and tools for weather observations for the analysis, e.g. Surface data: foundings, hip and buoy data, Satellite data, Radar data, Commercial aircraft data. All of these resources, along with various computational methods, can help to find weather patterns for a certain area. For weather prediction (forecasting) are mostly used current and past observations to predict weather in near future. Then, the result of using a mathematical model and historical data can be prognostic chart (the final forecast chart representing the atmosphere at a specified future time) or meteorological graphs. This chart can represent e.g. temperature, wind, humidity or amount of the solar irradiance.

One of the most important skill in forecasting is accuracy. Accuracy is arbitrary and relative, it's not clearly, objectively defined. The accuracy and skill should be more accurate than utilizing persistence (takes effect on a time frame of minutes to hours) or climatology (on time frame of hours to a few days).

Wireless sensor networks (WSN) have a lot of application areas. They are often located in the heavily nonaccessible places without electricity support of the power grid or without access for regular maintenance. Therefore, there are a necessary to advanced intelligent control strategies to achieve a proper functionality of WSN device operation. A broader survey was performed before the experiment, which is shunt in the second chapter.

## 2 Related work

Environmental monitoring systems are indispensable for the study of various natural phenomena. They are located in remote locations, which cause that their reliability and energy independence is very important.

In the following contribution ([10]), several methods of varying complexity are describe for prediction he total amount of daily solar energy available for harvest in the near future. All proposed methods are based solely on atmospheric surface pressure, with the aim of keeping the prediction algorithm as simple as possible.

The evolution of weather science as well as of high-performance computing and observing systems in the future is crucial for continuing the progress in Weather Prediction. Consequently, the present period is of fundamental importance for how weather forecasting and also climate science will evolve. These global predictions provide essential initial and boundary information for finer-scale limited-geographical-domain simulations of short-range detailed weather development. The following Review describe the fundamental scientific basis of numerical weather prediction. The numerical weather prediction is among the greatest of any area of physical science. Following paper ([4]) introduce scientific knowledge and technological advances over many years.

Seasonal climate forecasts are being used increasingly across a range of application sectors. Seasonal forecasts are made from ensembles of integrations of numerical models of climate. The paper ([12]) deals with the reliability of regional temperature and precipitation forecasts of the current operational seasonal forecast system of the European Center for Medium-Range Weather Forecasts, universally regarded as one of the world-leading operational institutes producing seasonal climate forecasts. In the ([8]), A method of estimating the economic value of weather forecasts for decision-making is described. In the paper, the method has recently been used for user-oriented verification of probability forecasts. The method is illustrated using site-specific probability forecasts generated from the ECMWF ensemble prediction system and deterministic forecasts from the ECMWF high-resolution global model. In the paper Value of probability forecasts and Comparison of probability and deterministic forecasts is presented.

In ([2]), the forecasting is increasingly showing value for the improved scheduling of wind energy, and as shown above, such forecasts can have substantial value even if they are not perfectly accurate. Using physics-based forecasting models, real-time wind and energy data from the wind plants, and computational learning systems such as artificial neural nets or support vector machines. Wind forecasting tools are a critical element in minimizing the impact costs and ensuring reliability with larger amounts of wind energy on the grid, and the approaches and reasonable expectations for state-of-the-art wind forecasting methods are described.

In the paper ([3]) discuss the issue of renewable energies is that the output of these kinds of systems depending on variability of weather conditions that cannot be predicted and controlled. They indicate that the short-term forecast is going to be essential for effectively integrating solar energy sources, being a very useful tool for the reliability and stability of the grid ensuring that an adequate supply is present. In this paper a new methodology for forecasting the output of a generator based on artificial neural network is introduce.

In the harvest environmental energy and regulation of their usage to satisfy their demand is discussed. There are describe prediction strategies that use weather forecasts, which are more accurate than prediction strategies based on the past, and are capable of improving the performance of a variety of systems. Also the analysis of the weather forecast, observational, and energy harvesting data to formulate a model that translates a weather forecast to a solar or wind energy harvesting prediction, and quantify its accuracy.

This contribution [6] solve the contribution of power production by photovoltaic (PV) systems, an efficient use of the fluctuating solar power production and the management of the electricity grids and for solar energy trading. An efficient use of the solar power will highly benefit from forecast information on the expected power. In paper is discussed an approach to predict regional PV power output according to the three days ahead provided by the European Centre for Medium-Range Weather Forecasts (ECMWF). The main goal is the description and evaluation of the approach of irradiance forecasting. This is a necessity for PV power prediction. At the end of the paper, an approach to derive weather specific prediction intervals for irradiance forecasts is presented.

The paper ([11]) solves weather forecasting error in renewable distributed energy resources (DERs) , specifically the solar energy prediction. The performance of historical and observed weather data errors is assessed using a solar PV generation forecasting model. At the end the comparison is mentioned (between the forecasted weather and the observed data).

### 3 Hardware Model of EWSN Node

This research is based on the simulation, which are realized through simulation framework. The simulation framework is proposed by prototype of the EWSN device. This device is designed as an energy harvesting node. The current version of the prototype has following parameters: 32-bit RISC microcontroller (MCU)



ARM Cortex-M0+ and it is housed in a watertight (IP67) case. The device is equipped with a solar panel, a supercapacitor serving as energy storage, primary batteries for backup, an SD-card data store, and a wireless transmitter. The circuitry is realized in three printed circuit boards: the main motherboard equipped with MCU, and the solar panel and signal conditioning boards mounted by board-to-board connectors. For more detailed information read in [5].

The node has implemented a firmware, which include following parameteres: a duty cycle mode with Sleep mode interleaved between two active states, three wake-up operations modes when it is activated. According to the criteria for sensing and transmitting the appropriate mode is operated. If criterias do not meet, sleep mode is activated. Other alternatives of operating modes are the following modes: Sensing mode, Transmission mode and Standby mode. Sensing mode collects data from sensors and store it on a small internal non-volatile memory device. Transmission mode is used for transmitting all data to the network (all data from the internal memory device is transferred to a large, permanent internal storage device - SD-card). Standby mode serves for the node wakes up and calculates state of energy storage (SoES).

The basic parameters of the hardware model are: solar panel area of 648 mm<sup>2</sup> with energy efficiency of 21 %. The power supply voltage is 3.3 V, the total energy buffer capacity is 750 J. These parameters have been gained during standard operation measurements on experimental setup and used as input parameters for the simulator. More detailed information you can find in ([5]).

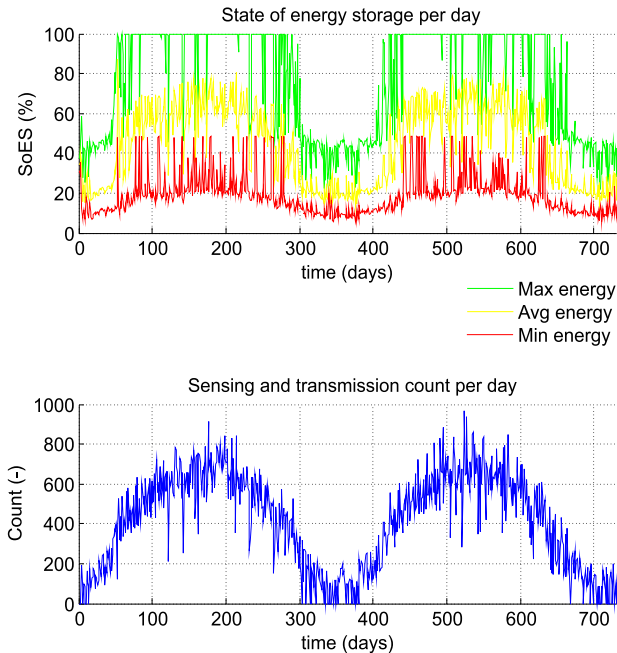
## 4 Simulation Framework and Input Data

For these experiments is used previously published simulation framework (see Konecny et al. (2019)). The simulation framework serves to simulate the EWSN node and for evaluating the control algorithm. The simulation framework is used for simulating the historical data from environment where WSN node is usually located. Individual blocks are more detailed describe in previous mentioned contribution.

The data manager block read historical data and arrange the input for energy source block. Energy source produces energy and charges an energy storage represented by energy storage block. The simulation block represents the simulation procedure and controls the simulation process. The controller block is basically the firmware of the EWSN node.

The simulations described in this contribution use five years of data from the Fairview Agricultural Drought Monitoring station (AGDM) in Alberta, Canada [1], located at 56.0815° latitude, -118.4395° longitude, and 655.00 m elevation. The data set solar irradiance measurements in W/m<sup>2</sup> measured at 5-minute intervals continuously from 2008 to 2012. The simulation runs in 1-minute iterations with the assumption that solar irradiance remains constant in every 1-minute iteration over each 5-minute interval [5].

In the graph it is possible to see basic simulation based on the decision-making process of the timer controller. The next step to improve the algorithm



**Fig. 1.** Two years simulation output: Up SoES maximum, minimum and average level in each day; Down total sensing cycles per day

will be to add a prediction parameter to improve the power management of the node and thus the device as a whole WSN. m

#### 4.1 Proposal of Forecast Simulation

In this contribution, the weather forecasting is used to predict the amount of the energy which will be available for WSN (Wireless Sensor Network) device. In this case, it is possible to define an EWSN, which characterize Environmental WSN. The EWSN can collect environmental data from environment surroundings. Among these data (parameters) temperature measurements, light monitoring, soil monitoring and gas analysis (see [7]), solar irradiance, wind monitoring (see [2]).

For predicting the weather condition based on historical data a short-term forecast will be used. In the experiment we suggest to use a short-range forecast for 1,2 and 3 days. For regional forecasts, one of the important paramentr is forecast accuracy. This parametr is increasing in dependency on the size of the region. For example, for the complete area of Germany, the rRMSE amounts to 13 % see in [6]. Values for prediction are calculated as an average of given values obtained from historical data and then used for prediction. Together with the forecast accuracy gained.

## 5 Conclusion

Methods and research related to WSN and weather prediction are presented in the article. The thesis proposes a method for this prediction, together using parameters and knowledge obtained from the research. A basic simulation was performed based on historical data, which is currently extended with a new controller using a prediction.

## References

1. Alberta agriculture and rural development. AgroClimatic Information Service (2013), <http://agriculture.alberta.ca/acis/>
2. Ahlstrom, M.L., Zavadil, R.M.: The role of wind forecasting in grid operations & reliability. In: 2005 IEEE/PES Transmission & Distribution Conference & Exposition: Asia and Pacific. pp. 1–5. IEEE (2005)
3. Almonacid, F., Pérez-Higueras, P., Fernández, E.F., Hontoria, L.: A methodology based on dynamic artificial neural network for short-term forecasting of the power output of a pv generator. *Energy conversion and Management* 85, 389–398 (2014)
4. Bauer, P., Thorpe, A., Brunet, G.: The quiet revolution of numerical weather prediction. *Nature* 525(7567), 47 (2015)
5. Konecny, J., Prauzek, M., Borova, M., Janosova, K., Musilek, P.: A simulation framework for energy harvesting in wireless sensor networks: Single node architecture perspective. 2019 23rd International Conference Electronics, ELECTRONICS 2019 (2019)
6. Lorenz, E., Hurka, J., Heinemann, D., Beyer, H.G.: Irradiance forecasting for the power prediction of grid-connected photovoltaic systems. *IEEE Journal of selected topics in applied earth observations and remote sensing* 2(1), 2–10 (2009)
7. Musilek, P., Prauzek, M., Krmer, P., Rodway, J., Barto, T.: Intelligent energy management for environmental monitoring systems. *Smart Sensors Networks: Communication Technologies and Intelligent Applications* pp. 67 – 94 (2017)
8. Mylne, K.R.: Decision-making from probability forecasts based on forecast value. *Meteorological Applications* 9(3), 307–315 (2002)
9. Richardson, L.F.: *Weather prediction by numerical process*. Cambridge University Press (2007)
10. Rodway, J., Musilek, P., Lozowski, E., Prauzek, M., Heckenbergerova, J.: Pressure-based prediction of harvestable energy for powering environmental monitoring systems. In: 2015 IEEE 15th International Conference on Environment and Electrical Engineering (EEEIC). pp. 725–730. IEEE (2015)
11. Sangrody, H., Sarailoo, M., Zhou, N., Tran, N., Motaleb, M., Foruzan, E.: Weather forecasting error in solar energy forecasting. *IET Renewable Power Generation* 11(10), 1274–1280 (2017)
12. Weisheimer, A., Palmer, T.: On the reliability of seasonal climate forecasts. *Journal of the Royal Society Interface* 11(96), 20131162 (2014)

# Data processing using PLC and MCU based on IoT

Antonín Gavlas

Department of Cybernetics and Biomedical Engineering, FEECS,  
VŠB – Technical University of Ostrava, 17. listopadu 15,  
708 33 Ostrava – Poruba, Czech Republic  
antonin.gavlas@vsb.cz

**Abstract.** An article is based on comparing of process data within PLC and MCU using Cloud platforms. The last advances in computation and communication technologies are taking shape in the form of IoT (Internet of Things), M2M (Machine to Machine) technology, Industry 4.0 and Cyber Physical Systems. Internet of Things connects an enormous number of devices. Devices within IoT need small number of sensors and control data, but with numerous messages. Today Cloud services work with the volume of these data and support large scale IoT systems. This paper represents a comparison of solutions Industrial and Commercial IoT.

**Keywords:** Industrial IoT, Commercial IoT, PLC, MCU, Cloud platforms.

## 1 Introduction

The world around us develops very quickly. Gradually it increases demands of people and companies on the technologies that surround us every day. The industry is increasingly focusing on more efficient use of resources, increasing productivity, reducing operating costs or safety of workers. For all of that it is possible to use technology Internet of Things (IoT). IoT is a network of interconnected objects (things) that are uniquely addressable with the fact that this network is based on standardized communications protocols allowing the exchanging and sharing of data and information. [1] [2]

### 1.1 Development of IoT

In terms of the development of IoT it was gradually formed two main directions, but they do not compete with each other. These directions are focused on their unique area of use (Fig. 1). The first segment (Industrial IoT) is based on M2M (Machine to Machine) part and it adds the possibility of analyzing data through Cloud platform. Communication between devices within IoT is built on a different principle than M2M. Existing M2M solution generally works on preprogrammed communication. IoT contains “things”, which communicate with each other randomly and all the time. [3] [5]

Within this segment it is possible to create a definition for Industrial Internet of Things (IIoT), which represents application of the IoT to the manufacturing industry. It improves manufacturing by allowing accessibility of far greater amounts of data and far more efficiently than before. Companies look for benefits from lower consumption

as a result of predictive maintenance, improved safety and more operational efficiency. The second segment focuses on consumers - consumer products, appliances, IT, telecommunication equipment and more. Electronic devices are used to simplify and improve everyday life in home automation, smart devices (washing machines, televisions, lighting and more) or portable electronics. [6] [7] [8]

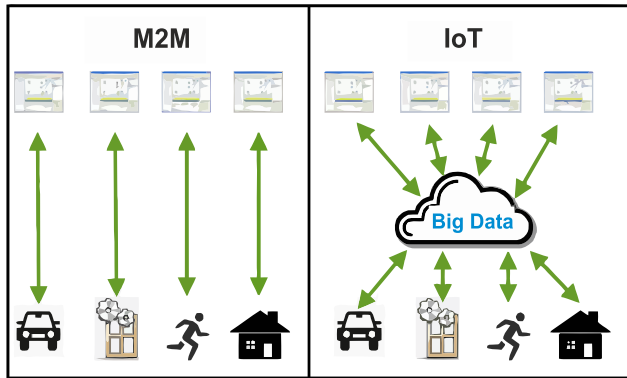


Fig. 1. Elementary difference between M2M and IoT. [4]

## 2 Possibilities of data processing

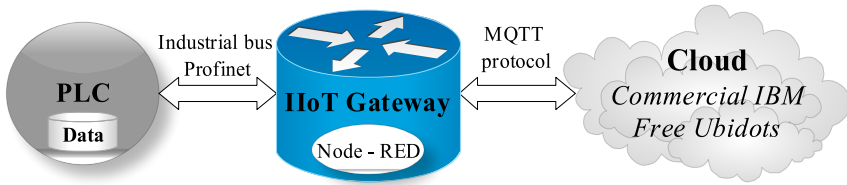
From the technological point of view, there are several possible ways to communicate within different devices. In industry, however, it is very often better to use a wired connection (e.g. industrial ethernet or profibus), which leads to increased reliability of the solution. It is also possible to use wireless communication and not only for the Commercial IoT segment. It mostly includes Wi-Fi, Bluetooth, NFC, ZigBee and more. There are also many different communication protocols for IoT solutions. It is possible to use for example HTTP/HTTPS&Websockets, CoAP (XMPP) and MQTT. In this study is MQTT the most important protocol within practical demonstration of reached results. [9] [10] [11]

## 3 Design of solution

At the beginning it is important to determine difference between traditional control (programming in available software interface from manufacturer) and offered control. It is necessary to compile wrote program and upload it to PLC or MCU. During testing these steps have to be often repeated and results are mostly immediately visible.

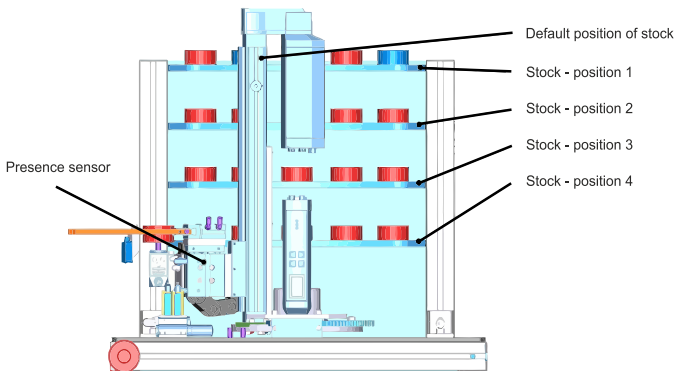
### 3.1 Industrial IoT solution

Industrial solution represents cooperation between PLC, IIoT Gateway and Cloud platforms (Fig. 2). It allows the device will be remotely controlled through transferring of process data between the PLC and IIoT Gateway (it must be connected to the internet).



**Fig. 2.** Communication between publishers and subscribers based on MQTT.

This part contains PLC, which controls a mechatronic system. Pucks are step by step modified through six workplaces for the potential customer who will receive the finished product. Last workplace uses to store finished products - stock of pucks (Fig. 3). Within Industrial IoT it is necessary to use PLC and device, which is able to send process data to Cloud platforms via internet. In this study it used an intelligent industrial IoT gateway. This gateway (Siemens Simatic IoT 2040) is used to store process data from PLC to Cloud platforms and then it controlled the real devices remotely through the web application. It's a reliable gateway that can be used as an interface between Cloud platforms and production. It is also an economical and safe alternative for control some part of device based on PLC. It is possible to use various communication protocols (MQTT, SQLITE3 and more). The shield is made of durable industrial components (IP20 protection). It allows continuous operations even in demanding conditions. [12]



**Fig. 3.** Part of mechatronic system – stock of pucks.

### 3.2 Commercial IoT solution

Commercial solution uses MCU and Cloud platform. It allows the device will be remotely controlled and received relevant information for tracking current status. It used MCU ESP8266 for control of whole process. The main part of this system is a Tensilica 106, 32-bit microcontroller unit and a Wi-Fi transceiver. The device can be programmed like an Arduino or similar MCU and it is possible to work with inputs, outputs or communication ports. For testing our IoT system it was used several NodeMCU modules.

It is available programming in different programming environments as Arduino IDE, Scratch, Processing and others and also through many languages (C, Python). For purpose of this paper it was using the Arduino IDE and “USB to Serial” communication for programming and checking the status of our system. There are also different communication interfaces to cooperate with other devices - Serial, I2C and SPI. ESP32 is a microcontroller (MCU) combining Wi-Fi and Bluetooth interface with a Xtensa micro-processor. In general, it’s a powerful version of the NodeMCU, with more communication and interaction options. This device was designed for mobile, wearable and IoT applications. The ESP32 unit was connected through MQTT protocol to receive information about active alarm states. Each alarm situation was connected to one of LED on the ESP32. For testing the MQTT communication it used buttons on the Cloud dashboard. Each button was controlled manually. It is also possible to create this signal through alarm. Each alarm state includes a logical statement of received process data, which controls an output or generates a message. Distant monitoring system was designed for experimental testing of MQTT protocol. Temperature and humidity were monitored. When triggered alarm events were used to represent MQTT messages. Our experimental system consists of described NodeMCU and ESP32. The data acquisition was performed with NodeMCU units with using HTTP protocol. Each unit measured temperature and humidity in the place of deployment. For this measurement were used digital temperature and humidity sensors. [13] [14]

### 3.3 Comparing of Industrial and Commercial IoT solutions

The average latency of Ubidots Cloud was evaluated on MCU and PLC (Fig. 4). The latency was measured by timer and it was calculated average latency of every 10 messages. The latency was probably affected by the quality of service of MQTT broker.

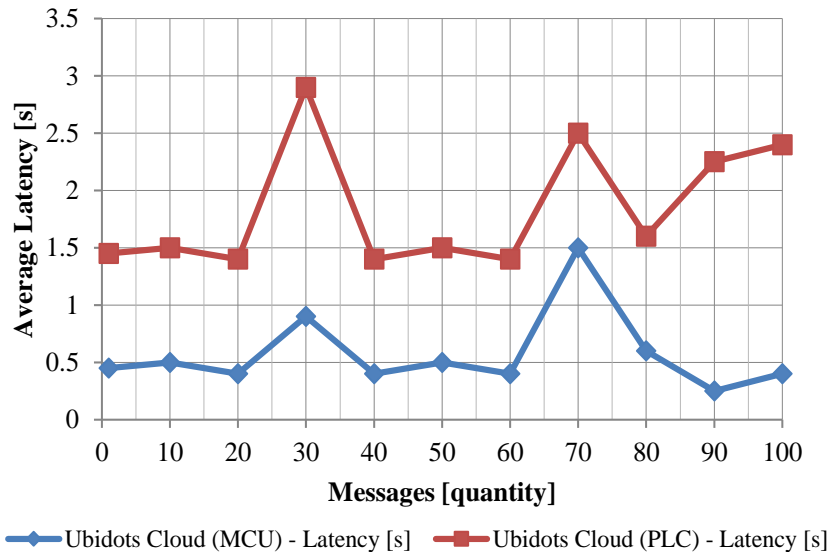


Fig. 4. Comparing of average latency of MQTT communication (Ubidots Cloud)

Graph on Fig. 5 shows comparison of Cloud platforms from different companies. First platform Ubidots Cloud was evaluated by MCU. Second one platform IBM Cloud was evaluated by PLC. Solution from company IBM reacts with maximum time, which is equals about 0.6 seconds. The second Cloud, platform Ubidots shows (in comparison with MCU) worse results. Delay through comparing with IBM Cloud was up to almost 1.5 seconds.

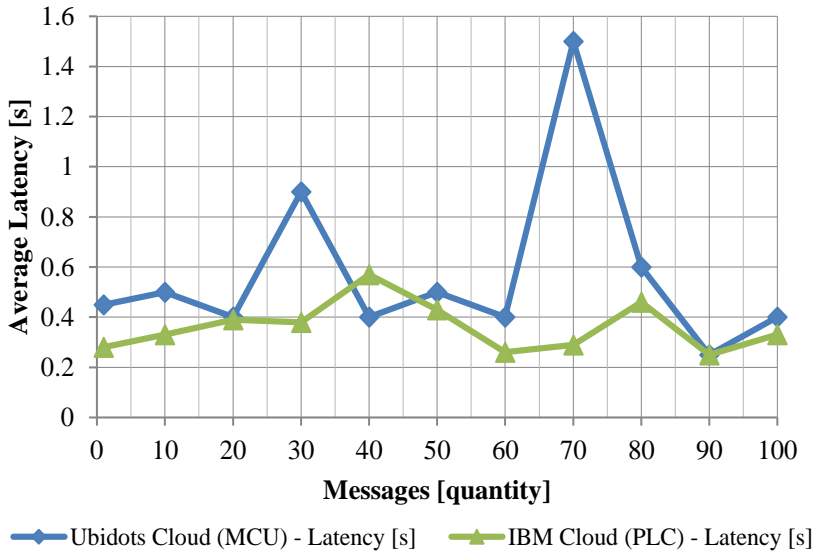


Fig. 5. Comparing of average latency of MQTT communication (Ubidots and IBM Cloud)

## 4 Conclusion

It is not existing best solution, which someone will use within IoT. Using of Industrial and Commercial IoT depends on the use case. As they are very vast fields covering everything from home to industrial automation, it is definitely possible to use some kinds of very diversified protocols. In this study was used protocol MQTT, which worked very well, but only in some situations. In terms of random moments it was changed a latency, which was increased up to 4 seconds per new unique value. Cloud platform Ubidots was mostly at least about a second slower than industrial part of similar solution. It can be dangerous in time critical tasks. Possibilities of security are available for example in form "Last Will and Testament". It works as a fuse in the event of faults and a failure of communications or device. IBM Cloud platform was fast enough with a maximum average latency about 0.6 seconds.



## 5 Acknowledgement

This work was supported by the project SP2018/160, „Development of algorithms and systems for control, measurement and safety applications IV" of Student Grant System, VSB-TU Ostrava.

## 6 References

1. GREENGARD, Samuel.: The internet of things. Cambridge: MIT Press (2015), ISBN 978-0-262-52773-6.
2. Bloom, G., Alsulami, B., Nwafor, E. and Bertolotti, I. C.: Design patterns for the industrial Internet of Things. 14th IEEE International Workshop on Factory Communication Systems (WFCS), Imperia, Italy, pp. 1-10 (2018). doi: 10.1109/WFCS.2018.8402353
3. Internet of things, <http://i2ot.eu/internet-of-things/>, last accessed 2019/07/09.
4. M2M vs IoT, <http://gyantemple.com/full.php?ID=196>, last accessed 2019/07/09.
5. What is M2M, <https://www.link-labs.com/blog/what-is-m2m>, last accessed 2019/07/09.
6. Meng, Z., Wu, Z., Muvianto, C. and Gray, J.: A Data-Oriented M2M Messaging Mechanism for Industrial IoT Applications. IEEE Internet of Things Journal, vol. 4, no. 1, 236-246 (2017).
7. Ruppert, T. and Abonyi, J.: Industrial Internet of Things based cycle time control of assembly lines. IEEE International Conference on Future IoT Technologies (Future IoT), Eger, pp. 1-4 (2018). doi: 10.1109/FIOT.2018.8325590
8. Petrenko, A. S., Petrenko, S. A., Makoveichuk, K. A. and Chetyrbok, P. V.: The IIoT/IoT device control model based on narrow-band IoT (NB-IoT). IEEE Conference of Russian Young Researchers in Electrical and Electronic Engineering (EIConRus), Moscow, pp. 950-953 (2018). doi: 10.1109/EIConRus.2018.8317246
9. Shinde, K. S. and Bhagat, P. H.: Industrial process monitoring using IoT. International Conference on I-SMAC (IoT in Social, Mobile, Analytics and Cloud) (I-SMAC), Palladam, pp. 38-42 (2017). doi: 10.1109/I-SMAC.2017.8058374
10. Katsikeas, S. et al.: Lightweight & secure industrial IoT communications via the MQ telemetry transport protocol. IEEE Symposium on Computers and Communications (ISCC), Heraklion, pp. 1193-1200 (2017), doi: 10.1109/ISCC.2017.8024687
11. Ferrari, P., Sisinni, E., Brandão, D. and Rocha, M.: Evaluation of communication latency in industrial IoT applications. IEEE International Workshop on Measurement and Networking (M&N), Naples, pp. 1-6 (2017). doi: 10.1109/IWMN.2017.8078359
12. Industrial IoT Gateway, <https://w3.siemens.com/mcms/pc-based-automation/en/industrial-iiot/pages/default.aspx>, last accessed 2018/07/22.
13. ESP 8266 Datasheet, [https://www.espressif.com/sites/default/files/documentation/0a-esp8266ex\\_datasheet\\_en.pdf](https://www.espressif.com/sites/default/files/documentation/0a-esp8266ex_datasheet_en.pdf), last accessed 2019/07/10.
14. ESP32 Datasheet, <https://everythingesp.com/>, last accessed 2019/07/10.

# Connecting demonstration stand for the education purposes to the university network

Matěj Golembiovský

Department of Cybernetics and Biomedical Engineering, FEECS,  
VŠB – Technical University of Ostrava, 17. listopadu 15,  
708 33 Ostrava – Poruba, Czech Republic  
matej.golembiovsky@vsb.cz

**Abstract.** This thesis discussed the issues and challenges associated that may occur when trying to connect demonstration stands to university networks.

## 1 Introduction

This paper introduces the Control system demonstration stand Docekal et al., 2018 that was designed for the teaching purposes at the Faculty of Electrical Engineering and Computer Science, Technical University of Ostrava. This demonstration stand allows simple implementation of control algorithms in REXYGEN environment and tests on the real hardware.

Technically, these demonstration stands have proven to be very useful, but after several semesters of teaching there has been a demand for easy transportability between classrooms. However, meeting this requirement has brought many challenges related to the topology and rules of the university network.

## 2 Problem Analysis

The described demonstration stands can be used for teaching of several subjects. However, since these subjects are taught in different classrooms with different student occupancy, it is necessary to ensure their easy transportability. A part of the transportability is ensured by their physical dimensions, but at workplaces it is also necessary to prepare a source of electricity and connection to the university network. Connection to the power supply is not a problem as all workplaces are equipped with wall sockets.

On the other hand, there are several possibilities of connecting to the university network.

### 2.1 Direct Connection via Wi-Fi Network

To use this option, each device needs to be equipped with a USB Wi-Fi dongle. It is then possible to connect to the university Wi-Fi Network. This option would probably be the best solution, as the products could be used throughout the university without any additional claims. In practice, however, this would mean

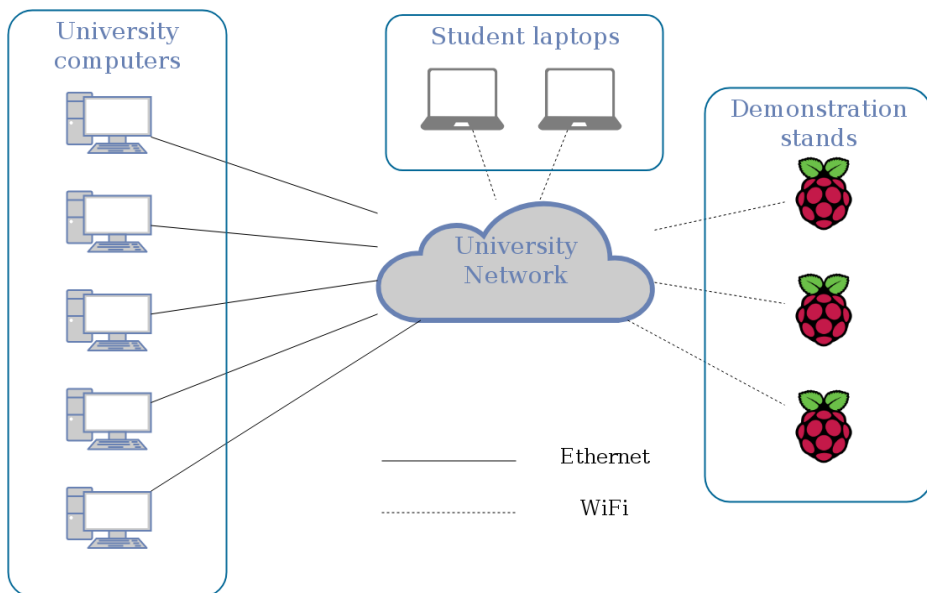


Fig. 1: Network topology for the direct wifi connection.

having to be able to assign these devices to a specific address. According to the helpdesk, this is not possible since it requires significant intervention to the university Wi-Fi network topology and configuration. Moreover, this intervention could have an impact on the efforts to isolate all clients on the Wi-Fi network, thus potentially also having a negative impact on the security of other connected clients.

## 2.2 Direct Connection via Wired Network

This solution requires building an infrastructure for this connection in each classroom where the products are to be used. This would involve installing 20 - 30 Ethernet cables and possibly other networking hardware. The difficulty of this option then increases with the number of classrooms in which the devices are intended to be used. Moreover, before each lesson, the devices would have to be connected by an extra cable to each device, which could lead to the potential problems associated with this step.

## 2.3 Connection via Central Demonstration Stand

In this configuration, the individual devices are connected to one central device via Wi-Fi. This device is then connected to the university network via an Ethernet cable. This solution combines ease of use and transportability of the first solution with the second solution so the whole concept is feasible. This solution also has the disadvantages of not having the ability to influence the university

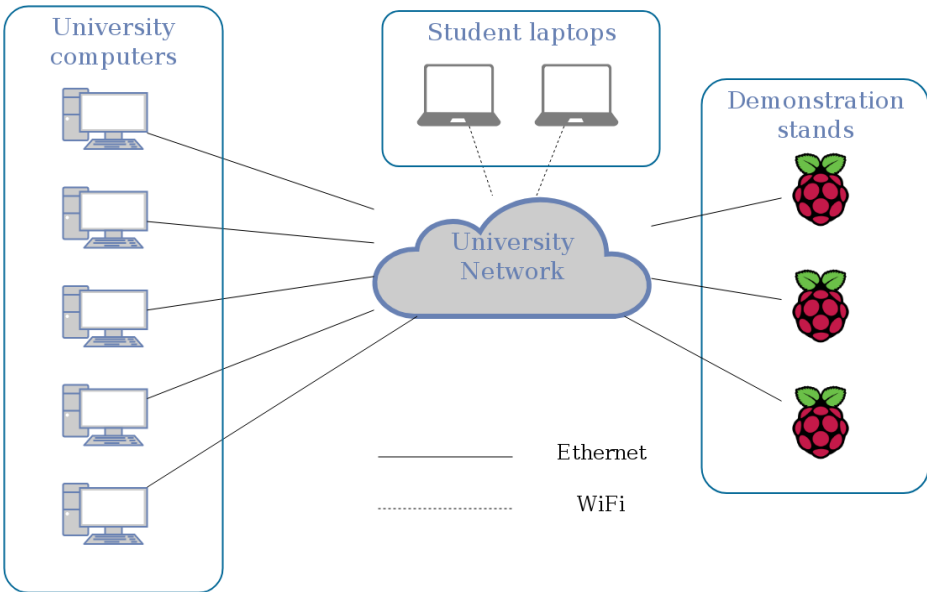


Fig. 2: Network topology for the direct ethernet connection.

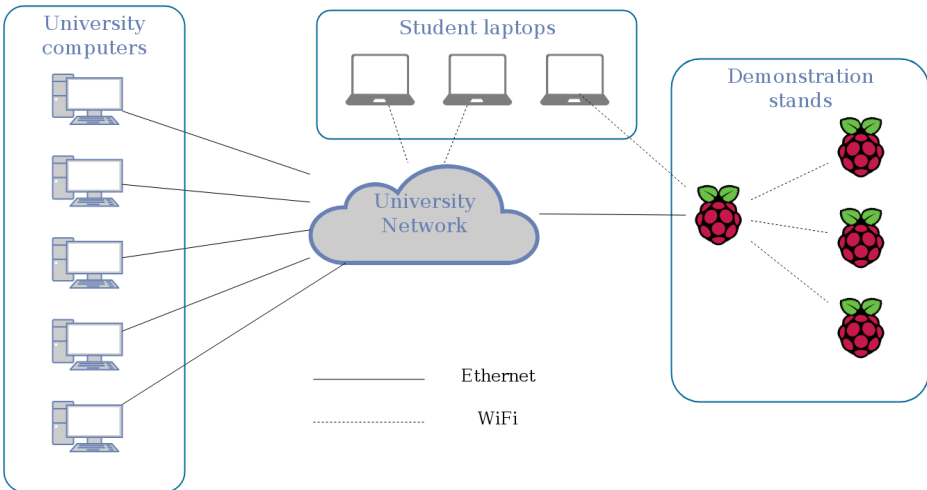


Fig. 3: Network topology for the central stand routing.

network in any way. This solution may also have some advantages. In case students bring their own laptops, they can also connect to the central device and thus do not need to use university computers or network. Theoretically, it would be possible to run this configuration without any network connection.

### 3 Solution

Of the above mentioned options, a connection via central demonstration stand was chosen as the most advantageous functional option. As already mentioned, we do not have the ability to influence the university network in any way. So we have to work with what we have and that is the only IP address assigned based on the MAC address on the Ethernet interface of the central fixture. This IP address is visible from the university network, so students working on both university computers and their laptops connected to the university network can access and work with this device via Wi-Fi.

However, since the aim is that each student can work with demonstration stands individually, it is necessary to ensure that the central demonstration stand allows to distinguish which product the student is trying to access. This is achieved through a port forward. Therefore, it seems that all students access the central fixture, but instead it sends out requests based on the requested port to the corresponding demonstration stand.

### 4 Implementation

For successful commissioning it is necessary to have:

- SD card (min 4GB),
- Raspberry Pi with Wi-Pi or Wi-Fi version
- Raspberry Pi with supported Wi-Fi module and REXYGEN installed.

We will start the installation by working on a central demonstration stand where it is necessary to put the Wi-Fi AP into operation and set the Wi-Fi interface so that it has a static IP address and is able to provide DHCP services on this interface. First, install the necessary packages and disable the services that are not configured:

---

```
sudo apt-get update
sudo apt-get upgrade

sudo apt-get install dnsmasq hostapd

sudo systemctl stop dnsmasq
sudo systemctl stop hostapd
```

---

To continue, set up a static IP address on the wlan0 interface:

---

```
sudo nano /etc/network/interfaces
```

---

```
# The loopback network interface
auto lo
iface lo inet loopback
```

```
# The primary network interface
```

```
allow-hotplug eth0
iface eth0 inet dhcp
```

```
allow-hotplug wlan0
iface wlan0 inet static
    address 192.168.4.1
    netmask 255.255.255.0
    network 192.168.1.0
    broadcast 192.168.1.255
```

---

Then configure a DHCP server to assign addresses to demonstration stands based on their MAC:

---

```
sudo nano /etc/dnsmasq.conf
```

---

```
dhcp-host=b8:27:eb:0e:f8:d5,REX1,192.168.4.11,45m
```

---

Next, set the Wi-Fi configuration for AP:

---

```
sudo nano /etc/hostapd/hostapd.conf
```

---

```
interface=wlan0
driver=nl80211
ssid=REXHost
hw_mode=g
channel=7
wmm_enabled=0
macaddr_acl=0
auth_algs=1
ignore_broadcast_ssid=0
wpa=2
wpa_passphrase=rexcorerexcore
wpa_key_mgmt=WPA-PSK
wpa_pairwise=TKIP
rsn_pairwise=CCMP
```

---

In the last step, set NAT and Port Forwarding:

---

```
sudo iptables -t nat -A POSTROUTING -o eth0 -j MASQUERADE
sudo iptables -t nat -A PREROUTING -i eth0 -p tcp --dport 9002 -j DNAT --to
192.168.4.11:22
sudo sh -c "iptables-save > /etc/iptables.ipv4.nat"
sudo nano /etc/rc.local
```

---

For demonstration stands it is then only necessary to set up automatic connection to the Wi-Fi Network established by the central demonstration stand.

## 5 Conclusion

This article discussed the issues and challenges associated that may occur when trying to connect demonstration stands to university networks. These proposed examples were solved at the network of Technical University Ostrava, but they can be used by the teachers and provide them the general knowledge of the approaches in connecting the demonstration stands to networks with specific infrastructure. The outlined solution is also interesting from the point of view that one can avoid using the university network.

## References

DOCEKAL, Tomas; GOLEMBIOVSKY, Matej, 2018. Low cost laboratory plant for control system education. *IFAC-PapersOnLine*. Vol. 51, no. 6, pp. 289–294. Available from DOI: [10.1016/j.ifacol.2018.07.168](https://doi.org/10.1016/j.ifacol.2018.07.168).

# A Hardware Communication Interface by NXP FlexIO Module

Libor Chrástecký, Jaromír Konečný, Martin Stankuš, and Michal Prauzek

Department of Cybernetics and Biomedical Engineering, FEECS,  
VŠB – Technical University of Ostrava, 17. listopadu 15,  
708 33 Ostrava – Poruba, Czech Republic  
{libor.chrastecky, jaromir.konecny, martin.stankus,  
michal.prauzek}@vsb.cz

**Abstract.** This paper focuses on the possibility of using specialized peripherals of microcontrollers to create a low-energy hardware solution for the InternetOfThings (IoT) communication interface. This solution uses NXP FlexIO peripherals and RFC1662 is used as the reference communication standard. RFC1662 communication standard is implemented through software and hardware approaches, during testing the total power consumption is measured. In conclusion the authors evaluate the time and energy consumption between the software implementation running on a central processing unit (CPU) and the hardware implementation using specialized peripherals, NXP FlexIO. The measured data show that the hardware implementation is effective in terms of time and power consumption and this approach can be used in IoT devices.

## 1 Introduction

The most of today's InternetOfThings (IoT) devices are designed as low-cost and low-power embedded platforms [1]. Generally, current IoT design goals requires modern approaches which can achieve minimal power consumption and minimal processing times [2]. This research direction is very important especially in battery-powered or harvesting IoT platforms [3].

Low-power devices operate usually in duty-cycle scenario [4] when run and sleep modes change in regular or adaptive intervals [5]. There are two possible approaches to power reduction. First method is based on absolute power consumption reduction in run and sleep mode [6]. Second method aims on effective computing algorithms [7] which allow to minimize time spend in run modes and therefore a total power consumption could be decreased.

This contribution shows possibilities of special microcontroller (MCU) module usage to reduce processing times in low-power communication protocols implementation. The NXP FlexIO module demonstrates a hardware-oriented approach to implement communication protocol represented by RFC1662 which can be used at IoT embedded devices. A transfer of computational tasks from central processing unit (CPU) to special peripherals such as FlexIO causes increase of instant supply current demands in a run mode [8]. Therefore a trade-off between task duration and power supply demands must be examined and then we are able to select a proper approach for target application.



## 2 Implementation and Testing

This section brings an overview of particular FSM implementation in terms of software and hardware approach. In testing subsection parameters of testing procedure are presented.

### 2.1 Implementation

In the experimental section we designed a FSM to compare software implementation with hardware approach using FlexIO module. FSM implementation represents RFC1662 protocol and the goal of this experiment is evaluation in term of energy demands. The FSM implementation using data link layer RS-486 is depicted in the Figure 1.

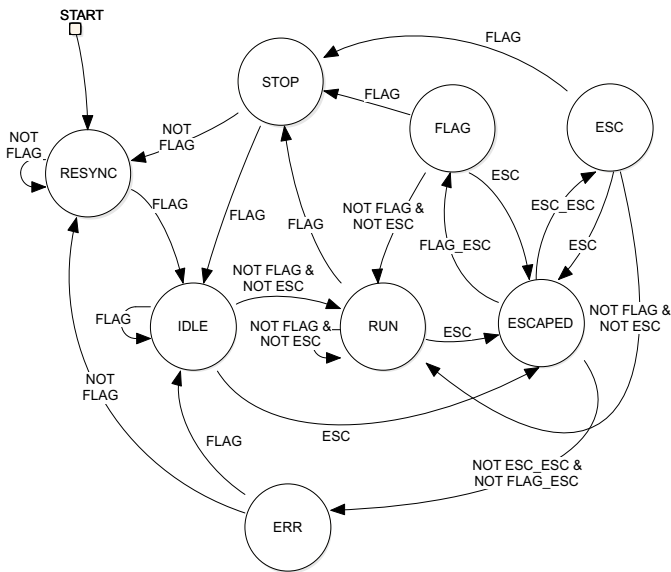
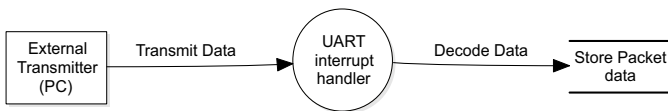


Fig. 1. Design of finite state machine representing RFC1662 functionality

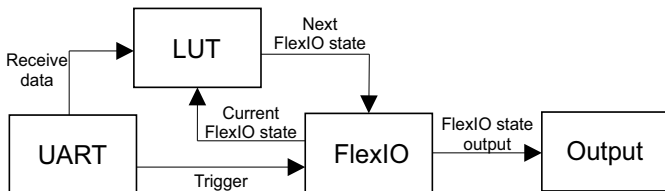
A device implementing FSM starts in RESYNC state, because communication might already running and unchecked start may cause a communication error. In RESYNC state FSM expects the FLAG, i.e. start or end of the message. After receiving the FLAG, the FSM changes the state into IDLE. If FSM receives FLAG again, the state will be not changed and the start of message is indicated again. If FSM receives (in IDLE) other character than FLAG, FSM changes state to RUN state and this state is dedicated to message content reception. If FLAG character is received in RUN state, FSM goes to STOP state and entire frame is received.

If FSM receives ESC character in RUN, IDLE, ESC, or FLAG state, FSM expects an escape sequence and active state is changed to ESCAPED state. The ESCAPED state means that one of two special characters (ESC\_ESC and FLAG\_ESC) is expected. If FSM receives ESC\_ESC or ESC\_FLAG, the FSM enters ESC or FLAG state respectively and corresponding value is written to receiving data buffer. If FSM receives other character than ESC\_ESC or ESC\_FLAG in ESCAPED state, the message is corrupted and FSM goes to ERR state and waits for FLAG character. The FLAG character can also be received in FLAG or ESC state and also indicates the end of received frame, so FSM goes to STOP state.



**Fig. 2.** Basic scenario of software finite state machine design

**Software design** Software implementation uses Universal Asynchronous Receiver Transmitter (UART) module as a physical layer and is depicted in figure 2. FSM implementation is coded in C language and it is running in CPU core. Each received byte causes an interrupt and received characters are read and processed by C-coded algorithm.



**Fig. 3.** Functional diagram of hardware approach using FlexIO

**Hardware design** Hardware implementation also uses UART as the physical layer (see figure 3) and the FSM is implemented using FlexIO module. Each state is denoted as 3-bit value, ie. 0 – 7 and these values are stored in look-up table LUT.Output. The process starts by receiving one byte by UART and the received byte and current FlexIO state together form an input address of the look-up table, where the next FlexIO state value is located. The value of the next

state is written to FlexIO input and then the FlexIO timer trigger is activated by Trigger MUX Control (TRGMUX). This event will cause state changing.

Each state processes a specific action, which is defined by FSM. Each action launches a Direct Memory Access (DMA) channel and DMA engine performs target action (e. g. constant moved to defined memory space). DMA events are represented in the figure 3 by the action arrows.

## 2.2 Testing procedure

For evaluation purposes a testing application in C# language was designed. The application allows to send data to the testing setup while the test itself includes evaluation of frame reception with different sizes, ESC characters amount and errors count. The tests aims for comparison of hardware and software approaches in terms of processing duration and total energy demands.

**Table 1.** Testing message parameters

Testing	Parameters
Message lenght	500/1000/1500
Number of ESC character within message	0/10/20
Number of Errors within message	0/1

Table 1 an shows overview of experimental testing parameters. The transmitting speed in UART peripheral is set to 115200 Baud and the maximum packet size is 1500 bytes. Test is designed to evaluate responces to frames without any error and frames with one error.

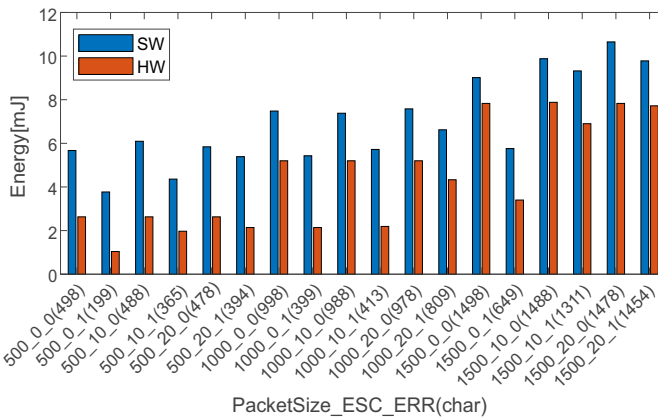
## 3 Results

The power consumption of hardware and software approaches was evaluated. The selected testing setup operates at 3.3V and the measured active current for the software implementation was 15.52 mA and for the hardware implementation was 16.59 mA, both values were measured by picoAmmeter Keithley 6485. The hardware implementation using the FlexIO module has a higher power consumption, this is because this solution uses more hardware peripherals (e.g. DMA) than the software implementation.

The total processing times for software and hardware approaches (obtained by DSOX2024A Oscilloscope) are presented in the table 2. For each testing frame described by amount of characters in frame, the results display the receiving time for software and hardware implementation and energy saving by FlexIO approach. The average transmission time for software approach is 136.4 ms and 80.3 ms for hardware approach using FlexIO module. The hardware approach achieves shorter processing times because the solution does not need CPU operation and only uses hardware modules such as DMA, FlexIO and TRGMUX.

**Table 2.** Results of algorithm processing times

Packet	Char in packet	SW time [ms]	HW time [ms]	Time (HW-SW) [ms]	Energy (HW-SW) [%]
500_0_0	498	110.8	48	62.8	54
500_0_1	199	73.6	19	54.6	72
500_10_0	488	119	48	71	57
500_10_1	365	85.2	36	49.2	55
500_20_0	478	114	48	66	55
500_20_1	394	105.2	40	66.2	60
1000_0_0	998	146	95	51	30
1000_0_1	399	106	39	67	61
1000_10_0	998	144	95	49	29
1000_10_1	413	111.6	42	71.6	62
1000_20_0	978	148	95	53	31
1000_20_1	809	129.2	79	50.2	35
1500_0_0	1498	176	143	33	13
1500_0_1	649	112.4	62	50.4	41
1500_10_0	1488	193	144	49	20
1500_10_1	1311	182	128	56	26
1500_20_0	1478	208	143	65	27
1500_20_1	1454	191	141	50	21
Average	826.9	136.4	80.3	56.1	37



**Fig. 4.** Bar graph comparison between energy consumption in hardware and software implementation

The figure 4 shows the differences between total power consumption of software and hardware approach. In all test cases, the hardware approach has faster frame processing and lower power demands even with higher instant power consumption. The average consumption of a hardware implementation is approx-

imately 37% less than a software implementation. In the same time we have to note that there is a disadvantage of a hardware implementation that uses significantly more memory space than software approach because the hardware implementation needs to encode the received characters through lookup tables to the 3-bit values that the FlexIO module handles.

## 4 Conclusion and Future Work

This paper introduces and test communication interface featuring FlexIO module as FSM communication protocol for standard byte-oriented point-to-point serial communication RFC1662. This approach represents hardware based method to save energy in IoT communication scenarios. For determine and compare time and energy saving was created reference software FSM implementation. The implementation of FSM via the FlexIO peripheral achieves better results in terms of total energy efficiency and processing time. Also, the FlexIO approach allows to transfer the necessary computational power from CPU to HW modules and thus CPU computing power can be used to perform other tasks

In the future, we are considering implementing of this method in battery-powered or harvesting embedded or IoT platforms where lower energy demands could extend operating time.

## References

1. Miorandi D., Sicari S., Pellegrini F. De, and Chlamtac I., "Internet of things: Vision, applications and research challenges," *Ad Hoc Networks*, vol. 10, no. 7, pp. 1497–1516, 2012.
2. Georgiou K., Xavier-De-Souza S., and Eder K., "The iot energy challenge: A software perspective," *IEEE Embedded Systems Letters*, vol. 10, no. 3, pp. 53–56, 2018.
3. Raj A. and Steingart D., "Review – power sources for the internet of things," *Journal of the Electrochemical Society*, vol. 165, pp. B3130–B3136, 2018.
4. Vigorito C., Ganesan D., and Barto A., "Adaptive control of duty cycling in energy-harvesting wireless sensor networks," *2007 4th Annual IEEE Communications Society Conference on Sensor, Mesh and Ad Hoc Communications and Networks, SECON*, pp. 21–30, 2007.
5. Musilek P., Prauzek M., Kromer P., Rodway J., and Barton T., "Intelligent energy management for environmental monitoring systems," *Smart Sensors Networks: Communication Technologies and Intelligent Applications*, pp. 67–94, 2017.
6. Prauzek M., Musilek P., and Watts A., "Fuzzy algorithm for intelligent wireless sensors with solar harvesting," *IEEE SSCI 2014 - 2014 IEEE Symposium Series on Computational Intelligence - IES 2014: 2014 IEEE Symposium on Intelligent Embedded Systems, Proceedings*, pp. 1–7, 2014.
7. Sampson A., Dietl W., Fortuna E., Gnanapragasam D., Ceze L., and Grossman D., "Enerj: Approximate data types for safe and general low-power computation," *Proceedings of the ACM SIGPLAN Conference on Programming Language Design and Implementation (PLDI)*, pp. 164–174, 2011.
8. Patil V., Mane Y., and Deshpande S., "Fpga based power saving technique for sensor node in wireless sensor network (wsn)," *Studies in Computational Intelligence*, vol. 776, pp. 385–404, 2019.

# Hybrid Methods for Processing of Fetal Electrocardiogram

René Jaroš and Radek Martinek

Department of Cybernetics and Biomedical Engineering, FEECS,  
VŠB – Technical University of Ostrava, 17. listopadu 15,  
708 33 Ostrava – Poruba, Czech Republic  
{rene.jaros, radek.martinek}@vsb.cz

**Abstract.** This paper focus on the design and implementation of a state-of-the-art type of hybrid extraction system for noninvasive fetal electrocardiogram processing. The proposed system combines advantages of individual adaptive and non-adaptive algorithms. The pilot study reviews two innovative hybrid systems - ICA-ANFIS-WT and ICA-RLS-WT. These systems leverage advantages of independent component analysis (ICA), adaptive neuro-fuzzy inference system (ANFIS) algorithm or recursive least squares (RLS) algorithm and wavelet transform (WT) algorithm.

**Keywords:** Noninvasive fetal electrocardiography, fetal heart rate variability monitoring, hybrid methods.

## 1 Introduction

Fetal electrocardiography (fECG) is a very promising method of electronic fetal monitoring based on sensing and evaluating electrical activity of the fetal heart. The main parameter monitored in clinical practice is the fetal heart rate (fHR). Besides it, morphological analysis of fECG signal (ST segment analysis, QT segment analysis, etc.) can be performed. In order to estimate high quality fECG signal suitable for diagnostic purposes, advanced signal processing methods must be applied. At present, methods combining several algorithms (hybrid fECG signal extraction methods) and using multichannel signal inputs appear to be very perspective. Very good results are achieved by hybrid methods combining independent component analysis (ICA) and some adaptive algorithm [1, 2, 3, 4].

## 2 Methods

### 2.1 Independent Component Analysis

Independent component analysis is based on assumption that sources in signals are statistically independent. Recorded sounds by electrodes placed on maternal abdomen can be marked by indexes  $x_1$  to  $x_n$ . Maternal heart is one signal source

$s_1$  and fetal heart is second signal source  $s_2$  (physiologically, different forms of noise are also present). This can be generally expressed by equation (1), where  $\mathbf{A}_{\text{mix}}$  is mixing matrix provided by maternal body and  $\mathbf{s}$  is vector of source signals. To separate source signals, it is necessary to estimate matrix  $\mathbf{W}$ , which is inverse to matrix  $\mathbf{A}_{\text{mix}}$  see equation (2) [2, 3, 4].

$$\mathbf{x} = \mathbf{A}_{\text{mix}} \cdot \mathbf{s}. \quad (1)$$

$$\mathbf{s} = \mathbf{W} \cdot \mathbf{x}. \quad (2)$$

## 2.2 Adaptive Neuro Fuzzy Inference System

This algorithm is basically fuzzy expert system which works as a multilayered feed-forward neural network, that uses least mean square (LMS) algorithm in feed-forward way and backpropagation algorithm in backward way. Adaptive neuro fuzzy inference system is basically composed of 5 feed-forward layers and their outputs are calculated by equations (3) to (7). First layer is input and adaptive layer, where fuzzification of input linguistic variables is carried out. Second and third layers are composed only of nonadaptive nodes. Fourth layer is composed of adaptive nodes and normalization nodes are in output of this layer. The last layer composed of one non-adaptive node called summation [5, 6].

$$o_{1,i} = \mu_{A_i}(x); o_{1,i} = \mu_{B_i}(y). \quad (3)$$

$$o_{2,i} = w_i = \mu_{A_i}(x) \cdot \mu_{B_i}(y). \quad (4)$$

$$o_{3,i} = \bar{w}_i = \frac{w_i}{w_1 + w_2}. \quad (5)$$

$$o_{4,i} = \bar{w}_i f_i = \bar{w}_i \cdot z_i = \bar{w}_i(p_i x + q_i y + r_i). \quad (6)$$

$$o_{5,i} = \sum_i \bar{w}_i f_i = \frac{\sum_i w_i f_i}{\sum_i w_i}. \quad (7)$$

## 2.3 Recursive Least Squares Filter

Adaptive algorithms calculate error  $e(n)$  by subtraction real output of the system  $y(n)$  from the desired output  $d(n)$ . Main goal of this algorithm is to adjust coefficients  $w(n)$  to obtain the output  $y(n)$ , which is most similar to the desired ideal output  $d(n)$ . The advantage of this algorithm is that it uses the values of previous error estimates and has very high performance in time-varying environments. The main weakness of this algorithm is problems with stability. Its aim is to minimize the result of the objective function  $\xi$ , see equation (8). The required

output  $p$  can be expressed by equation (9), where  $\lambda$  denotes the forgetting factor being in the interval  $\langle 0, 1 \rangle$ . Most often, the forgetting factor ranges from 0.95 to 0.99. To reduce the computational complexity, the  $N_{\text{RLS}}$  filter order is used, which indicates the final number of previous values processed [7, 8].

$$\xi(n) = \sum_{k=1}^n p_n(k) e_n^2(k). \quad (8)$$

$$p_n(k) = \lambda^{n-k}. \quad (9)$$

## 2.4 Wavelet Transform

When applying discrete WT (DWT), it is necessary to choose the type of maternal wavelet  $\Psi$  and the decomposition level  $n$ . The Daubechies wavelet type seems to be the most suitable, so hybrid extraction system. In the first decomposition stage, the signal is decomposed by the Low-pass filter to one  $cA$  approximation component and by the high-pass filter to one detailed  $cD$  component. In the second decomposition stage, the approximation component of the signal is divided into another one approximation component and one detailed component. This is happening until the final selected degree of decomposition. Equation (10) is used to describe DWT. The reverse DWT contains, at its input, signal  $c$  composed of the last approximation component and of all the detailed components from the highest degree of decomposition to the lowest one. This composite signal is adjusted by thresholding before the DTW is completed. Equation (11) is used to calculate the inverse DWT [9].

$$DWT(f) = F(j, k) = \hat{f}(j, k) = \int_{-\infty}^{\infty} f(t) \cdot \Psi_{j,k}^*(t) dt. \quad (10)$$

$$DWT^{-1}(F) = f(t) = \sum_{j,k} c_{j,k} \cdot \Psi_{j,k}(t). \quad (11)$$

## 3 Hybrid System Description

In Fig. 1, a block diagram of the hybrid system implemented can be seen. The methods employed consist of several steps which are performed successively to complete the successful extraction of the fECG signal. Extracting the fECG signal using both hybrid methods and without using the WT algorithm can be seen in Fig. 2, which shows a graphical user interface for extracting fECG signals.

First, at least 2 measured aECG signals are fed to the preprocessing block where the initial signal adjustment is performed. The input signals are labelled as  $AE_1$  to  $AE_n$ . It is possible to select any filter of a certain band, but, in our case, the FIR filter was chosen with cut-off frequencies from 10 to 15 Hz (based on study by Sameni et al. in 2010 [10]).

Signals after preprocessing are then brought to the ICA algorithm block. In this block, the number of components  $n_{\text{ICA}}$ , the convergence criterion  $\delta_{\text{ICA}}$  and



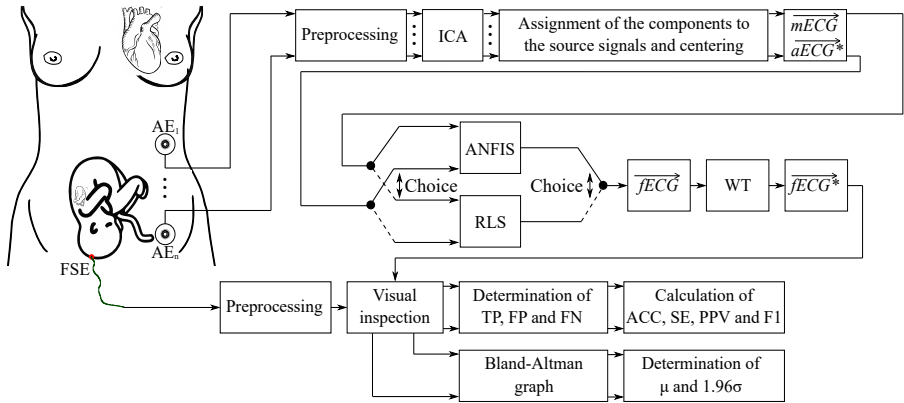


Fig. 1. Block diagram of the hybrid system.

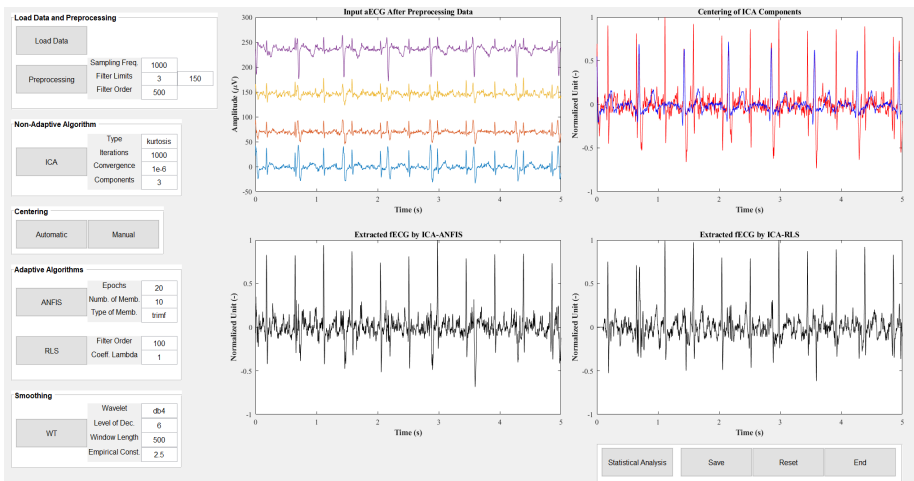


Fig. 2. Graphical user interface - extraction block.

the maximum number of iterations of the cycle  $k_{ICA}$  can be selected. The scheme described shows that, in most cases, one component practically corresponds to the mECG signal, the second component corresponds to the aECG signal with the enhanced fECG signal at the same amplitude level as the mECG signal (marked as aECG\*), and the third component corresponds to noise.

The individual components are in a different order each time the ICA algorithm is started, they have an altered amplitude due to standardization within the cycle, the components are rotated, and moreover, the components are time-shifted by several samples. For this reason, the output components are fed to an auto-centering block where the components are first differentiated and, then, rotated in the right direction. Subsequently, the component corresponding to the mECG signal is amplitude and time aligned, based on the mQRS complexes,

with the component corresponding to the aECG\* signal with enhanced fECG signal. Finally, re-standardization is performed because amplitude adjustments occur during centring. In the remaining course of the program, the output signals then have a dimensionless unit, and, thus, output fECG signals too.

Thus, the signals are ready for entering the adaptive algorithm and for the subsequent extraction of the fECG signal. It is now possible to select either the extraction of the fECG signal using the ANFIS algorithm, or the RLS algorithm. Using the ANFIS algorithm, it is possible to select the shape of membership functions  $\mu_{ANF}$ , the number of membership functions  $k_{ANF}$  and the number of epochs  $n_{ANF}$ . Conversely, when using the RLS algorithm, the  $N_{RLS}$  filter order and the forgetting coefficient  $\lambda_{RLS}$  must be selected. The advantage of this algorithm is the fact that it works faster than the ANFIS algorithm.

The output fECG signals from the adaptive algorithms are initially repeatedly standardized, and, then, they are adjusted (smoothed) in the last block using the WT algorithm. The reason for smoothing the fECG signals is to highlight the R-peaks for the subsequent estimation of the fHR variable over time, which is the primary task of this work. For this algorithm, the type of maternal wavelet  $\Psi_{WT}$ , the level of decomposition  $n_{WT}$ , the length of the window  $l_{WT}$  for adaptive thresholding and the empirical constant  $K_{WT}$  are to be set.

The statistical evaluation of this hybrid system is based determining of true positive (TP), false positive (FP) and false negative (FN) values and on calculation of accuracy (ACC), sensitivity (SE), positive predictive value (PPV) and harmonic mean between SE and PPV (F1). Next evaluation is based on plotting fHR variability and Bland-Altman graphs and determining of mean value  $\mu$  and standard deviation  $1.96\sigma$  between estimated fHR variability and reference fHR variability.

## 4 Conclusion

Hybrid methods combine the benefits of both adaptive and non-adaptive approaches, such as accuracy, stability, and minimization of the number of measuring electrodes. This study shows that this approach is very promising for the extraction of fECG and very accurate for the needs of determining fHR as the main parameter observed in current clinical practice. The subject of further research should be deeper morphological analysis, such as ST segment, QT interval or T/QRS ratio analysis.

## Acknowledgment

This article was supported by the Ministry of Education of the Czech Republic (Project No. SP2019/85 and SP2019/118). This work was supported by the European Regional Development Fund in the Research Centre of Advanced Mechatronic Systems project, project number CZ.02.1.01/0.0/0.0/16\_019/0000867 within the Operational Programme Research, Development and Education. This work was supported by the European Regional Development Fund in A Research

Platform focused on Industry 4.0 and Robotics in Ostrava project, CZ.02.1.01/0.0/0.0/17\_049/0008425 within the Operational Programme Research, Development and Education. This article was also a part of project VI20172019071.

## References

1. JAROS, Rene; MARTINEK, Radek; KAHANKOVA, Radana. Non-adaptive methods for fetal ECG signal processing: A review and appraisal. *Sensors*. 2018, vol. 18, no. 11, pp. 3648.
2. MARTINEK, Radek; KAHANKOVA, Radana; JEZEWSKI, Janusz; JAROS, Rene; MOHYLOVA, Jitka; FAJKUS, Marcel; NEDOMA, Jan; JANKU, Petr; NAZERAN, Homer. Comparative effectiveness of ica and pca in extraction of fetal ecg from abdominal signals: Towards non-invasive fetal monitoring. *Frontiers in physiology*. 2018, vol. 9, pp. 648.
3. KAHANKOVA, Radana; JAROS, Rene; MARTINEK, Radek; JEZEWSKI, Janusz; WEN, He; JEZEWSKI, Michal; KAWALA-JANIK, Aleksandra. Non-adaptive methods of fetal ECG signal processing. *Advances in Electrical and Electronic Engineering*. 2017, vol. 15, no. 3, pp. 476–490.
4. GUPTA, Abhinav; SRIVASTAVA, M. C.; KHANDELWAL, Vineet; GUPTA, Abhilekh. A Novel approach to fetal ECG extraction and enhancement using blind source separation (BSS-ICA) and adaptive fetal ECG enhancer (AFE). In: *2007 6th International Conference on Information, Communications & Signal Processing*. IEEE, 2007, pp. 1–4.
5. ASSALEH, Khaled. Extraction of fetal electrocardiogram using adaptive neuro-fuzzy inference systems. *IEEE Transactions on Biomedical Engineering*. 2006, vol. 54, no. 1, pp. 59–68.
6. NASIRI, Maryam; FAEZ, Karim; NASRABADI, Ali Motie. A new method for extraction of fetal electrocardiogram signal based on Adaptive Neuro-Fuzzy Inference System. In: *2011 IEEE International Conference on Signal and Image Processing Applications (ICSIPA)*. IEEE, 2011, pp. 456–461.
7. MARTINEK, Radek et al. Non-invasive fetal monitoring: A maternal surface ECG electrode placement-based novel approach for optimization of adaptive filter control parameters using the LMS and RLS algorithms. *Sensors*. 2017, vol. 17, no. 5, pp. 1154.
8. MARTINEK, Radek; ZIDEK, Jan; BILIK, Petr; MANAS, Jakub; KOZIOREK, Jiri; TENG, Zhaosheng; WEN, He. The use of lms and rls adaptive algorithms for an adaptive control method of active power filter. *Energy and Power Engineering*. 2013, vol. 5, no. 04, pp. 1126.
9. CHOUAKRI, S. A.; BEREKSI-REGUIG, F.; AHMALDI, S.; FOKAPU, O. Wavelet denoising of the electrocardiogram signal based on the corrupted noise estimation. In: *Computers in Cardiology, 2005*. IEEE, 2005, pp. 1021–1024.
10. SAMENI, Reza; CLIFFORD, Gari D. A review of fetal ECG signal processing; issues and promising directions. *The open pacing, electrophysiology & therapy journal*. 2010, vol. 3, pp. 4.

# Fetal Cardiac Activity Monitoring: An Overview

Radana Kahánková and Radek Martinek

Department of Cybernetics and Biomedical Engineering, FEECS,  
VŠB – Technical University of Ostrava, 17. listopadu 15,  
708 33 Ostrava – Poruba, Czech Republic  
{radana.kahankova, radek.martinek}@vsb.cz

**Abstract.** The fetal electrocardiogram and phonocardiogram are carriers of a huge amount of valuable information that, if measured and extracted properly, could be helpful in increasing the quality of fetal monitoring. This paper aims to summarize the results of the scientific work of the student under the supervision of associate professor Radek Martinek. It was focused mainly on the measurements of the fetal cardiac activity by means of two different methods.

## 1 Introduction

Intrapartum surveillance became possible in 1821 with the discovery of the fetal heart sounds by Kergaradec. Subsequently, obstetric stethoscope was developed which allowed the determination of mean heart frequency. The obstetricians were thus able to assess fetal health status from the changes occurring in strength and rate of fetal heart beats. Furthermore, it enabled the diagnosis of fetal life or death, allowed determination of multiple pregnancy, fetal presentation and position. This method of fetal monitoring is known as *intermittent auscultation*.

In the late 1960s, the electronic fetal monitoring (EFM) was enabled with the first electronic fetal monitor based on measuring and evaluating the audible fetal heart beats (i.e. phonocardiography) and ECG recordings. Nevertheless, these methods suffer from a large amount of noise, especially those produced by the maternal body. These signals overlap with the useful signal and their suppression is challenging. Therefore, this technique was later replaced by the cardiotocography (CTG), which is the most common technique in intrapartum surveillance nowadays. This technique is able to estimate average fetal heart rate (fHR) and capture the uterine contractions. This is possible by means of piezoelectric transducer and the pressure-sensitive contraction transducer (tocodynamometer), respectively.

However, the accuracy of the method is often questioned due to its false-positive profile. The measurement is sensitive on the fetal as well as maternal movement, the placement of the sensors and also the thickness of the abdominal wall of the measured body, i.e. the maternal body mass index. Moreover, the evaluation of the recordings differs among the expert obstetricians which leads to significant intra-observer disagreement.

Due to the progress in electronics and computer science, the current trends in the research focused on fetal monitoring are moving back towards the first non-invasive techniques – fECG and fPCG. A large amount of methods for the suppression of the maternal component has been introduced by the authors, both for fECG (e.g. [1] – [8]) and fPCG (e.g. [9] – [12]) signals. The main advantage of these techniques over the CTG is their ability to detect the beat-to-beat (BTB) heart rate variability. In contrast to CTG, which in principle averages the fetal heart beats, fPCG and fECG estimate fHR directly from the recorded signal by detecting the features corresponding to each cardiac cycle.

In this paper, we introduce the fPCG and fECG as promising methods for fHR monitoring. In contrast to fECG, the electronic monitoring of the fetal heart sounds by means of fPCG can be carried out by a low-cost device, such as in [13]. However, this method is affected by many factors, including the parameters of the measuring probe. Therefore, in order for the method to be accurate, the individual elements of the measuring system must be chosen carefully. Thus herein, we investigate the influence of the individual parts of the fetal phonocardiogram.

There is a need for the tests with real data. The problem is the lack of suitable real data available for the public use. There is an existing cooperation between the authors and university hospital on creating a database of the real data that can be used for experiments. This paper introduces the pilot projects that aimed to produce the real fPCG and fECG data. In case of fPCG, the first step was to find the optimal configuration of the measurement system – the probe placement is dependent on the position of the fetal heart. Contrary, in case of fECG measurement, both electrode placement and measurement system configuration significantly influence the quality of the output signal. Therefore, the aim of the research was to investigate the above mentioned factors in order to create the database of the real fPCG and fECG signals.

## 2 Experiments

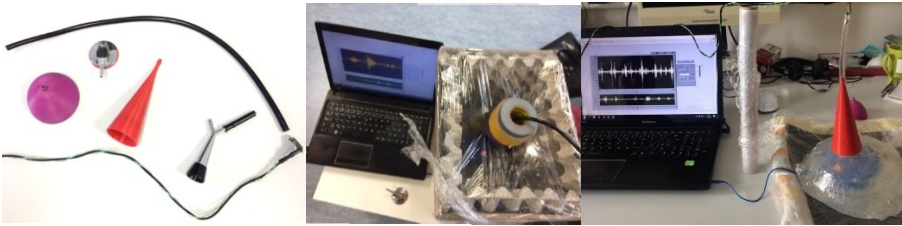
### 2.1 Fetal Phonocardiograph Elementary Parts

According to the available literature and the initial tests, the parts of the measuring system that attenuate the acoustic signal and that were selected for further tests are as follows: the length of the tubing system type and shape of the stethoscope heads to receive sound. Seven different tubing lengths (2, 10, 20 30, 40, 50, and 60 cm) and four different heads (Bell-shaped, Pinard-shaped, Classic Stethoscope, Fetoscope) were tested. The influence of these parts was investigated using different data (synthetic and real signals) as well as variable transmission systems (mobile acoustic box, phantom of a pregnant woman abdomen, real pregnant subject).

In the first part of the experiments, an acoustic mobile box was used to investigate the influence of different stethoscope heads on the standard range of audible frequencies (20 to 20,000 Hz). The aim of the experiment was to find the most suitable stethoscope head able to capture or absorb the frequencies in the range of the fPCG signal. The acoustic mobile box was created from cardboard egg trays and the stretch foil. In

the box, the speaker producing the acoustic signals was placed and connected to the notebook as well as the measuring system, which ensured the synchronization of both systems.

In the second part of the experiments, a phantom of pregnant woman was used to investigate the influence of different stethoscope heads and the tubing system length on the synthetic fPCG signal. The signal was generated using the generator of artificial signals introduced in [14]. This way we aimed to determine the most suitable combination of both stethoscope head and the tubing system length to capture the fPCG signal. The low-cost phantom of the pregnant woman abdomen was created from the jelly, which is used to imitate the abdomen, and covered with stretch foil. The phantom included the speaker producing the synthetic fPCG signals. Again, the synchronization of both systems was ensured by connecting the measuring system as well as the speaker to the notebook. Examples of the above-mentioned elementary parts and the experiments are depicted in Fig. 1.



**Fig. 1.** Examples of the elementary parts of fetal phonocardiograph (left), the experimental workloads consisting of the laptop, the measuring system acoustic mobile box (middle), and the Phantom of the pregnant woman abdomen (right).

The results were summarized in the paper, which was accepted for *The 16th International Conference on Programmable Devices and Embedded Systems, PDeS 2019*. The results revealed that the flat stethoscope head is the most suitable for the construction of fetal phonocardiograph. In terms of the tubing system, the shorter the tube, the better. The most suitable tubing length according to our experiments is 2 cm long. This configuration of the fetal phonocardiograph was verified by the tests in the clinical practice in both human and animal subjects and compared with ECG reference.



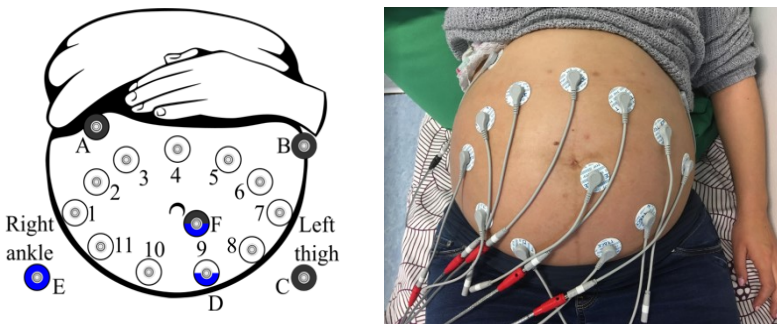
**Fig. 2.** The verification of the fPCG measurement system on human and animal subject.

## 2.2 Influence of System Configuration on NI-fECG Signal Measurement

In the pilot study we investigated the influence of various parameters on the quality of electronic fetal monitoring based on non-invasive fetal electrocardiography. The investigation was carried out as a necessary step in development of an embedded system for fetal monitoring designed as a wearable device. The experiments included measurements of four different configurations on a subject at 34th week of pregnancy by means of 2.0 generation g.USBamp biosignal amplifier from g.tec medical engineering company. The study results in the recommendation of the most suitable system configuration and the electrode placement in terms of the signal quality and the clinical feasibility. Four different configurations of the measurement system were tested:

1. *Jezewski*. This configuration was used in the ADFECGDB database (Jezewski *et al.*, 2012). It includes 4 SEs (1, 2, 4, and 7), the GND (C) placed on the left thigh and the reference (D) on the bottom of the abdomen.
2. *Behar*. This configuration was used in the NIFEADB database (Behar *et al.*, 2019). It includes 4 SEs (1, 3, 4, 5, and 7), the GND (A) placed on the left thigh and the reference (D) on the bottom of the abdomen.
3. *Vullings*. The configuration introduced in the investigation of Vullings (2010) includes 8 SEs (2, 3, 5, 6, 8, 9, 10, and 11), the GND (B) placed on the left waist, and the reference (F) is placed adjacent to the navel.
4. *Taylor*. This configuration of Taylor *et al.* (2003) includes 12 sensing electrodes (1 – 11); the GND (F) is placed adjacent to the navel and the common reference (E) on the right ankle.

The experiments included measurements on a real subject in 34<sup>th</sup> week of pregnancy. The total of 14 electrodes were positioned on the abdomen in the way to cover most of the commonly used electrode deployment as shown in fig. 2.



**Fig. 3.** Measurement deployment. Left: Sensing electrodes (white 1 – 11), ground reference (black A, C, F), and common reference electrode (blue D, E, F); Right: Measurement deployment in real subject at 34<sup>th</sup> week of pregnancy.

Table 1 summarizes the above mentioned configurations, the SE of best quality and the description of the signal features. Besides the ratio between fetal and maternal component, the shape and orientation of the QRS complexes are among the most important factors for the quality of the maternal ECG suppression. For extraction algorithms, the QRS complexes should be either negative or positive. Contrary, if the QRS complex is biphasic, the algorithms show lower performance.

This article investigated the influence of system configuration on the quality of NI-fECG monitoring. The main factors that were considered and tested were the electrode placement and the hardware system configuration. The results showed that the electrode placement herein denoted as Behar is the most suitable in terms of the signal quality and the clinical feasibility. Moreover, the paper introduced the optimal system configuration to ensure high quality input signals. The results were summarized in the paper, which was accepted for *The 16th International Conference on Programmable Devices and Embedded Systems, PDeS 2019*.

**Table 1.** Configurations tested

Configuration	List of SEs	GND	Ref.	Best SE	m:f ratio	mQRS
Jezewski	1, 2, 4, 7	C	D	3, 4	Low	Positive
Behar	1, 3, 4, 5, 7	A	D	2, 3, 4	Low	Neg./biphasic
Vullings	2, 3, 5, 6, 8 – 11	B	F	5, 6	High	Positive
Taylor	1 – 11	F	E	2, 3, 9, 7	High	biphasic

### 3 Conclusion

When recording the data, a lot of factors decreasing the signal quality must be considered. In this paper, the author introduced the latest stage of her research. It was mainly focused on investigating the influence of specific factors, such as the electrode placement and system configuration, on the quality of recorded signal.

Besides that in the earlier stages of the research, the author tested the influence of the electrode placement and the extraction algorithm setting on the signal quality [1], the influence of the gestation age on the extraction system performance [6]. The author also tested a wide variety of methods for the suppression of the maternal component for fECG (e.g. [1] – [8]) and fPCG (e.g. [9] – [12]) signals.

This was necessary step in order to develop an embedded system for fetal monitoring designed as a wearable device for pregnant subjects. In the future research, it is necessary to test the configurations as well as the performance of the extraction algorithms for the different subject, in different stage of pregnancy and different fetal positions.



## References

1. MARTINEK, Radek; KAHANKOVA, Radana; NAZERAN, Homer; KONECNY, Jaromir; JEZEWSKI, Janusz; JANKU, Petr; BILIK, Petr; ZIDEK, Jan; NEDOMA. *Non-Invasive Fetal Monitoring: A Maternal Surface ECG Electrode Placement-Based Novel Approach for Optimization of Adaptive Filter Control Parameters Using the LMS and RLS Algorithms*. *Sensors*, 2017, 17.5: 1154, DOI:10.3390/s17051154. (WoS, IF= 3,031, SCOPUS)
2. MARTINEK, Radek, KAHANKOVA, Radana; et al. Comparative effectiveness of ica and pca in extraction of fetal ecg from abdominal signals: Towards non-invasive fetal monitoring. *Frontiers in physiology*, 2018, 9: 648. (WoS, IF= 3.201, SCOPUS)
3. KAHANKOVA, Radana, et al. Non-adaptive methods of fetal ECG signal processing. *Advances in Electrical and Electronic Engineering*, 2017, 15.3: 476-490.
4. KAHANKOVA, Radana; MARTINEK, Radek; BILIK, Petr. Non-invasive Fetal ECG Extraction from Maternal Abdominal ECG Using LMS and RLS Adaptive Algorithms. In: *International Afro-European Conference for Industrial Advancement*. Springer, Cham, 2016. p. 258-271.
5. KAHANKOVA, Radana; MARTINEK, Radek; BILIK, Petr. Fetal ECG extraction from abdominal ECG using RLS based adaptive algorithms. In: *2017 18th International Carpathian Control Conference (ICCC)*. IEEE, 2017. p. 337-342.
6. KAHANKOVA, Radana, et al. Influence of gestation age on the performance of adaptive systems for fetal ECG extraction. *Advances in Electrical and Electronic Engineering*, 2017, 15.3: 491-501.
7. JAROS, Rene; MARTINEK, Radek; KAHANKOVA, Radana. Non-adaptive methods for fetal ECG signal processing: A review and appraisal. *Sensors*, 2018, 18.11: 3648. (WoS, IF= 3,031, SCOPUS)
8. KAHANKOVA, Radana, et al. Adaptive Linear Neuron for Fetal Electrocardiogram Extraction. In: *2018 IEEE 20th International Conference on e-Health Networking, Applications and Services (Healthcom)*. IEEE, 2018. p. 1-5.
9. MARTINEK, Radek; NEDOMA, Jan; FAJKUS, Marcel; KAHANKOVA, Radana; KONECNY, Jaromir; JANKU, Petr; NAZERAN, Homer. *A Phonocardiographic-Based Fiber-Optic Sensor and Adaptive Filtering System for Noninvasive Continuous Fetal Heart Rate Monitoring*. *Sensors*, 2017, 17.4: 890, DOI:10.3390/s17040890. (WoS, IF= 3,031, SCOPUS)
10. KAHANKOVA, R.; MARTINEK, R. Comparison of Fetal Phonocardiogram Wavelet Denoising Methods. In: *2018 IEEE Signal Processing in Medicine and Biology Symposium (SPMB)*. IEEE, 2018. p. 01-04.
11. KAHANKOVA, Radana, et al. Least Mean Squares Adaptive Algorithms Optimization for Fetal Phonocardiogram Extraction. *IFAC-PapersOnLine*, 2018, 51.6: 60-65.
12. KAHANKOVA, Radana; MARTINEK, Radek. Wavelet Transform Decomposition for Fetal Phonocardiogram Extraction from Composite Abdominal Signal. In: *International Conference on Advanced Engineering Theory and Applications*. Springer, Cham, 2018. p. 125-133.
13. KOLARIK, Jakub, KAHANKOVA, Radana, MARTINEK, Radek. A Low-cost Device for Fetal Heart Rate Measurement. *IFAC-PapersOnLine*, 2018, 51.6: 426-431.
14. JOSEPH, Anthony, MARTINEK, Radek; KAHANKOVA, Radana; Simulator of foetal phonocardiographic recordings and foetal heart rate calculator. In: *Journal of Biomimetics, Biomaterials and Biomedical Engineering*. Trans Tech Publications, 2018. p. 57-64.

# Evaluation of different methods used for recognition of lens types

Pavel Kodytek

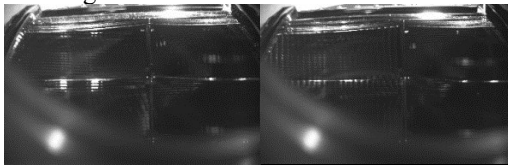
Department of Cybernetics and Biomedical Engineering, FEECS,  
VŠB – Technical University of Ostrava, 17. listopadu 15,  
708 33 Ostrava – Poruba, Czech Republic  
pavel.kodytek@vsb.cz

**Abstract.** The paper deals with the problem of lens classification using statistic evaluation of reliability of selected image processing techniques. Classified lenses are divided into two categories based on the raster on the lens. Image processing techniques that are designed to classify lenses with a lines raster and grid raster are pattern matching, and evaluation of frequency domain. Frequency domain is acquired with fast Fourier transform and thresholding over magnitude of complex number is performed to shrink the number of unwanted frequencies. To simplify the outcome of an FFT to single number, a sum of nonzero elements in frequency domain is computed and decision is made based on confidence intervals. As the last part of problem, we test a full dataset of images, and we calculate if either recognition algorithm is suitable for a real usage.

**Keywords:** Lens classification, Reliability, Statistic

## 1 Introduction

In the modern word of automatization 4.0 the human used knowledge is being replaced with a machine. This leads not only to improve of the reliability, but also to a shorter TTM (time to market) for a created unit. As a part of this process we also implement different automated test systems, which collect and process different types of data from all possible sources and provide a system with a final result. One of the possible inputs for the system is image captured from a camera. These systems then use different image processing algorithms, and based on the image processing techniques they either accept or decline the tested unit (set of units). In this paper we will try to differentiate between two types of lenses, which can be classified based on the raster of the lens. A set of tests have been performed to create a processing scene, where with specific light source and camera, we acquire an image for evaluation.



**Fig. 1:** Image of the lens. Left one is image with lines raster, and right one is image with grid raster.

For image processing we designed two types of algorithm, where first one is based on the pattern matching, and second one uses fast Fourier transform.

## 2 Pattern matching

Template matching or pattern matching techniques are operations, performed over the images (original image, and pattern image) to find a cross correlation function.

$$C_{i,j} = \sum_{x=0}^{M-1} \sum_{y=0}^{N-1} g(x,y)f(x+i,y+j), \quad (1)$$

Where  $f(x,y)$  is value of original pixel at coordination's  $[x,y]$ ,  $g(x,y)$  is a value for pixel at coordination's  $[x,y]$  for pattern image  $g$ , and  $i,j$  represents the offset of pattern from original coordination's.  $M,N$  is a total image size, and boundaries are created so the images wont overlap in blank space. [1]

The final analysis is done over each acquired grayscale image, and visualization process is created to highlight the matched pattern region, and percentage of match. To pick a region of interest we are looking for a local maxima in percentage scale over all  $i,j$  coordination's based on equation 1.

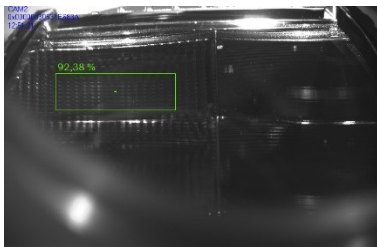


Fig. 2: Pattern matching algorithm on lens with grid raster.

## 3 Evaluation in frequency domain

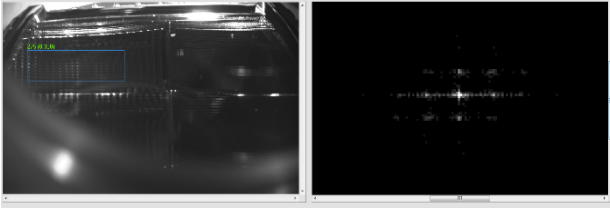
Second approach to classify the lens type is based on frequency domain. To implement a frequency domain on image, we do not use a Fourier transform, which require a continuous time domain signals, but we instead discretize the signals (as an image), and we apply discrete Fourier transform. [2]

$$F(k,l) = \sum_{x=0}^{M-1} \sum_{y=0}^{N-1} f(x,y) \times e^{-i2\pi\varphi}, \quad (2)$$

$$\varphi = \frac{kx}{M} + \frac{ly}{N}, \quad (3)$$

DFT is sampled and does not contain all frequencies. As long as a Fourier transform is process given by equations 2 and 3, and takes a quite a long time, we use a fast Fourier transform for image analyzing process. To further minimize the computation time, and also to improve the reliability of lens classification, we do not evaluate a whole image,

but only a small part of the image. In order to visualize the image as and grayscale image, we only take a magnitude of complex number.



**Fig. 3:** Visualization of FFT and right image is an magnitude of all complex numbers in scale 0-255.

Because the frequency domain, and magnitude visualization can be vague for an industry, we shift the frequency domain into one number. This is done through thresholding of the amplitudes of frequency spectrum, and by making a total count of non-zero elements after thresholding. This can also be expressed of taking a count of items in set B, where B is subset of set A, containing all elements that are greater than a certain value. This is highly depended on size of the region of interest, where we compute the FFT.

## 4 Measurement of reliability

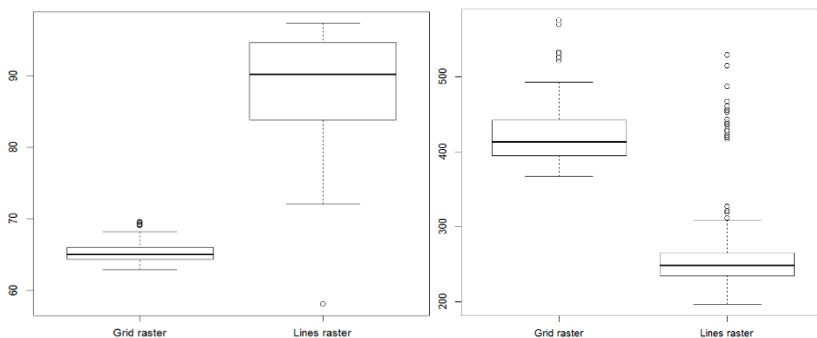
For the measurement of reliability, we collected image samples of total 690 lenses. They were unevenly divided to lenses with line raster, total of 646, and lenses with a grid raster, rest 44.

To make a clear evaluation, a automatic programing loop was created to process a same image with both algorithms mentioned, and values of non-zero magnitude elements in frequency domain, and percentage of match were recorded for comparison.

Pattern used to evaluate both types of lenses was a section of line type lens, and same pattern was used to evaluate a grid type lens as well. In case of selecting a different pattern, we would have to make a false positive or false negative testing as well. Before evaluating a mentioned set, both sets were manually selected to not contain an error images, which were created as an off product of automated capturing. Most of the pictures were missing a lens, or were affected by a strong light source, and therefore images contained over saturated areas.

## 5 Results

All datasets were first tested with tested using basic statistic average and dispersion. As a result of this test we plot a Boxplot of measured data for pattern matching and FFT. The final assumptions are made with hypothesis testing. For both we test normality based on Shapiro-Wilk normality test.



**Fig. 4:** Boxplots for a) Pattern matching on left and b) FFT on right

### Shapiro–Wilk test

- Significance level:  $\alpha = 0.05$
- $H_0$ : Data distribution is equal to normal distribution
- $H_A$ : Data distribution is not equal to normal distribution

**Tab.1:** P-values for Shapiro-Wilk normality test of pattern matching results and FFT

Da-taset	p-value PM	p-value FFT
Lines	7.0E-23	5.4E-33
Grid	1.4E-05	9.3E-06

For both datasets we reject null hypothesis on significance level 5%. Lines raster (Shapiro-Wilk test, p-value  $\ll 0.001$ ). Grid raster (Shapiro-Wilk test, p-value  $\ll 0.001$ ).

### 5.1 Pattern match

To make a statistic proof of a reliability of lens classification with a pattern matching, we make a parametric hypothesis test.

**Proof :** *By contradiction*

Since we like to prove, that both datasets have a different Average or in case a median, we need to prove it with a contradiction, where we negate that both the average values or in our case medians are the same.

---

 Testing for parameter  $X_{0,5}$ 


---

- Selected test: Mann-Whitney test
- $H_0: X_{0,5\_lines} = X_{0,5\_grid}$
- $H_A: X_{0,5\_lines} > X_{0,5\_grid}$
- Significance level:  $\alpha = 0.05$
- p-value =  $\ll 0.001$  (RKWard)

We reject null hypothesis, and medians for our datasets are not equal (Mann-Whitney test, p-value  $\ll 0.001$ ).

We selected a Mann-Whitney test, because it does not require the normality of datasets, which we rejected previously with Shapiro-Wilk test. Because we rejected a null hypothesis, we can conclude that the datasets have different medians, and the proof with contradiction is complete. As we were able to proof with empiric observations, we are able to make a reliable classification based on pattern matching algorithm to separate both types of lenses.

Final values for image classification based on pattern matching results in % of equivalence were set to: from 0 % to 60 % is a unknown item, and the error was presented. From 60% to 75% is a lens with a grid raster, and from 75% above is the line raster lens.

## 5.2 FFT

In case of FFT values, we also select a Mann-Whitney test, because both datasets do not have a normal distribution, and proof is also done with contradiction.

---

 Testing for parameter  $X_{0,5}$ 


---

- Selected test: Mann-Whitney test
- $H_0: X_{0,5\_lines} = X_{0,5\_grid}$
- $H_A: X_{0,5\_lines} < X_{0,5\_grid}$
- Significance level:  $\alpha = 0.05$
- p-value =  $\ll 0.001$  (RKWard)

We reject null hypothesis, and medians for our datasets are not equal (Mann-Whitney test, p-value  $\ll 0.001$ ).

Even thou we proved a difference of medians with a contradiction, we did not assume a stability of the classification, because an empiric evaluation of box plot. With a second testing, on significance level 0.01 we also reject null hypothesis, so we tested a confidence interval for both datasets, which we used to set a intervals.

Final values for image classification based on sum of non-zero elements in magnitude of frequency spectrum acquired with FFT were set to intervals  $\langle 180,340 \rangle$ , for lines raster, and  $\langle 340,600 \rangle$  to be grid raster. Anything else was unknown item, and set NOK.

**Tab.2:** Classification based on set intervals for FFT classification.

	Lines raster	Grid raster
Correct Classification	619	44
Wrong Classification	27	0

The final test for evaluation of lenses with non-zero elements of Fourier transform was done with a set numbers for a classification. Since all the images were labeled with a correct type of lens, a programming loop was created to evaluate all of them, and compare a real result with a computer classification. Results of correct and incorrect classification for both types of lenses are shown in Tab. 6. The grid raster lenses were classified with 100% success, however the lines raster lenses had 27 incorrect guesses, which is 4.17 %.

The problem of overlapping in datasets can be part of properties of FFT. In our case this can be issue of changing light, or present of dust on the lens. These will lead to a rise of high frequencies in frequency domain. Also, the number of non-zero elements is highly depended on the size of region of interest, therefore making a bigger ROI will lead to different values.

## 6 Conclusion

A two methods for lens classification were evaluated with statistic methods in this paper. A results of pattern matching, where a both type of lenses were evaluate with same pattern shows a no overlapping, and therefore went to a successful classification of lens type. The second approach, which used a sum of non-zero elements of frequency domain computed with a fast Fourier transform, proved to be useable at the confidence level 5%. The final test showed that out of 690 lenses, 27 were classified incorrectly.

## 7 References

KLINGER, THOMAS. IMAGE PROCESSING WITH LABVIEW AND IMAQ VISION. UPPER SADDLE RIVER, NJ: PRENTICE HALL PTR, c2003. ISBN 0-13-047415-0.

SOJKA, EDUARD, JAN GAURA A MICHAL KRUMNIKL. MATEMATICKÉ ZÁKLADY DIGITÁLNÍHO ZPRACOVÁNÍ OBRAZU [ONLINE]. VYSOKÁ ŠKOLA BĀŇSKÁ – TECHNICKÁ UNIVERZITA OSTRAVA, 2011 [CIT. 2018-10-04]. DOSTUPNÉ Z: [HTTP://MRL.CS.VSB.CZ//PEOPLE/SOJKA/DZO/MZDZO.PDF](http://mrl.cs.vsb.cz/people/sojka/dzo/mzdzo.pdf).

# Acoustic Sensor for Multi-Area Application

Jakub Kolařík and Radek Martinek

Department of Cybernetics and Biomedical Engineering, FEECS,  
VŠB – Technical University of Ostrava, 17. listopadu 15,  
708 33 Ostrava – Poruba, Czech Republic  
{jakub.kolarik, radek.martinek}@vsb.cz

**Abstract.** From the vibration analysis generated by biological and mechanical systems, it is possible to determine whether there has been a fundamental change in their time or frequency domain. This analysis can provide information about the internal state of the system and its dynamics without the need for invasive intervention. In addition, the measured data can be used together with advanced signal processing algorithms (neural networks or machine learning) to create a predictive maintenance and diagnostic system. This work describes a modular measuring device based on closed acoustic tube. Acoustic tube parameters are measured and optimized for use in remote monitoring in electronically disturbed or chemically hazardous environments.

**Keywords:** Vibrations measurement, Acoustic tube, Pressure tube

## 1 Introduction

In this work, the issue of vibration measurement and sound analysis was chosen as an area that has a fundamental impact on the diagnosis of biological and mechanical systems. This idea was based on demand on development of sophisticated sensor systems as part of initiative of SMART technologies and Industry 4.0 (see [1][2] and [3]). According to current trends, the classical concept of electromechanical sensors is in decline and multiple sensor systems based on light and optical methods (optical gates, image recognition, etc.) have been preferred.

The paper is a follow-up to previous work, which aims to develop a modular sensor system. Sensor modularity would be accomplished using replaceable sensor modules. The task of these modules would be to transfer the measured processes, in the sense of a basic physical quantity converter, to an acoustic and pneumatic signal, detectable by a measuring microphone. For each modification of the sensor system, it is necessary to determine the requirements for the sensor device according to the dynamics of the measured events. These requirements include the desired sampling rate, A/D converter range, or pre-processing and signal filtering to prevent aliasing. As rapid prototyping technology, 3D printing is suitable for sensor module design. The specific print material will be selected according to the application requirements (e.g. according to the flexibility or temperature resistance of the material). One of the goals of this project is to be competitive with optical fiber technology, while keeping the sensor cost of manufacturing low.



## 2 Sensor description

This chapter describes the measuring equipment hardware. The device prototype was developed primarily for biomedical purposes, more specifically for the measurement of fetal phonocardiography. Later, this measuring platform has found use in other fields of our research by development of different sensor modules. These sensing modules are developed for the following applications:

- Biomedical applications,
- industrial applications,
- traffic applications,
- construction industry,
- smart city and housing.

To date, several prototype sensor modules have been built for biomedical and industrial applications.

### 2.1 Sensor Principle

The sensor works on the principle of measuring the pressure change inside the tube. The tube is terminated on one side by a measuring microphone, and the other end contains a membrane, or the end is sealed.

For this sensor, the microphone measures minor pressure changes inside the tube. Depending on the type of embodiment, these pressure changes are caused by the movement of the diaphragm or by vibrations acting on the tube surface.

### 2.2 Sensor Parameters

In this part of the thesis are presented two versions of sensor design. The difference in these systems lies in the hardware used. As proof of concept were used system for virtual instrumentation by NI and the low-cost device of own design as example of final product.

NI hardware parameters:

- G.R.A.S microphone Type 40 PP,
- DAQ card with NI 9234 module,
- sampling rate 51.2 kHz.

Low-cost hardware parameters:

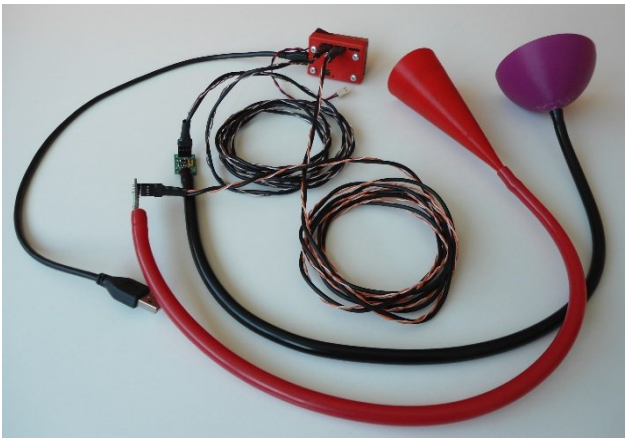
- Electret microphone model PUM-5250L-R,
- low-noise operational amplifier OPA172,
- microcontroller unit (MCU) STM32F373,
- sampling rate 5k Hz.

### 3 Biomedical Application Area

This chapter describes the selection of signal measurement areas. Following the previously solved problems of analysis of mechanical and biological processes, the measurement of vital functions was chosen, namely the cardiac and respiratory cycle. To measure these vital signs, a measurement module adapted for measuring phonocardiography (PCG), seismocardiography (SCG) and ballistocardiography (BCG) were used.

#### 3.1 Phonocardiography

One of the first versions of this sensor was a fetal phonocardiograph (see Fig. 1.). For the signal processing and analysis, we developed LabVIEW application which included a detection algorithm. This algorithm allows to determine fetal heart rate, which is a vital parameter for fetal well-being assessment. Preliminary tests [4] were promising and reveal, that some aspects of work need to be separately tested and improved [5]. The future research should include detailed study of factors influencing quality of the recorded signal, such as stethoscope heads, tube length, the number of tubes, etc. Based on these findings, the individual parts of the stethoscope should be reinvented.

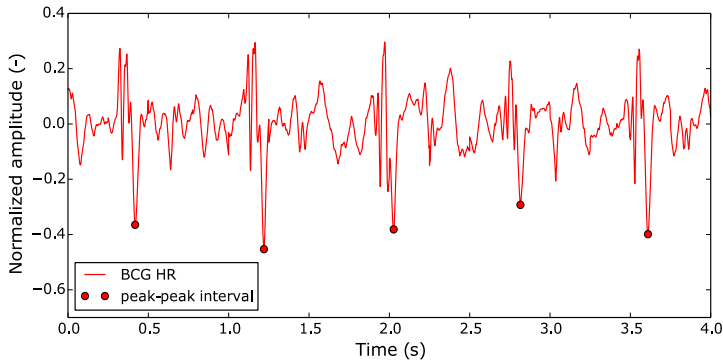


**Fig. 1.** Prototype Sensor for Fetal Phonocardiography

#### 3.2 Seismocardiography

The second area of application of the sensor was measurement of seismocardiography (SCG) during magnetic resonance imaging (MRI). The SCG is a method for studying the mechanical vibrations which are produced by cardiovascular activity. Common sensors used for SCG monitoring are accelerometers. They can measure acceleration in three axis and give complete information about the heart movement. In special cases, such as monitoring CA during MRI, the accelerometer cannot be standardly used. The measured signal would be influenced by changing magnetic field and induced currents. The presented equipment was different from the standard SCG monitoring tools and was therefore studied in detail. It relies on non-magnetic materials which also do not

affect MRI examination. One of the most significant changes in standardized SCG measurement is that our system measures the acceleration in one vector perpendicular to the location of the sensor on the patient's chest. The patient's SCG is measured through pressure changes within the tube as a result of minor movements of the skin below the sensor. These pressure changes are transmitted by a tube and then measured in a magnetic resonance (MR) control room using a microphone (see Fig. 2.) located at the end of the tube. Synchronized electrocardiograph measurements were used as reference.



**Fig. 2.** Heart rate measured by SCG in MRI

### 3.3 Ballistocardiography

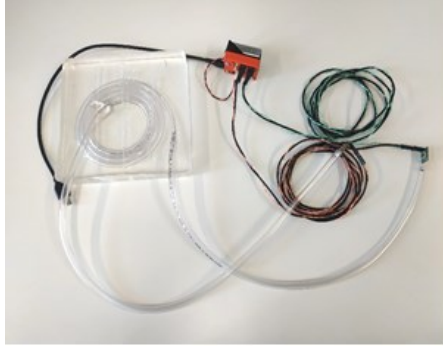
The last type of heart activity measurement was ballistocardiography (BCG). In this case, the sensor was built into a pad on which the patient was lying inside the MR. The signal measured by this sensor corresponded to the movement of the body due to the expulsion of blood into the bloodstream depending on the heart activity. The pressure change inside the line was sensed, as in the previous case, using a microphone at the end of the tube in the control room.

## 4 Industrial Application Area

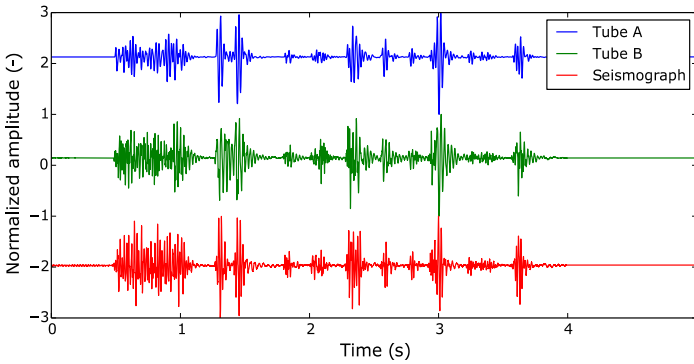
The industrial version of the sensor does not contain a membrane; This system has a direct relationship between the volume and the pressure of the gas enclosed inside the tube at constant temperature. This sensor version can be used for the building industry, transport, but also security activities (occupancy sensor).

### 4.1 Seismograph for Blasting Operation

One of the first tests in the industrial area was carried out when measuring rock blasts. Individual materials were tested in these trials. A modified sensor that consisted of a spirally twisted tube is shown in Figure 3. Our measurements (see Fig. 4.) were comparable with experimental systems based on optical fibers and also reference commercial seismograph.



**Fig. 3.** Prototype Sensor for Vibration Measurement



**Fig. 4.** Measured signals using two types of tube materials [a) PVC, b) PUR with polyester nylon cord] and reference signal from a commercial seismograph

## 4.2 Seismograph for Traffic Monitoring

A modified version of the sensor (see Fig. 3.) will be used to analyze the vibrational manifestations of vehicles to determine their speed, number or type of vehicles. This information can be useful in analyzing road congestion, detour planning, and optimizing approach routes for the Integrated Rescue System state departments. Another useful feature is the detection and classification of events such as car accidents or noise limits.

## 5 Conclusion

The presentation device has been successfully used in several areas as a suitable alternative to the currently used commercial sensors with many times higher price and comparable results. When using this sensory system, due to its lower cost requirements, it is possible to deploy in larger quantities and thus obtain a more complex overview of the measured phenomenon (e.g. Blasting operation).

The device was adapted for remote monitoring of cardiac activity, measuring seismic activity of blasting operation or measure speed of traffic. Measuring system has proven its immunity to interference by acoustic interference and has retained the shape of the transmitted signal compared to commercial sensors. The key to the further development of this work will improve the sensitivity, noise reduction, acquisition of new information and extend the possible uses.

The most studied problematic was cardiac activity measurement. In case of seismocardiography monitoring, the shape of the heart curve was instable due to dependency on the location of the probe. Despite this, the heart rate measurement by SCG was much more stable than the ECG measurement, which contain strong noise from magnetic resonance.

Future work will no longer be primarily focused on measuring CA but analyzing the vibrations produced by traffic to determine speed of vehicles and their type.

### Acknowledgment

This article was supported by the Ministry of Education of the Czech Republic (Project No. SP2019/85). This work was supported by the European Regional Development Fund in the Research Centre of Advanced Mechatronic Systems project, project number CZ.02.1.01/0.0/0.0/16 019/0000867 within the Operational Programme Research, Development and Education. This work was supported by the European Regional Development Fund in A Research Platform focused on Industry 4.0 and Robotics in Ostrava project, CZ.02.1.01/0.0/0.0/17 049/0008425 within the Operational Programme Research, Development and Education.

This work was supported by the project SP2019/107, „Development of algorithms and systems for control, measurement and safety applications V" of Student Grant System, VSB-TU Ostrava.

### References

1. Otahalova, T., Slanina, Z., and Vala, D., "Embedded sensors system for real time biomedical data acquisition and analysis", *IFAC Proceedings Volumes (IFAC-PapersOnline)* 11(part 1), 261-264 (2012).
2. Nudzikova, P. and Slanina, Z., "User identification by biometric methods", *Advances in Intelligent Systems and Computing* 423, 181-190 (2016).
3. Walendziuk, W., Sawicki, A. Telemetric measurement system of beehive environment conditions. *Proceedings of SPIE - The International Society for Optical Engineering*, 9290, art. no. 92901G, 2017. DOI: 10.1117/12.2073050
4. Kolarik, J., Golembiovsky, M., Docekal, T., Kahankova, R., Martinek, R., & Prauzek, M. (2018). A Low-cost Device for Fetal Heart Rate Measurement. *IFAC-PapersOnLine*, 51(6), 426-431.
5. Kolarik, J., Soustek, L., & Martinek, R. (2018, September). Examination and Optimization of the Fetal Heart Rate Monitor: Evaluation of the effect influencing the measuring system of the Fetal Heart Rate Monitor. *In 2018 IEEE 20th International Conference on e-Health Networking, Applications and Services (Healthcom)* (pp. 1-4). IEEE.

# Numerical SW Tools for Solutions of Optimal Control Problems

Filip Krupa

Department of Cybernetics and Biomedical Engineering, FEECS,  
VŠB – Technical University of Ostrava, 17. listopadu 15,  
708 33 Ostrava – Poruba, Czech Republic  
filip.krupa@vsb.cz

**Abstract.** The paper gives an overview of various ready-to-use numerical software solutions capable of solving optimal control problems (OCP). It summarizes basic properties, licensing policy, approach and formulation of OCP. The paper presents a case study which compares chosen SW tools in terms of achieved results. This is done for a mathematical model of a single pendulum on the cart which represents a highly complex and nonlinear system that is suitable to be used as a benchmark.

**Keywords:** Optimal control, SW tool, Dynamic optimization, Trajectory generation, State transition problem.

## 1 Introduction

The motivation of this paper is to give a brief overview of some of the software tools available in the market that are used to solve the optimal control problem (OCP). The goal is to ultimately provide the user with enough knowledge of the toolbox, problem formulation and certain other aspects to know which toolbox fits their problem definition.

When a dynamic system is considered, the process of determining its control and state trajectory over a finite amount of time, to optimize the cost function is known as optimal control. Solving it analytically turns out to be quite a challenge as the variables and complexity of the system increases. The numerical method is divided into two classes: indirect and direct methods. Indirect approach solves the problem by converting the optimal control into a boundary value problem. As a result, the optimal solution is found by solving a system of differential equations that satisfies endpoint [1]. Direct approach solves the problem by transitioning infinite optimization problem to finite optimization problem.

The late 1980's saw a transformation in the available tools for solving optimal control problems. These software tools could solve the most challenging optimal control problems one could realistically pose. Earlier software programs used compiled languages such as FORTRAN, but in recent years, MATLAB has become much more popular for solving optimal control problems. This increased appeal for MATLAB emanates from the fact that it is an extremely easy environment in which to program and the case for using Matlab becomes even stronger as the availability of NLP solvers is much more evident.

## 2 Mathematical formulation

An optimal control problem is formed as follows. Evaluating the state trajectory  $(t) \in R^n$ , the control trajectory  $u(t) \in R^m$ , the vector of static parameters  $p \in R^q$ ,

initial time,  $t_0 \in R$  and the final time,  $t_f \in R$  which will optimize the cost function, according to (1):

$$J = \varphi[x(t_0), t_0, x(t_f), t_f; p] + \int_{t_0}^{t_f} L[x(t), u(t), t; p] dt \tag{1}$$

where  $\varphi$  represents Mayer’s term and  $L$  represents Lagrange’s term. Both the terms form together a formula known as Bolza formula.

It is subject to the dynamic constraints (i.e., differential equation constraints), according to (2):

$$x'(t) = f[x(t), u(t), t; p] \tag{2}$$

and the path constraints, according to (3):

$$C_{min} \leq C[x(t), u(t), t; p] \leq C_{max} \tag{3}$$

and the boundary conditions, according to (4):

$$\varphi_{min} \leq \varphi[x(t_0), t_0, x(t_f), t_f; p] \leq \varphi_{max} \tag{4}$$

The state, control, and static parameter can each be written in the component form, according to (5):

$$\begin{aligned} x(t) &= [x_1(t) \dots x_n(t)] \\ u(t) &= [u_1(t) \dots u_m(t)] \\ p &= [p_1 \dots p_q] \end{aligned} \tag{5}$$

The differential equation of Eq. (2) describes the dynamics of the system while the performance index is a measure of the “quality” of the trajectory. When it is desired to minimize the performance index, a lower value of  $J$  is “better”; conversely, when it is desired to maximize the performance index, a higher value of  $J$  is “better [1].”

### 3 Overview of software tools in the field of OCP

This section talks about the various tools chosen that solve the optimal control problem.

Here is a list of tools selected for this survey: DYNOPT, PSOPT, GPOPS II, PyTrajectory, OptimTraj, POCP, ACADO, TOMLAB.

#### 3.1 DYNOPT

Dynamic programming is most often used to solve the optimization problem. In such cases, there can be a ton of possible solutions, but the task at hand is to obtain an optimal (minimum or maximum) value. We call such a solution to be an optimal solution.

DYNOPT is a set of MATLAB functions for determination of optimal control trajectory given the description of the process, the cost to be minimized, subject to equality and inequality constraints [2].

**Basic Overview:** DYNOPT requires a system that has its first derivatives by the state and control variables, the user can decide on the number of iterations, objective function evaluation. The user must choose the setting according to the problem definition.

**Problem formulation:** The general formulation for DYNOPT is given by (6):

$$\begin{aligned} \min u(t) J[x(t_f)] \\ x'(t) = f[t, x(t), u(t)], x(0) = x_0 \end{aligned}$$

$$\begin{aligned}
h[t, x(t), u(t)] &= 0 \\
g[t, x(t), u(t)] &\leq 0 \\
x(t)^L &\leq x(t) \leq x(t)^U \\
u(t)^L &\leq u(t) \leq u(t)^U
\end{aligned} \tag{6}$$

**Availability:** DYNOPT has gained a good momentum in the optimal control world due to its performance, price, simplicity and the fact that the source code is freely available. It optimizes a given performance index evaluated at the final conditions subject to the constraints which can be evaluated at the initial conditions or over the full-time interval or at the final conditions.

### 3.2 PSOPT

PseudoSpectral Optimal Control solver PSOPT is an open source optimal control package written in C++ that uses direct collocation methods, including Legendre and Chebyshev pseudo spectral discretization, as well as local transcriptions such as trapezoidal or Hermite-Simpson [3].

**Basic overview:** It usually uses the p-method where a single segment is used, and convergence is obtained by incrementing the degree p of the polynomial. It displays good convergences in states, controls and co-states.

**Problem formulation:** The problem formulation for PSOPT to minimize the cost function is as follows. Evaluate control trajectories,  $u(t), t \in (t_0, t_f)$ , state trajectories,  $x(t), t \in (t_0, t_f)$ , static parameters, p and time,  $t_0, t_f$ .

Once these parameters are obtained, the following cost function can be minimized, according to (7):

$$J = \Sigma \left[ \varphi[x(t_f), p, t_f] + \int_{t_0}^{t_f} L[x(t), u(t), p, t] dt \right] \tag{7}$$

**Availability:** The software is distributed under the terms of the GNU Lesser General Public License LGPL. PSOPT is compatible with the Ubuntu Linux operating system and has been ported to be compiled by Microsoft Visual Studio 2008 under Win 7 [4].

### 3.3 GPOPS II

GPOPS-II is the next-generation of general-purpose optimal control software. GPOPS-II is new MATLAB software intended to solve general nonlinear optimal control problems. GPOPS-II implements the new class of variable-order Gaussian quadrature methods where a continuous-time optimal control problem is approximated as a sparse nonlinear programming problem (NLP) [5].

**Basic overview:** It allows inclusion of integral constraints and highly general boundary conditions, highly accurate costate estimation, the inclusion of the NLP solver IPOPT, interface to be able to call the NLP solver SNOPT.

**Problem formulation:** Let  $p \in [1, \dots, P]$  be the phase number where P as the total number of phases. The optimal control problem is to determine the state,  $\mathbf{y}^{(p)}(\mathbf{t}), \mathbf{t} \in \mathbb{R}^{n_y^{(p)}}$ , the control,  $\mathbf{u}^{(p)}(\mathbf{t}), \mathbf{t} \in \mathbb{R}^{n_u^{(p)}}$ , integrals,  $\mathbf{q}^{(p)} \in \mathbb{R}^{n_q^{(p)}}$ , phase start times,  $t_0^{(p)} \in \mathbb{R}$ , phase final times,  $t_f^{(p)} \in \mathbb{R}$ , in all phases  $p \in [1, \dots, P]$ , along with the static parameters  $\mathbf{s} \in \mathbb{R}^{n_s}$ , that minimize the objective functional, satisfying constraints, according to (8) [6]:



$$\begin{aligned}
 J &= \Phi(e^{(1)}, e^{(2)}, \dots, e^{(P)}, s) \\
 \dot{y}^{(p)}(t) &= a^{(p)}(y^{(p)}(t), u^{(p)}(t), t, s) \quad (p = 1 \dots P)
 \end{aligned} \tag{8}$$

**Availability:** The disadvantage of using the latest GPOPS II is that the licenses must be purchased for academic purpose and the NLP solver SNOPT is not included. It must be purchased separately. The tool can be purchase at [7].

### 3.4 PyTrajectory

PyTrajectory is a Python library for trajectory generation for nonlinear control systems. It relies on solving a boundary value problem (BVP) via a collocation method. It is used for the determination of the feed forward control to achieve a transition between desired states of a nonlinear control system.

When it comes to the control of technological processes, a much important task falls upon planning and designing the trajectories. This problem falls under the two-point boundary value problem with free parameters. The main task that this method focuses on is the transition of a control system between the desired states.

**Basic overview:** PyTrajectory uses cubic spline functions as candidates to converge. Splines are piecewise polynomials with global differentiability.

**Problem formulation:** The optimal control problem is defined by cost functions consisting of two parts, Mayer term penalizing starting and end points, and Lagrange term penalizing transition. The boundary value problem uses cost function with only the Mayer term. The result is feed-forward control for the entered nonlinear system.

**Availability:** Python version 2.7 is required to work with this library. There are also some dependencies on the other libraries necessary to install before PyTrajectory [8].

### 3.5 OptimTraj

OptimTraj is a Matlab library designed for solving continuous time single phase trajectory optimization problems [9].

**Basic overview:** It has no dependencies outside Matlab, most methods support analytical gradients, helpful with debugging and experimenting, it solves problems with an integral cost function, boundary cost function, continuous dynamics and it uses Trapezoidal direct collocation method, Hermite-Simpson direct collocation methods, Runge-Kutta 4th order multiple shooting, Chebyshev-Lobatto orthogonal collocation.

**Problem formulation:** The optimal control problem is solved by minimizing the following objective function, according to (9) [9]:

$$\text{Min} J_B(t_0, t_f, x(t_0), x(t_f) + \int_{t_0}^{t_f} J_P(\tau, x(\tau), u(\tau)) d\tau \tag{9}$$

The user must provide with a suitable initial guess for  $t_0, t_f, x(t), u(t)$ .

**Availability:** OptimTraj is published under The MIT License (MIT) Copyright (c) 2016 Matthew P. Kelly. It is free of charge and the author allows the right to use, modify and publish [10].

### 3.6 POCP

POCP is a Matlab package aimed at solving approximately nonlinear optimal control problems for which all the problem data are polynomial.

**Basic overview:** The initial condition is fixed when the set C1 consists of only one point, a more general framework is considered when the initial condition is not known, it can be quite helpful to use where the horizon T is fixed or not, the sequence of lower bounds on the optimal value of the OCP is relaxed.

**Problem formulation:** Consider a continuous time system described by the differential equation, according to (10) [11]:

$$\dot{x}(t) = f(t, x(t), u(t)) \quad (10)$$

Then, the total cost to be minimized is defined, according to (11):

$$J(0, T, x(0), u(\cdot)) = \int_0^T h(t, x(t), u(t)) dt + H(x(T)) \quad (11)$$

where T is the horizontal length of the time interval.

**Availability:** To compute polynomial sub solutions of the HJB equation, the optimization modelling toolbox YALMIP must be installed as well. POCP is a free Matlab package consisting of an archive file downloadable from [12].

### 3.7 ACADO

ACADO Toolkit is a software environment and algorithm collection written in C++ for automatic control and dynamic optimization. It provides a general framework for using a great variety of algorithms for direct optimal control, including model predictive control as well as state and parameter estimation.

**Basic overview:** The syntax of ACADO Toolkit is as intuitive as possible, moreover, the syntax of ACADO for Matlab is familiar to both Matlab users and ACADO Toolkit users.

**Problem formulation:** Consider a dynamic system which is given, according to (12):

$$\dot{x}(t) = f(t, x'(t), x(t), z(t), u(t), p, T) \quad (12)$$

With differential states  $x$ , time varying control inputs  $u$ , and parameters  $p$ .

Then, the total cost to be minimized is defined, according to (13):

$$\Phi[x(\cdot), z(\cdot), u(\cdot), p, T] = \int_{t_0}^T L(\tau, x(\tau), z(\tau), u(\tau), p, T) d\tau + M(x(T), p, T) \quad (13)$$

**Availability:** It requires Matlab as well as a C++ compiler.

### 3.8 TOMLAB

The TOMLAB Optimization Environment is a powerful optimization and modelling package for solving applied optimization problems in Matlab for research and academic purpose.

**Basic overview:** The user must define the problem once and all the available solvers are used. Still, one of its main features remains its full modelling environment in Matlab. It can integrate completely with PROPT (Optimal control platform).

**Problem formulation:** The formulation for TOMLAB is given, according to (14):

$$\begin{aligned} & \min f(x) \\ & x^L \leq x \leq x^u \\ & b^L \leq Ax \leq b^u \\ & c^L \leq c(x) \leq c^u \end{aligned} \quad (14)$$

**Availability:** A valid license is required to run the TOMLAB solvers.

## 4 CONCLUSIONS

The paper presented gives a brief overview of the various tools available in the market to solve the optimal control problem through numerical approach, and the properties of these software tools give the user an idea as to which tool will suit one's problem definition.

The most evident observation made is the state trajectories obtained after computation satisfies the fundamental requirement placed by the problem definition. Considering a state-transition problem, there can be up to infinity number of different control signals capable of transitioning the system between predefined initial and final states. This is corresponding to a boundary-value problem (BvP), or it can be considered as a optimal control problem with the Mayer's term only. When adding Lagrange's term, in this case representing a minimum-energy problem, there is the only one solution expected. However, using different SW tools, obtaining identical results of the same job is quite challenging as these tools have many variabilities in their settings.

## 5 REFERENCES

1. Rao, Anil V. "A survey of numerical methods for optimal control." *Advances in the Astronautical Sciences* 135.1 (2009): 497-528.
2. Cizniar, M., M. Fikar, and M. A. Latifi. "MATLAB dynamic optimisation code DYNOPT." *User's Guide. Bratislava, Slovak Republic* (2006).
3. Becerra, Victor M. "Solving complex optimal control problems at no cost with PSOPT." *2010 IEEE International Symposium on Computer-Aided Control System Design*. IEEE, 2010.
4. Patterson, Michael A., and Anil V. Rao. "GPOPS-II manual: A general-purpose MATLAB software for solving multiple-phase optimal control problems version." (2015): 1-72.
5. Patterson, Michael A., and Anil V. Rao.(2015) "GPOPS-II manual: A general-purpose MATLAB software for solving multiple-phase optimal control problems version." Available online: <http://www.gpops2.com/>
6. Kunze, Andreas, O. Schnabel, and C. Knoll.(2016) "PyTrajectory Documentation, 2015." Available online:<https://www.python.org/download/releases/2.7/>
7. Kelly, M. "OptimTraj: Trajectory optimization library for matlab." (2016).
8. Kelly, M.(2016) "OptimTraj: Trajectory optimization library for matlab." Available online: <https://github.com/MatthewPeterKelly/OptimTraj>
9. Henrion, Didier, Jean B. Lasserre, and Carlo Savorgnan. "POCP: a package for polynomial optimal control problems." *2009 European Control Conference (ECC)*. IEEE, 2009.
10. Henrion, Didier, Jean B. Lasserre, and Carlo Savorgnan.(2009) "POCP: a package for polynomial optimal control problems." Available online: <https://pocoproject.org/download.html>
11. Ariens, David, et al. "Acado for Matlab user's manual." *Optimization in Engineering Center (OPTEC)* 1 (2010).
12. Holmström, Kenneth, Anders O. Göran, and Marcus M. Edvall. "Users guide for TOMLAB/SNOPT." *Mälardalen University, Department of Mathematics and Physics, Västerås, Sweden*(2008). Holmström, Kenneth, Anders O. Göran, and Marcus M. Edvall.(2008) "Users guide for TOMLAB/SNOPT." Available at: <http://tomopt.com>

# Model of Retinal Vasculature from Images Taken by RetCam 3 with Using the Morphological Operation Methods

Alice Křestánová and Marek Penhaker

Department of Cybernetics and Biomedical Engineering, FEECS,  
VŠB – Technical University of Ostrava, 17. listopadu 15,  
708 33 Ostrava – Poruba, Czech Republic  
{alice.krestanova, marek.penhaker}@vsb.cz

**Abstract.** This paper includes information about segmentation retinal vasculature of prematurity babies from images, which were taken by RetCam3. The segmentation is based on the morphological operation methods. For testing was used dataset about 22 images with different contrast. The data were provided by Clinic of Ophthalmology in University Hospital Ostrava. The method seems available for the next assessment of blood vessels tortuosity. Assessment of tortuosity is important for disease evaluation of retinopathy of prematurity.

**Keywords:** retinal blood vessels, RetCam3, morphological operation, segmentation, ROP, retinopathy of prematurity, tortuosity, MATLAB

## 1 Introduction

Retinopathy of prematurity (ROP) represents a vasoproliferative disease, which affects the immature retinal blood vessels of the retina in prematurity infants. This disease occurs in children born before the 32<sup>nd</sup> gestation week and children with a birth weight of less than 1.500 g. Hypoxemia or hypercapnia of newborns is another possible risk of ROP. For the ROP diagnostics, RetCam3 is conventionally used. It is a device from Clarity Medical Systems that allows for retrieve the retina of premature infants. Images from RetCam3 have a resolution 640x480 pixels. At the images, there are observable objects as the retinal blood vessels, optical nerve and retinal lesions. One of the symptoms of this disease is the tortuosity. Up to now, the curvature has been evaluated by the ophthalmologists by manually or by visual comparison of multiple images. For this reason, it is necessary to automatically extract the vascular system from image with a view to further evaluation of tortuosity. Since the tortuosity was not represent by a parameter, which it corresponds with the blood vessels curving [1], [2], [3]

## 2 Related Work

This paper deals with image processing of retinal images taken by the RetCam3. In related work have been processed predominantly images taken by fundus camera with higher resolution (605x700 pixels versus RetCam3 640x480 pixels). [4], [5]

Therefore, the recently reported segmentation methods do not have to be effectively applied in the RetCam 3 images. [6], [7]

This fact predetermines that low resolution images represent a challenging area for the medical image segmentation. [8] Method uses extraction of the green channel from color image was taken by RetCam3, noise filter is applied and mapping vascular system of retina on black background. [9]

In different approach an image has been pre-processed by grayscale image conversion, Gaussian blur, Laplace edge detection, noise removal, image binarization and removal of isolated areas. Segmentation has been enhanced by branch detection techniques and endpoint detection. [10]

Segmentation of retinal blood vessels based on Gabor's transformation. In this pre-processing image, extraction of the green chrominance component of image, image sharpening, histogram adaptation and median filtration were separated. Gabor's filters use Gabor's wave, which reliably detects the shape of the blood vessels system. [11]

Segmentation methods which have been applicate on images taken by fundus camera are described below. Segmentation of retinal blood vessels on the base of method clustering K-means. [12] Segmentation based on tracking is applied to local operators representing the blood vessels system. Blood vessel tracking begins at the initialization point, detects the center of the blood vessel lines or their surroundings by analyzing the orthogonal pixels in the tracking directions. [13]

Supervised method has been used training sets. The original image is processed by wavelet operation that allows to divide image into several levels based on the extraction features. The tracking method is based on combination of vessel directions and eight Hessian matrix vectors used for segmentation of the vascular system. [15], [16] Segmentation of the retinal blood vessels using neural networks utilizing a 7D features vector composed of gray shades and feature representing the invariant moment. The multilayer forward neural network is used for training and classification. [14]

Unsupervised method can be used using a fuzzy C-means clustering algorithm, that uses language descriptions to decide whether it is or it is not a vessel. Fuzzy tracking is based on the determination of membership of functions in two language values. [17], [18]

Different approach image pre-processing, when the RGB image was converted to the HSI color model. Additionally, it was used an adaptive histogram to increase the contrast and average filter to remove a noise. The next step for segmentation image is Top-hat transformation. [19]

### **3 Proposal of Morphological Segmentation of Retinal Blood Vessels**

This segmentation method is based on a sequence of the morphological operations. It has been tested on 22 retinal images of prematurity infants with the retinopathy of prematurity taken by the RetCam 3. The retinal images are divided into 11 contrast images and 11 non-contrast images. We have deliberately performed testing on worse quality

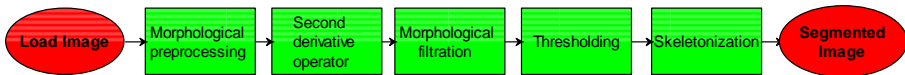
images in order to evaluate objective effectivity and robustness of the morphological image segmentation.

In the first step of the algorithm for segmentation of retinal blood vessels is morphological preprocessing, when vascular system is segmented from other anatomical retinal structures in images (e.g. optical disc). The aim of the morphological preprocessing is emphasized vasculature and preserved transitions of the bifurcation of the vascular system. The algorithm has been used difference between supreme  $I_c$  and infim  $I_B$  of morphological opening operation applied to the original image with two linear structural elements with different sizes. [20]

Removing linear shapes from the image corresponds to replacing them (local) backgrounds. The local background of the image is obtained by opening the boundary of the linear length  $B$  by a length in many ways, where  $i$  is represented 12 structural elements in  $0 - 165$  degrees.

The result of this morphological preprocessing is the emphasis on linear structure (blood vessels). Second derivative operator is used to emphasizing thin vascular structures. Morphological filtration is removed nonlinear bright parts.

Then binary mask of image is created by the hysteresis thresholding. Two binary images  $I_{low}$  and  $I_{high}$  are created:  $I_{low}$  is created by thresholding with low thresholding value  $t_{low}$  and  $I_{high}$  is created by thresholding with high thresholding value  $t_{high}$ . The segmentation output is represented by the binary segmentation mask, where the white pixels represent the detected blood vessels, contrarily the adjacent retinal structures are suppressed, as black. Skeletonization of the mask allows to identify points in the image, where blood vessels are crossed (bifurcations, transitions). [20] The entire image segmentation process is shown below (see Fig. 1.)



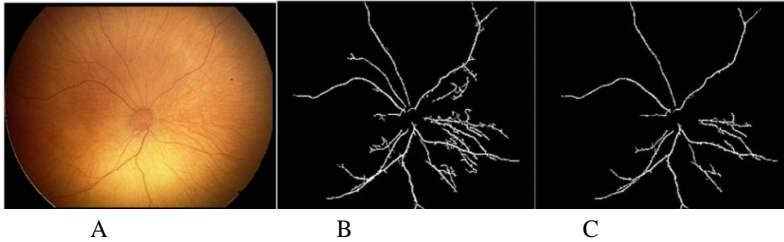
**Fig. 1.** Algorithm for modelling and extraction of retinal vascular system based on morphological segmentation.

**Table 1.** Parameters settings for the segmentation procedure of the blood vessels system

Parameters	Values
Linear length of the structural element for vascular amplification	11
Linear length of the structural element for the removal of blood vessels	11
Length of linear smoothing filter	7-15
Threshold value of tagged image (higher value)	15-50
Threshold value of mask image (lower value)	10-40
Defining removing objects that are smaller than (in pixels)	180
Fill holes smaller than (in pixels)	10

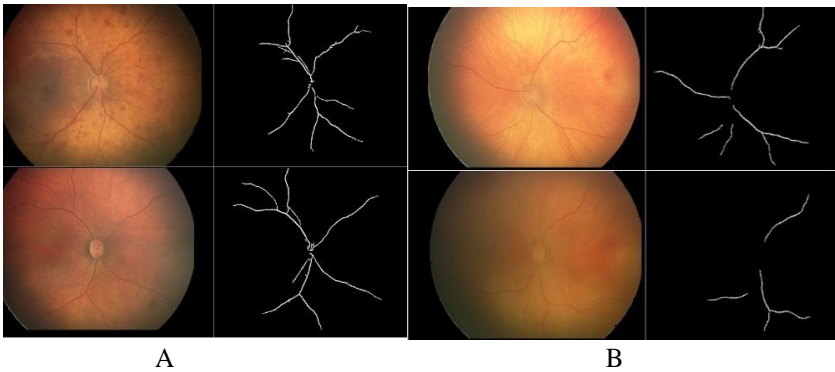
The setting parameters were mostly the same, only setting of the threshold value was changed depending on the contrast of the image. In some cases, the length of the linear smoothing filter was changed to achieve maximally sensitized detection of vascular system at minimal noise levels. The Fig. 2. shows a segmentation of the retinal blood

vessels from native image, when setting two different threshold values. Images show that when lower threshold values are set, the image also shown fine background vessels, while with higher threshold setting, the image shows the major vessels of the vascular system and eliminates the smaller blood vessels.



**Fig. 2.** Native image (A), Segmented image with setting threshold parameters (15, 25) (B), Segmented image with setting threshold parameters (30, 50) (C).

In Fig. 3, there is situated comparison of contrast and non-contrast images after morphological segmentation.



**Fig. 3.** Comparative segmentation analysis of contrast retinal images (A) and non-contrast images (B).

## 4 Conclusion

In the clinical ophthalmology, the segmentation of retinal vasculature belongs to one of the most frequent tasks being necessary regarding a proper diagnosis of the ROP. This disease is clinically examined by the RetCam 3, which generates data in lower resolutions. Such fact predetermines weaker contrast amongst individual retinal structures including the retinal blood vessels.

The proposed method based on the morphological segmentation is able to reliably identify individual blood vessels even in the noisy environment.

The blood vessels model should serve as a classification tool allowing for the tortuosity differentiation. We suppose calculation a set of the curvature features, which will be calculated from the proposed model. Such feature vector will serve as a base for classification and prediction of the pathological signs of the tortuosity.

## References

1. Kubicek J., Timkovic J., Krestanova A., Augustynek M., Penhaker M., Bryjova I.: Morphological Segmentation of Retinal Blood Vessels and Consequent Tortuosity Extraction. *Journal of Telecommunication, Electronic and Computer Engineering*. Vol 10, No 1 - 4, 73 - 77 (2018)
2. Jomier J., Wallace D.K., Aylward S.R. Quantification of Retinopathy of Prematurity via Vessel Segmentation. In: Ellis R.E., Peters T.M. (eds) *Medical Image Computing and Computer-Assisted Intervention - MICCAI 2003*. MICCAI 2003. LNCS, vol 2879. Springer, Berlin, Heidelberg (2003)
3. Chee R., Patel S. N., Jonas K. E. Gupta M. P. Cambell J. P., Chiang M. F., Chan R. V. P.: Current Trends in Telemedicine for Retinopathy of Prematurity. *Journal of Ophthalmology*. Vol 16, No 1 (2017)
4. Jan J., Odstrcilik J., Gazarek J., Kolar R., Retinal image analysis aimed at blood vessel tree segmentation and early detection of neura layer deterioration, *Computerized Medical Imaging and Graphics*, Volume 36, Issue 6, Pages 431-441, (2012).
5. Fraz M. M., Remagnino P. et al. Blood vessel segmentation methodologies in retinal images - A survey. *Computer methods and programs in biomedicine* 108 (1), Pages 407-33. (2012)
6. Meng Li, Zhenshen Ma, Chao Liu, Guang Zhang, and Zhe Han, Robust Retinal Blood Vessel Segmentation Based on Reinforcement Local Descriptions, *BioMed Research International*, vol. 2017, Article ID 2028946, 9 pages, (2017).
7. Patwari M. B., Manza R. R., Rajput Y. M., Saswade M. Deshpande N., Automatic Detection of Retinal Venous Beading and Tortuosity by using Image processing Techniques. *International Journal of Computer Applications (0975 – 8887) Recent Advances in Information Technology*, 2014.
8. Poletti E., Florin D., Grisan E., Ruggeri A., Automatic Vessel Segmentation in wide-field Retina Images of Infants with Retinopathy of Prematurity. 2011 Annual International Conference of the IEEE Engineering in Medicine and Biology Society, Boston, MA, USA (2011).
9. Jayadev,Ch., Vinekar A., Mohanachandra P., Desai S., Suveer A., MANGALES S., Bauer N., Shetty B. Enhancing Image Characteristics of Retinal Images of Aggressive Posterior Retinopathy of Prematurity Using a Novel Software, (RetiView). *BioMed ReSearch International*. (2015).
10. Turior R., Chutinantvarodom P., Uyyanonvara B., Automatic tortuosity classification using machine learning approach. *Applied Mechanics and Materials*. Vols. 241 - 244 (2013). pp 3143 – 3147.
11. Kubicek J., Kosturikova J., Penhaker M., Augustynek M., Kuca K.. Segmentation based on Gabor Transformation with Machine Learning: Modeling of Retinal Blood Vessels System from RetCam images and Tortuosity Extraction. Volume 297: *New Trends in Intelligent Software Methodologies, Tools and Techniques*. Pages 270 – 283. (2017)
12. Mapayi T., Tapamo J. R., Vipiri S., Adio A. O. Automatic Retinal Vessel Detection and Tortuosity Measurement. *Image Analysis and Stereology*. Pages 117 – 135 (2016).



13. Kaur M., Dr Talwar R. Review on: Blood Vessel Extraction and Eye Retinopathy Detection. *International Journal of Computer Science and Information Technologies*. Vol. 5(6), (2014), 7513 - 7516
14. Fraz M. M., Remagnino P., Hoppe A., Uyyanonvara B., Rudnicka A. R., Owen C. G., Barman S. A., Blood Vessel Segmentation Methodologies in Retinal Images – A Survey. *Computer methods and programs in biomedicine*. Volume 108, Issue 1, Pages 407 – 433, (2012)
15. S. Gregory, D. Trevor, I. Piotr, *Nearest-Neighbor Methods in Learning and Vision: Theory and Practice (Neural Information Processing)*, MIT Press, (2006)
16. L. Xu, S. Luo, A novel method for blood vessel detection from retinal images, *Bio-Medical Engineering Online* 9 (2010) 14.
17. Y.A. Tolias, S.M. Panas, A fuzzy vessel tracking algorithm for retinal images based on fuzzy clustering, *IEEE Transactions on Medical Imaging* 17 (1998) 263–273.
18. G.B. Kande, P.V. Subbaiah, T.S. Savithri, Unsupervised fuzzy based vessel segmentation in pathological digital fundus images, *Journal of Medical Systems* 34 (2009) 849–858.
19. Nazari A., Mustafa M., Zulkifley M. Segmentation of Retinal Blood Vessels By Top.hat Multi-scale Detection for Optic Disc Removal. *Jurnal Teknologi*. Vol. 77, Issue 6, Pages 47 – 53, (2015)
20. Heneghan C., Flynn J., O’Keefe M., Cahill M. Characterization of Changes in Blood Vessel Width and Tortuosity in Retinopathy of Prematurity Using Image Analysis. *Medical Image Analysis*. Vol. 6(4), Pages 407 – 29. (2002)

# Biological Signal Processing Using MATLAB Modular Processing System: An Overview

Martina Ládrová and Radek Martinek

Department of Cybernetics and Biomedical Engineering, FEECS,  
VŠB – Technical University of Ostrava, 17. listopadu 15,  
708 33 Ostrava – Poruba, Czech Republic  
martina.ladrova@vsb.cz

**Abstract.** Biological signals bring a valuable information about the function of the human body, such as the heart, brain or muscle activity, improving the successful diagnosis of its diseases and abnormalities. However, the biological signal is a very weak signal requiring suitable way of processing, so it is necessary to find new or improve existing processing methods. The paper aims to summarize the results of the student's scientific work under the supervision of associate professor Radek Martinek. It focuses mainly on the signal processing using the system implemented by the student in MATLAB environment.

**Keywords:** Biological Signal Processing, Digital Signal Processing, Signal Filtration, Adaptive filtration.

## 1 Introduction

Because the biological signals are often corrupted by many types of artifacts or interference, the signal processing makes up the important part of their analysis and thus, facilitates a correct interpretation and a further diagnosis. The signal filtering and processing enables to eliminate or remove the undesirable components of the signal so that the more valuable information can be extracted. The sources of the noise can be physiologic (e.g. reciprocal influence of the different organs on each other, biological rhythms, patient's moving, movement of the electrode-electrolyte interface) or the environment where the signal recording takes place. The noise sources are typical for each individual biologic signal, depending on a way how a signal is measured, which sensors are used (e.g. different types of interference corrupt an electrical signal in the comparison with an acoustic signal, etc.) and also, what is the frequency range of the signal.

As a reaction on the development in digital signal processing, connected with the increase in the performance of the microprocessor technique (multi-core processors, field-programmable gate arrays), the software which can be available in clinical practice, is more and more evolved. So, the authors implemented the modular signal processing application created in MATLAB software for the purposes of the education and testing of the several today well-known processing methods.

## 2 Software description

The implemented system represents a tool for the testing processing methods and enables the user to compare more techniques of the processing of the corrupted signal. The system offers the possibility to add a mixture of the available types of interference to the processed signal and evaluate the precision of the processing by computing of the signal-to-noise ratio (SNR) and determining the shape distortion of the signal during the filtration by correlation coefficients. After each change of the processed signal (e.g. adding the interference or filtering), these criteria are computed and the user can compare the values of the original signal, corrupted signal and filtered signal, when also the graphic representation is displayed – time waveforms of the signals, their frequency spectra and spectrograms which shows frequency distribution in time. The whole program contains five basic parts: loading a signal, it's resampling, adding an interference, filtration or other processing methods and last, analysis. From the techniques of processing, the digital filters, adaptive noise canceler (ANC), wavelet transform (WT), empirical mode decomposition (EMD), derivation, independent (ICA) and principal component analysis (PCA) were chosen to implement such as the basic exemplars of the processing methodology used in biological signal processing. Summary of the options of the implemented software when working with signals is described in Table 1.

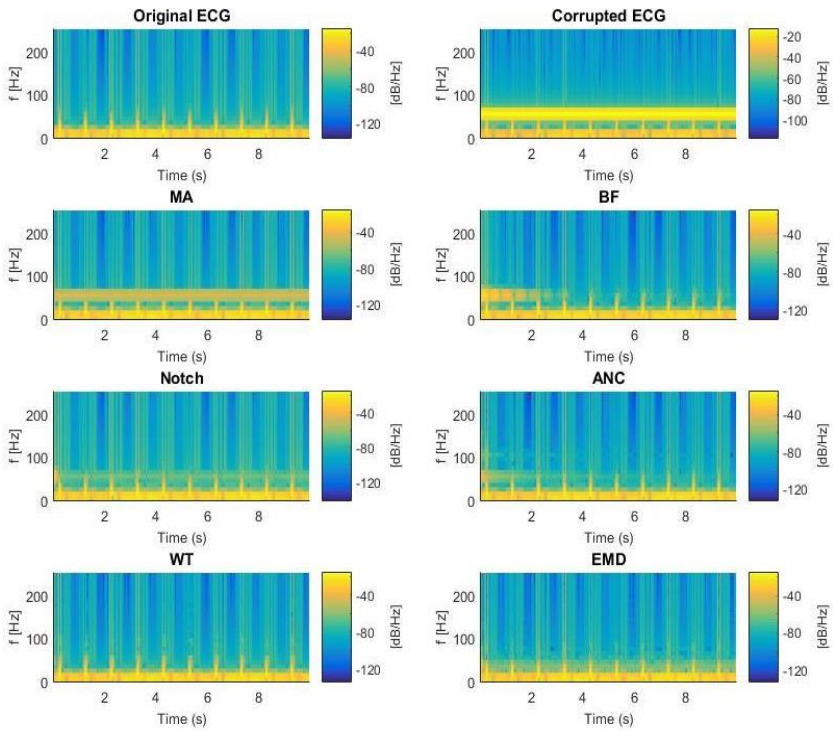
**Table 1.** Summary of the software functions.

Sampling	Noise	Filtration	Processing	Analysis
Linear	Power line interference 50/60 Hz	FIR filter	WT	Fixed peak detector
Nearest neighbor	Gauss trend	IIR filter	EMD	Adaptive peak detector
Cubic	Linear trend	Moving average	Derivation	Frequency power
Cubic spline	Random noise	Notch filter	ICA	Envelope
	Low-frequency drift	ANC	PCA	
	White noise			

### 3 Results and publications

For the experimental results, see [1],[2], authors tested the following methods of processing: moving average filter, Butterworth filter, notch filter, ANC, WT and EMD when applied on the ECG (electrocardiogram), EMG (electromyogram) and PCG (phonocardiogram) signals. In publications, the problematics of the ECG and EMG measuring and elimination of artifacts is discussed. The papers focus on the elimination of the power line interference (PLI) which originates due to the magnetic field distributed by human body by the power supply. The PLI means added sinusoidal and harmonic components on frequency 50 Hz (in Europe) or 60 Hz (in North America) to the signal and brings the significant problem due to its amplitude up to 50 % of the signal amplitude and the signal frequency range which contains also the PLI frequency. In the case of the recording when it is not possible to reduce the monitored range under 50 Hz, it is necessary to use other type of signal processing than the simple low pass filtering.

In [1], the results of the well-known methods of ECG signal filtration are compared: moving average filter, Butterworth filter, notch filter, ANC, WT and EMD. The signal after filtration is evaluated using signal-to-noise ratio (SNR), correlation coefficient and Bland-Altman analysis. The PLI was mixed with a signal in three levels of corruption, when SNR of the corrupted signal was -10, -5 and 5 dB, so the suitability of individual methods was tested in the wide range of signal distortion. The results showed that the SNR improvement is dependent on the interference level – in general, filtration of less corrupted signal results in lower SNR improvement. What is interesting, some of tested methods (WT, ANC) reach a highest SNR improvement and correlation coefficients only in one interference level but on the contrary, in other levels, they drop behind other processing methods. When comparing the chosen processing techniques, the spectrograms (see Fig. 1) showed the main problems of filtering in frequency domain – a time delay of the filtration. In the case of the BF, there is a delay up to 2 seconds when filter eliminated PLI only in part and its frequency component remained in signal with quite high power. This can be reduced by implementing a filter with lower order but for the price of the less efficient denoising in the rest of the signal. On the other hand, methods such as WT od EMD eliminated noise through whole time scale but characterized by their higher complexity and computational cost. According Bland-Altman analysis, notch filter, ANC, WT and EMD are methods with very good performance and they can be considered as accurate thanks to the very small difference of filtered signal in comparison with the original signal.



**Fig. 1.** Spectrograms of the original signal, corrupted signal and filtered signals using given filtration methods.

The elimination of PLI in EMG signal is proposed in [2], when notch filter, ANC and WT are compared also in SNR, correlation and Bland-Altman analysis. Concerning the results, ANC filter proved to be the most suitable method from the tested techniques of EMG signal processing in the case of PLI removal. Otherwise the notch filter reached the similar correlation coefficient values approaching to 1, but the in SNR, the ANC overcame the notch filter by at least 21 dB. On the other hand, the WT method did not prove its suitability for the elimination of PLI in EMG signal with the SNR 0,26 dB and correlation 0,24.

The other experiments dealing with the elimination of the different types of interference in PCG signal using WT and EMD were performed in conference paper which has not been published yet. Also, the authors are working in present on the research of the problematics of the biological signals in general; it focuses on way of their measuring, problems with artifacts and interference which occur in the signals and, mainly, the processing methods which are proposed in the contemporary literature, comparing their advantages and disadvantages.

## 4 Conclusion and future work

In spite that the digital signal processing is the frequently discussed topic and the research makes progress quickly, the advanced processing methods of the biological signals are not introduced into the medical practice because of their complexity and computational costs. The aim of the future research is to gain the satisfying results of these techniques which would be used in the practice and so simplify the work to the physicians, improve the diagnostic information and enhance the patient's comfort.

In present, the student's area of interest is moving into the problematics of the measuring the biological signals in the environment of magnetic resonance, which presents the other important part of the biological signal processing. In this environment, the signals are distorted by many artifacts, which should be eliminated for the accurate analysis of the signal. Currently, the authors are preparing the research publication focusing on this topic, specifically the triggering in cardiac magnetic resonance imaging.

## References

1. M. Ladrova et al., "Power Line Interference Elimination in ECG Signals", *Journal of Biomimetics, Biomaterials and Biomedical Engineering*, Vol. 41, pp. 105-115, 2019
2. M. Ladrova et al., "Methods of Power Line Interference Elimination in EMG Signal", *Journal of Biomimetics, Biomaterials and Biomedical Engineering*, Vol. 40, pp. 64-70, 2019

# The Control Design with REXYGEN in Industrial and Educational Applications

Jakub Němčík

Department of Cybernetics and Biomedical Engineering, FEECS,  
VŠB – Technical University of Ostrava, 17. listopadu 15,  
708 33 Ostrava – Poruba, Czech Republic  
jakub.nemcik@vsb.cz

**Abstract.** The REXYGEN Control System is a professional advanced tool for design and implementation of complex control systems that belongs to softPLC category. It covers the entire process starting from simulation of functionality of the application before deployment, through implementation on real-time target, towards analysis, diagnostics and visualization. It is also compatible with Simulink environment, and the way of implementation of control algorithm is very similar. It easily allows performing in-the-loop simulations (SIL, PIL, HIL) and creation of remote and virtual laboratories. The created control scheme is finally compiled and uploaded into a chosen real-time target. There is a wide variety of hardware platforms and real-time operating systems supported. The paper gives an overview of possibilities of its use in educational process and industrial applications, using both classical and advanced control algorithms.

**Keywords:** REXYGEN, control design, control algorithm, simulation, SIL, PIL, virtual laboratory.

## 1 Introduction

The REXYGEN control system is an advanced tool for design and implementation of complex algorithms for automatic control. The algorithms are composed from individual function blocks, which are available in extensive function block libraries. These libraries cover not only all common fields of automation and regulation but offer also a variety of elements for high-level control algorithms. Moreover, a user defined function block can be used for creating unique algorithms in special applications. If the license of Matlab®-Simulink® system is available, it is possible to benefit from its compatibility with the REXYGEN control system and exploit its simulation capabilities for testing the designed algorithms before deployment (See [1]).

This control system is designed for use in automatization, feedback systems, robotics and sensory systems. It is a package of multiple tools that together form a compact platform for development and operating of systems in this field. The main advantage of this system is the use of graphic programming interface which is very intuitive. In this interface, even the complicated algorithms are easy to read, as they consist of standard blocks capable of changing parameters which are part of the REXYGEN libraries, interconnected via conductors displaying data flow between individual blocks. It is also possible to color individual blocks in such a way that functional units are clearly distinguishable.

Resulting control tasks can then be opened in Simulink tool which simplifies testing of these algorithms. It is possible to use all standard tools of Matlab and Simulink; for example, for identification and subsequent simulation of the controlled setup which leads to further speeding up of the development of complex control tasks.

The interpreter of control algorithms itself supports a range of platforms. Resulting application can therefore be run on Linux IPC, WinPAC, Raspberry Pi etc. Interpreter controls running and timing of individual tasks which are run in form of preemptive multitasking.

## 2 Educational applications

### 2.1 Classical control algorithms and modern control theory

The REXYGEN control system has been primarily developed to support implementation of classical PID control algorithms, focusing on implementation in the industrial practice. There are two main blocks, PIDU and PIDMA capable of performing all necessary functionalities important for industrial purposes. These blocks support two-degree of freedom configuration, bumpless connection, anti-windup connection, and autotuning. They can be widely and effectively used both in engineering applications and educational purposes. Moreover, algorithms based on modern control theory can be implemented as well (See [1]).

The term "modern control theory" dates to 1960's to distinguish between approach based on state-space description and classical theory based on input/output description. Nowadays, both approaches (state-space and transfer function) shade into each other. Characteristic feature of modern control theory is use of mathematical model for description of regulated processes. If the model is specified in detail, then engineering task concerning design of controller can be formulated as optimization problem where an expert adjusts parameters of criteria (optimization) function and constraints instead of setting up controller's constants. One of the main advantages of this approach is that some features of solutions (such as stability in linear quadratic control) are assured implicitly. However, counting on precise mathematical model brings out some lack of modern control theory which makes up motivation for new so-called robust methods that makes it possible to include certain types of uncertainties into the model (See [4]).

Here are typical topics falling under algorithms based on modern control theory: modification of PID controllers in practical industrial operation (approximation of derivative term, windup effect, Smith predictor), LQR (Linear Quadratic Regulator) and LQG (Linear Quadratic Gaussian Regulator), adaptive control, robust control, predictive control, etc.

Some of advanced control algorithms, such as optimization-based predictive control, or any other highly customized algorithms can be implemented within external programs. In this case, the core of computational load is handled by external application running on the same platform as the one hosting REXYGEN runtime and exchanges the data via EPC or SILO blocks. This approach can also be used in case of using some other situations, like image processing via a camera.

Moreover, there is a possibility to use the REXLANG block which is a user programmable block usually used if standard blocks are insufficient and it is necessary to implement a user-defined function.



Next subchapters describe chosen educational case studies performed over recent years with the use of REXYGEN control system (See [3]).

### 2.2 Ball on spool

Laboratory model of Ball on spool (See [5]) was created for enhancement of educational activities at the Department of Cybernetics and Biomedical engineering. The ball is placed on the spool which is connected to the shaft and drive. The main control task is to keep the ball at the top (unstable) upright position by appropriate control provided by the drive affecting the spool. It is also capable of performing the “swing-up” control task 5.

Physical setup of the model is presented in Fig. 1. It is composed of the drive and shaft connected to spool with a ball on the top, while the feedback is provided by ultrasonic distance sensor and IRC position sensor.

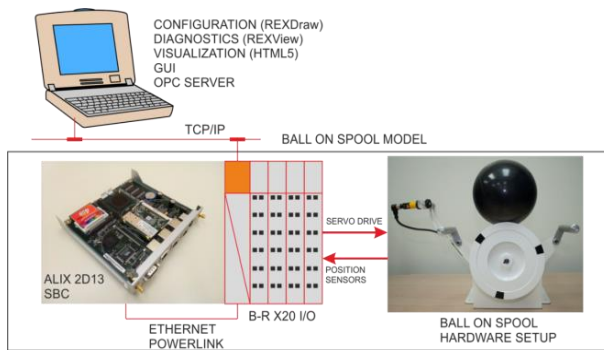


Fig. 1. Physical model of Ball on spool with interconnection of hardware parts

### Design of LQR Controller:

State-space description of simplified Ball on Spool model derived in previous section is a base for LQR design according Fig. 2. It is particularly based on LQR Matlab function.

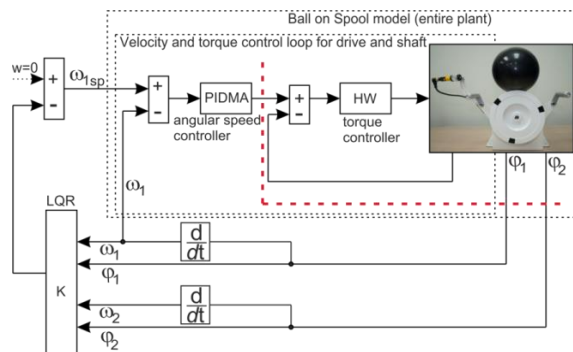


Fig. 2. Control loop with LQR controller

### Implementation of LQR Controller:

Structure of control loop according Fig. 3 contains one “internal” embedded hardware torque controller, one “external” automatically tuned PID controller represented by PIDMA block, and one state-space controller. Moreover, the scheme contains all other necessary blocks for data processing and regulation. Interface between hardware and software parts is marked by a red dashed-line. Yellow “flags” in the scheme represents blocks for I/O interfaces, blue blocks stand for controllers, see Fig. 3.

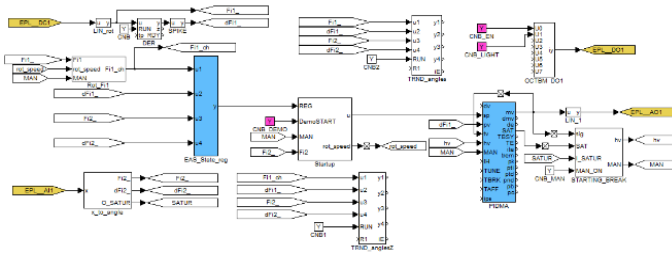


Fig. 3. Ball on spool control in REXYGEN control system

### 2.3 Ball on plate

A control algorithm will be able to stabilize the ball on any chosen position. The original configuration of the model was upgraded to use RPi with REXYGEN.

The ball is captured with a Raspberry PI + Raspberry Camera using external OpenCV-based application. The position is analysed and written to RPI’s RAMDISK in two separate files. REXYGEN continually reads these files to get the coordinates and uses a control algorithm to tilt the plate and move the ball to the desired position.

An Arduino UNO is connected to the Raspberry, it is the device which receives signals from the plate and command motors to tilt the plate.

### 2.4 Helicopter model

The original apparatus (See [7]) was upgraded so that it is composed of a Helicopter connected to an Arduino UNO. Two PWM are used (one for each rotor). There are two sensors which gives the position angles of the helicopter to the Raspberry PI. Finally, a third PWM is used to control the weight (which represent a disturbance). The Raspberry PI can be connected to a Personal Computer thanks to a FTP Server. We can upload new algorithm and access to the visualization in a wireless way.

### 2.5 Magnetic levitation

This apparatus (See [6]) presents an example of a mechatronic system with one input and one output and aims to regulate the position of the steel ball levitating in the magnetic field. The mechanical design consists of a coil and an inductive sensor that provides feedback in the control circuit. The action intervention is the value of the current flowing through the coil, according to which the steel ball is less or more attracted.

The control system consists of SBC PC Engines ALIX 2D13 connected to B&R IO modules via ethernet Powerlink.

### 2.6 Low-cost educational stand

This training stand was designed to support practical exercises in control theory. It can demonstrate the basic principles of open-loop and closed-loop control.

The list of exercises on the learning stand: button-controlled LED, PWM-controlled intensity of LED, 2<sup>nd</sup> order system composed of two RC circuits in series, 2<sup>nd</sup> order system composed of two RC circuits in series and PWM-controlled LED, PWM-controlled DC motor.

### 2.7 Virtual laboratories and SIL/PIL/HIL

The virtual laboratory is an interactive environment for creating and conducting simulated experiments: a playground for experimentation. The idea of virtual laboratory is very clearly described in [8]: virtual laboratory is a computer-based activity where students interact with real apparatus via a computer link, yet the student is remote from that apparatus.

Below are given two examples of application of these techniques.

#### Application of PIL approach for inverted pendulum:

Definition of PIL claims that simulation of the plant model is synchronized with the control algorithms running on the embedded target at full rate (as fast as possible). It is in accordance with one of the reasons why PIL is designed for, namely choice of appropriate sampling period and verification if the needed performance of embedded target is achieved.

However, the real-time synchronization on both sides (embedded target and simulation of the plant model) does not clash the definition. It is secured by RexCore - a runtime core running on the target device (Linux IPC, WinPAC, Raspberry Pi etc.). It handles timing and execution of all algorithms and provides various services. The individual tasks are executed using preemptive multitasking.

The block scheme of PIL model used for inverted pendulum is depicted on Fig.6.

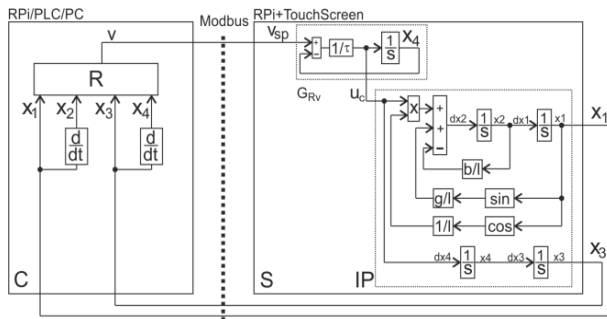


Fig. 4. PIL model for inverted pendulum

### 2.8 Triple inverted pendulum

Triple inverted pendulum is one of the most challenging benchmarks in the field of control theory as it is strongly underactuated, there are two free joints and the swing up and stabilizations are performed by the movement of the cart. There is a strong need

for PIL simulator which was created and used to test the control design before deployment. It uses a very fast FPGA-based computer hosting REXYGEN control system, very precise counters and wireless data transfer from the encoders to the control system.

### 3 Industrial applications

The REXYGEN control system is especially effective in application with high level of research and advanced customized algorithms. Below are given some chosen examples in the industry: Parallel robot with degrees of freedom, rope robot with 6 degrees of freedom, nuclear reactor power regulator, temperature shock stand, robot for aggressive environment.

### 4 Conclusion

The highest "performance/price" ratio of REXYGEN Controls solutions is usually achieved in control and diagnostic systems of non-standard, prototype, experimental and research machines, technologies, stands and robotic manipulators, where a complete design and development of the control system is requested.

### References

1. Koziorek, J., Ozana, S., Srovnal, V. and Docekal, T. (2019). *Modeling and Simulations in Control Software Design. In Analytic Methods in Systems and Software Testing* (eds R. S. Kenett, F. Ruggeri and F. W. Faltin). doi:10.1002/9781119357056.ch12
2. Rxygen - Documentation. Rxygen [online]. Plzeň: REX Controls, 2016 [cit. 2019-08-08]. Dostupné z: <https://www.rxygen.com/documentation-and-support/>
3. REXYGEN - User guide. Rxygen [online]. Plzeň: REX Controls, 2016 [cit. 2019-08-08]. Dostupné z: [https://www.rxygen.com/doc/PDF/ENGLISH/RxygenGettingStarted\\_UniPi\\_ENG.pdf](https://www.rxygen.com/doc/PDF/ENGLISH/RxygenGettingStarted_UniPi_ENG.pdf)
4. BUBNICKI, Zdzisław. *Modern control theory*. New York: Springer, c2005. ISBN 3540239510.
5. OŽANA, Štěpán, Martin PIEŠ, Radovan HÁJOVSKÝ a Tomáš DOČEKAL. Use of REX Control System for the Ball on Spool Model. *Journal of electrical engineering. Slovenská technická univerzita*, 2015, 66(4), s. 214-219. ISSN 1335-3632.
6. OŽANA, Štěpán. Možnosti řízení a vizualizace výukových fyzikálních modelů pomocí řídicího systému REX. *Automa. FCC Public*, 2015, **2015**(1), s. 12-13. ISSN 1210-9592.
7. OŽANA, Štěpán, Petr VOJČINÁK, Martin PIEŠ a Radovan HÁJOVSKÝ. Control Design of Mixed Sensitivity Problem for Educational Model of Helicopter. *Advances in Electrical and Electronic Engineering. VŠB - Technical University of Ostrava*, 2014, 12(5), s. 488-500. ISSN 1336-1376
8. S. Ozana and T. Docekal, "The concept of virtual laboratory and PIL modeling with REX control system," 2017 21st International Conference on Process Control (PC), Strbske Pleso, 2017, pp. 98-103. doi: 10.1109/PC.2017.7976196

# Statistical analysis of electrogastrographic signals before and after food intake

David Oczka and Martina Litschmannová

Department of Cybernetics and Biomedical Engineering, FEECS,  
VŠB – Technical University of Ostrava, 17. listopadu 15,  
708 33 Ostrava – Poruba, Czech Republic  
david.oczka@vsb.cz

**Abstract.** Electrogastronomy is quite old method for measurement of electrical activity of stomach, although there are no standardized procedures in its measurement. In this work we tried one of experimental procedure to measure electrogastronomy signals and we statistically compared power of activity of starving and power after specific meal. Statistical analysis was done to check if power of electrical activity after meal is different from activity of starving.

**Keywords:** EGG, gTec amplifier, statistical analysis

## 1 Introduction

Electrogastronomy is diagnostic method for measurement of bioelectrical potentials of stomach. Signals are measured using device called electrogastronomer which outputs record called electrogastronomogram. Electrogastronomy is usually used for measurement of stomach motility i.e. motion of stomach during its activity. Measurement could be invasive, measured directly inside of stomach, or non-invasive, measured via skin. Although, invasive measurement affects stomach activity, because of electrode as artificial object inside of stomach. Experimentally was found that electrical activity of stomach takes place on specific frequencies. These frequencies are: 310 mHz called bradygastria, 630 mHz called normogastria and 940 mHz called tachygastria.

## 2 Design and implementation

Electrogastronomic measurement does not have any standardized layout of electrodes, therefore experimental one was used. Used layout was discussed with clinician from practice. Layout of electrodes is consisted of three electrodes, one for measurement, one for reference and last for grounding of measured subject person. Very sensitive bio-amplifier, made by company gTec, was used for measurement. It has resolution of microvolts, therefore is very sensitive on environmental electrical noises. For measurement sampling frequency of 128 Hz was used.

Electrodes used during measurement was standardized Ag/AgCl cup electrodes for measurement of electroencephalography i.e. measurement of electrical potentials of brain. For better conductivity cup electrodes were filled with conductive gel. Place on the skin was firstly abraded and cleaned using alcohol solution.

Before measurement, all subjects had to follow following rules: starving for at least 6 hours, thirsting for at least 2 hours and no medication affecting stomach motility for at least 2 days.



**Fig. 1.** Layout of measuring electrodes.

There were 3 measurements done for 3 subjects 23-25 years old. At beginning electrogastrogram was measured after starving for all subjects for time of 10 minutes. After these measurements, all subjects got meal of specific weight of 200 grams. There were 3 types of meal: yogurt, scrambled eggs with slice of bread and pork steak. After meal there was pause of measurement for 15 minutes because of inertia of stomach. Measurement after meal then took 25 minutes. Each measurement with different meal was done on different day.

### 3 Results

After measurements analysis of data was done. Signals were filtered using wavelet transformation to remove parasitic electrocardiographic signal i.e. electrical signals originated from heart activity. After filtration time-frequency spectral analysis was done to extract power of signal at specific frequencies for electrogastrography. Such processed data were used for statistical analysis. It is important to notice that all values of power are expressed as attenuation, meaning that lower attenuation mean higher power.

In tables below are listed basic parameters of processed datasets. For each subject are listed median, standard deviation and variance.

**Table 1.** Basic statistical parameters for data of subject 1. Attenuation in dB.

F (mHz)	310			630			940		
	$x_{0.5}$	$\sigma$	$\sigma^2$	$x_{0.5}$	$\sigma$	$\sigma^2$	$x_{0.5}$	$\sigma$	$\sigma^2$
Starving	48.433	6.749	45.548	48.753	6.697	44.843	49.295	6.738	45.393
Yogurt	56.374	7.073	50.018	56.762	7.081	50.128	57.264	6.769	45.817
Starving	61.520	7.214	52.030	61.767	7.241	52.424	62.254	7.200	51.838
Sc. eggs	56.756	6.652	44.239	57.094	6.690	44.739	57.604	6.900	47.569
Starving	62.155	6.382	40.726	62.534	6.380	40.697	63.192	6.430	41.344
Steak	38.006	6.500	42.246	38.111	7.020	49.233	38.582	6.988	48.687

**Table 2.** Basic statistical parameters for data of subject 2. Attenuation in dB.

F (mHz)	310			630			940		
	$x_{0.5}$	$\sigma$	$\sigma^2$	$x_{0.5}$	$\sigma$	$\sigma^2$	$x_{0.5}$	$\sigma$	$\sigma^2$
Starving	46.246	7.419	55.037	46.566	7.395	54.674	46.929	7.342	53.900
Yogurt	58.159	7.441	55.363	58.325	6.880	47.333	58.390	6.830	46.645
Starving	55.425	11.711	137.138	55.710	11.724	137.448	56.035	11.714	137.205
Sc. eggs	57.511	6.252	39.081	57.815	6.278	39.405	58.323	6.283	39.465
Starving	100.455	7.339	53.862	100.803	7.010	49.132	100.927	10.707	114.639
Steak	87.483	8.504	72.317	87.824	8.967	80.390	88.418	8.506	72.350

**Table 3.** Basic statistical parameters for data of subject 3. Attenuation in dB.

F (mHz)	310			630			940		
	$x_{0.5}$	$\sigma$	$\sigma^2$	$x_{0.5}$	$\sigma$	$\sigma^2$	$x_{0.5}$	$\sigma$	$\sigma^2$
Starving	55.567	6.874	47.251	55.916	6.985	48.790	56.419	6.843	46.820
Yogurt	53.597	6.736	45.369	54.077	6.730	45.283	54.552	6.470	41.856
Starving	64.145	7.709	59.429	64.492	7.688	59.099	64.947	7.542	56.870
Sc. eggs	63.626	6.788	46.068	64.004	6.809	46.358	64.618	6.681	44.634
Starving	59.458	6.521	42.525	59.842	6.389	40.814	60.348	6.080	36.954
Steak	51.375	5.754	33.106	51.670	5.736	32.899	52.188	5.693	32.406

At first, to pick right statistical test, data needs to be checked if its distribution is normal. As it is noticeable in table below, in majority of cases, normality is rejected. Exception is starving activity of subject 3 for scrambled eggs measurement. It could be expressed as error of measurement, non-compliance with rules or specific activity of stomach of subject 3. Even if we have such result, parametric tests require same distribution of both datasets.

**Table 4.** p-values of  $\chi^2$  test to verify normality of data distribution.

Subject	1			2			3		
	310	630	940	310	630	940	310	630	940
Starving	<< 0.001	<< 0.001	<< 0.001	<< 0.001	<< 0.001	<< 0.001	<< 0.001	<< 0.001	<< 0.001
Yogurt	<< 0.001	<< 0.001	<< 0.001	<< 0.001	<< 0.001	<< 0.001	<< 0.001	<< 0.001	<< 0.001
Starving	<< 0.001	<< 0.001	0.002	0.001	<< 0.001	0.001	<b>0.006</b>	<b>0.028</b>	<b>0.070</b>
Sc. eggs	<< 0.001	<< 0.001	<< 0.001	<< 0.001	<< 0.001	<< 0.001	<< 0.001	<< 0.001	<< 0.001
Starving	<< 0.001	<< 0.001	<< 0.001	<< 0.001	<< 0.001	<< 0.001	<< 0.001	<< 0.001	<< 0.001
Steak	<< 0.001	<< 0.001	<< 0.001	<< 0.001	<b>0.023</b>	<< 0.001	<< 0.001	<< 0.001	<< 0.001

As stated above, normality of datasets was rejected and therefore non-parametric test for evaluation was used. In this case Wilcoxon’s test was used. Null hypothesis of test is stated as medians of both datasets are same. As alternative hypothesis we choose that median of dataset of starving activity is not equal to median of dataset of activity after meal i.e. attenuation after meal is different than attenuation before meal which means that power of activity is different after meal.

$$H_0: \chi_{0,5}^{starving} = \chi_{0,5}^{after\ meal}$$

$$H_A: \chi_{0,5}^{starving} \neq \chi_{0,5}^{after\ meal}$$

**Table 5.** p-values of Wilcoxon’s test.

Subject	1			2			3		
	310	630	940	310	630	940	310	630	940
Starving Yogurt	<< 0.001	<< 0.001	<< 0.001	<< 0.001	<< 0.001	<< 0.001	<< 0.001	<< 0.001	<< 0.001
Starving Sc. eggs	<< 0.001	<< 0.001	<< 0.001	<< 0.001	<< 0.001	<< 0.001	<b>0.622</b>	<b>0.408</b>	<b>0.248</b>
Starving Steak	<< 0.001	<< 0.001	<< 0.001	<< 0.001	<< 0.001	<< 0.001	<< 0.001	<< 0.001	<< 0.001

## 4 Conclusion

Based on results of statistical tests described in tables above, we can claim that power of electrical activity of stomach is different after meal in comparison with activity of starving for all subjects except subject 3 and meal scrambled eggs. It can be explained by occurrence of error of measurement, non-compliance of rules or specific reaction of stomach of subject 3.

## 5 References

1. KOCH, Kenneth L a Robert Morris STERN. Handbook of electrogastrography. New York: Oxford University Press, 2004.
2. PENHAKER, Marek. Lékařské diagnostické přístroje: učební texty. Ostrava: VŠB – Technická univerzita Ostrava, 2004. ISBN 80-248-0751-3.
3. TROJAN, Stanislav. Lékařská fyziologie. Vyd. 3., dopl. a rozš. Praha: Grada, 1999. ISBN 80-7169-788-5.



# Simulation of ultrasonic wave with 2 MHz frequency using convective wave equation

Tomáš Ondraczka

Department of Cybernetics and Biomedical Engineering, FEECS,  
VŠB – Technical University of Ostrava, 17. listopadu 15,  
708 33 Ostrava – Poruba, Czech Republic  
tomas.ondraczka@vsb.cz

**Abstract.** This paper deals with the simulation of propagation of the ultrasonic wave in water. The piezoelectric sensor is activated by four rectangular impulses with 2 MHz frequency. Time of all four impulses is 1.8  $\mu$ s.

Results of the simulation are the spread of electrical potential through the piezoelectric sensor, the spread of ultrasonic wave through a cylindrical tube filled with water and record of received echoes from the reference of the tube and the water level.

**Keywords:** Piezoelectric sensor, ultrasound, high frequency, ultrasonic reflection.

## 1 Introduction

The high frequency simulations are important for design and verification of the product. The problem with high frequency simulations is long computing time and high hardware requirements. The advanced methods need to be used for decreasing these disadvantages. Classic method of acoustic pressure can't be used.

Acoustic pressure works with all geometry, so the mesh of the geometry must be computed through whole geometry for the definition of the space where the acoustic pressure is computed. The problem is that the mesh will be very fine for this type of geometry and because of the high frequency of the ultrasonic wave (2 MHz) the wavelength will be small. Because of these problems, the number of elements for computation will be very high (tens of millions). This will cause that compute time for the simulation will be so long and hardware requirements so high, that the practical use of the model will not be possible.

To eliminate these problems the simulation of the model is solved by a method known as convective wave equation. This method has the advantage that it can narrow the number of equations needed to compute the model. This solution decreases computation time and has lower requirements for the hardware.

Model is designed in software Comsol Multiphysics 5.3a. The Comsol was chosen for its ability to solve Multiphysics such as piezoelectric effect.

## 2 Methods

There are two methods used for this type of simulation. The first is ray tracing, the second is the Finite element method. [2]

### 2.1 Ray tracing

It is a method that calculates the path and intensity of the beams emitted from the source.

In Comsol Multiphysics this method is known as ray acoustics interface. This method can be used for this type of model. [1]

The ray acoustics method is based on sending beams from the source of acoustic waves and then receive the beams by the receiver after their reflection from certain points in the geometry of the examined space. After receiving the beams, their path and intensity are determined [3, 5]

#### Advantages.

The biggest advantage of ray acoustics is the decomposition of the signal into rays, which are then counted sequentially. This will significantly speed up the simulation. [1, 2]

#### Disadvantages.

The disadvantage lies in the reconstruction of the received beams. There is a loss of phase information for each beam. For this reason, the resulting signal cannot be reconstructed using a piezoelectric effect. Ray tracing can't be used for this type of model. [1, 2]

### 2.2 Finite element method (FEM)

The method is based on discretizing a large number of elements in the model to a certain acceptable finite number. One of the methods it uses FEM is convected wave equation [3, 4].

The convected wave equation method is based on the discontinuous Galerkin method.

#### Advantages.

The advantage is memory saving due to discretization of elements. It also allows the output of the method to be converted to electrical output. [1, 2]

#### Disadvantages.

The biggest disadvantage is the relatively high time required for the calculation. [1, 2]

### 3 Description of the geometry

The geometry of the model is composed of two main components. The first component is composed of three parts and the second component has also three parts.

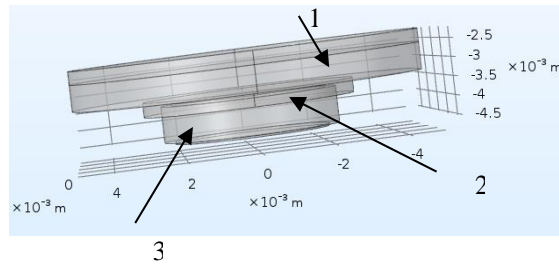
#### 3.1 First component

The lower part of the component is a piezoelectric sensor. This part emits the ultrasonic waves. Zero potential is on the bottom part of the sensor and the positive potential is on the upper part. The diameter is 5 mm and height is 1 mm.

The upper part of the component is the lower part of the cylindrical tube in with the ultrasound spreads. The diameter is 10 mm and height is 1 mm.

Last part of the first component is a conductive adhesive. This part connects the sensor with the lower part of the tube. The diameter is 6 mm and height is 0.5 mm.

Complete geometry of the first component is shown in Fig. 1.



**Fig. 1.** The complete geometry of the first component. (1) Lower part of the tube, (2) conductive adhesive, (3) piezoelectric sensor.

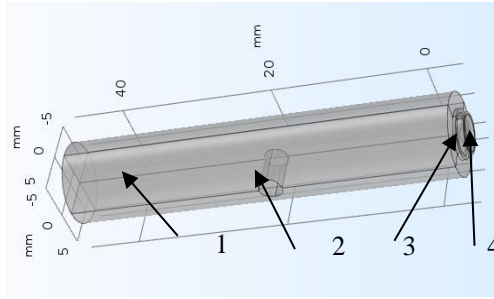
#### 3.2 Second component

The geometry of the second component is composed of a cylindrical tube filled with water. The diameter is 10 mm and height is 50 mm. In height of 20 mm is a reference which has cylindrical geometry and is perpendicularly connected to the inner wall of the tube. Reference diameter is 3 mm and height is 5 mm.

The second part of the second component is a piezoelectric sensor. The diameter is 5 mm and height is 1 mm.

The third part of the second component is a conductive adhesive, which connects the tube and piezoelectric sensor. The diameter is 6 mm and height is 0.5 mm.

Complete geometry of the second component is shown in Fig. 2.



**Fig. 2.** The complete geometry of the second component. (1) cylindrical tube, (2) reference, (3) conductive adhesive, (4) piezoelectric sensor.

## 4 Settings of the solution

A solution of the simulation is divided into three parts referred as studies which are dependent on each other. Each study gives its results and pasts them to study which follows.

### 4.1 First study (Inverse Piezoelectric Effect)

The first study has two results. The first result is spread of electrical potential through the piezoelectric sensor and conductive adhesive (Fig. 1) which is caused by the input signal.

The second result is spreading of acoustic pressure through the lower part of the tube (Fig. 1).

The solution is computed by the method of acoustic pressure. Because the geometry of the lower part of the tube (Fig. 1) is not as difficult to compute. It has only  $87.22 \text{ mm}^3$  so it is not necessary to use a method of the convective wave equation.

The second part of the first study pasts its results to the second study.

### 4.2 Second study (Ultrasound Propagation)

Second study deals in propagation of the ultrasonic wave through a cylindrical tube (Fig. 2).

Because the volume of the tube is significantly higher than in the first study ( $3889 \text{ mm}^3$ ) method of convective wave equation must be used. Reasons are described above.

Results from the second study are passed to the third study.

### 4.3 Third study (Piezoelectric Effect)

Third study deals in the computation of how long it takes to get the ultrasonic waves which were reflected by reference and the water surface. The water surface is represented by the top surface of the cylindrical tube (Fig. 2).

The results are recorded in the graph of floating potential over time.

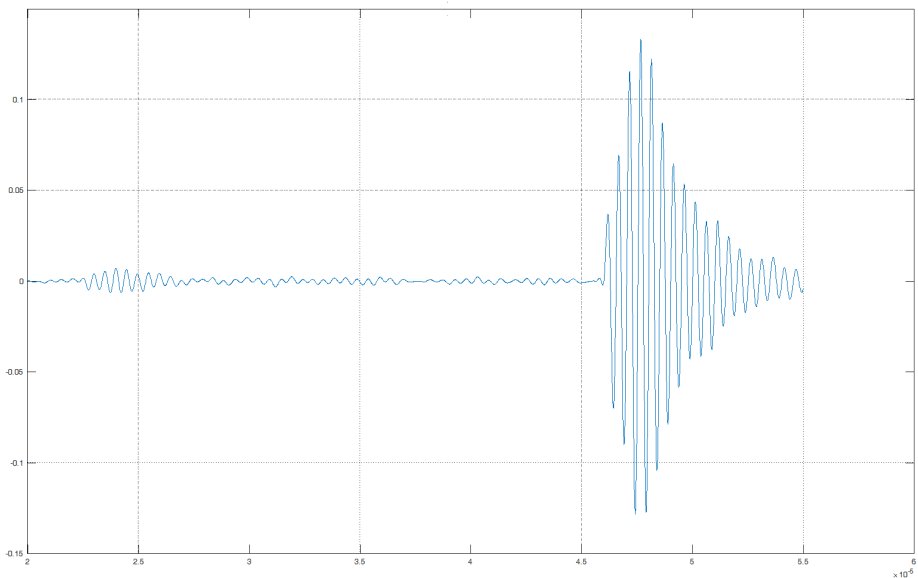
## 5 Results

The result of the simulation is shown just for third study (Piezoelectric Effect). The first and second study are just for passing results.

### 5.1 Result of the third study

The result of the third study is the computation of how long it takes to get the ultrasonic waves which were reflected by reference and the water surface.

The result of the study is shown in Fig. 3. It is a graph of floating potential over time. It shows the reflected ultrasonic waves received by the piezoelectric sensor. The first reflection is from reference and is received in simulation time  $40 \mu\text{s}$ . The second reflection is formed water surface and is received in simulation time  $85 \mu\text{s}$ . Water surface has 50 mm distance from the piezoelectric sensor.



**Fig. 3.** Graph of floating potential over time. Echo of the ultrasound wave with time  $2.2 \mu\text{s}$  is a reflection of the ultrasonic wave from the reference and Echo of the ultrasound wave with time  $4.7 \mu\text{s}$  a reflection of the ultrasonic wave from the water surface.

## 6 Conclusion

Simulation of the ultrasound wave, which has a frequency of 2 MHz and spreads in a tube which is filled with water gives results.

In the Fig. 3 we can see echo with time  $2.2 \mu\text{s}$  of the ultrasound wave acquired as reflection from reference and echo with time  $4.7 \mu\text{s}$  acquired as reflection from water surface. The echoes are clearly visible. Base on this results the model is working.

The hardware for computation of the model was Intel Core i7 8750H Coffee Lake, RAM 16GB DDR4, NVIDIA GeForce GTX 1060 6GB, SSD PCIe 512GB. The computation time was 6 days 5 hours. When the classic FEM method of acoustic pressure was used the simulation crashed on memory.

The computation time shows that the FEM method convected wave equation decreased hardware requirements needed for successful simulation.

This model is verification for measurement of water level using ultrasound. Water level is low if the echo from the water surface is reflected earlier than echo reflected from the reference.

## 7 Acknowledgement

This work was supported by the project SP2019/107, „Development of algorithms and systems for control, measurement and safety applications V” of Student Grant System, VSB-TU Ostrava.

## References

1. **Pryor, R. W.:** Multiphysics Modeling Using COMSOL: A First Principles Approach. Sudbury: Jones and Bartlett Publisher, USA (2011). ISBN 978-0-763-77999-3.
2. **Zimmerman, W. B.:** Multiphysics Modelling with Finite Element Methods. New Jersey: World Scientific Publishing, USA (2006). ISBN 9-812-56843-3.
3. COMSOL: Application Gallery: Flow duct. Application No.: 1371. {<https://www.comsol.com/model/flow-duct-1371>}
4. COMSOL: Application Gallery: Radially Polarized Piezoelectric Transducer. Application No.: 6147. {<https://www.comsol.com/model/radially-polarized-piezoelectric-transducer-6147>}
5. COMSOL: Application Gallery: Small Concert Hall Acoustics. Application No.: 20145. {<https://www.comsol.com/model/small-concert-hall-acoustics-20145>}

# Design of a Bioimpedance Measurement Device Based on AD5933 Impedance Converter

Martin Schmidt and Marek Penhaker

Department of Cybernetics and Biomedical Engineering, FEECS,  
VŠB – Technical University of Ostrava, 17. listopadu 15,  
708 33 Ostrava – Poruba, Czech Republic  
martin.schmidt@vsb.cz

**Abstract.** Non-invasive measurement of bioimpedance can provide information about the structure of the studied object. This method is often applied on the human body for estimation of body composition, for respiration rate measurements or for monitoring of changes in fluid distribution. Devices for measuring bioimpedance can be built for a low price using the AD5933 impedance converter. This work outlines the process of building such a device and focuses on the features of the AD5933 and difficulties encountered when using this impedance converter for bioimpedance measurements. The proposed device is controlled by Arduino Nano microcontroller board, it is capable of measuring bioimpedance with relative error of impedance magnitude lower than 3 %, as tested on a model of human body impedance using R and C components at measured frequencies between 10 and 50 kHz.

**Keywords:** Bioimpedance, Bioelectrical impedance, AD5933

## 1 Introduction

Bioimpedance is a measurement of electrical impedance of certain parts of the human body. Impedance is defined as the ratio between voltage and current. Because the membranes of human cells have a capacitive character, human body bioimpedance is frequency dependent. For this reason, AC current is required for correct measurement of bioimpedance. The most often used frequency range is between 100 Hz to 1 MHz with currents of hundreds of micro amperes. [1, 2]

Single frequency bioimpedance analysis is a method of measuring bioimpedance at one frequency. It is often used for body composition estimations at frequency of 50 kHz. A method of using multiple measurement frequencies is called Multi frequency bioimpedance analysis. The highest amount of frequencies is used in Bioimpedance spectroscopy, which is a method of measuring bioimpedance along the whole spectrum of frequencies in a given range. [2]

There have been several studies using the AD5933 impedance converter for bioimpedance measurements. Thanks to its small size it can also be used in wearable systems. [3, 4] In this application however, there is a disadvantage to this solution, as the

AD5933 draws up to 10 mA of current not counting the external circuitry needed. This consumption can significantly decrease battery lifetime. [4]

An advantage of the AD5933 is that it can be easily controlled by a microcontroller and provide a versatile low-cost solution to bioimpedance measurement devices. [5, 6] Bioimpedance measurement devices using the AD5933 have also been developed for specific applications, including impedance plethysmography [7], in vitro monitoring of the growth of single cells [8], blood glucose measurements [9], nutritional status monitoring in hemodialysis patients [10] and also body composition measurements. [11]

## 2 Designing the proposed device

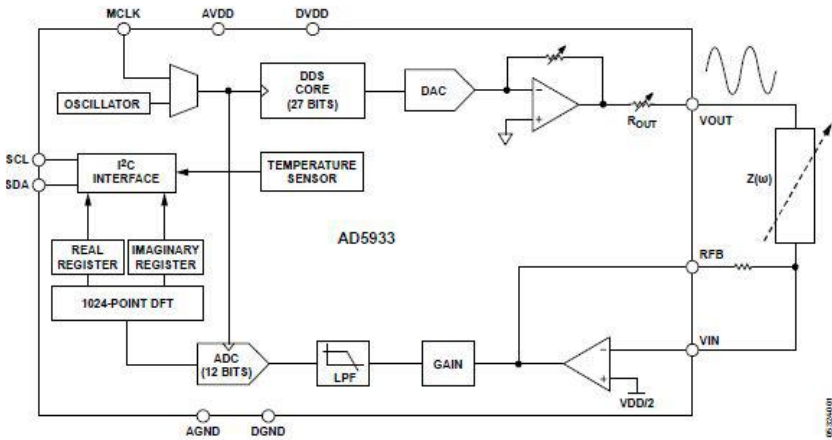
The proposed device is designed to measure bioimpedance using the AD5933 controlled by Arduino Nano microcontroller board.

### 2.1 The AD5933 Impedance Converter

Fig. 1 shows the simplified schematic of the AD5933 integrated circuit, taken from the datasheet of the device. The output measurement signal is a sinewave made by 27-bit direct signal digital synthesis. The signal is then converted by digital-to-analog converter to analog signal. Resistor  $R_{OUT}$  connected to the output pin represents the internal resistance of the AD5933 and it is always added to the measured impedance, unless a voltage follower with a low output impedance is added to the circuit.

The signal from  $V_{OUT}$  pin passes through the measured unknown impedance to the input pin  $V_{IN}$ , where it goes through a programmable amplifier that can be set to a gain of 1 or 5. After filtering out high-frequency noise, integrated AD converter of the AD5933 converts the measured signal to a digital signal again. Discrete Fourier transform is used to obtain real and imaginary values for individual measured frequencies. These values are then sent via I2C to the microcontroller and the microcontroller can then use them to compute the impedance magnitude and phase angle.





**Fig. 1** Schematic of the AD5933

## 2.2 Control of the AD5933

Microcontroller board Arduino Nano was used in this work to control the AD5933. It controls the chip by programming its registers via I<sup>2</sup>C communication. The chip control register contains 16 bits and by writing to this register, the chip can be initialized and a frequency sweep for impedance measurement can be started. The measurement sweep measures impedance at one frequency at a time and increments the frequency until it reaches the highest frequency point in the sweep. After completing the measurement, the chip goes to standby mode.

The initial frequency register contains 24 bits, in which the lowest measuring frequency is given. When measuring, this frequency increases in steps. The values of this step are given by another register of 24 bits. The number of times the frequency measurement will be increased by this step is indicated by the 16-bit register with a maximum value of 511. It can therefore be measured at a maximum of 512 different frequencies in one measurement.

## 2.3 Measurement circuit

The proposed device is controlled by a serial line terminal software installed on a PC, which is connected to the Arduino Nano by USB. Arduino then programs the registers of the AD5933 and initiates the frequency sweep to measure the impedance of the connected device under test. The measurement signal passes through a high-pass filter to remove the DC offset, which could cause polarization of cells when measuring on a human body. The signal is amplified, and the DC offset is again added to it for correct sampling by the analog to digital converter in the AD5933. The block diagram of the device is shown in figure 1.

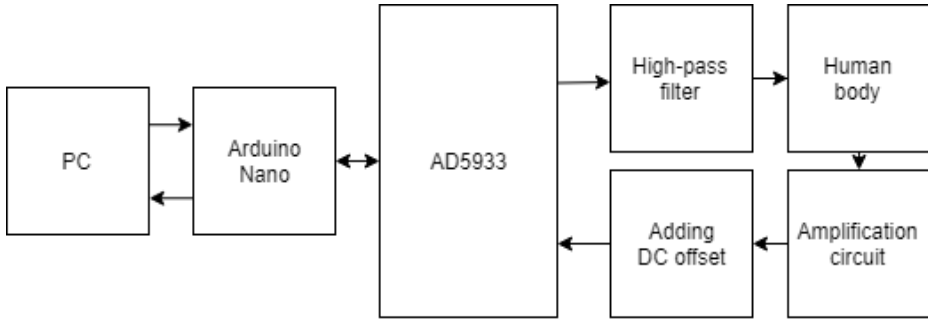


Fig. 2 Block diagram of the device.

### 3 Testing and Evaluation

The accuracy of the device was tested on a model of human body impedance. The circuit consists of a resistor modeling extracellular fluid resistance  $R_e$  with a resistance of  $676.2 \Omega$ , connected in parallel with capacitor with capacitance of  $3.2 \text{ nF}$  and resistor with resistance of  $888.8 \Omega$ . The capacitor represents cell capacitance and resistor intracellular fluids' resistance. Exact values of the components used are shown in figure 3.

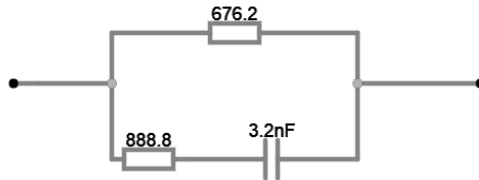


Fig. 3 Human body impedance model.

The measured impedance values were compared with calculated values for the model at given frequencies. Impedance values of the model were calculated using the following equations, equation 1 determines the resistance and equation 2 solves the reactance of the model.

$$R = \frac{R_i R_e (R_e + R_i) + R_e X_c^2}{(R_e + R_i)^2 - X_c^2} \tag{1}$$

$$X = \frac{X_c R_i R_e - R_e X_c (R_e + R_i)}{(R_e + R_i)^2 - X_c^2} \tag{2}$$

$$|Z| = \sqrt{X^2 + R^2} \tag{3}$$

$$\varphi = \arctg\left(\frac{X}{R}\right) \quad (4)$$

To get the magnitude of the impedance, equation 3 is used. Using equation 4 provides the phase angle of the model. Given that the reactance is frequency dependent, the calculations were made for each measurement frequency. Table 1 summarizes the measured and calculated values along with the relative errors at all measured frequencies.

**Table 1.** Impedance values of the model

Frequency	Value	Calculated	Measured	Relative error
10 kHz	Z	650 $\Omega$	651 $\Omega$	0.2 %
	$\varphi$	7.34 $^\circ$	6.97 $^\circ$	5.0 %
20 kHz	Z	593 $\Omega$	610 $\Omega$	2.9 %
	$\varphi$	12.53 $^\circ$	11.98 $^\circ$	4.4 %
30 kHz	Z	539 $\Omega$	550 $\Omega$	2.0 %
	$\varphi$	15.20 $^\circ$	14.10 $^\circ$	7.2 %
40 kHz	Z	497 $\Omega$	510 $\Omega$	2.6 %
	$\varphi$	15.98 $^\circ$	14.80 $^\circ$	7.4 %
50 kHz	Z	468 $\Omega$	480 $\Omega$	2.6 %
	$\varphi$	15.80 $^\circ$	13.90 $^\circ$	12.0 %

## 4 Conclusion

The results of the testing measurements show that the device is capable of measuring bioimpedance at frequencies between 1 and 100 kHz with relative errors of impedance magnitude of less than 3 %. Relative errors of phase angle were higher, up to 12 % at the highest frequency used, which was 50 kHz.

The device can be controlled by a computer connected to Arduino via USB. The future development will focus on improving the accuracy of the device as well as making the device portable without the need for a PC to control it.

## References

1. MARTINSEN, Orjan G.; GRIMNES, Sverre. *Bioimpedance and bioelectricity basics*. Academic press, 2011.
2. KHALIL, Sami; MOHKOTAR, Mas; IBRAHIM, Fatimah. The theory and fundamentals of bioimpedance analysis in clinical status monitoring and diagnosis of diseases. *Sensors*, 2014, 14.6: 10895-10928.

3. BRENIUC, Liviu; DAVID, Valeriu; HABA, Cristian-Győző. Wearable impedance analyzer based on AD5933. In: *2014 International Conference and Exposition on Electrical and Power Engineering (EPE)*. IEEE, 2014. p. 585-590.
4. ROSSI, Stefano, et al. A low power bioimpedance module for wearable systems. *Sensors and Actuators A: Physical*, 2015, 232: 359-367.
5. AL-ALI, Abdulwadood, et al. Design of a Portable Low-Cost Impedance Analyzer. In: *BIODEVICES*. 2017. p. 104-109.
6. CHABOWSKI, Konrad, et al. Simple wide frequency range impedance meter based on AD5933 integrated circuit. *Metrology and Measurement Systems*, 2015, 22.1: 13-24.
7. FERREIRA, Javier; SEOANE, Fernando; LINDECRANTZ, Kaj. Portable bioimpedance monitor evaluation for continuous impedance measurements. Towards wearable plethysmography applications. In: *2013 35th Annual International Conference of the IEEE Engineering in Medicine and Biology Society (EMBC)*. IEEE, 2013. p. 559-562.
8. CHEN, Ching Jung, et al. Development of a portable impedance detection system for monitoring the growth of mouse L929 cells. *Journal of the Taiwan Institute of Chemical Engineers*, 2012, 43.5: 678-684.
9. KAMAT, D. K.; BAGUL, Dhanashri; PATIL, P. M. Blood glucose measurement using bioimpedance technique. *Advances in Electronics*, 2014, 2014.
10. ZHANG, Guanghao, et al. A bioelectrical impedance phase angle measuring system for assessment of nutritional status. *Bio-medical materials and engineering*, 2014, 24.6: 3657-3664.
11. NOVELETTO, F., et al. Low-cost body impedance analyzer for healthcare applications. In: *II Latin American Conference on Bioimpedance*. Springer, Singapore, 2016. p. 56-59.

# Development and design of module for signal modulation

Miroslav Schneider

Department of Cybernetics and Biomedical Engineering, FEECS,  
VŠB – Technical University of Ostrava, 17. listopadu 15,  
708 33 Ostrava – Poruba, Czech Republic  
miroslav.schneider@vsb.cz

**Abstract.** This paper deals with design and execution of modules designed for demonstration of functionality of signal conditioning circuits for university students. Modules are designed to create a modular system designed for research purposes of behavior of individual elements when changing any of the characteristic parameters. Modules are also used in teaching. A standardized xls protocol document is created to work with each module. The activities included in the original protocol text for working with each individual type of frequency filtering, frequency modulation, and amplitude modulation modules are described herein. Furthermore, the text does not discuss concrete circuit design and component selection.

## 1 Introduction

The issue of modulation and signal conditioning is still an interesting case. Therefore, a modular system for testing and research purposes was designed, which can also serve as a study aid. The system consists of signal conditioning modules starting with filter modules, AM, FM modulator modules, demodulators, mixers, amplifiers, and voltage dividers. The following are presented in more detail:

- Filtration using high-pass, low-pass, band-pass, band-stop filters designed as RLC circuits.
- Frequency Modulation (FM)

## 2 About modules

Each of the modules must be suitably connected with both input and output pins to laboratory instruments such as oscilloscopes, function generators, and DC power supplies for active modules. Therefore, it is necessary that each of the protocols begins with an understanding of the correct wiring of the entire hardware configuration and the rules of proper use of these laboratory instruments. The modules circuits designs are inspired by resources [1],[3],[4].

Then there is a part of the measurement with instructions for working with the module, which are specific for each type of the mentioned modules. These sections are detailed in the section dealing with the module.

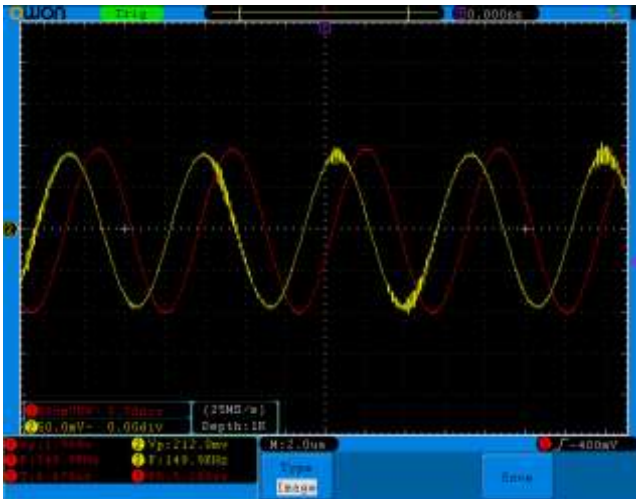
The final part of the protocol deals with repetition of work with the module when changing any of the input parameters of the processed signal and gaining user feedback on the acquired knowledge while working with the used module. The feedback consists of several questions related to the knowledge of the theoretical functionality of the module used and its comparison with the measured data.

Oscilloscopes are used in these tasks to investigate the waveforms of the input signal to the output and to investigate the possible phase shift. Function generators are used as input signal sources for adjustment. The user can thus test the behavior of the examined module at different frequencies and different shapes of the periodic signal.

## 2.1 Filtration modules

Filtration is solved by filters of the type of high pass filter, low pass filter, band pass filter, band stop designed as RLC circuits. Several custom solutions have been designed and manufactured for each of the above-mentioned types of frequency filters so that the user can practically test the behavior of the filter circuit when changing the parameters of RC components in particular. For clarity and eventual replacement of the defective module, all modules were provided with the original code number.

The measurement of the frequency filter module is carried out as follows. The user receives the input harmonic signal in the form of  $f_{\text{sin}}$  frequency parameters, peak to peak  $U_{\text{ppsin}}$  voltage values and  $U_{\text{offset}}$  voltage offset, for example:  $f_{\text{sin}} = 150 \text{ kHz}$ ,  $U_{\text{ppsin}} = 2000 \text{ mV}$ ,  $U_{\text{offset}} = 0 \text{ V}$ . The user is continuously guided through the protocol to generate he also controlled the output signal with an oscilloscope. The possible display of the signals then looks as in the Fig. 1.



**Fig. 1.** The input generated CH1 signal and output adjusted CH2 signal

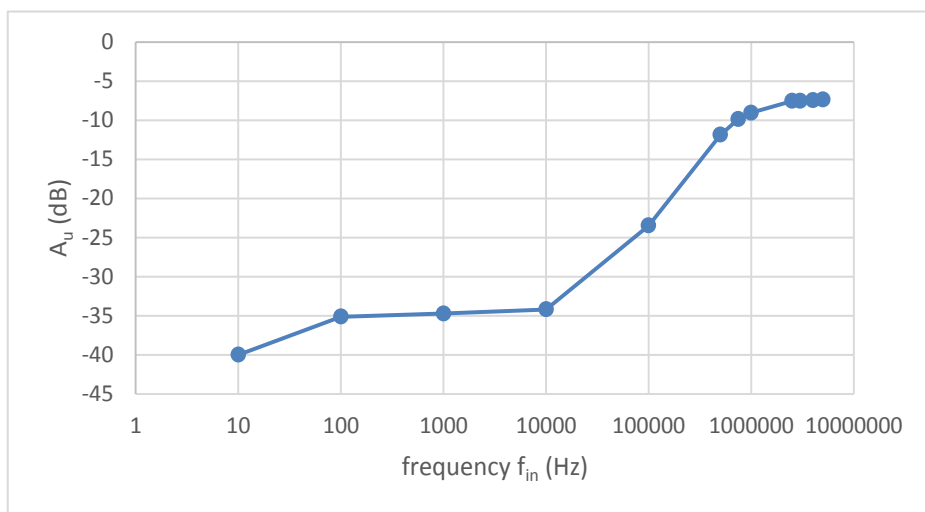
The user-student finds out that at this particular frequency the filter module used dampens the amplitude. With this section, the user has verified that the filter module actually works. In the following part of the thesis, the task is to measure the frequency

amplitude and phase characteristics by changing the frequency of the input signal and then bring all of the measured values into the appropriate table of the xml file. The formulas (1), (2), (3) are used to calculate the required parameters. The graphs are then drawn from the data in the table, from which the user can find out what type of filter it is.

$$A_u = \frac{U_{ppOUT}}{U_{ppIN}} [-] \tag{1}$$

$$\varphi = \frac{\Delta t}{T} \cdot 360 [^\circ] \tag{2}$$

$$A_u = 20 \cdot \log \frac{U_{ppOUT}}{U_{ppIN}} [dB] \tag{3}$$



**Fig. 2.** Output signal attenuation  $A_u$  (dB) dependence on input signal frequency  $f_{in}$  (Hz)

The figure Fig. 2 shows that this is a high-pass filter. Because the solution of each module is modular, the user can test the behavior of the filters after they are interconnected. The user can also investigate the behavior of the used RLC filters when changing their load resistance.

From the figure Fig. 3, the user then evaluates whether the phase level is frequency dependent. Using the relations (1), (3) for finding the breaking frequency, the relation is assuming that the gain  $A_0 = -3$  dB for  $f_0$ , where is  $A_0 = A_u$ .

In the last part, the investigated filter module is compared with an ideal filter with the same breaking frequency. An ideal filter is a system that completely rejects sinusoidal inputs of the form  $x(t)=A \cos \omega_0 t, -\infty < t < \infty$ , for  $\omega_0$  in certain frequency ranges, and does not attenuate sinusoidal inputs whose frequencies are outside these ranges. There are four basic types of ideal filters: lowpass, highpass, bandpass, and band-stop via [2].

By comparing the user with an overview of the quality of the filter used, the modules can be used for research purposes to obtain the highest quality filter for the given task.

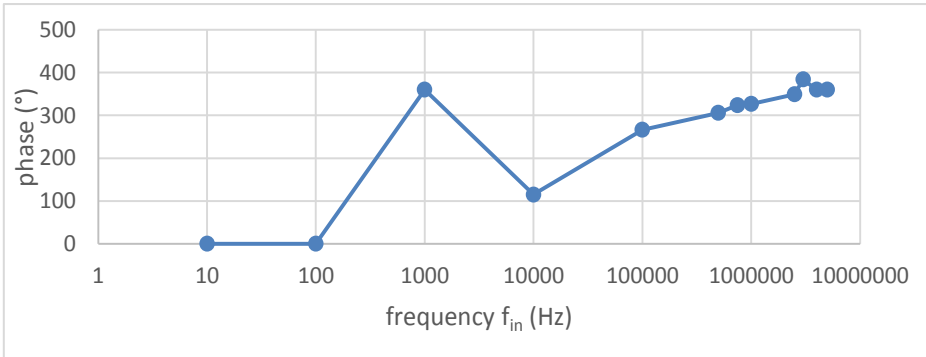


Fig. 3. Phase dependence on input signal frequency  $f_{in}$  (Hz)

## 2.2 Frequency Modulation (FM)

To work with these modules as voltage-controlled oscillators, in the first part of the measurement task, the setting of the value of the control DC input signal  $U_{offset}$  is entered. If the fixture is not damaged, the output terminals will receive a periodic signal, the future carrier wave, on the oscilloscope. Subsequently, the parameters of this periodic signal  $f_{out}$ ,  $U_{ppOut}$ ,  $U_{max}$ , Signal symmetry are investigated. An example of the captured wave of the generated signal is in the Fig. 4.

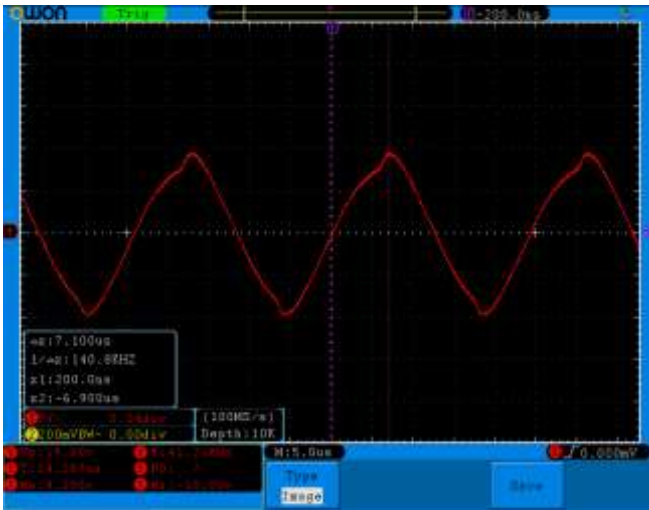
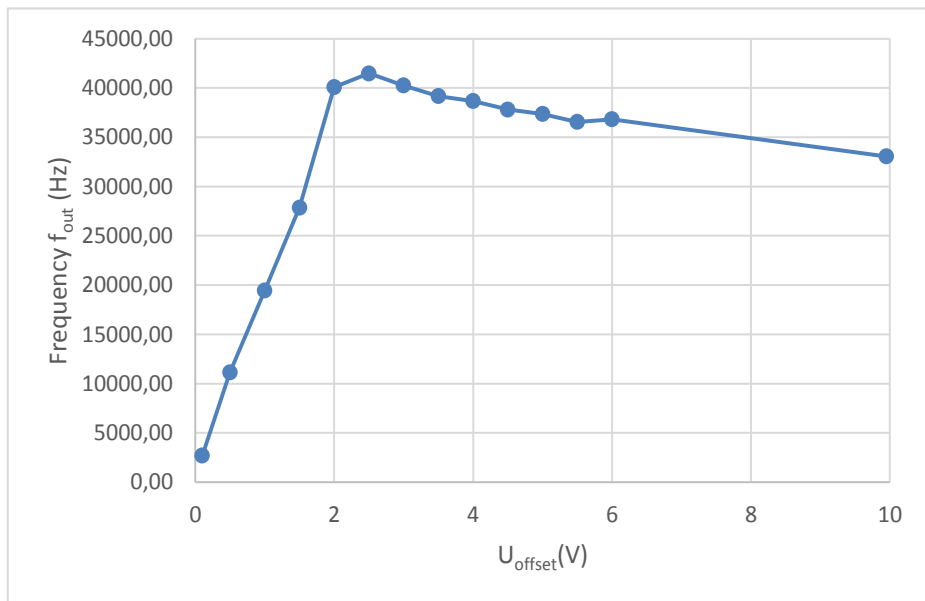


Fig. 4. Output of voltage controlled oscillator

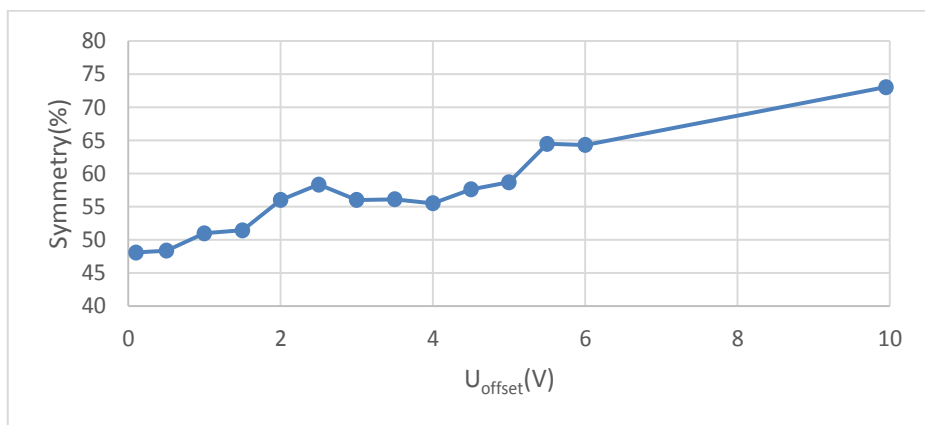
These parameters are written to the appropriate xls file table for each control voltage level according to the instructions. From the recorded data, the user is then instructed



to create a frequency response of the image and dependence of the change in symmetry of the output signal.



**Fig. 5.** Output frequency  $f_{out}$  (Hz) on supply voltage  $U_{offset}$  (V)



**Fig. 6.** Symmetry  $sym_{out}$  (%) on supply voltage  $U_{offset}$  (V)

The symmetry of the output signal is monitored as a signal quality factor, when a signal with a symmetry of about 50% is considered a quality signal. The frequency modulator module is equipped with a tuning element for eventual adjustment of this parameter.

In the next part, the user will use the obtained output frequency characteristics  $f_{out}$  on the control voltage  $U_{offset}$  for the frequency modulation of the information on the input

pin of the module. From the characteristic, the user selects the desired carrier frequency at the logic 1 and 0 state of the control information rectangular signal, for example as in the figure Fig. 7  $f_{\log 1} = 39 \text{ kHz}$ ,  $U_{\text{offsetLog1}} = 2 \text{ V}$ ,  $f_{\log 0} = 4 \text{ kHz}$ ,  $U_{\text{OffsetLog0}} = 0.1 \text{ V}$ .

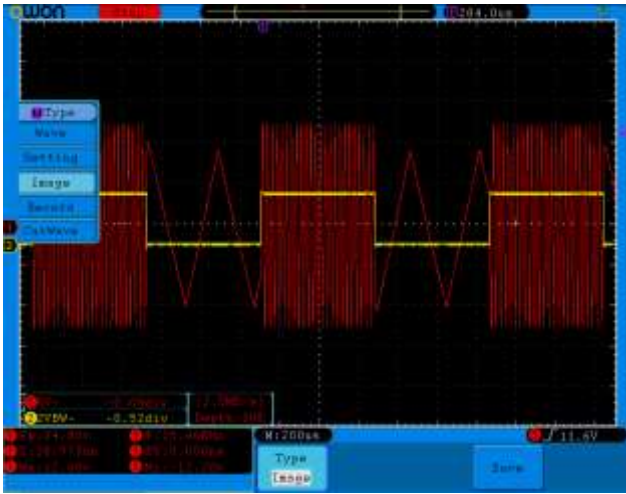


Fig. 7. FM output signal depending on the input control signal

### 3 Conclusion

Problems of this article are very broad, therefore only two of the prepared modules were chosen for demonstration of results.

The correct functionality and usability of this modular research solution has been tested on practical exercises of the subject dealing with this condition. Repeated measurements, more than 20 measurements on each of the 30 modules, confirmed the theoretical imperfection of the non-ideal filter within the accuracy class of the structural elements used. In the next period, this test system will be expanded to include elements dealing with digital signal modulations.

### References

1. PROKEŠ, Aleš. *Rádiové přijímače a vysílače: přednášky*. Brno: Vysoké učení technické, 2002. ISBN 80-214-2263-.
2. KAMEN, Edward W. HECK, Bonnie S. *Fundamentals of signals and systems using the Web and MATLAB®*. 2nd ed. Upper Saddle River, NJ: Prentice Hall, c2000. ISBN 0-13-017293-6.
3. HÁJEK, Karel, SEDLÁČEK, Jiří. *Kmitočtové filtry*. Praha: BEN - technická literatura, 2002. ISBN 80-7300-023-7.
4. Mohylova, J., Puncocar, J., Zajaczek, S. (2018) Band stop filter with a synthetic inductor with series resistance and a real operational amplifier. *Advances in Electrical and Electronic Engineering*, 16 (1), pp. 109-117.

# Smart sensors and technology of project Broadband<sup>LIGHT</sup> for “Smart City” concept

Lukáš Šoustek

Department of Cybernetics and Biomedical Engineering, FEECS,  
VŠB – Technical University of Ostrava, 17. listopadu 15,  
708 33 Ostrava – Poruba, Czech Republic  
lukas.soustek@vsb.cz

**Abstract.** This article deals with using smart sensors and the possibility of intelligent camera systems within the “SMART City” concept. There are discussed modern camera systems application areas. The original benefit of the study is the real implantation of a modular control system within the unique Broadband<sup>LIGHT</sup> testing polygon (parking of the Faculty of Electrical Engineering and Computer Science, VŠB-TUO, Czech Republic). There are analysed both used hardware components and designed software for working with them.

**Keywords:** Smart City, public lighting network, camera safety, parking guidance and information system

## 1 INTRODUCTION

In today's advanced computer systems, it is not desirable to use the device as a single-purpose device, but it is an effort to use all the possibilities offered by the device. Camera systems are often used only as a security system but can also be used for object counting or presence detection, such as parking lots occupancy monitoring system or system for counting amount of peoples in shop.

On VSB-Technical University of Ostrava they are working on development of parking guidance and information system on university parking place covered with project polygon Broadband Light which solved new possibilities of reusing an old public lamp power network.

During repetitive replacement of public street light luminaires an old spark lamp has been replacement with new LED luminaires with their own power management system. This change the need for control of public light network (PLN) by turning on and off the power on the whole street to the power on / off of each single luminaire with extra features such as continuous control of output power or diagnostics via the con-

trol unit and integrated data communication (2, s. 2-5). By using new types of luminaires it is possible to change the character of the power control of PLN with permanently available (24h) supply voltage. This allows continuous operation of additional smart devices such as camera systems, sensory systems or sound warning systems and much more. The polygon's philosophy is to incorporate new technologies into the “smart city” concept.

## 1.1 Project

In the project of polygon parking they are testing possibilities of using the public light network for different technologies and their mutual cooperation. As part of the polygon network, there are 10 public light poles providing 3 types of communication (one sided, bilateral, alternating, crosswalk and two separate light points). They test not only camera systems and the possibilities, but also “smart sensors” as a weather station, light intensity sensor, air pollution sensor. Also deal with monitoring and distribution of energy in the form of 2 measuring nodes (power supply in switchboard and output of solar power plants), electric charging station, photovoltaic power plants. As addition students are dealing with real time improvement of electric power quality (4, s. 3). Also they are testing various methods of data transmission for larger areas of lighting networks such as wired: Ethernet, fiber optic, Ethernet over power line, wireless: Wi-Fi, LTE and new ways unidirectional data transmission through visible light from a lighting device to a target device equipped with a camera or photo detector (3, s.1). The main advantage is the openness of the project for students with the possibility of deploying and testing their own sensor system in real environmental conditions. To test the light technical parameters, a computer model of the parking lot with lighting distribution Figure1 was created.



Fig. 1. Model of parking place

## 2 CONTROLLING SYSTEM

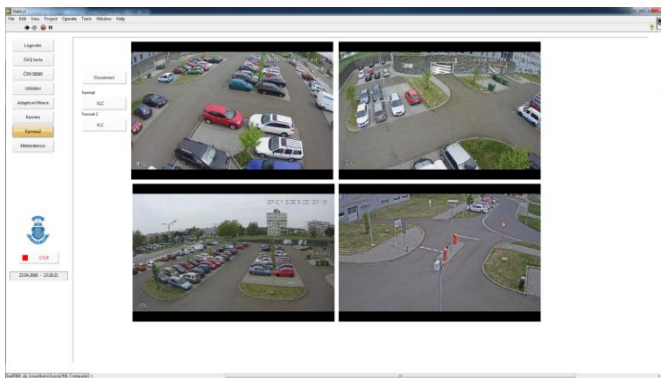
The goal of the project polygon parking is not only to create a mutually cooperating HW but also to unify the control of individual elements under a single programming

environment using idea of virtual instrumentation. Due to its versatility and wide range of features, National Instruments LabVIEW has been chosen as the default development environment. It was developed LabVIEW applications for setting and reading camera parameters, retrieving single frames and video for online preview of the guarded area, applying video recording to a storage medium (basic security system functions) Figure 3. It is currently monitoring the consumption and, in general, all the power parameters of the entire PLN of polygon according to the EN 50160 standard "Voltage characteristics of electricity supplied from the public distribution network". Last but not least, is possible to control the brightness level of individual luminaires. Luminaire control is performed by sending commands using the MQTT protocol to a dedicated server (just control luminaires and lighting devices such as Christmas lights).



**Fig. 2.** The control room

Application for control and monitoring of parking is built in the client - server style, when the main executive kernel initiates individual clients (plugins) which are already independent functional units Figure 3.



**Fig. 3.** Camera safety system plugin

## 2.1 Camera control system

The camera control application was a bit more challenging because from all the safety cameras in project there is only a single company (Axis) worked with the developers

of the development environment (National Instruments), so the only camera has suitable drivers and can work with a standard package of functions (Vision acquisition software). The same about communication specification there are only general documents with a list of standard commands and their structures for some dedicated camera types. So the first step for the fast verification of camera communication was to test standard commands by trial and error. Here were identified the commands using RTSP protocol and 3rd party software VLC media player to control the camera, however, such a solution from the perspective of the end application of the polygon management is not "clear" solution, in addition it was not able to control all the camera parameters. So studying deeper in specification was found the only one document with the basics of using the http protocol to communicate with cameras (DAHUA\_IPC\_HTTP\_API). By combining the RTSP knowledge with the information from the document + source codes from the manufacturer's http website to control the camera, was created our own command database for specific camera types (Axis, Dahua) Figure 4. An example of the same rtsp command for the Axis and Dahua cameras that turns on the video preview of the captured camera scene:

```
rtsp://10.11.2.251/axis-
media/media.amp?videocodec=h264&resolution=1280x720
rtsp://login:password@10.11.5.252:554/cam/realmonitor?cha
nnel=1&subtype=0
```

Examples of http commands again for both types of cameras, this time the command asks to turn on the video preview of the scanned camera scene and available camera resolution:

```
http://10.11.2.251/axis-
cgi/mjpg/video.cgi?resolution=640x480&fps=15&camera=1
http://login:password@10.11.5.252/axis-
cgi/mjpg/video.cgi?channel=0&subtype=1
http://10.11.2.251/axis-
cgi/param.cgi?action=list&group=Properties.Image.Resoluti
on
http://login:password@10.11.5.252/cgi-
bin/configManager.cgi?action=getConfig&name=Encode
```

As is evident, the commands vary considerably depending on the camera type and internal firmware. Another complication was with absence of direct image or video conversion from the http text stream to LabVIEW image format in the development environment, the problem solved Consynea's LabVIEW library called "Multimedia for LabVIEW".

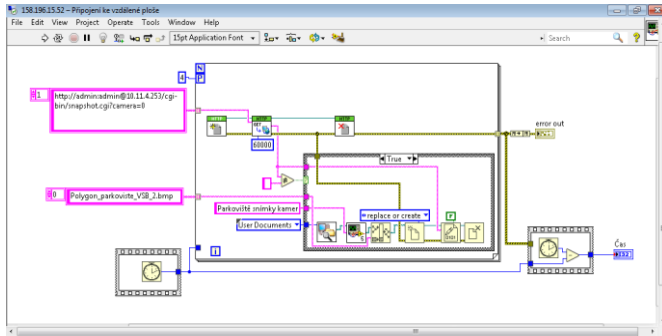


Fig. 4. Code for reading camera pictures

## 2.2 Camera systems

Currently there are 3 types of cameras in operation - professional security camera (Axis P14351e), cheap version of security camera (Dahua IPC HDBW1220E) and cheap version of universal camera (Raspberry PI). The primary purpose of all of these cameras is to provide security - monitoring the parking for online preview or recording in the event of some damage was happened.

Another feature beyond the normal requirements is object detection / object counting. These functions meet all the cameras some with the need to upload a 3rd party application, others have these features already integrated from the manufacturer. Another possible utilization of camera is the function of the outdoor light intensity detector - the camera basically measures the brightness of the points in the scanned scene, only this value recalculates mostly to an 8-bit binary word, which is proportionally distorted by the properties of the optical system and the sensor settings of the camera. Equation for light intensity recalculation shows (1) where  $L_s$  - Intensity[cd/m<sup>2</sup>],  $N_d$  - Pixel number,  $K_c$  - Calibration constant,  $f_s$  - Lens light parameter,  $t$  - Exposition time,  $S$  - ISO picture sensitivity (1, s. 7).

$$LS=N_dK_c \cdot fs2t \cdot [cd/m^2] \quad (1)$$

The problem with camera security types is the unavailability of current values for all the key parameters to calculate, or the inability to set these parameters fixed for testing. The parameter problem has been overcome with the universal Raspberry PI camera, where created our own code in which are all the parameters available. The output of this detector application is the numerical value of the light intensity in the selected image area. This information is used in the polygon luminaire power management system in the form of delayed proportional light intensity control.

## RESULTS

Project itself is realised and it's working for around 2 years now. All the devices are fully operable, working and they are making long term stability tests. A few weeks before was made some changes into controlling software to achieve new modern visual with new graphic functions but it is still in development stage. Raspberry PI camera light detector was made and tested for real light intensity control using testing luminaire in office and it as working properly so it is prepared for final installation to polygon.

## ACKNOWLEDGMENT

This article was supported by the Ministry of Education of the Czech Republic (Project No. SP2019/85 and SP2019/118). This work was supported by the European Regional Development Fund in the Research Centre of Advanced Mechatronic Systems project, project number CZ.02.1.01/0.0/0.0/16\_019/0000867 within the Operational Programme Research, Development and Education. This work was supported by the European Regional Development Fund in A Research Platform focused on Industry 4.0 and Robotics in Ostrava project, CZ.02.1.01/0.0/0.0/17\_049/0008425 within the Operational Programme Research, Development and Education.

## REFERENCES

1. HISCOCKS P.D., ENG P., Measuring Luminance with a Digital Camera. *Syscomp electronic design*, 2014
2. KUNCICKY Radim, KOLARIK Jakub, SOUSTEK Lukas, KUNCICKY Lumir, MARTINEK Radek. IoT Approach to Street Lighting Control Using MQTT Protocol. In: *AETA 2018 - Recent Advances in Electrical Engineering and Related Sciences: Theory and Application*. Cham: Springer International Publishing, 2020, 2020-04-13, s. 429-438. Lecture Notes in Electrical Engineering. DOI: 10.1007/978-3-030-14907-9\_42. ISBN 978-3-030-14906-2.
3. MARTINEK, Radek, DANYS Lukas, JAROS Rene. Visible Light Communication System Based on Software Defined Radio: Performance Study of Intelligent Transportation and Indoor Applications. *Electronics*, 2019, 8(4). DOI: 10.3390/electronics8040433. ISSN 2079-9292.
4. MARTINEK, Radek, RZIDKY Jaroslav, JAROS Rene, BILIK Petr, LADROVA Martina. Least Mean Squares and Recursive Least Squares Algorithms for Total Harmonic Distortion Reduction Using Shunt Active Power Filter Control. *Energies*. 2019, 12(8). DOI: 10.3390/en12081545. ISSN 1996-1073.



# Wireless Measurement of Environmental Quantities by use of IQRF Technology

Jan Velička, Martin Pieš, Radovan Hájovský, and Štěpán Ožana

Department of Cybernetics and Biomedical Engineering, FEECS,  
VŠB – Technical University of Ostrava, 17. listopadu 15,  
708 33 Ostrava – Poruba, Czech Republic  
{jan.velicka,martin.pies,radovan.hajovsky,stepan.ozana}@vsb.cz

**Abstract.** The paper focuses on the design and implementation of a comprehensive monitoring system that allows long-term monitoring of selected environmental quantities especially in the interior of buildings and visualizing them using modern SW tools. The measured quantities in this case include CO<sub>2</sub> concentration, temperature, humidity and atmospheric pressure. The sensor part of the system uses Figaro CDM7160, Bosch BME280 and Microchip MCP9802 sensors. The IQMESH network is based on the advanced IQRF wireless technology that allows coverage of vast areas with the wireless monitoring system. Measured data from individual measurement modules is sent using Raspberry Pi or via commercial Internet gateways to native IQRF cloud storage. From there, it is forwarded through a script to a MySQL database running on the university www server, which subsequently provides for processing and visualization using the Grafana SW system.

## 1 INTRODUCTION

Historically speaking, the indoor carbon dioxide(CO<sub>2</sub>) concentrations used to be lower than today. Previously, wood was burned for heating. Later, gas or oil heaters were used, which also needed a sufficient supply of oxygen from the air. With the arrival of electric heaters and central heating rooms are being gradually sealed for economic reasons. Nowadays, technologies (plastic windows, etc.) allow the creation of a sealed environment where natural ventilation has decreased about 40 times according to: [15]. Even if today rooms are no longer heated by burning, some CO<sub>2</sub> sources persist. The largest of all is man. Another large indoor source of CO<sub>2</sub> is smoking of tobacco products. The concentration of carbon dioxide affects air quality. For indoor spaces, the CO<sub>2</sub> concentration should be less than 1000 ppm. When this concentration is exceeded, there is a reduction in mental performance, attention deficit disorder, and with higher excess severe headaches, malaise, etc. Exceeding the concentration of 5000 ppm signifies serious health risks. The Government Decree 361/2007 Coll. states the permissible value of exposition limit (PEL) for CO<sub>2</sub> of 5000 ppm. The maximum value of the highest permissible concentration (HPC) with which a person can meet per shift is 25000 ppm.

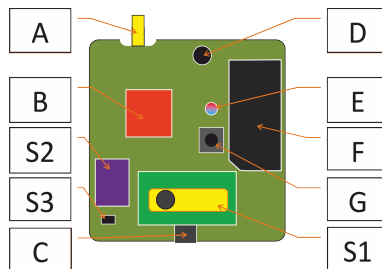
## 2 MEASUREMENT CHAIN DESIGN

For the monitoring of the air quality in the offices of the Department of Cybernetics and Biomedical Engineering, a measurement chain has been designed, the core element of which is the wireless measuring node, hereinafter called RMCD (Room Measurement of Carbon Dioxide).

The designed measurement chain consists of RMCD wireless measuring nodes and a central unit. The measured quantities are: CO<sub>2</sub> concentration, temperature, relative humidity and atmospheric pressure of the ambient air. The used sensors have digital output with IIC bus communication. Measured information from these sensors is sent via IQRF transceivers (hereinafter IQRF NODE) see [14].

- Sensor 1 - CO<sub>2</sub> sensor - Figaro CDM7160
- Sensor 2 - Temperature, humidity, atm. pressure sensor - Bosch BME280
- Sensor 3 - Temperature sensor - Microchip MCP9802

Where **A** indicates the SMA antenna connector, **B** is the IQRF transceiver, **C** is the charging micro USB connector, **D** is the piezo siren, which indicates CO<sub>2</sub> concentration above 5000 ppm. **E** is a three-colour RGB LED whose meaning is in Table 1. Module **F** is a step-up converter which increases the voltage of the backup Li-Pol battery to 5 V [12]. **G** indicates the user button that can be used to signal the CO<sub>2</sub> concentration when operating the RMCD on battery power. **S1** indicates the Figaro CDM7160 calibrated carbon dioxide concentration sensor. **S2** indicates the Bosch BME280 temperature, relative humidity and atmospheric pressure sensor. **S3** indicates temperature sensor Microchip MCP9802. The block diagram of RMCD design is shown in Figure 1. The indicated concentrations of carbon dioxide are summarized in Table 1.



**Fig. 1.** Physical diagram of RMCD wireless measuring node

The number of measured quantities can be updated as necessary. In most cases, it is intended to use the full version. If necessary, it is possible to select a variant according to the current measurement requirement. The selection is made by writing a constant to the EEPROM that is part of the IQRF transceiver. The

information on the variant is stored in HWPID as part of the DPA packet, see [14] and [11]. The following variants can be selected:

- Full version (measurement of all available quantities)
- Measurement of CO<sub>2</sub> concentration only
- Measurement of temperature only
- Measurement of temperature, humidity and atmospheric pressure only
- Router in IQMESH (no measurement)

**Table 1.** Indicated concentrations of RMCD

Value of CO <sub>2</sub> (ppm)	LED color	Comment
<600	Violet (R+B)	Outside area
600 - 799	Blue (B)	Ventilated room
800 - 999	Green (G)	Recommended concentration
1000 - 1499	Orange (R+G)	Acceptable concentration
>1499	Red (R)	Need to ventilate

The current CO<sub>2</sub> concentration is indicated comprehensively optically (RGB LED) and acoustically (Piezo siren). This signalling is functional even without communication in the IQMESH network. If the permanent signalling is switched off, it is possible to temporarily activate it by pressing the user button (in Figure 1 marked as G). The acoustic sound signalling is independent of optical signalling. Battery life was measured for various modes. Several configurations of RMCD operation were tested. The first configuration was to change the data transmission interval to either 1 minute or 10 minutes. The second configuration was to switch the RGB LED indication to either the RGB LED permanently on or the RGB LED permanently off. In this mode, the RGB LED is turned on-demand via the user button. The battery life is summarized in Table 2.

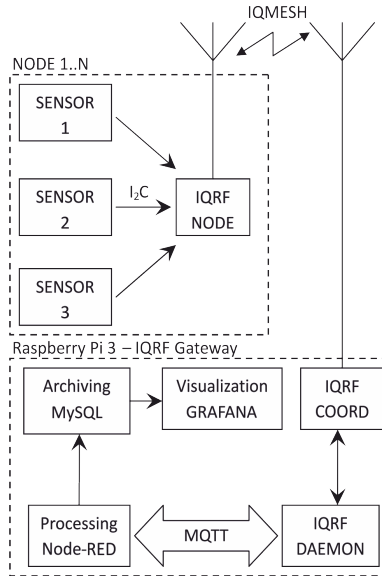
**Table 2.** Comparison of battery life in various modes

	Sending 1 min	Sending 10 min
RGB LED active	16-20 hours	22-24 hours
RGB LED on-demand	32-34 hours	36-39 hours

### 3 PROCESSING AND VISUALIZATION

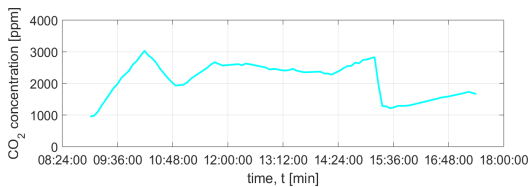
Data transfer is based on communication in the IQMESH network based on IQRf modules, see [10]. The IQRf module of the network coordinator (IQRf

COORD) is connected to Pi through the SPI bus, see [1, 2]. The communication with the network coordinator is provided by the IQRF-Daemon application. Data is transferred between IQRF-Daemon and Node-RED via MQTT. In an application created in Node-RED, the measured data is converted into a readable form and stored in a MySQL database. System Grafana is used for visualization. Block diagram of processing, archiving and visualization of measured data are draw on Figure 2.



**Fig. 2.** Block diagram of processing, archiving and visualization of measured data

In the software system Grafana (see Figure 3 ) an application was created for visualization of the measured data. The courses for the selected time interval and the last measured value are displayed. The measured data can be displayed in the Grafana environment as the time course of the individual environmental variables.



**Fig. 3.** Daily record of the measured environmental quantities in the laboratory EB305, FEECS, VSB-TUO

## 4 CONCLUSIONS

The designed and implemented comprehensive monitoring system is designed to monitor indoor air quality, mainly in the classrooms and laboratories of the Department of Cybernetics and Biomedical Engineering, VŠB - TU Ostrava. However, it is possible to deploy it in other school facilities, offices or households. Part of the monitoring system is also an application for processing and archiving of measured data. Data is processed using a Node-RED application. Processed data is stored in a MySQL database. The Grafana environment was used to visualize the measured values. Visualizations of time courses and actual values were created. Measured values are evaluated in the period in which people are expected to stay in a given room. Based on these values it was possible to determine what part of the period of occupation is spent by people in an inappropriate environment. Based on the determined facts it is possible to recommend changing or modifying the ventilation method in the rooms. Based on such changes, the work environment of students and employees could be improved. Based on experience with the pilot operation of the created monitoring system, it is possible to design its next version, which will be extended by other sensors and functionality. Other options present themselves in sensor data evaluation. Based on measured data, it would be possible to identify alarm states based on changes in individual measured quantities.

## References

1. Bazydło, P., Dabrowski, S., Szewczyk, R.: Wireless temperature measurement system based on the iqrF platform. *Advances in Intelligent Systems and Computing* 317, 281–288 (2015)
2. Calvo, I., Gil-García, J., Recio, I., López, A., Quesada, J.: Building IoT applications with Raspberry Pi and low power iqrF communication modules. *Electronics (Switzerland)* 5(3) (2016)
3. Dedek, J., Golembiowski, M., Slanina, Z.: Sensoric system for navigation of swarm robotics platform. In: Barbulescu, L., Roman, M., Popescu, E., Popescu, D., Sendrescu, D. (eds.) 18<sup>th</sup> International Carpathian Control Conference, ICC 2017. pp. 429–433. Institute of Electrical and Electronics Engineers Inc. (2017)
4. Fajkus, M., Nedoma, J., Bednarek, L., Vasinek, V., Martinek, R., Bilik, P., Vanus, J.: Analysis usability of the energetically passive sensors for the load monitoring of production press machines. In: Kolcun, M., Kurimsky, J., Kolcunova, I. (eds.) Proceedings of the 9<sup>th</sup> International Scientific Symposium on Electrical Power Engineering, ELEKTROENERGETIKA 2017. pp. 692–695. Technical University of Kosice (2017)
5. Gecova, K., Vala, D., Slanina, Z., Walendziuk, W.: Air condition sensor on KNX network. In: Linczuk, M., Romaniuk, R. (eds.) Proceedings of SPIE - The International Society for Optical Engineering. vol. 10445. SPIE (2017)
6. Hajovsky, R., Pies, M.: Use of iqrF technology for large monitoring systems. In: Milik, A. (ed.) IFAC-PapersOnLine. vol. 28, pp. 486–491 (2015)
7. Konecny, J., Kelnar, M., Prauzek, M.: Advanced waste rock exploring by mobile robot. In: 2<sup>nd</sup> International Conference on Machinery Electronics and Control Engineering. pp. 913–917 (2012)

8. Musilek, P., Prauzek, M., Krömer, P., Rodway, J., Barton, T.: Smart Sensors Networks: Communication Technologies and Intelligent Applications, chap. Intelligent Energy Management for Environmental Monitoring Systems, pp. 67–94. Elsevier Inc. (2017)
9. Pies, M., Hajovsky, R.: Monitoring environmental variables through intelligent lamps. In: Joukov, N., Kim, K.J. (eds.) Lecture Notes in Electrical Engineering. vol. 425, pp. 148–156 (2018)
10. Pies, M., Hajovsky, R.: Using the iqrf technology for the internet of things: Case studies. In: Joukov, N., Kim, K.J. (eds.) Lecture Notes in Electrical Engineering. vol. 425, pp. 274–283 (2018)
11. Prauzek, M., Krömer, P., Rodway, J., Musilek, P.: Differential evolution of fuzzy controller for environmentally-powered wireless sensors. Applied Soft Computing Journal 48, 193–206 (2016)
12. Slanina, Z., Dedek, J., Golembiovsky, M.: Low cost battery management system. Journal of Telecommunication, Electronic and Computer Engineering 9(2-5), 87–90 (2017)
13. Slanina, Z., Docekal, T.: Energy meter for smart home purposes. In: Tarassov, V., Abraham, A., Kovalev, S., Sukhanov, A., Snasel, V., Vasileva, M. (eds.) Advances in Intelligent Systems and Computing. vol. 680, pp. 57–66. Springer Verlag (2018)
14. s.r.o., I.T.: Iqrf - technology for wireless (2018), <https://www.iqrf.org/>
15. Vanus, J., Martinek, R., Bilik, P., Zidek, J., Dohnalek, P., Gajdos, P.: New method for accurate prediction of CO<sub>2</sub> in the smart home. In: IEEE Instrumentation and Measurement Technology Conference. vol. 2016-July. Institute of Electrical and Electronics Engineers Inc. (2016)
16. Vanus, J., Sykora, J., Martinek, R., Bilik, P., Koval, L., Zidek, J., Fajkus, M., Nedoma, J.: Use of the software pi system within the concept of smart cities. In: Kolcun M., Kurimsky J., K.I. (ed.) Proceedings of the 9<sup>th</sup> International Scientific Symposium on Electrical Power Engineering, ELEKTROENERGETIKA 2017. pp. 513–517. Technical University of Kosice (2017)

# Embedded systems powered by piezoelectric transducers

Martin Vitásek, Michal Prauzek, and Jaromír Konečný

Department of Cybernetics and Biomedical Engineering, FEECS,  
VŠB – Technical University of Ostrava, 17. listopadu 15,  
708 33 Ostrava – Poruba, Czech Republic  
{martin.vitasek, michal.prauzek, jaromir.konecny}@vsb.cz

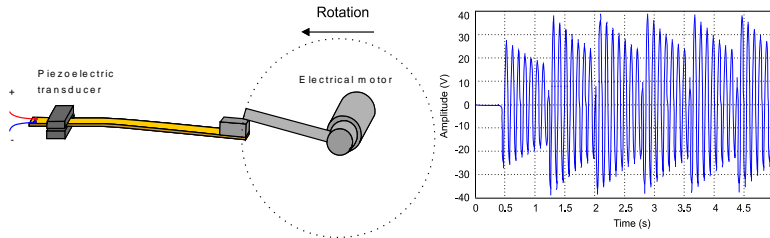
**Abstract.** This contribution presents a pilot study on powering battery-less embedded systems. The study is focused to energy harvesting from vibrational kinetic energy using piezoelectric transducers. First, the authors describe a testing setup consisting of piezoelectric transducer, DC/DC converter with energy storage, and evaluation microcontroller platform (FRDM KL25Z). Basic principles of energy generation and implementation of testing low power algorithm is also described in this part. Three types of experiments have been conducted for two voltage configurations including charging speed, continuous operation and discharge test. Results presented in this article concentrate on power supply voltage (1.8 V and 3.3 V), total efficiency (67.16 % and 76.75 %) and operation times (24.28 s and 15 s) of the embedded system.

## 1 Introduction

Nowadays, the number of electronic embedded devices is increasing which is associated with trend of Internet-of-Things (IoT). Many of the current research challenges stem from the mass deployment of IoT sensors in many application domains such as environmental sensors [1], industrial sensors [4], wearables [2], [3], etc. Each of this electronic embedded device needs to be powered by electrical energy. This brings the need for effective power supply solutions. One of the solutions is use an alternative energy sources based on energy harvesting. It opens a promising field of study due to the widespread implementation of such devices in many application domains [1]. The powering solution described in this contribution is based on vibration energy harvesting using a piezoelectric converter. Target applications are low power embedded systems such as smart IoT sensors applicated in areas where ambient kinetic energy is available [5]. Sensors can be implemented in transportation vehicles [6], [7], industrial facilities [8], etc. Design of embedded systems without batteries powered by kinetic energy harvester is a complex task requires compliance with the energy-neutrality condition [9]. For long term operational time are often used different technical solutions such as low power electronic design, low power wireless communications, energy saving algorithms etc. This article is divided into several sections which describes basic experimental setup, experimental setup principle of function, obtained results and brief outline of future work.

## 2 Experimental setup description

The goal of the experimental work is to evaluate an MCU-driven battery-less embedded system powered by energy harvested using a piezoelectric converter. For testing purposes, a vibration generator was implemented using electrical motor (see Fig. 1).

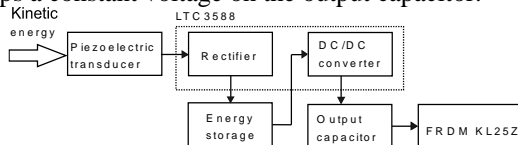


**Fig. 1.** Kinetic energy excitation of piezoelectric beam by electrical motor and output voltage of the piezoelectric transducer.

The motor rotates with frequency of 1.33 Hz, emulating energy obtained from the environment. An arm attached to the shaft bends the piezoelectric beam. The beam tip starts vibrating with frequency of 10 Hz when the arm releases the tip. The resonant frequency of the beam depends on its length and the mass of the weight located at its end. When the resonant frequency of the beam matches the frequency of the kinetic source frequency, the beam works in the optimal regime.

Vibrations of the beam result in dynamic deformations of the piezoelectric material in the inner layer of the piezoelectric converter. Therefore, the kinetic energy is transformed to alternating electrical voltage on transducer output (see Fig. 1) based on direct piezoelectric effect. Fig. 2 shows a block diagram of the testing setup. Its input is the kinetic energy harvested by the piezoelectric transducer. Alternating current from the piezoelectric converter enters the energy harvester module.

The energy conversion and storage module are based on the integrated circuit LTC3588. The alternating voltage is rectified and then stored to the energy storage device implemented using an electrolytic capacitor with capacitance of 100  $\mu\text{F}$ . When the energy storage voltage surpasses a preset threshold, the DC/DC converter starts operating in the step-down mode. The DC/DC converter operates with efficiency of 60-90 %, and it keeps a constant voltage on the output capacitor.



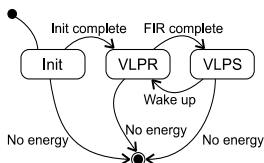
**Fig. 2.** A block diagram of the testing setup; it describes the path from the kinetic energy transducer to the load represented by the evaluation MCU board (FRDM KL52Z).

The testing platform is based on the evaluation board FRDM KL25Z with ARM-Cortex M0+ MCU. Board is powered by the harvested kinetic energy converted by LTC3588. The FRDM board was modified and unused peripherals on the board were



disconnected to minimize its power consumption. The resulting power supply current drawn by the board is 700-800  $\mu\text{A}$  in Very Low Power Run (VLPR) mode, and 15.3  $\mu\text{A}$  in Very Low Power Stop (VLPS) mode.

To evaluate the capability of the development board to run programs in VLPR mode, a testing firmware was implemented. A 7th order FIR filter operating in duty-cycle scenario (switching VLPR and VLPS modes in a predefined interval) was implemented as a testing algorithm.



**Fig. 3.** A finite state machine of the implemented firmware (duty-cycle scenario - switching VLPR and VLPS modes in a predefined interval).

The testing algorithm was implemented as a finite state machine (FSM) (see Fig. 3). After the initial kinetic energy conversion, the microcontroller enters the INIT state. After peripheral initialization, the system instantly enters the VLPR mode and runs the FIR filter algorithm. When FIR calculations are completed, the system sets the low-power timer to 4 seconds and the FSM transitions to the VLPS mode where the system stops all peripherals and awaits a wake-up signal from the low-power timer. This setup allows a 4 seconds duty-cycle operation when the microcontroller switches between the two low power modes (VLPR and VLPS). If there is lack of energy for the system operation, it gets a low voltage flag and immediately stops operation.

### 3 Results and evaluation

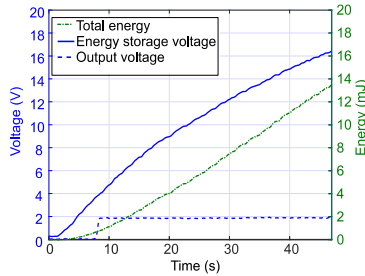
The following parameters were measured and logged:

- Supply current to development board
- Time log of energy storage voltage
- Time log of output capacitor voltage

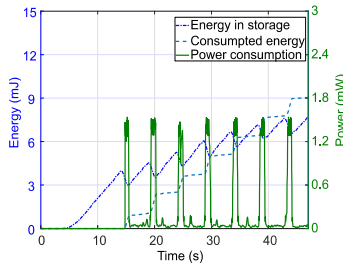
High-precision measurement instruments (obtained by DSOX2024A Oscilloscope) were used to capture the very low supply current drawn by the development board. Current measurements were performed using a precise pico-ammeter with analogue voltage output that corresponds to the instantaneous value of the measured current. This output was connected to one of four oscilloscope channels. All voltage time logs were connected to the remaining channels.

Supply voltage for KL25Z microcontroller ranges from 1.71 – 3.6 V. For evaluation purposes, two configurations of the DC/DC converter output voltage (1.8 V and 3.3 V) were used to perform three types of experiments. In the following, measurements for the 1.8 V case are presented in a graphical form. Both configurations are compared in a summary table at the end of this section.

The goal of the first experiment (Fig. 4) was to obtain information about the speed of charging of the energy storage device by the kinetic energy. The electrical motor (Fig. 1) started to rotate when the storage device was completely depleted, and the shaft first hit the transducer arm in 1.25 seconds. The transducer started converting the kinetic energy and the DC/DC converter started operating when the storage device reached a pre-set threshold (in approximately 8 seconds). The energy storage reference voltage of 15 V, corresponding to 11.25 mJ of energy stored in the capacitor, was reached at time 40.48 seconds, or 39.23 seconds after the first hit of the beam tip.



**Fig. 4.** First experiment – charging the energy storage device without load for 1.8 V output capacitor.

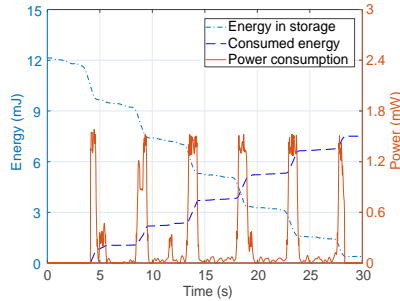


**Fig. 5.** Second experiment – operation with continuous delivery of kinetic energy for 1.8 V output capacitor.

The second experiment examined the possibility of permanent system operation with a continuous delivery of kinetic energy. Fig. 5 shows the time log of the current stored energy, total energy consumption and instantaneous input power. The piezoelectric converter delivered enough energy for continual operation of the experimental device. It was also observed that when the energy storage voltage raises, the DC/DC converter operates with lower efficiency due to its step-down topology (higher voltage drop causes lower efficiency). Therefore, the delivered energy is in balance with the instantaneous power consumption.

The third experiment demonstrates discharging from the reference state of charge (11.25 mJ/15 V). After the initialization of the energy buffer, the experimental device was connected and no energy is supplied from the piezoelectric transducer. The goal

was to evaluate the maximum operation time for the experimental setup. Fig. 6 shows the details of the instantaneous and total power consumption, as well as the amount of energy remaining in the storage device. In the examined configuration, the system can operate for 24.28 seconds.



**Fig. 6.** Third experiment – discharging from reference energy level without delivery of kinetic energy for 1.8 V output capacitor.

**Table 1.** Overall of experimental testing.

	1.8 V	3.3 V
VLPR current	0.764 mA	0.706 mA
VLPS current	0.018 mA	0.020 mA
Average current	0.167 mA	0.164 mA
Average power	0.298 mW	0.539 mW
Operation time	24.28 s	15.00 s
Utilized energy	7.245 mJ	8.089 mJ
Energy loss	3.538 mJ	2.450 mJ
Unused energy	0.382 mJ	0.676 mJ
Total energy	11.165 mJ	11.216 mJ
Total efficiency	67.16 %	76.75 %

Overview of the results is presented in Table 1 for both output capacitor configurations (1.8 V and 3.3 V). The numerical results are averages of 10 trial runs for each experiment. For both configurations, the difference between supply currents was not significant. But due to the different supply voltage, there was a significant difference in terms of power consumption: it affects the operation time and lower voltage configuration can prolong the operation by 62 % with same amount of initial energy.

In terms of energy utilization and total energy efficiency, the observation is reverse. The 3.3 V configuration can utilize more energy than 1.8 V configuration, i.e. its total energy efficiency is higher. This is caused primarily by the operation efficiency of the DC/DC converter, because the voltage drop is principally lower in the 3.3 V case.

## 4 Conclusions

This article explores the possibility to use kinetic vibration energy for powering battery-less microcontroller based embedded systems. For converting vibrational energy to electrical energy is used piezoelectric energy harvesting transducer based on direct

piezoelectric effect. The configuration of a testing system is described in the first part of this article. For testing purposes, electrical motor is used as a vibration source. Three evaluation experiments were performed under two power supply voltage levels (1.8 V and 3.3 V). There are two important conclusions based on the observed behaviour of the tested system. First, microcontroller based electronic circuit has significantly higher power consumption at 3.3 V. It is caused by static power consumption of integrated circuits. In addition, higher clock frequency results in higher dynamic power consumption. It looks like the lower voltage and lower clock frequency results in lower power consumption but second conclusion is the reverse of the first observation. When using higher output voltage, the DC/DC converter operates with a higher efficiency due to the relatively lower voltage drop from the energy storage device. Therefore, only static consumption is considered, then higher supply voltage has a substantial advantage in terms of utilized energy and total efficiency. Both observations can be used to select a voltage level appropriate for a given application. For further reduce overall energy consumption of microcontroller-based system could be used advanced techniques such as dynamic voltage scaling or dynamic clock frequency scaling.

## References

1. Prauzek, M., Konecny, J., Borova, M., Janosova, K., Hlavica, J., Musilek, P.: "Energy harvesting sources, storage devices and system topologies for environmental wireless sensor networks: A review," *Sensors (Switzerland)*, 2018.
2. Zhao, J., You, Z.: "Models for 31-mode PVDF energy harvester for wearable applications," *Scientific World Journal*, vol. 2014, 2014.
3. Suhaimi, K., Ramlan, R., Putra, A.: "A combined softening and hardening mechanism for low frequency human motion energy harvesting application," *Advances in Acoustics and Vibration*, vol. 2014, 2014.
4. Zhang, X., Fang, J., Meng, F., Wei, X.: "A novel self-powered wireless sensor node based on energy harvesting for mechanical vibration monitoring," *Mathematical Problems in Engineering*, vol. 2014, 2014.
5. Khan, F. U., Ahmad, I.: "Review of energy harvesters utilizing bridge vibrations," *Shock and Vibration*, vol. 2016, 2016.
6. Maurya, D., Kumar, P., Khaleghian, S., Sriramdas, R., Kang, M. G., Kishore, R. A., Kumar, V., Song, H. -, Park, J. -. J., Taheri, S., Priya, S.: "Energy harvesting and strain sensing in smart tire for next generation autonomous vehicles," *Applied Energy*, vol. 232, pp. 312 – 322, 2018.
7. Wang, Y., Zhu, X., Zhang, T., Bano, S., Pan, H., Qi, L., Zhang, Z., Yuan, Y.: "A renewable low-frequency acoustic energy harvesting noise barrier for high-speed railways using a helmholtz resonator and a pvdf film," *Applied Energy*, vol. 230, pp. 52 – 61, 2018.
8. Kim, K. -, Cho, J. Y., Jeon, D. H., Ahn, J. H., Hong, S. D., Jeong, Y. -, Nahm, S., Sung, T. H.: "Enhanced flexible piezoelectric generating performance via high energy composite for wireless sensor network," *Energy*, vol. 159, pp. 196 – 202, 2018.
9. Musilek, P., Prauzek, M., Krömer, P., Rodway, J., Bartoň, T.: "Intelligent energy management for environmental monitoring systems," *Smart Sensors Networks: Communication Technologies and Intelligent Applications*, pp. 67–94, 2017.

# Application of Transformation Methods on Pathological ECG Records

Jaroslav Vondrák and Marek Penhaker

Department of Cybernetics and Biomedical Engineering, FEECS,  
VŠB – Technical University of Ostrava, 17. listopadu 15,  
708 33 Ostrava – Poruba, Czech Republic  
{jaroslav.vondrak, marek.penhaker}@vsb.cz

## Abstract.

This work deals with the application of transformation methods to pathological electrocardiographic records of patients to get vectorcardiographic record. Before processing the data it was necessary to filter the measured signals from interfering components in the signal. After the transformed curve thus obtained, a comparison was made with the curve measured by Frank's lead system, where both curves were measured simultaneously. The comparison between the curves was calculated in each signal sample. Thus, the absolute deviations were the algebraic differences of the actual values of the individual records in the respective samples. After these calculations, it was concluded that Kors regression method at lead X and Y achieved the most accurate transformation results. The QLSV method, which is primarily derived for the QRS complex of the heart cycle, achieved the most accurate results for the lead Z.

**Keywords:** Heart, Frank's lead system, VCG, ECG, Transformation ECG to VCG, Heart attack

## 1 Introduction

The heart, as a muscle pump, performs two basic vital functions - it collects blood from all parts of the body and then pumps it into the lungs, and collects oxygenated blood from the lungs, which it then pumps into the whole body. For these functions to be performed correctly by the heart, the heart must be able to generate and conduct electrical impulses that lead to heart contraction. These electrical impulses are measured and recorded by various measurement methods collectively called electrocardiography, which will bring us a 2D record. However, there is a method that allows us to record in three levels. This ECG-based method is called vectorcardiography. This method does not provide as clear information as electrocardiography, but still has some potential that can be used in certain situations. Today, however, the primary role is played by the ECG record, which remains the most frequently used cardiology examination. This work presents possibilities of transformation of ECG record to VCG record. [1, 3, 4]

Vectorcardiography is a diagnostic method that deals with spatial recording of electrical manifestations of the heart. It is another form of recording the electrical manifestations of the heart sensed from the body surface. The leakage system is rectangular, thus better matching the representation of the electric field of the heart in three-dimensional space. The aim of vectorcardiography is to obtain projection of instantaneous vector changes into three mutually perpendicular anatomical planes: frontal, sagittal and horizontal plane. Projections of voltage vectors have the character of closed vectorcardiographic loops. By tracking the motion of the instantaneous electrical summation vector in space and time, we get three loops corresponding to P wave, QRS complex, and T wave. The resulting image is called a vectorcardiogram. Frank's lead system is used for vectorcardiogram measurements. [1, 3, 5]

The aim of this work is to take advantage of vectorcardiography, which can be beneficial in terms of diagnostics. Using transformation methods that transform the electrocardiographic curve into a vectorcardiographic curve, the rate of variation will be evaluated in comparison with the curve measured by Frank's lead system. This data analysis will serve for future use of transformation methods for individual pathological records.

## 2 Materials and methods

### 2.1 Patients records

Data with ECG signal records from the “PhysioBank” database were selected for practical processing. The National Metrology Institute in Germany PTB provides the PhysioNet ECG database with a wide range of ECG records. From this server a database called “The PTB Diagnostic ECG Database” was selected, where each ECG record contains 15 simultaneously measured signals, which are obtained from a 12-lead system (I, II, III, aVR, aVL, aVF, V1-V6) together with Frank's lead system (vx, vy, vz). Individual records are digitized with a sampling frequency of 1000 Hz. Each ECG record is also accompanied by a header file (.hea) containing information about the patient - age, sex, diagnosis, treatment, etc. Five ECG patient records who had a myocardial infarction were selected for this treatment. [12]

### 2.2 Transformation methods

Transformation methods are used to convert an electrocardiographic curve into a vectorcardiographic curve. The Levic and Dower transforms can be used to recalculate the electrical activity of the heart ECG and VCG. In this way, signals obtained from I. and II. Einthoven's lead and six thoracic leads to transform into a three-dimensional image.

Transformation of classical 12-lead ECG to VCG is realized by mathematical methods by multiplying two matrices. The first matrix consists of eight lines representing the leads V1 - V6, I, II and the second transformation matrix, which is given by the appropriate method. Each line has one ECG lead (V1 - V6, I, II). The resulting matrix consists of three rows representing the VCG values of the x, y and z leads. [6, 7, 8]

### Quasi orthogonal Kors method

The assumption on which this method builds is that the lead X is to some extent analogous to lead V<sub>6</sub> and lead Y is analogous to lead II. The negative half of V<sub>2</sub> is partly similar to Z. All input leads have coefficients equal to zero except for three selected leads analogous to orthogonal leads. The Kors method is given by the following equations:

$$X = V_6 \quad (1)$$

$$Y = II \quad (2)$$

$$Z = -0,5 \cdot V_2 \quad (3)$$

### Kors regression method

This method belongs to statistical methods where Kors used mathematical regression. The coefficients for the regression method were derived mathematically with simultaneous measurement of ECG and VCG, and it is these coefficients that enable the transformation of ECG into VCG. During transformation, the matrix of ECG leads is multiplied with the matrix of regression coefficients.

### Inverse Dower transform

The basis of this method is the use of mathematical pseudoinversion of the Dower method of ECG derivation from VCG. Orthogonal leads X, Y and Z are determined by a linear combination of 8 leads.

### QLSV method

Least-square value, or least squares method. This method, which minimizes the mean quadratic error of the QRS complex, is based on a regressive approach. The transformation matrix was again derived from the mean quadratic errors. [2, 5, 6, 9, 11]

## 2.3 Signal processing

During the recording of biological signals, the disturbance that distorts the signal is recorded along with the desired signal. Therefore, it is necessary to filter out unwanted components in the signal before the next data process. The components that need to be removed from the signal are: network interference, signal zero line variation, and myopotential interference.

There are a number of methods to eliminate network interference. In this particular case the method of FIR filtering - Hamming window was chosen. Filtration takes place offline (filtration from the measured record), where a high-order filter could be used, which ensures the necessary slope. [14]

Other interfering signals include misalignment of the zero signal isolation. It occurs at low frequencies in the range of 0–3 Hz and is caused by respiratory phenomena, slow patient movements or at the skin-electrode interface with a half-cell voltage. This interference cannot be avoided, but can be filtered out by various methods. The Lynn principle filtering method was chosen to eliminate this interference. It is a filtration

based on comb filters that have an even distribution of zero poles around the perimeter of the unit circle.

After applying the appropriate transformation methods to the input ECG records, a comparison was then made in individual record samples according to the same rules. In these samples the individual deviations (percentages) from the directly measured vector cardiogram according to Frank's lead system were assessed. Thus, the absolute deviations were the algebraic differences of the actual values of the individual records in the respective samples. Since this difference in values may be negative due to the "orbiting" of the transformation curve around the curve measured by Frank's lead system, the absolute value of the difference of all values in each sample was made. Absolute error is defined as the difference between the measured value (M) and the actual value (S) of the measured quantity (4).

$$\Delta = M - S \tag{4}$$

$$\delta = \frac{\Delta}{M} \cdot 100 \tag{5}$$

Relative values are the percentage of absolute values where the 100 % value was taken into account for the algebraic difference between the maximum and minimum values of the Frank curve. The relative error is given by the ratio (5). [6, 10, 13]

### 3 Evaluations and results

In this work the above transformation methods were applied to all patient records. The resulting curves were then compared with the curves measured by Frank's lead system. Signal filtering has been performed which, if not filtered, can cause signal distortion, which can lead to misdiagnosis. An example of the use of the Kors regressive transformation method and filtration of the signal can be seen in Figure 1.

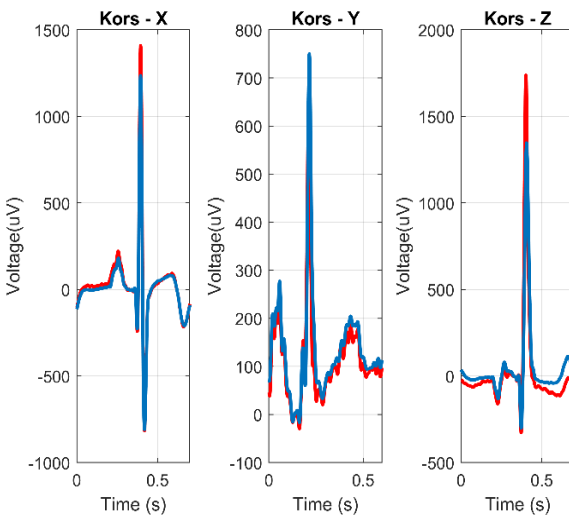


Fig. 1. Kors regressive method for one ECG cycle



**Table 1.** Average similarity of transformation methods.

Method	Lead X (%)	Lead Y (%)	Lead Z (%)
Kors regressive	0,9884	0,9856	0,9835
Inverse Dower	0,9776	0,9749	0,9734
QLSV	0,9782	0,9756	0,9844
Quasi orthogonal	0,9753	0,9725	0,9743

In Table 1 it can be seen that the most accurate method for lead X and Y is the Kors regression method for the first patient record with heart attack. For lead Z, the QLSV method achieves the best results. Despite the small percentage differences between the individual transformation methods, it is always necessary to select the most accurate one, because, despite small differences, misdiagnosis may subsequently occur.

**Table 2.** Summarization of results

	Transformation method					
	Kors regressive			QLSV		
Patient	Lead X	Lead Y	Lead Z	Lead X	Lead Y	Lead Z
1.	0,9884	0,9856	0,9835	0,9882	0,9756	0,9844
2.	0,9881	0,9861	0,9828	0,9879	0,9766	0,9850
3.	0,9886	0,9860	0,9827	0,9877	0,9798	0,9855
4.	0,9879	0,9859	0,9835	0,9872	0,9778	0,9860
5.	0,9883	0,9857	0,9836	0,9876	0,9758	0,9848

Table 2 summarizes the two transformation methods that achieved the highest percent similarity to the directly measured transformation curve. If we work with the whole heart cycle, it is better to use the Kors regression method. But most cardiac arrhythmias are related only to some part of the heart cycle, therefore, it is necessary to choose a transformation method by which the coefficients were derived just for the desired part of the heart cycle, for example for QRS complex is derived QLSV transformation method which has the best results in lead Z.

## 4 Conclusion

The results of this work will serve as an initial step for further analysis of the application of transformation methods to pathological records of the electrocardiogram. Patient records with a history of heart attack were selected. These records were subsequently processed in the Matlab software environment, where these data were adjusted by necessary filtration before evaluation. After these modified data, four transformation methods were applied to the electrocardiographic record. Correlation with the curve measured by Frank's lead system was made from the transform curves thus obtained. The comparison was performed in each sample of the selected cardiac record from which the mean deviation was calculated. Of the five patient records with myocardial infarction, the X and Y lead was best for the Kors regression transformation method. For lead Z, QLSV achieved the best results.

The next step is to focus on specific sections of the heart cycle using transformation methods and Laufberger octant vectorcardiography. These findings can assist clinicians in the detection of cardiac arrhythmias by measuring a common 12-lead ECG.

## 5 References

1. AUGUSTYNIAK, Piotr. On the Equivalence of the 12-Lead ECG and the VCG Representations of the Cardiac Electrical Activity. In: 10th International Conference on System-Modelling-Control. 2001. p. 51-56.
2. STRAŠKRÁBOVÁ, Bc. Alžběta. Analysis of animal ECG. Ostrava, 2017. Diplomová práce. VSB – Technical University of Ostrava. Vedoucí práce Ing. Martin Augustynek, Ph.D
3. PENHAKER, Marek a Martin AUGUSTYNEK. Zdravotnické elektrické přístroje 1. 1. vyd. Ostrava: VSB - Technical University of Ostrava, 2013, 411 s. ISBN 978-80-248-3107-7.
4. O'ROURKE, Robert A., Richard A. WALSH a Valentí FUSTER. Kardiologie: Hurstův manuál pro praxi. Praha: Grada, 2010. ISBN 978-80-247-3175-9
5. MALMIVUO, Jaakko. a Robert. PLONSEY. Bioelectromagnetism: principles and applications of bioelectric and biomagnetic fields. New York: Oxford University Press, 1995. ISBN 9780195058239
6. VOZDA, Michal; CERNY, M. Methods for derivation of orthogonal leads from 12-lead electrocardiogram: A review. Biomedical Signal Processing and Control, 2015, 19: 23-34.
7. DAWSON, Drew, et al. Linear affine transformations between 3-lead (Frank XYZ leads) vectorcardiogram and 12-lead electrocardiogram signals. Journal of electrocardiology, 2009, 42.6: 622-630.
8. KORS, Jan A. Lead transformations and the dipole approximation: Practical applications. Journal of electrocardiology, 2015, 48.6: 1040-1044.
9. MAHESHWARI, Sidharth, et al. Frank vectorcardiographic system from standard 12 lead ECG: An effort to enhance cardiovascular diagnosis. Journal of electrocardiology, 2016, 49.2: 231-242.
10. SCHRECK, David M.; FISHBERG, Robert D. Derivation of the 12-lead electrocardiogram and 3-lead vectorcardiogram. The American journal of emergency medicine, 2013, 31.8: 1183-1190.
11. BELLOCH, J. A., et al. Comparison of Different Methods for the Derivation of the Vectorcardiogram from the ECG and Morphology Descriptors. In: 2007 Computers in Cardiology. IEEE, 2007. p. 435-438.
12. The PTB Diagnostic ECG Database. <https://physionet.org> [online]. Germany, 2016 [cit. 2019-07-23]. Available from: <https://physionet.org/physiobank/database/ptbdb/>
13. GULDENRING, Daniel, et al. Transformation of the Mason-Likar 12-lead electrocardiogram to the Frank vectorcardiogram. In: 2012 Annual International Conference of the IEEE Engineering in Medicine and Biology Society. IEEE, 2012. p. 677-680.
14. MIKULÁŠ, Karol. Generátor rušení signálu EKG. Brno: Vysoké učení technické v Brně, Fakulta elektrotechniky a komunikačních technologií, 2010.

# Similarity comparison of LZ78, LZW and Fuzzy methods with different approaches of generating data

Martin Bielik and Jan Platoš

Department of Computer Science, FEECS,  
VŠB – Technical University of Ostrava, 17. listopadu 15,  
708 33 Ostrava – Poruba, Czech Republic  
{martin.bielik.st, jan.platos}@vsb.cz

**Abstract.** This paper explains comparison algorithms such as LZ78, LZW, FCD and our approaches of generating and comparing data to gather the most accurate result of the similarity between two documents. The first chapter of this paper deals with the basics of similarity problem. Later in the second chapter LZ78 and LZW algorithms are described in deep. The third and fourth chapters describe FCD and Fuzzy approaches. In the experimental part, our approaches to the generating example data and our results in comparison to other approaches are discussed.

**Keywords:** LZ78, LZW, FCD, algorithm, Fuzzy

## 1 Introduction

The similarity of the data is used daily for comparing new text documents against old ones to detect plagiarism. It is also used for problems related to publishing the same news several times from several sources. Nowadays, there are a lot of algorithms for detecting the percentage of similarity. Their approaches are described later. The similarity is divided into two types:

- Meaningful
- Lexical

This article is related to lexical similarity, which means that words are compared according to exact match, not by their meaning. Lexical similarity changes text to some kind of sequences of words later called as phrases and create vocabulary from it, next that vocabulary is used for comparison with another vocabulary created from the second document to calculate similarity.

At first, LZ78 and LZW algorithms for generating data will be described. Later Fuzzy similarity and FCD algorithms will be characterized and compared with different dictionaries that were created with our methods. Finally, our method of generating data and filtering dictionaries together with results that we achieved will be defined.

## 2 LZW (Lempel-Ziv-Weich)

### 2.1 LZ78

LZ78 is the dictionary-based algorithm, that achieves compression by referencing repeating phrases in the dictionary with indexes to these phrases that were saved before. Entries in the dictionary consist of index and character, in our case characters are replaced with words [3].

### 2.2 LZW

LZW is the variation of LZ78, as it encodes the input data, it achieves compression by replacing sub-strings that have occurred previously with references into the dictionary [2]. If phrases do not repeat (the data is a stream of symbols in more or less random order), LZW is not going to be able to compress the data very well.

LZW algorithm is mostly used in the Unix system for compress files or to compress GIF/PDF files (old versions of ZIP, ARC) [2]. Nowadays LZW was overcome by newer algorithms such as Huffman Coding.

Encoding:

1. Insert to result in the dictionary all phrases with the length of one (insert all words)
2. Start at the beginning of the document and iterate all words
3. Insert new word to phrase and check phrase against dictionary
  - (a) If the phrase is founded, increase the count of the phrase
  - (b) If the phrase is not founded, insert the new phrase to the dictionary, clear phrase and move to next word in the document (remember to move by one word, not by the length of phrase)
4. Go to step 3

In our solution algorithm LZW is used for compressing text documents or paragraphs to the series of phrases and in other way decoded. These phrases are then used for the comparison algorithm to find a level of similarity. To find other ways, the resulting dictionary of generated phrases was filtered by removing one, two, or three-word phrases.

## 3 FCD (Fast Compression Distance)

The idea of FCD starts with usage of previously generated dictionaries with LZW method. These dictionaries are then calculated with the formula:

$$FCD(x, y) = \frac{|D(x)| - |\cap(D(x), D(y))|}{|D(x)|}$$

where  $|D(x)|$  and  $|D(y)|$  are counts of all items in the dictionaries and  $|\cap(D(x), D(y))|$  is the number of phrases that are same in both dictionaries. The result value of that formula is the number between 0 and 1 where 0 means minimum distance and 1 means maximum. That number represents the level of similarity for two selected dictionaries [4].

## 4 Fuzzy similarity

Let  $F(X)$  is the class of all fuzzy sets of universe  $X$ .

Definition 1. (See [1]) A function  $Sim : F(X) \times F(X) \rightarrow [0, 1]$  is called a similarity measure if  $Sim$  satisfies the following properties:

- (S1)  $Sim(X, \emptyset) = 0$  and  $Sim(A, A) = 1$  for all  $A \in F(X)$ .
- (S2)  $Sim(A, B) = Sim(B, A)$  for all  $A, B \in F(X)$ .
- (S3) For all  $A, B, C \in F(X)$ ,  $Sim(A, C) \leq \min(Sim(A, B), Sim(B, C))$  whenever  $A \subseteq B \subseteq C$ .

Particularly, a similarity measure  $Sim$  is called a strict similarity measure if it also satisfies

- (S4)  $Sim(A, B) = 1 \Leftrightarrow A = B$  for all  $A, B \in F(X)$ .

A novel approach that is motivated by the FCD, NCD, Fuzzy similarity and other mentioned algorithms and variants was developed. Its main goal is to increase the precision of the measurement. This novel approach is inspired by Fuzzy sets and their comparison. We named our approach Fuzzy Document Similarity (FDS).

The basic idea is very similar to the principle behind the FCD approach. The dictionary, which is created using the LZ (Lempel–Ziv) principle, stores only the information about the presence of a phrase in a document. The suggestion is to append and utilize the information about the frequency of each phrase. This step significantly improves the amount of information stored in the dictionary. The phrase frequencies are not ideal measures. Therefore, is necessary to convert them into the form which is more suitable for further processing. It is proposed to use frequency normalization [5].

### 4.1 Similarity computation

Let  $A$  is a document. Then we denote  $P(A)$  a set of phrases from the dictionary, created for the document  $A$ .

We denote function  $f_A : P(A) \rightarrow N$  that  $f_A(p)$  is a frequency of a phrase  $p$  in document  $A$ .

We denote  $g_A : P(A) \rightarrow [0, 1]$  that  $g_A(p) = \frac{f_A(p)}{\sum_{p \in P(A)} f_A(p)}$  is a normalized frequency of a phrase  $p$  in document  $A$ .

Then an extended function  $g_A^*(p)$  such that, was defined.

$$g_A^*(p) = \begin{cases} g_A(p), & \text{if } p \in P(A) \\ 0, & \text{otherwise} \end{cases} \quad (1)$$

We define a fuzzy set that corresponds to the document  $A$  as

$$(P(A), g_A) = \{(p, g_A(p)) \mid p \in P(A)\}.$$

The similarity of the two documents will then be measured as a similarity of the corresponding fuzzy sets.

There is a lot of approaches for fuzzy set similarity measurement [1] based on different aggregation functions of the degree of memberships.

In this approach, the measurement based on the operations of t-norm and t-conorm [1] was used.

$$a \oplus b = \min(a, b)$$

$$a \otimes b = \max(a, b)$$

The similarity function  $FDS(A, B)$  between documents  $A$  and  $B$  is defined as

$$FDS(A, B) = \frac{\sum_{p \in P(A) \cup P(B)} (g_A^*(p) \oplus g_B^*(p))}{\sum_{p \in P(A) \cup P(B)} (g_A^*(p) \otimes g_B^*(p))}. \quad (2)$$

The proposed measure of FDS gives us a resulting similarity in the range  $[0, 1]$ . If  $FDS(A, B) = 1$  then it means that the two documents  $A$  and  $B$  are the same, they have the same content; they are equal. The documents  $A$  and  $B$  have the highest difference, and they have nothing in common if  $FDS(A, B) = 0$ .

We can easily modify Equation 2 for computing similarity between two fuzzy sets  $(P(A), g_A)$  and  $(P(B), g_B)$  as

$$Sim((P(A), g_A), (P(B), g_B)) = \frac{\sum_{p \in P(A) \cup P(B)} (g_A^*(p) \oplus g_B^*(p))}{\sum_{p \in P(A) \cup P(B)} (g_A^*(p) \otimes g_B^*(p))}. \quad (3)$$

It is easy to show that  $Sim$  is similarity in sense Definition 1.

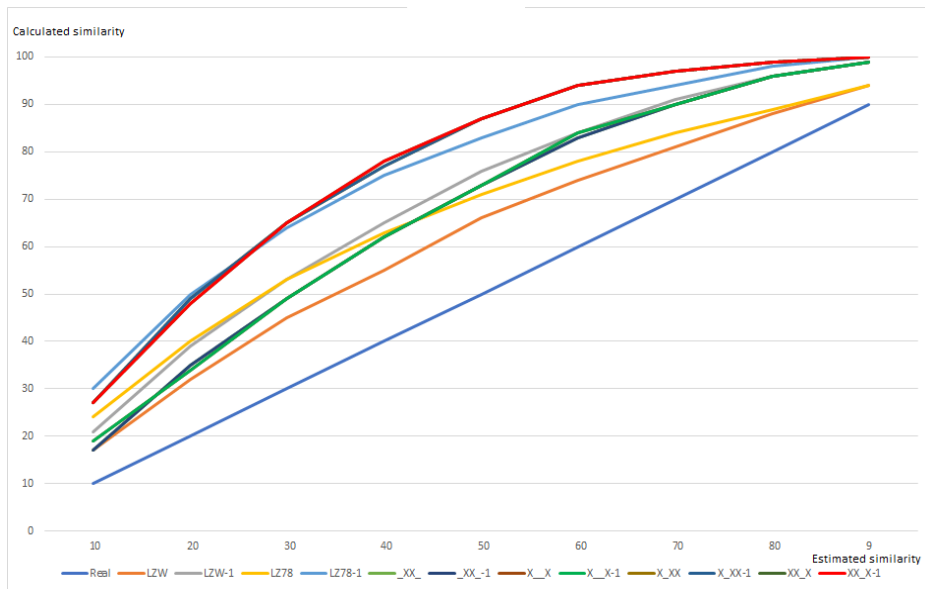
## 5 Experimental section

### 5.1 Data generation

For testing purposes we used our tool to generate data. The script basically takes the database of words and create 100 original files. Then for each original file, the script also creates 100 different versions of that file (for each percentage of similarity 1-100%). For example in the original file with 1000 words, changing 10 words means that the new file is 99% similar to the original. Basically, with that approach, it is possible directly say what is the percentage of similarity between two files and then compare results from our solution with real results.

### 5.2 Results and discussion

Results of our work were compared with other methods on our generated datasets. Considering a wide range of files, we had enough resources to get multiple results and made an average percentage of similarity for each method which made our results more accurate.



**Fig. 1.** Comparison of methods

Figure no.1 shows results from our idea of skipping words and creating different phrases, but it did not work at all. Even removing one-word phrases from dictionaries made no difference in the end-results. Our results had the best results in 10% - 15% and 75% - 90% of similarity but still worse than LZW or LZ78 methods. Other “mid-level” percentage provide much higher estimated similarity than real ones. LZW algorithm proved to be the best algorithm to estimate the similarity between document sets in compare to our methods or LZ78. In the graph, we can see both options of skipping 1-word phrases and no skipping these phrases at all (for example LZW-1 means skipping one-word phrases). Orange and yellow lines show LZW and LZ78 methods while other lines (\_XX\_, X\_X, X\_XX, XX\_X) show our results. “\_” in our names of methods means skipping of word in phrase, for example in phrase “conclusion and future work” with the method X\_X will generate “conclusion work” phrase.

Skipping one-word phrases proved to be an incorrect approach. In figure no.1 we can see XX\_X-1, LZ78-1, X\_XX-1 as worst options for estimating similarity. We can say that all other approaches proved to be in interval between LZW and LZW-1 from results point side of view.

## 6 Conclusion and future work

In this article, LZW, FCD and Fuzzy similarity algorithms were described. With experiments based on fuzzy similarities revealed that different approaches to fuzzy set creation lead to different results. These results were described in the previous section that tells us that our way of skipping one-word phrases does not

provide more accurate results as same as skipping words in phrases to generate new phrases.

There is still much to explore in our idea with methods such as substitution or combining phrases and their counts of occurrences.

## Acknowledgment

This work was supported by the projects SP2019/135 “Parallel processing of Big Data V” of the Student Grant System, VSB-Technical University of Ostrava.

## References

1. G. Deng, Y. Jiang, J. Fu, Monotonic similarity measures between intuitionistic fuzzy sets and their relationship with entropy and inclusion measure *Information Sciences*
2. T. A. Welch, A technique for high-performance data compression, *Computer*, 17 (6) (1984),
3. M. Li, Y. Zhu, Image classification via LZ78 based string kernel: A comparative study, *Lecture Notes in Computer Science (including subseries 475 Lecture Notes in Artificial Intelligence and Lecture Notes in Bioinformatics)*, 3918 LNAI (2006), pp. 704–712.
4. D. Cerra, M. Datcu, A fast compression-based similarity measure with applications to content-based image retrieval, *Journal of Visual Communication and Image Representation*, 23 (2) (2012), pp. 293–302.
5. V. Novák, I. Perfilieva, J. Močkoř, *Mathematical Principles of Fuzzy Logic*. 495 Kluwer, Boston, (1999).



# Knowledge Base for the TIL-Script Inference Machine; Polymorphic Deduction System

Michal Fait

Department of Computer Science, FEECS,  
VŠB – Technical University of Ostrava, 17. listopadu 15,  
708 33 Ostrava – Poruba, Czech Republic  
michal.fait@vsb.cz

**Abstract.** In this article, I am going to summarise what I have been working on during the last academic year. First, I dealt with the design of the knowledge base for the TIL-Script inference machine. In addition, within the half year mobility research stay in the University of Milano, I was working on the polymorphic deduction system with Giuseppe Primiero, who was my mentor.

**Keywords:** TIL-Script, knowledge base, inference machine

## 1 Introduction

The research area, which is now gaining a lot of interest, is the natural language processing and analysis. There are large corpora of text data that need to be processed in order to extract necessary pieces of information from these data. For these purposes, it is advisable to apply hyperintensional logic, because natural language is so rich that the object of predication denoted by one language term can be the very meaning of another expression. In particular, sentences expressing attitudes of knowing or believing, where the intensional analysis leads to the paradox of logical-mathematical omniscience or idiocy, serve as a typical example. For the hyperintensional analysis of natural language, it appears to be an ideal system of Transparent intensional logic (TIL).

Natural language sentences are automatically formalized in the form of TIL constructions [1] We translate these constructions into the TIL-Script language, which is a computational variant of TIL. The corpora of natural language texts written in the TIL-Script language serve as a basis of explicit knowledge for the needs of deriving implicit knowledge contained in the analysed texts. For this purpose, we can make use of the deduction apparatus for TIL [2] and for the TIL-Script language [3].

## 2 Tool for the analysis of the TIL-Script file and creation of the knowledge base

Within the work on the project, I have been extending and improving the module implemented in the Prolog language, which processes the TIL-Script file. As first, the module performs a syntactic check of the file, whether the file corresponds to the formal grammar of the TIL-Script. The module also creates derivations trees of TIL-Script constructions. A sample of the structure of such a derivation tree is illustrated in Fig. 1.

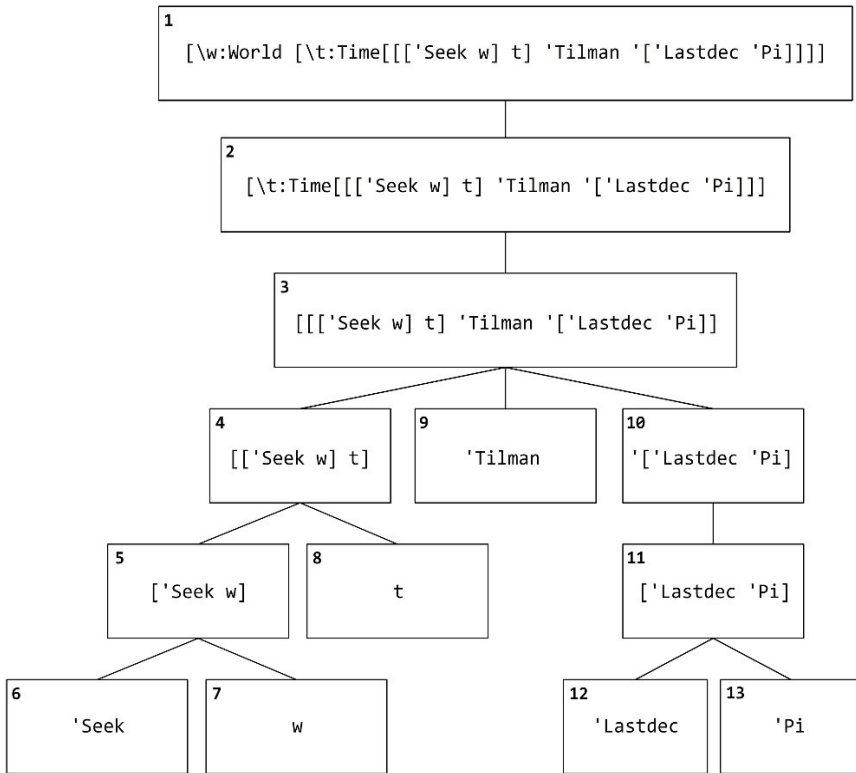


Fig. 1. Illustration of the derivation tree

Afterwards the module goes through the structure of the tree using depth-first search strategy and performs the type checking (for more details see [4]) and context recognition [5]. In the case of syntax errors or incorrect typing, the module types a warning message into the console. Output of this module is a knowledge base in the form of the XML file that contains definitions of entities, definitions of variables and derivations trees of constructions, where each construction has assigned the context in which the construction occurs and the type of a produced object. The module was later extended with the possibility to perform substitution of identicals with respect to

a context in which a given construction occurs [6]. The module thus produces new constructions where substitution rules have been applied.

The XML knowledge base consists of several sections – *entities*, *variables* and *constructions*.

Each XML element *entity* has the following attributes:

- **name** – the name of an entity
- **type** – the type of an entity

Each XML element *variable* has the following attributes:

- **name** – the name of a variable
- **productType** – the type of an object produced by the variable

XML elements for representing constructions have name *construction* and have the following attributes.

- **ID** – ID of a construction
- **type** – type of an object that a given construction is typed to produce
- **construction** – expression of the construction in the TIL-Script language
- **constructionType** – the kind of a construction (Closure, Trivialisation, Variable, Composition, ...)
- **occurrence** – context in which the construction occurs

A simple sample of the resulting knowledge base is shown in Fig. 2 (for the sake of simplicity, the ID and constructionType attributes are removed from the sample to make it easier to read).

```
<?xml version="1.0" encoding="UTF-8"?>
<source>
  <entities/>
  <variables>
    <variable name="x" productType="Real" />
  </variables>
  <explicitConstructions>
    <construction occurrence="Intensional" type="(Real Real)" construction="[\x [* x x]]">
      <construction occurrence="Intensional" type="Real" construction="[* x x]">
        <construction occurrence="Intensional" type="(Real Real Real)" construction="**" />
        <construction occurrence="Intensional" type="Real" construction="x" />
        <construction occurrence="Intensional" type="Real" construction="x" />
      </construction>
    </construction>
  </explicitConstructions>
  <implicitConstructions />
</source>
```

**Fig. 2.** XML knowledge base

### 3 Inference machine

Inference machine will be implemented within the “Question-Answer” system proposed in [7]. The system input will be a knowledge base containing constructions in an XML file that is the output of the module for processing type checking and context recognition, presented in Section 2. In this inference machine we are going to implement the deduction system for TIL presented in [2].

The system will be implemented in the C# language using the .NET framework. As the first step, I have proposed an object model for representation of constructions, types and definition of the TIL-Script language. This model is presented by Fig. 3.

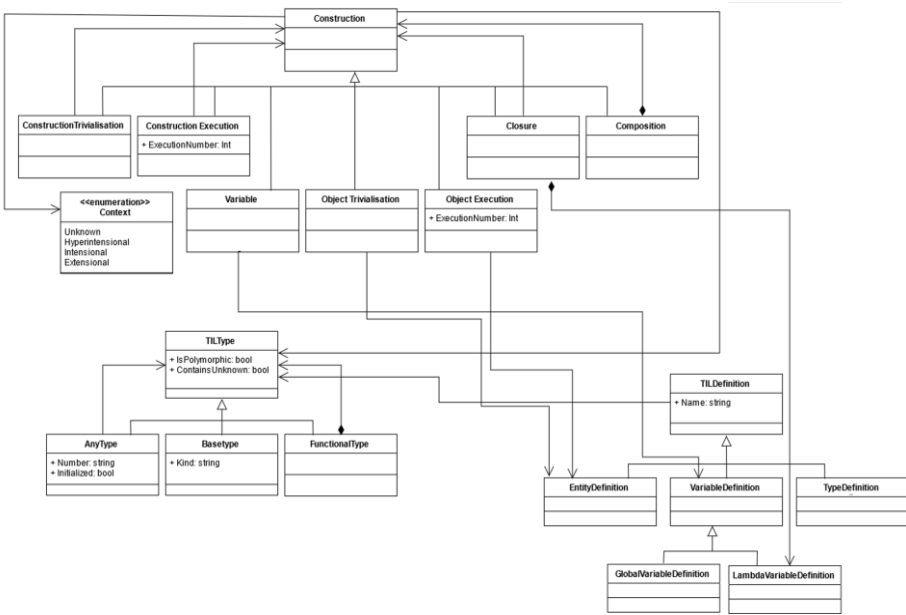


Fig. 3. Object model of the system

The core of the system is the Construction class from which the classes representing particular constructions are derived. To represent the Trivialisation (or Execution) of construction or object, the classes are created separately, because of the different behaviour of these constructions. The class Construction uses the composite design pattern; each molecular construction contains a reference to its subconstructions. An atomic construction contains a reference to an entity definition or to variable definition. Each construction also contains a reference to the instance of the class representing the type of the produced object. Classes for representing types are designed similarly to classes representing constructions. The TILtype class serves as a basic one, from which each kind of type is derived (base type, functional type or polymorphic type). The types also use the composite design pattern.

## 4 Polymorphic deduction system

I am currently working within my half-year mobility under the programme “Science without borders” with mentor Giuseppe Primiero on the deduction system for polymorphic typed  $\lambda$ -calculus. The design of the system is built purely syntactically as it is common in  $\lambda$ -calculi. The goal is, among other things, to give to logicians and philosophers who are not experts in TIL though they are familiar with typed  $\lambda$ -calculus or so-called ‘proof-theoretical semantics’, an insight into deduction in TIL. Compared to  $\lambda$ -calculi that are based on the simple type theory, the system will make it possible to work not only in the intensional level of functions and their values as it is common in the  $\lambda$ -calculi, but also at the hyperintensional level of constructions of functions and their values, as it is the case of the TIL system. The proposed system also includes rules for switching between levels. In this chapter I will briefly introduce basic foundations of the system.

### 4.1 Types

Due to the syntactic nature of the system, we assign types to terms of the language. The terms of the hyperintensional  $\lambda$ -calculus denote TIL constructions of objects or the objects themselves. Therefore, if we are talking about the “type of a term” then it is the type of the entity denoted by the term. If the term denotes a construction, then it has assigned the construction type, i.e.  $*^T$  (we do not specify the order of construction), where the superscript  $T$  stands for the type of the product produced by this construction. The type definition is as follows:

$$\begin{aligned} T &::= B \mid (T T_1 \dots T_n) \\ B &::= o \mid \iota \mid \tau \mid \omega \mid *^T \end{aligned}$$

The type can be atomic, i.e. base type or construction type  $*^T$ . We use the same epistemic base as in TIL, i.e. the set  $\{o, \iota, \tau, \omega\}$ . Functional types are  $(T T_1 \dots T_n)$ , i.e. the types of partial mappings from  $T_1 \times \dots \times T_n$  into  $T$ . For assigning of type  $T$  to term  $t$  we use a colon, i.e.  $t:T$ .

### 4.2 Form of the Judgement

There is an important role of variables in judgements.

$$\begin{aligned} \text{Variable} &::= x_i, x_j, \dots \\ \text{Term} &::= t_i, t_j, \dots \\ \text{Judgement} &::= \text{Variable}:T \mid \text{Term}:T \\ \text{Context} &::= \Gamma = \{x_1:T_1, \dots, x_n:T_n\} \\ \text{Hypothetical judgement} &::= \text{Context} \vdash \text{Judgement} \end{aligned}$$

### 4.3 Typing rules

$$\frac{}{x_i: T \vdash x_i: T} \textit{assumption}$$

The following two rules are modified rules of lambda calculus for  $\lambda$ -abstraction and application of a function to an argument, hence the TIL rules for Closure and Composition.

$$\frac{\Gamma, x_1: T_1, \dots, x_n: T_n \vdash t: T}{\Gamma \vdash \lambda x_1 \dots x_n t: (T T_1 \dots T_n)} \textit{closure}$$

$$\frac{\Gamma \vdash \lambda x_1 \dots x_n t: (T T_1 \dots T_n) \quad \Gamma_1 \vdash t_1: T_1 \dots \Gamma_n \vdash t_n: T_n}{\Gamma, \Gamma_1, \dots, \Gamma_n \vdash t[x_1/t_1 \dots x_n/t_n]: T} \textit{composition}$$

*Note:* The *composition* rule comprises also  $\beta$ -reduction by name. It serves essentially for determining the type of the resulting term.

$$\frac{\Gamma \vdash t: T}{\Gamma \vdash t': *^T} \textit{trivialisation}$$

$$\frac{\Gamma \vdash t: *^T}{\Gamma \vdash t': T} \textit{execution}$$

The system also contains extensional deduction rules. The following is a demonstration of Conditional proof and Modus ponendo ponens rules:

Conditional proof (CP)

$$\frac{\Gamma, t_i: o \vdash t_j: o}{\Gamma \vdash t_i \supset t_j: o}$$

Modus ponendo ponens (MPP)

$$\frac{\Gamma \vdash t_i \supset t_j: o \quad \Gamma' \vdash t_i: o}{\Gamma, \Gamma' \vdash t_j: o}$$

## 5 Conclusions and future work

In this paper I introduced the knowledge base for the TIL-Script inference machine and presented an outline of the object model for representation of constructions and TIL-Script definitions. I am currently implementing and testing this object model. The next step will be the implementation of deduction rules for the truth functions and for the quantifiers specified in [2].

During my mobility under the mentor Giuseppe Primiero we have designed foundations of the polymorphic deduction system. We are currently dealing with context recognition in the system. Further research goals include, inter alia, solving technical complications arising from dealing with partial functions and improper constructions that fail to produce an object. Last but not least, we are going to deal with  $\beta$ -reduction by value vs. by name, because the latter is not an equivalent conversion in the logic of partial functions.

**Acknowledgements.** This research has been supported by the Grant Agency of the Czech Republic, project No. GA18-23891S “Hyperintensional Reasoning over Natural Language Texts”, by the internal grant agency of VSB-Technical University of Ostrava, project No. SP2018/172, “Application of Formal Methods in Knowledge Modelling and Software Engineering”, by the EU project “Science without borders”, No. CZ.02.2.69/0.0/0.0/16\_027/0008463, and by the Moravian-Silesian regional program No. RRC/10/2017 “Support of science and research in Moravian-Silesian region 2017”.

## 6 References

1. Horák, A. (2002): *The Normal Translation Algorithm in Transparent Intensional Logic for Czech*. Brno, PhD thesis, Masaryk univerzity, Faculty of Informatics.
2. Duží, M., Menšík, M. (2018): Inferring knowledge from textual data by natural deduction. To appear in *Computación y Sistemas*.
3. Duží, M., Menšík, M., Pajr, M., Patschka, V. (2019): Natural Deduction System in the TIL-Script Language. *Frontiers in Artificial Intelligence and Applications*, vol. 312: Information Modelling and Knowledge Bases XXX, pp. 237-255, Amsterdam: IOS Press.
4. Duží, M., Fait, M. (2019a): Type checking algorithm for the TIL-Script language. *Frontiers in Artificial Intelligence and Applications*, vol. 312: Information Modelling and Knowledge Bases XXX, pp. 219-236, Amsterdam: IOS Press.
5. Duží, M., Fait, M. (2016): The algorithm of context recognition in TIL. In *proceedings of the Tenth Workshop on Recent Advances in Slavonic Natural Language Processing, RASLAN 2016*, Horák A., Rychlý P., Rambousek, A. (eds.), Tribun EU s.r.o, pp. 51-62.
6. Fait, M., Duží, M. (2020): Substitution rules with respect to a context. In *Lecture Notes in Electrical Engineering 554*, I. Zelinka, P. Brandstetter, T.T. Dao, Vo. H. Duy, S.B. Kim eds., AETA 2018 – Recent Advances in Electrical Engineering and Related Sciences: Theory and Applications, pp. 55-66, Springer.
7. Duží, M., Fait, M. (2019b): Question-Answering system in the TIL-Script language. In the *proceedings of the 29th International Conference on Information Modelling and Knowledge Bases - EJC 2019*.

# Distributed Processing in Dynamically Growing Networks

Tomáš Janečko

Department of Computer Science, FEECS,  
VŠB – Technical University of Ostrava, 17. listopadu 15,  
708 33 Ostrava – Poruba, Czech Republic  
tomas.janecko@vsb.cz

**Abstract.** This paper presents a description of the data analysis and data coordination methods operated by IOTA in merging together with distributed ledgers. Based on the different interconnection network models and communication setups have been measured the performance behaviors of the monitored network. One of the primary meanings for IOTA is a new transaction settlement and data transfer layer for the Internet of Things (IoT). It is based on a new distributed ledger technology, the Tangle, which overcomes the inefficiencies of current Blockchain designs and introduces a new way of reaching consensus in a decentralized peer-to-peer systems.

**Keywords:** distributed ledger, parallel programming, data analysis, network model

## 1 Introduction

Nowadays, we see changes when people and machines need to transfer data and money simultaneously in real time in the decentralized environment without any transaction fees. Like the IT solution architecture evolves from monolithic applications to the microservices oriented applications, the same trend goes to the data transfer field at the global level. This means that even nano-transactions are possible without the need for a trusted intermediary of any kind.

In the increasing adoption of IoT technologies and industry is necessary to provide any system which will be able to handle massive load of microtransactions and data integrity for machines. For that was created cryptocurrency called IOTA which is the main token in the current network. To master this the [6] IOTA's distributed ledger does not consist of transactions grouped into blocks and stored in sequential chains, but as a stream of individual transactions entangled together.



## 2 Experiment Design

In our testing scenarios we reused features introduced by IOTA Reference Implementation (IRI) together with the currently running networks. The IOTA ecosystem provides in current state multiple isolated environments:

1. Mainnet - The main running network with real tokens
2. Devnet - The development network running the latest stable version of IRI which allows developers to work on their apps
3. Spamnet - The development network to help with collecting statistics and analyzing spam techniques
4. Canarynet - This network is specifically for testing new versions of IRI before they hit the Mainnet
5. Testnet1 - The future testing network environment

From the reasons to don't be influenced by other transactions we came into conclusion to build own Private Testnet environment.

### 2.1 Private Testnet Environment

To build robust, scalable, high available environment with the design, implementation and evaluation of parallel algorithms with focus on HPC (High Performance Computing) was selected solution composed by multiple nodes.

By default IOTA's design needs to challenge the distributed architecture with parallel approach of multiple nodes. Parallel computing describes that [1] interconnection networks provide mechanisms for data transfer between processing nodes or between processors and memory modules. Interconnection networks can be classified as **static** or **dynamic**.

Figure 1(a) illustrates a simple static network of four processing elements or nodes. Each processing node is connected via a network interface to two other nodes in a mesh configuration. Figure 1(b) illustrates a dynamic network of four nodes connected via a network of switches to other nodes.

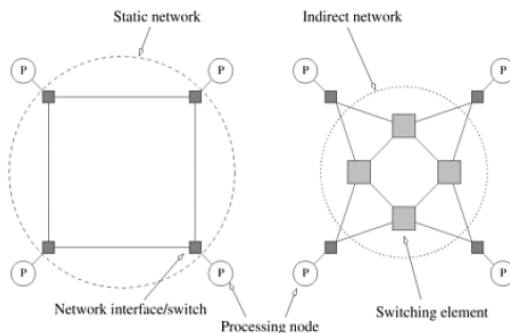


Fig. 1: Classification of interconnection networks: (a) a static network; and (b) a dynamic network

From the above findings the dynamic networks was the best solution for experiments in our private testing environment.

### 2.2 Transactions Distribution

Experiment simulated the real behavior of the isolated devices especially sensors which relate to the IoT field. The aim of the device is to continuously record data and track them into the distributed ledger.

Since the transactions are distributed around dynamically growing network we distinguish several types of transactions:

1. All transactions - all incoming transactions from the particular neighbor
2. Random transactions - transactions with "random tip" requests that the node send to this particular neighbor
3. New transactions - subset of All Transactions and count the transactions that current node has not seen yet
4. Invalid transactions - invalid transactions to be consumed by the network
5. Sent transactions - sum of all New Transactions from all neighbors minus the new transactions that received from the node it is sending to. Node broadcasts all new transactions that received to all other nodes

During the measured experiment period have been produced 5628 transactions and left 42 opened transactions (tips) and the transactions comparison against the remaining publicly available networks was presented. The results for particular type of transactions was following:



Fig. 2: All transactions

### 2.3 Dynamic Network Behavior and Visualization

The publicly available networks have a known problem which occurs when large number of transactions reference a single specific transaction which typically turns out to be a milestone. This prevents the tangle from growing organically by trapping incoming transactions inside of the blowball.

This issue was mitigated in our private tesnet by turning off the Coordinator node and providing the network only by distributed full nodes. The evolution of the entangled transactions incoming in time is visualized at Figure 3.

The enhanced legend for the vertices is:

- Violet vertex - Confirmed transaction
- Gray vertex - Unconfirmed transaction

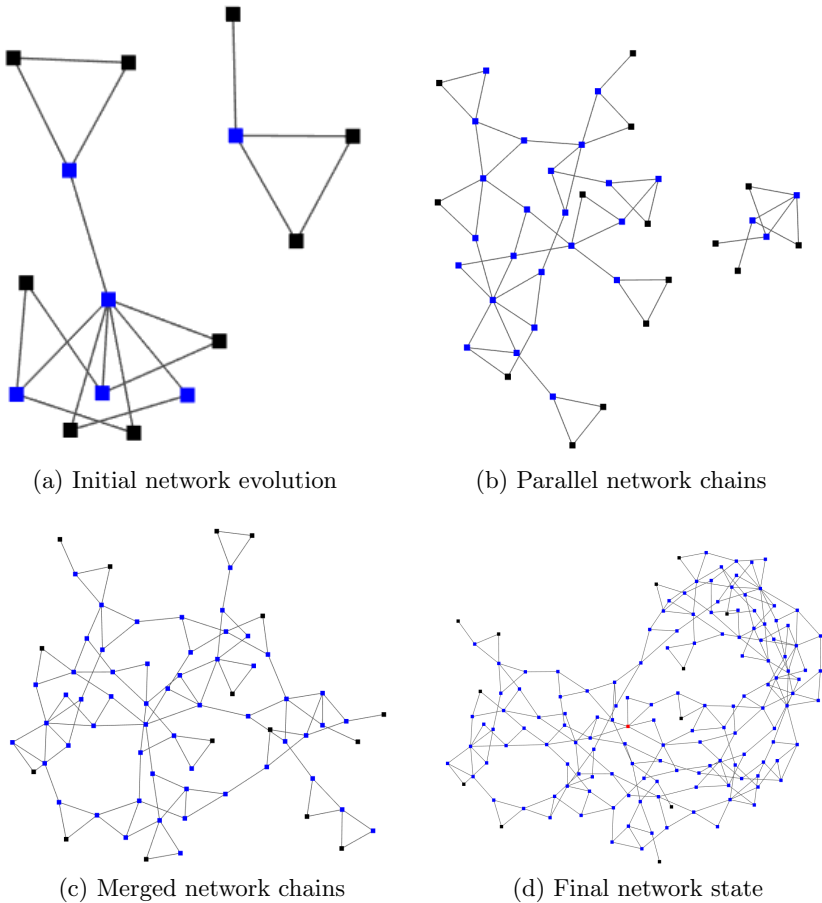


Fig. 3: Dynamic network - evolution A to D

### 3 Results

To produce the transparent outputs from our experiment was necessary to build brand new private network ecosystem. The fundamental approaches to our network comes from the general IOTA's practices, but they were enhanced to the experiment scope.

The important step was to isolate network from distracting influences like that somebody else might confirm transactions that we want to stay unconfirmed and unexpectedly broadcast them widely to the network. Together with this change was removed Coordinator node.

The network build by private custom nodes produced better results in the following fields:

- Blowballs syndrom
- TPS vs CTPS variance

The drawback of this approach was the decreased security aspect of the network, because the required amount of transactions incoming into the system was relatively low in compare to the production Mainnet.

In other words, [6] the input flow of "honest" transactions should be large compared to the attackers computational power. This indicates the need for additional security measures, such as checkpoints during the early days of a Tangle-based system.

### 4 Conclusion

In this paper was used the IOTA network for the data analysis and data coordination methods together with the parallelly distributed transactions. IOTA's tangle is unique among distributed ledger models and it forms a flexible architecture capable of organizing itself around estimative probabilities. This affords a training based data driven coordination ideally suited to unleashing machine learning technologies.

IOTA's tangle resembles a rudimentary neural network that propagates transactions, circulates data and allows for various ways in which data can map out meaningful cohesion. The tangle in that sense can be understood as a general framework for advancing Artificial Intelligence.

An important contribution of IOTA to the distributed ledger is the family of Markov Chain Monte Carlo algorithms it proposes in the framework. Markov Chain Monte Carlo are considered to be the only methods generally used to sample from and compute expectations with respect to complicated, multivariate and high dimensional probability distributions where no other methods are practical or adequately suited.

The purpose of MCMC's in the IOTA protocol is to select a tip transaction and follow its validations to a certain depth of acceptable certainty in traversing the correlated chains of the graph history.

Our experiment implementation open various options how the network could be vulnerable. The attacks could be performed by parasite chain attachment or by splitting attack which lead into double spending problem. The security of IOTA relies on an assumption that is an intrinsic feature of all decentralized, distributed and permissionless technologies: the ability for an attacker to exert undue influence over the network is infeasible because the resources required to do so are too great.

For further research we would like to focus how to run IRI in isolation where the core logic and database will be shard amongst different devices which behaves like a single full node. Similarly to swarm intelligence this enables a cluster of devices to efficiently make transactions without being a full node, but having reduced trust requirements from clients.

The results from these experiments was published at 3rd International Scientific Conference "Intelligent Information Technologies for Industry".

**Acknowledgement:** The following grants are acknowledged for the financial support provided for this research by Grant of SGS No. 2018/177, VSB-Technical University of Ostrava and under the support of NAVY and MERLIN research lab.

## References

1. Grama, A., Kumar, V., Gupta, A., & Karypis, G. (2003). Introduction to parallel computing. Pearson Education.
2. Newman, M., Barabasi, A. L., & Watts, D. J. (2011). The structure and dynamics of networks (Vol. 12). Princeton University Press.
3. Liu, B. (2007). Web data mining: exploring hyperlinks, contents, and usage data. Springer Science & Business Media.
4. Popov S.: The Tangle (2018). Version 1.4.3
5. Ahmad, S., & Alam, M. (2014). Balanced-ternary logic for improved and advanced computing. *Int J Comput Sci Inf Technol*, 5(4), 5157-5160.
6. IOTA Foundation: <https://www.iota.org> [Online; accessed 5-March-2019]
7. Gagniuc, P. A. (2017). Markov chains: from theory to implementation and experimentation. John Wiley & Sons.
8. Serfozo, R. (2009). Basics of applied stochastic processes. Springer Science & Business Media.
9. Rozanov, Y.A. (6 December 2012). Markov Random Fields. Springer Science & Business Media. p. 58. ISBN 978-1-4613-8190-7
10. Alemdar, H., Leroy, V., Prost-Boucle, A., & Ptrot, F. (2017, May). Ternary neural networks for resource-efficient AI applications. In 2017 International Joint Conference on Neural Networks (IJCNN) (pp. 2547-2554). IEEE.
11. Popov S., Saa o., Finardi P.: Equilibria in the Tangle (2018, March)

# Natural Gas Consumption Forecasting

Vojtěch Kotík and Jan Platoš

Department of Computer Science, FEECS,  
VŠB – Technical University of Ostrava, 17. listopadu 15,  
708 33 Ostrava – Poruba, Czech Republic  
{vojtech.kotik, jan.platos}@vsb.cz

**Abstract.** This paper presents current state of our research related to forecasting of natural gas consumption. Our main goal is to improve precision of existing forecasting methods by enriching dataset with new kinds of data which became available with rise of big data during last decade. We also plan to publish our dataset for general use to set new baseline for similar future researches.

**Keywords:** gas consumption prediction, neural network, big data

## 1 Introduction

Natural gas consumption forecasting is important field of interest since 1949 [1]-[16]. We have used all those mentioned articles to gain our basic insight. There are many reasons for importance of this field. Distribution network operators get high penalties for differences between their orders and real consumption. This creates high demand for precise consumption forecast tools. Distribution of natural gas is also complex logistic problem. Storing gas is very expensive. For example Turkey has available storage for only 5% of its consumption [2].

Until recent decade there was a significant lack of available datasets. Most researches in this area focused on annual, monthly or daily data. There were only few researches who had access to hourly consumption datasets and included them in their experiments [1].

None of those used datasets were published for another researchers. Our goal is to create baseline for all researchers who will conduct similiar research in the future.

Our steps towards this goal will be:

- Discover source of gas consumption data
- Obtain gas consumption data from source
- Clean obtained data into base dataset
- Define scope of input elements according to existing researches
- Obtain input data and enrich dataset
- Prepare first experiments on dataset

Dataset will be published after research with release of our complete paper.

## 2 Previous research

We have reviewed related researches to get basic knowledge of environment. Papers described in this part brought most important knowledge related to our research so far.

Very interesting research was conducted in Turkey [2] in 2011. This team used for prediction Autoregressive Integrated Moving Average (ARIMA) as time series analysis method. They have also tried artificial neural networks - Multi Layer Perceptron and Radial Basis Function Network. After experiments they combined those methods into Adaptive Neuro Fuzzy Inference System which includes artificial neural network and fuzzy interference system. Their dataset was based on weekly consumption reports from official publications. Prediction models used in their experiments were very close to each other in terms of prediction precision. They have not included any weather variables into dataset and relied solely on the consumption time series predictions.

Including weather input variables was one of key improvements contained in similar research performed by Croatian team [3]. Their dataset consisted of real historical consumption data from croatian gas distributor in hourly intervals. Their additional input variables included temperature prognoses for every six hours of the next day, wind velocity and direction, day type (working day, holiday and day after holiday), day of the week and season. Dataset included observations from January 1, 2008 to March 31, 2009. They have tested and trained two neural network algorithms - multilayer perceptron and radial basis function network with different activation functions. During research were identified problematic parts of day from 7:00 to 8:00 and from 12:00 to 16:00 with MAPE higher than 10%. This was identified as region specifics due to residents coming to work in the morning and heating their homes in the afternoon after their return from work. They have suggested further research of this matter due to fact that is was not explainable by the variations in type of day (working day, weekend, holiday).

Another specifics of regional differences influencing natural gas consumption were described in Bangladesh [4]. Almost half of all primary energy used in the country comes from use of natural gas. Their main contribution was including economic variables into dataset - total GDP and GDP per capita and population. One of key insights from their research was discovering possible suppression of demand within the country due to statistically insignificant response of natural gas consumption to changes in prices and population. This suggests to policymakers to try price increase to influence demand.

Including solar radiation into dataset was one of another interesting ideas [5]. There were previous researches investigating effect of solar radiations on buildings but none of them investigated influence on gas heating of buildings. They have observed data on two different scales: model house and residential sector of local distribution company. Based on results they recommended including solar radiation into forecasting model because it helps to improve accuracy. Most significant problem regarding this method now is lack of weather prediction which includes solar radiation.

### 3 Dataset

Most important part of our work so far was creating the dataset. We have reviewed many possible sources of gas consumption and weather data.

Most viable source for gas consumption data was Pražská Plynárenská, natural gas distributor for Prague city. This company operates distribution network and provides to the public consumption data on the whole distribution network level. Data available for the public starts on 1.1.2010. Until 2013 are data available only in range from 6:00 to 22:00. All later data are available in hourly intervals for a whole days.

**Table 1.** Input variables in the dataset

Variable	Description
1	Date
2	Time
3	Day of week
4	Day before holiday
5	Holiday
6	Gas consumption
7	Air temperature
8	Atmospheric pressure reduced to sea level
9	Atmospheric pressure at 2 meters height
10	Wind direction
11	Wind speed

Due to fact that our gas consumption data are from Prague we searched for historic weather data from Prague. We have first tried weather archive of Prague Libuše weather station. Unfortunately this archive contained many missing values - sometimes even whole weeks of data were completely missing.

After that we tried including weather reports from nearby Kbely Airport. Airports are issuing regular METAR reports about weather situation at their local weather station and provide those informations to the pilots.

We have obtained datasets from both sources. It was necessary to do a lot of preprocessing due to insufficient validation during data collection and resulting noise.

Current dataset contains hourly data from 1.1.2013 to 30.6.2019 – approximately 57 000 data rows. Tool we prepared is automated to extend dataset with newer values when available. Structure of the dataset is described in Table 1.

We are searching for new more detailed weather archive sources to improve our dataset as weather proved to be a vital input during previous researches.

Archives of gas consumption of other Czech distribution network operators are also available and we plan to include those into dataset as well in the future.

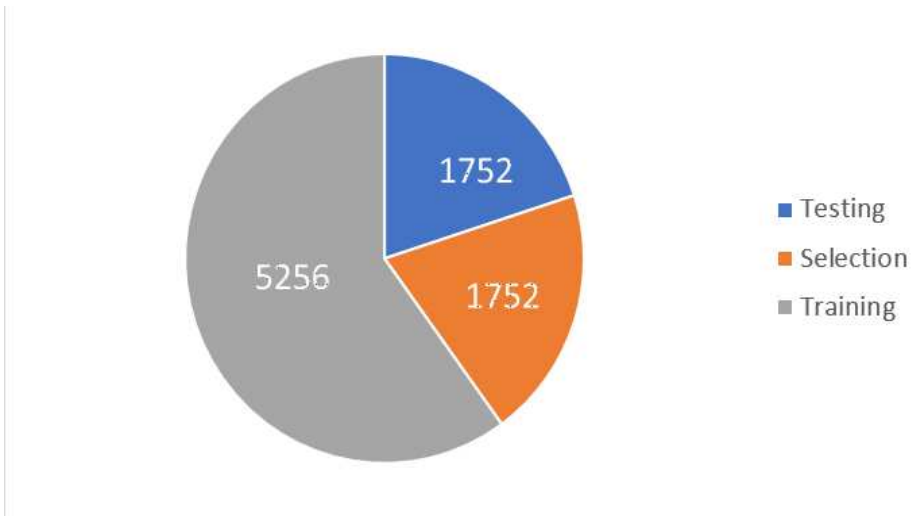


## 4 First experiments

Due to interesting previous results [2], [3], [8], [16] we chose neural networks for first experiments performed on the dataset.

We have extracted subset from the dataset. Selected subset contained following features:

- Data from 1.1.2013 to 31.12.2013
- Input variables included as specified in Table 1
- 8760 valid data rows
- 979 missing values were substituted by their means
- Dataset was divided for training as in Figure 1.



**Fig. 1.** Distribution of dataset for neural network training

Before training we have performed evaluation of correlations between selected input variables and gas consumption. Result are available in Table 2.

For initial experiments we have used multi layer perceptron neural network with one hidden layer. Activation function used was hyperbolic tangent. We have used normalised square error as error method and Quasi-Newton method as optimization algorithm.

Training of neural networks and experiments were performed on Intel Xeon E5450 CPU.

Best precision reached so far was 0.029 MSE on selection part of dataset which was not used during training process. Final training error was 0.014 MSE. This training included 1000 epochs. Correlations analysis also enabled first insight into real usability of our input variables and suggested guidelines for further selection of new input variables.

**Table 2.** Correlations between input variables to gas consumption

Variable	Type	Consumption
Date	Linear	0.966289
Temperature	Linear	-0.885091
Humidity	Linear	0.314330
Pressure	Linear	-0.242133
Time	Linear	0.191149
Wind direction	Linear	0.147478
Pressure 2	Linear	-0.127784
Wind speed	Linear	0.056574
Day of week	Linear	-0.035618
Holiday	Logistic	0.017295
Before holiday	Logistic	0.004638

## 5 Conclusion and further research

We have prepared suitable dataset and proved its usability by first experiments with neural networks. Outputs of those experiments sets guidelines for our further research which will include experiments on full dataset, including more weather input variables, including consumption data from more gas distribution network operators and use of more complex algorithms like Convolutional neural networks.

## References

1. Soldo, B.: Forecasting natural gas consumption. *Applied Energy* 92 (2012) 26-37
2. Kaynar, O., Yilmaz, I., Demirkoparan, F.: Forecasting of natural gas consumption with neural network and neuro fuzzy system, *Energy Education Science and Technology Part A* (2011) 221-238
3. Tonkovic, Z., Zekic-Sušac, M., Somolanji, M.: Predicting natural gas consumption by neural networks, ISSN 1330-3651, UDC/UDK 665.612 : 004.032.26
4. Wadud, Z., Dey, H.S., Kabir, A., Khan, S.I.: Modeling and forecasting natural gas demand in Bangladesh, *Energy Policy* 39 (2011) 7372-7380
5. Soldo, B., Potočnik, P., Šimunovic, G., Šaric, T., Govekar, E.: Improving the residential natural gas consumption forecasting models by using solar radiation, *Energy and Buildings* 69 (2014) 498-506
6. Verhulst, M.J.: The theory of demand applied to the French gas industry, *Econometrica* (1950), 18(1) 45-55
7. Tinic, S.M., Harden, B.B., Janssen, C.T.: Estimation of rural demand for natural gas, *Manage Sci* (1973) 20(4) 604-616
8. Khotanzad, A., Elragal, H.: Natural gas load forecasting with combination of adaptive neural networks, *Proceedings of the international joint conference on neural networks*, vol. 6 (1999) 4069-4072
9. Potocnik, P., Thaler, M. Govekar, E., Grabec, I., Poredos, A.: Forecasting risks of natural gas consumption in Slovenia, *Energy policy* (2007) 35 4271-4282

10. Timmer, R.P., Lamb, P.J.: Relations between temperature and residential natural gas consumption in the Central and Eastern United States, *Appl Meteorol Climatol* (2007), 353-357
11. Ma, H., Wu, Y.: Grey predictive on natural gas consumption and production in China, *Proceedings of the 2009 2nd Pacific-Asia conference on web mining and web-based application* (2009) 91-94
12. Reynolds, D.B., Kolodziej, M.: North American natural gas supply forecast: the Hubbert method including the effects of institutions, *Energies* (2009) 335-337
13. Beierlein, J.G., Dunn, J.W., McConnon Jr., J.G.: The demand for electricity and natural gas in the northeastern United States, *Rev Econ Statist* (1981), 403-408
14. Khotanzad, A., Elgaral, H., Lu, T-I.: Combination of artificial neural-network forecasters for prediction of natural gas consumption, *IEEE Trans Neural Networks* (2000) 464-473
15. Gil, S. Deferrari, J.: Generalized model of prediction of natural gas consumption, *J Energy Resources Technol* (2004) 90-98
16. Viet, N.H., Mandziuk, J.: Neural and fuzzy neural networks in prediction of gas consumption, *Neural Parallel Scientific Comput* (2005), 265-286

# Co-authorship Network Dataset – StanBerk

Jakub Plesník and Miloš Kudělka

Department of Computer Science, FEECS,  
VŠB – Technical University of Ostrava, 17. listopadu 15,  
708 33 Ostrava – Poruba, Czech Republic  
[jakub.plesnik@vsb.cz](mailto:jakub.plesnik@vsb.cz)

**Abstract.** In this article, we present a collaboration network that we call “StanBerk”. We provide brief overview of the network’s origin, methods that have been used for construction of such network and problems that we encountered during the process. Further in this article, we present a basic statistical analysis of network, provide more detailed explanation of the structure and roles of important people in the network, and visualize this network using multiple methods for extracting as much information as possible.

## 1 Introduction and Related Work

In the last two decades, the analysis of real-world networks has received extraordinary attention. One of the data-source are social networks, which are growing at an enormous rate. Notable and long-investigated sources in this area are co-authorship and, in general, collaborative networks.

Liu et al. [1] provides a good overview of Social Network Analysis, co-authorship networks and a combination of both. Barabasi et al. [2] presented and analyzed in detail a network model inspired by the evolution of co-authorship networks. The research presented by Ramasco et al.[3] falls into the same area. Many other researchers uses a DBLP as source of collaboration networks, for example, work that reviews so-called six degrees of separation phenomenon in DBLP-DB by Elmacioglu E et al. [4]. Problems and solutions of data mining from databases like a DBLP is described by Osmar R. Zaiane et al. [5]. Also Kudělka et al. [6] provides deep analysis of co-authorship networks from DBLP.

## 2 Dataset

The name StanBerk comes from a combination of the names of two very prestigious universities Stanford University and University of California Berkeley. We have created a collaboration network of employees and researchers from these two universities, based on co-authorship of publications listed in DBLP <sup>1</sup>. In the preparation phase we have obtained a list of individuals gathered from the websites of each university and used it as input for the application that construct the collaboration network. The application is using DBLP API to obtain data about

---

<sup>1</sup> <https://dblp.uni-trier.de/>

authors and their publications. DBLP API documentation is accessible through the DBLP website <sup>2</sup>. The whole process of network construction is displayed in Figure 1. In the first step we used person search endpoint for obtaining the person’s unique identifier called “urlpt”. Then we sent a request to the person publication endpoint in order to get a list of all of their publications. We were saving all this information to memory for further network construction.

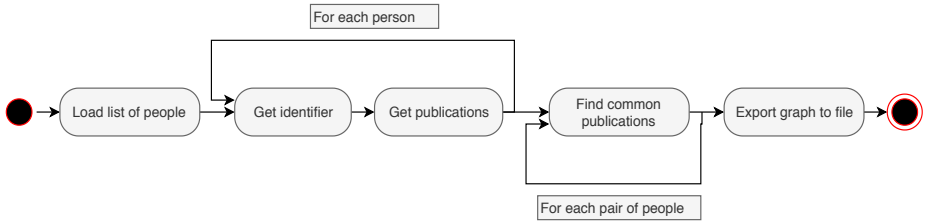


Fig. 1: Diagram of network construction

When we had all data downloaded from DBLP we used it to build a collaboration network. Each person in the input list represents one Node with its “id” as a unique identifier and label for the author’s name. The author’s name is suffixed with the first letter of their university’s name with dots on both sides (e.g.: “.B.”). The weight of edge represents the number of common publications between two authors. In the final network, we included only nodes with a non-zero degree.

During the development of the application, we have encountered a problem with the network’s construction. This problem was caused by technical limitations on the side of DBLP. The API has set a limit of requests per minute so each request had to have been followed by a 1 - 1,5 sec pause to ensure that request won’t be rejected. This significantly increases the time complexity.

We have computed basic attributes for 3 variations of the network that can be seen in Table 1. First two variations contain only members of a given university. The last variation contains nodes from both Stanford and Berkeley.

### 3 Network Visualization

In Figure 1 we can see the visualization produced with the Force Atlas 2 layout. The blue nodes belong to Berkeley and the yellow belong to Stanford. In Figure 2c we can see a denser connection between the blue nodes and a higher average degree. We can easily identify the most important nodes if we assume that the importance is based on degree. For example, we can assume that David A. Patterson, Michael Jordan, and Joseph M. Hellerstein are very important for this network hence for the academic field of these universities. To support this

<sup>2</sup> <https://dblp.uni-trier.de/xml/docu/dblpxmlreq.pdf>

Table 1: Network attributes

Attribute	Stanford	Berkeley	StanBerk
Nodes	127	89	216
Edges	284	349	788
Average degree	4.472	7.89	7.29
Connected Components	8	4	2
Diameter	8	7	8
Modularity	0.692	0.508	0.606
Density	0.035	0.089	0.034
Avg. Clustering Coef.	0.411	0.464	0.375

claim, we can search for more information about these people and verify the importance of their roles. Further observations reveal that yellow nodes create smaller clusters/groups that are densely connected, but with a lower degree. In the layout, these groups are more distant to each other and create some sort of surroundings around nodes of Berkeley.

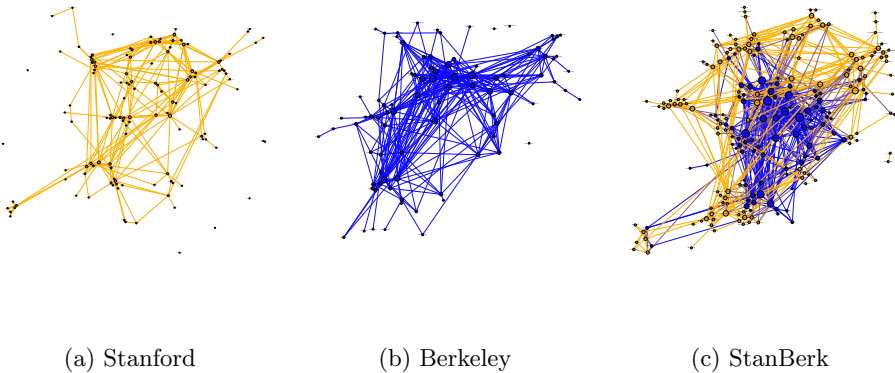


Fig. 2: StanBerk

## 4 Existence of Prominent Nodes

An interesting question is which nodes play an important role in the network, for this purpose we follow the definition of prominent nodes from Kudělka(2019) et al. [7]. We have used an algorithm that produces a list of a strongly prominent nodes. With a brief observation, we noticed that these nodes have a connection to members of both universities. In real networks, there are many reasons why one

person may belong to more than one community. Talking about this particular case, the most obvious reason why one person may have a real-life connection to both universities, or to the individuals in that university, is the migration of that person. By migration, we mean for example that one person studied at university A but continued his academic career as a lecturer in university B or just studied at both. We have found several cases just like this one with only small variations.

**Pieter Abbel** is a roboticist known for his work on reinforcement learning. In the academic field, he holds a Ph.D. title in the field of Computer Science from Stanford (2008). The same year he finished his Ph.D. studies and became a professor at UC Berkeley. We assume that his connection to Berkeley was made or supported by his advisor, Andrew Ng, professor at UC Berkeley.

**David A. Patterson** is well known for his big contribution to RISC processor design, for which he also won a Turing Award. Patterson served as Chair of the Computer Science Division at UC Berkeley, Chair of the Computing Research Association, and President of ACM. He has advised several notable Ph.D. candidates, including Christos Kozyrakis. Christos is a Professor of Electrical Engineering and Computer Science at Stanford University, holding a Ph.D. degree from UC Berkeley. Patterson also co-authored seven books, including two on the topic of computer architecture with John Hennessy, who is a former President of Stanford University.

**Ion Stoica** is a computer scientist that specializes in fields such as cloud computing, networking or big data. He is a professor at UC Berkeley. Stoica's connection is made through past Ph.D. students, where he had the role of co-advisor. Both his students are from Stanford and other advisors are also from Stanford. Another connection is through the company Databrick. Stoica is a co-founder and member of the board of directors together with Matei Zaharia, who is a professor at Stanford University.

It's important to note that all mentioned above are very important for the whole network structure and without aspect that they connect people from the different group together, the whole network may look very different.

## 5 Evolution of the Network

As we mentioned in section 2, where we describe how the network was constructed, StanBerk contains information about the date of release for the publication. We use this timestamp information to create edges that exist only for a specific year of publication. In cases where there are multiple edges between two nodes at the same time, we use the SUM strategy to project a number of edges to one edge with a specific weight. For visualization, we created 3 snapshots that are created in a 5 years time frame each. Thanks to the data format, there is a simple way to generate different snapshots of the network in tools such a Gephi.

In Figures 3 and 4 are examples of the visualization of the network evolution. Figure 3 uses standard Force Atlas 2 layout. Figure 4 uses terrain visualization that is great addition for revealing local structures of the network.

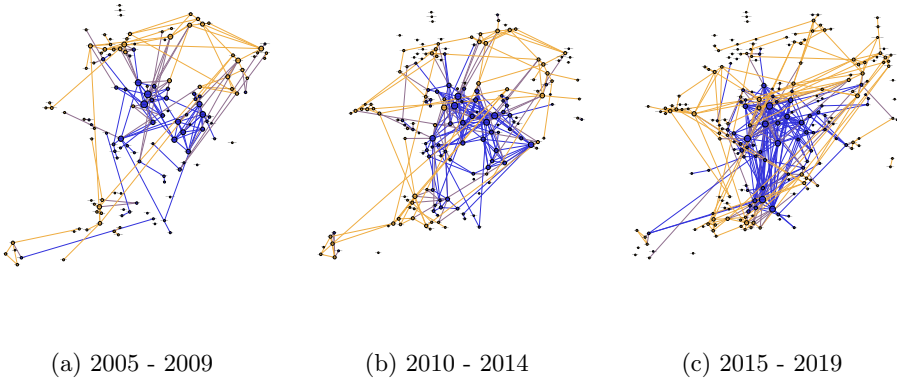


Fig. 3: Evolution of the network in standard layout

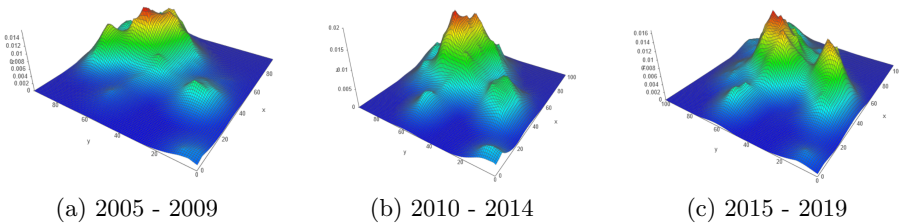


Fig. 4: Evolution of the network in terrain visualization

## 6 Summary

In this article, we have presented a new dataset that we created and described some of its characteristics. Also, we have presented various ways to visualize the network. We have identified nodes in the role of highly prominent nodes that have a very important role in the network, and we tried to reveal the motivation for the behavior of these people.

## References

1. X. Liu, J. Bollen, M.L. Nelson, H. Van de Sompel, Co-authorship net-works in the digital library research community, *Information Processing & Management*, vol. 41 (2005)
2. A.-L. Barabasi, H. Jeong, Z. Néda, E. Ravasz, A. Schubert, and T. Vicsek. Evolution of the social network of scientific collaborations. *Physica A: Statistical mechanics and its applications*, 311(3):590–614, 2002.
3. J. J. Ramasco, S. N. Dorogovtsev, and R. Pastor-Satorras. Self-organization of collaboration networks. *Physical review E*, 70(3):036106, 2004.



4. Elmacioglu E, Lee D (2005) On six degrees of separation in DBLP-DB and more. *ACM SIGMOD Record* 34:33. doi: 10.1145/1083784.1083791
5. Zaiane OR, Chen J, Goebel R (2007) DBconnect. In: *Proceedings of the 9th WebKDD and 1st SNA-KDD 2007 workshop on Web mining and social network analysis - WebKDD/SNA-KDD '07*. ACM Press
6. M. Kudelka, E. Ochodkova, S. Zehnalova *Around Average Behavior: 3-lambda Network Model*
7. M. Kudelka, E. Ochodkova, S. Zehnalova and J. Plesnik *Ego-zones: Non-symmetric Dependencies Reveal Network Groups with Large and Dense Overlaps Applied Network Science (2019)(Accepted)*

# Swarm Malware

Lukáš Révay

Department of Computer Science, FEECS,  
VŠB – Technical University of Ostrava, 17. listopadu 15,  
708 33 Ostrava – Poruba, Czech Republic  
`lukas.revay.st@vsb.cz`

**Abstract.** This paper summarizes all related work, which has been done within swarm intelligent malware. It covers parts related to environment setup, architecture, implementation and testing. Whole environment is virtualized and based on Docker. This minimizes impacts on real computers when it comes to testing or erroneous scenarios. Malware implementation in C++ is fully supported by virtual environment which can be fully used for swarm improvements. Outcome from this work should be a theoretical setup of environment where malware particles are doing distributed denial of service (DDoS) coordinated attack to some http server. After this theoretical work the practical implementation and simulation shall be done to see if the optimized attack brings expected results.

**Keywords:** docker, C++, qt, pso, swarm, swarm-bot, s-bot, ddos, http server, linux, alpine

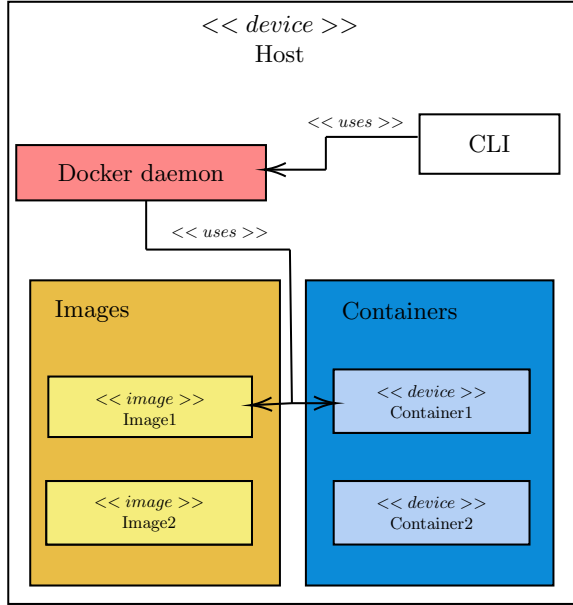
## 1 Introduction

This work seamlessly follows and extends the malware based environment which was set up in previous work [3]. Additional implementations like sensors and network communication are practical. Still there are ongoing implementations and because of that the theoretical concepts are ahead of implementations. Theoretical idea of the swarm based network malware is the added value of this paper. This is the main reason why this work is done and all related stuff which has been already implemented fully supports this theoretical concepts.

## 2 Virtual environment

Current work continues with virtual environment which is backbone infrastructure for swarm malware development and testing. It allows multiple users to share improvements via docker images without influencing each other on architectural or even code level [3]. Such kind of separation of a virtual environment and virtual connected computers allows making such attacks without any harm or even impact in real computers.

Alpine based image was set up as an environment which fully supports program execution. To prepare such image it was defined which tools are needed to fit the needs. These tools have been added into image as illustrated here. Also libraries which are required as prerequisites for program run are parts of this Fig. 1.



**Fig. 1.** An illustration representing hosting of docker artifacts together with command line interface (CLI) used for control

### 3 Particle swarm optimisation

Particle swarm optimisation (PSO) algorithm is convergent where all particles at a particular iteration will eventually wander around global best position. If this happens, then the movement of those particles would not be too significant hence make PSO computation ineffective. At this point decision will be made whether search will continue or not. This determines whether the convergence properties found a solution that can already be considered successful or not. Whole solution is more robust. This is caused by communication over network where is necessary to synchronize and inform particles about  $G_{best}$  [1] position in whole swarm. This information will be used in next iteration.

In this simulation attractiveness is then the HTTP server port which has the higher priority than another open ports. Objective function is not so complex even multi-modal. PSO can be utilized because of particles and sensors data from s-bots (more about s-bot 4.1), where each particle has its velocity according to the equation

$$v_i(t+1) = v_i(t) + c_1.r_1(P_i - x_i(t)) + c_2.r_2(G_{best} - x_i(t)) \quad (1)$$

and position

$$x_i(t+1) = v_i(t+1) + x_i(t) \quad (2)$$

Each particle computes its own fitness. Environment where particles move happens is discrete and finite [4]. This space is separated into groups related to

sub-networks based on IP addresses. Whole swarm is able to move via such space and share important information. Discrete character of this environment changes the equations a bit. It is not surprise that we can get rid of  $x_i(t)$  (in equation 1) part because it makes no sense to count the fitness based on IP address. This also gives us answer that whole position is totally discreet. It is not necessary then, to use this equation 2. What is still important for the solution is inside objective function.

### 3.1 Objective function

The task in this work was to find the HTTP server in network. Bring the particles as near as possible to this node. What does it mean near in network domain? In this case it means one hop far from this target is the nearest position. Each particle shall be on this position. If this is not possible, caused by higher number of particles than zero hop distance nodes, than the remaining particles will stay on one or n-th level of hop counts. The best positions of all particles are when all are a the sub-network where a target exists. It can be easily proven that all particles zero hop far are those which are on the same sub-network.

To make it general let say that the objective function will take into account number of open ports or specific port and also hops to target. Let say particle which finds a node with ten open ports on target node one hop far, will have better position than particle with five founded open ports and one hop far from target node. It is clear that the objective function 3 counts only with discrete values related to ports and hops, but for this demonstration ,academic purposes and further investigation this is enough.

$$P = \text{open\_ports\_count} - \text{hops\_count} \quad (3)$$

Objective function takes care only about hops count and open ports. Of course it can happen that prematurely searching ends in starting sub-network (network where swarm is initialised). This can be easily avoided when the algorithm will be changed a bit in way that will not stop with DDoS attack. There can be also another improvement that during infiltration on system the virus can scan for specific files where it can gather information(hosts file, routing table, known hosts in ssh, etc.) for movement into another network.

## 4 Swarm bot

Thinking about movements of the particle in any space brings the same problems which needs to be solved in space of network devices. Similar solutions are already done in swarm bots [2] solutions. Because the difference is just in domain where this is used it was decided to apply some parts of this solutions also in this work.

Each s-bot is a fully autonomous mobile robot capable of performing basic tasks such as autonomous navigation, perception of the environment and grasping of objects. In addition to these features, an s-bot is able to communicate with other s-bots and physically connect to them in flexible ways, thus forming a swarm bot [2].

## 4.1 S-bot

S-bot is a fully autonomous robot and is equipped with all the sensors necessary for navigation and movements [2]. Environment the bots are operating in this work is not so general for movements. This causes a different usage of sensors.

```

59
60 | QStringList* IPPortScanner::extractByQuery(const QString &xpathQuery)
61 | {
62 |     log->info(QString("Extracting ip's from network scan"));
63 |     QFile file(fileName);
64 |
65 |     if(!file.exists()) {
66 |         throw QString("Cannot find scanned file %1 .").arg(fileName);
67 |     }
68 |
69 |     bool isFileOpened = file.open(QFile::ReadOnly);
70 |
71 |     if(!isFileOpened) {
72 |         throw QString("Cannot open file %1 which represents scan.").arg(fileName);
73 |     }
74 |
75 |     QDomQuery query;
76 |     bool canRead = query.setFocus(&file);
77 |     query.setQuery(xpathQuery);
78 |
79 |     if(!canRead) {
80 |         throw QString("Cannot read from file %1 which represents scan.").arg(fileName);
81 |     }
82 |
83 |     QStringList * result = new QStringList;
84 |
85 |     if(query.isValid()) {
86 |         query.evaluateTo(result);
87 |     } else {
88 |         throw QString("Invalid xpath string.");
89 |     }
90 |
91 |     file.close();
92 |     return result;
93 | }

```

**Fig. 2.** Part of code used for port scanning utilizing nmap.

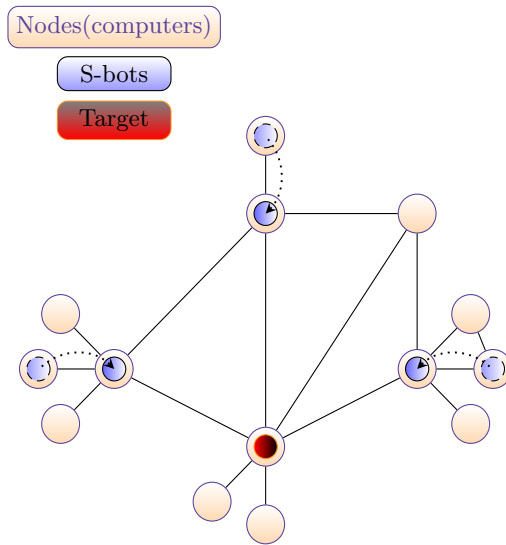
In this domain sensors like cameras or infrared sensor are not necessary. Tools like ping, telnet, traceroute, finger and etc. are sensors which can be utilized in this domain related to IP addresses space. Part of code implementig sensor utilizing nmap is visible on Figure 2.

There are used words like particle and s-bot in this paper. To make it clear, let's assume that s-bot and particle are synonyms when it comes to swarm intelligence particle is more precise. In case of swarm bot 4 and self intelligence the s-bot will be used.

## 5 Particle move

Particles movements as described on Figure 3. are crucial prerequisites for swarm. To keep the basic principles of movements that is the backbone of this solution was the important part. Movements of each particle obey rules which are necessary for swarm. The movement itself consists of few steps until it is finished.

States of particles like copy and then delete do the the job which finally causes a movement over the network. Before deletion the particle had to start another instance of itself. Move state does the movement to destination. This kind of setup provides all unnecessary stuff which fulfills requirements of swarm bot.



**Fig. 3.** Particles move in virtual network

## 6 Conclusion and future improvements

Aim of this work was to find possible solutions for further implementations, partly implements swarm intelligence and make the separation of components for better testing, demarcation of responsibility and future improvements. Crucial thing to solve was also the network setup in virtual environment described in chapter 3.1. Most of these problems are solved theoretically. In specific time these theoretical solutions will become part of the platform implementation.

Future improvements should add possibilities to spy particles communication on real time, to see which particle has for example the best solution, how the swarm reacts when topology of network changes, when some particle from swarm

is not reachable and other changes related to firewalls not running ssh's blocked ports and so on.

The results from this paper has been already published in "Journal of Advanced Enginnering And Computation".

## Acknowledgment

The following grants are acknowledged for the financial support provided for this research: Grant of SGS No. SP2019/137, VSB Technical University of Ostrava.

## References

1. Hu, X., Eberhart, R.C.: Adaptive particle swarm optimization: detection and response to dynamic systems 2, 1666–1670 (2002)
2. Nolfi, S., Denebourg, J.L., Floreano, D., Gambardella, L., Mondada, F., Dorigo, M.: Swarm-bots: Swarm of mobile robots able to self-assemble and self-organize. *Ercim News* 53, 25–26 (2003)
3. Revay, L.: From malware testing to virtualization. *Procedia Computer Science* 150, 751 – 756 (2019), <http://www.sciencedirect.com/science/article/pii/S187705091930345X>, proceedings of the 13th International Symposium "Intelligent Systems 2018" (INTELS'18), 22-24 October, 2018, St. Petersburg, Russia
4. Sabir, M.R., Mian, M.S., Sattar, K., Fahiem, M.A.: Ip address space management using aggregated fixed length subnet masking. In: 2007 International Conference on Electrical Engineering. pp. 1–4 (April 2007)

# Intelligent Malware

Lubomír Sikora

Department of Computer Science, FEECS,  
VŠB – Technical University of Ostrava, 17. listopadu 15,  
708 33 Ostrava – Poruba, Czech Republic  
lubomir.sikora@vsb.cz

**Abstract.** The focus of my work is to use artificial intelligence techniques in a malware in order to create a testing subject for further behavioral analysis of similar technology. Artificial intelligence techniques in this work are swarm intelligence algorithms: Ant Colony Optimization (ACO), Self Organizing Migration Algorithm (SOMA). Other techniques like Artificial Neural Networks (ANN) was used as well. The work also introduces caste system within a swarm. The main idea is to store knowledge about a file system into a graph (network). The applications of the malware could be cyber security as well as cyber weapons e.g. spyware thus xware is more appropriate name. It consists of multiple virus instances (individuals), these instances can communicate between each other and the whole system is decentralized.

**Keywords:** artificial intelligence, malware, cyber security, cyber weapon, artificial neural network, file system, swarm intelligence

## 1 Introduction

With new age comes also new threats. In cyberspace, where never-ending progress is present, rages a war between cyber security and cyber weapons or just a war between antivirus and malware. It is very important to companies specializing in antivirus software to have access to new technologies before malware creators. Unfortunately, this statement is not always true. Hackers create more and more sophisticated pieces of code utilizing more and more sophisticated pieces of technology. The one that rises today is non-other then artificial intelligence. My work is focused on the creation of such artificial intelligence malware in order to examine its behavior.

My intelligent malware can be described by swarm intelligence. In swarm intelligence algorithms are individuals moving through space searching for the best solution using some behavioral pattern. For example, in Ant Colony Optimization (ACO) the decision of an individual is determined by combining two factors; knowledge of space and a pheromone. In Self Organizing Migrating Algorithm (SOMA) the decision is determined by the position of the best individual (leader). In almost all those algorithms play its role randomness as part of behavior. Randomness refers to something called mutation (perturbation, or



disturbance). My technique uses these principles and mimics some of those algorithms namely ACO and SOMA. It consists of virus instances (individual) it uses some behavior patterns (ACO, SOMA).

In the following sections of the paper, these methods will be explained. Section 3 describes ACO variant of malware. Section 4 is focused on SOMA. Section 5 describes the caste system of the virus. My latest interest is to incorporate an artificial neural network. In section 6 will be shown theoretical utilization of this technology into my work. In section 7 are mentioned some results showing the potential use of tried approaches (ACO, SOMA). And finally section 8 conclusions. How does the malware work is noted in the next section 2

## 2 General functionality

The malware consist of few parts. The behavioral pattern explained in later chapters, movement of one virus instance from file to file (the malware can infect \*.exe files), infecting mechanism itself.

In order to use algorithms like ACO or SOMA, the searching space should be mapped from the tree structure of the file system into something more reasonable or the algorithm itself is slightly modified to fit the tree structure. Details are noted in later sections.

Previous lines mentioned searching for the best solution. Used algorithms are searching algorithms. In this case, these algorithms are searching for files. The essence of the file is given by fitness function. The function can evaluate files based on their properties (probability of being important or malicious) In this case, the fitness of the file was just its size for demonstrative purposes. But, some more sophisticated evaluation can be used e.g. how many times the file was executed by the user or some contextual properties could be taken into account (what files are nearby or name of the directory the file is in).

When it comes to moving from file to file, command-line arguments are used to memorize the state of the virus instance. It has to be created a new virus instance on the next file and the old one must be deleted. The appending method was used as an infection mechanism. Command-line arguments were used to transfer build string matching the structure and knowledge of the virus instance. More information can be found in [5].

## 3 Ant Colony as intelligent behavior

This section is focused on using ACO as a behavioral pattern in the malware [3]. One virus instance is one ant in a colony. All instances together make the whole swarm. ACO is graph-ready algorithm so the tree structure of the file system is not a big problem. The solution to this minor problem is to map the tree into a graph mimicking some properties of the tree: files nearby each other should be near also in the graph. For those purposes, the Barabasi-Bianconi graph building algorithm was used [1]. The probability of being the neighbouring node (file) of some important node (file) is greater than to have as a neighbour some

unimportant node (file). When a random walker goes through the graph it has greater probability to visit important nodes (files with greater fitness value). Now the swarm intelligence obtained in the file system is stored in properties of the graph for example centralities (betweenness, eigenvector, closeness, etc.).

The result of this behavior is a nicely balanced graph with spread intelligence across all nodes. For more information read [5].

## 4 SOMA as intelligent behavior

The next approach was about using a different algorithm. The SOMA algorithm was chosen. The main disadvantage of other algorithms than ACO is that they are not suitable for graph (tree) structure of the search space. In this case, the algorithm was slightly modified to accommodate that. The accommodation consisted of a way the algorithm makes jumps across space. In this case, jumps were performed proportionally to the path length and the number of files in between the starting file and the final file. In each jump, there was a chance to change detection to a random location.

The distance between files was computed as a number of directories in between. If two files share the same directory, the distance is 0. If the first file is in folder residing in the directory of the second file or vice versa, the distance is 1. This metric is useful in determining the final file of the path. The file must be far enough (the distance must be greater than the path length for the particular migration).

The principle of storing information in the graph is the same but execution is different. The edge was added from the current file to the leader file, file with the best fitness value, in each step of the migration path. Only the edge from the best file of the path has a bigger weight. SOMA in comparison with ACO is not that effective due to the fact the SOMA is more elite oriented. The leader is far more important. The resulting information in the graph is denser at the elite nodes (files with greater fitness value). The rest of the graph is more similar to a random structure. So, there is a little chance for a newly spotted file that the file will be the new best node according to centralities. The file will simply be overcome by the strength of older leaders.

For more information about SOMA see [2]

## 5 Caste System

The next level is to introduce the caste system. The idea is to have more types of virus instances. The first type is explorers and the other type is executors. Explorers walk down the file system and create the network. Executors walk the network in a random manner and perform some code on visited files. There is a bigger chance to visit better files because they have a better place within the network. Executors can be further divided into levels. Each of those can perform its part of code. The code can be independent of the state of the file. But, more interestingly, it can be dependent on the previously visited executors.

Firstly a level 0 executor performs the code, then a level 2 executor can perform its code only when a level 1 executor previously performed its code on the file etc. Executors can even achieve a level up by visiting files. The better the file, the bigger the amount of experience it gets. When the executor gets enough experiences, its level is increased.

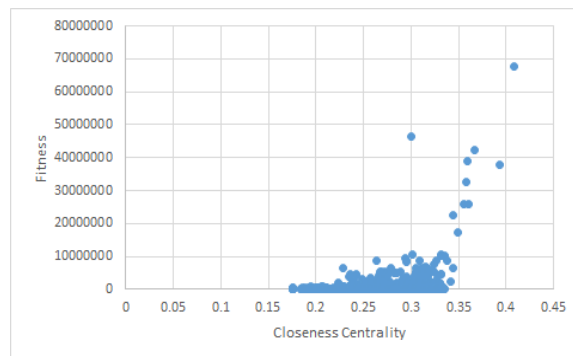
This system is independent of the behavior the virus instance follows. More information can be found in [6]

## 6 Artificial Neural Network Utilization in malware

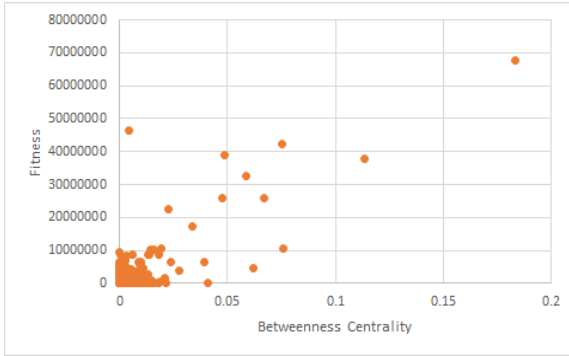
The next step is to utilize one of the most important tools of artificial intelligence; artificial neural networks. Neural networks have countless utilization in computer science. ANN can be used as classifiers. So, in intelligent malware or xware, because maliciousness is not a necessity, ANNs could be used for stealing computation power, or they can classify files as potentially malicious or harmless. The main idea is to make them decentralized. One virus instance should be one neuron and neurons should independently communicate with each other. A good example of such independent behavior is spiking neural network SNN [4]. In SNN there is no need for synchronization like in feed forward neural networks.

## 7 Results

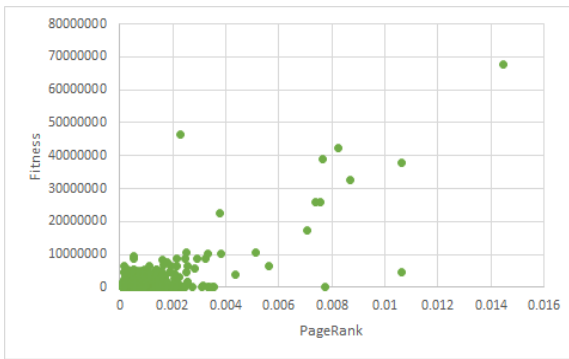
As previously stated the main idea is to create a network storing some information about the file system “swarm intelligence”. Two main methods were introduced: ACO and SOMA. The later was too much leader oriented so the final network is not the quality of the ACO solution. On the other hand, ACO performed well when it comes to the quality of the network. The information was spread evenly across the whole network. Better files have a better place within the network, better value of most centralities.



**Fig. 1.** Fitness Closeness Centrality dependency example for ACO



**Fig. 2.** Fitness Betweenness Centrality dependency example for ACO



**Fig. 3.** Fitness PageRank dependency example for ACO

More detailed result about ACO version can be found in [5]

## 8 Conclusion

When it comes to AI behavior pattern the ACO pattern is a better solution from tested ones. It provides good enough network that stores information in its structure. In future work, I will try to utilize an ANN in the file system.

## References

1. Bianconi, G., K. Darst, R., Iacovacci, J., Fortunato, S.: Triadic closure as a basic generating mechanism of communities in complex networks. *Physical Review E* 90 (07 2014)
2. Davendra, D., Zelinka, I. (eds.): *Self-Organizing Migrating Algorithm*. Springer International Publishing (2016), <https://doi.org/10.1007/978-3-319-28161-2>
3. Dorigo, M., Stützle, T.: *Ant Colony Optimization*. Bradford Company, Scituate, MA, USA (2004)
4. Rozenberg, G., Bäck, T., Kok, J.: *Handbook of Natural Computing*. Handbook of Natural Computing, Springer Berlin Heidelberg (2012)
5. Zelinka, I.: *Evolutionary algorithms, swarm dynamics and complex networks : methodology, perspectives and implementation*. Springer, Berlin, Germany (2018)
6. Zelinka, I., Das, S., Sikora, L., Šenkeřík, R.: Swarm virus - next-generation virus and antivirus paradigm? *Swarm and Evolutionary Computation* 43, 207–224 (Dec 2018), <https://doi.org/10.1016/j.swevo.2018.05.003>

# Skeleton Action Recognition Based on Singular Value Decomposition

Radek Simkanič

Department of Computer Science, FEECS,  
VŠB – Technical University of Ostrava, 17. listopadu 15,  
708 33 Ostrava – Poruba, Czech Republic  
radek.simkanic.st@vsb.cz

**Abstract.** A new method using SVD to recognise human activities is introduced in this work. The primary focus was on the problems like different duration of activities, inaccurate placement of the joints, and, especially, total loss of information about where the joint is at given times. It was necessary to develop a robust model for these problems. This was achieved by using timestamps while computing SVD for the description and approximation of the trajectory. Also, the timeline of the activity is divided into logical hierarchical time parts using temporal pyramid decomposition.

**Keywords:** 3D action feature · human action recognition · SVD

## 1 Introduction

Human action recognition is one of the important interesting topics in computer vision and image analysis. This field has a potential for many applications such as medical applications, public surveillance, or even entertainment. Today the RGBD sensors are cheap for the public, and they can be used in the research of human activities recognition. The depth maps from these devices can be used to get the approximate pose of the human skeleton and joints. In some cases, the use of depth sensors is not appropriate (e.g. environmental conditions or surroundings) and a conventional camera is needed. The skeleton can be captured also from RGB images obtained from a camera using, e.g., OpenPose [1]. The skeleton pose captured from each frame of depth maps or RGB images can be used for recognition of human activities.

The rest of the paper is organised as follows. In Section 2 the details of proposed method are stated. The experimental results are reported in Section 3. The conclusion can be found in Section 4.

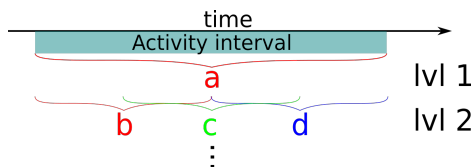
## 2 Proposed method

The main idea of the proposed method, based on the sequences of skeletons, for activity recognition is based on approximation of joints trajectories using

singular value decomposition (SVD). The time information is lost if the SVD is applied to the data in a classical way. In this paper, we have tried two approaches to suppress the loss of time information when using SVD. The first approach how to keep the time information is to calculate SVD on each part of a given activity. The second approach is to insert the time information directly into the matrix, that is used for SVD. In order to achieve this, the timeline of the activity is divided into several shorter time intervals, and SVD is then applied to these time intervals. The premise of this method is that the location of the beginning and the end of the activity is obtained beforehand. The robust model is developed that is relatively resistant to noise and independent of the duration of the activity. We focused on two types of noise in skeletal sequence. The first type is inaccurate placement of the joint, and the second is total loss of information about where the joint is at given times.

It is appropriate to convert the classic coordinates of skeleton joints to directional vectors of skeletal bones. This ensures that the activity recognition is invariant on the rotation of the skeleton. The individual directional vectors which represent rotation of bones is denoted by  $d_{i,t}$ , where  $i$  is the index of directional vector of bone, and  $t$  is the frame number. The directional vectors are computed from two joints between which the bone is located.

The first intuitive approach how to keep the time information is to divide the data into several parts. This principle is commonly used in statistics, where SVD is calculated for a given time horizon (e.g. one year). In our case, the first suitable solution to get more local time intervals is creating a hierarchical time pyramid of the time intervals. The first level of the pyramid uses the whole time interval. In each consequent level, the main interval is divided into several smaller sub-intervals that overlap. At each additional level, the sub-interval size is reduced by half, and the overlap between two sub-intervals is the half of their length. This process is shown in Figure 1.



**Fig. 1.** The dividing of activity timeline  $a$  into a few parts  $b$ ,  $c$ , and  $d$ .

The second approach is to create timestamps which are then used for SVD computation. These timestamps provide certain consistency of data, such as data order, even with occasional complete loss of information about the location of the joints. Each captured skeleton frame in activity interval is timestamped by  $\tau_t = \frac{N}{t} * c$ , where  $N$  is length of sequence,  $t$  is the actual index of the sequence frame and  $c$  is a regulation coefficient of the step size of the timeline.

The singular value decomposition (SVD)  $A = USV^T$  is used for trajectory approximation of directional vectors of bones for each temporal part. The angles of fitted planes and variance are used for description and approximation of the trajectory. The feature extraction from specific temporal parts of each directional vector  $d_{i,t}$  and temporal information  $\tau_t$  is used for creating the matrix  $A$  as follows.

$$A_{i,b,e} = \begin{bmatrix} d_{i,b,x} & d_{i,b,y} & d_{i,b,z} & \tau_b \\ d_{i,b+1,x} & d_{i,b+1,y} & d_{i,b+1,z} & \tau_{b+1} \\ \vdots & \vdots & \vdots & \vdots \\ d_{i,e,x} & d_{i,e,y} & d_{i,e,z} & \tau_e \end{bmatrix}, \quad (1)$$

where  $i$  is identifier of directional vector of bone,  $b$  and  $e$  are indices of the beginning and the end of the temporal part. The  $x$ ,  $y$ , and  $z$  are the denominations for the individual dimensional indices of a directional vector  $d_{i,t}$ .

The variance values contained on the diagonal of the matrix  $S$  obtained via SVD is subsequently converted to a unit vector  $s$ , which is one of the features for recognition. The orthonormal vectors from the right singular matrix  $V^T$  represent fitted planes to data from the matrix  $A$ . The matrix  $V^T$  can be used as a next feature for recognition, but this matrix contains duplicate values therefore it is appropriate to convert it to angles:

$$V_{\alpha_j} = \arctan \left( \frac{\sqrt{\sum_{k=1}^4 V_{k,j}^2 - V_{j,j}^2}}{V_{j,j}} \right), \quad (2)$$

where the index  $j \in \{1...4\}$  selects the orthonormal vector that is present in the  $j$ -th row of the matrix  $V^T$ , and  $k \in \{1...4\}$  is element index of this vector. The final feature vector for a specific time interval and concrete directional vector looks like as:

$$a = (s_1, \dots, s_4, V_{\alpha_1}, \dots, V_{\alpha_4}) \quad (3)$$

All these subset feature vectors are concatenated into one big and subsequently used for recognition. Recognition is done by SVM with intersection kernel in our case.

### 3 Experiments

In this section, we evaluate the proposed method using two different datasets where the Kinect or Kinect-like sensors are used for data collection: MSR-Action3D [4] and Florence3D-Action [6]. Two techniques are used to demonstrate the accuracy of the new method: (i) ACC (accuracy) by the formula  $ACC = \frac{TP+TN}{TP+TN+FP+FN}$ , (ii) the harmonic mean of precision and sensitivity  $F1 = \frac{2 \cdot TP}{2 \cdot TP+FP+FN}$ . **MSR-Action3D dataset** [4] contains 20 action types of class where each action is performed by 10 human subjects who repeat the same action 2 or 3 times. The skeleton consists of 20 joints with 3D coordinates. The skeleton poses are inaccurate and in some frames do not correspond to real



poses and some actions are similar to each other. The original standard protocol proposed by Li. et al.[4] is divided into three subsets AS1, AS2 and AS3. Each subset contains 8 action types that share some action types between them. One half (odd id's) of the samples of subjects is used for training and the other half is used for validation. The second used protocol is provided in Wang et al. [8]. This protocol is not divided into subsets, but the test is applied over all action types of the entire dataset (this protocol is noted like "All" in this paper). The decomposition for cross-subject training and testing are divided in the same way. **Florence3D-Action** [6] contains 9 action types of class. 10 human subjects repeat every action two or three times. The dataset contains several classes which are problematic because they are very similar to each other. The collection contains 215 sequences.

**Table 1.** The experimental results of proposed method on the MSR-Action3D dataset via cross-subject decomposition. AS1 - AS3 is provided by Li. et al. [4] protocol and All is provided by Wang et al. [8] protocol.

AS1		AS2		AS3		All	
F1 %	ACC %	F1 %	ACC %	F1 %	ACC %	F1 %	ACC %
72.38	93.10	75.89	93.97	89.19	97.30	73.26	97.33

**Table 2.** Comparison average of AS1-AS3 accuracies provided via cross-subject by protocol Li. et al. [4].

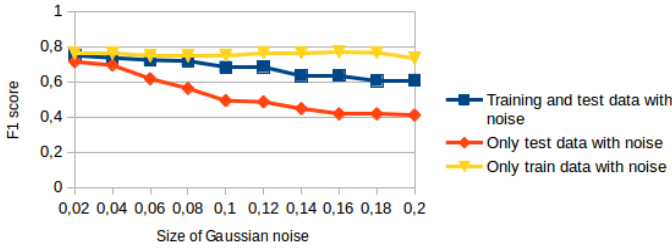
Methods	ACC (%)
Yang et al. [10]	83.3
Liu et al. [5]	84.07
Gowayyed et al. [3]	91.26
Du et al. [2, 9]	94.49
Our	94.79

**Table 3.** The experimental results of proposed method on the Florence3D datasets via cross-subject (S1:1) decomposition validation protocol of [11] and leave-one-actor-out (LOAO) validation protocol of [6].

Methods	S1:1 (%)		LOAO (%)	
	F1	ACC	F1	ACC
Vemulapalli et al. [7]	–	90.88	–	–
Seidenari et al. [6]	–	–	–	82
Our	72.22	93.83	71.63	93.70

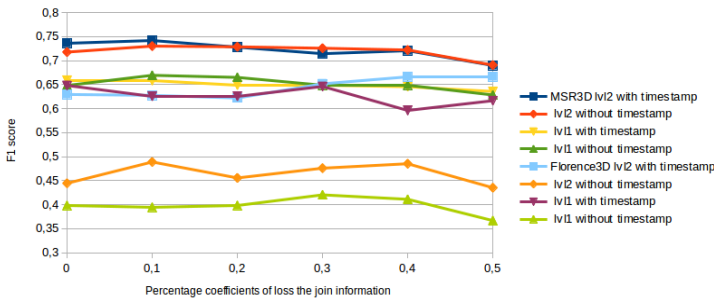
Primarily, two levels of pyramid decomposition and the constant  $c$  equal 1 are used for experiments. The comparison of our method on the MSR-Action3D dataset is presented in Table 2. The individual accuracies over the dataset are shown in Table 1. The comparison over Florence3D dataset is shown in Table 3.

The robustness of proposed method to noisy data is tested on the MSR-Action3D dataset with the cross-subject protocol and all classification classes. The Gaussian noise is added to the original coordinates of the skeletons joint.



**Fig. 2.** The progress of F1 score when applying Gaussian noise to the positions of skeleton joints. The x-axis depicts the standard deviation of the position disturbance. The yellow curve in the chart represents the training on original and noisy data and the red curve represents the evaluation on original and noisy data. The noise data with original data are included for training and subsequently testing is shown on blue curve on the chart.

These coordinates are also used for computing SVD and used for training and/or testing phase. The standard deviation of the position disturbance is in the range from 0.02 to 0.2. The demonstration is shown in Figure 2.



**Fig. 3.** Analysis of robustness to loss of coordinates data of joints.

The next analysis include testing the robustness of the proposed method to loss of coordinates data of joints. This analysis is important because, due to various occlusions, information about the location of the joint can be lost. The benefit of the temporal information contained in matrix  $A$  is demonstrated here and this principle is tested against the variant without these temporal information. It can be observed that the principle of temporal information in the matrices  $A$  is very important especially for the dataset Florence3D but the changes of accuracy are minimal for a dataset MSR-Action3D. The next demonstration of this analysis is usefulness of temporal pyramid decomposition. The demonstration is shown in Figure 3. This use of SVD for activity recognition seems to be well applicable.

## 4 Conclusion

This article has presented a new method for the description of space-time data applied to activity recognition. The method uses SVD decomposition of the matrix  $A$ . The matrix  $A$  contains the values of directional vectors, and, also the temporal information. The experiments proved that the use of temporal information helps to make human activities better recognizable. Furthermore, it has been shown that it is important to divide the data into individual time parts by using the temporal pyramid decomposition. The main goal, which is the robustness of the method to noise and mainly the loss of location information of joints, has been fulfilled even with the preservation of similar recognition accuracy as state-of-the-art methods.

## References

1. Cao, Z., Hidalgo, G., Simon, T., Wei, S.E., Sheikh, Y.: OpenPose: Realtime Multi-Person 2D Pose Estimation using Part Affinity Fields. arXiv e-prints arXiv:1812.08008 (Dec 2018)
2. Du, Y., Wang, W., Wang, L.: Hierarchical recurrent neural network for skeleton based action recognition. 2015 IEEE Conference on Computer Vision and Pattern Recognition (CVPR) (2015)
3. Gowayyed, M.A., Torki, M., Hussein, M.E., El-Saban, M.: Histogram of oriented displacements (hod): Describing trajectories of human joints for action recognition. In: Proceedings of the Twenty-Third International Joint Conference on Artificial Intelligence. pp. 1351–1357. IJCAI '13, AAAI Press (2013), <http://dl.acm.org/citation.cfm?id=2540128.2540323>
4. Li, W., Zhang, Z., Liu, Z.: Action recognition based on a bag of 3d points. In: 2010 IEEE Computer Society Conference on Computer Vision and Pattern Recognition - Workshops. pp. 9–14. IEEE (2010)
5. Liu, Z., Zhang, C., Tian, Y.: 3d-based deep convolutional neural network for action recognition with depth sequences. *Image and Vision Computing* 55, 93100 (2016)
6. Seidenari, L., Varano, V., Berretti, S., Bimbo, A.D., Pala, P.: Recognizing actions from depth cameras as weakly aligned multi-part bag-of-poses. 2013 IEEE Conference on Computer Vision and Pattern Recognition Workshops (2013)
7. Vemulapalli, R., Arrate, F., Chellappa, R.: Human action recognition by representing 3d skeletons as points in a lie group. 2014 IEEE Conference on Computer Vision and Pattern Recognition (2014)
8. Wang, J., Liu, Z., Chorowski, J., Chen, Z., Wu, Y.: Robust 3d action recognition with random occupancy patterns. In: *Computer Vision ECCV 2012*, pp. 872–885. Springer, Berlin (2012)
9. Wang, J., Liu, Z., Wu, Y., Yuan, J.: Mining actionlet ensemble for action recognition with depth cameras. In: 2012 IEEE Conference on Computer Vision and Pattern Recognition. pp. 1290–1297. IEEE (2012)
10. Yang, X., Tian, Y.: Effective 3d action recognition using eigenjoints. *Journal of Visual Communication and Image Representation* 25(1), 211 (2014)
11. Zhu, Y., Chen, W., Guo, G.: Fusing spatiotemporal features and joints for 3d action recognition. 2013 IEEE Conference on Computer Vision and Pattern Recognition Workshops (2013)

# Text Topic Detection Based on Topic Modeling and Feature Selection

Yujia Sun<sup>1,2</sup> and Jan Platoš<sup>1</sup>

<sup>1</sup>Technical University of Ostrava, 17. listopadu 2172/15,  
708 00 Ostrava-Poruba, Czech Republic

<sup>2</sup>Hebei GEO University, No. 136 East Huai'an Road, Shijiazhuang Hebei China  
yujia.sun.st@vsb.cz

**Abstract.** Text data is the most natural way to store and exchange information. Text mining technology and topic detection are the effective methods in information retrieval field to detect potential knowledge patterns hidden in massive text data. This paper studies text data topic mining and visualization technology. First, text information is processed via tokenization and stop words removal. Then, a topic model based on latent semantic relationships and feature selection is used to mine hidden topic information in text data. Finally, t-SNE technology is used to visualize the clustering results. The experiment results show that the LDA model is best used with text data that has clear semantic information and logical relationships.

## 1 Introduction

Today, the need of large data collection processing increase. Such type of data can has very large dimension and hidden relationships. Analyzing this type of data leads to many errors and noise. Therefore, dimension reduction techniques are applied[1]. In natural language processing, Latent Semantic Indexing (LSI) and Latent Dirichlet Allocation (LDA) are well known in the area of feature vector dimension reduction of text[2, 3, 4]. This work, focuses on LSI, LDA and Chi-square[5] methods, comparing the performance of these three methods for extracting feature words on a publicly available data set from BBC news. In order to properly contrast LSI, LDA and Chi-square, t-SNE[6] technology is used to illuminate the success of the clustering process.

## 2 METHODS

### 2.1 Topic Modeling

Topic modeling is one of the most well-known techniques used to decisively reduce the dimensionality of document representation and it can be easily applied to large volumes of data.

This study considers the two most widely used topic modeling techniques Latent Semantic Indexing (LSI) and Latent Dirichlet Allocation (LDA).

LSI is an indexing and retrieval method that uses a mathematical technique called singular value decomposition (SVD) to identify patterns in the relationships between terms and concepts contained in an unstructured collection of text. LSI is based on the principle that words used in the same contexts tend to have similar meanings.

SVD is a matrix decomposition technique. It decomposes the original data set matrix  $A$  into three matrices  $U$ ,  $\Sigma$  and  $V$ .

$$A_{m \times n} = U_{m \times m} \Sigma_{m \times n} V_{n \times n}^T \quad (1)$$

In the above decomposition,  $U$  and  $V$  are two orthogonal matrices with dimensions  $m \times m$  and  $n \times n$ . Matrix  $\Sigma$  will be constructed, which has only diagonal elements and all other elements are 0. These diagonal elements are called singular values, and they correspond to singular values in the original data set matrix  $A$ , after matrix  $A$  singular value is the number of  $r$ , other singular values are set to 0, which means that there are only  $r$  important features in data set  $A$ , while the rest are noise or redundant features. Aiming to create a new matrix of significantly lower dimension and less sparse in relation to the original matrix  $A$ , we reduce the square matrix  $\Sigma$ , retaining the top singular values. Hence, LSI requires a set parameter: the number of topics.

LDA is a soft clustering algorithm that is ideal for text. Given a set of documents, LDA models, the topics this set of documents may have been created from. LDA is a three-layer Bayesian model of words-documents-corpora. Each document is represented as a finite mixture of a set of latent topics and each topic is described by a distribution of words. It is closely related to probabilistic latent semantic indexing and the main difference is that LDA assumes that the topic distribution follows a sparse Dirichlet prior. The input for LDA consists of a document-word matrix  $DW$ , where  $DW_{ij}$  represents the frequency of word  $j$  in document  $i$ . LDA then produces a set of topics  $T$ , a topic-word matrix  $TW$ , and a document topic matrix  $DT$ .  $TW_{kj}$  specifies the probability of word  $j$  in topic  $k$ , while  $DT_{ik}$  represents the probability of topic  $k$  in document  $i$ . These probabilities are numeric values ranging between 0 and 1.

## 2.2 Feature Selection

Feature selection is a process in which a subset of the terms occurring in the training set are selected and used exclusively as features in text classification. Feature selection serves two main purposes. First, it makes classifier training and application more efficient by decreasing the size of the effective vocabulary. Second, feature selection often increases classification accuracy by eliminating noise features.

This study uses the Chi-square statistic ( $\chi^2$ ), which measures the independence of two variables in mathematical statistics. Given category  $c_k$  and feature  $t_i$ ,  $t_i$  owns significant category information if it has a high Chi ( $t_i, c_k$ ) value. The value of  $t_i$  is calculated as follows:

$$\begin{aligned}
Chi(t_i) &= \max_{c_k} \{Chi(t_i, c_k)\}, Chi(t_i, c_k) \\
&= \frac{N(a_{ik}d_{ik} - b_{ik}e_{ik})^2}{(a_{ik} + b_{ik})(a_{ik} + e_{ik})(b_{ik} + d_{ik})(e_{ik} + d_{ik})}.
\end{aligned} \tag{2}$$

Where  $N$  represents the total number of messages,  $a_{ik}$  represents the frequency that  $t_i$  and  $c_k$  co-occur,  $b_{ik}$  represents the frequency that  $t_i$  does not occur in  $c_k$ ,  $e_{ik}$  represents the frequency that class  $c_k$  occurs and does not contain feature  $t_i$ , and  $d_{ik}$  represents the frequency that neither  $c_k$  nor  $t_i$  occur.

### 2.3 t-SNE

T-distributed Stochastic Neighbour Embedding (t-SNE) is a machine learning algorithm for visualization. It is also a nonlinear dimensionality reduction technique well-suited for embedding high-dimensional data for visualization in a low-dimensional space of two or three dimensions. Specifically, it models each high-dimensional object with a two- or three-dimensional point in such a way that similar objects are modeled by nearby points and dissimilar objects are modeled by distant points with high probability. This algorithm is extensively applied in image processing, NLP, genomic data and speech processing.

## 3 Experimental results and analysis

The data used here is the British Broadcasting Corporation (BBC) news data set in the form of raw text documents, for a total of 2225 text files from the BBC news website corresponding to stories in five topical areas from 2004-2005. The text documents are arranged into 5 folders containing the class label (business, entertainment, politics, sports and technology) and each contains new articles related to that class label.

For the topic modeling and feature selection process, the separated words must be input, so the word data set must be segmented. The data set language is English, and all punctuation marks, numbers, the word segmentation can be completed only by spaces. In addition, stop words have been removed, therefore the words obtained in this step are all representative words, and these segmented texts become texts composed of discrete, disordered collections of word strings. Table 1 shows the top 10 feature words in descending order of weight in the topic model extracted by LSI. Table 2 shows the top 10 feature words in descending order of weight in the topic model extracted by LDA. Table 3 shows the top 10 feature words in descending order of weight extracted by Chi-square.

**Table 1.** Top 10 feature words by LSI.

technology	sports	politics	business	entertainment
People	win	labor	growth	film
company	play	elect	economic	award
Time	game	part	rate	star
Firm	match	Lib Dem	price	Oscar
government	England	tax	quarter	actor
Work	injuries	Dem	economy	actress
UK	champion	lib	rise	director
World	cup	conserve	fall	comedy
Plan	Ireland	chancellor	interest rate	movie
report	team	leader	bank	festival

**Table 2.** Top 10 feature words by LDA.

technology	sports	politics	business	entertainment
people	game	government	company	film
game	play	labor	market	award
mobile	win	elect	firm	music
technology	time	part	bank	star
phone	player	people	sale	show
service	England	plan	growth	actor
user	world	public	price	band
computer	match	tax	economic	song
music	team	lord	month	director
time	second	law	government	Oscar

**Table 3.** Top 10 feature words by Chi-square.

technology	sports	politics	business	entertainment
phone	season	Dem	stock	chart
device	championshi p	liber	economy	actress
online	team	prime	price	band
Microsoft	Chelsea	lib	market	album
digit	rugby	chancellor	analyst	singer
mobile	injury	secretary	economic	Oscar
software	champion	conserve	profit	actor
technology	coach	part	oil	award
computer	match	elect	growth	star
user	cup	labor	bank	film

In order to properly contrast LSA, LDA and Chi-square, we instead use a dimensionality-reduction technique called t-SNE, which will also serves to better illuminate the success of the clustering process. Now that these  $n$ \_topics-dimensional

vectors have been reduced to two-dimensional representations, we can plot the clusters. t-SNE clustering of LSI topics is shown in Fig. 1. t-SNE clustering of LDA topics is shown in Fig. 2. t-SNE clustering of Chi2 topics is shown in Fig. 3.

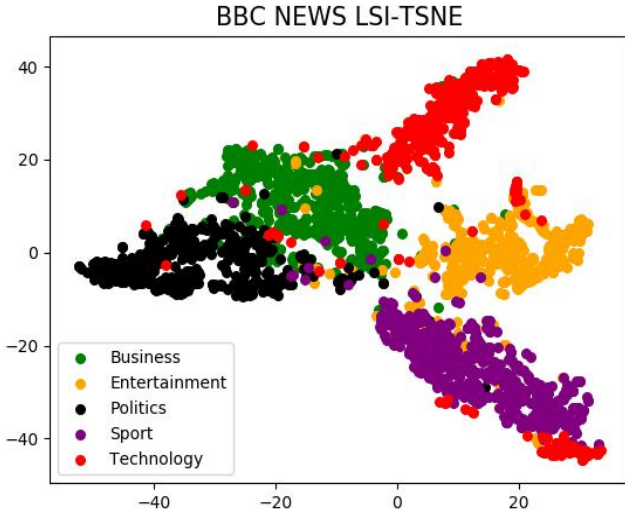


Fig. 1. t-SNE clustering of LSI topic.

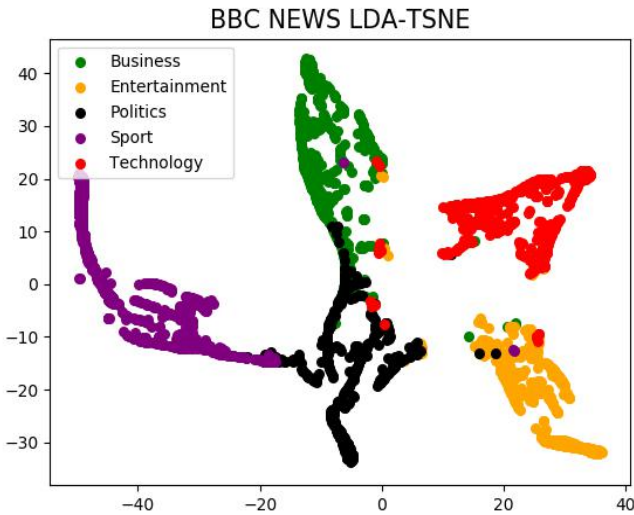
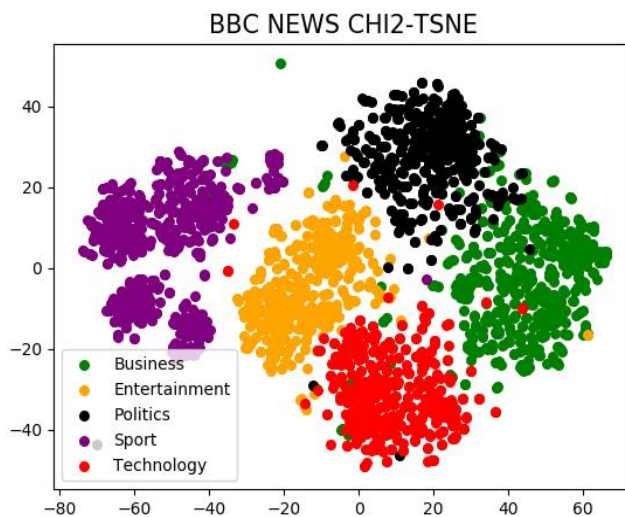


Fig. 2. t-SNE clustering of LDA topics.





**Fig. 3.** t-SNE clustering of Chi-square topics.

## References

1. Platos, J., Gajdos, P., Kromer, P., Snase, V.: Non-negative Matrix Factorization on GPU. Second International Conference 2010, Vol 87, pp. 21-30. Springer, Heidelberg(2010).
2. Berry, M., Browne, M.: Understanding Search Engines. Mathematical Modeling and Text Retrieval, Siam (1999).
3. Snasel, V., Gajdos, P., Abdulla, H.M.D., Polovincak, M.: Concept Lattice Reduction by Matrix Decompositins. DCCA (2007).
4. Blei, D.M., Ng, A.Y., Jordan, M.I.: Latent Dirichlet Allocation. Journal of Machine Learning Research, 3, 993-1022 (2003).
5. Chi2 Feature selection Homepage, <https://nlp.stanford.edu/IR-book/html/htmledition/feature-selectionchi2-feature-selection-1.html>.
6. Van der Maaten, L., Hinton, G.E.: Visualizing Data using t-SNE. Journal of Machine Learning Res.9, 2579-2605 (2008).
7. Platos, J., P., Kromer.: Prediction of Multi-class Industrial Data. International Conference on Intelligent Networking and Collaborative Systems 2013, pp.64-68. (2013)
8. Snasel, V., Nowakova, J., Xhafá, F., Barolli, L.: Geometrical and topological approaches to Big Data. Journal of Future Generation Computer Systems, 286-296 (2017).

## Publications

Yujia Sun, Jan Platoš: CAPTCHA Recognition Based on Kohonen Maps. INCoS(2019)

# Crowdsourcing-enhanced N-grams Algorithm for Text Document Classification

Petr Šaloun, David Andrešič, and Barbora Cigánková

Department of Computer Science, FEECS,  
VŠB – Technical University of Ostrava, 17. listopadu 15,  
708 33 Ostrava – Poruba, Czech Republic  
{petr.saloun, david.andresic, barbora.cigankova.st}@vsb.cz

**Abstract.** Classification is one of the most common tasks in a world of natural language processing. Although it is still performed best by human, there are applications where we prefer speed over perfect correctness of classification. This opens a space for natural language processing that transforms the text into a form understandable by some classifier, such as K-mean neighbor, Decision tree or Support Vector Machine. But we can still use the human element to improve the accuracy by means of crowdsourcing.

The aim of this work is to design and bring to the real world text document classifier based on N-grams classification algorithm with an interface allowing to evaluate and improve the classifier accuracy using crowdsourcing. Beside the data collection, it will also serve to evaluate classification accuracy and thus enlarge the classifier's training set.

We tested our approach on two data sets where it performed very well even across different languages. That led to a real-world application introduction at the beginning of 2019 in cooperation of two universities: VŠB-TUO and OU.

**Keywords:** classification, text documents, natural language processing, N-grams, crowdsourcing

## 1 Introduction

Despite the advance in text classification using Natural language processing (NLP), humans still perform best, which opens a space to a human-assisted classification (e.g. by means of crowdsourcing). In this work we describe our experiences and preliminary result with Czech text document classification. We also briefly summarize today text document classification (focused on Czech language) and the crowdsourcing and its advantages.

We tested our approach on two data sets and compared results with and without crowdsourcing. This work is also a continuation of our previous work [1].

## 2 Natural Language Processing and Algorithms Overview

During the process of text documents classification, following steps must usually be performed [2]:

- Removing stop words, tags and other pre-processing,
- Extraction of significant attributes from the text [2].

Today algorithms utilizes either stochaistic approaches or machine learning. *Naive Bayes Classifier* [3] has e.g. an advantage in high accuracy with small training data set. *Term Frequency-Inverse Document Frequency (TF-IDF)* is a statistic metric that measures an importance of words in the given document [4] [2]. *Latent Semantic Analysis (LSA)* is based on an analysis of relationships between sets of documents and their words [5][6]. *Support Vector Machines* is a method of machine learning based on an idea of decision planes [7][8]. *N-gram* is a tuple of items belonging to some sequence (e.g. words or letters) used (among others) for text document classification where the beginning and ending of a word is marked by a special character [9]. Its great advantage is the language independence because there is no pre-processing required and there is also some tolerance to typos and grammatical errors.

The whole NLP process has several phases [11]. One of the most important is morphological [10], syntactic and semantic analysis. Text processing usually requires some pre-processing as well: transformation to a lower case, removing of special characters, stop words and tokenization. There there is also stemming and lemmatization [12][13]. The Czech language is usually considered to be difficult language for processing. One of the very few usable frameworks for it is Apache Lucene<sup>1</sup> that contains Czech stop words, stemmer and tokenizer. Lemmatizer can be compensated by Majka [14].

### 2.1 Crowdsourcing

Can be defined as a way of work where the activity is outsourced to the crowd [15] as a general call [16]. Its basic idea is therefore the collective intelligence [17]. Pros and cons of this approach are summarized e.g. in [18]. Ways how to motivate the crowd then in [19].

## 3 Prototype and Preliminary Results

From all the available algorithms we eventually chose the N-grams with implementation based on [9] but with removing of stop words which allows to

<sup>1</sup> Apache Lucene: <https://lucene.apache.org>

begin in profile from the beginning of the list. Our classifier is also working with longer profiles due to psychological nature of our texts. Beside the classification, our classifier also determines key words of each class. Five of them with greatest weights are then recommended to selected users which should confirm our hypothesis about more accurate classification for those contributions with pre-defined key words. Calculations of key words are realized by TF-IDF algorithm modified for classes according to [20]. Errors in classification are corrected directly by users. Such contribution is then added to the training set.

*Language data set* contained texts in Czech, Slovak and English. Each class contained 40 texts with from 20 to 60 words. Both training and test set contained 20 texts for each class. The source of these texts was the DATAKON conference (2010, 2012, 2013 and 2014). Texts were of technological nature. Results can be seen in Tab. 1 and they exceeded our expectations for Czech and Slovak language. The language independence of the algorithm was confirmed.

*Psychological data set* contained less balanced and structured texts difficult to classify even for human. It contained 85 texts in categories like personal issues and illnesses (63), work, finance and school (8) and relationships, family and work (14). Training and test data were divided in 80:20 ratio. Results can be seen in Tab. 1. In each class was one incorrectly classified document. We suppose that it is caused by the nature of the text (the beginning of the document was describing a different topic) or marginal cases difficult to classify even by human.

**Table 1.** Classification accuracy for language and psychological data sets.

Language set		Psychological set	
Class	Accuracy	Class	Accuracy
English	20/20	Personal issues	12/13
Slovak	20/20	Work, finances, school	1/2
Czech	20/20	Relationships, family, employment	2/3

The topic of contributions in crowdsourcing interface was a *"life of non-formal caretakers and the influence of caretaking on it"* with following classes: *motivation, benefits and consequences, caretakers support and needs of caretakers*. Training set contained 180 texts with 2 sentences (at max.) in 4 classes. Contributions were added and evaluated by students of LF OU. Incorrectly classified were used to extend the training set. There were 8 contributions added (2 for each class) by a single author (which means similar dictionary). In first phase, one contribution was added which led to a zero accuracy caused by different nature in compare to training data. After the data synchronization, second phase with another contribution followed with accuracy 50%. Although we can

see an improvement in accuracy and learning of the classifier, we cannot make any conclusions from such small sample.

## 4 Conclusion

The main goal of this work was to create a prototype of text documents classifier based on N-grams algorithm with crowdsourcing interface for improving the accuracy. The first data set confirmed language independence of N-grams algorithm. Second (psychological) data set handled very well as well (it classified incorrectly only contributions difficult even for humans). Eventually, human assisted with classification which to extension of the training data set with formerly incorrectly classified documents. With respect to a small number of these texts we cannot make any conclusions although we can see some improvement. Further work will include a confirmation of hypothesis about increasing the accuracy by suggesting recommended key words and extension of the training set with formerly incorrectly classified documents. This work is closely related to our other work described in [21]. Here, we focused mostly on just N-grams algorithm and an implementation of crowdsourcing interface. Results led to a realization of the whole project in cooperation of two universities: VŠB-TUO and OU at the beginning of 2019 in a form of real-world application.

*Acknowledgements* The following grants are acknowledged for the financial support provided for this research: Grant of SGS No. SGS 2018/177, VSB-Technical University of Ostrava and TA ČR No. TL01000299.

## References

1. Šaloun, P., Andrešič, D., Cigánková, B.: Crowd Sourcing as an Improvement of N-Grams Text Document Classification Algorithm. In: Proc. of the 16th annual workshop WOFEX 2018 (2018).
2. KARMAN, S. Senthamarai; RAMARAJ, N. Similarity-Based Techniques for Text Document Classification. *Int. J. SoftComput*, 2008, 3.1: 58-62.
3. OPITKA, P.; ŠMAJSTRLA, V. "PRAVDĚPODOBŇOST A STATISTIKA," [In Czech] (Probability and statistics) 2013. [Online]. Available: <https://homen.vsb.cz/oti73/cdpast1/KAP02/PRAV2.HTM>. [Accessed on 4. 3. 2018].
4. "Tf-idf : A Single-Page Tutorial - Information Retrieval and Text Mining," [Online]. Available: <http://www.tfidf.com/>. [Accessed on 25. 12. 2017].
5. LANDAUER, Thomas K.; FOLTZ, Peter W.; LAHAM, Darrell. An introduction to latent semantic analysis. *Discourse processes*, 1998, 25.2-3: 259-284.
6. HÁJEK, Petr, et al. Možnosti využití přístupu indexování latentní sémantiky při předpovídání finančních krizí. *POLITICKÁ EKONOMIE*, [In Czech] (Possible use of indexed latent semantic approach for financial crisis prediction) 2009, 6: 755.
7. "Support Vector Machines (SVM)," TIBCO Software Inc, [Online]. Available: <http://www.statsoft.com/Textbook/Support-Vector-Machines>. [Accessed on 28. 12. 2017].

8. ŽIŽKA, J. "Studijní materiály předmětu FI:PA034," [In Czech] (Study materials to FI:PA034) [Online]. Available: [https://is.muni.cz/el/1433/podzim2006/PA034/09\\_SVM.pdf](https://is.muni.cz/el/1433/podzim2006/PA034/09_SVM.pdf). [Accessed on 29. 12. 2017].
9. CAVNAR, William B., et al. N-gram-based text categorization. *Ann arbor mi*, 1994, 48113.2: 161-175.
10. HABROVSKÁ, P. "Vybrané kapitoly z počítačového zpracování přirozeného jazyka," 2010. [In Czech] (Selected chapters from natural language processing) [Online]. Available: <http://www.inflow.cz/kratce-o-zpracovani-prirozeneho-jazyka>.
11. SCAGLIARINI, L.; VARONE, M. "Natural language processing and text mining," 11 April 2016. [Online]. Available: <http://www.expertsystem.com/natural-language-processing-and-text-mining/>. [Accessed on 15. 12. 2017].
12. KODIMALA, Savitha. Study of stemming algorithms. 2010.
13. RISUENO, T. "The difference between lemmatization and stemming," 28. 1. 2018. [Online]. Available: <https://blog.bitext.com/what-is-the-difference-between-stemming-and-lemmatization/>. [Accessed on 4. 3. 2018].
14. ŠMERK, P.; RYCHLÝ, P. "Majka – rychlý morfologický analyzátor," [In Czech] (Majka - quick morphological analyzer) 2009. [Online]. Available: <https://www.muni.cz/vyzkum/publikace/935762>. [Accessed on 15. 12. 2017].
15. ESTELLÉS-AROLAS, Enrique; GONZÁLEZ-LADRÓN-DE-GUEVARA, Fernando. Towards an integrated crowdsourcing definition. *Journal of Information science*, 2012, 38.2: 189-200.
16. SCHENK, Eric; GUITTARD, Claude. Crowdsourcing: What can be Outsourced to the Crowd, and Why. In: *Workshop on Open Source Innovation*, Strasbourg, France. 2009.
17. AITAMURTO, Tanja; LEIPONEN, Aija; TEE, Richard. The promise of idea crowdsourcing—benefits, contexts, limitations. *Nokia Ideasproject White Paper*, 2011, 1: 1-30.
18. KALSÍ, M. "Crowdsourcing through Knowledge Marketplace," 3. 3. 2009. [Online]. Available: [http://blog.spinact.com/knowledge\\_as\\_a\\_service/2009/03/crowdsourcing-through-knowledge-marketplace.html](http://blog.spinact.com/knowledge_as_a_service/2009/03/crowdsourcing-through-knowledge-marketplace.html). [Accessed on 2018 3. 4.].
19. KAUFMANN, Nicolas; SCHULZE, Thimo; VEIT, Daniel. More than fun and money. *Worker Motivation in Crowdsourcing-A Study on Mechanical Turk*. In: *AM-CIS*. 2011. p. 1-11.
20. VRL, NICTA. An unsupervised approach to domain-specific term extraction. In: *Australasian Language Technology Association Workshop 2009*. 2009. p. 94.
21. Andrešič, D., Ondrejka, A, Šaloun, P., Cepláková, R.: *Webový portál pro identifikaci poruchy osobnosti z psaného textu*. In: *Proc. of 12th Workshop on Intelligent and Knowledge oriented Technologies 2017* (2017).

# On the Particle Swarm Optimization Control

Lukáš Tomaszek

Department of Computer Science, FEECS,  
VŠB – Technical University of Ostrava, 17. listopadu 15,  
708 33 Ostrava – Poruba, Czech Republic  
lukas.tomaszek@vsb.cz

**Abstract.** In the present, many researchers study the metaheuristics algorithms. They try to analyze them and make them better. In our research, we are focusing on the control and metaheuristics algorithms. More specifically, we try to control the metaheuristics to increase their performance. In this article, the latest progress is reported. The study about the particle swarm optimization algorithm control is reviewed, and the latest results are shown here.

**Keywords:** particle swarm optimization algorithm, control, time delay auto synchronization, CEC 2014 benchmark, analytical programming

## 1 Introduction

In technology, we often deal with optimization tasks. Companies want to improve their processes, and each process can be understood as an optimization task in which we minimize the cost, or maximize the profit. These tasks are often very complex, and sometimes it is impossible to solve them by exact methods in a reasonable amount of time. For such tasks, metaheuristics can be used [5,15].

Today, there exist many metaheuristic algorithms like particle swarm optimization algorithm (PSO) [6], self-organizing migrating algorithm [1,22], differential evolution [14], and many others [2,21,20]. Also, researchers have been studying those algorithms and have improved their performance [3,7,17,19]. Each day, many new articles about the metaheuristics algorithms are presented, and also, there exist journals, which focuses on this topic only.

In our research, we are focusing on the combination of two different research area: metaheuristics and control. By control, we mean a process, where a system is controlled to the desired behavior. There exist many methods, conventional or unconventional, like time delay auto synchronization (TDAS) [9], extended time delay autosynchronization [10], control with analytical programming [11], or control with neural networks [8]. Our research tries to implement control into the metaheuristics algorithm, so it improves its performance.

This article reviews our recent research on the PSO control. In the following parts. Firstly the PSO is described. After, the PSO behavior is analyzed and controlled. In the end, the controlled and uncontrolled PSO is compared.

## 2 Particle swarm optimization algorithm

PSO was presented in 1995 by Eberhart and Kennedy [4]. Later, in 1998 Shi and Eberhart [12] added an inertia weight to this algorithm, but the velocity in this strategy the velocity may grow to infinity, so the maximal velocity restriction was added [13]. This is known as a standard PSO algorithm.

Before the algorithm starts, the parameters must be set. Parameters can be seen in Tab 1. After the parameters are set, the algorithm may start.

**Table 1.** PSO parameters

Parameter name	Remark
$w$	Controlling parameter
$c1$	Controlling parameter
$c2$	Controlling parameter
<i>Dimemsion</i>	Number of arguments in cost function
<i>ParticlesNumber</i>	Controlling parameter
<i>Iterations</i>	Stopping parameter

Firstly, the initial particles positions  $x$  are generated. The particles are generated randomly and distributed over the searching space according to equation

$$x_{i,j}^0 = r \cdot (x_{max,j} - x_{min,j}) + x_{min,j}, \quad (1)$$

where  $x_{i,j}^0$  is the value of  $i$ -th particle's  $j$ -th parameter at the beginning.  $r$  is a uniformly distributed random number from range  $(0, 1)$  and  $x_{max,j}$ ,  $x_{min,j}$  represent the maximal respectively the minimal value of the parameter  $j$ .

After, in each iteration, the particles are evaluated and the  $pBest_i$  and  $gBest$  positions are updated.  $pBest_i$  is the best found position by particle  $i$ .  $gBest$  is the global best-found position. The best position found by all particles. When the best positions are updated, the velocity  $v$  and a new particle position  $x$  is counted according to Eq. (2) respectively (3). This process is repeated until we reach the maximal number of iterations or the maximal number of function evaluations (MaxFEs).

$$v_{i,j}^{IT+1} = w \cdot v_{i,j}^{IT} + c_1 \cdot r_1 \cdot (pBest_{i,j} - x_{i,j}^{IT}) + c_2 \cdot r_2 \cdot (gBest_j - x_{i,j}^{IT}) \quad (2)$$

$$x_{i,j}^{IT+1} = x_{i,j}^{IT} + v_{i,j}^{IT} \quad (3)$$

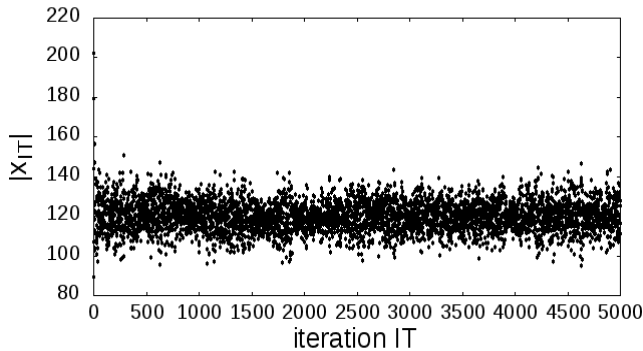
$x_{i,j}^{IT}$	The value of $i$ -th particle's $j$ -th parameter in iteration $IT$ .
$v_{i,j}^{IT}$	The velocity of $i$ -th particle's $j$ -th parameter.
$pBest_i$	The best found position by particle $i$ .
$gBest$	The best found position by all particles.
$r_1, r_2$	Uniformly distributed random numbers.
$c_1, c_2, w$	Controlling parameters.



In additional, the velocity is restricted to the interval  $(-v_{max}, v_{max})$ . This ensure that the velocity will not grow to infinity. If the counted velocity is greater or lower than  $v_{max}$ ,  $v_{max}$  respectively  $-v_{max}$  is used.

### 3 Particle analysis

The simplest analysis we can make is the change of the particle position. In other words, how the particle moves in the search space. Does in converge to a single point, or does the particle oscillate? The behavior of one particle, we can see in Fig. 1. Since the optimization tasks are multidimensional, we represent the position of the particle as a distance from the origin.



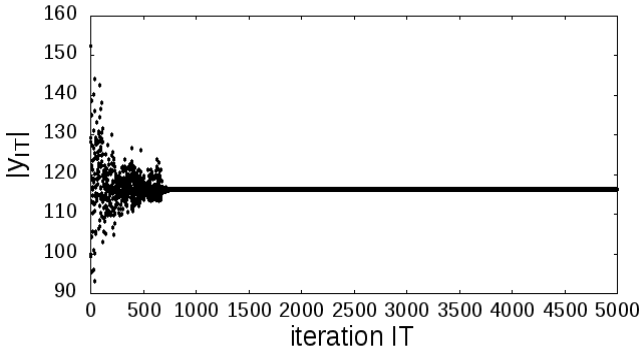
**Fig. 1.** Evolution of the vector size which represents a particle position

As we can see, the particle oscillates. This phenomenon is well known for PSO. With this behavioral, the particles never converge to a single point. They will oscillate, and algorithm performs exploitation more than exploration. Also, we do not know when the algorithm ends. Does the algorithm already find the best solution, or will it find a better solution later?

The behavior, we want to reach, may looks like on Fig. 2. The particle performs the search and converges to a single point, so we know that the algorithm ends.

### 4 Particle Swarm Optimization Control

In [16], we use the analytical programming [23] for the creation of the control equation, and several equations were found. The examples, we can see bellow, (4) - (7). All equations were capable to control the particle into the desired state, but the most interesting is (5). This equation is the same as TDAS control, so it was used in the next research.



**Fig. 2.** Required behavior of the particle

$$(x^{IT-1} - x^{IT}) \cdot k, \text{ where } k = 0.2487 \tag{4}$$

$$x^{IT-1} - x^{IT} + k, \text{ where } k = 0.1601 \tag{5}$$

$$x^{IT-1} - x^{IT} + \frac{1}{x^{IT}} + k, \text{ where } k = 0.1676 \tag{6}$$

$$\frac{2 \cdot x^{IT-1}}{x^{IT} - k_1} (x^{IT-1} - x^{IT}) \cdot k_2, \text{ where } k_1 = 0.4053, k_2 = 0.2838 \tag{7}$$

## 5 Controlled Particle Swarm Optimization Algorithm

Based on [16], we proposed a novel controlled PSO algorithm in [18]. The control was applied to all particles, so they all try to reach one periodical behavior as soon as possible. In the ideal condition, this point will be a global optimum. The main change is in application of control to a position update. See (8). The mark  $c$  represents the control input given by the (4).

$$x_{i,j}^{IT+1} = x_{i,j}^{IT} + v_{i,j}^{IT} + c \tag{8}$$

As it was reported in [18], based on the comparison on the CEC 2014 benchmark functions, the novel controlled PSO is significantly better than standard PSO. The novel controlled PSO converge faster, and reaches similar or statistically better results than standard PSO. In fact, with the inertia weight set to 0.9 the controlled PSO found statistically better results on 25 out of 25 functions, and with inertia weight set to 0.7 the controlled PSO found statistically better results on 13 out of 25 functions and were worst only on 2 functions out of 25, but on the functions, where the results were same, the controlled PSO found the final result during fist 100 000 FEs, and the standard PSO needs 500 000 FEs.

## 6 Conclusion

Till now, all articles mainly present the novel idea about the control, and how we can look at the metaheuristics from a different perspective. This area seems to be promising, and according to our knowledge, nobody looks at the metaheuristics from the control view.

In this article, we mainly wanted to report the progress about the control of the metaheuristics algorithms during last year. Since now, we were capable to apply the control to a standard PSO algorithm and improve its performance, but the novel algorithm still needs some improvement to overperform the up to date algorithms. For example, the novel algorithm converges very fast, so the population reset may increase the performance. Also, the switching between the control and uncontrol may be applied, but this will be the main tasks of our future research.

## References

1. Davendra, D., Zelinka, I., et al.: Self-organizing migrating algorithm. New optimization techniques in engineering (2016)
2. Davis, L.: Handbook of genetic algorithms (1991)
3. Diep, Q.B., Zelinka, I., Das, S.: Self-organizing migrating algorithm pareto. In: MENDEL. vol. 25, pp. 111–120 (2019)
4. Eberhart, R., Kennedy, J.: A new optimizer using particle swarm theory. In: Micro Machine and Human Science, 1995. MHS'95., Proceedings of the Sixth International Symposium on. pp. 39–43. IEEE (1995)
5. Glover, F.W., Kochenberger, G.A.: Handbook of metaheuristics, vol. 57. Springer Science & Business Media (2006)
6. Kennedy, J.: Particle swarm optimization. Encyclopedia of machine learning pp. 760–766 (2010)
7. Lynn, N., Suganthan, P.N.: Heterogeneous comprehensive learning particle swarm optimization with enhanced exploration and exploitation. Swarm and Evolutionary Computation 24, 11–24 (2015)
8. Miller, W.T., Werbos, P.J., Sutton, R.S.: Neural networks for control. MIT press (1995)
9. Pyragas, K.: Continuous control of chaos by self-controlling feedback. Physics letters A 170(6), 421–428 (1992)
10. Pyragas, K.: Control of chaos via extended delay feedback. Physics letters A 206(5-6), 323–330 (1995)
11. Šenkeřík, R., Oplatková, Z., Zelinka, I., Jašek, R.: Application of analytic programming for evolutionary synthesis of control law—introduction of two approaches. In: Advances in Intelligent Modelling and Simulation, pp. 253–268. Springer (2012)
12. Shi, Y., Eberhart, R.: A modified particle swarm optimizer. In: Evolutionary Computation Proceedings, 1998. IEEE World Congress on Computational Intelligence., The 1998 IEEE International Conference on. pp. 69–73. IEEE (1998)
13. Shi, Y., Eberhart, R.C.: Parameter selection in particle swarm optimization. In: International conference on evolutionary programming, pp. 591–600. Springer (1998)
14. Storn, R., Price, K.: Differential evolution—a simple and efficient heuristic for global optimization over continuous spaces. Journal of global optimization 11(4), 341–359 (1997)

15. Talbi, E.G.: *Metaheuristics: from design to implementation*, vol. 74. John Wiley & Sons (2009)
16. Tomaszek, L., Chadli, M.: On the particle swarm optimization control using analytic programming and self organizing migrating algorithm. In: 2019 IEEE Congress on Evolutionary Computation (CEC). IEEE (2019)
17. Tomaszek, L., Zelinka, I., Chadli, M.: On the leader selection in the self-organizing migrating algorithm. In: MENDEL. vol. 25, pp. 171–178 (2019)
18. Tomaszek, L., Zelinka, I., Chadli, M.: On the particle swarm optimization improvement using time delay auto synchronization. In: 2019 IEEE 58th Conference on Decision and Control (CDC). IEEE (2019)
19. Xu, G., Cui, Q., Shi, X., Ge, H., Zhan, Z.H., Lee, H.P., Liang, Y., Tai, R., Wu, C.: Particle swarm optimization based on dimensional learning strategy. *Swarm and Evolutionary Computation* 45, 33–51 (2019)
20. Yang, X.S.: Firefly algorithm, stochastic test functions and design optimisation. arXiv preprint arXiv:1003.1409 (2010)
21. Yang, X.S., Deb, S.: Cuckoo search via lévy flights. In: 2009 World Congress on Nature & Biologically Inspired Computing (NaBIC). pp. 210–214. IEEE (2009)
22. Zelinka, I.: Soma—self-organizing migrating algorithm. In: *New optimization techniques in engineering*, pp. 167–217. Springer (2004)
23. Zelinka, I., Davendra, D., Senkerik, R., Jasek, R., Oplatkova, Z.: Analytical programming—a novel approach for evolutionary synthesis of symbolic structures. In: *Evolutionary algorithms*. IntechOpen (2011)

# Comparison of range query performance for UB-tree and R-tree

Lukáš Zátopek and Michal Krátký

Department of Computer Science, FEECS,  
VŠB – Technical University of Ostrava, 17. listopadu 15,  
708 33 Ostrava – Poruba, Czech Republic  
{lukas.zatopek, michal.kratky}@vsb.cz

**Abstract.** In this article, we review the UB-tree – a multidimensional data structure. This data structure utilizes a space filling curve called the Z-curve together with a linear data structure called the B-tree. Since regions of the UB-tree are not overlapped, it can be a good alternative to the well-known R-tree. As a result, we depict a preliminary comparison of both data structures where mainly the performance of range query algorithms are compared.

**Keywords:** UB-tree, BUB-tree, space filling curve, Z-curve, Z-address, Z-region, multidimensional indexing, B-tree, range query

## 1 Introduction

The multidimensional range query or k-NN query [6] over multidimensional data are utilized in some applications [4]. Although a lot of multidimensional data structures supporting these queries have been introduced in last decades, only some of them are utilized in practise, for example the *R-tree* (introduced in [3] by Antonin Guttmann). Since there are some weak points of the R-tree, for example the overlapping of minimal bounding rectangles, other data structures try to improve the weak points. The Universal *B-tree* (UB-tree) introduced in [2] by Rudolf Bayer is one of them. For this purpose, it uses the well known *B-tree*, introduced in [1] by Rudolf Bayer and Edward M McCreight, together with a space filling curve called the *Z-curve* [5]. In this way there is an ordering of all points in the discrete multidimensional space, i.e. we can compute an order of each point using *Z-address*.

The goal of this article is to describe properties of the UB-tree and to compare the UB-tree with the R-tree. In Section 2 we briefly compare both trees. We present the range query algorithm. We describe the *Z-address* and its properties as well as *Z-region*. Section 3 depicts a comparison of *UB-tree* and *R-tree* data structures. In last section we conclude with directions of our future work.

## 2 The UB-tree

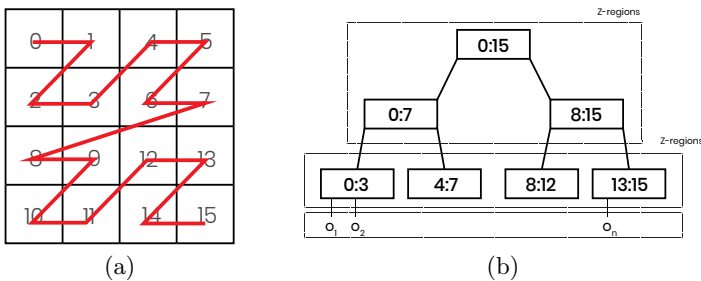
### 2.1 Introduction

The *UB-tree* utilizes a linear data structure, the *B-tree*, to index a multidimensional data. The data are linearized into one dimension within aid of space filling curve, called the *Z-curve*. The *Z-curve* produces the *Z-address*.

The *Z-address* is represented as a binary string computed with a bit interleaving algorithm where each tuple value is iterated bit by bit. Table 1 depicts the calculation of *Z-address*. The *Z-address* provides an information about a position in a space. If a bit is set to 0 then it is situated at the lower half of domain. Whereas 1 bit indicates localization in the upper half of domain. The *Z-address* represents a point in space space and in conjunction with the *UB-tree* is represented at leaf level.

Inner node is represented as *Z-region* which is in fact, an interval. The *Z-region* is determined by two bounding points (*Z-addresses*). The lower bound is denoted as *Alpha*, whereas the upper bound is denoted as *Beta*. The *Z-regions* divide a space into the partitions which create hierarchy of nested *Z-regions*. Thus the root node of the UB-tree represents the whole space whereas items of leaf node represent tuples.

In Figure 1, a 2-dimensional space  $4 \times 4$  filled with the Z-curve and the related UB-tree are shown.



**Fig. 1.** (a) Two dimensional space  $4 \times 4$  filled with Z-curve. (b) The UB-tree nodes create a hierarchy of the Z-regions. Indexed object are at leaf level.

### 2.2 Range Query Algorithm

The range query retrieves all tuples of a multidimensional space in a query hyper rectangle. The query hyper rectangle is defined as an interval which consists of two bounding points denoted as  $Q_{low}$ ,  $Q_{high}$ , where  $Q_{low}$  needs to be lower than  $Q_{high}$ . We need to traverse through the whole tree from the root to it's leaves.

**Table 1.** Calculation of the Z-address for 2-dimensional point [4,9]

The navigation code		
Dimension	Number	Bit representation
0	4	0100
1	9	1001
Z-address		
01100001		

In each item (Z-region) of an inner node, it is necessary to compute whether the region is intersected with the query rectangle. We call such an algorithm as the linear or exponential intersection algorithm. In each tuple of a leaf node, we test whether the tuple is in the query hyper rectangle. The result is a list of all items (Z-addresses) which have an intersection with the query box. Let us show a general range query algorithm for the UB-tree:

*input:* A query box  $qb$

*output:* The result of tuples retrieved from the UB-tree

1. Node  $n \leftarrow$  the root node.
2. Iterate all items of  $n$ .
  - (a) If  $n$  is an inner node, do the following:
    - If an item (Z-region) is intersected by  $qb$ , store the node index and the item on a stack. Continue with the node referenced with the item, go to Step 2.
  - (b) If  $n$  is a leaf node, do the following:
    - If an item (Z-address) is in  $qb$ , add the item in the result.
    - Pop the node index from the stack and continue with the node, go to Step 2.
3. Finish the algorithm as soon as the stack is empty.

The core algorithm of the range query algorithm is the intersection of Z-region and query rectangle. In original papers [2] this algorithm is not sufficiently described. In [7], a new range query algorithm is introduced, authors describe two algorithms: linear and exponential. Both algorithms are based on a comparison of Z-addresses and Z-region. The linear algorithm brings a significant improvement over the exponential one: it tries to merge individual semi-results of the computation into groups. As a result, the amount of generated semi-results is significantly lower.

### 2.3 An example

Let us have a Z-region where the first point called *alpha* is determined by [21,4], whereas the last point called *beta* is determined by [18,13]. We calculate Z-addresses for these points. We find the minimum amount of hyper quadrants [7]

for the *Z-region* which need to be tested if any of them have an intersection with query box.

In Table 2, we show results of linear and exponential algorithms for the *Z-region*. Both algorithms produce a different number of navigation codes. The navigation code is a geometric representation of *Z-address*, thus these terms are therefore equivalent. The upper group represents those navigation codes which have lower navigation code than *Beta* bound, whereas the lower group represent those which have higher navigation code than *Alpha* bound. The entirely between group represents all navigation codes which lie between the bounds. If we inspect the results of both algorithms, we see that the linear algorithm merges the multiple results into the one, hence the name reduced group. When the space dimension is higher, the reduction is higher.

**Table 2.** Examples of results for linear and exponential intersection algorithms

Results comparison	
Reduced upper group	Upper group
01 1X	
01 00 11 1X	01 00 11 10 01 00 11 11
01 00 11 01	01 00 11 01
01 00 11 00 1X	01 00 11 00 10 01 00 11 00 11
01 00 11 00 01	01 00 11 00 01
Reduced lower group	Lower group
01 0X	
01 10 0X	01 10 00 01 10 01
01 10 10 00	01 10 10 00
01 10 10 01 0X	01 10 10 01 00 01 10 10 01 01
01 10 10 01 10	01 10 10 01 10
Reduced upper group	Entirely between
01 01	01 01

Let us note that the linear algorithm generates 2 navigation codes which do not have a couple within the exponential algorithm. We remove those navigation codes because we want two disjoint sets. Thus, navigation codes 01|1X and 01|0X are removed. In general, the linear algorithm generates 9 navigation codes whereas the exponential algorithm generates 13 navigation codes.



### 3 Experiments

In our experiments, we compare the range query performance of the UB-tree and R\*-tree. We use the highly selective range queries with the result set including one tuple. The linear intersection algorithm is used in the UB-tree. The average processing times of the range queries are depicted in Table 3.

**Table 3.** Range query performance

Range query processing time		
<b>R-tree</b>		
<b>Dimension</b>	<b>Avg. time [s]</b>	<b>Tuples count</b>
6	0,0098	500 000
12	0,2	
18	0,37	
24	0,4	
<b>BUB-tree</b>		
<b>Dimension</b>	<b>Avg. time [s]</b>	<b>Tuples count</b>
6	1,2	500 000
12	21,2	
18	23,75	
24	37,54	

Evidently, the range query algorithm of the R-tree is more efficient than the algorithm of the UB-tree. We have found out that one of the main problem of such a poor performance of the UB-tree is the frequent calculation of the Z-addresses. Consequently, it is necessary to use an improved version of the algorithm. Preliminary results of the algorithm are shown in Table 4.

**Table 4.** Comparison of two Z-address calculation algorithms

Processing time of Z-address calculation for 500 000 tuples (ms)				
<b>Dimension:</b>	<b>4</b>	<b>8</b>	<b>16</b>	<b>32</b>
<b>Dimension:</b>	<b>4</b>	<b>8</b>	<b>16</b>	<b>32</b>
Bit-interleaving	725	1274	2544	5103
Improved algorithm	62	209	676	2309

## 4 Conclusion and future plans

The results clearly show that the performance of the range query algorithm for the BUB-tree is lower than for the well-known R-tree. After the performance testing, we found out that the performance problem is not an intersection algorithm, but the frequently used transformation of a Z-address to an Euclidean tuple. Moreover, we want to apply some optimizations of the UB-tree range query algorithm.

## References

1. R. Bayer and E. McCreight. Organization and Maintenance of Large Ordered Indices. In *Proceedings of the 1970 ACM SIGFIDET (Now SIGMOD) Workshop on Data Description, Access and Control*, SIGFIDET '70, pages 107–141, New York, NY, USA, 1970. ACM.
2. Rudolf Bayer. The universal B-tree for multidimensional indexing: General concepts. In Takashi Masuda, Yoshifumi Masunaga, and Michiharu Tsukamoto, editors, *Worldwide Computing and Its Applications*, pages 198–209, Berlin, Heidelberg, 1997. Springer Berlin Heidelberg.
3. Antonin Guttman. R-trees: A Dynamic Index Structure for Spatial Searching. In *Proceedings of the 1984 ACM SIGMOD International Conference on Management of Data*, SIGMOD '84, pages 47–57, New York, NY, USA, 1984. ACM.
4. Dinesh P. Mehta and Sartaj Sahni. *Handbook Of Data Structures And Applications (Chapman & Hall/Crc Computer and Information Science Series.)*. Chapman & Hall/CRC, 2004.
5. G. M. Morton. A computer oriented geodetic data base and a new technique in file sequencing. Technical report, IBM, Ottawa, Canada, 1966.
6. Hanan Samet. *Foundations of multidimensional and metric data structures*. Elsevier/Morgan Kaufmann, 2006.
7. Tomáš Skopal, Michal Krátký, Jaroslav Pokorný, and Václav Snášel. A new range query algorithm for Universal B-trees. *Information Systems*, 31:489–511, 09 2006.

# Mountain pass algorithm for boundary value problems with $p$ -Laplacian

Michaela Bailová

Department of Applied Mathematics, FEECS,  
VŠB – Technical University of Ostrava, 17. listopadu 15,  
708 33 Ostrava – Poruba, Czech Republic  
michaela.bailova@vsb.cz

**Abstract.** Many engineering problems lead to finding critical points of nonlinear functionals. If the functional has a certain geometry, we can use mountain pass theorem to prove the existence of its nontrivial critical points. We focus on some specific quasilinear boundary value problems with  $p$ -Laplacian. The approach introduced here is based on the fact that the process of solving such problems coincide with finding critical points of corresponding functionals with mountain pass geometry. In the paper, we formulate alternative version of the mountain pass theorem. Subsequently, we introduce an algorithm and analyze its theoretical background. We use the algorithm for finding solutions of a given problem.

**Keywords:**  $p$ -Laplacian operator, quasilinear elliptic PDE, critical point, Mountain Pass Theorem, mountain pass algorithm

## 1 Introduction

Many engineering problems lead to finding critical points of nonlinear functional. Our research is focused on functionals with certain geometry. The approach introduced in this paper is based on the fact that we can use so called Mountain pass theorem to prove the existence of critical points of such functionals.

In this paper, we study the quasilinear elliptic boundary value problem with  $p$ -Laplacian operator

$$\begin{cases} -\Delta_p u = u^3 & \text{in } \Omega, \\ u = 0 & \text{on } \partial\Omega, \end{cases} \quad (1)$$

where

$$\Delta_p u = \operatorname{div}(|\nabla u|^{p-2} \nabla u),$$

$\Omega$  is a bounded domain in  $\mathbb{R}^2$  with Lipschitz boundary and  $p \in (\frac{4}{3}, 4)$ . Let us note that, if we take  $p = 2$ , (1) turns into a well known problem with classical Laplace operator. The approach introduced here is based on the fact that the process of solving (1) correspond to finding critical points of the following functional

$$J(u) = \frac{1}{p} \int_{\Omega} |\nabla u|^p \, dx - \frac{1}{4} \int_{\Omega} u^4 \, dx. \quad (2)$$

As it was shown in [2], we can prove the existence of nontrivial critical points. The recent research aims on appropriate numerical algorithm. We pay the highest attention to the analytical background of the algorithm. Consequently, we use it to compute numerical solutions.

## 2 Analytical background

In WOFEX 2018, we used classical version of the mountain pass theorem to prove the existence of nontrivial critical points.

Let us now introduce a different approach, inspired by [4], exploiting the geometry of (1). Instead of a set of curves connecting 0 and  $e$ , we can consider all rays with the initial point at the origin. Each ray is determined by a vector  $w$ . Let us first define  $\bar{c}$  as a minimax value over all rays with the origin in 0, i.e.

$$\bar{c} := \inf_{\substack{w \in W_0^{1,p}(\Omega) \\ w \neq 0}} \max_{t \geq 0} J(tw). \quad (3)$$

. It can be shown that the value  $\bar{c}$  is well defined. The most important output of our recent research is the following theorem that provides some alternative version of the classical mountain pass theorem.

**Theorem 1.** *The value  $\bar{c}$  is the critical value of  $J$ , i.e. there exists  $w \in W_0^{1,p}(\Omega)$  such that*

$$\begin{aligned} J(w) &= \bar{c}, \\ \langle J'(w), v \rangle &= 0 \quad \forall v \in W_0^{1,p}(\Omega). \end{aligned}$$

*Proof.* The proof of 1 will be published in a paper that is currently in progress.

## 3 Numerical algorithm

The algorithm introduced here is based on the approach introduced above. Let us now briefly summarize the steps of the algorithm. At the beginning, an arbitrary nonzero vector  $w$  is chosen. Then, the algorithm finds  $t^* > 0$  such that

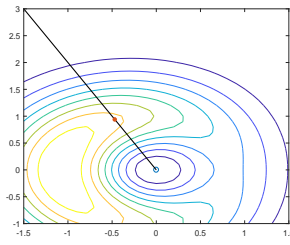
$$J(t^*w) = \max_{t > 0} J(tw)$$

and sets  $w_1 = t^*w$ . This step is called the maximization.

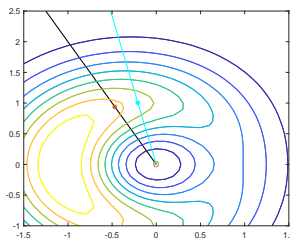
If  $\|\nabla J(w_1)\| \leq \varepsilon$ , where  $\varepsilon$  is a desired tolerance, the algorithm returns  $w_1$  and stops.

Otherwise, the algorithm moves  $w_1$  in the descent direction  $v$  until the value of  $J$  is reduced. This step is called the minimization.

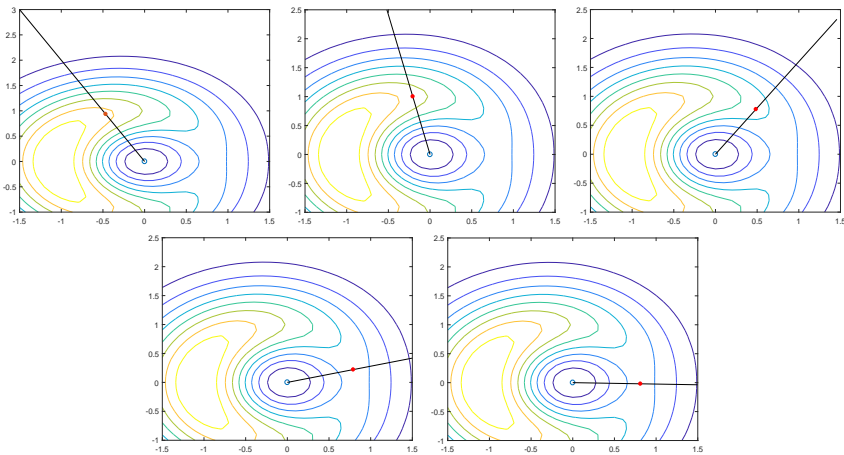
In the figure 3, we can see the iterations of the algorithm for the function  $f(x, y) = (x^2 + y^2)e^{1-x^2-y^2}(2-x)$ .



**Fig. 1.** Maximization



**Fig. 2.** Minimization



**Fig. 3.** The first iterations and a result

### 3.1 Descent direction

The choice of  $v$  is not difficult if  $p = 2$ , the space  $W_0^{1,2}(\Omega)$  is a Hilbert space, so we can take  $v = \frac{\nabla J(w_1)}{\|\nabla J(w_1)\|_{1,2,0}}$ , where

$$\|w\|_{1,2,0} = \left( \int_{\Omega} |\nabla w|^2 \, dx \right)^{\frac{1}{2}}.$$

If  $p \neq 2$ , the situation is more complicated. The way how to choose the descent direction is also a subject of our research and will appear in the prepared paper. Let us show the main idea for  $p = 2$ . Finding the steepest descent direction is similar to finding  $v_0 \in W_0^{1,2}(\Omega)$

$$\langle J'(u), v_0 \rangle = \max_{v \in W_0^{1,2}(\Omega), \|v\|_{1,2,0}=1} \langle J'(u), v \rangle. \tag{4}$$

Note that

$$\langle J'(u), v \rangle = \int_{\Omega} \nabla u \nabla v \, dx - \int_{\Omega} u^3 v =: F(u) \in \left( W_0^{1,2}(\Omega) \right)^*.$$

From the Riesz theorem,  $(\exists! w_0 \in W_0^{1,2}(\Omega)) (\forall v \in W_0^{1,2}(\Omega))$ :

$$\langle J'(u), v \rangle = \int_{\Omega} \nabla u \nabla v \, dx - \int_{\Omega} u^3 v = (w_0, v) = \int_{\Omega} \nabla w_0 \nabla v \, dx. \tag{5}$$

Thus,  $w_0$  can be computed as a solution of the following linear elliptic equation

$$\begin{cases} \Delta w_0 = \Delta u + u^3 & \text{in } \Omega \\ w_0 = 0 & \text{on } \partial\Omega. \end{cases} \tag{6}$$

The equation can be solved using finite element method. Let us now focus on the choice of  $v_0$ . From (5) and the properties of the inner product, we get

$$\max_{v \in V_0^h(\Omega), \|v\|_{1,2,0}=1} \langle J'(u), v \rangle = \max_{v \in V_0^h(\Omega), \|v\|_{1,2,0}=1} (w_0, v) = (w_0, \frac{w_0}{\|w_0\|_{1,2,0}}).$$

In other words, for each  $u \in W_0^{1,2}(\Omega)$ , we can take  $v_0 = -\frac{w_0}{\|w_0\|_{1,2,0}}$  and get a steepest descent direction.

If  $p \neq 2$ , we can use similar ideas, but the process is more complicated. A way how to find a descent direction, is also an object of our research.

## 4 Numerical experiments

Thanks to the research on the choice of the descending direction for  $p$  different from 2, we made some improvement of the algorithm itself. Due to the behavior of the solutions, we chose the appropriate  $L_p$  norm

$$\|w\|_p = \left( \int_{\Omega} |w|^p \, dx \right)^{\frac{1}{p}}$$

to measure the numerical error. To approximate the value of  $\Delta_p u(x_{ij})$ , we use the following formulas:

$$\nabla u(x_{ij}) = \left( \frac{u(x_{(i+1)j}) - u(x_{(i-1)j})}{2h}, \frac{u(x_{i(j+1)}) - u(x_{i(j-1)})}{2h} \right) =: (g_1(x_{ij}), g_2(x_{ij})),$$

$$\Delta_p u(x_{ij}) = |\nabla u(x_{ij})|^{p-2} \left( \frac{g(x_{(i+1)j}) - g(x_{(i-1)j})}{2h} + \frac{g(x_{i(j+1)}) - g(x_{i(j-1)})}{2h} \right).$$

We compute the elements of a vector  $\Delta_p u_{ij} + u_{ij}^3$ .

In the tables 1, 2, we can see the results for the desired precision  $\varepsilon = 10^{-4}$ . The discretization step in the first table was, due to the limits of the computer, set to  $h = \frac{1}{64}$ .

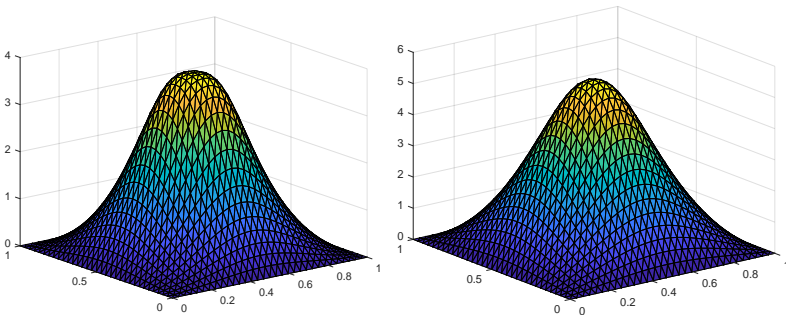
**Table 1.** Results for various  $p$

$p$	$\ \Delta_p u + u^3\ _p$	$J(u)$	it
$\frac{3}{2}$	0.008966	4.873499	315
$\frac{11}{6}$	0.003284	4.111440	9
$\frac{7}{3}$	0.007015	3.468336	12
3	0.042863	4.168312	65

**Table 2.** Results for various  $h$

$p$	$\ \Delta_p u + u^3\ _p$			
	$h = \frac{1}{40}$	$h = \frac{1}{60}$	$h = \frac{1}{80}$	$h = \frac{1}{100}$
$\frac{3}{2}$	0.022477	0.013102	0.008967	0.006686
$\frac{11}{6}$	0.010294	0.005182	0.003284	0.002347
$\frac{7}{3}$	0.016374	0.009712	0.007015	0.005565
3	0.072862	0.053032	0.042863	0.036525

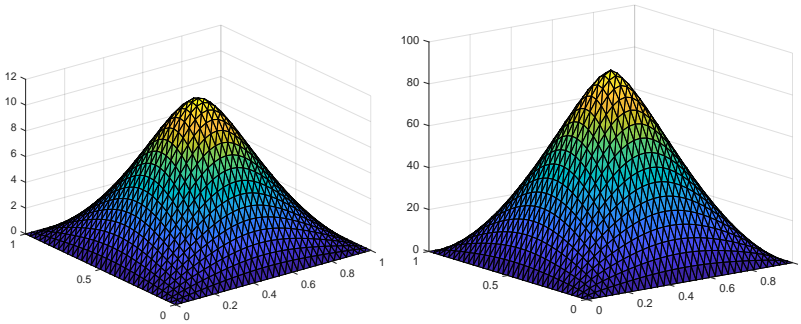
The result of the algorithm can be seen in the figure 4.



**Fig. 4.** Solution for  $p = \frac{3}{2}$  and  $p = \frac{11}{6}$ .

## 5 Conclusion

Our recent research is mainly focused on formulation of the ideas and proofs mentioned here. Another goal is to develop the alternative version of the moun-



**Fig. 5.** Solution for  $p = \frac{7}{3}$  and  $p = 3$ .

tain pass theorem introduced here and find some general assumptions of the theorem. Moreover, we will concentrate on the problem of descent directions for  $p$  different from 2. Consequently, we will develop the theory and the algorithm presented in this paper and focus on more general problems with the mountain pass geometry

$$\begin{cases} -\Delta_p u = f(x, u(x)) & \text{in } \Omega, \\ +\text{boundary conditions on } \partial\Omega, \end{cases} \tag{7}$$

where  $f : \mathbb{R}^2 \rightarrow \mathbb{R}$  is a function that is nonlinear with respect to  $u$ . There are also many approaches how to improve the algorithm that can be used and combined with respect to the problem.

Then, we can focus on saddle point problems, the analytical background and appropriate algorithms.

## References

1. Ambrosetti, A., Rabinowitz, P.H.: Dual variational methods in critical point theory and applications. *Journal of Functional Analysis* 14(4), 349 – 381 (1973)
2. Bailová, M.: Quasilinear boundary problem with p-laplacian. *Proceedings of Wofex 2018*
3. Bisgard, J.: On mountain pass type algorithms. *Nonlinear Differential Equations and Applications NoDEA* 20(4), 1499–1518 (Aug 2013)
4. Ding, Z., Costa, D., Chen, G.: A high-linking algorithm for sign-changing solutions of semilinear elliptic equations. *Nonlinear Analysis: Theory, Methods and Applications* 38(2), 151 – 172 (1999)
5. H Rabinowitz, P.: *Minimax methods in critical point theory with applications to differential equations* 65 (01 1986)
6. Haim, B., Louis, N.: Remarks on finding critical points. *Communications on Pure and Applied Mathematics* 44, 939–963
7. Jabri, Y.: *The Mountain Pass Theorem: Variants, Generalizations and Some Applications*. *Encyclopedia of Mathematics and its Applications*, Cambridge University Press (2003)
8. Willem, M.: *Minimax theorems*. Birkhauser, Boston (1996)



# Modeling hydro-mechanical processes in fractured porous media

Michal Bérés<sup>1,2</sup> and Radim Blaheta<sup>2</sup>

<sup>1</sup>Department of Applied Mathematics, FEECS,  
VŠB – Technical University of Ostrava, 17. listopadu 15,  
708 33 Ostrava – Poruba, Czech Republic

<sup>2</sup>Institute of Geonics of the CAS,  
Studentská 1768, 708 00 Ostrava-Poruba, Czech Republic  
`michal.beres@vsb.cz`

**Abstract.** This contribution describes recent development and implementation of two finite element numerical models: mechanical deformation of an elastic body with fractures and the flow in saturated fractured porous media with fractures. Both models share one mesh of a domain with a fracture network. We consider an iterative coupling of these models, as the hydro-mechanical coupling is important in many applications. The key issue in the modeling of mechanical response is the choice of contact conditions in fractures and the numerical realization ensuring these conditions. The resulting contact problem is solved using the FETI method and the SMALSE algorithm. Resulting values of fracture aperture serve as an input to the hydraulic model. The numerical model of the saturated flow uses an extra mesh for fractures, which are modeled as lower-dimensional objects. The coupling between the flow in the fractures and the porous matrix is realized via suitable Robin boundary conditions. Calculated pore and fracture pressure are then used as an input to the mechanical model.

**Keywords:** Hydro-Mechanical coupled model, fractured porous environment, contact mechanics

## 1 Hydro-mechanical stationary model

We consider the following model

$$-\nabla \cdot (k\nabla p) = s \text{ in } \Omega, \quad (1)$$

$$-\operatorname{div}(C : \varepsilon(u)) + \alpha_B \nabla p = f \text{ in } \Omega. \quad (2)$$

Equation (1) describes the flow in saturated porous media  $\Omega$  with the pore pressure  $p$ , hydraulic conductivity  $k$  and the source term  $s$ . The deformation of  $\Omega$  is described by the elasticity equation (2) with the displacement  $u$ , the small strain tensor  $\varepsilon(u)$ , the elasticity tensor  $C$  and the volume force with density  $f$ . For the steady state with no changes of pressure and displacement in time the Biot poroelasticity model becomes only one-way coupled system (1)-(2).

The coupling is only via contribution of the fluid pressure in the pores to the momentum balance equation (2).  $\alpha_B$  is the Biot-Willis constant, we will use  $\alpha_B = 1$ . The system (1), (2) is completed by mixed boundary conditions on  $\partial\Omega = \Gamma_p \cup \Gamma_v$  for flow and  $\partial\Omega = \Gamma_u \cup \Gamma_\sigma$  for elasticity.

Note that the system (1), (2) become fully coupled if  $k = k(u)$ , which will happen for the case of hydro-mechanical (H-M) model with fractures.

## 2 Darcy flow in fractured media

Let us consider a domain  $\Omega$  with the boundary  $\partial\Omega$  and one fracture  $\gamma$  (interface inside  $\Omega$ , curve for  $\Omega \subset \mathbb{R}^2$ ), see [3]. For  $x \in \gamma$  let us denote by  $n(x)$  a unit normal to  $\gamma$  and define two sides or faces  $\gamma^+$  and  $\gamma^-$ . We use the following formulation

$$\begin{aligned} -\nabla \cdot (k_m \nabla p_m) &= s_m \text{ in } \Omega, \\ -k_m \nabla p_m \cdot n^\pm &= \alpha_f (p_m - p_f) \text{ on } \gamma^\pm \\ p_m &= \hat{p} \text{ on } \Gamma_p, \\ -k_m \nabla p_m \cdot n &= \hat{g} \text{ on } \Gamma_v \end{aligned}$$

coupled with

$$\begin{aligned} -\nabla_t \cdot (k_f \nabla_t p_f) &= s_f - k_m (\nabla p_m|_{\gamma^+} - \nabla p_m|_{\gamma^-}) \cdot n \text{ on } \gamma \\ p_f &= \hat{p}_f \text{ on } \partial\gamma_p \\ -k_f \frac{\partial p_f}{\partial t} &= \hat{g}_f \text{ on } \partial\gamma_v \end{aligned}$$

The first set of equations describes the flow in the porous matrix with Robin boundary conditions on the interface between the domain and the fracture. The second set of equations describes the flow in the fracture as the lower dimensional flow with the corresponding contribution from the Robin condition.

For intersecting fractures we add the continuity and balance equations in the intersections. The sample solution of the Darcy flow in the fractured porous media (using permeability obtained from mechanical response - fracture aperture and the cubic law, see section 4) can be seen in figure 2.

## 3 Linear elasticity in fractured media

In the case of the linear elasticity, the fractures behave as the contact area of the deformable body. We work with fracture aperture, which cannot be negative (or lower than given threshold). The fracture aperture is defined as  $a(x) = a_0(x) + [d(x)]^+$  for  $x \in \gamma$ , where  $d(x)$  is the displacement jump on  $\gamma$  defined as  $d(x) = [u_+(x) - u_-(x)] \cdot n(x)$ . Non-penetration condition  $d(x) \geq 0$  in the discrete form of the problem is evaluated per segment of the fracture network and can be rewritten as nonlinear inequality condition  $B_I(u)u \geq 0$ . We assume that there

are no slips inside the fractures and the mapping of corresponding nodes in the fracture stays unchanged after the deformation. We solve the problem using total FETI and the SMALSE method, see [4]. The problem is solved in its dual form:

$$\begin{aligned} \min_{R^T B^T \lambda = R^T b} \quad & \lambda^T B A^+ B^T \lambda - \lambda^T B A^+ b, \\ & \lambda_I \geq 0 \end{aligned}$$

where  $B = [B_E^T, B_I^T]^T$ ,  $B_E$  are equality constrains from TFETI and  $R$  is the kernel of  $A$  (matrix of linear elasticity).

We linearize inequalities by freezing  $B_I^k = B_I(u_k)$  and update them only in some outer iterations (every time we reach more precise solution) of the SMALSE method. These updates are marked by triangles in the figure 1. The figure 1 shows the convergence of projected gradient ( $g_p$ ), equality constraints ( $Gu$ ) and the SMALSE parameters  $M, \rho$ . We use adaptive version of algorithm which switch between updating  $\rho$  and  $M$  depending on convergence of  $g_p/Gu$ .

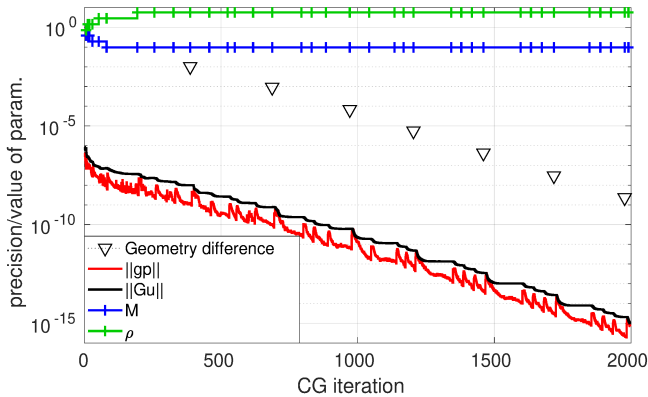


Fig. 1. Sample convergence of SMALSE method for fixed pressure

The sample solution of deformation and stresses int the fractured media (under the pressures coming from the hydraulic model) can be seen in figure 3.

### 4 Iterative coupling of H-M model

We have two interconnected models in the porous continuum  $\Omega$  with fractures  $\gamma_i : i = 1, \dots, nf$ .

*Hydraulic part:* solves the flow with input parameters  $k_m, k_{fi}$  and  $\alpha_{fi}$  of hydraulic conductivity in  $\Omega$  and  $\gamma_i$  and transport of fluid from fractures to  $\Omega$ . Moreover, the conductivity  $k_f$  depends on the fracture aperture  $a_f$ , which is provided by the mechanical model. We assume dependence  $k_f = k_f(a_f)$  derived from idealized Poisseuille flow leading to so called cubic law,

$$k_f = k_f(a, x) = \frac{a(x)^2}{12\mu\eta}, \quad x \in \gamma,$$

where  $\mu$  is the viscosity of fluid and  $\eta$  account from fracture roughness and deviation from the idealized case.

*Mechanical part:* elastic deformation of body with fractures with input parameters being Lamè moduli as well as pore pressure  $p_m$  in  $\Omega$  and fluid pressure  $p_f$  in fractures.

*Coupled H-M iterative model:* the steady state solution  $(p_m, p_f, u)$  of the coupled H-M problem is computed iteratively. Starting from an initial guess we use simple Picard iterations

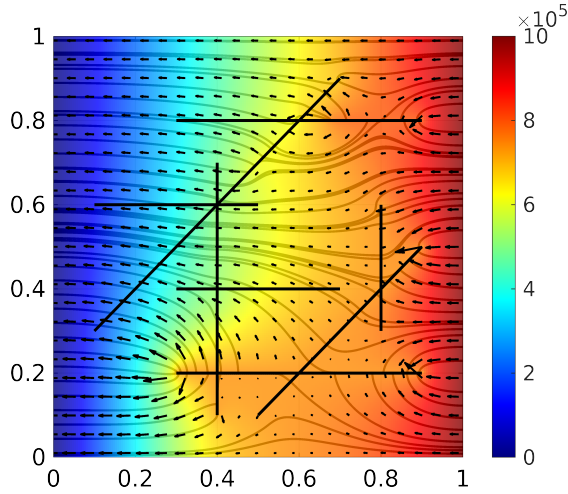
$$(p_m^i, p_f^i, u^i) \rightarrow (p_m^{i+1}, p_f^{i+1}, u^i) \rightarrow (p_m^{i+1}, p_f^{i+1}, u^{i+1}).$$

For the demonstration we use  $k_m = 10^{-15}, k_f = 10^{-6} \cdot a^2, \alpha_f = 10^{-6}$ , no-flow condition on the upper and bottom boundary and pressure drop  $10^6$  from left to the right side of the boundary for the hydraulic part of the problem. Lamè moduli  $\lambda = \mu = 10^9$ , zero normal displacement at the boundary,  $p_f$  as the acting force in the fracture boundary and  $\nabla p$  as the forcing term for the mechanical part of the problem. Figure 2 shows the Darcy flow in the domain and figure 3 shows the norm of the stress tensor and the absolute value of the displacement.

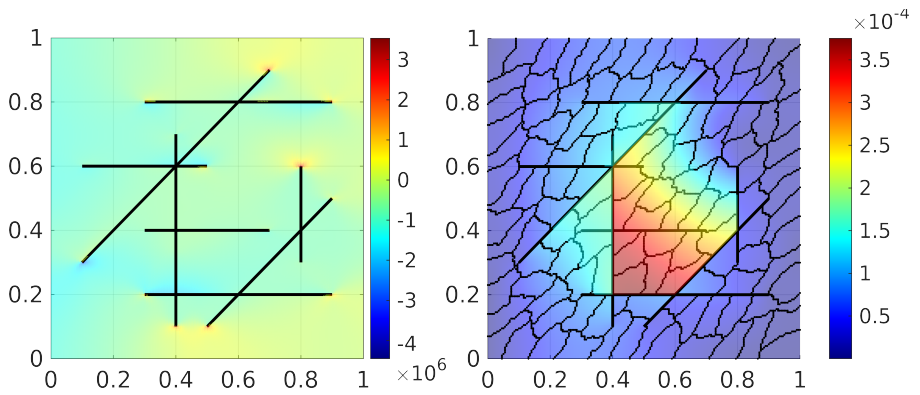
### 4.1 Convergence of coupling iterations

The convergence of the coupling iterations is shown in Fig. 4. We measure the coupling convergence as the relative difference in pressure in fractures  $\left\| \frac{p_f^{i+1} - p_f^i}{p_f^i} \right\|$  and fracture aperture (derived from  $u^i$ )  $\left\| \frac{a^{i+1} - a^i}{a^i} \right\|$ . We assume four different configurations, which differs in the source and sink sides (always in opposite) of the domain (first configuration has source on the right side and than shifting clockwise). The convergence curves in figure 4 correspond to 30 solutions of configuration 2. These solutions correspond to random samples of fracture permeability  $\log_{10} k_0^{(i)} \sim \mathcal{N}(-6, 1), i = 1, \dots, 4$  ( $k_f^{(i)} = k_0^{(i)} \cdot a^2$ ).

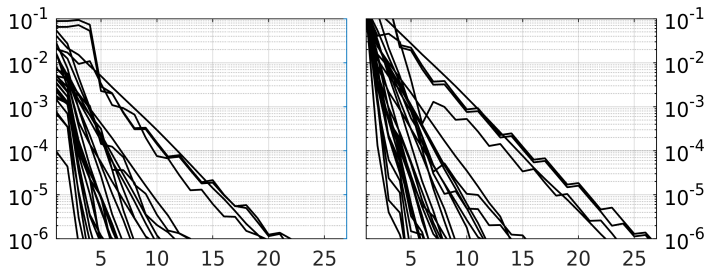
More thorough testing of the coupling convergence can be seen in Fig. 5. Here we show histograms of the number of the coupling iterations needed to reach the tolerance  $10^{-6}$ . We use the previous setting and show results for all configurations. The results show that the coupled solver is stable for our set of problems.



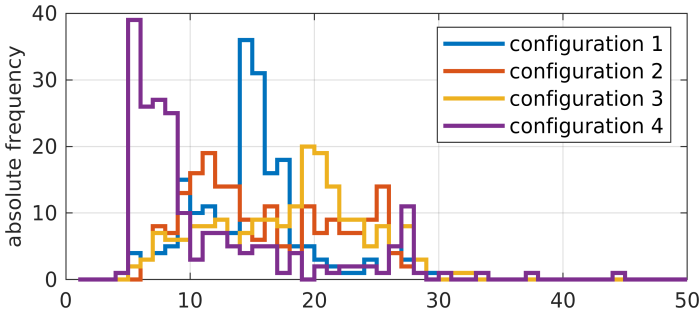
**Fig. 2.** Sample solution of hydraulic problem (coloring - pressure, streamlines and arrows - flux)



**Fig. 3.** Sample solution of mechanical problem: stress, displacement



**Fig. 4.** Relative difference between consecutive coupling iterations - left: pressure in fractures, right: fracture aperture



**Fig. 5.** Number of coupling iterations until reaching the precision  $10^{-6}$  (200 random samples)

## 5 Conclusion and future work

The presented work concerns a numerical realization of coupled H-M model for continua with fractures. We restricted to steady-state but generalization for evolution HM could be straightforward. The convergence of iterative coupling is dependent on the geometry of the problem. Some fracture distribution can lead to an oscillation in the convergence, which needs some stabilization between coupling iterations, which would lead to a slower convergence. This should be mainly because we solve the steady-state problem, which can have (due to nonlinearity in linear elasticity with contacts) multiple solutions (local minima). Still, there is a lot of questions concerning properties of the HM model, accuracy, efficiency and robustness of the numerical realization.

The HM model has a lot of applications, but many of them suffer from a lack of knowledge about the parameters. This was also our motivation to build this model because we are interested in Bayesian inverse approach for such problems. The work in this direction is in progress, see [1,2].

## References

1. Blaheta, R., Béréš, M., Domesová, S., Pan, P.: A comparison of deterministic and Bayesian inverse with application in micromechanics. *Applications of Mathematics*, 63(6), 665–686. 2018
2. Blaheta, R., Beres, M., Domesova, S., Horák, D.: Bayesian inversion for steady flow in fractured porous media with contact on fractures and hydro-mechanical coupling. *Computational Geosciences* (submitted)
3. Martin, V., Jafre, J., Roberts, J. E.: Modeling fractures and barriers as interfaces for flow in porous media. *SIAM SISC*, 2005
4. Dostál, Z., Kozubek, T., Sadowská, M., Vondrák, V.: Scalable algorithms for contact problems. Springer, 2016

# Acceleration of adaptive MCMC methods in Bayesian inversion using surrogate models

Simona Domesová

Department of Applied Mathematics, FEECS,  
VŠB – Technical University of Ostrava, 17. listopadu 15,  
708 33 Ostrava – Poruba, Czech Republic  
Institute of Geonics of the CAS,  
Studentská 1768, 708 00 Ostrava-Poruba, Czech Republic  
`simona.domesova@vsb.cz`

**Abstract.** This paper is motivated by the Bayesian approach to the solution of inverse problems governed by computationally demanding forward models. The result of the Bayesian inversion is the posterior probability distribution which contains all the available information about unknown parameters including the prior information and the information from measurements. The implementation involves the use of Markov chain Monte Carlo (MCMC) sampling methods to provide samples from the posterior distribution. Typically, each iteration of these methods requires an evaluation of the forward model which makes this procedure computationally expensive. To reduce the number of forward model evaluations, the sampling process can be accelerated using surrogate models. In this context, a surrogate model is an approximation of the forward model with a significantly cheaper evaluation. Recent literature offers several possibilities of utilizing surrogate models to accelerate MCMC methods. This paper overviews these possibilities and compares them with an adaptive MCMC method which is based on the delayed acceptance Metropolis-Hastings algorithm and incorporates a surrogate model which is updated during the sampling process. Numerical experiments show the ability of this method to reduce the number of forward model evaluations.

**Keywords:** Adaptive MCMC, delayed acceptance, inverse problem, posterior sampling, surrogate model

## 1 Introduction

In mathematical modeling, inverse problems governed by computationally demanding forward models, e.g. by partial differential equations and their systems solved using numerical methods, are often encountered. The aim of inverse problems is to identify unknown parameters of the model based on observed data. The observations are typically corrupted by noise; therefore, the use of deterministic optimization methods to find the unknown parameters is not suitable.

The Bayesian inversion is a proper tool to solve these identification problems; however, its numerical realization requires large computing resources and the development of efficient sampling methods.

Consider a forward model  $G : \mathbb{R}^n \rightarrow \mathbb{R}^m$  and observed data  $\mathbf{y} \in \mathbb{R}^m$  satisfying

$$\mathbf{y} = G(\mathbf{u}) + \boldsymbol{\eta},$$

where  $\mathbf{u} \in \mathbb{R}^n$  is the vector of unknown parameters, which is treated as a random vector. The random vector  $\boldsymbol{\eta} \in \mathbb{R}^m$  represents the additive noise with known joint probability distribution. The Bayesian approach also naturally includes the prior knowledge of the parameters available from experience (independent of the observations). Briefly, the aim of the Bayesian approach is to describe the joint probability distribution of the random vector  $\mathbf{u} \in \mathbb{R}^n$  called posterior distribution. The posterior probability density function  $\pi(\mathbf{u}|\mathbf{y})$  is given by the Bayes' theorem as

$$\pi(\mathbf{u}|\mathbf{y}) \propto f_{\boldsymbol{\eta}}(\mathbf{y} - G(\mathbf{u})) \pi_0(\mathbf{u}), \quad (1)$$

where  $f_{\boldsymbol{\eta}}$  is the probability density function (pdf) of the noise,  $\pi_0$  is the prior pdf and  $\propto$  denotes a proportionality. The computational complexity of the Bayesian inversion is given by the process of generating samples from the posterior distribution using MCMC methods. This paper focuses on the numerical realization of the Bayesian inversion and especially on the use of surrogate models for the acceleration of the computations. A surrogate model  $\tilde{G} : \mathbb{R}^n \rightarrow \mathbb{R}^m$  is an approximation of  $G$  which should be much cheaper to evaluate.

## 2 The use of surrogate models in MCMC methods

Recent research papers propose various MCMC methods that involve surrogate models. Some of these methods are directly intended for the use with arbitrary non-intrusive surrogate models and others are simply modifiable for this purpose, see e.g. [3] and [4]. There are also other approaches linked with a specific approximation of the forward model, see e.g. [5]; however, such approaches are outside the scope of this paper. Since the methods mentioned below are based on the basic Metropolis-Hastings (MH) algorithm, its principle is briefly outlined before explaining the use of surrogate models. The rest of this section describes more advanced sampling methods and their use with surrogate models.

**The MH algorithm** forms a basic frame of many advanced sampling methods. Its algorithm is simple. Assume, a sample  $\mathbf{u}^{(t)}$  is given and a proposal  $\mathbf{x}$  was generated from a proposal distribution with pdf  $q(\cdot|\mathbf{u}^{(t)})$ . To obtain  $\mathbf{u}^{(t+1)}$

- accept  $\mathbf{x}$  with probability  $\min \left\{ 1, \frac{q(\mathbf{u}^{(t)}|\mathbf{x})\pi(\mathbf{x}|\mathbf{y})}{q(\mathbf{x}|\mathbf{u}^{(t)})\pi(\mathbf{u}^{(t)}|\mathbf{y})} \right\}$ ,
- otherwise set  $\mathbf{u}^{(t+1)} = \mathbf{u}^{(t)}$ .



This procedure constructs a Markov chain with limiting distribution equal to the posterior, for details see [9]. With this algorithm, the forward model is evaluated for each proposed sample. Therefore, the basic form of the MH algorithm cannot be used in practice when  $G$  is a complicated forward model.

**The delayed acceptance MH (DAMH) algorithm** proposed in [3] works with an approximation  $\tilde{\pi}$  of the posterior distribution. Using a surrogate model  $\tilde{G}$ , this approximation can be constructed as  $\tilde{\pi}(\mathbf{u}|\mathbf{y}) \propto f_{\eta}(\mathbf{y} - \tilde{G}(\mathbf{u})) \pi_0(\mathbf{u})$ . The algorithm includes an extra pre-acceptance step that uses only the cheap approximation  $\tilde{\pi}$  to decide about the proposed sample. If the sample is not pre-accepted, the forward model is not evaluated. Therefore, if  $\tilde{\pi}$  is a good approximation of  $\pi$ , the total number of forward model evaluations can be significantly reduced. To obtain  $\mathbf{u}^{(t+1)}$

- pre-accept  $\mathbf{x}$  with probability  $\tilde{\alpha}(\mathbf{u}^{(t)}, \mathbf{x}) = \min \left\{ 1, \frac{q(\mathbf{u}^{(t)}|\mathbf{x})\tilde{\pi}(\mathbf{x}|\mathbf{y})}{q(\mathbf{x}|\mathbf{u}^{(t)})\tilde{\pi}(\mathbf{u}^{(t)}|\mathbf{y})} \right\}$ ,  
otherwise set  $\mathbf{u}^{(t+1)} = \mathbf{u}^{(t)}$ .
- If  $\mathbf{x}$  is pre-accepted, accept it with probability  
 $\min \left\{ 1, \frac{\tilde{\alpha}(\mathbf{x}, \mathbf{u}^{(t)})q(\mathbf{u}^{(t)}|\mathbf{x})\pi(\mathbf{x}|\mathbf{y})}{\tilde{\alpha}(\mathbf{u}^{(t)}, \mathbf{x})q(\mathbf{x}|\mathbf{u}^{(t)})\pi(\mathbf{u}^{(t)}|\mathbf{y})} \right\}$ , otherwise set  $\mathbf{u}^{(t+1)} = \mathbf{u}^{(t)}$ .

This algorithm can be also understood as the standard MH algorithm with a modified proposal pdf  $\tilde{q}(\cdot|\mathbf{u}^{(t)})$ , for its specification see [3].

**The adaptive DAMH algorithm (ADAMH)** is basically the DAMH algorithm modified by the adaptive construction of the enhanced error model, see [4]. More specifically, a stochastic model of the error between the exact forward model and a fixed surrogate model is being constructed. Therefore,  $\tilde{\pi}$  and thus also the modified proposal pdf  $\tilde{q}$  changes during the sampling process. Due to the updates of  $\tilde{q}$ , the produced chain of samples is not a Markov chain and this algorithm belongs to the category of adaptive MCMC methods. This algorithm was intended for the use with a state-dependent reduced-order model; however, the principle of the algorithm allows the use of any surrogate model.

**The DAMH algorithm with surrogate model updates (DAMH-SMU)** previously described in author's paper [6] is a different adaptive version of the DAMH algorithm. Similarly to the ADAMH algorithm, the approximated posterior distribution is being updated using new snapshots obtained during the sampling process. However, in this case, the posterior distribution updates are realized via updates of the surrogate model. With each pre-accepted sample  $\mathbf{x}$ , the exact posterior pdf is calculated, which involves the evaluation of  $G(\mathbf{x})$ . Each of these snapshots can be used to update the surrogate model. Due to these updates, the algorithm also belongs among the adaptive MCMC methods.

The main difference between this and the ADAMH algorithm is that the ADAMH algorithm uses a fixed surrogate model during the whole sampling

process. However, this fact also limits the DAMH-SMU algorithm to the use of surrogate models that can be easily updated when a new snapshot is available. For the possibility of surrogate model updates, non-intrusive methods are considered. A suitable choice is e.g. the stochastic collocation method or the radial basis functions interpolation (see [6] for details), which is also used in the numerical experiments in the following section.

### 3 Numerical experiments

This numerical experiments aim at the comparison of DAMH based sampling methods described above (DAMH, ADAMH, DAMH-SMU) in terms of the reduction of the number of forward model evaluations. A brief analysis of the DAMH algorithm shows that the sampling efficiency corresponds to the ratio of accepted samples to all pre-accepted samples. In other words, when designing a DAMH based method, the aim is to reduce the number of samples that were pre-accepted and then rejected, because these samples waste computation time on useless evaluations of  $G$ .

For testing purposes, 5000 samples from the same posterior distributions were generated using these three methods and the numbers of accepted, pre-rejected and rejected samples (with a total sum of 5000) were recorded. The ratio between accepted and other samples is mostly influenced by the choice of the proposal pdf  $q$ ; therefore, a fixed proposal distribution which approximately resulted in a ten percent acceptance rate was used in all experiments. The RBF surrogate model was constructed using  $N$  snapshots produced by a short preliminary run of the standard MH algorithm. For the DAMH and the ADAMH algorithm, this surrogate model remained fixed during sampling; in the case of the DAMH-SMU algorithm, it served as the initial surrogate model. Under these conditions, the quality of the methods was compared via the number of rejected samples. All algorithms were run 10 times with different seeds of the generator of pseudo-random numbers. The whole experiment was repeated for several values of  $N$  and for two different posterior distributions.

As a model problem, a simple one-dimensional linear elasticity problem with unknown material parameters  $k_1, \dots, k_n$  was considered:

$$\begin{cases} -(k(x)u'(x))' = -0.1 & x \in (0, 1) \\ u(0) = 0 \\ ku(1)' = 0 \end{cases}, \text{ where } k(x) = \begin{cases} k_1 & x \in \langle 0, \frac{1}{n} \rangle \\ \vdots \\ k_n & x \in \langle 1 - \frac{1}{n}, 1 \rangle \end{cases}.$$

The observation is a noisy measurement of the value  $u(1)$ . This defines a forward model  $G: \mathbb{R}^n \rightarrow \mathbb{R}$  which can be expressed analytically and evaluated for virtually no cost. This makes it possible to carry out relatively extensive tests. The prior distribution of the random vector  $(k_1, \dots, k_n)$  is assumed to be Gaussian with independent components from  $\mathcal{N}(10; 1.5)$ . The Gaussian noise  $\eta$  with the distribution  $\mathcal{N}(0; 2 \cdot 10^{-4})$  is considered. The posterior distribution of the random vector  $\mathbf{u} = (k_1, \dots, k_n)$  is given by (1).

Figure 1 shows the results of the numerical experiments governed by this model problem with two ( $n = 2$ ) and four ( $n = 4$ ) random variables. The horizontal axis (with logarithmic scale) corresponds to the number of snapshots used to construct the RBF surrogate model; more snapshots lead to a more accurate surrogate model. The vertical axis corresponds to the number of rejected samples; lower value basically means that the DAMH based algorithm has a better approximation  $\tilde{\pi}$  of  $\pi$ . Depicted graphs are averages of 10 sets of results obtained for different random seeds. These results show that further updates of the initial surrogate model can significantly reduce the number of forward model evaluations in comparison to the fixed surrogate.

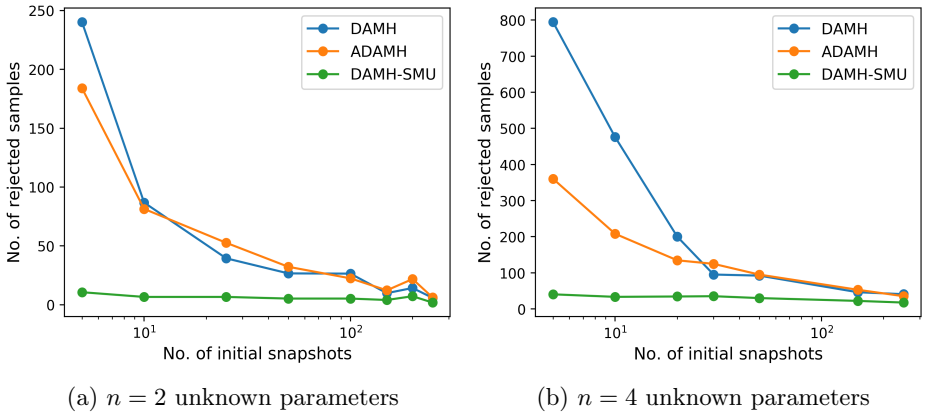


Fig. 1: The number of samples rejected by the DAMH/ADAMH/DAMH-SMU algorithm depending on the number of snapshots used to construct the initial surrogate model (lower value is better; scale of horizontal axis is logarithmic)

These results can also be interpreted in terms of the computation time reduction. For example, in the case of the 4-parametric model problem, the DAMH algorithm with fixed surrogate model based on 20 snapshots rejected approximately 200 samples on average. Using the surrogate model updates, this number was reduced to 35 samples. Considering the 10 percent acceptance rate (approximately 500 accepted samples), the updates saved about 24 percent ( $1-535/700$ ) of the computation time. Note that this comparison does not cover the computational demands of the surrogate model updates in the DAMH-SMU algorithm and of the enhanced error model construction in ADAMH. However, these costs are usually almost negligible in comparison to the cost of typical forward model evaluations. For applications governed by complex forward models see publications [2,8] that solve the identification of hydraulic conductivity parameters on several materially homogeneous subdomains, [7] that considers unknown material in the form of a Gaussian random field and [1] that solves the identification of fracture aperture governed by a hydro-mechanical forward model.

## 4 Conclusions

According to the previous research, the DAMH algorithm can significantly accelerate the sampling process compared to the basic MH algorithm. The results presented in this paper show that the process can be further accelerated using surrogate model updates. The sampling quality increases with the length of the generated chain, since with a high number of available snapshots, the surrogate model is more accurate.

The DAMH-SMU approach is limited to the use of suitable non-intrusive surrogate models and in fact, the choice of the method of surrogate model construction directly controls the efficiency of the sampling process. The DAMH performance can potentially be higher with a fixed approximated posterior pdf  $\tilde{\pi}$  constructed by methods that do not allow further updates. However, construction of such approximation  $\tilde{\pi}$  is highly problem-specific. On the other hand, the advantage of easily updatable non-intrusive methods lies in their general use which is almost independent of the properties of the forward model.

Author's current research focuses on establishing theoretical properties of the proposed adaptive MCMC algorithm including the ergodicity and the stationarity of the target posterior distribution.

## References

1. Blaheta, R., Béréš, M., Domesová, S., Horák, D.: Bayesian inversion for steady flow in fractured porous media with contact on fractures and hydro-mechanical coupling. *Computational Geosciences* (submitted)
2. Blaheta, R., Béréš, M., Domesová, S., Pan, P.: A comparison of deterministic and Bayesian inverse with application in micromechanics. *Applications of Mathematics* 63(6), 665–686 (2018)
3. Christen, J.A., Fox, C.: Markov chain Monte Carlo Using an Approximation. *Journal of Computational and Graphical Statistics* 14(4), 795–810 (2005)
4. Cui, T., Fox, C., O'Sullivan, M.J.: Bayesian calibration of a large-scale geothermal reservoir model by a new adaptive delayed acceptance Metropolis Hastings algorithm. *Water Resources Research* 47(10) (2011)
5. Cui, T., Marzouk, Y.M., Willcox, K.E.: Data-driven model reduction for the Bayesian solution of inverse problems. *International Journal for Numerical Methods in Engineering* 102(5), 966–990 (2015)
6. Domesová, S.: The Use of Radial Basis Function Surrogate Models for Sampling Process Acceleration in Bayesian Inversion. In: *AETA 2018*, vol. 554, pp. 228–238. Springer International Publishing, Cham (2020)
7. Domesová, S., Béréš, M.: Inverse Problem Solution using Bayesian Approach with Application to Darcy Flow Material Parameters Estimation. *Advances in Electrical and Electronic Engineering* 15(2), 258 – 266 (2017)
8. Domesová, S., Béréš, M.: A Bayesian Approach to the Identification Problem with Given Material Interfaces in the Darcy Flow. In: *High Performance Computing in Science and Engineering*, vol. 11087, pp. 203–216. Springer International Publishing, Cham (2018)
9. Robert, C.P., Casella, G.: *Monte Carlo Statistical Methods*. Springer Texts in Statistics, Springer New York, New York, NY (2004)

# Parallel methods for solving the parabolic problem

Ladislav Foltyn

Department of Applied Mathematics, FEECS,  
VŠB – Technical University of Ostrava, 17. listopadu 15,  
708 33 Ostrava – Poruba, Czech Republic  
ladislav.foltyn@vsb.cz

**Abstract.** In a paper, we present our recent results about solving parabolic problems. One possible way to solve transient heat equation in parallel is to use the semi-discrete scheme, where only a spatial domain is discretized. The time derivative is approximated by some stepping scheme like Euler method or Crank-Nicolson method, etc. As a parallel solution of the semi-discrete problem, we use the Parareal algorithm, which is based on the predictor-corrector scheme. We also present a combination of the Parareal with a non-overlapping domain decomposition method. Another attempt to solve the parabolic problem is to use space-time finite element method, by which the whole space-time domain is discretized. In this case, we used the same DDM as for the Parareal and we use it only for the spatial domain so appropriate subdomains are prolonged along the time interval.

**Keywords:** semi-discretization, Parareal, space-time FEM, domain decomposition method

## 1 Parabolic problem

Consider following general heat equation

$$\begin{aligned} c_H \frac{\partial u}{\partial t}(\mathbf{x}, t) - \Delta_{\mathbf{x}} u(\mathbf{x}, t) &= f(\mathbf{x}, t) \quad \forall (\mathbf{x}, t) \in \Omega \times (0, T) = Q_T, \\ u(\mathbf{x}, t) &= 0 \quad \forall (\mathbf{x}, t) \in \Gamma \times (0, T), \\ u(\mathbf{x}, 0) &= u_0(\mathbf{x}) \quad \forall \mathbf{x} \in \Omega, \end{aligned} \tag{1}$$

where  $\Omega \subset \mathbb{R}^n$ ,  $n = 1, 2, 3$  is a bounded domain with Lipschitz boundary ( $n = 2, 3$ ) and  $\Gamma = \partial\Omega$ ,  $c_H > 0$  is a given heat capacity constant,  $f(\mathbf{x}, t): Q_T \mapsto \mathbb{R}$  is a given source term,  $u_0(\mathbf{x}): \Omega \mapsto \mathbb{R}$  is given initial condition.

## 2 Semi-discrete scheme

After multiplication of (1) by test function, integration by parts over the spatial domain and using Gelfand triple  $(H_0^1(\Omega), L_2(\Omega), H^{-1}(\Omega))$ , we obtain a weak

formulation

$$\left\{ \begin{array}{l} \text{find } u(t) \in L_2(0, T; H_0^1(\Omega)) \text{ with } u'(t) \in L_2(0, T; H^{-1}(\Omega)) \text{ such that} \\ \frac{d}{dt}(u(t), v)_{L_2(\Omega)} + a(u(t), v) = \langle f(t), v \rangle \forall v \in H_0^1(\Omega) \text{ a.e. in } (0, T), \\ u(0) = u_0 \in L_2(\Omega), \end{array} \right. \quad (2)$$

where  $f \in L_2(0, T; H^{-1}(\Omega))$  and  $\langle \cdot, \cdot \rangle: H^{-1}(\Omega) \times H_0^1(\Omega) \rightarrow \mathbb{R}$  represents duality pairing. The problem has a unique solution, see [2, 5].

Further, by considering a finite dimensional space  $\mathcal{V}^h \subset H_0^1(\Omega)$ , a discrete solution  $u_h(\mathbf{x}, t)$  and a discrete test function  $v_h(\mathbf{x})$  given by

$$u_h(\mathbf{x}, t) = \sum_{j=1}^N u_j(t) \varphi_j(\mathbf{x}), \quad v_h(\mathbf{x}) = \sum_{i=1}^N v_i \varphi_i(\mathbf{x}), \quad (3)$$

where  $\varphi_i(\mathbf{x})$  is a FEM basis function, we arrive at the system of ODEs

$$\begin{aligned} M \frac{d\mathbf{u}}{dt}(t) + A\mathbf{u}(t) &= \mathbf{b}(t) \\ \mathbf{u}(0) &= \mathbf{u}_{0,h}, \end{aligned} \quad (4)$$

where  $u_{0,h}$  is an approximation of  $u_0$  in  $\mathcal{V}^h$ ,  $\mathbf{u}(t) = (u_j)(t)$ ;  $M = (m_{ij})$ ,  $m_{ij} = (\varphi_j, \varphi_i)_{L_2(\Omega)}$ ;  $A = (a_{ij})$ ,  $a_{ij} = a(\varphi_j, \varphi_i)$ ;  $\mathbf{b}(t) = (b_i)(t)$ ,  $(b_i)(t) = \langle f(t), \varphi_i \rangle$ . At least, the time derivative is approximated by some stepping scheme like explicit/implicit Euler method or Crank-Nicolson method, etc.

### 2.1 Parareal

The Parareal allows us to divide the parabolic problem along the time interval into  $n$  independent problems which could be solved in parallel. It is based on the predictor-corrector method. First, we compute some “predictive” values and then we correct them by a more precise solution. The Parareal scheme is available in [3]. We also coupled the Parareal with the non-overlapping DDM, see [1, 4]. Given DDM is used only in the spatial domain and in that part of the Parareal algorithm where we have to solve the fine solution.

### 2.2 Numerical experiments

**Parareal convergence rate** For simplicity consider the 1D parabolic problem

$$\begin{aligned} c_H \frac{\partial u}{\partial t}(x, t) - \frac{\partial^2 u}{\partial x^2}(x, t) &= 0 & x \in (0, 2), t \in (0, 2], \\ u(0, t) = u(2, t) &= 0 & t \in (0, 2], \\ u_0(x) = u(x, 0) &= 1 - (x - 1)^2 & x \in (0, 2). \end{aligned}$$

In our example we use  $c_H = 2$ . We aim to the convergence rate of the Parareal with increasing number of independent time subdomains. The error is computed in the sense of  $H^1$ -norm

$$\int_{\Omega} [u(x, 2) - u_h(x, 2)]^2 + [\nabla(u(x, 2) - u_h(x, 2))]^2 \, d\mathbf{x}, \tag{5}$$

where  $u(x, 2)$  is an approximate solution of pure sequential method and  $u_h(x, 2)$  is an approximate solution of the Parareal. The spatial step is  $h = \frac{1}{128}$ , the coarse time step is  $\Delta t = \frac{1}{2^i}$ ,  $i = 2, 3, 4, 5$  and the fine time step is  $\delta t = \frac{1}{2^{5-i} \cdot 128}$ ,  $i = 2, 3, 4, 5$ .

**Table 1.** Errors after  $k$  Parareal steps.

$\Delta T$	$k = 1$	$k = 2$	$k = 3$	$k = 4$	$k = 5$	$k = 6$
$\frac{1}{4}$	$5.91 \cdot 10^{-2}$	$7.24 \cdot 10^{-3}$	$4.80 \cdot 10^{-4}$	$2.07 \cdot 10^{-5}$	$4.56 \cdot 10^{-6}$	$1.33 \cdot 10^{-6}$
$\frac{1}{8}$	$3.24 \cdot 10^{-2}$	$2.51 \cdot 10^{-3}$	$1.18 \cdot 10^{-4}$	$4.23 \cdot 10^{-6}$	$1.84 \cdot 10^{-6}$	$1.38 \cdot 10^{-6}$
$\frac{1}{16}$	$1.69 \cdot 10^{-2}$	$7.26 \cdot 10^{-4}$	$1.99 \cdot 10^{-5}$	$4.01 \cdot 10^{-7}$	$6.32 \cdot 10^{-8}$	$4.54 \cdot 10^{-8}$
$\frac{1}{32}$	$8.61 \cdot 10^{-3}$	$1.94 \cdot 10^{-4}$	$2.86 \cdot 10^{-6}$	$3.10 \cdot 10^{-8}$	$1.13 \cdot 10^{-9}$	$5.36 \cdot 10^{-10}$
$\frac{1}{64}$	$4.33 \cdot 10^{-3}$	$4.98 \cdot 10^{-5}$	$3.78 \cdot 10^{-7}$	$2.14 \cdot 10^{-9}$	$2.18 \cdot 10^{-11}$	$5.49 \cdot 10^{-12}$

In Table 1 we could see that if we use as much processors as we are able to, we obtain solution quite faster.

**Parareal coupled with DDM** For this purpose we consider 2D heat equation

$$\begin{aligned} c_H \frac{\partial u}{\partial t}(\mathbf{x}, t) - \Delta_{\mathbf{x}} u(\mathbf{x}, t) &= 1 & \forall (\mathbf{x}, t) \in \Omega \times (0; 2], \\ u(\mathbf{x}, t) &= 0 & \forall (\mathbf{x}, t) \in \partial\Omega \times (0; 2], \\ u(\mathbf{x}, 0) &= \sin(\pi x) \sin(\pi y) & \forall \mathbf{x} \in \Omega, \end{aligned} \tag{6}$$

where  $\Omega = (0; 1)^2$ ,  $c_H = 25$ . We can't use the same 1D problem as in the previous case, because if we use mentioned DDM technique to the 1D parabolic problem we obtain the direct solution. It makes no sense for us while studying the improvement of the Parareal coupled with DDM. In this case of 2D heat equation, we focus on a number of CG iterations which are needed to obtain the fine solution up to  $k = 6$  Parareal iterations. Coarse time step is  $\Delta t = \frac{1}{4}$ , i.e. we have 8 time subintervals. Fine time step is  $\delta t = \frac{1}{64}$ . Coarse spatial step is  $H = \frac{1}{4}$ , i.e. we obtain 4 spatial subdomains.

We could see in Table 2 that we get fewer numbers of iterations in the case with the use of DDM. This is just a fraction of a possible success. We also have to study how used DDM affect the convergence rate of the Parareal but given results are out of the scope of the paper due to satisfying its length.

**Table 2.** Numbers of CG iteration for  $2 \times 2$  DDM subdomains.

	$h = \frac{1}{4}$	$h = \frac{1}{8}$	$h = \frac{1}{16}$	$h = \frac{1}{32}$
without DDM	2334	3864	8796	17970
with DDM	2304	2688	2688	3072
improvement	1.0130	1.3705	3.2723	5.8496

### 3 Space-time FEM

Derivation of a weak formulation for space-time FEM is quite similar to the previous one. There is only one difference, we also integrate the original formula over the time interval, so we obtain

$$\left\{ \begin{array}{l} \text{find } u \in L_2(0, T; H_0^1(\Omega)) \text{ with } u' \in L_2(0, T; H^{-1}(\Omega)) \text{ (} u \in U \text{) s. t.} \\ m(u, v) + a(u, v) = \langle f(t), v \rangle \quad \forall v \in V, \\ u(\mathbf{x}, 0) = u_0 \quad \forall \mathbf{x} \in \Omega, \end{array} \right. \quad (7)$$

where

$$\begin{aligned} V &= \{w \in L_2(0, T; H_0^1(\Omega)) : w(\mathbf{x}, 0) = 0 \quad \forall \mathbf{x} \in \Omega\}, \\ m(u, v) &= c_H \cdot \int_0^T \int_{\Omega} \frac{\partial u}{\partial t}(\mathbf{x}, t) v(\mathbf{x}, t) \, d\mathbf{x} \, dt, \\ a(u, v) &= \int_0^T \int_{\Omega} \nabla_{\mathbf{x}} u(\mathbf{x}, t) \nabla_{\mathbf{x}} v(\mathbf{x}, t) \, d\mathbf{x} \, dt, \\ \langle f, v \rangle &= b(v) = \int_0^T \int_{\Omega} f(\mathbf{x}, t) v(\mathbf{x}, t) \, d\mathbf{x} \, dt. \end{aligned}$$

We assume that a solution  $u(\mathbf{x}, t)$  can be splitted into a form  $u(\mathbf{x}, t) = u_H(\mathbf{x}, t) + u_0(\mathbf{x}, t)$  for  $(\mathbf{x}, t) \in \Omega \times (0, T)$ . Further, we assume finite dimensional spaces  $U^h \subset U$ ,  $V^h \subset V$  and that the discrete solution  $u_H^h(\mathbf{x}, t)$  and the discrete test function  $v_h(\mathbf{x}, t)$  are given by

$$u_H^h(\mathbf{x}, t) = \sum_{j=1}^N u_j \varphi_j(\mathbf{x}, t), \quad v_h(\mathbf{x}, t) = \sum_{i=1}^N v_i \varphi_i(\mathbf{x}, t). \quad (8)$$

We arrive at the system of linear equations

$$(\mathbf{M} + \mathbf{A}) \cdot \mathbf{u} = \mathbf{b} - (\hat{\mathbf{M}} + \hat{\mathbf{A}}) \cdot \mathbf{u}_0, \quad (9)$$



where  $\mathbf{u} = (u_j)$ ;  $\mathbf{u}_0 = (u_0^j)$ ;  $\mathbf{M} = (m_{ij})$ ,  $m_{ij} = m(\varphi_j, \varphi_i)$ ;  $\mathbf{A} = (a_{ij})$ ,  $a_{ij} = a(\varphi_j, \varphi_i)$ ;  $\mathbf{b} = (b_i)$ ,  $b_i = \langle f, \varphi_i \rangle$ . The matrices  $\hat{\mathbf{M}}$ ,  $\hat{\mathbf{A}}$  correspond to initial condition  $\mathbf{u}_0$ .

### 3.1 Numerical examples

Consider the same 2D problem (6) as in the previous section. We focus on the use of given DDM to the parabolic problem. Mentioned DDM was introduced only for elliptic problems so the results are uncertain for the considered 2D heat equation.

In this case, the spatial domain is discretized into right-angled isosceles triangles by the step  $h$ . The time interval is divided with the step  $\Delta t$ , so an individual space-time element forms a prism with triangle base. We assume an approximate solution  $u_h(\mathbf{x}, t)$  and a test function  $v_h(\mathbf{x}, t)$  in a form

$$u_h(\mathbf{x}, t) = \sum_{j=1}^N u_j \cdot \varphi_j(t) \cdot \psi_j(x, y) , \quad v_h(\mathbf{x}, t) = \sum_{i=1}^N v_i \cdot \varphi_i(t) \cdot \psi_i(x, y) , \quad (10)$$

where  $\varphi(t)$ ,  $\psi(x, y)$  are piecewise linear functions.

We solve non-symmetric problem

$$(\mathbf{M} + \mathbf{A})\mathbf{u} = \mathbf{b} - (\hat{\mathbf{M}} + \hat{\mathbf{A}})\mathbf{u}_0. \quad (11)$$

The time step is  $\Delta t = \frac{1}{2}$ , i.e. we obtain 4 time layers in each space-time subdomain. Due to the non-symmetry of the problem the GMRES method is used.

**Table 3.** Numbers of iterations, time step  $\Delta t = \frac{1}{2}$  (GMRES method).

	$h = \frac{1}{4}$	$h = \frac{1}{8}$	$h = \frac{1}{16}$	$h = \frac{1}{32}$	$h = \frac{1}{64}$
no precond.	9	33	73	150	286
Subdomains	Preconditioned system				
$2 \times 2$	9	12	14	16	16
$4 \times 4$		16	19	21	22
$8 \times 8$			13	15	17
$16 \times 16$				11	12

We could see in Table 3 that there could be a possibility of use of given DDM to the parabolic problems because the numbers of iterations seems to be quite stable after preconditioning. To confirm that results, we have to do more experiments and provide analysis for the heat equation.

## 4 Outlooks

In the future work, we focus how the Parareal convergence rate is affected by the use of DDM. Also we provide an analysis of the use of DDM for parabolic problem.

## 5 Publications

We don't have any indexed publications, yet, only conference proceedings. We are going to provide an article of recent results about the Parareal in Applications of Mathematics published by Institute of Mathematics, Czech Academy of Sciences. Also, after providing the analysis of mentioned DDM to the parabolic problem, we plan to publish these results in an appropriate journal.

## 6 Grants and Awards

Work is partly supported by SGS grant no. SP2019/84, VŠB – Technical university of Ostrava.

## References

1. Bramble, J. H., Pasciak, J. E., Schatz, A. H.: The Construction of Preconditioners for Elliptic Problems by Substructuring. I. Mathematics of Computation, vol. 47, no. 175, p. 103, (1986).
2. Grossmann, C., Roos, H.-G., Stynes, M.: Numerical Treatment of Partial Differential Equations. Berlin, Heidelberg: Springer Berlin Heidelberg, (2007).
3. Lions, J.-L., Maday, Y., Turinici, G.: Résolution d'EDP par un schéma en temps  $\llcorner$  pararéel  $\lrcorner$ . Comptes Rendus de l'Académie des Sciences – Series I – Mathematics, vol. 332, no. 7, pp. 661-668, (2001).
4. Lukáš, D., Bouchala, J., Vodstrčil, P., Malý, L.: 2-Dimensional primal domain decomposition theory in detail. Applications of Mathematics, vol. 60, no. 3, pp. 265-283, (2015).
5. Zeidler, E.: Nonlinear functional analysis and its applications I-IV. Springer, Berlin, (1990).

# Estimating Parameters of Gaussian Mixtures using Variational Bayesian Approach

Petra Kozielová

Department of Applied Mathematics, FEECS,  
VŠB – Technical University of Ostrava, 17. listopadu 15,  
708 33 Ostrava – Poruba, Czech Republic  
`petra.kozielova@vsb.cz`

**Abstract.** In this paper we will estimate Gaussian mixture's parameters for model with  $n$  components with the help of Variational Bayesian algorithm. In order to find values of these parameters we need to compute posterior distribution. Since it's impossible to find it in a closed form, our goal will be it's approximation. The variational approximation involves choosing the suitable distribution family for parameters, which are considered hidden variables. Then we look for closest distribution to the posterior distribution in sense of Kullback-Leibler divergence. This problem can be considered an optimization problem.

## 1 Bayesian statistics

In Bayesian statistics parameters are understood as random variables with probability distribution, which expresses knowledge about values of unknown parameters and describes uncertainty about their values. When we estimate these parameters we need to have some knowledge about them which is given in advance and it's called prior knowledge. The source of this knowledge can be for example physical model or results of previous experiment, or some personal believe about parameters. The prior knowledge is described by prior density function which helps us to express known limitations of values of parameters. But it can be also a source of problems, because we sometimes don't have suitable prior information in advance and finding it can be difficult.

Next we have information from obtained data, which is characterized by likelihood function and it describes our statistical model.

Let us consider a random variable (data)  $x$ , which depends on an unknown parameter  $\theta$ . Then we express joint density  $p(x, \theta)$  as

$$p(x, \theta) = p(x|\theta)p(\theta),$$

where  $p(\theta)$  is prior density function and  $p(x|\theta)$  is parametric model, also called a likelihood function.

When we combine information from data and prior information together, we will get posterior information, which provides complex image about unknown parameter. Posterior density is given by following expression

$$p(\theta|x) = \frac{p(x|\theta)p(\theta)}{p(x)},$$

where  $p(x)$  is normalization constant. Posterior density is used for exploring the hidden data structure so we can estimate what the next data will look like.

Usually there is a problem with computing posterior density, so we use methods which approximate this density, which are Markov chain Monte Carlo methods [3] or Variational Bayesian methods [1]. In this article we will deal only with Variational Bayesian methods. When we use Variational approximation we need to find suitable probabilistic distribution which is closest to posterior distribution. Derivation of this distribution results in iteration equations and it's very demanding but the computing is much faster than MCMC algorithm.

## 2 Variational approximation

We will now consider the probabilistic model of hidden random variables (parameters) and observed random variables (data) described by graphical model [2], for which we compute posterior distribution. The relationship between the variables is described by the model and a prior distribution. The aim of the Variational Bayesian methods is to derive approximation of the posterior distribution.

Firstly we introduce variational family of distributions of hidden variables, which is parametrized by variational parameters. The approximate posterior distribution is searched as a member of this family which is closest to posterior distribution. Distance between these distributions is measured with Kullback-Leibler divergence. The resulting distribution is called variational distribution. We will denote it by  $q$ . In our case we consider mean-field variational approximation, which means we demand mutual independence between hidden variables.

In variational derivation we minimize KL divergence of variational distribution and posterior distribution.

## 3 Model description

We will consider mixture model with  $J$  Gaussian components. Hidden variables are: means  $\mu = (\mu_1, \dots, \mu_J)$ , precisions  $\tau = (\tau_1, \dots, \tau_J)$ , component weights  $\alpha = (\alpha_1, \dots, \alpha_J)$  and numbers of components  $c_n$  determining from which component observed data  $x_n$  come from. This mixture model can be described by graphical model in Figure 1, which helps to describe conditional independences between variables.

Data  $x_n$  are normally distributed:

$$x_n | \mu, \alpha, \tau, c_n \sim \mathcal{N}(x_n | \mu_{c_n}, \sigma_{c_n}^2) = \prod_{j=1}^J \left( \frac{1}{\sqrt{2\pi}} \tau_j^{1/2} \exp\left(-\frac{\tau_j}{2} (x_n - \mu_{c_n})^2\right) \right)^{\delta(c_n, j)}$$

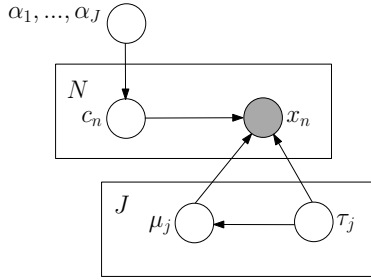


Fig. 1. Graphical mixture model with  $J$  components

Weights  $\alpha$  are from Dirichlet distribution, the distributions of pairs  $\mu_j, \tau_j$  are Normal-gamma and values  $c_n$  are from Discrete distribution:

$$\begin{aligned} \tau_j &\sim \mathcal{G}(a_j, b_j) \\ \mu_j | \tau_j &\sim \mathcal{N}(\bar{\mu}_j, (k_j \tau_j)^{-1}) \\ \alpha &\sim \mathcal{Dir}(d_1, \dots, d_J) \\ c_n | \alpha &\sim D(\alpha_1, \dots, \alpha_J), \end{aligned}$$

where

$$\begin{aligned} p(\alpha, \mu_1, \tau_1, \dots, \mu_J, \tau_J, c_1, \dots, c_n) = \\ p(\alpha | d_1, \dots, d_J) \left( \prod_{j=1}^J p(\tau_j | a_j, b_j) p(\mu_j | \bar{\mu}_j, (k_j \tau_j)^{-1}) \right) \left( \prod_{n=1}^N p(c_n | \alpha_1, \dots, \alpha_J) \right) \end{aligned}$$

for some prior parameters  $a_j, b_j > 0, \bar{\mu}_j \in \mathbb{R}, k_j > 0, d_j > 0$ .

In order to find a suitable variational family we rearrange the joint distribution

$$p(x, c, \mu, \alpha, \tau) = p(\mu, \alpha, \tau) \prod_{n=1}^N p(c_n | \alpha) p(x_n | \mu, \tau, c_n).$$

After series of derivations, we obtain that conditional distribution  $p(\mu, \tau, \alpha | x, c)$  equals the product of Normal-gamma distributions and Dirichlet distribution:

$$\begin{aligned} \mathcal{Dir}(\alpha | d_{N_1}, \dots, d_{N_J}) \otimes \mathcal{NG}(\mu_1, \tau_1 | \mu_{N_1}, k_{N_1}, a_{N_1}, b_{N_1}) \otimes \dots \\ \dots \otimes \mathcal{NG}(\mu_J, \tau_J | \mu_{N_J}, k_{N_J}, a_{N_J}, b_{N_J}), \end{aligned}$$

where

$$\begin{aligned}
 a_{N_j} &= a_j + \sum_{n=1}^N \frac{1}{2} \delta(j, c_n) \\
 k_{N_j} &= k_j + \sum_{n=1}^N \delta(j, c_n) \\
 b_{N_j} &= b_j + \frac{1}{2} \sum_{j=1}^J k_{N_j} \left( \frac{k_j \bar{\mu}_j^2 + \sum_{n=1}^N x_n^2 \delta(j, c_n)}{k_{N_j}} - \left( \frac{k_j \bar{\mu}_j + \sum_{n=1}^N x_n \delta(j, c_n)}{k_{N_j}} \right)^2 \right) \\
 \mu_{N_j} &= \frac{k_j \bar{\mu}_j + \sum_{n=1}^N x_n \delta(j, c_n)}{k_{N_j}}
 \end{aligned}$$

Now we express full conditional distribution  $p(c_n = j | x_n, \mu, \tau, \alpha)$  for  $j$ -th component:

$$\begin{aligned}
 p(c_n = j | x_n, \mu, \tau, \alpha) &= \frac{\alpha_j \frac{1}{\sqrt{2\pi}} \tau_j^{1/2} \exp\left(-\frac{\tau_j}{2} (x_n - \mu_j)^2\right)}{\sum_{\tilde{j}=1}^J \alpha_{\tilde{j}} \frac{1}{\sqrt{2\pi}} \tau_{\tilde{j}}^{1/2} \exp\left(-\frac{\tau_{\tilde{j}}}{2} (x_n - \mu_{\tilde{j}})^2\right)} \\
 &\stackrel{\text{def.}}{=} \frac{\kappa_j}{\sum_{\tilde{j}=1}^J \kappa_{\tilde{j}}}.
 \end{aligned}$$

Now we select the variational family to be a family of a distributions with densities  $q(\alpha, \mu, \tau, c)$  such that

$$q(\alpha, \mu, \tau, c) = q(\alpha) q(\mu_1, \tau_1) \dots q(\mu_J, \tau_J) q(c_1) q(c_N)$$

and the marginal densities are of the same type as the corresponding full conditional densities of the posterior density.

After expressing conditional distributions  $p(\mu, \tau, \alpha | x, c)$  and  $p(c_n = j | x_n, \mu, \tau, \alpha)$  in form of exponential family, we can compute variational parameters  $\lambda, \phi_n$  as expected values of natural parameters of these conditional distributions:

$$\begin{aligned}
 \lambda = E_q \left[ a_{N_1} - \frac{1}{2}, \dots, a_{N_J} - \frac{1}{2}, -b_{N_1} - \frac{1}{2} k_{N_1} \mu_{N_1}^2, \dots, -b_{N_J} - \frac{1}{2} k_{N_J} \mu_{N_J}^2, \right. \\
 \left. k_{N_1} \mu_{N_1}, \dots, k_{N_J} \mu_{N_J}, -\frac{k_{N_1}}{2}, \dots, -\frac{k_{N_J}}{2}, d_{N_1}, \dots, d_{N_J} \right]^T
 \end{aligned}$$

$$\phi_n = E_q [\ln \kappa_1, \dots, \ln \kappa_J]^T$$

After computing these expected values, we get that variational parameters are expressed as:

$$\lambda = \left( a_1 + \frac{1}{2} \sum_{n=1}^N \theta_{n1}, \dots, a_J + \frac{1}{2} \sum_{n=1}^N \theta_{nJ}, -b_1 - \frac{1}{2} k_1 \bar{\mu}_1^2 - \frac{1}{2} \sum_{n=1}^N x_n^2 \theta_{n1}, \dots, \right. \\ \left. -b_J - \frac{1}{2} k_J \bar{\mu}_J^2 - \frac{1}{2} \sum_{n=1}^N x_n^2 \theta_{nJ}, k_1 \bar{\mu}_1 + \sum_{n=1}^N x_n \theta_{n1}, \dots, \right. \\ \left. k_J \bar{\mu}_J + \sum_{n=1}^N x_n \theta_{nJ}, -\frac{1}{2} \left( k_1 + \sum_{n=1}^N \theta_{n1} \right), \dots, -\frac{1}{2} \left( k_J + \sum_{n=1}^N \theta_{nJ} \right) \right),$$

where

$$\theta_{nj} = q(c_n = j), \quad \sum_{j=1}^J \theta_{nj} = 1$$

and

$$\phi_n = \left( \left( \psi(d_{N_1}^*) - \psi(d_{N_1}^* + d_{N_2}^*) - \ln \sqrt{2\pi\sigma_1^2} \right) + \frac{-x_n^2 + 2x_n\mu_{N_1}^* - (\sigma_{N_1}^*)^2 - (\mu_{N_1}^*)^2}{2\sigma_1^2}, \right. \\ \left. \left( \psi(d_{N_2}^*) - \psi(d_{N_1}^* + d_{N_2}^*) - \ln \sqrt{2\pi\sigma_2^2} \right) + \frac{-x_n^2 + 2x_n\mu_{N_2}^* - (\sigma_{N_2}^*)^2 - (\mu_{N_2}^*)^2}{2\sigma_2^2} \right),$$

where parameters marked with symbol \* are common parameters of variational distribution  $q$  and can be transformed into natural parameters.

### 4 Application

This algorithm will be applied on blood pressure data. The data can be understood as mixture with 2 components, where the first component includes the pressures measured at night and second pressures measured during the day, where the day pressures has a greater weight.

## References

- [1] Matthew D Hoffman, David M Blei, Chong Wang, and John Paisley. Stochastic variational inference. *The Journal of Machine Learning Research*, 14(1):1303–1347, 2013.
- [2] Thomas Dyhre Nielsen and Finn Verner Jensen. *Bayesian networks and decision graphs*. Springer Science & Business Media, 2009.
- [3] Christian Robert and George Casella. *Monte Carlo statistical methods*. Springer Science & Business Media, 2013.



# PCDeflation: A High-performance Deflation Preconditioner in PETSc

Jakub Kružík<sup>1,2</sup> and David Horák<sup>1,2</sup>

<sup>1</sup>Institute of Geonics of the CAS,  
Studentská 1768, 708 00 Ostrava-Poruba, Czech Republic

<sup>2</sup>Department of Applied Mathematics, FEECS,  
VŠB – Technical University of Ostrava, 17. listopadu 15,  
708 33 Ostrava – Poruba, Czech Republic  
jakub.kruzik@vsb.cz

**Abstract** This paper presents PCDeflation - a general, multilevel, high-performance deflation preconditioner in PETSc. Deflation is a well known scheme for accelerating the solution of linear systems solved by Krylov subspace iterative methods. Moreover, deflation can be combined with a preconditioner to further improve the numerical behaviour of a Krylov subspace iterative method as well as the time to solution. The presented numerical experiments illustrate the effectiveness of deflation. As far as we know, PCDeflation is the first implementation of a general deflation scheme available in any major library for scientific computing.

## 1 Introduction

Many problems in engineering, finance, etc. eventually lead to a system of linear equations of the form

$$\mathbf{A}\mathbf{x} = \mathbf{b}, \quad (1)$$

where  $\mathbf{A}$  is  $n$ -dimensional (possibly complex valued) matrix.

The Krylov subspace iterative methods represent a class of algorithms often best suited for the solution of such systems. A Krylov subspace iterative method finds a solution on a Krylov subspace with respect to some optimality condition. Examples of well-known Krylov subspace iterative methods include Conjugate Gradients (CG) and GMRES. CG optimality condition is that the error of the solution minimizes the  $\mathbf{A}$ -norm of the error, while the optimality condition for the GMRES is the minimization of the Euclidian norm of the residual  $\mathbf{r} = \mathbf{A}\mathbf{x} - \mathbf{b}$ .

In order to accelerate the convergence of a Krylov subspace iterative method, we often need a good preconditioner. However, there also exists a complementary approach to the preconditioning known as deflation. The deflation utilizes a deflation space that should represent slowly converging components of the solution. The deflation removes (deflates) the deflation space from the space the Krylov subspace iterative method operates on and thus further accelerates the convergence.

In this work, we present PCDeflation - our high-performance implementation of the deflation as a general preconditioner in PETSc [4]. PETSc (Portable, Extensible Toolkit for Scientific Computation) is a widely-utilized suite of data

structures and routines for the scalable (parallel) solution of scientific applications. PCDeflation is currently available in the main (master) branch of PETSc and will be available from the next stable release (3.12, due to be released in fall 2019) onward.

The paper is divided as follows. The next section describes deflation as a preconditioner. The third section introduces the implementation. Finally, we present some numerical experiments.

## 2 Deflation Preconditioner

The deflation, introduced for CG in [15,5], works by splitting the solution of Equation (1) into two parts. The first part represents the solution on the deflation space and is directly obtained. The second one is computed by a Krylov subspace iterative method that operates only on the  $\mathbf{A}$ -conjugate complement of the deflation space.

Let us define a full rank deflation matrix

$$\mathbf{W} = (\mathbf{w}_1, \mathbf{w}_2, \dots, \mathbf{w}_m) \in \mathbb{C}^{n \times m}, m < n$$

and let  $\mathcal{W}$  be a subspace spanned by columns of  $\mathbf{W}$ . Then we can denote a projector

$$\mathbf{P} = \mathbf{I} - \mathbf{W} (\mathbf{W}^H \mathbf{A} \mathbf{W})^{-1} \mathbf{W}^H \mathbf{A} = \mathbf{I} - \mathbf{Q} \mathbf{A}$$

onto an  $\mathbf{A}$ -conjugate complement of  $\mathcal{W}$ .

Given an arbitrary initial guess  $\mathbf{x}_{-1}$  and defining the residual  $\mathbf{r}_{-1} = \mathbf{b} - \mathbf{A} \mathbf{x}_{-1}$  we can choose the initial guess for a Krylov subspace iterative method  $\mathbf{x}_0$  to be

$$\mathbf{x}_0 = \mathbf{x}_{-1} + \mathbf{W} (\mathbf{W}^H \mathbf{A} \mathbf{W})^{-1} \mathbf{W}^H \mathbf{r}_{-1} = \mathbf{x}_{-1} + \mathbf{Q} \mathbf{r}_{-1}. \quad (2)$$

It is easy to show that  $\mathbf{x}_0$  is the exact solution of (1) in  $\mathcal{W}$  and therefore  $\mathbf{r}_0$  is orthogonal to  $\mathcal{W}$ . If we use  $\mathbf{x}_0$  as the initial guess for CG, we obtain the InitCG method [6]. In general, we call using this initial guess for a Krylov subspace iterative method InitDef.

If the columns of  $\mathbf{W}$  are exact eigenvectors then, in exact arithmetic, we achieved the restriction of the Krylov subspace iterative method on the  $\mathbf{A}$ -conjugate complement of the deflation space. However, in the case of general  $\mathbf{W}$ , we need to apply  $\mathbf{P}$  either as left or right (with the required correction) preconditioner, i.e.,

$$\mathbf{P} \mathbf{M}^{-1} \mathbf{A} \mathbf{x} = \mathbf{P} \mathbf{M}^{-1} \mathbf{b} \quad \text{or} \quad \mathbf{A} \mathbf{P} \mathbf{M}^{-1} \mathbf{y} = \mathbf{b},$$

where  $\mathbf{M}^{-1}$  is an additional preconditioner.

The preconditioner works by shifting to zero (deflating) some eigenvalues of the preconditioned operator. The eigenvalues can also be shifted to any value by using the coarse problem correction, which can enhance the numerical stability of deflation.

For some spaces, the analysis of the preconditioning effect of deflation is easy. For example, if the deflation space consists of eigenvectors of  $\mathbf{A}$ , the corresponding eigenvalues are deflated while the rest of the spectrum stays the same [9]. While the deflation using eigenvectors is one of the most efficient, the eigenvectors are usually not available and very expensive to compute [9]. Thus some approximations are generally used. One of these is wavelet-based spaces that were introduced in [8].

### 3 The Implementation

We implemented deflation as a general preconditioner in PETSc and named it PCDeflation. It is available in the master branch and will be included in the next stable release (3.12) that is due to be released in fall of 2019.

The code is based on an implementation of the deflated CG (DCG) method that we wrote for PERMON [3] toolbox for quadratic programming. This implementation is described in [9] where the numerical behaviour, as well as the performance of the method, is also presented.

The implementation as a preconditioner instead of DCG implementation as an extension of the CG method has a clear advantage as it can be used to solve more general problems. For example, it is no longer required that the system matrix  $\mathbf{A}$  is symmetric positive semi-definite or a different variant of some Krylov subspace iterative method, better suited for a given problem and computational environment, can be used. Moreover, PCDeflation can handle complex-valued problems.

The method's bottleneck is the solution of the deflation coarse problem (CP) - that is the solution of the inverse  $(\mathbf{W}^H \mathbf{A} \mathbf{W})^{-1}$  contained in the projector  $\mathbf{P}$ . Since the dimension of the CP operator is usually significantly smaller than that of the system operator  $\mathbf{A}$ , a fully parallel solution is commonly dominated by solver communication. Communication avoiding techniques are used to reduce communication and improve performance. The CP operator is redistributed and solved by ranks contained in MPI subcommunicators. Such partial parallelization leads to improved data locality and reduced communication, which significantly improves the performance [18]. PCDeflation further improves upon partial parallelization compared to our previous implementation by using only single subcommunicator instead of redundant solves on multiple subcommunicators. The new approach reduces set up time by decreasing the number of matrix entries that need to be communicated. In the solve phase, the communication volume (both size and number of messages) needed to redistribute the input vector is also decreased, while the communication needed to make the output vector fully distributed slightly increases [14].

Regardless of the communication optimizations, a good solver for CP is needed. If the deflation space is large, a natural solver is a Krylov subspace iterative method preconditioned by deflation. The recursive deflation application is known as a multilevel deflation [7]. PCDeflation was from onset designed to be multilevel. The bottom level CP is solved by a direct solver which for

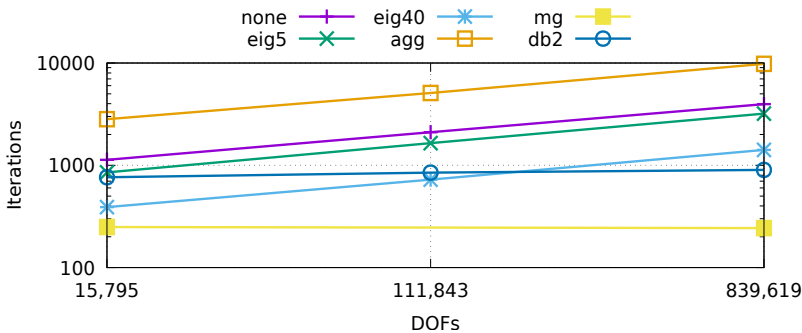
PCDeflation is by default SuperLU(`_DIST`) [12,13] if available. When not on a bottom level, a flexible Krylov subspace iterative method [16] is used. When a flexible Krylov subspace iterative method is also used for the solution of the original system, a significant reduction of CP solvers precision can be allowed, which leads to a further decrease of CPs solution cost.

The deflation preconditioner can be turned on and fully controlled from the command line or by interface function. PCDeflation computes a deflation space if the user provides none. Automatically computable spaces are subdomain aggregations and wavelet-based [8]. See PCDeflation documentation [10] for available options.

## 4 Numerical Experiments

The ARCHER [2] supercomputer was used to compute the numerical experiments. We used the CG method to showcase both the numerical behaviour as well as the performance of our implementation.

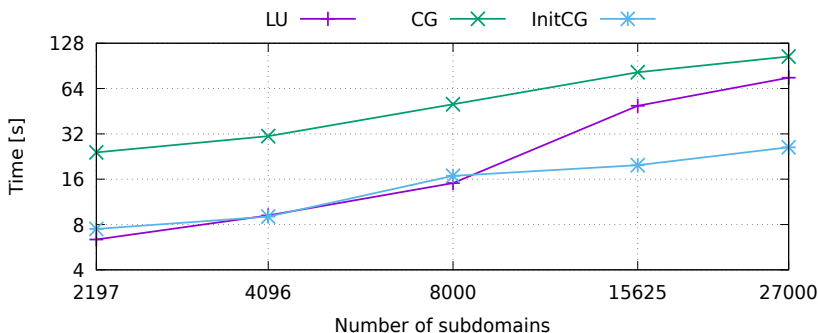
The first set of benchmarks used in the numerical experiments include all 236 SPD matrices from SuiteSparse Matrix collection, 2D Laplace on a rectangular domain with a hole and 3D linear elasticity multi-material cantilever beam discretized with MFEM [1], and 2D Laplace discretized by boundary element method on an L-shaped domain. The results with appropriate discussion can be found in [9]. A comparison of numerical scalability of CG (none) and DCG with 5 and 40 eigenvectors (eig5, eig40) belonging to the smallest eigenvalues, subdomain aggregations (agg), geometric multigrid prolongations (mg), and Haar wavelet (db2) deflation spaces is depicted in Figure 1.



**Figure 1.** Number of iterations for various deflation spaces on 3D elasticity benchmark [9].

Another benchmark comes from [11]. In Figure 2, InitDef variant of CG (InitCG) with 100 eigenvectors as the deflation space computed by SLEPc [17] (included in time) is compared against the unpreconditioned CG method and LU decomposition computed by SuperLU\_DIST on a solution of FETI coarse

problem of a 3D problem with 1,000 right-hand sides. The results show that accelerating FETI coarse problem solution with deflation significantly improves the scalability of the whole FETI method for a large number of computational cores (one subdomain belongs to one core).



**Figure 2.** Comparison of CG, InitCG and LU direct solver on a FETI coarse problem of a 3D benchmark with 1,000 right-hand sides [11].

## 5 Conclusion

This work describes PCDeflation - a general, high-performance preconditioner implementing deflation. PCDeflation is available in PETSc library for scientific computing. As far as we know, this is the first available open-source implementation of deflation that is not tied to a specific Krylov subspace iterative method.

The numerical experiments demonstrate the usefulness of deflation schemes for Krylov subspace iterative methods. A significant reduction in the number of iterations, as well as time to solution, can be achieved by using appropriate deflation spaces. Using novel wavelet-based deflation or multigrid prolongation operators yields very good results on a wide variety of benchmarks solved by deflated CG. Often, the number of iterations, as well as the time to the solution, can be decreased by a factor of more than 3.

Future research will include the relaxation of precision for coarse problems solution in the multilevel deflation.

## Acknowledgements

PCDeflation was created by the first author while on a research stay with Prof. Reinhard Nabben at the Institute of Mathematics, TU Berlin. This work has been supported by The Ministry of Education, Youth and Sports from the National Programme of Sustainability (NPU II) project IT4Innovations excellence in science - LQ1602; by the grant of SGS No. SP2018/165, VSB - Technical

University of Ostrava. The work has also been performed under the PRACE-DECI14 project PERMON and the computer resources provided by Edinburgh Parallel Computing Centre (EPCC).

## References

1. MFEM: Modular finite element methods. [mfem.org](http://mfem.org)
2. ARCHER web page (2019), <http://www.archer.ac.uk/>
3. PERMON web page (2019), <http://permon.vsb.cz/>
4. Balay, S., Abhyankar, S., Adams, M.F., Brown, J., Brune, P., Buschelman, K., Dalcin, L., Eijkhout, V., Gropp, W.D., Kaushik, D., Knepley, M.G., May, D.A., McInnes, L.C., Mills, R.T., Munson, T., Rupp, K., Sanan, P., Smith, B.F., Zampini, S., Zhang, H., Zhang, H.: PETSc Web page (2019), <http://www.mcs.anl.gov/petsc>
5. Dostal, Z.: Conjugate gradient method with preconditioning by projector. *International Journal of Computer Mathematics* 23(3-4), 315–323 (1988)
6. Erhel, J., Guyomarc’h, F.: An augmented conjugate gradient method for solving consecutive symmetric positive definite linear systems. *SIAM Journal on Matrix Analysis and Applications* 21(4), 1279–1299 (2000)
7. Erlangga, Y.A., Nabben, R.: Multilevel projection-based nested krylov iteration for boundary value problems. *SIAM J. Scientific Computing* 30, 1572–1595 (2008)
8. Kružík, J., Horák, D.: Wavelet based deflation of conjugate gradient method. In: *Proceedings of the Fifth International Conference on Parallel, Distributed, Grid and Cloud Computing for Engineering*. Civil-Comp Press, Stirlingshire, UK (2017)
9. Kružík, J.: Implementation of the Deflated Variants of the Conjugate Gradient Method. Master’s thesis, VSB - Technical University of Ostrava (2018)
10. Kružík, J.: PCDeflation documentation (2019), <https://www.mcs.anl.gov/petsc/petsc-dev/docs/manualpages/PC/PCDEFLATION.html>
11. Kružík, J., Horák, D., Hapla, V., Cermak, M.: Comparison of selected FETI coarse space projector implementation strategies. *Parallel Computing* (2019), under review
12. Li, X.S.: An overview of SuperLU: Algorithms, implementation, and user interface. *ACM Trans. Math. Software* 31(3), 302–325 (September 2005)
13. Li, X.S., Demmel, J.W.: SuperLU\_DIST: A scalable distributed-memory sparse direct solver for unsymmetric linear systems. *ACM Trans. Mathematical Software* 29(2), 110–140 (June 2003)
14. May, D.A., Sanan, P., Rupp, K., Knepley, M.G., Smith, B.F.: Extreme-scale multigrid components within PETSc. In: *Proceedings of the Platform for Advanced Scientific Computing Conference*. pp. 5:1–5:12. PASC ’16, ACM, New York, NY, USA (2016)
15. Nicolaidis, R.A.: Deflation of conjugate gradients with applications to boundary value problems. *SIAM Journal on Numerical Analysis* 24(2), 355–365 (1987)
16. Notay, Y.: Flexible conjugate gradients. *SIAM Journal on Scientific Computing* 22(4), 1444–1460 (2000)
17. Roman, J.E., Campos, C., Romero, E., Tomas, A.: SLEPc users manual. Tech. Rep. DSIC-II/24/02 - Revision 3.9, D. Sistemes Informàtics i Computació, Universitat Politècnica de València (2018)
18. Vašatová, A., Tomčala, J., Sojka, R., Pecha, M., Kružík, J., Horák, D., Hapla, V., Čermák, M.: Parallel strategies for solving the FETI coarse problem in the PERMON toolbox. In: *Programs and Algorithms of Numerical Mathematics*. pp. 154–163. Institute of Mathematics CAS (2017)

# Quaternions and dynamics of particles

Ondřej Markovič

Department of Applied Mathematics, FEECS,  
VŠB – Technical University of Ostrava, 17. listopadu 15,  
708 33 Ostrava – Poruba, Czech Republic  
ondrej.markovic@vsb.cz

**Abstract.** This paper presents my first steps in simulations of granular matter dynamics. First, I looked at the kinematics of particulate flows, then the description of rotation using quaternions.

**Keywords:** particles, particulate flows, modeling, kinematics, dynamics, numerical integration, ODE, quaternion, rotation

## 1 Studies

### 1.1 Dynamics of particles

The study of granular matter dynamics led me to kinematics of particulate flows and book [3]. I began with kinematics of single particle. To understand the kinematics, we need to introduce position  $r$ , velocity  $v$  and acceleration  $a$  and their relations

$$v = \frac{dr}{dt} = \dot{r}, \quad a = \frac{dv}{dt}.$$

We do not simply apply velocity or the acceleration, but the change of position of particle is given by force applied to it. This leads to the known Newton's second law of motion

$$F = ma.$$

We can also study behavior of system of  $n$  particles using center of mass

$$r_{cm} = \frac{\sum_{i=1}^n m_i r_i}{\sum_{i=1}^n m_i}.$$

Force applied to the system is given only by external forces  $F_i^{EXT}$  as the sum of all internal forces  $F_i^{INT}$ , forces between particles in the system, is equal to zero. Thus

$$\sum_{i=1}^n m_i \ddot{r}_i = M \ddot{r}_{cm} = \sum_{i=1}^n F_i^{EXT}.$$

Total force  $F_i^{tot}$  applied to  $i$ -th particle is split into three components: the near-field interaction force  $F_i^{nf}$ , contact force  $F_i^c$  and friction force  $F_i^f$

$$F_i^{tot} = F_i^{nf} + F_i^c + F_i^f.$$

As it was mentioned I studied the description of rotation using quaternions. The reason behind it was for me to incorporate rotational force into the total force in upcoming year.

The near-field interaction force applied to particle  $i$  is given by central forces between two particles  $i$  and  $j$ . The forces are that of attraction and repulsion and they depend solely on the distance between two particles. The near-field interaction force is given as

$$F^{nf} = \sum_{j \neq i}^n \left( \underbrace{\alpha_{1ij} \|r_i - r_j\|^{-\beta_1}}_{\text{attraction}} - \underbrace{\alpha_{2ij} \|r_i - r_j\|^{-\beta_2}}_{\text{repulsion}} \right) n_{ij},$$

where  $\alpha, \beta$  are simple parameters and  $n_{ij}$  is unit normal vector between two particles.

The contact force is the normal force that is active when two particles collide. It is derived from the momentum conservation principle. The friction force is the tangential force of the collision, calculated from the contact force and the coefficient of friction.

To simulate the motion of particles I followed with numerical integration for ordinary differential equations, starting with the simple Euler method. Following the first simulations, few changes to the basic model were studied, such as “swarm like systems” given only by near-field interaction forces.

## 1.2 Quaternions

Quaternions were studied from the books [1, 2] for description of rotation of granular matter particles. Quaternions are given by ordered sequence  $(a, b, c, d)$  also known as components. With imaginary units  $(i, j, k)$  they create the cartesian form

$$q = a + bi + cj + dk.$$

The imaginary units relations are the most important part of quaternion algebra. They are given as

$$\begin{aligned} i^2 = j^2 = k^2 = ijk = -1, \\ ij = -ji = k, \quad jk = -kj = i, \quad ki = -ik = j. \end{aligned}$$

The set of all quaternions is denoted by  $\mathbb{H}$  after William Rowan Hamilton.

Quaternion  $q \in \mathbb{H}$ , can be divided into scalar and vector part

$$q = S(q) + V(q),$$

where

$$\begin{aligned} S(q) &= a, \\ V(q) &= bi + cj + dk. \end{aligned}$$



It can be also divided in terms of components into real and imaginary part as

$$\begin{aligned} \operatorname{Re}(q) &= a, \\ \operatorname{Im}(q) &= (b, c, d). \end{aligned}$$

Now let us introduce the basic properties. For quaternion written as  $x = x_0 + x_1i + x_2j + x_3k$ , the sum of two quaternions  $x, y \in \mathbb{H}$  is given as

$$\begin{aligned} x + y &= S(x) + S(y) + V(x) + V(y), \\ x + y &= x_0 + y_0 + (x_1 + y_1)i + (x_2 + y_2)j + (x_3 + y_3)k. \end{aligned}$$

Product of two quaternions  $x, y \in \mathbb{H}$  is given as

$$\begin{aligned} xy &= x_0y_0 - (x_1y_1 + x_2y_2 + x_3y_3) + \\ &\quad + x_0(y_1i + y_2j + y_3k) + y_0(x_1i + x_2j + x_3k) + \\ &\quad + (x_2y_3 - x_3y_2)i + (x_3y_1 - x_1y_3)j + (x_1y_2 - x_2y_1)k, \\ xy &= \operatorname{Re}(x)\operatorname{Re}(y) - \operatorname{Im}(x)\operatorname{Im}(y) + \operatorname{Re}(x)\operatorname{Im}(y)(i, j, k) + \\ &\quad + \operatorname{Re}(y)\operatorname{Im}(x)(i, j, k) + (\operatorname{Im}(x) \times \operatorname{Im}(y))(i, j, k), \end{aligned}$$

where the known signs for scalar and cross product are used.

- quaternion multiplication is non-commutative:  $xy \neq yx$
- quaternion multiplication is associative:  $(xy)z = x(yz)$
- quaternions are distributive in addition:  $x(y+z) = xy+xz, (x+y)z = xz+yz$
- quaternions are commutative in scalar multiplication  $\alpha: \alpha(xy) = x(\alpha y)$

In the same way as in complex numbers we have conjugate quaternion to  $q \in \mathbb{H}$  denoted as  $\bar{q} = S(q) - V(q)$  and absolute value  $|q| = \sqrt{\bar{q}q}$ . Unit quaternion is defined as  $x \in \{q; q \in \mathbb{H}, |q| = 1\}$  and inverse quaternion as  $q^{-1} = \frac{\bar{q}}{|q|^2}$ . Quaternion  $q \in \mathbb{H}$  is called pure if  $S(q) = 0$ .

The most important quaternion function for the study of rotation is the exponential function. For  $q \in \mathbb{H}$  it is given as

$$\begin{aligned} e^q &= e^{S(q)}e^{V(q)}, \\ &= e^{S(q)} (\cos(\gamma) + \mu \sin(\gamma)), \end{aligned}$$

where  $\gamma = |V(q)|, \mu = V(q)/|V(q)|$ .

We can also represent quaternions in many different ways, one of them is representation by real matrix  $\mathcal{M}_{\mathbb{R}}(q) \in \mathbb{R}^{4 \times 4}$  as

$$\mathcal{M}_{\mathbb{R}}(q) = \begin{bmatrix} q_0 & q_1 & q_3 & q_2 \\ -q_1 & q_0 & -q_2 & q_3 \\ -q_3 & q_2 & q_0 & -q_1 \\ -q_2 & -q_3 & q_1 & q_0 \end{bmatrix}$$

or the complex matrix  $\mathcal{M}_{\mathbb{C}}(q) \in \mathbb{C}^{2 \times 2}$  as

$$\mathcal{M}_{\mathbb{C}}(q) = \begin{bmatrix} q_0 + q_1 i & -q_2 + q_3 i \\ q_2 + q_3 i & q_0 - q_1 i \end{bmatrix}.$$

The use of quaternion rotation has become more popular as the rotation using the Euler angles suffers from gimbal lock.

To describe rotation in 3D we represent point in space by pure quaternion  $q$ . Then the rotation of point in space is given by  $\mathcal{R}(q)$  as

$$\mathcal{R}_r(q) = pq\bar{p},$$

where

$$p = e^{\frac{\gamma}{2}r},$$

$r$  unit pure quaternion represents axis around which we rotate and  $\gamma$  is the angle of rotation. Quaternions can also be used for description of system of particles.

## 2 Activity report

I had two presentations at the Department of applied mathematics seminar. The presentations were made from the studies of 2018/2019. I also attended the NUMTA2019 conference in Italy. Its main topic was the introduction of grossone and its future use. I sent also two applications to HPC-Europa3 programme. However, both were denied. In next period I am going to implement these studies into PERMON toolbox and to combine quadratic programming algorithms with domain decomposition approach of FETI type to solve large-scale simulations in parallel.

## References

1. Ell, T., Bihan, N., Sangwine, S.: Quaternion Fourier Transforms for Signal and Image Processing. FOCUS Series, Wiley (2014)
2. Rodman, L.: Topics in Quaternion Linear Algebra. Princeton Series in Applied Mathematics, Princeton University Press (2014)
3. Zohdi, T.: An Introduction to Modeling and Simulation of Particulate Flows. Computational Science and Engineering, Society for Industrial and Applied Mathematics (SIAM, 3600 Market Street, Floor 6, Philadelphia, PA 19104) (2007)

# An Optimization Approach to Solving the Kohn-Sham Equation

Martin Mrovec<sup>1,2</sup>

<sup>1</sup>IT4Innovation, VŠB – Technical University of Ostrava,  
17. listopadu 15, 708 33 Ostrava – Poruba, Czech Republic

<sup>2</sup>Department of Applied Mathematics, FEECS,  
VŠB – Technical University of Ostrava, 17. listopadu 15,  
708 33 Ostrava – Poruba, Czech Republic  
`martin.mrovec@vsb.cz`

**Abstract.** The paper presents results of using the optimization approach in the area of Electronic Structure Calculations. It follows the previous research where this approach has been tested for solving the Hartree-Fock Equation. Currently we are interested in the Kohn-Sham Equation with a slightly different structure. The paper shows a comparison of the convergence of chosen numerical methods, namely the Direct Inversion of the Iterative Subspace and the Inexact Restoration Method based algorithm, for solving the nonlinear eigenvalue problem. The numerical experiments are performed on the modeling of the potential curve of the Hydrogen Fluoride molecule.

## 1 Introduction

Electronic Structure Calculations belong to very challenging tasks. We are currently interested in electronic structures of closed-shell molecules, more specifically the ground state energy and related electronic charge density based on the Density Functional Theory (DFT). The solution process usually consists of two parts. First, the precomputing phase is performed for getting coefficients which are necessary during the second part. The computational part consists of solving of a nonlinear Eigenvalue Problem (EVP). It is usually solved by the iteration of the Self Consistent Field (SCF) accelerated by the Direct Inversion of the Iterative Subspace (DIIS) [1]. Since its introduction, the DIIS approach has been extensively developed. Despite significant improvements, we may still encounter convergence issues related to DIIS (even in current prominent computational codes, such as Molpro). Thus, we should consider an alternative approach, e.g. the optimization one, where the problem is transformed to a Quadratically Constrained Minimization Problem. There are known algorithms, such as Trust Region methods, for solving such kind of optimization problems. We use methods inspired by the Inexact Restoration Method (IRM) published in [2]. This study is focused on a comparison of the mentioned approaches where the numerical experiments have been performed on a simple two-atomic system. Preliminary results have been presented in [3] where the Hartree-Fock Equation has been solved. Here, the same system of particles is studied, but the calculations are done at the level of the Local Density Approximation (LDA).

## 2 Kohn-Sham Equation

The standard form of the Kohn-Sham (KS) Equation can be written as

$$\left( -\frac{1}{2}\Delta + V_{\text{ext}}(\mathbf{r}) + V_{\text{H}}(\mathbf{r}) + V_{\text{xc}}(\mathbf{r}) \right) \phi_i(\mathbf{r}) = \varepsilon_i \phi_i(\mathbf{r}). \quad (1)$$

This equation can be understood as a non-linear eigenvalue problem (EVP). Equation (1) is usually solved within a finite dimensional basis. Given a  $N_b$ -dimensional basis, each orbital can be written as

$$\phi_i(\mathbf{r}) = \sum_{j=1}^{N_b} c_{ji} \mu_j(\mathbf{r}) \quad (2)$$

and the discretized form of the KS Equation as matrix equation

$$\mathbf{F}(\mathbf{C})\mathbf{C} = \mathbf{M}\mathbf{C}\mathbf{A}. \quad (3)$$

The unknown of our problem is represented by coefficient matrix  $\mathbf{C} \in \mathbb{R}^{N_b \times N}$ . For an easier expressing of the energy functional it is suitable to use the so-called density matrix  $\mathbf{Z}$  where  $\mathbf{Z} = \mathbf{C}\mathbf{C}^T$ . Equation (3) has to be solved iteratively. Using an initial guess, matrix  $\mathbf{F}$  is assembled and the EVP is solved. The process is repeated with the new coefficient matrix until the Self-Consistency is reached. For a stabilization of the convergence, the DIIS mixing procedure is usually used [1]. However, this procedure does not always ensure the convergence (see the Comparison section).

## 3 Optimization Approach

Within the basis given by Eq. (2), the Kohn-Sham Energy functional can be written as a function of unknown matrix  $\mathbf{Z}$  such that

$$E(\mathbf{Z}) = \text{Trace}[2\mathbf{H}\mathbf{Z} + \mathbf{J}(\mathbf{Z})\mathbf{Z}] + E_{\text{xc}}(\mathbf{Z}) \quad (4)$$

where  $\mathbf{H}$  represents the kinetic part and the nuclear potential,  $\mathbf{J}$  represents the Hartree potential. The aim is to find a minimum of such functional. The structure of the density matrix brings the following equality constraints

$$\mathbf{Z} = \mathbf{Z}^T, \quad \mathbf{M}\mathbf{Z}\mathbf{M} = \mathbf{Z}, \quad \text{Trace}(\mathbf{M}\mathbf{Z}) = N \quad (5)$$

so the optimization problem is quadratically constrained. The Kohn-Sham energy functional is generally not quadratic (as in the Hartree-Fock case) which is caused by the exchange-correlation term. This term has to be evaluated by a numerical integration. For gradient based optimization methods we have to write down the gradient of the energy functional with respect to the unknown matrix  $\mathbf{Z}$ , i.e.

$$\nabla_{\mathbf{Z}} E(\mathbf{Z}) = 2(\mathbf{H} + \mathbf{J}(\mathbf{Z})) + \nabla_{\mathbf{Z}} E_{\text{xc}}(\mathbf{Z}). \quad (6)$$

Analogously to the energy formula, the last term has to be evaluated elementwise by a numerical integration. The integral formula depends on the level of the approximation of the exchange-correlation energy. For example within the LDA it corresponds to the evaluation of exchange-correlation potential matrix  $\mathbf{V}_{xc} \in \mathbb{R}^{N_b \times N_b}$  used in the standard eigenvalue approach, i.e..

$$[\mathbf{V}_{xc}^{LDA}]_{ij} = \int_{\mathbb{R}^3} \frac{\delta E_{xc}^{LDA}(\rho_{\mathbf{z}})}{\delta \rho_{\mathbf{z}}(\mathbf{r})}(\mathbf{r}) \mu_i^*(\mathbf{r}) \mu_j(\mathbf{r}) d^3\mathbf{r}, \tag{7}$$

We should notice that, in principle, the evaluation of  $\nabla_{\mathbf{z}} E(\mathbf{Z})$  corresponds to the evaluation of the Kohn-Sham Matrix  $\mathbf{F} \in \mathbb{R}^{N_b \times N_b}$  and thus the computational complexity is identical. The same idea can be applied at the level of the GGA approximation. Unfortunately, a further generalization for higher levels of approximation of  $E_{xc}$  (within standard KS Theory) may be problematic because conditions for evaluating  $\mathbf{V}_{xc}$  bring additional constraints that are difficult to be explicitly derived. However, this approach is applicable within the Generalized KS theory. For algorithmic purposes it is suitable to transform the optimization problem by defining an alternative unknown matrix  $\mathbf{X} = \mathbf{M}^{\frac{1}{2}} \mathbf{Z} \mathbf{M}^{\frac{1}{2}}$ . Then the optimization problem transforms to

$$\min f(\mathbf{X}) = E\left(\mathbf{M}^{-\frac{1}{2}} \mathbf{X} \mathbf{M}^{-\frac{1}{2}}\right) \tag{8}$$

subject to

$$\mathbf{X} = \mathbf{X}^T, \tag{9}$$

$$\mathbf{X}\mathbf{X} = \mathbf{X}, \tag{10}$$

$$\text{Trace}(\mathbf{X}) = N. \tag{11}$$

## 4 Algorithm

The optimization algorithm we use is based on the Inexact Restoration Method (IRM) published in [2]. This iterative method is designed for solving optimization problems with equality constraints which describe feasible set  $\Omega$ . In the published form the algorithm is not well-suited for using in the DFT calculations. Thus, necessary modifications had to be done. Each iteration consist of the following steps:

1. **Restoration Phase** - Given an iterate  $\mathbf{X}_k$  which does not belong to  $\Omega$ , the restoration phase calculates its projection  $\mathbf{Y}_{k+1} = P_{\Omega}(\mathbf{X}_k)$ . Generally, this procedure requires a knowledge of the spectrum of  $\mathbf{X}_k$ . However, due to the some properties of  $\mathbf{X}_k$  guaranteed by the previous iteration it can be performed by so-called McWeeny purification procedure given by iterative process

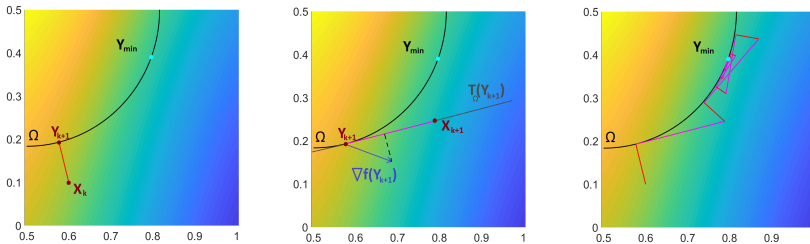
$$\mathbf{Y}_k^{j+1} = 3\left(\mathbf{Y}_k^j\right)^2 - 2\left(\mathbf{Y}_k^j\right)^3. \tag{12}$$

Such approach requires only an estimate of the largest eigenvalue which is dramatically cheaper to calculate than in case of standard EVP approach.

2. **Calculation of the descent direction** - Since the evaluation of the gradient of the energy function requires  $\mathcal{O}(N_b^2)$  numerical integrations, for finding a descent direction we should omit any iterative procedure. As an optimal direction the gradient descent one is chosen. Next, the projection of the direction to the tangent set  $T_\Omega(\mathbf{Y}_k)$  has to be calculated. The searching of the next iterate within the tangent set is a necessary step for applicability of the purification procedure in phase 1.
3. **Optimum within the tangent set** - The next iteration is calculated as  $\mathbf{X}_{k+1} = \mathbf{Y}_k + t_k \mathbf{E}_k$  where step length  $\mathbf{E}_k$  in the tangent descend direction is determined using the Golden Ratio Linesearch which minimizes the number of energy evaluations (and thus the numerical integrations). The computationally critical part of the calculation of the energy is the evaluation of the charge density for all quadrature points. However, the structure of the problem enables us to reduce the computational costs to roughly two evaluations of the density. The original energy function is replaced by its lagrangian defined as

$$L(\mathbf{X}, \Lambda) = f(\mathbf{X}) + \text{Trace}(\Lambda(\mathbf{X}^2 - \mathbf{X})) \quad (13)$$

where, at given point  $\mathbf{Y}_k \in \Omega$ , the matrix of Lagrange multipliers is suitably approximated.



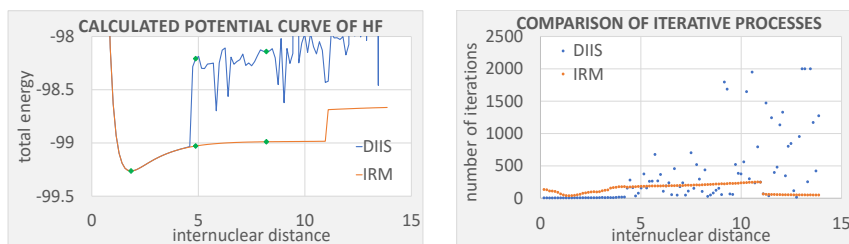
**Fig. 1.** left - restoration phase of the algorithm, center - gradient projection onto tangent set and linesearch, right - convergence to minimum

## 5 Comparison of DIIS and IRM-based algorithm

For the numerical experiments we have chosen the calculation of the potential curve of the Hydrogen Fluoride. It means that we want to calculate the dependence of the ground state energy of the system on the distance between nuclei. The interval of distances we are interested is between  $0.173 a_0$  to  $13.863 a_0$  ( $a_0$  is the Bohr radius, as the energy unit we use the Hartree energy) so it contains the nuclear repulsion wall, the equilibrium and a significant portion of the attraction part. The interval has been divided into 100 points providing an appropriate number of measurements. For each distance we have solved the KS Equation (with exchange-correlation term based on LDA) using

1. **Self-Consistent Field approach with DIIS** - As a residual for the assembly of the DIIS matrix and for the purposes of the stopping criterion we have used  $\mathbf{E} = \mathbf{F}(\mathbf{Z})\mathbf{ZM} - \mathbf{MZ}\mathbf{F}(\mathbf{Z})$  which corresponds to [1]. The DIIS matrix has not been assembled for all the previous iterations but only for  $k$  last iterations. There has been set a maximal value of  $k$  (experiments have been done for  $k_{\max}$  between 6 and 10, however no significant effect to the stability has been observed). Furthermore, the DIIS matrix size has been reset to 1, if its conditional number reaches given threshold.
2. **Optimization approach with IRM-based algorithm** - As a stopping criterion the Frobenius norm of the energy function gradient projection onto the tangent set has been chosen. It is closely related to the residual used in the standard DIIS approach.

We have been focused on the correctness of the result and on the number of the iterations required to get the same accuracy. The stopping criterion threshold has been set to  $10^{-5}$ . As a basis set we have chosen pc-1 basis [5], which consisted of  $N_b = 20$  contracted Gaussian-type orbital basis functions. Number of electrons is equal to 10, i.e.  $N = 5$  eigenvectors had to be computed. In all cases the initial approximation has been chosen as the zero matrix so the initial Kohn-Sham matrix consisted only of the kinetic part and the nuclear potential part.

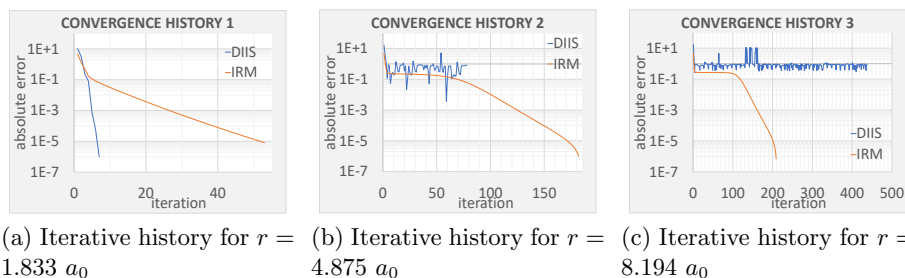


(a) Calculated potential curve of HF molecule (b) Number of iterations with respect to internuclear distance

**Fig. 2.** Convergence of the algorithms

## 6 Conclusions and Outlooks

An optimization approach based on IRM has been presented. It has shown a good convergence behavior, thus it can be understood as a well-suited alternative to the standard solution of a non-linear EVP (iteration of SCF accelerated with DIIS). Although the number of iterations of our approach can be higher, the algorithm demonstrates its robustness in configurations where the standard one fails to converge. As an limitation of the IRM-based algorithm, we should mention that it is generally a local optimizer. The consequence of this property can be observed at higher distances of the potential curve where the algorithms end



**Fig. 3.** Selected histories of the iterative process

up in a different local minimum. Currently, we are working on a global optimization strategy based on the Swarm Intelligence [6]. Using such algorithm, we can find a point within a basin of attraction of the global minimum and then the IRM-based algorithm will converge to the right minimum. Currently, numerical experiments with different atomic systems (e.g. CrC) are running and a paper is in preparation.

## 7 Acknowledgement

This work was supported by The Ministry of Education, Youth and Sports from the National Programme of Sustainability (NPS II) project IT4Innovations excellence in science - LQ1602. The work was also supported by SGC Grants No. SP2018/178, SP2019/162, SP2019/84, VŠB - Technical University of Ostrava, Czech Republic. The calculations have been performed using the resources of the IT4Innovations National Supercomputing Center of the Czech Republic.

## References

1. Pulay, P.: Convergence acceleration of iterative sequences. the case of scf iteration. *Chem. Phys. Lett.*, vol. 73(issue 2):393–398, 1980.
2. Martínez, J. M., Martínez, L., Pisnitchenko, F.: Inexact restoration method for minimization problems arising in electronic structure calculations. *Computational Optimization and Applications*, vol. 50(issue 3):555–590, 2011.
3. Mrovec M.: Convergence Study of Different Approaches of Solving the Hartree-Fock Equation on the Potential Curve of the Hydrogen Fluoride. *AETA 2018 - Recent Advances in Electrical Engineering and Related Sciences: Theory and Application. Lecture Notes in Electrical Engineering*, vol 554. Springer, Cham
4. Saad, Y., Chelikowsky, J. R., Shontz, S. M.: *Numerical Methods for Electronic Structure Calculations of Materials*. *SIAM Review*. 2010, DOI: 10.1137/060651653, ISSN 0036-1445, Zbl 1185.82004
5. Pritchard, B. P., Altarawy, D., Didier, B., Gibson, T. D., Windus, T. L.: A New Basis Set Exchange: An Open, Up-to-date Resource for the Molecular Sciences Community, 2019, Manuscript in Preparation
6. Kennedy, J., Eberhart, R.: Particle swarm optimization; *Neural Networks*, 1995; *Proceedings.*, IEEE International Conference, vol.4: 1942-1948



# Duality Based Solver for the Navier-Stokes Problem

Jan Pacholek

Department of Applied Mathematics, FEECS,  
VŠB – Technical University of Ostrava, 17. listopadu 15,  
708 33 Ostrava – Poruba, Czech Republic  
jan.pacholek.st@vsb.cz

**Abstract.** The paper deals with the Navier-Stokes flow with the Dirichlet and Neumann boundary conditions. Using the P1-bubble/P1 finite element approximation of the velocity-pressure formulation, we arrive at a system of equations, which we solve by the Shur complement method and the Oseen iterations. An implementation is done in MATLAB environment with ENSIGHT used as a graphic program for interpreting the results of experiments done on a L-shaped domain.

## 1 Introduction

Let  $\Omega$  be a bounded domain in  $\mathbb{R}^2$  with a sufficiently smooth boundary  $\partial\Omega$  that is split into three nonempty disjoint parts:  $\partial\Omega = \bar{\gamma}_D \cup \bar{\gamma}_N$ . We consider the model of a viscous incompressible Newtonian fluid modelled by the Navier-Stokes system with the Dirichlet and Neumann boundary conditions on  $\gamma_D$  and  $\gamma_N$ , respectively:

$$\left. \begin{aligned} -2\nu \operatorname{div} D(\mathbf{u}) + (\mathbf{u} \cdot \nabla) \mathbf{u} + \nabla p &= \mathbf{f} && \text{in } \Omega, \\ \nabla \cdot \mathbf{u} &= 0 && \text{in } \Omega, \\ \mathbf{u} &= \mathbf{u}_D && \text{on } \gamma_D, \\ \boldsymbol{\sigma} &= \boldsymbol{\sigma}_N && \text{on } \gamma_N. \end{aligned} \right\} \quad (1)$$

We are searching for a vector function representing the flow velocity field  $\mathbf{u} : \Omega \rightarrow \mathbb{R}^2$ ,  $\mathbf{u} = (u_1, u_2)$  and a scalar function representing the pressure field  $p : \Omega \rightarrow \mathbb{R}$ , where  $\nu > 0$  is the dynamic viscosity,  $\mathbf{f} : \Omega \rightarrow \mathbb{R}^2$  describes the forces acting on the fluid,  $\mathbf{u}_D : \gamma_D \rightarrow \mathbb{R}^2$  and  $\boldsymbol{\sigma}_N : \gamma_N \rightarrow \mathbb{R}^2$  are the Dirichlet and Neumann boundary data, respectively. Further

$$\boldsymbol{\sigma} = 2\nu D(\mathbf{u})\mathbf{n} - p\mathbf{n} \text{ on } \partial\Omega$$

is the stress vector on  $\partial\Omega$ .  $D(\mathbf{u})$  is then the symmetric gradient, where for

$$\nabla \mathbf{u} = \begin{pmatrix} \nabla u_1 \\ \nabla u_2 \end{pmatrix} = \begin{pmatrix} \frac{\partial u_1}{\partial x_1} & \frac{\partial u_1}{\partial x_2} \\ \frac{\partial u_2}{\partial x_1} & \frac{\partial u_2}{\partial x_2} \end{pmatrix}$$

we define  $D(\mathbf{u})$  as

$$D(\mathbf{u}) = \frac{1}{2}(\nabla\mathbf{u} + (\nabla\mathbf{u})^T) = \begin{pmatrix} \frac{\partial u_1}{\partial x_1} & \frac{\frac{\partial u_1}{\partial x_2} + \frac{\partial u_2}{\partial x_1}}{2} \\ \frac{\frac{\partial u_1}{\partial x_2} + \frac{\partial u_2}{\partial x_1}}{2} & \frac{\partial u_2}{\partial x_2} \end{pmatrix}.$$

## 2 Weak formulation and algebraic problem

Now we introduce the description of the problem (1) using integrals that is known as the weak formulation. Applying Green’s theorem, we will reduce the requirements on the smoothness of the solution, similarly to [2].

We multiply the first equation in (1)

$$-2\nu\operatorname{div}D(\mathbf{u}) + (\mathbf{u} \cdot \nabla)\mathbf{u} + \nabla p = \mathbf{f},$$

by the test function  $\mathbf{v} = (v_1, v_2)$  and we integrate:

$$-2\nu \int_{\Omega} \operatorname{div}D(\mathbf{u}) \cdot \mathbf{v} dx + \int_{\Omega} (\mathbf{u} \cdot \nabla)\mathbf{u} \cdot \mathbf{v} dx + \int_{\Omega} \nabla p \mathbf{v} dx = \int_{\Omega} \mathbf{f} \cdot \mathbf{v} dx.$$

Using Green’s theorem, we arrive at:

$$-2\nu \int_{\Omega} D(\mathbf{u}) : D(\mathbf{v}) dx + \int_{\Omega} (\mathbf{u} \cdot \nabla)\mathbf{u} \cdot \mathbf{v} dx - \int_{\Omega} p(\nabla \cdot \mathbf{v}) dx = \int_{\Omega} \mathbf{f} \cdot \mathbf{v} dx + \int_{\partial\Omega} \boldsymbol{\sigma} \cdot \mathbf{v} dx, \tag{2}$$

where  $D(\mathbf{u}) : D(\mathbf{v}) = D_1(\mathbf{u}) \cdot \nabla v_1 + D_2(\mathbf{u}) \cdot \nabla v_2$ .

Equation

$$\nabla \cdot \mathbf{u} = 0$$

can be then multiplied by the test function  $q$ , which is sufficiently smooth:

$$\int_{\Omega} q(\nabla \cdot \mathbf{u}) dx = 0. \tag{3}$$

If we look at equation (2), we can notice that the line integral can be separated into two parts, such that:

$$\int_{\partial\Omega} \boldsymbol{\sigma} \cdot \mathbf{v} dx = \int_{\gamma_D} \boldsymbol{\sigma} \cdot \mathbf{v} dx + \int_{\gamma_N} \boldsymbol{\sigma} \cdot \mathbf{v} dx.$$

The integral over  $\gamma_N$ , with consideration of the Neumann boundary condition, has the following form:

$$\int_{\gamma_N} \boldsymbol{\sigma} \cdot \mathbf{v} dx = \int_{\gamma_N} \boldsymbol{\sigma}_N \cdot \mathbf{v} dx$$

and we join it with the volume integral on the right side of (2).

Now we define appropriate forms, which will describe our problem:

$$\begin{aligned}
 a &: (H^1(\Omega))^2 \times (H^1(\Omega))^2 \times (H^1(\Omega))^2 \rightarrow \mathbb{R}, & a(\mathbf{w}, \mathbf{u}, \mathbf{v}) &= a_0(\mathbf{u}, \mathbf{v}) + a_1(\mathbf{w}, \mathbf{u}, \mathbf{v}), \\
 a_0 &: (H^1(\Omega))^2 \times (H^1(\Omega))^2 \rightarrow \mathbb{R}, & a_0(\mathbf{u}, \mathbf{v}) &= -2\nu \int_{\Omega} D(\mathbf{u}) : D(\mathbf{v}) dx, \\
 a_1 &: (H^1(\Omega))^2 \times (H^1(\Omega))^2 \times (H^1(\Omega))^2 \rightarrow \mathbb{R}, & a_1(\mathbf{w}, \mathbf{u}, \mathbf{v}) &= \int_{\Omega} (\mathbf{w} \cdot \nabla) \mathbf{u} \cdot \mathbf{v} dx, \\
 b &: L^2(\Omega) \times (H^1(\Omega))^2 \rightarrow \mathbb{R}, & b(q, \mathbf{v}) &= - \int_{\Omega} q(\nabla \cdot \mathbf{v}) dx, \\
 l &: (H^1(\Omega))^2 \rightarrow \mathbb{R}, & l(\mathbf{v}) &= \int_{\Omega} \mathbf{f} \cdot \mathbf{v} dx + \int_{\gamma_N} \boldsymbol{\sigma}_N \cdot \mathbf{v} dx.
 \end{aligned}$$

Furthermore, we define the set of functions on which we search for the solution:

$$V_D = \{ \mathbf{v} \in (H^1(\Omega))^2 : \mathbf{v} = \mathbf{u}_D \quad \text{on } \gamma_D \}.$$

We consider the test functions  $\mathbf{v}$  belonging to  $V_D$ . Using these forms, we arrive at the following weak formulation of (1)

$$\left. \begin{aligned}
 &\text{Find } (\mathbf{u}, p) \in V_D \times L^2(\Omega) \text{ so that} \\
 &a(\mathbf{u}, \mathbf{u}, \mathbf{v}) + b(p, \mathbf{v}) = l(\mathbf{v}) \quad \forall \mathbf{v} \in V_D \\
 &b(q, \mathbf{u}) = 0 \quad \forall q \in L^2(\Omega).
 \end{aligned} \right\} \tag{4}$$

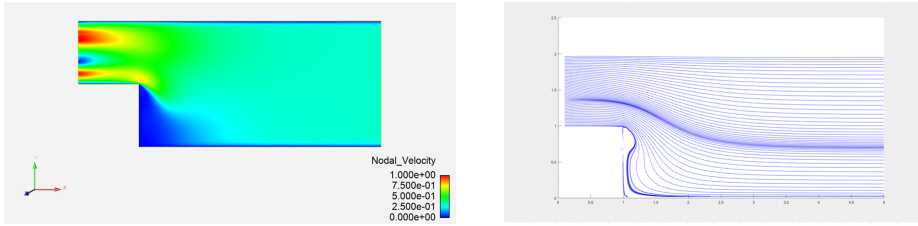
We approximate (4) by the mixed finite element method based on the P1-bubble/P1 finite elements [1], which, after elimination of bubble components, leads to the following problem:

$$\begin{pmatrix} A & B_u^T \\ B_l & -E \end{pmatrix} \begin{pmatrix} u \\ p \end{pmatrix} = \begin{pmatrix} b \\ c \end{pmatrix}, \tag{5}$$

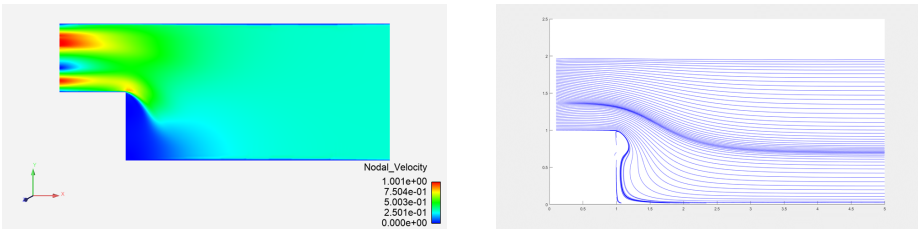
where  $A \in \mathbb{R}^{n_u \times n_u}$  is nonsingular with diffusion and convective matrices added together,  $B_u, B_l \in \mathbb{R}^{n_u \times n}$  are full row rank stiffness matrices,  $b \in \mathbb{R}^{n_u}$ ,  $E \in \mathbb{R}^{n \times n}$  is symmetric, positive semi-definite matrix, which together with vector  $c \in \mathbb{R}^n$  arise from the elimination of the bubble components. To solve the system of equations we use the Shur complement method and Oseen iterations with BiCGSTAB as the inner solver.

### 3 Numerical experiments

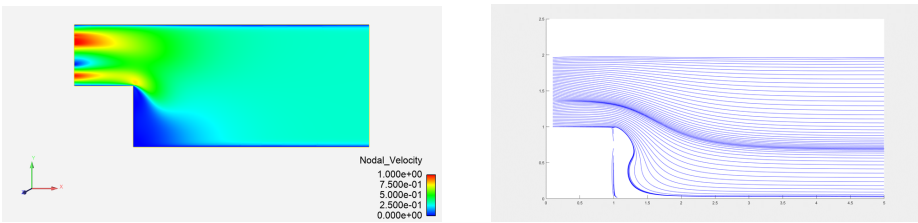
We consider the L-shaped domain  $\Omega = (0, 5) \times (0, 2) \setminus \bar{\mathcal{S}}$ ,  $\mathcal{S} = (0, 1) \times (0, 1)$  with  $\mathbf{f} = \mathbf{0}$ ;  $\gamma_D = \gamma_{top} \cup \gamma_{left}$  with  $\gamma_{top} = (0, 5) \times \{2\}$ ,  $\gamma_{left} = \{0\} \times (1, 2)$ ,  $\mathbf{u}_D|_{\gamma_{top}} = \mathbf{0}$ , and  $\mathbf{u}_D|_{\gamma_{left}} = (4(x_2 - 2)(1 - x_2), 0)$ ;  $\gamma_N = \{5\} \times (0, 2)$  with  $\boldsymbol{\sigma}_N = \mathbf{0}$ . Each picture then represents different values of  $\nu$  and the respective velocity field inside  $\Omega$ .



**Fig. 1.** Velocity field and contours in L-shaped domain with  $\nu = 0.001$



**Fig. 2.** Velocity field and contours in L-shaped domain with  $\nu = 0.0001$



**Fig. 3.** Velocity field and contours in L-shaped domain with  $\nu = 0.00001$

## Conclusion

We have successfully implemented a working MATLAB code for solving the Navier-Stokes equations with the Dirichlet and Neumann boundary conditions. For future work, we would like to implement a version for the stick-slip boundary conditions, which will require use of the semi-smooth Newton method or the interior point method, with a possible extension to 3D problem.

## References

1. Koko, J.: Vectorized Matlab codes for the Stokes problem with P1-bubble/P1 finite element. <https://www.isima.fr/~jkoko/Codes/StokesP1BubbleP1.pdf>.
2. Pacholek, J.: Semi-smooth Newton method for solving the Stokes equations with monotonously increasing slip condition. Diploma thesis, VŠB-TU Ostrava (2017).

# Fitting of potential energy surfaces using neural networks

Stanislav Paláček

Department of Applied Mathematics, FEECS,  
VŠB – Technical University of Ostrava, 17. listopadu 15,  
708 33 Ostrava – Poruba, Czech Republic  
stanislav.palacek@vsb.cz

**Abstract.** There exist complex systems for which nonadiabatic molecular dynamics calculations are impractical or impossible to perform in reasonable time using ab initio methods. For this reason it is required to have quick and computationally cheap way to obtain potential energy or other quantities necessary for nonadiabatic molecular dynamics calculations on ab initio level of accuracy. It would be more convenient to perform ab initio calculations on some appropriately chosen configuration points and fit the potential energy surface by making the use of neural networks. For creating and training neural networks a software package called *neuron4dyn* has been implemented using FORTRAN language.

## 1 Artificial neural networks

Artificial neural networks (ANN) are computing systems inspired by the biological neural networks that form brains. Such systems are learned on examples without a need of programming any task specific rules. ANNs have found many applications. Typically they are widely used in an image recognition. They can learn to identify images that contain for example a dog by learning on images which have been manually labeled as *dog* or *no dog*. Basic units of such ANNs are nodes commonly called neurons. An artificial neuron has several inputs and only one output. Mathematically it can be described by equation:

$$y = \phi\left(\sum_{j=1}^n w_j x_j + b\right), \quad (1)$$

where  $x_1, \dots, x_n$  are the input signals,  $w_1, \dots, w_n$  are the synaptic weights of the neuron,  $b$  is the bias,  $\phi$  is the activation function,  $y$  is the output signal of the neuron. Activation function  $\phi: \mathbb{R} \rightarrow \mathbb{R}$ , also referred to as transition function define the output of a neuron. There exist several types of activation functions. Most widely in output neurons are used identity function:

$$\phi(x) = x \quad (2)$$

and in internal neurons are used sigmoid function:

$$\phi(x) = \frac{1}{1 + e^{-x}}. \quad (3)$$

There exist a lot of ways how to interconnect neurons in ANNs, however feedforward neural networks (FFNN) are very typical. Neurons are grouped into layers and signals travel from the first layer (the input layer) to the last layer (the output layer). Each neuron from the current layer is connected with each neuron of the next forward layer. Different layers can have different transition functions. FFNN is also called as multilayer perceptron.

For multilayer feedforward network universal approximation theorem applies which claims that [1]: *The standard multilayer feedforward networks with a single hidden layer that contains a finite number of hidden neurons, and with arbitrary activation function are universal approximators in  $C(\mathbb{R}^m)$*  This theorem has been proved by Cybenko [2] for FFNN with sigmoidal activation functions in the hidden layer and more generally by Hurnik [3] for any transition function in hidden layer.

## 2 Learning algorithms

A scalar cost function  $E$  is very important in learning of any neural network, it gives us measure how good or bad the prediction of neural network is in comparison with the expected value. Ideally, we want the cost function to be zero. In learning process weights and biases of a neural network are gradually adjusted until good predictions are obtained.

### 2.1 Backpropagation

Backpropagation followed by a gradient descent method, [4] chapter 7, is basic and most widely used learning algorithm of neural networks. Topology of FFNN permits to calculate the gradient of cost function with respect to the parameters of neural network analytically. Backpropagation algorithm is a recursive algorithm and is derived on the basis of the chain rule.

Let  $w_{ij}^k$  be the weight of the connection from  $i$ -th neuron in layer  $k-1$  to the  $j$ -th neuron  $k$ -th layer. For simplicity the bias of  $j$ -th neuron in  $k$ -th layer will also be denoted as  $w_{0j}^k = b_j^k$ . Outputs of  $i$ -th neuron from  $(k-1)$ -th layer will be denoted  $o_i^{k-1}$  and  $o_0^{k-1} = 1$  is a bias signal. Then the activation of  $j$ -th neuron in  $k$ -th layer is  $a_j^k = \sum_{i=0}^{R_{k-1}} o_i^{k-1} w_{ij}^k$ , where  $R_{k-1}$  is the number of neurons in layer  $k-1$ . Output of  $j$ -th neuron from  $k$ -th layer is  $o_j^k = \sigma_k(a_j^k)$ , where  $\sigma_k$  is the activation function of neurons in  $k$ -th layer. Backpropagation algorithm is then given by the following set of equations:

$$\frac{\partial E}{\partial w_{ij}^k} = \delta_j^k o_i^{k-1}, \quad (4)$$

$$\delta_j^k = \sigma'_k(a_j^k) \sum_{l=1}^{R_{k+1}} w_{jl}^{k+1} \delta_l^{k+1} \quad (5)$$

$$\delta_j^M = \sigma'_M(a_j^M) \frac{\partial E}{\partial o_j^M}, \tag{6}$$

where  $M$  denotes the output layer of FFNN. The following steps are performed during the learning process. Feed-forward propagation, evaluation of  $\delta_j^M$  for the output layer using equation 6, backpropagation from last hidden to the first hidden layer of  $\delta$  using equation 5 and finally evaluation of gradient of the cost function using equation 4. After computing all partial derivatives the network weights are updated in the negative gradient direction

$$\Delta w_{ij}^k = -\gamma \frac{\partial E}{\partial w_{ij}^k}, \tag{7}$$

where  $\gamma$  defines a step length.

### 2.2 Global extended Kalman filter

Beside gradient descent method there exist alternatives for training of neural networks. One such alternative is global extended Kalman filter (GEKF). More detailed description of this algorithm can be found in [5] and more general informations about Kalman filters can be found in [6]. GEKF training algorithm as is given in [5] is based on the following recursion formulas:

$$\mathbf{K}_k = \lambda^{-1} \mathbf{P}_{k-1} \mathbf{H}_k [\mathbf{I} + \lambda^{-1} \mathbf{H}_k^T \mathbf{P}_{k-1} \mathbf{H}_k]^{-1} \tag{8}$$

$$\mathbf{P}_k = \lambda^{-1} \mathbf{P}_{k-1} - \lambda^{-1} \mathbf{K}_k \mathbf{H}_k^T \mathbf{P}_{k-1} + \mathbf{Q}_k \tag{9}$$

$$\mathbf{w}_k = \mathbf{w}_{k-1} + \mathbf{K}_k \boldsymbol{\xi}_k \tag{10}$$

Vector  $\mathbf{w}_k$  represents the estimate of the parameters of a neural network at step  $k$ . Symbol  $\mathbf{K}_k$  is the Kalman gain matrix, and  $\boldsymbol{\xi}_k = \mathbf{y}_k - \hat{\mathbf{y}}_k$  is an error vector. Here  $\mathbf{y}_k$  is the target output vector and  $\hat{\mathbf{y}}_k$  is the output of the network. Symbol  $\mathbf{P}_k$  represents an approximate error covariance matrix,  $\mathbf{H}_k$  is a matrix of derivatives of the network outputs with respect to all trainable parameters.  $\mathbf{Q}_k$  is the process noise covariance matrix. This algorithm attempts to find parameters of NN which minimize a cost function written in the form of  $\sum_{p=1}^k \boldsymbol{\xi}_k^T \boldsymbol{\xi}_k \lambda^{k-p}$ . The errors are summed over all the  $k$  iterations, but the exponential weighting factor  $\lambda^{k-p}$  provides significant weighting only for more recently encountered samples. There exists a variant of GEKF were the value of  $\lambda$  is adjusted after each presentation of training example according to

$$\lambda_k = \lambda_0 \lambda_{k-1} + 1 - \lambda_0, \tag{11}$$

where  $\lambda_0$  is a constant ranging between 0.99 – 0.9995 and initial value of  $\lambda$  is chosen from the range between 0.95 – 0.99. This forgetting strategy is due to the

reason, that at the early stage of optimization iterations are relatively inaccurate. The noise covariance matrices,  $\mathbf{Q}_k$ , have to be specified for all the training data and similarly, the approximate error covariance matrix  $\mathbf{P}_k$ , have to be initialized at the beginning of training. GEKF training is carried out sequentially. After each presentation of the training pattern the error vector  $\boldsymbol{\xi}_k$  is computed by propagating through the network. The Matrices of derivatives  $\mathbf{H}_k$  can be calculated using the backpropagation algorithm. Using equations 8 and 9 Kalman gain matrix  $\mathbf{K}_k$  can be recalculated and approximate error covariance matrix  $\mathbf{P}_k$  updated. Using equation 10 parameters of NN are updated.

Adaptive global extended Kalman filter (AGEKF) is an adaptive variant of GEKF. In this variant after the first epoch, i.e. after all training data set is presented, calculations of  $\mathbf{K}_k$  and update of  $\mathbf{P}_k$  and  $\mathbf{w}_k$  are skipped if  $\boldsymbol{\xi}_k$  is smaller than some given fraction of the root mean square error.

### 3 Representation of PES by NN

In a representation of potential energy surface (PES) by neural networks symmetries of a system must be properly taken into account. There exist many approaches to do so. Translation and rotation symmetry can be simply incorporated by a proper choice of some internal coordinates. Another problem is the incorporation of permutation symmetries, i.e. the invariance of the potential energy surface with respect to the permutation of identical particles. Several approaches have been proposed to do so, most frequently used being the approaches of Behler and Parrinello [7]. Another approach consists in using of Permutation Invariant Polynomials (PIP) [8],[9] or, more conveniently seemed to be usage of Fundamental Invariants (FI) [10].

The Approach of Behler and Parrinello is appropriate for large molecules and clusters. In this approach the symmetry of the system is introduced by using symmetry functions which describe the chemical environment of each atom. The overall energy is then given as a sum of atomic contributions. Every atom is represented by a unique FFNN with atoms of same kind being represented by the same neural network.

In the PIP neural network fitting, primary and secondary invariant polynomials are used as the input to the network which are able to conclusively describe all permutationally invariant possibilities. An Inconvenience with the PIP is, that the number of polynomials increases exponentially with the degree of bound.

In the FI neural network fitting approach a subset of invariant polynomials (known as fundamental invariants) is used as the input vector to the network. FI contain the least number of invariants which can generate all the invariant polynomials [11],[12]. Mathematical background of fundamental invariants was developed decades ago. The fundamental invariants can be calculated with Kings's algorithm [13] using computer program called Singular [14].



## 4 Neuron4dyn

As an instrument for the use of artificial neural networks in potential energy surface representations I have been developing my own software package called neuron4dyn. It is possible to use neuron4dyn to construct a single feedforward neural network as well as structured neural networks compound of feedforward neural networks which can have shared parameters. This allows to construct neural networks of Behler and Parrinello type. As a learning methods gradient descent and Adaptive Global Extended Kalman filter have been implemented.

## 5 Test calculations

First I have tested neuron4dyn on a model potential of a triatomic system  $A_2B$ . The FI approach has been used. I found out that it is more convenient for the learning process to first transform mutual distances using exponential formula  $p_i = e^{-r_i}$  and calculate FI from the transformed internal coordinates  $p_i$ . Neuron4dyn has been also applied to fitting of  $N_2He^+$  PESs calculated using multireference methods as implemented in the MOLPRO software package [15]. A preliminary analysis of fitted potentials shows that they are not as precise as we need. However a deeper analysis has shown that this may be due to some artifacts in the underlying multireference aculations. The problem is under further investigation.

Neuron4dyn also will be applied to fitting of PES of  $He_2^+$  cluster using the Behler and Parrinello approach. Study of this problem has started and is still in solution.

## 6 Conclusion

A software package neuron4dyn has been implemented for creating and training neural networks. Gradient descent and Adaptive Global Extended Kalman filter have been implemented as learning methods. Neuron4dyn is designed for fitting of PESs and have been applied on system  $N_2He^+$ . On the other hand it can be used also on different types of problems concerning of neural networks. Noteworthy, the neuron4dyn package has further been used in applied calculations related to the optimization of production process in glass industry. Interestingly, the same methodology as that developed by Behler and Parrinello for molecular complexes could be used in those applied calculations with only modest modifications.

## References

1. Balázs Csanád Csáji: Approximation with Artificial Neural Networks (2001)
2. Cybenko, G.: Approximations by superpositions of sigmoidal functions (1989)
3. Kurt Hornik: Approximation Capabilities of Multilayer Feedforward Networks (1991)

4. Raul Rojas: *Neural Networks - A Systematic Introduction*, Springer-Verlag, Berlin, New-York, (1996), <http://page.mi.fu-berlin.de/rojas/neural/index.html.html>
5. T. B. Blank and S. D. Brown: Adaptive, global, extended Kalman filters for training feedforward neural networks, *Journal of Chemometrics*, vol. 8, no. 6, pp. 391–407, (1994)
6. Haykin, Simon S., ed. 2001: *Kalman Filtering and Neural Networks*. Adaptive and Learning Systems for Signal Processing, Communications, and Control. New York: Wiley.
7. Behler, Jörg, and Michele Parrinello: Generalized Neural-Network Representation of High-Dimensional Potential-Energy Surfaces. *Physical Review Letters* 98 (14). (2007) <https://doi.org/10.1103/PhysRevLett.98.146401>.
8. Jiang, Bin, and Hua Guo: Permutation Invariant Polynomial Neural Network Approach to Fitting Potential Energy Surfaces. III. Molecule-Surface Interactions. *The Journal of Chemical Physics* 141 (3): 034109. (2014) <https://doi.org/10.1063/1.4887363>.
9. Z. Xie and J. M. Bowman: Permutationally Invariant Polynomial Basis for Molecular Energy Surface Fitting via Monomial Symmetrization, *Journal of Chemical Theory and Computation*, vol. 6, no. 1, pp. 26–34, Jan. (2010).
10. K. Shao, J. Chen, Z. Zhao, and D. H. Zhang: Communication: Fitting potential energy surfaces with fundamental invariant neural network, *J. Chem. Phys.*, vol. 145, no. 7, p. 071101, Aug. 2016.
11. H. Derksen a G. Kemper: *Computational Invariant Theory*. Berlin, Heidelberg: Springer Berlin Heidelberg, (2015)
12. R. P. Stanley, Invariants of finite groups and their applications to combinatorics, *Bulletin of the American Mathematical Society*, vol. 1, no. 3, pp. 475–512, May 1979.
13. King, Simon A.: Minimal Generating Sets of Non-Modular Invariant Rings of Finite Groups. *Journal of Symbolic Computation* 48 (January): 101–9. (2013) <https://doi.org/10.1016/j.jsc.2012.05.002>.
14. Decker, W.; Greuel, G.-M.; Pfister, G.; Schönemann, H.: *SINGULAR 4-1-2* — A computer algebra system for polynomial computations. <http://www.singular.uni-kl.de> (2019).
15. MOLPRO, version 2019.2, a package of ab initio programs, H.-J. Werner, P. J. Knowles, G. Knizia, F. R. Manby, M. Schütz, and others , see <https://www.molpro.net>.

# Proof of Concept: Balancing Predictive Relevance of Biochemical Activities Employing SVM Classification and Platt's Calibration

Marek Pecha

Department of Applied Mathematics, FEECS,  
VŠB – Technical University of Ostrava, 17. listopadu 15,  
708 33 Ostrava – Poruba, Czech Republic  
`marek.pecha@vsb.cz`

**Abstract.** In this paper, we present a proof of concept that deals with balancing predictive relevance of biochemical activities in order to employ conventional supervised machine learning technique, namely Support Vector Machines. As a technique for a problem of balancing, we propose the Platt's calibration. The qualities of models improved using the calibration are demonstrated on single-target classification; the data of ligand bioactivities were exported from the ExCAPE database.

**Keywords:** SVM; PermonSVM; chemogenomics; single-target; MPRGP; Platt's calibration;

## 1 Ligand-based Supervised Biochemical Activity Modelling

*In silico* computational supervised modelling based on ligand profiles is widely used as a complementary method in the pharmaceutical industry, specifically in the early stage of drug design and development to obtain an indication of probable off-target interactions. The aim is to train a model that generalizes the biological activities of chemical compounds (ligands) by reusing information from former *in vitro* laboratory experiments. A common approach to the biological target (proteins, genes) prediction is to exploit a panel of structure-analysis ligand models, such as SAR (Structure-Activity Relationship) and QSAR (Quantitative SAR), with one model per target. Then, using statistical learning, we train a classification or regression model used to predict categorical or numerical values for new compounds, respectively. The suggested strategies on how to train the models are the single and multi-target schemes; in our text, we focus on single-target (Active-vs-Inactive) approach.

Several methods and tools are typically utilized for constructing such models. The most popular ones are Deep Neural Networks (DNNs) and Support Vector Machines (SVMs). Despite the fact that Deep Learning (DL) is getting favoured in recent years, the SVMs are still applicable. One of the most advantages of

the SVMs approach is that they find learning functions maximizing geometric margins, unlike generally composed functions produced by DNNs.

However, SVMs have a serious drawback; they are sensitive to imbalanced datasets, outliers, and small multivariance among training samples, which could be a cause of preferencing one group over another. Therefore, we propose an additional model calibration that transforms the SVM classification model output into a probability distribution over classes.

## 2 Support Vector Machines for No-Bias Classification

SVMs belong to conventional machine learning techniques, and they are practically used for both classification and regression. Unlike the DL underlying architecture, SVMs could be considered as the single perceptron problems that find the learning functions maximizing the geometric margins. Therefore, we can explain the qualities of a learning model and the underlying solver behaviour directly. In this paper, we focus only on the linear C-SVM for classification; we denote the C-SVM as SVM for simplification in further reading.

SVM was originally designed as a supervised binary classifier [1], i.e. a classifier that decides whether a sample falls into either Class A or Class B by means of a model determined from already categorised samples in the training phase of the classifier. Let us denote the training data as an ordered sample-label pairs such that

$$T := \{(\mathbf{x}_1, y_1), (\mathbf{x}_2, y_2), \dots, (\mathbf{x}_m, y_m)\},$$

where  $m$  is the number of samples,  $\mathbf{x}_i \in \mathbb{R}^n$ ,  $n \in \mathbb{N}$ , is the  $i$ -th sample and  $y_i \in \{-1, 1\}$  denotes the label of the  $i$ -th sample,  $i \leq m$ .

Standard SVM solves a problem of finding a classification model in a form of maximal-margin hyperplane

$$H = \langle \mathbf{w}, \mathbf{x} \rangle + b, \quad (1)$$

where  $\mathbf{w}$  is a normal vector of hyperplane  $H$  and  $b$  is its bias alongside origin. In the cases of the no-bias classification, we do not consider bias  $b$  in a classification model, but we include it into the problem by means of augmenting the vector  $\mathbf{w}$  and each sample  $\mathbf{x}_i$  with an additional dimension so that  $\hat{\mathbf{w}} \leftarrow \begin{bmatrix} \mathbf{w} \\ B \end{bmatrix}$ ,  $\hat{\mathbf{x}}_i \leftarrow \begin{bmatrix} \mathbf{x}_i \\ \beta \end{bmatrix}$ , where  $B \in \mathbb{R}$ , and  $\beta \in \mathbb{R}^+$  is a user defined variable (typically set to 1). Let  $p \in \{1, 2\}$  for purposes related to our application, then the problem of finding hyperplane  $\hat{H} = \langle \hat{\mathbf{w}}, \hat{\mathbf{x}} \rangle$  can be formulated as a constrained optimization problem in the following primal formulation

$$\arg \min_{\hat{\mathbf{w}}, \xi_i} \frac{1}{2} \langle \hat{\mathbf{w}}, \hat{\mathbf{w}} \rangle + \frac{C}{p} \sum_{i=1}^n \xi_i^p \text{ s.t. } \begin{cases} y_i \langle \hat{\mathbf{w}}, \hat{\mathbf{x}}_i \rangle \geq 1 - \xi_i, \\ \xi_i \geq 0 \text{ if } p = 1, i \in \{1, 2, \dots, n\}, \end{cases} \quad (2)$$

where  $\xi_i = \max(0, 1 - y_i \langle \hat{\mathbf{w}}, \hat{\mathbf{x}}_i \rangle)$  is the hinge loss function,  $C \in \mathbb{R}^+$  is a penalty that penalizes misclassification error. Value of  $C$  is user-defined or determined

using hyperparameter optimization (HyperOpt) techniques, e.g. grid-search combined with cross-validation (CV). Exploiting the Lagrange duality and evaluating Karush-Kuhn-Tucker conditions, we transform (2) into the dual formulations for both  $p = 1$  and  $p = 2$  so that

$$\arg \min_{\boldsymbol{\lambda}} \frac{1}{2} \boldsymbol{\lambda}^T \mathbf{H} \boldsymbol{\lambda} - \boldsymbol{\lambda}^T \mathbf{e} \text{ s.t. } \mathbf{o} \leq \boldsymbol{\lambda} \leq \mathbf{C} \mathbf{e}, \tag{3}$$

$$\arg \min_{\boldsymbol{\lambda}} \frac{1}{2} \boldsymbol{\lambda}^T (\mathbf{H} + \mathbf{C}^{-1} \mathbf{I}) \boldsymbol{\lambda} - \boldsymbol{\lambda}^T \mathbf{e} \text{ s.t. } \mathbf{o} \leq \boldsymbol{\lambda}, \tag{4}$$

respectively. The formulation (3) is called dual  $\ell_1$ -loss SVM and the formulation (4) is known as dual  $\ell_2$ -loss SVM, where  $\mathbf{H} = \mathbf{Y}^T \mathbf{G} \mathbf{Y}$ ,  $\mathbf{G} = \mathbf{X}^T \mathbf{X}$  denotes the Gramian matrix,  $\mathbf{X} = [\hat{\mathbf{x}}_1 \dots \hat{\mathbf{x}}_m]$ ,  $\mathbf{Y} = \text{diag}(\mathbf{y})$ ,  $\mathbf{y} = [y_1, y_2, \dots, y_m]^T$ ,  $\mathbf{e} = [1, 1, \dots, 1]^T \in \mathbb{R}^m$ ,  $\mathbf{o} = [0, 0, \dots, 0]^T \in \mathbb{R}^m$ . The Hessian associated with QP (Quadratic Programming) problem (3) is SPS (Symmetric Positive Semidefinite), it becomes SPD (Symmetric Positive Definite) using regularization by means of the diagonal matrix  $\mathbf{C}^{-1} \mathbf{I}$  in the formulation (4).

### 3 Model Calibration

Model calibration in sense of classification means transforming a raw prediction  $f(\mathbf{x})$  into a posterior class probability  $P(\text{class} \mid \text{input})$ . Generally, such calibration is required in order of improving classifier decision abilities that include a balance of class preference and cost-sensitive classification. In this section, we introduce a well-known calibration technique called Platt’s Calibration. In the original paper [6], Platt proposed approximating a posterior probability by a parametric form of a sigmoid function such that

$$P(y = 1 \mid \mathbf{x}) \approx P_{A,B}(y = 1 \mid \mathbf{x}) = \frac{1}{1 + \exp(Af(\mathbf{x}) + B)}, \tag{5}$$

where parameters  $A$ ,  $B$  are fitted using maximum likelihood estimation. The model (5) assumes the raw SVM output  $f(\mathbf{x}) := H(\mathbf{x}) = \langle \mathbf{w}, \mathbf{x} \rangle + b$  is proportional to the log odds of positive samples. In order to no-bias classification, we define  $\hat{f}(\hat{\mathbf{x}}) := \hat{H}(\hat{\mathbf{x}}) = \langle \hat{\mathbf{w}}, \hat{\mathbf{x}} \rangle$ . To avoid model overfitting, Platt suggested to use a new training set, i.e. calibration set, for training a calibrated model. Let us denote calibration dataset as an ordered set as follows

$$CA := \{(f_1, y_1), (f_2, y_2), \dots, (f_l, y_l)\},$$

where  $l$  is a number of the calibration samples,  $f_j$  is estimate of  $f(\mathbf{x}_j)$  or  $\hat{f}(\hat{\mathbf{x}}_j)$ ,  $j \in \{1, 2, \dots, l\}$ . Additionally, Platt proposed transformation of binary labels  $y_j$  to target probabilities  $t_j$  such that  $t_j = \frac{N_p+1}{N_p+2}$  iff  $y = +1$ , or  $t_j = \frac{1}{N_n+2}$  iff  $y = -1$ , where  $N_p$  and  $N_n$  are numbers of positive and negative calibration samples, respectively.

The best parameter setting, i.e.  $A^*$  and  $B^*$ , is determined by minimizing negative log likelihood of calibration data so that

$$\arg \min_{A,B} - \sum_{j=1}^l [ t_j \log(p_j) + (1 - t_j) \log(1 - p_j) ], \quad (6)$$

where  $p_j = \frac{1}{1 + \exp(Af_j + B)}$ . To solve (6), Hsuan-Tien Lin et. al [3] introduce the Newton method as more numerically stable method instead of using the Levenberg–Marquardt algorithm that was early suggested by Platt.

## 4 Benchmarks

In this section, we demonstrate technique of calibrating models, introduced in Section 3, related to Active-vs-Inactive no-bias classification, described in Section 2, on 3 targets, namely *abl1* (Abelson murine leukemia viral oncogene homolog 1 protein), *adora2a* (Adenosine  $A_{2A}$  receptor), *cnr1* (cannabinoid receptor type 1). In cooperation with V. Chupakhin (Janssen Pharmaceutica), we exported small (Proof of Concept) datasets of ligand bioactivities associated with targets above from ExCAPE database [7], then we split the data into training, calibration and test datasets, see Table 1.

**Table 1.** Proof of Concept (PoC) datasets: the training, calibration and test dataset descriptions related to *abl1*, *adora2a*, and *cnr1* targets.

Target (dataset)	#ligands (QSARs)	#active+	#inactive-
<i>abl1</i> (training)	640	312	328
<i>abl1</i> (calibration)	200	92	108
<i>abl1</i> (test)	160	81	79
<i>adora2a</i> (training)	640	343	297
<i>adora2a</i> (calibration)	200	105	95
<i>adora2a</i> (test)	160	95	65
<i>cnr1</i> (training)	640	392	248
<i>cnr1</i> (calibration)	200	123	77
<i>cnr1</i> (test)	160	110	50

As the tool for solving underlying SVM problems, we employ PermonSVM. The tool is a member of PERMON family packages and is built on top of PETSc and PermonQP, the PERMON core QP solver. We evaluate the performance of models on the test dataset using precision, sensitivity, and area under the curve receiver operating characteristic (AUC) scores. Presented experiments were run on the ANSELM supercomputer at IT4Innovations.

For training (uncalibrated) classification models, we choose the best penalty  $C_{BE}$  from the set  $\hat{C} = \{2^p, p \in \{-7, -6, \dots, 6, 7\}\}$  algorithmically employing the HyperOpt by means of grid-search combined with stratified 3-fold CV. The value of the best penalty  $C_{BE}$  is selected so that precision and sensitivity scores on validated datasets (produced by CV) are maximized. All initial guess components are set to  $0.99 * C$  as we propose in [5]. The relative norm of projected

gradient being smaller than  $1e-1$  [4] is used as stopping criterion for the MPRGP (Modified Proportioning and Reduced Gradient Projection) [2] algorithm in all presented experiments. The expansion step-size is fixed and determined such as  $\alpha = 2.0/\|\mathbf{H}\|_2$ , where  $\|\mathbf{H}\|_2 = \sqrt{\lambda_{max}(\mathbf{H}^T\mathbf{H})}$ .

Using PETSc implementation of the Newton method, the S-shaped calibration function is computed by minimizing cross-entropy (6) of calibration data as we mentioned in Section 3.

Instead of comparing the model qualities in probability sense using log loss or Brier score, we convert target probabilities to labels using optimal threshold (thr.), i.e.  $y = 1$  if  $p > \text{thr.}$ , that we try to achieve the balanced class predictive relevance. The optimal threshold is determined using grid-search so that absolute value of the difference of precision (Pre.) and sensitivity (Sen.) on the test dataset is minimized, and F1 score must be greater than 0.50, i.e. predictive ability of model must be better than random. Because of the PoC datasets are too small to utilize more than one processor core, all experiments were run on 1 MPI process. For both  $\ell 1$ -loss and  $\ell 2$ -loss SVM, achieved results are summarized in Table 2.

**Table 2.** abl1, adora2a, cnr1 targets: evaluation of performance scores associated with uncalibrated models with  $C_{BE}$  and calibrated models with optimal threshold (thr.) in a sense of labels (binary classification) on test datasets.

Target	Loss	Uncalibrated model				Calibrated model			
		$C_{BE}$	Pre. [%]	Sen. [%]	AUC	Thr.	Pre. [%]	Sen. [%]	AUC
abl1	$\ell 1$	$2^{-6}$	71.60	65.17	0.66	0.52	65.43	64.63	0.64
	$\ell 2$	$2^{-5}$	69.14	60.22	0.64	0.54	60.49	60.49	0.60
adora2a	$\ell 1$	$2^{-6}$	70.53	82.72	0.74	0.41	78.95	78.95	0.74
	$\ell 2$	$2^{-7}$	70.53	83.75	0.74	0.44	78.95	78.95	0.74
cnr1	$\ell 1$	$2^{-6}$	90.00	82.50	0.77	0.63	83.64	83.64	0.74
	$\ell 2$	$2^{-6}$	87.27	81.36	0.74	0.58	83.64	83.64	0.74

Regarding performance score, we consider the qualities of models as the same in the sense of predictive abilities if the difference between appropriate scores lies in 5% confidence interval. Looking at Table 2, we can observe,  $\ell 2$ -loss SVM produces uncalibrated models of the same qualities (adora2a) or slightly worse (abl1, cnr1) than  $\ell 1$ -loss SVM. The  $\ell 1$ -loss SVM trains models that are more robust of catching outliers during the training procedure. For both  $\ell 1$ -loss and  $\ell 2$ -loss SVM, elapsed times are summarized in Table 3.

**Table 3.** abl1, adora2a, cnr1 targets: elapsed time related to training of uncalibrated models including hyperparameter optimization.

Loss	Elapsed time [s] (HyperOpt + Training)		
	abl1	adora2a	cnr1
$\ell 1$	2.15	2.61	1.95
$\ell 2$	1.38	1.86	1.58

From the table Table 3, we can observe speedups 1.56 (abl1), 1.40 (adora2a), 1.22 (cnr1) in order to  $\ell_2$ -loss SVM. Readers, who are familiar with the MPRGP algorithm, can explore full report on GitHub page [git.io/fjHn](https://github.com/fjHn). After applying model calibration and proposed conversion, we obtain almost perfectly balanced predictive class relevance of models with slightly worse overall predictive abilities as we can see in Table 2.

## 5 Conclusions and Further Research

In this contribution, we presented proof of the concept associated with ligand-based supervised biochemical activity modelling. As a method for solving the problem above, we chose SVMs due to the advantage of theirs that they find a learning function maximizing geometric margin. However, SVMs have a serious drawback. They are sensitive to outliers, a small multivariance among training samples, and imbalanced datasets; therefore, in these cases, additional model calibration is required commonly. As the calibration technique, we propose to apply the Platt's calibration (PC). By the achieved results on 3 benchmarks, it seems, the PC should be suitable for balancing predictive class-relevance for both  $\ell_1$ -loss, and  $\ell_2$ -loss SVM. In our further research, we will focus on comparing PC with isotonic regression and benchmarking them on large-scale datasets.

## Awards and Grants

- The best paper award at conference AETA 2018
- Support Research in the Moravia-Silesia Region 2017 (RRC/10/2017)

## References

1. Cortes, C., Vapnik, V.: Support-vector networks. *Machine Learning* 20(3), 273–297 (Sep 1995)
2. Dostál, Z.: *Optimal Quadratic Programming Algorithms, with Applications to Variational Inequalities*, vol. 23. SOIA, Springer, New York, US (2009)
3. Lin, H.T., Lin, C.J., Weng, R.C.: A note on Platt's probabilistic outputs for Support Vector Machines. *Machine Learning* 68(3), 267–276 (aug 2007)
4. Pecha, M., Hapla, V., Horák, D., Čermák, M.: Notes on the preliminary results of a linear two-class classifier in the PERMON toolbox. In: *AIP Conference Proceedings*. vol. 1978 (2018)
5. Pecha, M., Horák, D.: Analyzing l1-loss and l2-loss Support Vector Machines implemented in PERMON toolbox. In: *Lecture Notes in Electrical Engineering*, pp. 13–23. Springer International Publishing (apr 2019)
6. Platt, J., et al.: Probabilistic outputs for Support Vector Machines and comparisons to regularized likelihood methods. *Advances in large margin classifiers* 10(3), 61–74 (1999)
7. Sun, J., Jeliaskova, N., Chupakhin, V., Golib-Dzib, J.F., Engkvist, O., Carlsson, L., Wegner, J., Ceulemans, H., Georgiev, I., Jeliaskov, V., Kochev, N., Ashby, T.J., Chen, H.: ExCAPE-DB: an integrated large scale dataset facilitating big data analysis in chemogenomics. *Journal of Cheminformatics* 9(1) (mar 2017)



# Coupling Parareal and Schwarz method

Ivo Peterek

Department of Applied Mathematics, FEECS,  
VŠB – Technical University of Ostrava, 17. listopadu 15,  
708 33 Ostrava – Poruba, Czech Republic  
ivo.peterek@vsb.cz

**Abstract.** In this paper we present recent results related to the coupling of the Parareal and Schwarz method for the transient heat equation. The standardized numerical solution of the transient heat equation is done by using FEM semi-discretization in the spatial domain. Then the time derivative is approximated by a time-stepping scheme, such as the Euler method. However, this approach does not allow the parallelization of the solution along the time axis. Therefore we focused on a combination of the Parareal and Schwarz method with overlap. This combination allows us to decompose solved problem arbitrarily in the whole space-time domain and brings the possibility of space-time parallelization.

**Keywords:** Parareal, Schwarz method, space-time parallelization, heat equation, parallel in time

## 1 Transient heat equation

We will consider following transient heat equation in 1 spatial dimension

$$\begin{aligned}c_H \frac{\partial u}{\partial t}(x, t) - \frac{\partial^2 u}{\partial x^2}(x, t) &= f(\mathbf{x}, t) \quad \forall (x, t) \in \Omega \times (0, T), \\u(x, t) &= 0 \quad \forall (x, t) \in \Gamma \times (0, T), \\u(x, 0) &= u_0(x) \quad \forall x \in \Omega,\end{aligned}\tag{1}$$

where  $c_H > 0$  is a given heat capacity constant,  $f(x, t)$  is a given source term,  $u_0(x)$  is given initial condition,  $\Omega \subset \mathbb{R}$  and  $\Gamma = \partial\Omega$ .

## 2 Finite elements method semi-discretization in space

Corresponding weak formulation to transient heat problem (1) is in the form written below

$$\left\{ \begin{array}{l} \text{find } u(t) \in L_2(0, T; H_0^1(\Omega)) \text{ with } u'(t) \in L_2(0, T; H^{-1}(\Omega)) \text{ such that} \\ \frac{d}{dt}(u(t), v)_{L_2(\Omega)} + a(u(t), v) = \langle f(t), v \rangle \quad \forall v \in H_0^1(\Omega) \text{ a.e. in } (0, T), \\ u(0) = u_0 \in L_2(\Omega), \end{array} \right.\tag{2}$$

where  $f \in L_2(0, T; H^{-1}(\Omega))$ ,  $\langle \cdot, \cdot \rangle: H^{-1}(\Omega) \times H_0^1(\Omega) \rightarrow \mathbb{R}$ .

We now consider a finite-dimensional subspace  $\mathcal{V}^h \subset H_0^1(\Omega)$  in order to get discrete solution of (2) by FEM . The solution is represented by the following system of ordinary differential equations

$$\begin{aligned} M \frac{d\mathbf{u}}{dt}(t) + A\mathbf{u}(t) &= \mathbf{b}(t) \\ \mathbf{u}(0) &= \mathbf{u}_{0,h}, \end{aligned} \tag{3}$$

where  $u_{0,h}$  is an approximation of  $u_0$  in  $\mathcal{V}^h$ ,  $M$  is mass matrix,  $A$  is stiffness matrix and  $\mathbf{b}$  is vector of right-hand side.

At this point we could use some time-stepping scheme, such as backward Euler’s method, for discretization in time. Instead we will now apply coupled Parareal and Schwarz method.

### 2.1 Coupled Parareal and Schwarz method

In the beginning, let’s introduce both of methods that we will use here.

The Parareal is originally a parallel in time method for solving ODE. The main idea of this method is to compute a coarse approximation of problem first and then use its values as initial conditions for independent subproblems with fine discretization, related to the original problem, one per each point of coarse discretization. After that, we iteratively use values from fine approximation for the correction of the solution. The algorithm of Parareal is described in [1].

The Schwarz method is a domain decomposition method for PDE. It’s based on the decomposition domain in the spatial dimension into multiple subdomains with overlapping. First, we guess boundary conditions on inner subdomains and then iteratively solve a problem on each subdomain and exchange boundary conditions between adjacent subdomains until we are satisfied with the precision of the solution. For more on Schwarz method see [2].

We now present a combination of the Parareal and Schwarz method. The start is just like in the Parareal with a coarse approximation of (3). For example, we may use implicit Euler’s method

$$\begin{aligned} \left( \frac{1}{\Delta T} M + A \right) \mathbf{u}_{c,1}^{n+1} &= \mathbf{b}(T^{n+1}) + \frac{1}{\Delta T} M \mathbf{u}_{c,1}^n, \\ \mathbf{u}_{c,1}^0 &= \mathbf{u}_{0,h}, \end{aligned} \tag{4}$$

where  $\Delta T$  is size of coarse discretization step  $\mathbf{u}_{c,k}^n$  is solution on coarse grid at point  $n$  in  $k$ -th iteration of Parareal and  $T^n$  is  $n$ -th point of coarse discretization in time. After that perform Parareal iterations which consist of:

1. Find solution on fine grid for independent initial boundary value problems on each interval  $(T^n, T^{n+1})$  with initial conditions from coarse approximation  $\mathbf{u}_{c,k}^n$ . Here we apply Schwarz method to split domains on which we solve these problems in space. We denote  $Q_i$  as a  $i$ -th subdomain on  $n$ -th interval  $(T^n, T^{n+1})$ . Problem related to each of this subdomains follows

$$\begin{aligned}
 c \frac{\partial u_{Q_i}}{\partial t}(x, t) - \frac{\partial^2 u_{Q_i}}{\partial x^2}(x, t) &= f(x, t), \quad x \in (x_{Q_i}^1, x_{Q_i}^2), \quad t \in (T^n, T^{n+1}), \\
 u_{Q_i}(x_{Q_i}^1, t) &= g_1(t), \quad t \in (T^n, T^{n+1}), \\
 u_{Q_i}(x_{Q_i}^2, t) &= g_2(t), \quad t \in (T^n, T^{n+1}), \\
 u_{Q_i}(x, T^n) &= p(x), \quad x \in (x_{Q_i}^1, x_{Q_i}^2),
 \end{aligned}$$

where  $x_{Q_i}^1$  and  $x_{Q_i}^2$  are boundary points of subdomain in space,  $g_1(t)$  and  $g_2(t)$  are boundary conditions and  $p(x)$  is corresponding part of initial condition. Then we solve each of these problems with Schwarz iterations. That means, in one Schwarz iteration, we have to solve each problem on fine grid with implicit Euler’s method (similar to (4) with different time step and initial condition) and then exchange boundary conditions between adjacent subdomains in each time interval  $(T^n, T^{n+1})$ . Finally, after enough Schwarz iterations for given precision, we obtain fine approximation of solution in coarse points and in Parareal iteration denoted as  $\mathbf{u}_{f,k}^n$ .

2. Compute jumps

$$S_k^n = \mathbf{u}_{f,k}^{n-1}(T^n) - \mathbf{u}_{c,k}^n$$

3. Propagate jumps

$$\begin{aligned}
 \left( \frac{1}{\Delta T} M + A \right) \delta_k^{n+1} &= \frac{1}{\Delta T} M (\delta_k^n + S_k^n), \\
 \delta_k^0 &= \bar{0},
 \end{aligned}$$

4. Update solution

$$\mathbf{u}_{c,k+1}^n = \mathbf{u}_{f,k}^{n-1}(T^n) + \delta_k^n$$

## 2.2 Numerical experiments

In this section, we study the convergence of the coupled Parareal and Schwarz method. Our focus is to compare results with Parareal without any DDM and see how usage of the Schwarz method affects its convergence. Consider following heat equation with given parameters

$$\begin{aligned}
 2 \frac{\partial u}{\partial t}(x, t) - \frac{\partial^2 u}{\partial x^2}(x, t) &= 0 & x \in (0; 2), t \in (0; 2], \\
 u(0, t) = u(2, t) &= 0 & t \in (0; 2], \\
 u_0(x) = u(x, 0) &= 1 - (x - 1)^2 & x \in (0; 2).
 \end{aligned}$$

The error is computed as difference in standard Euclidean norm between approximate solution  $\mathbf{u}_{SEQ}^{h, \Delta T}$  which is just solution of (3) by implicit Euler’s method and  $\mathbf{u}_{PAR}^{h, \Delta t}$  for solution obtained by Parareal algorithm only or  $\mathbf{u}_{PSW}^{h, \Delta t}$  in case of coupled Parareal and Schwarz method

$$\left\| \mathbf{u}_{PAR}^{h, \Delta t} - \mathbf{u}_{SEQ}^{h, \Delta t} \right\|,$$

respectively

$$\left\| \mathbf{u}_{PSW}^{h,\Delta t} - \mathbf{u}_{SEQ}^{h,\Delta t} \right\|.$$

In every experiment we use equal spatial and time steps  $h = \Delta T = \frac{1}{128}$  and  $\Delta t = \frac{\Delta T}{100}$  (fine solution time step). Size of subdomains and overlap is uniform. We present three experiments, in each one of them we fix one parameter of coupled Parareal and Schwarz method. The parameters of coupled method are following number of Schwarz iterations *SwIt* in each Parareal cycle, number of overlapping elements *OvEl* between two adjacent subdomains and a number of subdomains *NSub* in each time subinterval. Also we denote number of Parareal iteration as *k*.

In the first experiment we obtain errors for different *SwIt* = 3, 4, 5, 6 and compare them with Parareal without any DDM in Table 1. Other parameters have been fixed with values *Nsub* = 4 and *OvEl* = 10. For *SwIt* = 5 and more iterations we obtain exactly same errors as without DDM(to given precision of  $10^{-8}$ ).

	<i>k</i> = 1	<i>k</i> = 2	<i>k</i> = 3	<i>k</i> = 4	<i>k</i> = 5	<i>k</i> = 6
Parareal only	$2.31 \cdot 10^{-3}$	$3.31 \cdot 10^{-4}$	$7.10 \cdot 10^{-5}$	$1.71 \cdot 10^{-5}$	$4.34 \cdot 10^{-6}$	$1.13 \cdot 10^{-6}$
<i>SwIt</i> = 3	$3.03 \cdot 10^{-3}$	$4.04 \cdot 10^{-3}$	$4.03 \cdot 10^{-3}$	$4.03 \cdot 10^{-3}$	$4.03 \cdot 10^{-3}$	$4.03 \cdot 10^{-3}$
<i>SwIt</i> = 4	$2.31 \cdot 10^{-3}$	$3.32 \cdot 10^{-4}$	$7.15 \cdot 10^{-5}$	$2.67 \cdot 10^{-5}$	$2.65 \cdot 10^{-5}$	$2.65 \cdot 10^{-5}$
<i>SwIt</i> = 5	$2.32 \cdot 10^{-3}$	$3.32 \cdot 10^{-4}$	$7.11 \cdot 10^{-5}$	$1.71 \cdot 10^{-5}$	$4.34 \cdot 10^{-6}$	$1.13 \cdot 10^{-6}$
<i>SwIt</i> = 6	$2.32 \cdot 10^{-3}$	$3.32 \cdot 10^{-4}$	$7.11 \cdot 10^{-5}$	$1.71 \cdot 10^{-5}$	$4.34 \cdot 10^{-6}$	$1.13 \cdot 10^{-6}$

Table 1: Comparison of errors of the Parareal to the coupled Parareal and Schwarz method with a variable *SwIt*.

The second example was variable *OvEl* = 8, 12, 16, 20 other parameters were fixed as *Nsub* = 4 and *SwIt* = 3. Results in comparison with Parareal without additional DDM are shown in Table 2. In this case for 16 and 20 *OvEl* we obtain the same precision as for Parareal algorithm only.

	<i>k</i> = 1	<i>k</i> = 2	<i>k</i> = 3	<i>k</i> = 4	<i>k</i> = 5	<i>k</i> = 6
Parareal only	$2.31 \cdot 10^{-3}$	$3.31 \cdot 10^{-4}$	$7.10 \cdot 10^{-5}$	$1.71 \cdot 10^{-5}$	$4.34 \cdot 10^{-6}$	$1.13 \cdot 10^{-6}$
<i>OvEl</i> = 8	$2.12 \cdot 10^{-2}$	$2.24 \cdot 10^{-2}$	$2.24 \cdot 10^{-2}$	$2.24 \cdot 10^{-2}$	$2.24 \cdot 10^{-2}$	$2.24 \cdot 10^{-2}$
<i>OvEl</i> = 12	$2.31 \cdot 10^{-3}$	$6.31 \cdot 10^{-4}$	$6.18 \cdot 10^{-4}$	$6.18 \cdot 10^{-4}$	$6.18 \cdot 10^{-4}$	$6.18 \cdot 10^{-4}$
<i>OvEl</i> = 16	$2.31 \cdot 10^{-3}$	$3.32 \cdot 10^{-4}$	$7.11 \cdot 10^{-5}$	$1.71 \cdot 10^{-5}$	$8.43 \cdot 10^{-6}$	$8.37 \cdot 10^{-6}$
<i>OvEl</i> = 20	$2.31 \cdot 10^{-3}$	$3.32 \cdot 10^{-4}$	$7.11 \cdot 10^{-5}$	$1.71 \cdot 10^{-5}$	$4.34 \cdot 10^{-6}$	$1.13 \cdot 10^{-6}$

Table 2: Comparison of errors of the Parareal to the coupled Parareal and Schwarz method with a variable *OvEl*.

In the last of experiments we have fixed  $OvEl = 8$  and  $SwIt = 8$ . Then we provide errors for  $NSub = 2, 4, 8, 16$  and compare them with version of Parareal without DDM in Table 3. In this table, we observe that for  $NSub = 2, 4, 8$  the convergence is the same as without applying DDM. For  $NSub = 16$  the convergence starts to break, change of discretization,  $OvEl$  or  $SwIt$  may be needed if we plan to use more subdomains.

	$k = 1$	$k = 2$	$k = 3$	$k = 4$	$k = 5$	$k = 6$
Parareal only	$2.31 \cdot 10^{-3}$	$3.31 \cdot 10^{-4}$	$7.10 \cdot 10^{-5}$	$1.71 \cdot 10^{-5}$	$4.34 \cdot 10^{-6}$	$1.13 \cdot 10^{-6}$
$NSub = 2$	$2.31 \cdot 10^{-3}$	$3.31 \cdot 10^{-4}$	$7.10 \cdot 10^{-5}$	$1.71 \cdot 10^{-5}$	$4.34 \cdot 10^{-6}$	$1.13 \cdot 10^{-6}$
$NSub = 4$	$2.31 \cdot 10^{-3}$	$3.31 \cdot 10^{-4}$	$7.10 \cdot 10^{-5}$	$1.71 \cdot 10^{-5}$	$4.34 \cdot 10^{-6}$	$1.13 \cdot 10^{-6}$
$NSub = 8$	$2.31 \cdot 10^{-3}$	$3.31 \cdot 10^{-4}$	$7.10 \cdot 10^{-5}$	$1.71 \cdot 10^{-5}$	$4.34 \cdot 10^{-6}$	$1.13 \cdot 10^{-6}$
$NSub = 16$	$2.31 \cdot 10^{-3}$	$3.31 \cdot 10^{-4}$	$7.10 \cdot 10^{-5}$	$1.71 \cdot 10^{-5}$	$6.55 \cdot 10^{-6}$	$6.47 \cdot 10^{-6}$

Table 3: Comparison of errors of the Parareal to the coupled Parareal and Schwarz method with a variable  $NSub$ .

### 3 Conclusion

The conclusion is that for right choice of mentioned parameters the convergence of the Parareal algorithm is unaffected by DDM. The biggest advantage of coupling these two methods is possibility decomposition in the space-time domain, which may help us to obtain a solution faster than the sequential approach if enough parallel processing power is available.

### 4 Future work

We would like to try coupling of the Parareal method with more advanced DDM and study Parareal convergence more in-depth. We also plan to develop a parallel code for the proposed method and perform scaling tests on the HPC system.

### 5 Publications

At this time we don't have any indexed publications. An article of recent results about the Parareal and DDM is currently in preparation (in cooperation with Doc. Ing. Dalibor Lukas, Ph.D. and Ing. Ladislav Foltyn). We plan to publish it in Applications of Mathematics published by Institute of Mathematics, Czech Academy of Sciences.

## References

1. Lions, J.-L.; Maday, Y.; Turinici, G. *Résolution d'EDP par un schéma en temps << pararéel >>*. Comptes Rendus de l'Académie des Sciences – Series I – Mathematics, vol. 332, no. 7, pp. 661-668, Apr. 2001.
2. Toselli, A.; Widlund, O. *Domain Decomposition Methods-Algorithms and Theory*. Springer Science & Business Media, 2006.

# Use of generalized truncation for computer search for $(k, g)$ -graphs

Tom Raiman

Department of Applied Mathematics, FEECS,  
VŠB – Technical University of Ostrava, 17. listopadu 15,  
708 33 Ostrava – Poruba, Czech Republic  
tom.raiman.st@vsb.cz

**Abstract.** A  $(k, g)$ -graph is a graph with regularity  $k$  and girth  $g$ . We investigate the use of generalized truncation in improving the upper bound of  $(k, 6)$ - and  $(k, 8)$ -bound, where  $k = q + 2$  and  $q$  is a prime power. Then we compare these bounds against the so-called Sauer bound. Sauer bound is currently the best known constructive general upper bound for any  $(k, g)$ -graphs. We also discuss conditions under which one can reverse generalized truncation. We have done this with the aim of obtaining a tool for proving the existence or non-existence of the  $(57, 5)$ -Moore graph, but consider the use of this technique in general  $(k, g)$ -graph constructions.

**Keywords:** cage,  $k$ -regular graph, girth, Sauer bound, generalized truncation

## 1 Introduction

A  $(k, g)$ -graph is a  $k$ -regular graph of girth  $g$ . A  $(k, g)$ -cage is a smallest  $(k, g)$ -graph; its order is denoted by  $n(k, g)$ .

Given  $k \geq 2, g \geq 3$ , the  $(k, g)$ -order spectrum is the ordered sequence of all possible orders of  $(k, g)$ -graphs starting off the smallest order  $n(k, g)$ .

However, the orders  $n(k, g)$  of  $(k, g)$ -cages have been only determined for small sets of parameter pairs [1], thus determining the the  $(k, g)$ -order spectrum for a given pair  $k, g$  is a decisively hard problem, and except for the spectra of orders of  $(2, g), g \geq 3, (k, 3), k \geq 2, (3, 5), (3, 6)$ -graphs, and some families of  $(k, 4)$ -graphs determined in [3], no other full spectra are known.

The Moore bound gives a natural lower bound for the orders of  $(k, g)$ -graphs (and therefore also for the order  $n(k, g)$  of the  $(k, g)$ -cages).

$$n(k, g) \geq M(k, g) = \begin{cases} \frac{k(k-1)^{(g-1)/2}-2}{k-2}, & \text{if } g \text{ is odd,} \\ \frac{2(k-1)^{g/2}-2}{k-2}, & \text{if } g \text{ is even.} \end{cases} \quad (1)$$

It is known that the orders of the majority of cages exceed the value  $M(k, g)$ . Graphs for which  $n(k, g) = M(k, g)$  are called *Moore graphs*. Full survey of the cage problem can be found in [1].

In the 1960's, Erdős and Sachs introduced an upper bound for the order of  $(k, g)$ -cages. They were also able to prove that for any given pair of  $(k, g)$ , there exists a  $(k, g)$ -graph of any larger admissible order. Their results were later improved by Sauer. We will denote *Sauer's bound* by  $S(k, g)$  [5], [1]:

$$n(3, g) \leq S(3, g) = \begin{cases} \frac{4}{3} + \frac{29}{12}2^{g-2}, & \text{if } g \text{ is odd,} \\ \frac{2}{3} + \frac{29}{12}2^{g-2}, & \text{if } g \text{ is even.} \end{cases} \tag{2}$$

For  $k \geq 4$

$$n(k, g) \leq S(k, g) = \begin{cases} 2(k-1)^{g-2}, & \text{if } g \text{ is odd,} \\ 4(k-1)^{g-3}, & \text{if } g \text{ is even.} \end{cases} \tag{3}$$

We will call  $(k, g)$ -graphs of order at least  $S(k, g)$  *Sauer graphs*. The significance of these bounds lies in the fact that from the bound onward there exists a  $(k, g)$ -graph of any admissible order greater than or equal to the Sauer bound.

Now we recall lemmas for spectra of  $(k, 3)$ - and  $(k, 4)$ -graphs as well as a bound derived in [4] with respect to a condition for adding vertices to  $(3, g)$  graphs. We will use these results later.

**Lemma 1 ([3]).**

1. If  $k \geq 4$  is even, there exists a  $(k, 3)$ -graph of any order greater than or equal to the Moore bound  $M(k, 3) = k + 1$ .
2. If  $k \geq 3$  is odd, a  $(k, 3)$ -graph exists of every even order greater than or equal to the Moore bound  $M(k, 3) = k + 1$ .

**Lemma 2 ([3]).** For each integer  $k \geq 3$  and each even integer  $n \geq M(k, 4)$ , there exists a  $(k, 4)$ -graph of order  $n$ .

**Theorem 1 ([4]).** Let  $\Gamma$  be a  $(3, g)$ -graph. If  $\Gamma$  is of order at least  $\frac{1}{3}2^g - \frac{4}{3}$ , then there exists a  $(3, g)$ -graph of any greater even order.

## 2 Generalized truncation

In [2], authors defined the concept of generalized truncation. We will recall the definition and then use generalized truncation to improve the upper bounds for special classes of  $(k, 6)$ - and  $(k, 8)$ -graphs.

Let  $G$  be a finite  $k$ -regular graph, and let  $D(G)$  denote the set of *darts* of  $G$  obtained by associating each edge of  $G$  with two opposing darts. A *vertex-neighbourhood labelling* of  $G$  is a function  $\rho$  from the set  $D(G)$  into the set  $\{1, 2, \dots, k\}$  having property that for each set of darts emanating from a vertex  $v \in V(G)$  is a bijection onto  $\{1, 2, \dots, k\}$ .

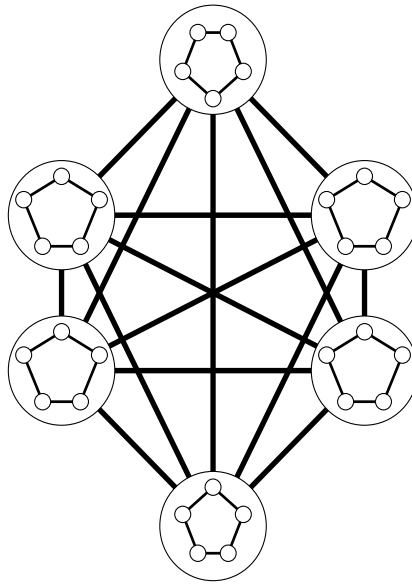
Let  $H$  be a graph of order  $k, V(H) = \{u_1, u_2, \dots, u_k\}$ . The *generalized truncation* of a  $k$ -regular graph  $G$  with a vertex-neighbourhood labelling  $\rho$  by the graph  $H$  (of order  $k$ ) is the graph  $T(G, \rho; H)$  obtained from  $G$  by replacing the vertices of  $G$  by a copy of the graph  $H$  as follows: each vertex  $v$  of  $G$  is replaced



by graph  $H$  attached to darts originally emanating from  $v$  according to the rule that  $u_i$  is attached to the dart labelled by  $i$ .

Following theorem shows the importance of generalized truncation for  $(k, g)$ -graphs.

**Theorem 2 ([2]).** *Let  $G$  be a finite  $(k, g)$ -graph with a vertex-neighbourhood labelling  $\rho$ , and let  $H$  be a  $(k', g')$ -graph of order  $k$ . The generalized truncation graph  $T(G, \rho; H)$  is a  $(k' + 1)$ -regular graph of girth not smaller than  $\min\{2g, g'\}$  and if  $g' \leq 2g$  then  $g'$  is the exact girth of  $T(G, \rho; H)$ .*



**Fig. 1.** Generalized truncation of  $K_6$  by  $C_5$

Next, we will use Theorem 2 together with Lemma 1 and Lemma 2 to improve the upper bounds for  $(k, 6)$ - and  $(k, 8)$ -graphs, where  $k = q + 2$  and  $q$  a prime power.

**Theorem 3.** *Let  $G$  be a  $(k, 3)$ -graph of order  $n$  and  $H$  be a  $(k', 6)$ -graph of order  $k$ . Then there exist  $(k' + 1, 6)$ -graphs of all orders  $n'k$ , with  $n' \geq n$ .*

*Proof.* Let  $G$  be a  $(k, 3)$ -graph of order  $n$  and  $H$  be a  $(k', 6)$ -graph of order  $k$ . We will replace each vertex  $v$  of  $G$  by graph  $H$ . Because graph  $H$  is of order  $k$  we will always point one edge of  $G$  to one vertex of  $H$ , thus the resulting graph will be  $(k' + 1)$ -regular graph. From Theorem 2 we know its girth is exactly 6, because  $g' = 6$ . Because we are replacing vertices of  $G$ , which is of order  $n$ ,

by graph  $H$ , which is of order  $k$ , the order of  $T(G, \rho; H)$  is  $nk$ . From Lemma 1, we know the spectra of  $(k, 3)$ -graphs, and because  $(k, 3)$ -graphs exist for all admissible orders, we have  $(k' + 1, 6)$ -graphs of orders  $n'k$ , for all  $n' \geq n$ .

**Theorem 4.** *Let  $G$  be a  $(k, 3)$ -graph of order  $n$  and  $H$  be a  $(k', 8)$ -graph of order  $k$ . Then there exist  $(k' + 1, 8)$ -graphs of all orders  $n'k$ , with  $n' \geq n$ .*

We will omit the proof of Theorem 4, because it follows along similar lines as the proof of Theorem 3. The only difference is that we use Lemma 2 in the proof.

Next, to conclude the section, we will prove that the bounds from Theorem 3 and Theorem 4 are better than the Sauer bound for case were  $k = q + 2$ , and  $q$  is a prime power. We will prove this for  $(k, 6)$ -graphs, since the case for  $(k, 8)$ -graphs would follow along similar lines. First, let us point out that  $H$  can be taken to be a Moore graph. This means that  $|H| = \frac{2(k-1)^4 - 2}{k-2}$ . Next, we observe that order of  $G$  is  $|G| = |H| + 1$ . This means that order of  $|T(G, \rho; H)| = |G||H| = 4k^2 + 2k$ . This order is smaller for  $S(k, 6) = 4(k - 1)^3$ , for all  $k \geq 4$ .

### 3 Reversibility of generalized truncation

In this section, we focus on the question of under which conditions we can reverse generalized truncation. By reversing generalized truncation we mean that we would have a graph that would be constructed by some amount of graphs  $H$  which would be a  $n$ -regular and these copies would be connected in some way with condition that the whole graph would be  $m$ -regular, where  $m > n$ . Of course one can ask what properties would have had the graph when we factor out the  $H$ -graphs and what conditions do we have satisfy if we want to get particular graph  $G$ , which would be  $k$ -regular with girth  $g$ . First there is the natural condition that the girth of the considered graph must be at least the double of size of graph we are trying to obtain. This condition is not strong enough, because then we potentially could connect two graphs we are trying to factor out with two edges if this does not imply shorter girth. If we tried to factor these graphs out we would get a multigraph. With this knowledge we could say that we need for the two graphs we are trying to factor out not to be connected by two edges and preserve the double of girth. This condition still is not strong enough. Imagine we are trying to factor out  $C_{12}$  from a  $(3, 10)$ -graph with the aim of obtaining a  $(12, 5)$ -graph. Let say that there would be  $C_{12,1}, C_{12,2}, C_{12,3}$  connected in a way that  $C_{12,1}$  is connected to  $C_{12,2}$ ,  $C_{12,2}$  is connected to  $C_{12,3}$  and  $C_{12,3}$  is connected to  $C_{12,1}$ , while preserving  $g = 10$ . Now if we would factor out all  $C_{12}$ 's from the  $(3, 10)$ -graph we would not obtain the desired  $(12, 5)$ -graph, but only a  $(12, 3)$ -graph. We want to prevent such a situation. So we need to define something like cycles of  $H$ -graphs in  $G$ .

Let  $G$  be a  $k$ -regular graph of order  $n$  and  $H$  be a  $k'$ -regular graph of order  $k$ . Let  $T(G, \rho; H)$  be a graph of generalized truncation. We denote each  $H$ -graph by  $H_1, H_2, \dots, H_n$ . The length of  $H$ -cycle in  $G$  is the length of cycle after which we end up in the starting  $H$ -graph and no  $H_i$  is repeated, where  $i \in \{1, 2, \dots, n\}$

with exception of initial  $H_j$ -graph, where  $j \in \{1, 2, \dots, n\}$ . The  $H$ -girth in  $G$  is the length of the smallest of  $H$ -cycles.

It is only natural to ask why would one want to reverse generalized truncation. First we state a theorem that gives us some insight, why it might be useful to reverse the generalized truncation.

**Theorem 5.** *Let graph  $I$  contain  $n$  distinct subgraphs that are isomorphic to graph  $H$  and let  $H$  be a  $(k', g')$ -graph of order  $k$ . If  $I$  is  $(k' + 1)$ -regular with  $H$ -girth being equal to  $g$ , then if we factor out  $H$ -graphs we obtain  $(k, g)$ -graph  $G$  of order  $n$ .*

*Proof.* First we will denote the  $n$  graphs that are isomorphic to  $H$  by  $H_1, H_2, \dots, H_n$ . Because  $H$  girth is equal to  $g$  it means that no two  $H_i, H_j$ -graphs, where  $i, j \in \{1, 2, \dots, n\}$  are connected by more than one edge. Because  $H_i$ -graphs are of order  $k$  and  $I$  is  $(k' + 1)$ -regular graph it follows that each  $H_i$ -graph is connected to  $k$  distinct  $H_j$  graphs. Thus if we factor out  $H$ -graphs to obtain graph  $G$ , than  $G$  is  $k$ -regular graph and is of order  $n$ , because there are  $n$  subgraphs  $H$  in  $I$ . Because we asked for  $H$ -girth to be equal  $g$  that means we must always go through  $g$   $H$ -subgraphs to get to initial subgraph thus the  $H$ -girth changes into girth  $g$  in graph  $G$ . Thus  $G$  is  $(k, g)$ -graph of  $n$ .

Now imagine that the  $(57, 5)$ -Moore graph does exist, it is of order 3250. If we truncate the  $(57, 5)$ -Moore graph with  $C_{57}$  we will obtain a  $(3, g)$ -graph of order  $3250 \cdot 57 = 185250$ , where  $10 \leq g \leq 57$ . With the knowledge of Theorem 5 we can start with potential truncated graph  $(3, g)$ -graph, where  $10 \leq g \leq 57$  and ultimately find the  $(57, 5)$ -Moore graph. First we will start with 3250 cycles  $C_{57}$ . Those will be our  $H$ -graphs. Next, we can start to create 3-regular, while preserving  $C_{57}$ -girth equal to 5. Thus we will create  $(3, g)$ -graph on 185250, where  $10 \leq g \leq 57$ . Now if any of these  $(3, g)$ -graphs exist and we factor out  $H$ -graph we will obtain back the  $(57, 5)$ -Moore graph. Now we can ask if we can somehow narrow the bound of  $g$  for potential  $(3, g)$ -graph. First, we try to limit  $g$  by Moore bound (1). Since  $M(3, 33) = 196608 > 185250$ , thus we can narrow upper bound for  $g \leq 32$ ,  $M(3, 32) = 131072$ . We think that it would be highly unlikely to find such  $(3, g)$ -graph, where  $27 \leq g \leq 32$ , that would at the same time satisfy the conditions we need. This is due to fact that such graph would have to be a record [1], especially considering the added condition for  $H$ -girth being equal to 5. We think that if our truncated  $(3, g)$ -graph does exist it is for  $g \in \{10, 11, \dots, 18\}$  ( $S(3, 18) = 158380 < 185250$ ).

We believe that this approach might help to resolve long standing question whether the  $(57, 5)$ -Moore graph does or does not exist. This is due to fact that we must be able to truncate the  $(57, 5)$ -Moore graph with  $C_{57}$ . This means if we cannot find truncated version of the  $(57, 5)$ -Moore graph than the  $(57, 5)$ -Moore graph does not exist. We also think that approach is better because it can be naturally parallelized for each  $g \in \{10, 11, \dots, 32\}$ . Plus as a bonus it is much more easy to find 3-regular than 57-regular graph, especially if we consider that we start with a 2-regular graph.

## 4 Conclusion

We presented three new theorems concerning generalized truncation. With Theorem 3 and Theorem 4 we were able to improve the upper bound for  $(k, 6)$ - and  $(k, 8)$ -graphs, where  $k = q + 2$ ,  $q$  is a prime power, hence we were able to extend characterized part of spectra of these graphs. We have also shown under which condition one can reverse generalized truncation. In this article we have mainly discussed the use of reverse truncation in connection with the  $(57, 5)$ -Moore graph, but the result of theorem 5 can be used to search for any  $(k, g)$ -cage or record. Of course it is necessary to use computer search.

## References

1. Exoo, G., Jajcay, R.: Dynamic cage survey. *Electron. J. Combin.* 15(16), 4 (2008)
2. Exoo, G., Jajcay, R.: Recursive constructions of small regular graphs of given degree and girth. *Discrete Mathematics* 312(17), 2612–2619 (2012)
3. Jajcay, R., Raiman, T.: Spectra of orders for  $k$ -regular graphs of girth  $g$ . *Discussiones Mathematicae Graph Theory* (2019)
4. Raiman, T.: New upper bounds for the orders of  $(k, g)$ -graphs. *WOFEX* pp. 219–223 (2018)
5. Sauer, N.: Extremaleigenschaften regularer graphen gegebener taillenweite, i and ii. *Sitzungsberichte Osterreich. Acad. Wiss. Math. Natur. Kl* pp. 27–43 (1967)

# Modelling of transient piezoelectricity – acoustic problem

Erika Straková and Dalibor Lukáš

Department of Applied Mathematics, FEECS,  
VŠB – Technical University of Ostrava, 17. listopadu 15,  
708 33 Ostrava – Poruba, Czech Republic  
{erika.strakova, dalibor.lukas}@vsb.cz

**Abstract.** In this paper, we will present piezo acoustic FEM analysis, which is important for simulating the behavior of piezoelectric sensors and actuators. The mathematical model of the piezoelectric level sensor includes the modeling of elastoelectric waves in the piezoelectric element, the modeling of acoustic waves in the fluid and the interaction of the two models.

**Keywords:** modelling of piezoelectricity, piezoelectricity - acoustic coupling problem, finite element method

## 1 Transient piezoelectricity problem

After deformation in some materials, e.g. quartz, volatage is produced between its surface. Conversely, when a volatage is applied to the piezoelectric material, it undergoes a mechanical distortion. Expansion of Maxwell's equations of electrostatics and equations of elasticity by the direct and the inverse piezoelectric effect gives the piezoelectric equations.

Let us consider a 3-dimensional computational domain  $\Omega$  with a Lipschitz boundary and the time interval  $(0, T)$ . The displacement vector field  $\mathbf{u}(\mathbf{x}, t)$  and the potential scalar field  $\phi(\mathbf{x}, t)$  are governed by (see [3], [4])

$$\begin{aligned}\rho \frac{d^2 \mathbf{u}}{dt^2} - \operatorname{div} \boldsymbol{\sigma} &= \mathbf{0}, \\ \boldsymbol{\sigma} &= c^E \boldsymbol{\varepsilon}(\mathbf{u}) + e^T \nabla \phi, \\ \operatorname{div} \mathbf{D} &= 0, \\ \mathbf{D} &= e \boldsymbol{\varepsilon}(\mathbf{u}) - \epsilon \nabla \phi,\end{aligned}\tag{1}$$

with boundary and initial conditions:

$$\begin{aligned}\mathbf{u} &= \mathbf{u}_\Gamma \quad \text{on } \Gamma_u \times (0, T), \\ \boldsymbol{\sigma} \cdot \mathbf{n} &= \boldsymbol{\sigma}_n, \quad \text{on } \Gamma_\sigma \times (0, T), \\ \phi &= \phi_\Gamma \quad \text{on } \Gamma_\phi \times (0, T), \\ \mathbf{D} \cdot \mathbf{n} &= D_n \quad \text{on } \Gamma_D \times (0, T), \\ \mathbf{u} &= \mathbf{0} \quad \text{in } \Omega \times \{0\}, \\ \mathbf{u},_t &= \mathbf{0} \quad \text{in } \Omega \times \{0\}.\end{aligned}$$

The high-order tensors  $c^E, e, \epsilon$  in Eq. (1) contain elastic stiffness constants, the piezoelectric stress constants and the electric permittivities for constant mechanical strain according to piezoelectric material, respectively. Components of strain tensor  $\epsilon$  are given by

$$\epsilon_{ij} = \frac{1}{2} \left( \frac{\partial u_i}{\partial x_j} + \frac{\partial u_j}{\partial x_i} \right).$$

For the purpose of weak form we consider Sobolev spaces:

$$\begin{aligned} \mathbf{V} &:= \{v \in \mathbf{H}^1(\Omega) := (H^1(\Omega))^d \mid T_{\Gamma_u}(\mathbf{v}) = 0\}, \\ \Pi &:= \{\varphi \in H^1(\Omega) \mid T_{\Gamma_\phi}(\varphi) = 0\}. \end{aligned}$$

Additionally, set

$$\mathbf{V}_{\Gamma_u} := \epsilon_{\Gamma_u} \mathbf{u}_\Gamma + \mathbf{V} \quad \text{and} \quad \Pi_{\Gamma_\phi} := \epsilon_{\Gamma_\phi} \phi_\Gamma + \Pi,$$

where  $\epsilon_\Gamma : H^{\frac{1}{2}}(\Gamma) \rightarrow H^1(\Omega)$  is extension operator.

The problem is to find  $\mathbf{u} \in L^2(0, T; \mathbf{V}_{\Gamma_u})$  and  $\phi \in L^2(0, T; \Pi_{\Gamma_\phi})$  satisfying  $\frac{d\mathbf{u}}{dt} \in L^2(0, T; \mathbf{L}^2(\Omega)), \frac{d^2\mathbf{u}}{dt^2} \in L^2(0, T; \mathbf{V}')$  such that (see [1], [2])

$$\begin{aligned} \int_\Omega \rho \frac{d^2\mathbf{u}}{dt^2} \cdot \mathbf{v} \, d\Omega + \int_\Omega C^E \epsilon(\mathbf{u}) : \epsilon(\mathbf{v}) \, d\Omega + \int_\Omega E^T \epsilon(\mathbf{v}) \cdot \nabla \phi \, d\Omega = \\ = \int_{\Gamma_\sigma} \boldsymbol{\sigma}_n \cdot T_{\Gamma_\sigma}(\mathbf{v}) \, d\Gamma \quad \forall \mathbf{v} \in \mathbf{V} \tag{2} \\ \int_\Omega E \epsilon(\mathbf{u}) \cdot \nabla \varphi \, d\Omega - \int_\Omega \epsilon \nabla \phi \cdot \nabla \varphi = \int_{\Gamma_D} D_n T_{\Gamma_D}(\varphi) \, d\Gamma \quad \forall \varphi \in \Pi. \end{aligned}$$

We discretize  $\Omega$  and approximate  $\mathbf{V}, \Pi$  by a finite element method. We obtain the following linear system

$$\underbrace{\begin{pmatrix} M & 0 \\ 0 & 0 \end{pmatrix}}_{\mathbb{M}} \underbrace{\begin{pmatrix} \hat{u}_{tt} \\ \hat{\phi}_{tt} \end{pmatrix}}_{x_{tt}} + \underbrace{\begin{pmatrix} K & B^T \\ B & A \end{pmatrix}}_{\mathbb{K}} \underbrace{\begin{pmatrix} \hat{u} \\ \hat{\phi} \end{pmatrix}}_x = \underbrace{\begin{pmatrix} f \\ g \end{pmatrix}}_z, \tag{3}$$

where the vectors  $\hat{u}, \hat{\phi}$  represent approximated values for  $\mathbf{u}, \phi$  at the nodes of computational domain  $\Omega$ . The matrices  $M_{uu}, K_{uu}, K_{u\phi}, K_{\phi\phi}$  are the discretizations of the bilinear forms on the left-hand sides of (2) and the vectors  $f, g$  arise from the linear forms on the right-hand sides of (2). To conduct a transient analysis we can apply the Newmark scheme, where at each time step we

- solve algebraic system of equations

$$\left( \mathbb{M} + \frac{(\Delta t)^2}{4} \mathbb{K} \right) x_{tt}^{(i+1)} = z^{i+1} - \mathbb{K} \left( x^i + \Delta t x_t^{(i)} + \frac{(\Delta t)^2}{4} x_{tt}^{(i)} \right),$$

- compute

$$\begin{aligned}
 x^{(i+1)} &= x^i + \Delta t x_t^{(i)} + \frac{(\Delta t)^2}{4} \left( x_{tt}^{(i)} + x_{tt}^{(i+1)} \right) \\
 x_t^{(i+1)} &= x_t^{(i)} + \frac{\Delta t}{2} \left( x_{tt}^{(i)} + x_{tt}^{(i+1)} \right).
 \end{aligned}$$

In practice we often deal with axisymmetric structures (e.g. cylinder), where only two coordinates  $r$  and  $z$  are needed to describe the problem. This class of problems is often referred to as two-dimensional axisymmetric problems. In the case of axisymmetric cylindrical geometry we obtain the following structure of matrices in (3)

$$\begin{aligned}
 M_{ij}^{\alpha\beta} &= 2\pi \int_{\underline{R}}^{\overline{R}} \int_{\underline{z}}^{\overline{z}} r \varphi_i^\alpha(r, z) \cdot \varphi_j^\beta(r, z) \, dr dz, \quad \alpha, \beta = r, z, \\
 K_{ij}^{\alpha\beta} &= 2\pi \int_{\underline{R}}^{\overline{R}} \int_{\underline{z}}^{\overline{z}} \left( \begin{bmatrix} \frac{\partial}{\partial r} & 0 \\ \frac{1}{r} & 0 \\ 0 & \frac{\partial}{\partial z} \\ \frac{\partial}{\partial z} & \frac{\partial}{\partial r} \end{bmatrix} \varphi_i^\alpha(r, z) \right)^T C^E \begin{bmatrix} \frac{\partial}{\partial r} & 0 \\ \frac{1}{r} & 0 \\ 0 & \frac{\partial}{\partial z} \\ \frac{\partial}{\partial z} & \frac{\partial}{\partial r} \end{bmatrix} \varphi_j^\beta(r, z) \, dr dz, \\
 B_{ij}^\beta &= 2\pi \int_{\underline{R}}^{\overline{R}} \int_{\underline{z}}^{\overline{z}} r (\nabla \varphi_i(r, z))^T E \begin{bmatrix} \frac{\partial}{\partial r} & 0 \\ \frac{1}{r} & 0 \\ 0 & \frac{\partial}{\partial z} \\ \frac{\partial}{\partial z} & \frac{\partial}{\partial r} \end{bmatrix} \varphi_j^\beta(r, z) \, dr dz, \\
 A_{ij} &= 2\pi \int_{\underline{R}}^{\overline{R}} \int_{\underline{z}}^{\overline{z}} r \nabla \varphi_i(r, z) \epsilon \nabla \varphi_j(r, z) \, dr dz,
 \end{aligned}$$

where  $\varphi_i$ ,  $i = 1 \dots n_{nodes}$  are two-dimensional nodal basis functions and  $C^E, E, \epsilon$  are axisymmetric matrices of piezoelectric material.

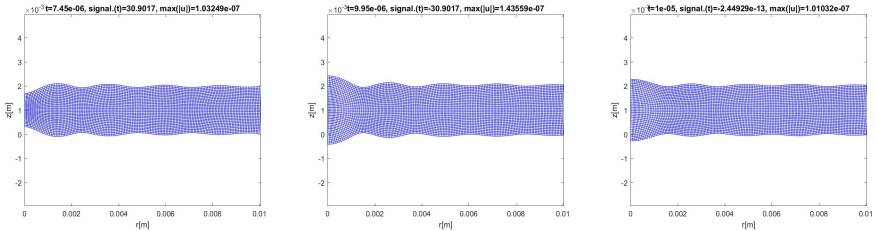


Fig. 1: Mechanical displacement of piezo cylinder with radius 0.2 m, thickness 0.02 m and Dirichlet boundary condition  $U(t) = 100 \sin(\omega t)$ ,  $f = 1$  MHz on  $\Gamma_\phi$ .

## 2 Piezoelectricity - acoustic coupling problem

The numerical simulation of coupled piezoelectricity–acoustic problems demands consideration of the coupling conditions at the interface  $\Gamma_{pf}$ . These conditions are incorporated as appropriate boundary conditions in the PDEs. Let us assume that deformations and electric potential of the piezoelectric system are the only source for the acoustic field ( $\phi = U$  on  $\Gamma_\phi$ ) and the boundary conditions at the outer boundary of  $\Omega_f$  are zero.

The weak form for the piezoelectricity domain  $\Omega_p$  and the fluid domain  $\Omega_f$  becomes

$$\begin{aligned}
 & \text{Find } \mathbf{u}, \phi, \psi, \text{ such that} \\
 & \int_{\Omega_p} \rho_p \frac{d^2 \mathbf{u}}{dt^2} \cdot \mathbf{v} \, d\Omega + \int_{\Omega_p} C^E \varepsilon(\mathbf{u}) : \varepsilon(\mathbf{v}) \, d\Omega + \int_{\Omega_p} E^T \varepsilon(\mathbf{v}) \cdot \nabla \phi \, d\Omega = \\
 & \hspace{25em} = \int_{\Gamma_{pf}} \frac{d\psi}{dt} (\mathbf{v} \cdot \mathbf{n}) \, d\Gamma, \tag{4} \\
 & \int_{\Omega_p} E \varepsilon(\mathbf{u}) \cdot \nabla \varphi \, d\Omega - \int_{\Omega_p} \epsilon \nabla \phi \cdot \nabla \varphi \, d\Omega = 0, \\
 & - \int_{\Omega_f} \frac{\rho_f}{c_f^2} \frac{d^2 \psi}{dt^2} \eta \, d\Omega - \int_{\Omega_f} \nabla \psi \nabla \eta \, d\Omega = \int_{\Gamma_{pf}} \rho_f \left( \frac{d\mathbf{u}}{dt} \cdot \mathbf{n} \right) \eta \, d\Gamma.
 \end{aligned}$$

After discretization  $\Omega$  we obtain the following linear system

$$\begin{pmatrix} -M_p & 0 & \\ 0 & 0 & 0 \\ 0 & 0 & -M_f \end{pmatrix} \begin{pmatrix} \hat{u}_{tt} \\ \hat{\phi}_{tt} \\ \hat{\psi}_{tt} \end{pmatrix} - \begin{pmatrix} 0 & 0 & C^T \\ 0 & 0 & 0 \\ C & 0 & 0 \end{pmatrix} \begin{pmatrix} \hat{u}_t \\ \hat{\phi}_t \\ \hat{\psi}_t \end{pmatrix} + \begin{pmatrix} K & B^T & 0 \\ B & -A_p & 0 \\ 0 & 0 & -A_f \end{pmatrix} \begin{pmatrix} \hat{u} \\ \hat{\phi} \\ \hat{\psi} \end{pmatrix} = \begin{pmatrix} 0 \\ g \\ 0 \end{pmatrix}. \tag{5}$$

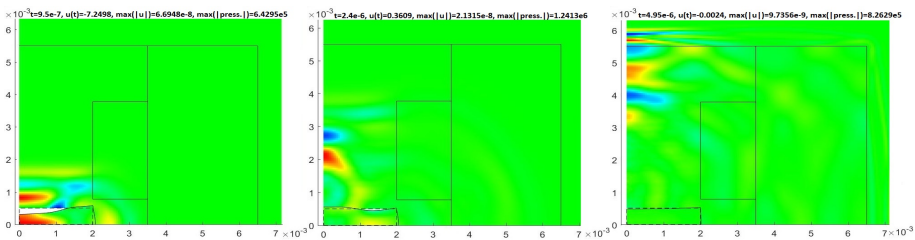


Fig. 2: Propagation of acoustic wave with  $U(t) = 100 \sin(\omega t) \exp(-2ft)$ ,  $f = 1$  MHz with standard parameters for acoustic media (speed of sound and density for water, air and plastic).



### 3 Future work

In the future we would like to finish parallel implementation of 3D transient piezo - acoustic simulation. In 01/2019 some results related to the analysis of piezo - acoustic FEM was presented in the SNA Conference in Ostrava.

### Acknowledgement

This work is supported by SGS grant no. SP2019/84, VŠB - Technical university of Ostrava.

### References

1. Gantner, A.: Mathematical Modeling and Numerical Simulation of Piezoelectrical Agitated Surface Acoustic Waves. Ph.D. thesis, University of Augsburg (6 2005)
2. Grossmann, C., Roos, H.G., Stynes, M.: Numerical Treatment of Partial Differential Equations. Springer (6 2007)
3. Kocbach, J.: Finite Element Modeling of Ultrasonic Piezoelectric Transducers. Ph.D. thesis, University of Bergen (9 2000)
4. Rupitsch, S.J.: Piezoelectric Sensors and Actuators: Fundamentals and Applications. Springer (6 2018)

# High-order boundary element method

David Ulčák

Department of Applied Mathematics, FEECS,  
VŠB – Technical University of Ostrava, 17. listopadu 15,  
708 33 Ostrava – Poruba, Czech Republic  
david.ulcak@vsb.cz

**Abstract.** In this paper, we introduce concept of high-order Boundary element method (BEM). The BEM provides alternative approach for solving boundary value problems in comparison to more conventional Finite element method (FEM). The methods are similar in principle, however, the formulation of problem follows different scheme, and BEM deals only with the boundary of the computational domain, thus producing likely smaller dimensions of matrices after discretization, which is remarkable when the surface/volume ratio of the domain is sufficiently low. Furthermore, finite-dimensional formulation may give better approximation when using basis consisting of polynomials of higher order. To deal with singular integrals for constructing BEM matrices, the logarithmic version of Gauss-Christoffel quadrature scheme is used. Although these calculations are numerical, for certain situations we can get elements of the single layer potential matrix exactly. We will focus on 2D problem, however, the logarithmic quadrature scheme can be particularly used also in 3D BEM, despite different fundamental solution appearing in boundary integral formulation.

**Keywords:** Boundary element method, polynomial basis, Gauss-Christoffel quadrature

## 1 High-order BEM

### 1.1 Potentials and boundary integral formulation

First of all, let us consider the fundamental solution to Laplace equation in 2D

$$G : \mathbb{R}^2 \times \mathbb{R}^2 \rightarrow \mathbb{R}, \quad G(\mathbf{x}, \mathbf{y}) = -\frac{1}{2\pi} \ln \|\mathbf{x} - \mathbf{y}\|. \quad (1)$$

It can be readily shown that for every domain  $\Omega$  such that  $\mathbf{x} \notin \Omega$  it holds  $\Delta_{\mathbf{y}}G(\mathbf{x}, \mathbf{y}) = 0$ , and more generally, in every domain containing  $\mathbf{x}$  it is  $\Delta_{\mathbf{y}}G(\mathbf{x}, \mathbf{y}) = \delta_{\mathbf{x}}$  in distributional sense, where  $\delta_{\mathbf{x}}$  is the Dirac distribution, centred in  $\mathbf{x}$ .

Now, let  $\Omega \subset \mathbb{R}^2$  be simply-connected Lipschitz domain and  $\Gamma_D, \Gamma_N \subset \partial\Omega$  such that  $\Gamma_D \cap \Gamma_N = \emptyset$ ,  $\Gamma_D \cup \Gamma_N = \partial\Omega$ . Considering the Poisson boundary

value problem

$$\left\{ \begin{array}{l} -\Delta u(x_1, x_2) = f(x_1, x_2) \text{ in } \Omega \\ u(x_1, x_2) = g(x_1, x_2) \text{ on } \Gamma_D \\ \frac{du}{dn}(x_1, x_2) = h(x_1, x_2) \text{ on } \Gamma_N \\ \text{diam}(\Omega) < 1, \end{array} \right. \quad (2)$$

for smooth enough initial data  $f, g, h$  and unknown  $u$  we can get the solution via Green’s third identity, which can be generalised (see e.g. [2]) for  $f \in L^2(\Omega)$ ,  $g \in H^{\frac{1}{2}}(\Gamma_D)$ ,  $h \in H^{-\frac{1}{2}}(\Gamma_N)$ ,  $u \in H^1_{\Delta}(\Omega)$ :

$$\begin{aligned} \forall \mathbf{x} \in \Omega : \quad u(\mathbf{x}) &= \int_{\Omega} f(\mathbf{y})G(\mathbf{x}, \mathbf{y})d\mathbf{y} + \int_{\Gamma} \gamma_N u(\mathbf{y})\gamma_D G(\mathbf{x}, \mathbf{y})d\ell(\mathbf{y}) - \\ &\quad - \int_{\Gamma} \gamma_D u(\mathbf{y})\gamma_{N, \mathbf{y}} G(\mathbf{x}, \mathbf{y})d\ell(\mathbf{y}) \quad (3) \\ &\stackrel{\text{notation}}{=} N(f) + \tilde{V}(\gamma_N u) - W(\gamma_D u), \end{aligned}$$

where  $\gamma_D$  is the trace operator and  $\gamma_N$  represents outer normal derivative operator. This identity follows from properties of the function  $G$ , the second Green’s identity and the limit approach to point  $\mathbf{x}$ . As the notation suggests, the integrals in the formula correspond with the potentials:  $N$  is the Newton (volume) potential,  $\tilde{V}$  the single-layer potential and  $W$  the double-layer potential.

It is clear that we would get the solution of the problem (2) immediately, only if we knew  $\gamma_D u$  on  $\Gamma_N$  and  $\gamma_N u$  on  $\Gamma_D$ . Using the mapping properties of each potential and limit approach to the domain’s boundary (see [3]), we eventually arrive at the weak formulation. For finding e.g.  $\gamma_N u$  on  $\Gamma_D$  it is as follows:

$$\begin{aligned} &\text{Find } t \in H^{-\frac{1}{2}}(\Gamma) \text{ such that} \\ \forall v \in H^{-\frac{1}{2}}(\Gamma) : \quad \langle v, Vt \rangle &= \left\langle v, \left( \frac{1}{2}I + K \right) g \right\rangle, \quad (4) \end{aligned}$$

where  $V = \gamma_D \circ \tilde{V}$ ,  $I$  is the identity operator,  $K$  is derived from  $\gamma_D \circ W$  and the duality pairing  $\langle v, w \rangle$  can be interpreted simply as  $\int_{\Gamma} v(x)w(x)d\ell(x)$  for  $v, w \in L^2(\Gamma)$ . This follows from the fact that space  $L^2(\Gamma)$  is a dense subspace of  $H^{-\frac{1}{2}}(\Gamma)$  in sense of the Riesz theorem, which, most importantly, guarantees the existence and uniqueness of solution, since the condition  $\text{diam}(\Omega) < 1$  ensures ellipticity of the operator  $V$ .

### 1.2 Numerical realization and polynomial basis

Henceforth the approach is analogous to FEM: We need to pick finite-dimensional subspace of our solution space, in this case  $H^{-\frac{1}{2}}(\Gamma)$ . To guarantee reasonable convergence rate, discretization of the domain’s boundary possibly should not contain significant differences among the elements of the mesh. Then, having  $n$  elements, we can define basis piecewise constant functions  $\psi_1, \dots, \psi_n$  for our subspace  $V^h$  such that the  $k^{\text{th}}$  basis function equals to 1 above the  $k^{\text{th}}$  element

and zero elsewhere. Furthermore, to approximate the space  $H^{\frac{1}{2}}(\Gamma)$  by piecewise continuous basis, we can use "classic" FEM-like hat functions  $\varphi_1, \dots, \varphi_n$ . However, we can use a set of polynomials up to certain degree above each element, acquiring the high-order BEM basis. In our approach, we use Legendre polynomials over each segment, thus the basis functions look as follows:<sup>1</sup>

$$\begin{aligned} \varphi_0^{(i)}(t) &= \chi_{\tau_i}(x)\varphi_i(t), \\ \psi_k^{(i)}(x) &= \chi_{\tau_i}(x)L_k(2t-1), \quad \varphi_1^{(i)}(t) = \chi_{\tau_i}(x)\varphi_{i+1}(t), \\ \varphi_k^{(i)}(t) &= \varphi_0^{(i)}(t)\varphi_1^{(i)}(t)L_{k-2}(2t-1). \end{aligned}$$

Formulation (4) then leads to the system of linear equations

$$\mathbb{V}\mathbf{t} = \left(\frac{1}{2}\mathbb{M} + \mathbb{K}\right)\mathbf{g}, \tag{5}$$

where

$$\mathbb{V}_{k,l}^{(i,j)} = \langle \psi_k^{(i)}, V\psi_l^{(j)} \rangle = -\frac{1}{2\pi} \int_{\Gamma} \psi_k^{(i)}(\mathbf{x}) \int_{\Gamma} \psi_l^{(j)}(\mathbf{y}) \ln \|\mathbf{x} - \mathbf{y}\| d\ell(\mathbf{y})d\ell(\mathbf{x}), \tag{6}$$

$$\mathbb{M}_{k,l}^{(i,j)} = \langle \psi_k^{(i)}, \varphi_l^{(j)} \rangle = \int_{\Gamma} \psi_i(\mathbf{x})\varphi_j(\mathbf{x})d\ell(\mathbf{x}), \tag{7}$$

$$\mathbb{K}_{k,l}^{(i,j)} = \langle \varphi_k^{(i)}, \varphi_l^{(j)} \rangle = \frac{1}{2\pi} \int_{\Gamma} \psi_i(\mathbf{x}) \int_{\Gamma} \varphi_j(\mathbf{y}) \cdot \frac{(\mathbf{x} - \mathbf{y}) \cdot \mathbf{n}(\mathbf{y})}{\|\mathbf{x} - \mathbf{y}\|^2} d\ell(\mathbf{y})d\ell(\mathbf{x}), \tag{8}$$

whereas the matrices are organized by blocks, having e.g.  $\mathbb{V}^{(i,j)}$  the block corresponding to integration over  $i^{\text{th}}$  and  $j^{\text{th}}$  segment.

For unknown function  $u$  regular enough, we can achieve solution with convergence rate exponential according to order of polynomial basis (see [3]). For more complex cases, the pairing of finer discretizations on less regular parts of computational domain with coarse mesh with higher-order basis on smoother part may give decent results.

## 2 Logarithmic Gauss-Christoffel quadrature

To deal with the integrals in (6),(7),(8), mainly for diagonal and sub-diagonal blocks of the matrix  $\mathbb{V}$ , we will need some efficient tool for integration. The general Gaussian quadrature, also known as Gauss-Christoffel quadrature, proves convenient in our case.

Let  $w \in L^1(a, b)$ , such that  $w > 0$  almost everywhere in  $\langle a, b \rangle$ . Then for  $f, g \in L^2(a, b)$ ,

$$(f, g)_{w,a,b} = \int_a^b w(x)f(x)g(x)dx \tag{9}$$

---

<sup>1</sup> Using  $t \in (0, 1)$  as parametrization variable for  $i^{\text{th}}$  segment.

is well-defined inner product. Through Gram-Schmidt process, we can obtain a set of polynomials orthogonal with respect to inner product (9). Roots of the  $n^{\text{th}}$  polynomial  $x_1, \dots, x_n$  serve as nodes in the quadrature formula

$$\int_a^b w(x)f(x)dx \approx \sum_{i=1}^n w_i f(x_i), \quad w_i = \int_a^b w(x) \prod_{\substack{j=1 \\ j \neq i}}^n \frac{x - x_j}{x_i - x_j} dx \quad (10)$$

which is exact for polynomial  $f$  up to degree  $2n - 1$ , which is the highest possible precision in sense of polynomial order. Numbers  $w_1, \dots, w_n$  are called weights and they satisfy  $\sum_{i=1}^n w_i = \int_a^b w(x)dx = \|w\|_{L^1(a,b)}$ . By putting  $w(x) = 1$ , we get aforementioned Legendre polynomials and Gauss-Legendre quadrature, used for evaluation of elements in matrices  $\mathbb{K}$  and  $\mathbb{M}$ . For non-polynomial  $f$  and more general (Jacobi-type) weight function  $w$ , it can be shown (see [4]) that if  $f$  is analytic, then the Gaussian quadrature converges exponentially with respect to  $n$ . However, our concern is to deal with singular logarithmic integrals in construction of  $\mathbb{V}$ , so we put  $w(x) = -\ln(x)$ ,  $a = 0$ ,  $b = 1$ . This quadrature has likely the same convergence rate for analytic  $f$ , proving by employing rational approximation. Nevertheless, our integrals contain only polynomial integrands. Let us see example of convergence for  $\int_0^1 h(x)dx$  for  $h_1(x) = \ln(x) \sin(\pi x)$  and  $h_2(x) = \ln(x)\sqrt{1 - x^2}$  in the Table 1:

**Table 1.** Comparison of Gauss-Legendre (GL) and logarithmic (log) quadratures

$n$	Error (GL) $h_1$	Error (log) $h_1$	Error (GL) $h_2$	Error (log) $h_2$
2	0.027	0.010	0.104	0.002
4	0.002	$2.32 \cdot 10^{-6}$	0.032	$8.94 \cdot 10^{-5}$
8	$1.54 \cdot 10^{-4}$	$6.66 \cdot 10^{-16}$	0.009	$4.11 \cdot 10^{-6}$
12	$3.25 \cdot 10^{-5}$	under $\varepsilon$	0.004	$6.24 \cdot 10^{-7}$
16	$1.07 \cdot 10^{-5}$	$\approx 0$	0.002	$1.59 \cdot 10^{-7}$
20	$4.48 \cdot 10^{-6}$	$\approx 0$	0.001	$5.47 \cdot 10^{-8}$

### 3 Numerical example

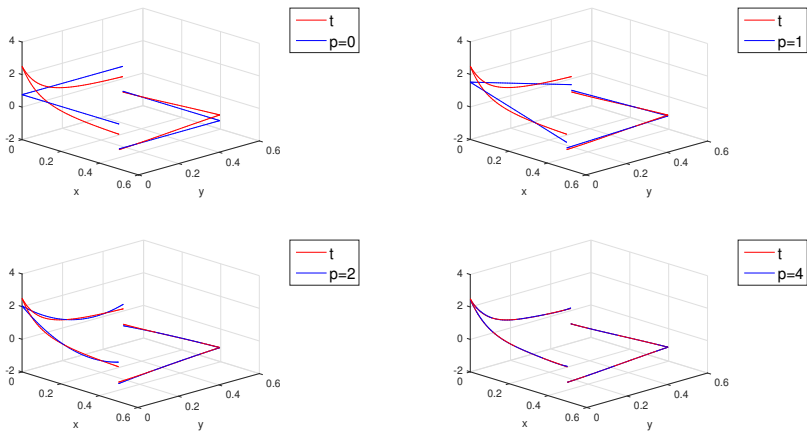
Using semi-analytic approach (Duffy’s substitution, properties of Legendre polynomials etc.) for matrix  $\mathbb{V}$  we can use logarithmic quadrature in both variables for diagonal blocks and in one of the variables for sub-diagonal blocks, calculating corresponding elements exactly up to computer precision. Non-diagonal blocks of  $\mathbb{M}$  as well as the diagonal blocks of  $\mathbb{K}$  can be easily shown to be zero. The rest of the elements in either matrix can be computed via Gauss-Legendre quadrature.

Finally, let us have a look on an academic example of convergence of high-order BEM for regular Laplace problem:

$$\tilde{u}(\mathbf{x}) = -\frac{1}{2} \ln \left\| \mathbf{x} + \frac{1}{10} \begin{bmatrix} 1 \\ 1 \end{bmatrix} \right\|, \quad \Omega = \left(0, \frac{1}{2}\right)^2$$

$$\begin{cases} -\Delta u = 0, & x \in \Omega \\ \gamma_D u = g, & x \in \Gamma, \end{cases} \quad g(x) = \tilde{u}|_{\Gamma}(x).$$

The Figure 1 depicts convergence of resulting approximation of  $\gamma_N u$ , the Figure 2 shows exponential convergence of p-BEM in comparison to superlinear convergence of classical BEM.



**Fig. 1.** Visual convergence of p-BEM for increasing order

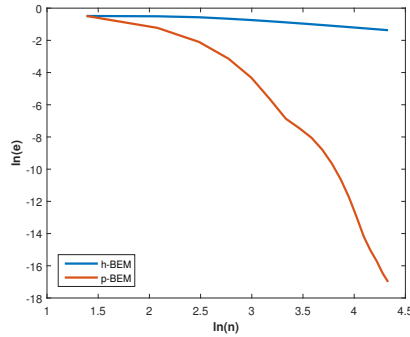


Fig. 2.  $L^2$ -norm of the solution error with respect to matrix dimensions

## 4 Future work

In the future, we would like to finish the logarithmic quadrature scheme for 3D BEM and focus more closely on high-order 3D BEM concept. We would also like to finish the proof of exponential convergence for logarithmic quadrature.

## 5 Publications

We have not published any paper on this topic yet, however, we would like to publish soon the paper on effective usage of logarithmic quadrature in 3D BEM, including the above-mentioned convergence proof. Some of the aforementioned results were presented on the SNA 19 conference in January 2019.

## 6 Grants and Awards

This work is partly supported by SGS grant no. SP2019/84, VŠB – Technical university of Ostrava.

## References

1. Davis, P. J., Rabinowitz, P.: Methods of numerical integration. Courier Corporation. (2007)
2. McLean, W. C. H.: Strongly elliptic systems and boundary integral equations. Cambridge university press. (2000)
3. Sauter, S.A., Schwab, C.: Boundary element methods, volume 39 of Springer Series in Computational Mathematics. Springer-Verlag. (2011)
4. von Sydow, B.: Error estimates for Gaussian quadrature formulae. Numerische Mathematik. 29(1), 59–64 (1977)

# Dealing with the variable selection problem in the analysis of mixed data

Adéla Vrtková

Department of Applied Mathematics, FEECS,  
VŠB – Technical University of Ostrava, 17. listopadu 15,  
708 33 Ostrava – Poruba, Czech Republic  
adela.vrtkova@vsb.cz

**Abstract.** The variable selection, also called feature selection, is a process of selecting a subset of the most relevant exploratory variables for the purpose of model construction. There are various methods which work on different basis. Some of them are almost perfectly automatic, some of them require further individual researcher's assessment. The specific properties of certain methods carry some advantages and disadvantages. In this paper, we provide overview of several methods which are widely-used for the purpose of variable selection in the context of mixed data analysis. We aim to gain important theoretical background of studied methods for the purpose of future extension of our current research which is focused on solving classification problems in medicine.

**Keywords:** mixed data, variable selection, univariate selection, stepwise regression, best-subset regression, LASSO regression, decision trees

## 1 Motivation

Mixed data are basically datasets containing both numerical and categorical variables. Naturally, solving real-life problems usually means dealing with the mixed data which is not a trivial problem. In our research, we focus on solving classification problems with statistical methods and machine learning methods. So far, we have applied widely-used methods, such as the logistic regression, neural networks or random forests. However, until now the variable selection problem, which is a vital part of the analysis process, has been dealt with mainly by the univariate selection which can be considered as quite elementary method. Therefore, extension for more advanced methods is currently the leading topic of our research.

We focused on well-known methods with wide literature background and strong support in R software community considering further application on real-life data. In this paper, firstly, the univariate selection will be described, followed by the stepwise and best-subset regression method, the LASSO regression and tree-based methods. Also, we provide notes, remarks and comments about their application.



This paper aims to provide the overview of methods which will be later used in combination with above-mentioned classification methods to finally find appropriate model for the prediction of clinical status of patients after an acute ischemic stroke. Obtained knowledge and results will be combined with conclusions derived from our previous work [10, 11] where we have already analysed above-mentioned data about patients after stroke.

## 2 Methodology

Firstly, it is necessary to explain that there are four general approaches of dealing with the variable selection problem [2]. Filter methods are applied before the application of the learning algorithm itself, so, it is completely independent, and it is usually based on the tools of statistical inference. Wrapper methods train a model for some or for all possible subsets of exploratory variables and the variable selection is then based on the model's error rate. In embedded methods, the variable selection process is built directly in the learning algorithm. Lastly, there is an approach which uses dimensionality reduction for a purpose of reduction of the number of exploratory variables by transforming them into a set of new variables. The last described approach is not suitable for our problem because of the transformation of the original set of exploratory variables.

### 2.1 Univariate Selection

The univariate selection method is one of the filter methods which assesses variables individually, e.g. with standard tools of statistical inference, i.e. hypotheses testing procedure. Considering the application before the classification learning algorithm, it means that the categories defined by the predicted (dependent, output) variable are compared within categories of the exploratory (independent, input) variables and only those with detected statistically significant difference are included in the learning algorithm. In the context of classification, using the ANOVA, the Kruskal-Wallis test or Chi-Squared test of independence is a common choice. Mathematical background of the statistical tests is available e.g. in [3].

The application of the univariate selection is very simple because statistical tests are implemented in various software. However, including the information about possible interactions among exploratory variables is completely missing and the univariate selection process doesn't help with multicollinearity. Anyway, this process could be useful in separating the most irrelevant exploratory variables and as a filter method, practically, it can be applied prior any classification algorithm. We applied this method in [10] and [11] as a primary selection procedure before application of the random forests algorithm and neural networks.

### 2.2 Stepwise and Best-Subset Regression

Both methods can be classified as wrapper methods. The stepwise regression is widely-used approach when dealing with the regression analysis, even though

various studies refer about its limitations and possible biased measures related to the quality of regression model [6]. However, when used carefully, the method can provide useful information. The stepwise regression uses forward selection, backward elimination or combination of both [5], [4]. The forward selection starts with no variables in the model and adds the variable which causes the most significant model-fit improvement. This continues until no significant improvement can be obtained. Analogously, the backward elimination is performed where the process starts with all variables in the model. The forward selection was used with the logistic regression in our latest paper [11].

The best-subset regression simply generates all possible subsets of exploratory variables and the performance of related regression model is evaluated [5], [4]. The result is a list of all possible models and their summary statistics. Then, the final choice depends on the researcher. This method is especially useful when the number of exploratory variables is small. On the other hand, its complexity becomes a disadvantage when working with larger datasets and both best-subset and stepwise regression don't automatically deal with possible multicollinearity. Unfortunately, in the prediction of clinical status of patients after stroke, the number of exploratory variables is too high to apply the best-subset regression.

### 2.3 LASSO Regression

The LASSO regression is an embedded method and it was formulated as an alternative to the ridge regression which primarily reduces multicollinearity but doesn't help with the variable selection. The LASSO regression can help us with both. Explanation of the gist of the LASSO regression requires providing wider mathematical background which is beyond the scope of this paper. So, for detailed theoretical background, let us refer to [5], [4] or [6].

Nevertheless, according to promising properties of the method, it seems that it could be perfect solution for our data. It can help us with the variable selection and moreover with multicollinearity. However, presence of categorical exploratory variables in analysed dataset means necessity of transformation to dummy variables which later could cause an issue during interpretation of the final model in a case that the algorithm would eliminate a part of a transformed categorical variable. So far, we haven't applied the LASSO regression on our dataset. The idea about this method arose from the discussion at last attended conference in June 2019 in Žilina, Slovakia [11], hence it remains for our future work.

### 2.4 Tree-Based Methods

Tree-based methods (or decision trees) belong to a category of embedded methods and they have been considered as one of the most flexible, easy-to-use and robust methods [1]. They are applicable to regression and classification problems (regression or classification trees) and specifically the random forests algorithm is one of the most popular machine learning algorithms.

The gist of standard random forests is quite simple. The algorithm starts with the selection of many bootstrap samples from the original dataset, where the number of bootstrap samples determines the number of trees (classification or regression trees). Then, a decision tree is built for each bootstrap sample and at each node, certain number of exploratory variables is chosen randomly to make the best split. In the end, the final prediction is calculated by averaging the predictions of regression trees or by identifying the most frequent prediction in classification trees. The alternative random forests algorithm which is based on conditional inference trees chooses subsets of exploratory variables by their statistically significant relationship with the predicted variable [9], [8].

We applied the random forests with conditional inference trees in [10] and [11] not just as a method for variable selection purpose but also as a classification algorithm with very promising results. As an embedded method, the algorithm combines the variable selection and the classification process which is its main advantage and we don't plan to make any adjustments or extensions.

### 3 Conclusion

This paper provided an overview of methods used for the variable selection in mixed data. This research work provided us important methodological background which will be crucial later during model building process. We described some methods which have already been used in our research, but we also described methods which we want to use in our future research (especially LASSO regression).

For future work, we would like to combine the classification methods - logistic regression, neural networks, and others - with explored variable selection methods to obtain final predictive model for clinical status of patients after ischemic stroke. The cooperation with the University Hospital Ostrava continues and the goal of building a decision-support tool for contributing to the ischemic stroke treatment is still of interest. In our previous work, we have already obtained satisfactory results. However, we aim to explore more possibilities rather than settle with the first satisfactory model and our main idea consists in complexity of the solution of the classification problem.

In 12/2018, in cooperation with the University Hospital Ostrava, a paper related to the topic of the analysis of ischemic stroke data was published in the Medical Science Monitor [7]. Findings presented in this paper are an essential part of the research which leads to the above-mentioned desirable decision-support tool. Also, in 06/2019, another paper [11] related to the topic was presented by the author in the International Conference on Information and Digital Technologies 2019 in Žilina, Slovakia.

## Acknowledgement

The author acknowledges the support of VSB - Technical University of Ostrava (Project No. SP2019/16) and the support of the Moravian-Silesian Region (RRC/10/2017).

## References

1. Breiman, L.: Random forests. *Machine learning* 45(1), 5–32 (2001)
2. Chandrashekar, G., Sahin, F.: A survey on feature selection methods. *Computers & Electrical Engineering* 40(1), 16–28 (2014)
3. DeGroot, M.H., Schervish, M.J.: *Probability and statistics*. Pearson Education (2012)
4. Friedman, J., Hastie, T., Tibshirani, R.: *The elements of statistical learning*, vol. 1. Springer series in statistics New York (2001)
5. James, G., Witten, D., Hastie, T., Tibshirani, R.: *An introduction to statistical learning*, vol. 6. Springer (2013)
6. Miller, A.: *Subset selection in regression*. Chapman and Hall/CRC (2002)
7. Procházka, V., Jonszta, T., Czerny, D., Krajca, J., Roubec, M., Hurtikova, E., Urbanec, R., Streitová, D., Pavliska, L., Vrtkova, A.: Comparison of mechanical thrombectomy with contact aspiration, stent retriever, and combined procedures in patients with large-vessel occlusion in acute ischemic stroke. *Medical science monitor: international medical journal of experimental and clinical research* 24, 9342 (2018)
8. Strobl, C., Boulesteix, A.L., Kneib, T., Augustin, T., Zeileis, A.: Conditional variable importance for random forests. *BMC bioinformatics* 9(1), 307 (2008)
9. Strobl, C., Boulesteix, A.L., Zeileis, A., Hothorn, T.: Bias in random forest variable importance measures: Illustrations, sources and a solution. *BMC bioinformatics* 8(1), 25 (2007)
10. Vrtková, A.: Predicting clinical status of patients after an acute ischemic stroke using random forests. In: *Information and Digital Technologies (IDT), 2017 International Conference on*. pp. 417–422. IEEE (2017)
11. Vrtková, A., Procházka, V.: Comparing the performance of regression models, random forests and neural networks for stroke patients' outcome prediction. In: *Information and Digital Technologies (IDT), 2019 International Conference on*. p. (Proceedings in preparation). IEEE (2019)

# On Almost Regular Graphs and on Social Networks

Jakub Závada

Department of Applied Mathematics, FEECS,  
VŠB – Technical University of Ostrava, 17. listopadu 15,  
708 33 Ostrava – Poruba, Czech Republic  
jakub.zavada@vsb.cz

**Abstract.** This work is a summary of my results achieved during my study in academic year 2018/2019. Since my research during the last academic year paid attention to more than one topic, all of these topics will be briefly mentioned in this text. The title of the article can hint that the article is about some connection between almost regular graphs and social networks, but these are only the two main disjoint topics of my research made up to now. The first topic is the orientation of almost regular graphs. I already presented this topic in the WOFEX last year. Our work on this topic was extended and was prepared for the publication during this year. The second topic is based on my research related to the doctoral course called Social Networks, which I completed this year. The last topic is the scheduling of tournaments. I have just started to work on this topic in June 2019, so there are no significant results, which can be presented in this text, but it is expected, that I will pay high attention to this topic during the next year and in my dissertation thesis.

**Keywords:** graph orientation, metric, social networks

## 1 Introduction

Since this work is divided into two main disjoint parts, the introduction is divided into two subsections. Each of these subsections is focused on one topic separately.

### 1.1 Graph Orientation Part

First part of the introduction is recalled from my WOFEX 2018 contribution. The work on orientations of almost regular graph is joint work with Petr Kovář, Michal Kravčenko, Matěj Krbeček, Michael Kubesa, and Adam Silber.

In general, orientation of a simple weighted graph  $G = (V, E, w)$  is an NP-complete problem [1], but the problem of the orientation of unweighted graphs (or graphs with equal weights) can be solved in  $O(|E|^2)$  time using the algorithm provided in [2]. This algorithm was slightly improved in [1], where it is shown that the problem can be solved in  $O(|E|^{\frac{3}{2}})$  time. An optimal orientation can be

found even faster for some special cases of graphs such as trees (with  $O(|V|)$  time complexity) [1] or planar graphs (with  $O(|E|)$  time complexity) [3].

Our aim was to solve the orientation problem optimally for another class of graphs, which we call almost regular graphs. We provide two algorithms. First of them is faster ( $O(|E|)$  time complexity), but the orientation found by this algorithm is not optimal for certain almost regular graphs. We show the conditions, which are necessary for finding an optimal orientation using the first algorithm. Our second algorithm is slightly slower, but can find an optimal orientation for every almost regular graph. We consider only connected graphs. Optimal orientation problem for disconnected graphs can be solved by applying the same algorithm on each component of the graph separately.

Results of this work can be used for the optimization of parallel computing in numerical methods.

## 1.2 Social Networks Part

One of my tasks to pass the Social Networks course was to read and try to find mistakes or better solutions of problems mentioned in [4]. Article [4] proposes a novel metric for 2-connected graphs, which reflects important properties of graphs of social networks. We can imagine the typical graph of a social network as a graph in which there are subgraphs of very high degree of connectivity. It can be illustrated for example in graphs of well-known internet social networks. Every user of the social network will be represented by a vertex in this graph and edge is between two vertices if and only if users represented by its endvertices are in a relation in the social network. It is easy to see that there will be subgraphs with high degrees of connectivity, because if user  $a$  knows user  $b$  and user  $b$  knows user  $c$ , then there is quite high probability, that user  $a$  knows also user  $c$ . Such dense subgraph, (often clique), can represent for instance family or group of classmates.

## 2 Orientations of Almost Regular Graphs

Almost regular graph is every graph  $G$  in which the difference between maximum degree  $\Delta(G)$  and minimum degree  $\delta(G)$  is at most two. Optimal orientation of  $G$  is such orientation (we orient every edge of  $G$  in exactly one way) that the maximum outdegree is minimized. An easy algorithm, which successfully finds optimal orientation in most almost regular graphs, is based on following process:

1. Check, whether all degrees in the graph are even. If so, skip step 2 and go to the step 3.
2. Insert new vertex  $v$  to the graph and connect it by an edge with all vertices of odd degree.
3. Graph is now Eulerian and we can find an Eulerian trail in the graph and orient all edges along the trail.
4. If vertex  $v$  was inserted in step 2, delete vertex  $v$ .

The orientation of connected almost regular graph found by this algorithm is optimal if  $\Delta(G) - \delta(G) \leq 1$  or  $\Delta(G)$  is even or the number of vertices of degree  $\Delta(G)$  is greater than the number of vertices of degree  $\delta(G)$ . All these conditions can be checked easily. Moreover if at least one of them is satisfied in an almost regular graph  $G$ , then the maximum outdegree in the optimal orientation of  $G$  is always  $\left\lceil \frac{\Delta(G)}{2} \right\rceil$ . If none of them is satisfied, then the maximum outdegree in the optimal orientation of  $G$  is either  $\left\lfloor \frac{\Delta(G)}{2} \right\rfloor$  or  $\left\lceil \frac{\Delta(G)}{2} \right\rceil$ . For this case we presented different algorithm based on the maximum flow problem.

More detailed information and proofs can be found in the text of my WOFEX 2018 contribution. Subsequent work after WOFEX 2018 was to show that there cannot exist different algorithm with linear (considering the number of vertices) time complexity which can decide, whether the value of maximum outdegree is  $\left\lfloor \frac{\Delta(G)}{2} \right\rfloor$  or  $\left\lceil \frac{\Delta(G)}{2} \right\rceil$ . Main idea was to find certain class of graphs and to show that the complexity cannot be linear for this class. Since this part is prepared for publication, but still not published, there cannot be given more information in this text. This article was notably coauthored by Petr Kovář and Matěj Krbeček.

### 3 Social Networks

In [4] there is given a novel metric for 2-connected graphs. The distance from vertex  $u$  to vertex  $v$  in this metric is defined as the length of the shortest closed trail in which both  $u$  and  $v$  are contained. Theorem 1 in [4] says that it is a metric, but it came out that there are slight mistakes in this proof. A different proof is presented here. It is not necessary for this proof to be so long, but all parts of the proof are described in details to make it as clear as possible.

**Theorem 1.** *If we define the distance from vertex  $u$  to vertex  $v$  in simple unweighted graph  $G = (V, E)$  as the length of the shortest closed trail which contains both  $u$  and  $v$ , this distance is a metric in every 2-edge-connected graph.*

*Proof.* We prove that all properties of metrics (nonnegativity, symmetry, and triangle inequality) are satisfied.

Nonnegativity: it is clear, that the length of any trail in unweighted graph cannot be negative.

Symmetry: it is clear from the definition of this distance – shortest closed trail which contains both  $u$  and  $v$  is clearly the same as shortest closed trail which contains both  $v$  and  $u$ .

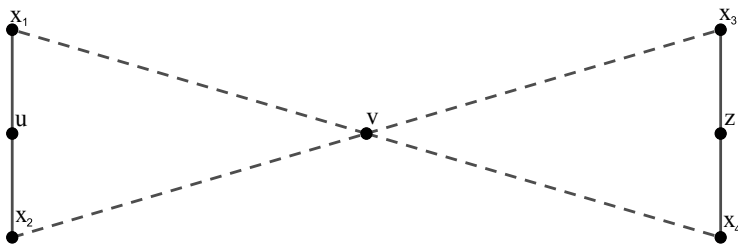
Triangle inequality: let  $d_{ct}(u, v)$  be the length of closed trail containing  $u$  and  $v$ , i.e. distance between vertices  $u$  and  $v$  in our definition of distance. Let  $CT(u, v)$  denotes a closed trail containing  $u$  and  $v$  and let  $|CT(u, v)|$  be the length of this trail. Our aim is now to show that for every  $u, v, z$  in  $V$  is  $d_{ct}(u, v) + d_{ct}(v, z) \geq d_{ct}(u, z)$ . Now we will assume, that we have found closed trails  $CT(u, v)$  and  $CT(v, z)$  of shortest possible length, i.e.  $|CT(u, v)| = d_{ct}(u, v)$  and  $|CT(v, z)| = d_{ct}(v, z)$ . These trails always exist in 2-edge-connected graph.

Vertex  $v$  is contained in both closed trails, so we can merge these two closed trails in  $v$  into one closed walk. Now there are three cases:

1. If  $CT(u, v)$  and  $CT(v, z)$  are edge disjoint, then closed walk created by merging  $CT(u, v)$  and  $CT(v, z)$  is also a closed trail of the length  $|CT(u, v)| + |CT(v, z)| = |CT(u, z)| \geq d_{ct}(u, z)$ .
2. If  $CT(u, v)$  contains  $z$  or  $CT(v, z)$  contains  $u$ , then trail  $CT(u, v)$ , or  $CT(v, z)$  respectively, can be selected to be  $CT(u, z)$  and clearly  $|CT(u, v)| + |CT(v, z)| > |CT(u, z)| \geq d_{ct}(u, z)$ .
3. In all remaining cases there is at least one common edge for  $CT(u, v)$  and  $CT(v, z)$ , but edges incident to  $u$  and  $z$  are not common (if some edge incident to  $u$  or  $z$  is contained in both  $CT(u, v)$  and  $CT(v, z)$ , then we have case 2). Figure 1 shows a subgraph  $H$  composed only of trails  $CT(u, v)$  and  $CT(v, z)$ . Edges which are not contained in  $CT(u, v)$  nor  $CT(v, z)$  are not shown in the figure. Dashed lines are used for trails. Notice that the length of trail  $x_i v$  can be zero in the case that  $uv$  is contained in  $CT(u, v)$ , or  $vz$  is contained in  $CT(v, z)$ , respectively. Then  $x_i = v$  for some  $i \in \{1, 2, 3, 4\}$ . But this is not a problem in the proof. We know that trail  $x_1 v$  has no common edge with  $x_2 v$  (otherwise  $CT(u, v)$  contains some edge repeatedly and so  $CT(u, v)$  is not a trail) and similarly  $x_3 v$  has no common edge with  $x_4 v$ . We know  $|CT(u, z)| + |CT(v, z)| > |h(H)|$ , where  $h(H)$  is the number of edges of subgraph  $H$ , because every edge of  $H$  is in  $CT(u, v)$  or  $CT(v, z)$  and at least one of these edges is in both  $CT(u, v)$  and  $CT(v, z)$ . Now it suffices to show that there exists some closed trail  $CT(u, z)$  in  $H$ , because then  $|CT(u, z)| + |CT(v, z)| > |h(H)| \geq |CT(u, z)| \geq d_{ct}(u, z)$  and triangle inequality is satisfied. Menger Theorem says that there exist exactly two edge disjoint paths between any two vertices of  $G$  if and only if  $G$  is 2-edge-connected. Two edge disjoint paths between  $u$  and  $z$  can together make required  $CT(u, z)$ , so according to Merge Theorem it suffices to show that  $H$  is 2-edge-connected, i.e. does not contain a bridge. So we can take edges one by one and for every edge check, whether it is a bridge or not. There are three types of edges in the schema. First of them are edges incident to  $u$  or  $z$ . If we delete one of these edges, the graph clearly remains connected, so these edges are not bridges. Second type are edges, which lie on exactly one of the trails  $x_i v$ . Removal of any such edge does not disconnect the graph. Last type are edges contained in two different trails. When we delete some of these edges, it will result in two "holes" in the schema. But one of the holes will be on the left side of  $v$  and the other on the right side of  $v$ . So the graph again remains connected. Graph  $H$  is 2-edge-connected and therefore there exists a closed trail  $CT(u, z)$ . The proof of the triangle inequality is finished.

This proof is better than the proof presented as proof of Theorem 1 in [4] also because the proof in [4] assumes 2-connectivity instead of the more general 2-edge-connectivity assumed here. I tried to do lots of more research regarding article [4] to improve results of the article, but most of it turned out to be





**Fig. 1.** Schema of subgraph  $H$  from the proof.

unsuccessful or useless. I also made a correction of some slight mistakes in the text [4].

## 4 Conclusion

During this academic year I paid more attention to the exams than to research. I passed all planned exams during first two years of my Ph.D. study, so during next years there will be more time for research. This article described two parts of my research. First part (orientations of almost regular graphs) is practically finished. It was presented also in the conference Graphs 2018 in Prague. For the second part (social networks) I suggested to continue by solving similar problem also for oriented graphs, because graphs of lots of social networks are oriented. I also mentioned third part of my research, which is only in the beginnings, but will be probably the most important during next years. This topic is scheduling of tournaments, which is related also to 1-factorizations or vertex labelings.

## References

1. Yuchi, A., Miyano, E., Ono, H., Zenmyo, K.: Graph orientation algorithms to minimize the maximum outdegree. 12th Computing: The Australasian Theory Symposium. pp. 11–20 (2006)
2. Venkateswaran, V.: Minimizing maximum indegree. Discrete Applied Mathematics. vol. 143, iss. 1–3, pp. 374–378 (2004)
3. Chrobak, M., Eppstein, D.: Planar orientations with low out-degree and compaction of adjacency matrices. Theoretical Computer Science. vol. 86, iss. 2, pp. 243–266 (1991)
4. Snášel, V., Dráždilová P., Platoš, J.: Closed trail distance in a biconnected graph. PLoS ONE. vol. 13, no. 8, pp. 1–12 (2018)

# VoIP simulation network by applying stochastic process methods

Ladislav Behaň

Department of Telecommunications, FEECS,  
VŠB – Technical University of Ostrava, 17. listopadu 15,  
708 33 Ostrava – Poruba, Czech Republic  
ladislav.behan@vsb.cz

**Abstract.** In many situations, it is necessary to detect and analyze VoIP attacks, monitor their progress and then prepare an effective defence against them. The best way how to detect attacks on VoIP infrastructure is by implementing VoIP honeypot. To attract the highest number of attackers possible, our VoIP honeypots create fake VoIP traffic among themselves. This feature is based on a Markov chains principle. In this paper, we provide a complete implementation of a SIP emulation model which ensures the exchange process of SIP signaling messages between the honeypots.

**Keywords:** honeypot, markov, chain, SIP, simulation

## 1 INTRODUCTION

Markov chains and their properties can be and are harnessed in various technology sectors such as data science. They are also remarkably useful in creating a diversity of real-world processes. They are widely employed in stock-market transaction models, game theory, various financial models, speech recognition or speech-to-text models, etc., which proves their versatility. [1]

To make the implemented model random as much as possible, we generate random variables using different types of distributions such as Poisson, Exponential, Binomial or Geometric. Our simulation network is controlled by probabilities obtained from data gathered by real VoIP provider. We emulate a common user behaviour including call session initiation, call pickup, call rejection and possibly timeout. Call features such as duration or ring time are drawn from the statistical population with the properties given by the chosen statistical distribution. [2, 3]

### 1.1 Design and implementation of the VoIP simulator

In the following text, we will focus on the simulation process of making and receiving phone calls.

For example, according to the processed data let's determine the number of VoIP calls that are performed let's say on Monday. There are over 40000 phone

calls made by call center agents made on Monday. As mentioned before, only a fraction of that number is to be used to simulate SIP signaling among honeypot distribution system.

So let's define a random experiment as a Poisson process (independent events occurring at time  $t$ , with the rate of  $\lambda$ ). If we define the random variable  $X$  - a number of events that occur in a time interval  $t$ , then we can consider  $X$  as a random variable with Poisson's distribution which is denoted as follows:

$$X \rightarrow Po(\lambda t) \tag{1}$$

Now we are going to fit the formula for Poisson random variables to suit our simulation model. As previously mentioned, we do not need thousands of calls per hour in our implementation that we have seen from the processed data, and  $\frac{1}{100}$  of total calls will be calculated. Our modified formula (2) is generating RV from PD where  $\lambda t$  is defined as  $nc_D$ , which  $nc$  represents a total number of calls at a certain day  $D$  (Monday = 40420 calls).

$$X \rightarrow Po\left(\frac{1}{100} * nc_D\right) \tag{2}$$

Consequently, for every day, we can generate RVs from PD that represent the total number of calls made in that given day. Next, we need to determine the number of calls that are made in each time slot of the day.

$$X \rightarrow Po\left(\frac{1}{100}nc_D * \frac{1}{100}cp_H\right) \Rightarrow Po\left(\frac{nc_D * cp_H}{10000}\right) \tag{3}$$

Where:

- $X \Rightarrow$  Random Variable from Poisson Distribution
- $nc_D \Rightarrow$  number of calls made in whole day
- $cp_H \Rightarrow$  ratio of calls made in certain time interval to  $nc_D$

The random selection results (RV PD) are processed in the following table, and the Poisson distribution graphs for calls at individual time intervals are shown in Figure 1.

Table 1: Monday call rate determination (RV=400)

Interval	Calls ( $cp_H$ )[%]	$\lambda t$	RV PD
00:00-05:59	0.00005	0	0
06:00-08:59	7.45	30	22
09:00-11:59	47.57	192	179
12:00-14:59	31.54	128	114
15:00-17:59	13.05	52	38
18:00-23:59	0.0037	1	2

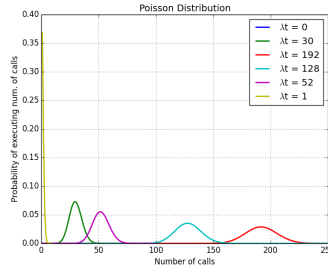


Fig. 1: Poisson Distribution Graph

Consequently, we have to determine how many calls will be successful. We know two parameters to determine a random variable from a particular distribution: the probability of a successful call and the total number of requests. Consider a trial having two possible outcomes: successful call or failed call. Suppose the trial is repeated several times and the repetitions are independent of each other. The total number of trials where the outcome turns out to be a success is a random variable whose distribution is called binomial distribution. Therefore, the most suitable distribution to generate RVs for this specific situation is Binomial distribution.

Therefore, for a binomial random variable to be defined, we must know its two parameters: the total number of Bernoulli experiments -  $n$ , and the probability of occurrence of the event (success) in each experiments -  $p$ . In short, The binomial random variable  $X$  is defined as the occurrence of the event (s) in Bernoulli's experiments. The random variable of the binomial distribution is defined with the following formula:

$$X \rightarrow Bi(n, p) \tag{4}$$

The probability function of a binomial random variable determines what is the probability that in  $n$  Bernoulli's attempts will be  $k$  successful attempts.

$$P(X = k) = \binom{n}{k} p^k (1 - p)^{n-k}; \quad 0 \leq k \leq n \tag{5}$$

The following table (Table 2) shows the number of total calls that will be made in each time slot of the day, and also includes the probability of a successful call that we obtained from the analysed data.

Table 2: Determination of the number of succesful calls (Monday)

Interval	Calls	Success probab.	RV PD
00:00-05:59	0	0	0
06:00-08:59	22	0.74	14
09:00-11:59	179	0.44	67
12:00-14:59	114	0.46	43
15:00-17:59	38	0.53	17
18:00-23:59	2	0.30	1

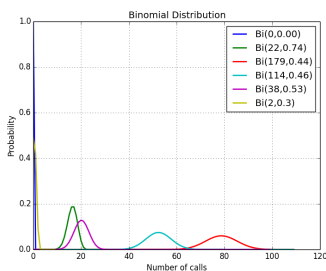


Fig. 2: Binomial Distribution Graph

HoneyPot draws random samples from the binomial distribution by using an inversion algorithm. To do so, it has to calculate the probability that  $P(X = x)$  for all values  $x$  from 0 through  $n$ . Then by using a pseudorandom number generator to generate samples uniformly from range 0 to 1, one can transform the calculated samples  $U[0, 1]$  into discrete numbers by using the probabilities calculated in the first step.

Another important parameter that is significant for real-time simulation of VoIP traffic is total call time. From the analyzed data it is clear that the average talk time is approximately 52.26 seconds. As discussed above, this time variable is also based on the exponential distribution.

$$EX = \frac{1}{\lambda}; \quad 52.26 = \frac{1}{\lambda}; \quad \lambda = 0.0019 \quad (6)$$

The chart of the resulting exponential distribution is shown in Figure 3.c.

The same procedure as the call length calculation is repeated for calculating the ring time before the call is answered. If we know that the average ring time is 10.042 seconds then  $\lambda$  parameter is:

$$X \rightarrow Exp\left(\frac{1}{10.042}\right) \Rightarrow Exp(0.099) \quad (7)$$

The resulting distribution function for ringtime is shown in the following figure (Figure 3.a).

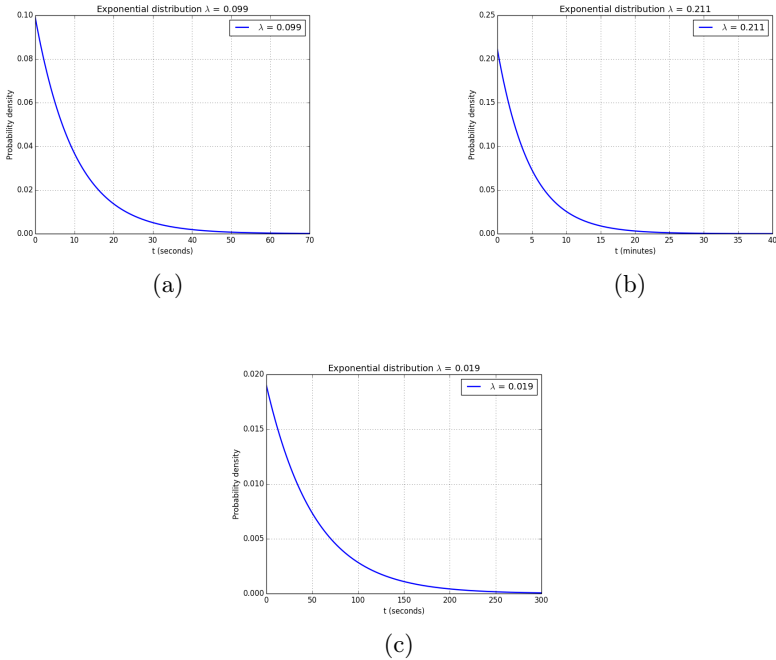


Fig. 3: Exponential Distribution PDFs.

Honeypot call rate value is controlled by the time they stay idle after individual SIP calls. Whenever honeypot  $n$  becomes idle (after registration or after hangup), there is a random value  $t_n$  sampled from an exponential distribution. Afterwards, a random call is placed at the end of this time value. However, during this inactive period, they can decide if they answer incoming calls from other participants connected to this VoIP honeypot distribution system.

To determine the time gap between every single INVITE call request, we need to calculate the average time gap between each call from our processed data. For example, if we know that between 15:00 and 18:00, 38 calls have to be made, then:

$$\overline{t_n} = \frac{t_{min}}{nc_H} \Rightarrow \frac{180}{38} = 4.737 \text{ min.} \tag{8}$$

From the graph (Figure 3.b), we can see that the time lags between each call will most likely gain values in the range from 0 to 20. The CDF calculation can verify the integrity of the statement:

$$P(X > t) = 1 - \epsilon^{-\lambda t} \Rightarrow 1 - \epsilon^{-0.211*20} = 0.014 \quad (9)$$

The result proved that the probability of the pause between individual calls being longer than 20 minutes is less than 2%.

After the time that honeypot was in an idle state, it decides to make a call by sending an INVITE request message to another participant connected to the honeypot network. The number to which the call is going to be realized is randomly selected from the list of online participants. Let  $c_n$  denote the callee that honeypot  $n$  is about to call. We determine  $c_n$  value from a categorical distribution.

$$c_n | P_n \propto \kappa(c_n; P_n) \quad (10)$$

such that  $P_n \propto \{P_n, 1, \dots, P_{n,N}\}$  is the normalized probability vector for honeypot  $n$ , where  $P_{n,m}$  is the probability that honeypot  $n$  calls other  $m$  honeypot. When the honeypot  $n$  randomly selects the callee, it sends INVITE request to start a conversation.

## 2 CONCLUSION

The article deals with an implementation of SIP traffic emulator using DTMC. The emulator is a part of our developed honeypot solution such that SIP traffic mutually generated by honeypots is able to attract more potential attackers and thus contribute to the creation of reputation databases of malicious sources. To implement such a honeypot we had to gather a lot of data from already deployed honeypots and also from real VoIP provider. To simulate SIP signaling and make it similar to real VoIP traffic, we defined call parameters by generating random variables using different types of statistical distributions such as Poisson, Exponential, Binomial, Geometric or Categorical.

## References

1. Lee, K., Caverlee, J., Webb, S. Uncovering social spammers: Social honeypots + machine learning (2010) SIGIR 2010 Proceedings - 33rd Annual International ACM SIGIR Conference on Research and Development in Information Retrieval, pp. 435-442.
2. Spitzner, L. Honeypots: Catching the insider threat (2003) Proceedings - Annual Computer Security Applications Conference, ACSAC, 2003-January, art. no. 1254322, pp. 170-179.
3. Kreibich, C., Crowcroft, J. Honeycomb - Creating intrusion detection signatures using honeypots (2004) Computer Communication Review, 34 (1), pp. 51-56.

# Development of LoRaWAN backend web application

Jakub Jalowiczor and Miroslav Vozňák

Department of Telecommunications, FEECS,  
VŠB – Technical University of Ostrava, 17. listopadu 15,  
708 33 Ostrava – Poruba, Czech Republic  
jakub.jalowiczor@vsb.cz

**Abstract.** The significant expansion of the Internet of Things (IoT) field and unique requirements of the IoT devices bring new technologies created exclusively to provide wireless connectivity for the IoT devices. Among many technologies suitable for building Low-Power WAN IoT networks, we can find LoRaWAN specification using a spread spectrum modulation technique LoRa (Long Range). Unlike some other LPWANs, the LoRaWAN is an open standard, and it allows us to build private networks. The paper deals with the development of a web application that serves as a backend for registration of end-devices to the LoRaWAN, and it provides access to the history of all uplink messages transmitted by end-devices and received by the network.

**Keywords:** LPWAN, LoRa, LoRaWAN, Internet of Things, MQTT protocol, The Things Network

## 1 Introduction

Nowadays, the Internet of Things (IoT) area is becoming increasingly popular. Considerable popularity of this area is due to the new technologies and market trends that allow interconnection of more devices, which can be smaller, simpler and less expensive at the same time[1]. Thanks to this expansion of the IoT field and unique requirements of the IoT devices, new technologies created exclusively to provide wireless connectivity for the IoT devices are developed. These technologies aim at achieving as low energy consumption as possible while maintaining a certain quality of transmission. Low-Power Wide-Area Network (LPWAN) technologies have common features to enable long-distance wireless communication with the lowest power consumption. LPWAN technologies are primarily designed to transfer a small amount of data at once. This type of networks include LoRa (Long Range) technology.

The paper is structured as follows: firstly, we briefly describe LoRa technology in the introductory part, the second section provides an overview of the network architecture. The section number three includes an explanation of The Things Network service and MQTT protocol together with a description of their usage in the solution. Explanation of the implemented KoIoT backend application, which is important for the end-users to retrieve the data sent to the LoRaWAN

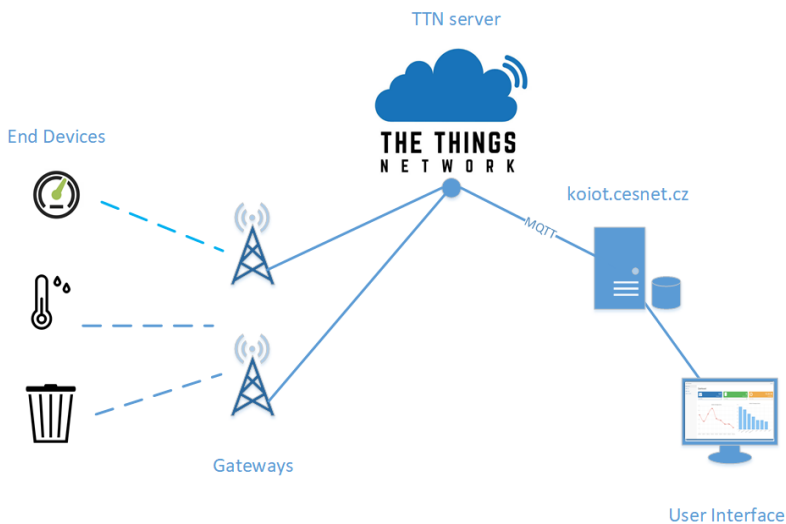


network, is presented in the section number four. The fifth section describes possible improvements. Finally, the sixth section summarizes our conclusions.

LoRa is a wireless modulation intended to ensure long-range low-power low-data-rate communication. The LoRa modulation has been patented by Semtech Corporation. The LoRa modulation is based on Chirp Spread Spectrum modulation, which is used in the military and for space communication, but LoRa is the first implementation for commercial usage. LoRaWAN defines communication protocol and system architecture for the network, while the physical layer LoRa provides a communication link. The LoRaWAN is an open standard, and it allows us to build private networks[2]. For comparison, another LPWAN technology called Sigfox[3] is managed by a network operator.

## 2 Network architecture

The network architecture consists of end-devices, gateways, The Things Network server, the KoIoT server and web application for end-users. The end-devices are different types of sensors that are capable of sensing specific variables of an external environment. LoRaWAN gateways serve as a bridge between wireless and wired part of the network. Each gateway is connected via Ethernet cable with the Internet to provide connection to The Things Network server, which is one of the main parts of the solution. Another main part is the KoIoT server, which is under our full management. It is intended to store data and serves as a backend web interface for end-users. The schematic representation of the architecture can be seen in Fig. 1.



**Fig. 1.** Diagram of the infrastructure

### 3 The Things Network and MQTT broker

The section deals with a description of used technologies and components, particularly The Things Network (TTN) and Message Queue Telemetry Transport (MQTT).

#### 3.1 The Things Network

TTN community deals with building a global open crowd-sourced Internet of Things data network using LoRaWAN. The network coverage is ensured by community members who can run their gateways. The advantage of this solution is that all gateways are free to use for every member of the community. In this manner, it creates extensive data connectivity, and therefore sensors can communicate with cities and businesses.

TTN provides MQTT broker for devices to allow them publishing, sending activation and messages. With the usage of a bridge, all information can be forwarded to a broker, which is running on the KoIoT server. This solution does not allow to register or unregister devices remotely, and therefore our solution uses application programming interfaces (API), built on a combination of protocols MQTT and HTTP, to streamline internal operations. The Things Network API brings developers a way to integrate their application with TTN. The Handler's Application Manager API allows managing applications and devices registered to TTN. This API contains several methods for different purposes. The API offers methods, which can do the following actions - registering, deleting, setting and getting of a new application or device[4].

#### 3.2 MQTT broker

MQTT is a messaging protocol designed to be standard for communication such as Machine-To-Machine (M2M). The basic methods of MQTT protocol are publish and subscribe, and these are used for high-efficiency communication in the IoT as the transition of messages implementation is flexible and simple. MQTT is built on top of the TCP protocol, and for the message delivery, four levels of Quality of Service (QoS) are defined. The QoS levels are an important feature on unreliable networks transferring critical information. MQTT consists of three components - subscriber, publisher, and broker. The subscriber can register for specific topics in order to receive messages by the broker when the publisher publish into topics of interest. The publisher has the function of a data sender. The broker has the role of a server because the clients (subscribers and publishers) do not communicate directly, but each message is forwarded by the broker. In this manner, the broker can handle security by checking authorization of the publishers and the subscribes[5,6].

There is plenty of software solutions for the MQTT broker, but in this solution, the Eclipse Mosquitto broker is used, and it runs on the KoIoT server, where access control list auth plugin is implemented. This plugin performs authentication through username and password, which are encrypted and stored in the PostgreSQL database on the server.

## 4 KoIoT server

Since a larger number of users use our solution of the LoRaWAN network, there must be a way to divide individual users in the system. TTN solution does not offer functionality to separate different users within one application and in this way authorization cannot be provided. Each user would have to use a specific application, which would be restrictive or even impossible for us as a network provider to manage the service in this way, as we could not have control under the devices. For this purpose, TTN is supplemented by the KoIoT server, where users can create their accounts with access only to their devices. Another reason for the KoIoT server is to offer insight into the history of all messages received for a given user, which is not supported by TTN server. TTN server allows only a few received messages to be displayed, which are deleted after a certain time elapsed.

The KoIoT server is created with the Java Spring Framework. This framework is divided into modules, and therefore the developer can choose which modules are needed. For KoIoT server, a combination of Spring Web model-view-controller (MVC), Java Spring Boot and Spring Security is used. These are deployed to create a standalone web application with embedded Tomcat, Jetty or Undertow and with comprehensive and extensible support for authentication and authorization[7].

For the registered end-users, the KoIoT backend web application serves for registration of new devices into the campus LoRaWAN network, for their managing, for access to the history of all uplink messages received by LoRaWAN network and for deleting of the previously registered device with subsequent cancellation of the registration from TTN. If a user is not registered, the only accessible pages are the page for registration into the KoIoT and the page for login to the KoIoT system. After registration and email confirmation, the user can log in and then the dashboard is shown. This dashboard provides a quick overview of interesting information, such as the number of user devices or the number of all messages received by LoRaWAN network, as well as graphs with information regarding a number of messages per device or per day. The KoIoT server provides web form for registering a new device. All devices owned by one user are shown in the table on a dedicated web page. The messages can be displayed separately for one device or together for all devices. One user can access only to devices that the user previously registered. The same is valid for messages - one user can access only to messages sent from the devices that are owned by the user. In this way, our solution can provide authorized access. The KoIoT user-interface can be seen on Fig. 2.

As mentioned above, the combination of MQTT and HTTP API is used. The HTTP API applies standard HTTP methods as POST and DELETE with proper JSON data-interchange format in the body to manage individual devices registered in TTN. Depending on the user's choice, different HTTP methods with different body content are applied. Because this HTTP API cannot be used to retrieve received messages, MQTT has to be deployed. Each message received by LoRaWAN gateway is forwarded to TTN from where the message

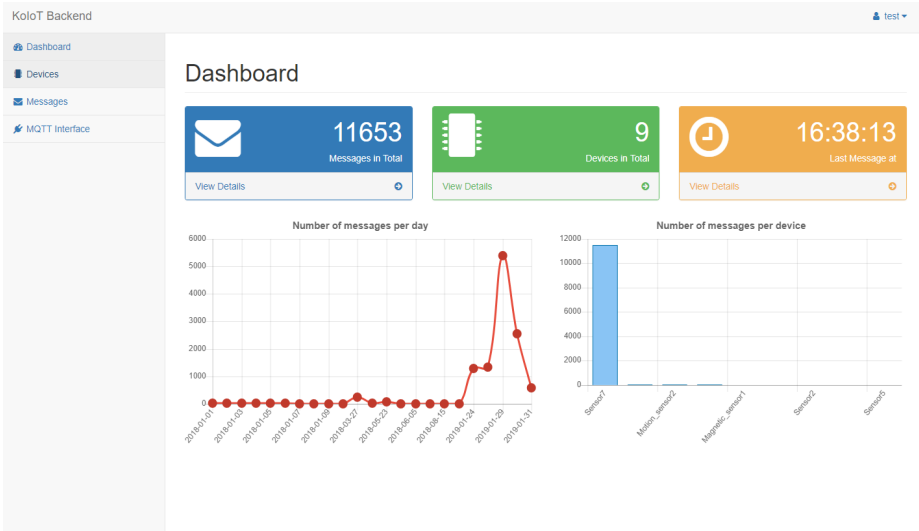


Fig. 2. Dashboard of the KoIoT backend web application

is published to MQTT Mosquitto Broker. Immediately after the MQTT Broker receives such a message, the message is inserted into the main database. The data inside this database are selected and showed to the KoIoT user depending on his queries.

## 5 Possible improvement

At this moment, the KoIoT server supports only the Over-the-Air Activation method of end-device activation. The activation is required in order to participate in a LoRaWAN network. In the Activation by Personalization (ABP) method, the end-device does not have DevEUI, AppEUI, and AppKey, which are necessary for another method of activation called OTAA to negotiate the session keys (NwkSkey and AppSkey). As a substitute, both session keys required for communication are pre-stored on the end-device. Thus no communication is needed to join the network. The ABP is less safe activation method as an end-device must use the same session keys throughout its lifetime, but the power consumption is lower[8,9].

## 6 Conclusions

The paper presents the network architecture and describes important parts of the infrastructure such as TTN, MQTT broker and the KoIoT server that serves as a web interface for end-users of the network.

As a future work, we would like to add missing integration of Activation by Personalization (ABP) end-device activation method.

## 7 Publications

Jalowiczor, J., Gresak, E., Rezac, F., Rozhon, J., Safarik, J., Dudzik, M.C., Ricklin, J.C.: Development and deployment of the main parts of LoRaWAN private network. *Autonomous Systems: Sensors, Processing, and Security for Vehicles and Infrastructure* 2019. 2- (2019).

## References

1. Rose, K., Eldridge, S., Chapin, L.: *The Internet Of Things: An Overview*. The Internet Society (2015)
2. LoRa Alliance: *LoRaWAN 1.1 Specification*. LoRa Alliance (2017)
3. Jalowiczor, J., Voznak, M.: Proposal and Implementation of Probe for Sigfox Technology. In: *AETA 2018 - Recent Advances in Electrical Engineering and Related Sciences: Theory and Application*. pp. 420-428. Springer International Publishing, Cham (2020)
4. The Things Network: *Application Manager API*. "The Things Network, <https://www.thethingsnetwork.org/docs/applications/manager/>"
5. Al-Fuqaha, A., Guizani, M., Mohammadi, M., Aledhari, M., Ayyash, M.: *Internet of Things: A Survey on Enabling Technologies, Protocols, and Applications*. 17, 2347-2376 (2015)
6. Katsikeas, S., Fysarakis, K., Miaoudakis, A., Van Bemten, A., Askoxylakis, I., Pappaefstathiou, I., Plemenos, A.: *2017 IEEE Symposium on Computers and Communications (ISCC)*. 1193-1200 (2017)
7. Spring: *Spring Boot*. Spring, <https://spring.io/projects/spring-boot>
8. Toussaint, J., El Rachkidy, N., Guitton, A.: *Performance analysis of the on-the-air activation in LoRaWAN*. *2016 IEEE 7th Annual Information Technology, Electronics and Mobile Communication Conference (IEMCON)*. 1-7 (2016)
9. Kim, J., Song, J.S.: *A Dual Key-Based Activation Scheme for Secure LoRaWAN*. *Wireless Communications and Mobile Computing*. 2017, 1-12 (2017)

# Influence of dry ice on a modulated optical beam on the basis of SDR for an FSO system

Jan Látal, Jakub Kolář, Jan Vitásek, and Lukáš Hájek

Department of Telecommunications, FEECS,  
VŠB – Technical University of Ostrava, 17. listopadu 15,  
708 33 Ostrava – Poruba, Czech Republic  
jan.latal@vsb.cz

**Abstract:** Basic atmospheric phenomena (mainly fog) influencing the optical beams, which was generated by a laser diode at a wavelength of 650 nm, will be introduced in this article. Also, the possibilities of the Software Defined Radio utilization, which can create different types of modulation (M-QAM, M-PSK) and can be used for evaluation of the influences of artificial atmospheric effect on the modulated optical beam in the acrylate box, will be presented. As an evaluative parameter, MER was chosen. The value of MER was changing depending on the concentration of CO<sub>2</sub>.

**Keywords:** FSO, fog, MER, modelling, modulation, scattering.

## 1 INTRODUCTION

Optical Wireless Communications (OWC) systems have become a new type of telecommunication networks in recent years. The OWC are not regulated by any national regulator of Radiofrequency (RF) spectrum and provide high bandwidth. This makes the OWC an attractive transmission tool for telecommunication operators. The unlicensed bands of OWC are very advantageous; nevertheless, there are problems with the transmission environment, which is the atmosphere. The atmosphere causes several problems in the form of plenty of physical phenomena which affect the optical beam. The atmosphere is a chaotic and unpredictable environment with dynamic changes. Many negative effects are in the atmosphere. Aerosols in the atmosphere cause the scattering of light, which happens on their particles. The scattering is described according to the Mie linear scattering which appears on particles comparable to the wavelength of light. These effects degrade the optical power or the beam shape. The fog, mist, turbulence and other atmospheric phenomena can affect the FSO link [1-3]. Modern methods of switching between FSO and RF are using for reliability and immunity improvement. Hybrid FSO/RF link has much better reliability and immunity against atmospheric effects [4-7]. In this article, the author's team focused on the effect of the simulated atmospheric phenomenon, which was a carbon dioxide fog, on the modulated optical beam Phase-Shift Keying or Quadrature Amplitude Modulation (PSK and QAM) with respect to the communication parameter Modulation Error Ratio (MER).

## 2 MEASUREMENT OF FOG EFFECT ON FSO LINK

We used the measuring (acrylate) box for our fog measurement experiment with the modulated FSO link in the laboratory. This acrylate box has a length of 2.5m and 0.5m in height and 0.5m in width. The box is used for stable conditions during experimental measurements. The carbon dioxide generated artificial fog.



**Fig. 1.** Measurement of fog influence on FSO link.

Subsequently, the acrylate box was placed on an iron mounting in front of it; the holder of the laser diode was installed on an aluminum structure, with the laser diode shooting at a right angle through the front of the measurement box. To ensure thermal and current stabilization of the laser diode (LD) on the transmission side, a Thorlabs set was used (TDC205C – setting regular part of the stream, TED200C – setting operating temperature, TLCLDM9 – holder of the laser diode with input for modulating voltage). One type of light source with a wavelength of 650 nm (types 650543A) was used. The LD 650 nm the output power was 5 mW. To generate the PRBS (pseudo-random bit sequenced) signal, a USRP NI 2920 was used: its output was linked to the LD and could change the size of the modulation voltage for the laser diode. Modulation of the laser diode was achieved using the RF input on the holder TCMLD9, which was driven by the current and thermal controller. The laser diode was placed inside laser driver TCMLD9, where circuit Bias-T is placed. This circuit allows bringing together the DC component from the current driver and modulation signal from RF input. This laser driver is also stabilized by temperature driver. To the RF input that was supplied by an SMA connector with an impedance ending of about 50  $\Omega$ , the modulating signal with a frequency up to 50 MHz could be added and the sample rate is 500 kHz, number of symbols was set to 500, any shaping filter was not used and the gain of the signal was set to 0 dB. This signal directly modulated the laser diode installed in front of the holder (TLCLDM9) equipped with a collimator (type marking A220TM-B) to focus the optical beam. The fog generator fueled the fog into the acrylate box. The optical beams went through the box. On the receiver side, there was a photodetector InGaAs Fixed Gain Detector PDA10CF-EC. The photodetector bandwidth was 150 MHz. The affected laser beam was converted back to an electrical signal by stimulating a photodetector and then was demodulated in the second device (USRP NI 2920). A computer connected to the controlled device (USRP NI 2920) provided the reading of the changes in the symbol speed or modulation format and qualitative parameter MER.

## 2.1 Sublimation of solid carbon dioxide

Dry ice is a solid phase of carbon dioxide, which emerges from desublimation during cooling under  $-78.5\text{ }^{\circ}\text{C}$ . Dropping the solid carbon dioxide in hot water causes rapid sublimation of the solid carbon dioxide and very concentrated carbon dioxide ( $\text{CO}_2$ ) gas is generated. The  $\text{CO}_2$  is heavier than air and sticks to the bottom of the box. The concentration gradually and spontaneously decreases with increasing time. The sublimation of solid carbon dioxide at different levels could be considered as certain kinds of smog ( $\text{CO}_2$  is an element of the smog). As many metropolitan cities in the world are burdened by smog pollution, this research could potentially contribute to a better understanding of optical communications in metropolitan areas.

## 3 The measurement procedure

Dry ice was used for fog simulation. The advantage is that there is not any melting process; the dry ice changes its state from solid to gas directly. This process is called sublimation. The measurement procedure was as follows. The same amount of dry ice (150 ml) was taken into the container by the gauge, then the dry ice was poured by 500 ml of hot water and a sublimation process happened. The created fog is cold; therefore it lies at the bottom of the box. Therefore, after the sublimation, the fan blew the fog over all box and measurements were started. The created fog caused zero visibility, therefore the MER parameter decreased to zero. Subsequent fog decay caused an increasing of MER values and the time was measured for each modulation in which the MER reached the original maximum value. The fog generation process is depicted in Fig. 2. The left is a sublimated fog that lies at the bottom of the box. The fog blowing is in the middle figure and the fog is blown on the right. Dry ice is a solid form of carbon dioxide ( $\text{CO}_2$ ).



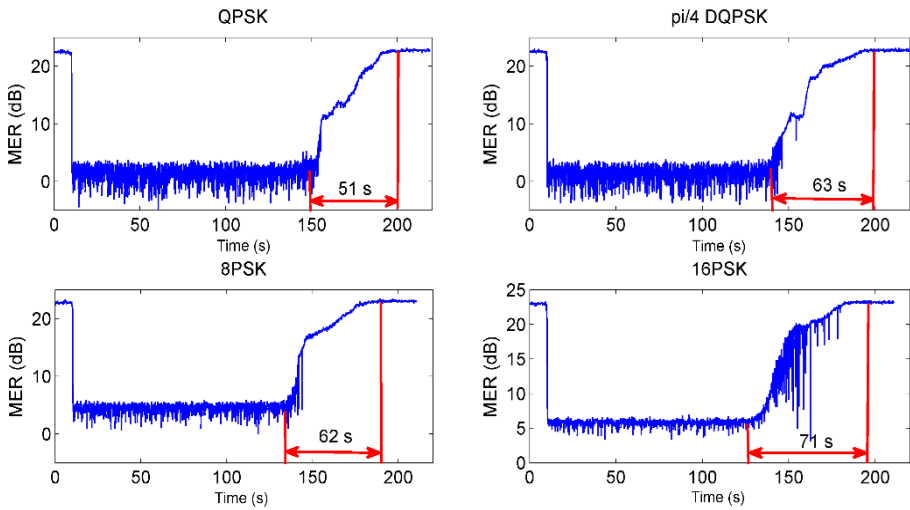
**Fig. 2.** The creation process of fog by sublimation of the dry ice (carbon dioxide  $\text{CO}_2$  gas).

As mentioned above, the time records of the MER parameter were recorded during the fog decay. The time, in which the MER returned to the original value, was determined from these waveforms. Each modulation was measured three times.



### 3.1 PSK modulation

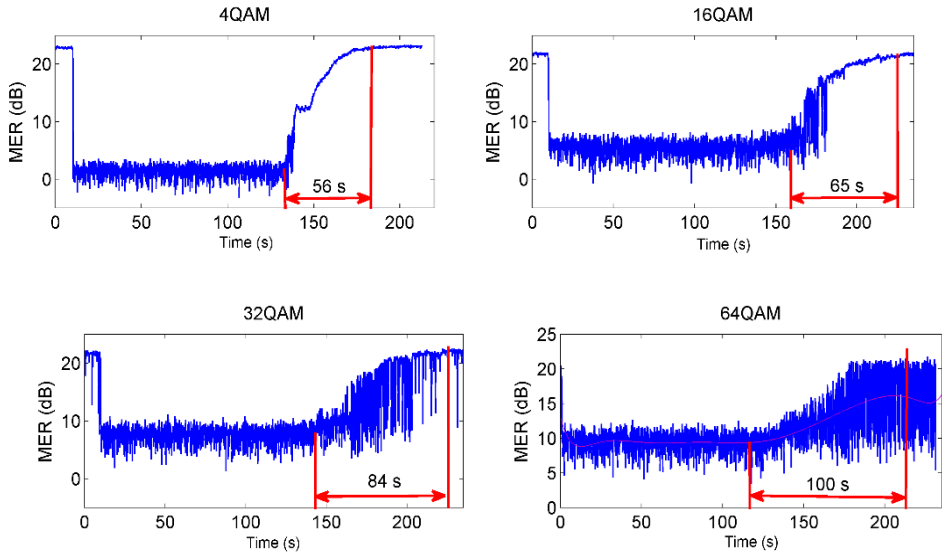
The time waveforms of PSK modulations are shown in Fig. 3. It is obvious that the individual waveforms are similar. Only in case 16PSK modulation, oscillations occurred with increasing of values. From  $\pi/4$  DQPSK, we can see a strong increase of rising time from minimal to maximal MER values for a given type of modulation. The  $\pi/4$  DQPSK has two advantages - the information is represented as the phase change, it allows an incoherent reception. In addition, it limits the effect of parasitic amplitude modulation. For the other 8PSK and 16PSK modulations, similar or longer delays of the MER transition state occur from the minimal to the maximal level.



**Fig. 3.** Time waveforms of PSK modulations by fog effect from the sublimation of dry ice (carbon dioxide CO<sub>2</sub> gas).

### 3.2 QAM modulation

The times to reach the original MER value are shown in Fig. 4 for QAM modulation with a different number of states. The MER values oscillated by modulations 16QAM and higher during fog decay, whereas the 4QAM modulation had a smooth rise until the MER reached the maximum level, respectively the original value. It is obvious that more complex QAM modulation formats are more demanding and the number of symbols has a major effect on the faultless communication behaviour through the MER parameter. For fibreless systems using QAM modulation, it is therefore necessary to provide additional RF connection, which in the case of strong fog would be able to switch to lower RF frequencies to prevent loss of communication or complete failure of the connection.



**Fig. 4.** Time waveforms of QAM modulations by fog effect from the sublimation of dry ice (carbon dioxide  $\text{CO}_2$  gas).

## 4 CONCLUSIONS

During the research of dry ice (carbon dioxide  $\text{CO}_2$  gas) behavior towards the FSO was shown, that the modulation formats of a more complex character such as QAM or multi-symbol modulations compensated very poorly the effect of generated fog in the box. However, it has to be said that nowadays the RF link is usually installed additionally to the FSO connections. The RF link is intended to increase the reliability of the FSO connection and, at the same time, acts as an additional communication source in case that the FSO connection degrades.

### Acknowledgement.

The research described in this article could be carried out thanks to the active support of the projects no. VI20172019071, CZ.1.07/2.3.00/20.0217.

### References.

1. R. Ramirez-Iniguez, S. M. Idrus, Z. Sun. *Optical wireless communications: IR for wireless connectivity*. CRC Press, Boca Raton (2008).
2. A. K. Majumdar, J. C. Ricklin, eds. *Free-space laser communications: principles and advances. Vol. 2*. Springer Science & Business Media, Berlin (2010).
3. F. Nadeem, V. Kvicera, M. S. Awan, E. Leitgeb, S. S. Muhammad, G. Kandus, *IEEE Journal on Selected Areas in Communications* 27, 1687–1697 (2009).
4. M. A. Esmail, H. Fathallah, M. S. Alouini, *IEEE Photonics Journal* 9, 1-12 (2017).
5. E. Leitgeb, H. Ivanov, T. Plank, P. Pezzeri, C. Pock, In *Proceedings of International Conference on Transparent Optical Networks (ICTON) '19*, Girona, Spain, 1-4 (2017).

6. B. Kebapci, F. Miramirkhani, H. Nouri, M. Uysal, In *Proceedings of International Conference on Transparent Optical Networks (ICTON) '19*, Girona, Spain, 1-5 (2017).
7. M. Ijaz, Z. Ghassemlooy, J. Pesek, O. Fiser, H. L. Minh, E. Bentley, *Journal of Lightwave Technology* 31, 1720–1726 (2013).

# Micro-bending sensor made from polydimethylsiloxane

Martin Novák

Department of Telecommunications, FEECS,  
VŠB – Technical University of Ostrava, 17. listopadu 15,  
708 33 Ostrava – Poruba, Czech Republic  
martin.novak.st@vsb.cz

**Abstract.** The paper describes the procedure for the production of micro-bending sensors from polydimethylsiloxane and their functionality based on attenuation behavior. I made three variations of sensors with a different number of deformation elements and tested their measuring ranges. One sensor was also tested in practice as a walking detector.

**Keywords:** Polydimethylsiloxane, PDMS, sensor, micro-bending, walking detector

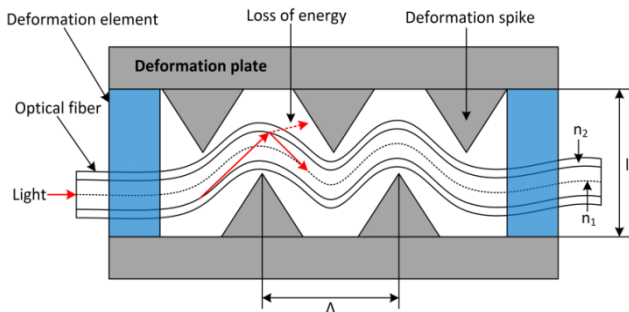
## 1 Introduction

Polydimethylsiloxane (PDMS) has several key properties. The first important feature of PDMS is the thermal resistance of the material. In the literature, a temperature of 350 ° C is given in the short term and 200 ° C in the long term. The second interesting feature is optical transmission (up to 93%), which makes it possible to use material for light-guide applications, imaging systems and sensor assemblies. Other important features of PDMS include resistance to various chemicals, acids, UV radiation and radiation. The essential feature for my application is the mechanical resistance of the material, especially the flexibility and small memory effect is very important for the proper functioning of the micro-motion sensors. [1]

## 2 Methods

Micro-bending sensors belong to the group of amplitude fiber sensors, by means of which it is possible to measure various physical quantities, typically pressure or temperature. At the point of the physical magnitude, the condition of total reflection on the core-shell interface is violated, as light (beam) strikes the core-shell interface at a different angle when the optical fiber geometry changes. There will be a decrease in the light energy (optical power) and thus increase the fiber attenuation. Figure 1 shows a typical arrangement of an optical fiber micro-bending sensor. In practice, multimode optical fibers with a core diameter of 50  $\mu\text{m}$  or 62.5  $\mu\text{m}$  are used in most cases. The micro-bending sensor consists of two opposing deformation plates on

which the deformation tips are placed. Two deformation elements are placed between these deformation plates, which are compressed under the effect of the physical quantity. The deformation tips will then deform the optical fiber that is placed between the spikes. [2]



**Fig. 1.** Typical arrangement of micro-bending sensor

The maximum losses in an optic cable occur if the wave number is equal to the difference in the wavenumbers of the conducted modes and radiated modes.

$$\beta - \beta' = \mp \frac{2\pi}{\Lambda} \tag{1}$$

where:  $\Lambda$  - period of micro-bending. [2]

There is a relationship to change the transfer of optical fiber depending on the change in the force  $\Delta F$  acting on the deformation plates

$$\Delta T = \left(\frac{\Delta T}{\Delta X}\right) \Delta F \left(K_f + \frac{A_s Y_s}{l_s}\right)^{-1} \tag{2}$$

where:  $\Delta X$  – change in the separation of the deformation boards,  $\Delta T/\Delta X$  - sensitivity,  $\Delta F$  - thickness,  $A_s$  – area of section,  $l_s$  - length of deformation element,  $Y_s$  – Youngs module of elasticity,  $K_f$  – the effective constant of elasticity of an optic cable. [2]

The effective constant of elasticity  $K_f$  is expressed

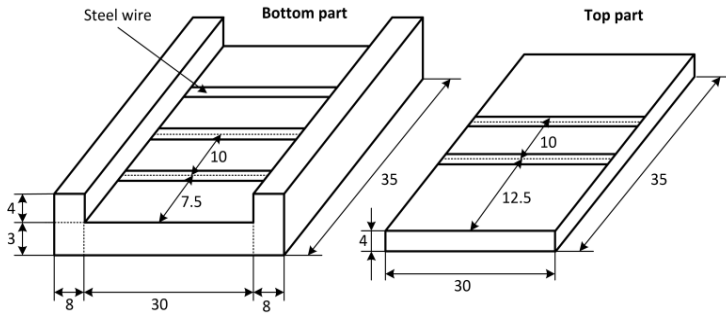
$$K_f^{-1} = \frac{\Lambda^3}{3\pi Y d^4 \eta} \tag{3}$$

where:  $Y$  – the effective Youngs module of electricity,  $d$  – the diameter of the optic fibre,  $\eta$  – number of diffractions. [2]

### 3 Experimental setup and measurement

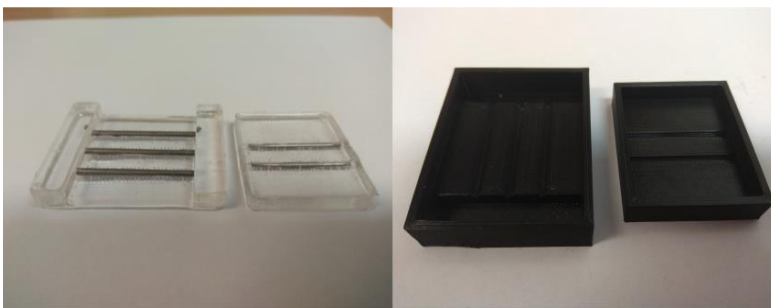
I chose the casting method for the production of micro-bending sensors, so I made three casting molds for 5, 11 and 15 deformation elements using a 3D printer. The

deformation element is, in this case, steel wire. From a safety point of view, this is the best variant of the deformation element from my point of view, because sharp points can damage the optical fiber in case of larger deformations. Figure 2 shows the sensor dimensions with 5 deformation elements. Other design variants are similar, only the sensor length changes.



**Fig. 2.** Dimensions of a micro-bending sensor with five steel wires

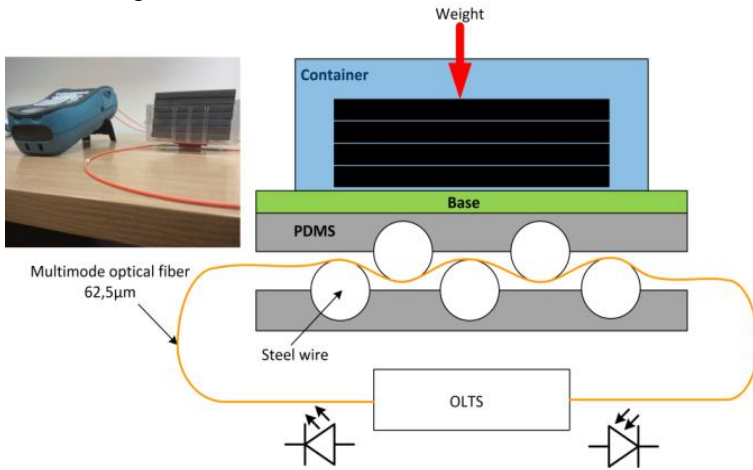
The surface of the casting mold was porous, so it was necessary to cover the mold with a thin layer of lubricant (eg oil) to prevent damage to the sensor. I inserted the 2 mm diameter deformation elements (steel wires) into the grooves in the casting mold and filled the mold with the prepared mixture of PDMS and curing agent. Here, the curing agent serves as a catalyst for starting the chemical reaction (PDMS curing process). The sample thus prepared was vulcanized for one hour in a temperature box at 70 ° C to accelerate the curing process. I repeated the whole procedure for other sensor variants. Figure 3 shows a casting mold printed on a 3D printer and a resultant sensor with five steel wires.



**Fig. 3.** A micro-bending sensor made from PDMS and a casting form

I inserted a multimode optical fiber with a core diameter of 62.5  $\mu\text{m}$  without secondary protection between the top and bottom of the sensor. I connected the first end of the optical fiber to the light source and the other to the photodetector (OLTS EXFO AXS 200/350). I placed the multimode optical fiber so that it passes through the center of the sensor. I placed a collecting container on the sensor into which I gradually

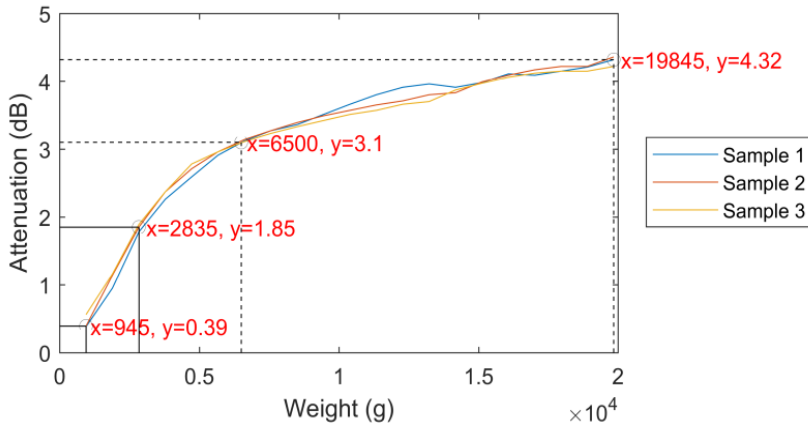
put the weights. Measurements were made at 850 nm. The complete measuring work-  
place is shown in Figure 4.



**Fig. 4.** Layout of the measuring work space

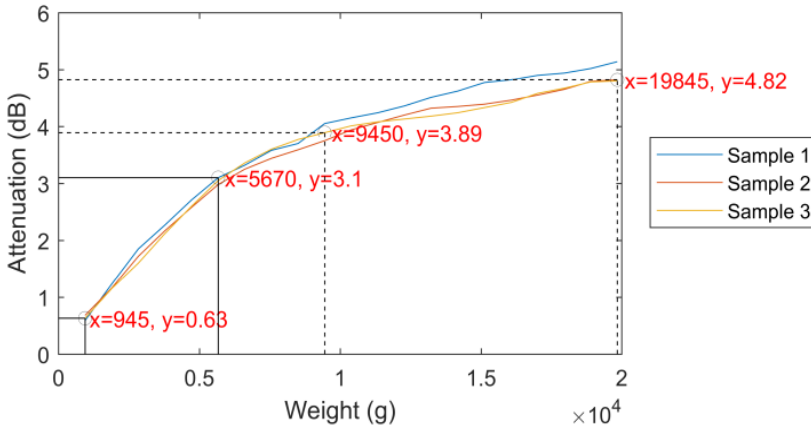
## 4 Results

For each design, I made three identical samples on which I performed attenuation measurements. The measuring ranges of the sensors and their coordinates are indicated in each graph. Figure 5 shows the measurement results for three micro-bending sensors with five steel wires.



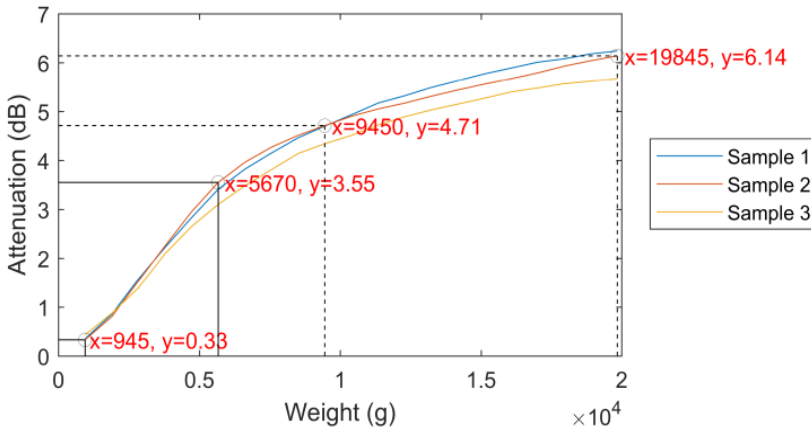
**Fig. 5.** Damping characteristics of micro-bending sensors with 5 steel wires

The plotted characteristics are very similar, so a very decent measurement repeatability is ensured. Sensor ranges are defined from 945-2835 g and 6500-19845 g (linear characteristic curve). Half of the optical power is lost at 5842 g.



**Fig. 6.** Damping characteristics of micro-bending sensors with 11 steel wires

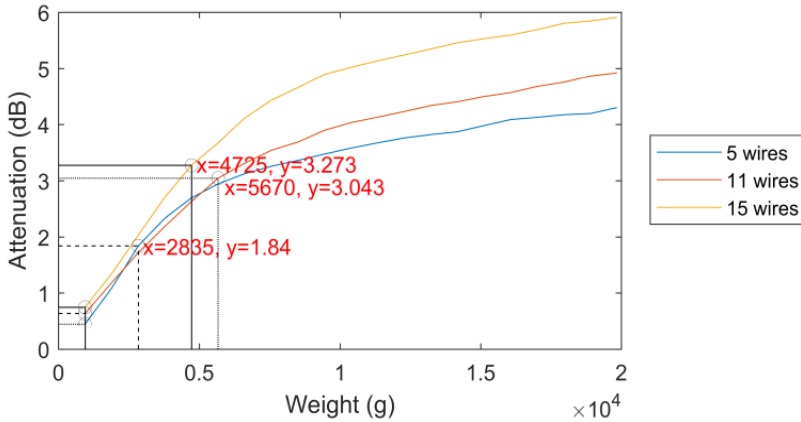
Figure 6 shows the attenuation characteristics for three micro-bending sensors with eleven steel wires. If we compare the results with the previous ones, we find that in the first measuring area there is a double increase of the range, while in the second area the decrease of the range by 2950g is seen. Half of the optical power is lost at 5481 g.



**Fig. 7.** Damping characteristics of micro-bending sensors with 15 steel wires

Figure 7 shows the attenuation characteristics of fifteen steel wire sensors. With this sensor variant, the measuring range no longer increases, only the characteristic slope changes. Loss of half the power corresponds to a weight of 4965 g.





**Fig. 8.** Comparing the damping characteristics of micro-bending sensors

Figure 8 shows a comparison of the sensor variants, the data being obtained by averaging all measured values within each sensor variant. For clarity, only the first measuring areas of the sensors are indicated in the graph.

## 5 Conclusion

Tested sensors are functional over the entire range of measured values. Sensor testing indicates that sensor ranges can be controlled by the number of steel wires or optical fiber arrangement in the sensor. The number of wires (bends) also affects the slope of the characteristics, a big difference is seen especially between the three and eleven steel wires. By reducing the distance between the steel wires, it may be possible to control the overall sensor range. I also used a five-steel wire sensor to detect passing people in the lab. It turned out that the sensor captured with 100 % success all passing people weighing from 70 to 95 kg. The attenuation was in the range of 5-7 dB.

## 6 References

1. S. Torino, B. Corrado, M. Iodice, G. Coppola, "Pdms-based microfluidic devices for cell culture," *Inventions*, vol. 3, art. no. 65, 2018.
2. M. Y. Rofianingrum, B. Widiyatmoko, E. Kurniawan, D. Bayuwati, I. Afandi, "Fiber optic load sensor using microbend-deformer," *Journal of Physics: Conference Series*, vol. 1191, art. no. 012007, 2019.

# Non-invasive heart rate sensor for magnetically interfered environments

Stanislav Žabka

Department of Telecommunications, FEECS,  
VŠB – Technical University of Ostrava, 17. listopadu 15,  
708 33 Ostrava – Poruba, Czech Republic  
stanislav.zabka@vsb.cz

**Abstract.** This article deals with the theme of the biomedical fiber-optic sensor as a sensor of the heart rate of the human body. The sensor is based on the Bragg grating structure. The basic advantage of the presented sensor against the conventional electrocardiography (ECG) sensors is the possibility of uses in the electromagnetically harsh environments (1.5 T and 3T). The presented article also summarizes the author's activities during three years of his study, his research and development activities related to the studies and research projects.

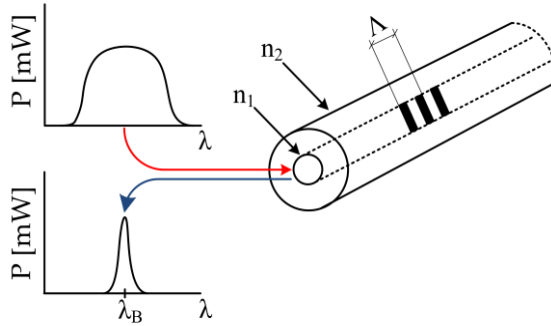
**Keywords:** optical fiber, sensors, heart rate, vital sign

## 1 Introduction

Allow me to introduce myself. My name is Mr. Stanislav Zabka. I am a doctoral student at the Faculty of Electrical Engineering and Computer Science at the Technical University of Ostrava. My education program is called Computer Science, Communication Technology and Applied Mathematics and field of study called Communication Technology. I am also working (part-time job) as Java developer in big software corporation and I am using these skills to achieve the best results when it comes to create software which handles and computes big data from sensors. In my third year of study I am extending my knowledge especially in the field of biomedical fiber-optic sensors. I am also part of five research projects. To the date 7/2019, I have a total of 15 accepted or published publications and 5 utility models.

## 2 About my project and dissertation work

During the first and second year of my study, I was to design a measurement scheme and forms for the creation of the fiber Bragg grating sensor [1] which can be used in the harsh magnetic resonance environments (1.5 T and 3 T). Schematic diagram of the Bragg grating sensor is shown in Figure 1.



**Fig. 1.** Schematic diagram of the Bragg grating sensor.

Parameter  $n_1$  denotes the refractive index of the core, parameter  $n_2$  the refractive index of the optical fiber sheath and  $\Lambda$  is the spatial period of the refractive index changes.

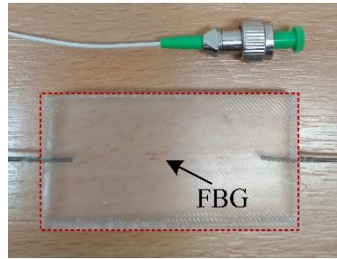
To implement the FBG sensor, I used a standard Bragg grating with polyimide recounting with a central Bragg wavelength of 1552.346 nm, a reflection spectrum width of 219 nm and a reflectance of 89 %. In laboratory environment, we tested the influence of encapsulation on the grating itself. The results show that encapsulation method has no effect on the optical and mechanical properties of the optical fiber grating. Sensitivity relations (1) to (2), as well as the central Bragg wavelength, the spectrum width, and reflectivity parameters, remain valid, which simplifies the design and manufacturing of the sensor. Also, there is a possibility of multiplexing of individual sensors for monitoring more patients when used for multiple MR scanners (one interrogation unit can be used).

$$\frac{1}{\lambda_B} \frac{\Delta\lambda_B}{\Delta\varepsilon} = 0,78 \cdot 10^{-6} \text{ } \mu\text{strain}^{-1}, \quad (1)$$

$$\frac{1}{\lambda_B} \frac{\Delta\lambda_B}{\Delta T} = 6,678 \cdot 10^{-6} \text{ } ^\circ\text{C}^{-1}, \quad (2)$$

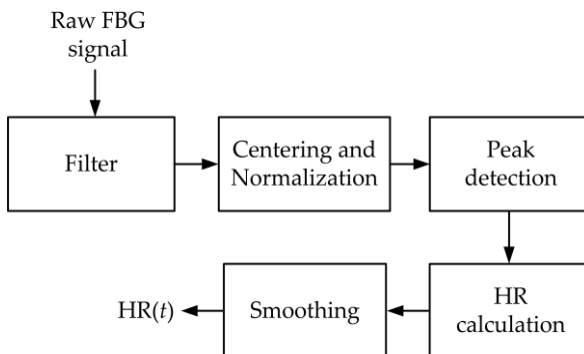
where  $\Delta\lambda_B$  is the changes in wavelength itself,  $k$  is the deformation coefficient,  $\varepsilon$  is the size of applied deformation,  $\alpha_\Lambda$  is the coefficient of applied thermal expansion,  $\alpha_n$  is the thermo-optic coefficient and  $\Delta T$  is the changes in temperature itself.

I have created a prototype of a measuring sensor which was tested in a real magnetic environment (3T MR scanner, Brno, CEITEC company) [2]. The sensor was created by the encapsulation of Bragg grating structure into polymer entitled polydimethylsiloxane (PDMS) [3]. This material is inert to the human body and also is inert to the electromagnetic interferences. For this reason, was this material chosen. Sensor dimensions are 30 mm length, 20 mm height and 5 mm width. Weight is 4 g. Real photo of the sensor is depicted in Figure 2.



**Fig. 2.** Real photo of the proposed FBG sensor.

The signal processing methodology is based on our previous research [3] and research [4-5]. Input raw signal from the FBG sensor represents the signal from the used FBG interrogator unit called FBGuard. The wavelength resolution of this instrument is 1  $\mu\text{m}$ , the output power is 1 mW and used sampling rate was 2 kHz. The resulted signal from the FBGuard is then filtered to remove any unwanted components formed by motion minor and major artifacts (movements of the human body like a moving of hands, legs, caught and etc.) and slow temperature drift by a third-order band-pass filter (a type of used filter was Butterworth). The cut-off frequencies of the filter were used 0.1 and 2 Hz. Another step includes centering, normalization, peak detection and final smoothing of the signal. Schematic diagram of the signal processing is shown in Figure 3.



**Fig. 3.** Schematic diagram of the signal processing.

Based on detection of the individual peaks (maxima), the respiratory rate (RR) is calculated according to the following formula (3):

$$RR = 60 / (t_n - t_{n-1}), \tag{3}$$

where  $t_n$  is the time mark of the  $n^{\text{th}}$  peak and  $t_{n-1}$  is the time mark of the previous peak.

The magnetic resonance environments are very problematic. It is necessary to design the measuring scheme correctly so that only the magnetically non-conductive materials are in the MR machine room.

For this reason, optical fibers with special protection, as well as special fasteners, have been used. Also, fibers had to exhibit very low attenuation (less than 0.2 dB/km). Evaluation unit with a computer and other necessary parts must be stored outside the MR room. All the measurements were processed online because doctors must have information about heart rate variability during the all measurement procedure. For this reason, I must propose a quick and robust software which was written in LabVIEW [6]. Measurement scheme is depicted in Figure 4.

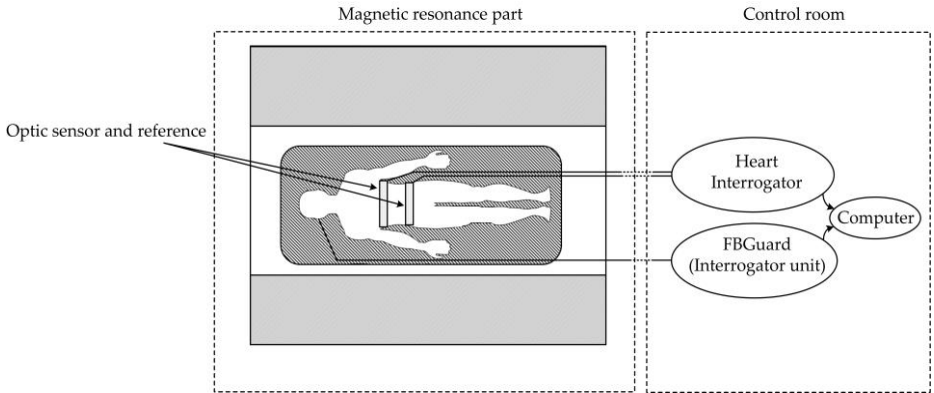


Fig. 4. Measurement scheme.

Figure 5 shows the real record obtained by the proposed FBG fiber-optic sensor in real MR 3T magnetic environment. Further, the curve obtained with a conventional ECG is shown. It is very easy to see that the ECG curve corresponds to a fiber-optic curve (number of maxims = number of heartbeats).

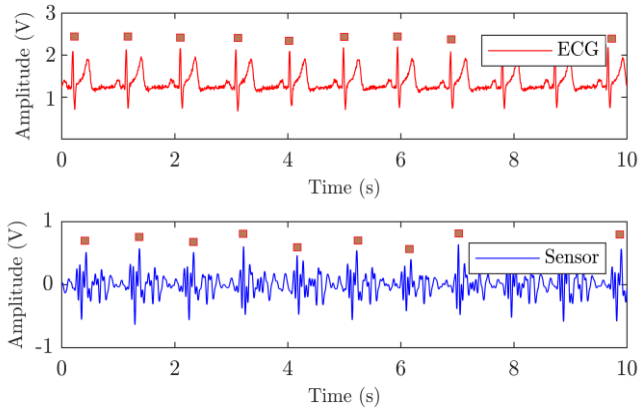


Fig. 5. Example of the course of heart rate (10s).

The key experimental results of heart rate measurements in the laboratory environment (six volunteers of both sexes) are summarized in Table 1. Data were compared by the objective medicine used the Bland-Altman method [7]. The

reproducibility is considered to be good if 95 % of the results lie within a  $\pm 1.96$  SD (Standard Deviation) range.

**Tab.1.** The key experimental results of heart rate measurements in the laboratory environment.

Subject	Rec. time (s)	HR	
		NoS sensor	Samples in $\pm 1.96$ SD (%)
Male1	725	812	<b>95.53</b>
Male2	545	640	<b>95.48</b>
Male3	695	889	<b>95.11</b>
Male4	525	668	<b>95.38</b>
Female1	485	755	<b>96.23</b>
Female5	535	621	<b>94.82</b>

Now we work on the very difficult but very interesting topic entitled cardiac triggering. We will try to use the proposed type of sensor to triggering the MR scanner. Actually, there is no presented study (Scopus and WoS databases), which demonstrated triggering the MR scanner by pure fiber-optic technology. Based on the consultation with doctors the possibility of retrospective/prospective filtration of cardiac artifacts arising during the measurement of functional MR and diffusion-weighted images (by the pure fiber-optic technology/sensors) can promise improvement of the output of these measurements, especially in the field of neurosurgery - refining the localization of functional brain centers, more accurate course of neural pathways, this may have a great future benefit in the treatment of brain tumors, but also, for example, in the treatment of epilepsy or mental illness.

### 3 Projects

As part of my studies, I was actively involved in solving 5 projects, namely:

1. Measuring the weight of trash bins, while being lifted by truck
2. SGS SP2017/79 - New types of photonic systems for IoT.
3. SGS SP2018/184 - Optical communication technologies and sensors.
4. SGS SP2019/80 - New Fiber Optic Technologies for Comm. and Sensors.
5. SGS SP2019/85 - Advanced Signal Processing Methods.

Now we prepare the project (ZETA Programme) to the Technology Agency of the Czech Republic (TA CR) which will focus on using fiber-optic technology in real MR environments with the cooperation of Faculty Hospital Ostrava (Assoc. prof. Dr. Petr Krupa, M.D. and Dr. Pavla Hanzlikova, M.D.).

## 4 Publications activities

From the date 9/2016 since to the date 9/2017, I have a total of 15 accepted or published papers and 5 utility models. Now we prepared a publication entitled "MR Fully-Compatible and Safe FBG Breathing Sensor: A Practical Solution for Respiratory Triggering". The paper is under review in journal IEEE ACCESS (Q1, IF 2018: 4.098).

## 5 Pedagogic part and other activities at the Department of Telecommunications

In the winter and summer semester, I was part of courses FYZ I and (Physics I) OK III (Optical communications III) as help for academic teachers.

## 6 Future work

Now I focus on the individual subjects of my Ph.D. studies. Also, I will be actively involved in above-mentioned projects and with my colleagues, in the near future we prepare a new article. Involving to the project (ZETA Programme) which will focus on using fiber-optic technology in real MR environments with the cooperation of Faculty Hospital Ostrava. Primary outputs of this project should be functional samples of MR-compatible FBG sensors.

## References

1. Dziuda, L., "Fiber-optic sensors for monitoring patient physiological parameters: A review of applicable technologies and relevance to use during magnetic resonance imaging procedures," (2015) *Journal of Biomedical Optics*, 20, pp. 010901.
2. Multimodal and Functional Imaging Laboratory, Brno, Czech republic, Central European Institute of Technology, (2019).
3. Nedoma, J., Fajkus, M., Martinek, R., Nazeran, H., "Vital Sign Monitoring and Cardiac Triggering at 1.5 Tesla: A Practical Solution by an MR-Ballistocardiography Fiber-Optic Sensor," (2019) *Sensors*, 19, pp. 470.
4. Dziuda, L., Skibniewski, F.W. "A new approach to ballistocardiographic measurements using fibre Bragg grating-based sensors," (2014) *Biocybern. Biomed. Eng.* 34, pp. 101-106.
5. Santelli, C., Nezafat, R., Goddu, B. "Respiratory bellows revisited for motion compensation: Preliminary experience for cardiovascular MR. *Magnetic Resonance in Medicine*," (2011), 65, pp. 1097-1102.
6. Elliott, C., Vijayakumar, V., Zink, W., Hansen, R., "National instruments LabVIEW: a programming environment for laboratory automation and measurement," (2007) *JALA: J. Assoc. Lab. Automation*, 12, pp. 17-24.
7. Bland, J.M., Altman, D.G. "Measuring agreement in method comparison studies," *Stat. Methods Med. Res.* (1999), 8, pp. 135-160.

# Study of neutron-rich nuclei within the Skyrme-Hartree-Fock Model and the Algebraic Collective Model

Mojgan Abolghasem and Petr Alexa

Department of Physics, FEECS,  
VŠB – Technical University of Ostrava, 17. listopadu 15,  
708 33 Ostrava – Poruba, Czech Republic  
{mojgan.abolghasem.st, petr.alex}@vsb.cz

**Abstract.** The present work resumes the study of nuclear shape and nuclear structure of neutron-rich nuclei in different mass regions obtained with the axial Skyrme-Hartree-Fock model+BCS and the algebraic collective model. In the chain of Te, Xe, Ba and Ce isotopes ground state deformations ( $\beta_2$  and  $\beta_3$ ) has been studied. For the chain of Ce and Nd isotopes the evolution of single-neutron and single-proton states around the Fermi level has been investigated. The structure of even-even xenon isotopes  $^{128,130}\text{Xe}$  has been studied to find whether they belong to  $O(5)$  or  $E(5)$  limits.

**Keywords:** atomic nuclei, nuclear models, deformation

## 1 Introduction

The study of neutron rich-nuclei constitutes one of the main topics in both experimental and theoretical nuclear structure research. New experimental radioactive beam facilities at ORNL, RIKEN or GANIL together with highly efficient arrays of HPGe detectors at neutron beam facilities (EXILL campaign at ILL) made this region accessible for spectroscopic studies [1–3].

Among the many methods used to study microscopic properties of nuclei the nuclear density functional theory (DFT) plays a central role [4, 5]. A very high quality description of nuclear properties in different mass regions can now be reached using the Skyrme-Hartree-Fock Model (SHF). This model provides the possibility to study the nuclear ground state properties and has the ability to describe the bulk properties of nuclei such as masses, radii or shapes. Since the method gives a good approximation of closed shell nuclei, for describing open shell nuclei the pairing correlations are essential. These effects are described by the BCS approximation [6].

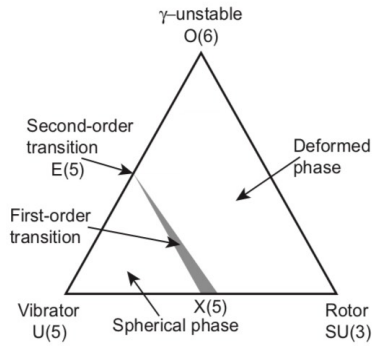
Our understanding of nuclear structure is considerably simplified due to a set of paradigms that are used as benchmarks describing idealized situations.

From a structural point of view, a spherical nucleus is one for which single-particle modes dominate while a deformed nucleus contains a strong collective component in its wave function. A spherical nucleus with a potential centered



at  $\beta = 0$  will possess an oscillator-like spectrum  $U(5)$  while a nucleus with a potential centered around a stiff, deformed  $\beta \neq 0$  minimum will have a rotor-like spectrum  $SU(3)$ .

In transitional nuclei, a given nuclear eigenstate may have a probability distribution spanning a range of different deformations. Different nuclear observables are sensitive to different aspects of the onset of deformation. For example, for the stiff oscillator, the energy of the first excited  $0^+$  is twice the energy of the first  $2^+$  state for small deformations and both energies are quite high. With increasing deformation the energy of the first  $2^+$  state (changing its nature from a vibrational to a rotational) decreases while the  $0^+$  state, retaining its vibrational character (evolving into a  $\beta$ -vibrational bandhead) increases its excitation energy.



**Fig. 1.** Analytical benchmarks in the Casten triangle.

An especially simple geometric description of nuclei near the critical point of the phase transition between spherical and deformed nucleus has been proposed by Iachello [7, 8]. The deformation potential is expected to be relatively flat in  $\beta$ , allowing the nucleus to assume either a spherical or a deformed shape with minimal energy penalty. Such a flat-bottomed potential can be approximated by an infinite square-well potential in the deformation variable  $\beta$ , termed  $E(5)$ , and describes a  $\gamma$ -soft transition. A square well with an additional stabilization in the  $\gamma$  degree of freedom termed  $X(5)$  is used for the description of axially-symmetric transitional nuclei. Thus, the  $E(5)$  and  $X(5)$  models provide analytical benchmarks for the interpretation of transitional nuclei as much as the structural limits described conveniently by the Casten triangle provide benchmarks for the interpretation of spherical or well-deformed nuclei (see Fig. 1).

Some aspects of the transition between spherical and deformed shapes can be also obtained using the algebraic collective model (ACM) [9] described in the next section.

## 2 Nuclear models

From the theoretical point of view the evolution of nuclear shapes and structural changes can be studied within algebraic models (e.g. ACM) or in a more fundamental microscopic approach (e.g. SHF+BCS model).

### 2.1 Skyrme density functional with BCS pairing

The Skyrme-Hartree-Fock model is the most widely used for investigations of nuclear ground state deformations. The Skyrme energy density functional (SDF)  $\mathcal{H}_{Sk}[J_d(\mathbf{r})]$  depends on a set of densities  $J_d(\mathbf{r})$  [4]. The Hartree-Fock (HF) Hamiltonian  $\hat{H}$  can be heuristically obtained by variation with up to first-order functional derivatives:

$$\hat{H} = \sum_i \varepsilon_i \hat{\alpha}_i^\dagger \hat{\alpha}_i = \sum_d \int \frac{\delta \mathcal{H}_{Sk}}{\delta J_d(\mathbf{r})} \hat{J}_d(\mathbf{r}) d\mathbf{r}, \quad (1)$$

where the single-quasiparticle energies  $\varepsilon_i$  are from HF+BCS.

There are plenty of SHF functional parameterizations available in the literature. We use a recent family of parameterizations derived from least-square fitting of its free parameters to a large pool of selected g.s. observables and other nuclear properties over the whole nuclear chart (incompressibility, symmetry energy, effective isoscalar and isovector masses) [10].

### 2.2 Algebraic collective model

The ACM, introduced as a computationally tractable version of the Bohr model [11] is characterized by a well defined algebraic structure [9]. We consider the ACM Hamiltonian of the form

$$\hat{H}(M, \alpha, \kappa, \chi) = \frac{-\nabla^2}{2M} + \frac{1}{2}M[(1 - 2\alpha)\beta^2 + \alpha\beta^4] - \chi\beta \cos 3\gamma + \kappa \cos^2 3\gamma, \quad (2)$$

where

$$\nabla^2 = \frac{1}{\beta^4} \frac{\partial}{\partial \beta} \beta^4 \frac{\partial}{\partial \beta} + \frac{1}{\beta^2} \hat{A} \quad (3)$$

is the Laplacian on the 5-dimensional collective model space and  $\hat{A}$  is the  $SO(5)$  angular momentum operator [12].

Such a Hamiltonian, expressed in terms of the quadrupole deformation parameters  $\beta$  and  $\gamma$  serves as a useful starting point for description of a wide range of nuclear collective spectra.

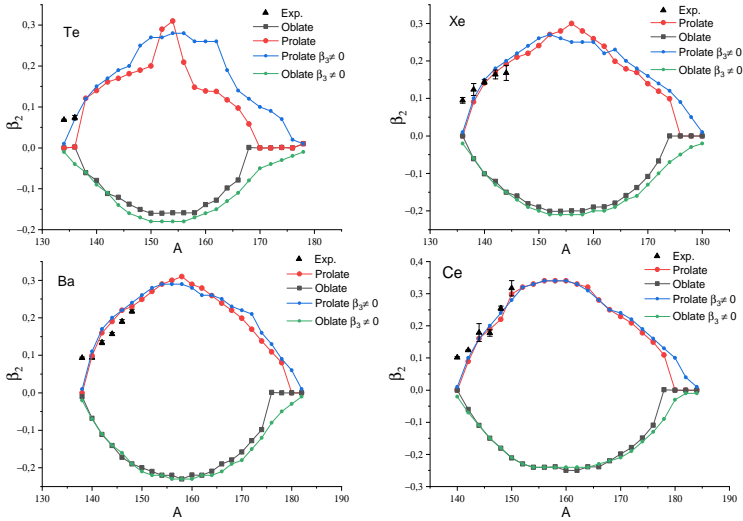
## 3 Results and conclusions

### 3.1 Evolution of nuclear shapes and structure in Te, Xe, Ba and Ce

The SHF+BCS model has been applied to chains of Te, Xe, Ba and Ce isotopes beyond  $N = 82$  to find their quadrupole and octupole deformations,  $\beta_2$  and

$\beta_3$  [13]. Among all tested Skyrme interaction parametrizations we confine that SV-sym34 fits the best experimental binding energies for these chains of isotopes.

All studied nuclei are characterized by prolate g.s. quadrupole deformation  $\beta_2$  for  $86 \leq N \leq 120$  with the exception of  $A > 156$  Te isotopes (see Fig. 2). Highest octupole deformations ( $\beta_3 > 0.08$ ) are predicted for  $^{144}\text{Ba}$ ,  $^{150}\text{Ba}$ ,  $^{148}\text{Ce}$ , and  $^{150}\text{Ce}$  for prolate shapes only. The potential energy curves (PEC) are rather flat in  $\beta_3$  thus resembling a phase-transition critical point and not a well-established octupole deformation.



**Fig. 2.** Comparison of calculated and experimental [14]  $\beta_2$  values with and without octupole deformation taken into account for the studied chains.

### 3.2 Single-particle levels in neutron-rich Ce and Nd isotopes isotopes

For selected Skyrme interaction parameterizations the evolution of single-neutron and single-proton states around the Fermi level along the two isotopic chains has been investigated and the results compared to existing experimental data from odd-Ce, odd-Pr, odd-Nd and odd-Pm nuclei [15].

Assignments of the experimentally observed levels in the studied region are mostly tentative and rather scarce [16]. The exceptions are  $^{153}\text{Pm}$  (4 assigned Nilsson configurations),  $^{153}\text{Nd}$  and  $^{155}\text{Pm}$  (2 assigned Nilsson configurations).

The parametrization SLy6 seems to fit best the g.s. spins and parities and assigned excited bandheads. Therefore, we recommend using the SLy6 parametrization for calculations of single-particle proton and neutron levels in odd- $A$  Ce, Pr, Nd and Pm isotopes.

### 3.3 Test of $E(5)$ symmetry in xenon isotopes

The main purpose of this study is to reexamine the basic properties of  $^{128}\text{Xe}$  and  $^{130}\text{Xe}$  within two different models, first within the ACM and subsequently within the SHF+BCS method, to shed more light on their closeness to the  $E(5)$  critical-point symmetry [17].

In order to identify a candidate for an  $E(5)$  transition in an isotopic chain it is important to specify a set of observables characteristic of  $E(5)$  behavior. A systematic search of the nuclear database for occurrence of experimental fingerprints of  $E(5)$  symmetry conducted by Clark and collaborators [18] pointed at the nucleus  $^{128}\text{Xe}$  as one of the possible realisations of this symmetry. The suggestion by Clark and collaborators for the critical point symmetry in  $^{128}\text{Xe}$  was mainly based on relative excitation energies, some absolute  $B(E2)$  decay strengths and the branching ratios of the  $0_2^+$  state and one branch from the  $0_3^+$  state. The  $B(E2)$  branching ratios further suggested that the crucial excited states were mixed in a two-level mixing scheme. However a necessity to improve the knowledge of absolute  $B(E2)$  values was pointed out to check for the consistency with the data.

For this purpose measurements of absolute  $E2$  decay strengths from both  $0_2^+$  and  $0_3^+$  states were reported in [19] in order to check qualitatively the assignments for the  $0^+$  states in  $^{128}\text{Xe}$ . The conclusion based on their analysis is that  $^{128}\text{Xe}$  lie between  $E(5)$  and  $O(5)$ , the main point of departure from  $E(5)$  being the decay pattern of the  $0^+$  states.

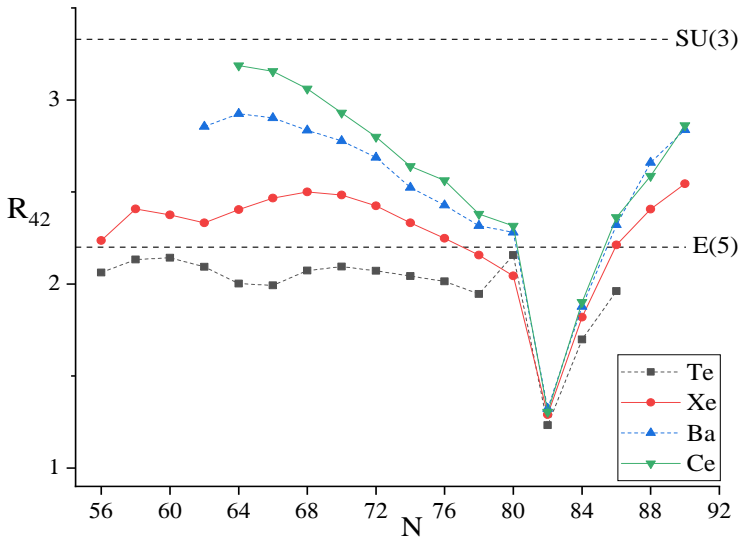
In Fig. 3 the evolution of the energy ratios  $R_{42} = E(4_1^+)/E(2_1^+)$  is shown for Te, Xe, Ba and Ce isotopic chains. We observe that for Xe isotopes far from neutron magic numbers  $N = 50$  and  $N = 82$   $R_{42}$  is fairly constant and close to a value of 2.4. Recall that in the  $O(6)$  limit  $R_{42} = 2.5$  while  $R_{42} = 2.20$  is expected for  $E(5)$ -like nuclei. One observes that the  $E(5)$ -like value of  $R_{42} = 2.20$  is best realized in Xe isotopes closer to the end of the major shell, i.e. near  $N = 78$  and at  $N = 86$ .

The ACM analysis of the  $^{128,130}\text{Xe}$  isotopes reveals that they are both characterized by very  $\gamma$ -soft potentials. Their experimental spectra contains a lot of characteristics typical for the  $E(5)$  transitional limit. Nevertheless there are also points of departure from the limit.

The main point of departure is the behavior of the first two excited  $0^+$  states, considered to be a robust test of the  $E(5)$  symmetry. We have shown that the data and our ACM calculations point towards an exchange of the role of those two states, the role of the first excited  $E(5)$   $0_2^+$  state being played by the observed  $0_3^+$  state.

On the other hand, the existence of the  $4_3^+$  state in  $^{128}\text{Xe}$  with the decay properties close to those expected in the  $E(5)$  limit favors the interpretation of  $^{128}\text{Xe}$  as a reasonable realisation of this critical-point symmetry.

The SHF+BCS calculations indicates that  $^{130}\text{Xe}$  might be closer to the  $E(5)$  limit, however the barrier height separating two almost symmetric prolate and oblate minima is still higher than one would expect for an  $E(5)$  nucleus.



**Fig. 3.** Experimental ratio  $R_{42}$  of the energy of the  $4_1^+$  state and the  $2_1^+$  state for isotopic chains of Te, Xe, Ba and Ce, compared to theoretical  $E(5)$  and  $SU(3)$  values.

### Acknowledgments

This work has been supported by SGS SP2018/84 and SP2019/26 projects.

### References

1. J.M. Allmond *et al.*, *Phys. Rev. Lett.* **118**, 092503 (2017).
2. B. Moon *et al.*, *Phys. Rev. C* **95**, 044322 (2017).
3. M. Jentschel *et al.*, *J. Instrum.* **12**, 11003 (2017).
4. M. Bender *et al.*, *Rev. Mod. Phys.* **75**, 121 (2003).
5. G.A. Lalazissis, P. Ring and D. Vretenar (eds.) *Extended Density Functionals in Nuclear Structure Physics*, Berlin, Springer (2004).
6. J. Suhonen, *From Nucleons to Nucleus*, Heidelberg, Springer (2007).
7. F. Iachello, *Phys. Rev. Lett.* **85**, 3580 (2000).
8. F. Iachello, *Phys. Rev. Lett.* **87**, 052502 (2001).
9. D.J. Rowe *et al.*, *Phys. Rev. C* **79**, 054304 (2009).
10. P. Klüpfel *et al.*, *Phys. Rev. C* **79**, 034310 (2009).
11. A. Bohr and B.R Mottelson, *Nuclear Structure II*, New York, Benjamin (1974).
12. D.J. Rowe and J.L. Wood, *Fundamentals of Nuclear Models: Foundational Models, Vol. 2*, Singapore, World Scientific (2010).
13. M. Abolghasem *et al.*, *Acta Phys. Polon. B* **50**, 555 (2019).
14. B. Pritychenko *et al.*, *Nucl. Data Sheets* **120**, 112 (2014).
15. M. Abolghasem *et al.*, submitted to *Acta Phys. Polon. B, Proceedings Supplement* (2019).
16. <http://www.nndc.bnl.gov/ensdf/>
17. M. Abolghasem *et al.*, submitted to *Phys. Scr.* (2019).
18. R.M. Clark *et al.*, *Phys. Rev. C* **69**, 064322 (2004).
19. L. Coquard *et al.*, *Phys. Rev. C* **80**, 061304(R) (2009).

# Bloch surface waves as a tool for refractive index sensing

M. Gryga, D. Ciprian and P. Hlubina

Department of Physics, FEECS,  
VŠB – Technical University of Ostrava, 17. listopadu 15,  
708 33 Ostrava – Poruba, Czech Republic

**Abstract.** A theoretical study of a new type of surface electromagnetic wave sensor, similar to a surface plasmon resonance (SPR) sensor, which utilizes a one-dimensional photonic crystal (1DPhC) instead of a metal film, is presented. Replacing the metal film in the SPR sensor by the 1DPhC has number of advantages including physical and chemical robustness, enhanced sensitivity, etc. 1DPhCs can be engineered to exhibit metal-like optical properties over given frequency intervals. Equivalently, the optical response of the 1DPhC can be described by an effective dielectric constant with a negative real value that permits the 1DPhC to support surface electromagnetic waves at frequencies within the forbidden transmission band. In our theoretical study, the 1DPhC is represented by a multilayer structure and we model the response of the system comprising a BK7 prism/multilayer/analyte in a Kretschmann configuration. For the system under study we express the reflectances of p- and s-polarized waves as a function of angle of incidence on the prism. Spectral reflectance is also presented. Dips in the reflectance spectra represent the coupling of light waves to surface modes and this can be confirmed by sensitivity to refractive index changes at the multilayer-analyte surface.

**Keywords:** surface electromagnetic waves, one-dimensional photonic crystal, Kretschmann configuration, BK7, sensor, analyte

## 1 Introduction

Recently, Bloch surface waves (BSW) have emerged as an attractive alternative to Surface plasmon polaritons (SPP) for sensing applications [1, 2].

Bloch surface waves are waves within the forbidden bandgap of photonic crystal. BSW is a surface electromagnetic excitation that exists at the interface between an optically active composite and a homogeneous dielectric. BSW can be excited at any wavelength by suitably changing the refractive index and thicknesses of the dielectric materials in the multilayer structure. This flexibility in the case of metals is limited.

BSWs are non-radiative electromagnetic modes, i.e., they do not exist in free space on their own. The BSW wavevector is longer compared to the free space wavevector at a given frequency. Thus, we need to provide an additional momentum to the wavevector of the incident wave so that it can satisfy the phase

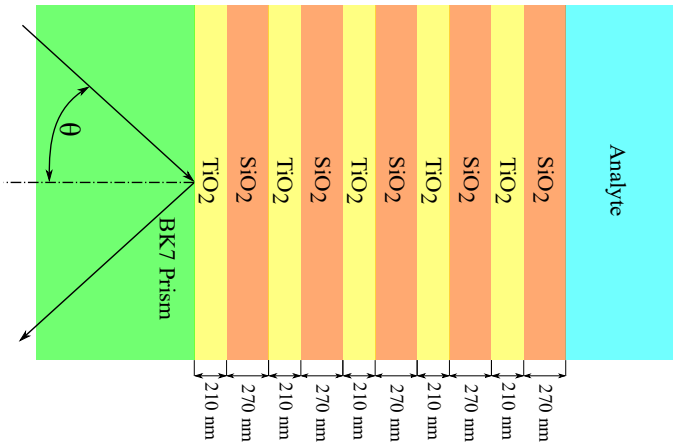
matching condition with the BSW wavevector. This is usually done by prism coupling technique, either using Kretschmann configuration or Otto configuration. In this study we use the Kretschmann configuration. BSW using the prism coupling is excited when the parallel wavevector ( $\beta$ ) on the top of the 1DPhC is equal to  $k_{\text{BSW}}$  as given by

$$\beta = k_{\text{BSW}} = k_0 n_{\text{glass}} \sin \theta \quad (1)$$

where  $k_0 = \frac{2\pi}{\lambda_0}$  is the free-space wave number,  $n_{\text{glass}}$  is the refractive index of the prism, and  $\theta$  is the angle of incidence of the incident wave.

## 2 Structure

Modeled structure is shown in fig. 1. It consists of 5-bilayers of  $\text{TiO}_2$  and  $\text{SiO}_2$ . As coupler prism BK7 was chosen. As analyte we consider air, and aqueous solutions of ethanol. Dispersion characteristics of all involved materials are used. The wavelength-dependent refractive index  $n_{\text{BK7}}(\lambda)$  for pure BK7 optical glass



**Fig. 1.** Schematic representation of theoretically modeled structure. It consists of 5-bilayers of alternating layers of  $\text{TiO}_2$  and  $\text{SiO}_2$  surrounded by two semi-infinite media (glass BK7 and analyte).

can be approximated by expression

$$n_{\text{BK7}}^2(\lambda) = 1 + \frac{1.03961212\lambda^2}{\lambda^2 - 0.00600069867} + \frac{0.231792344\lambda^2}{\lambda^2 - 0.0200179144} + \frac{1.01046945\lambda^2}{\lambda^2 - 103.560653} \quad (2)$$

where  $\lambda$  is wavelength in  $\mu\text{m}$ . We also consider wavelength ( $\lambda$ ) dependent refractive index of both  $\text{TiO}_2$  [3] and  $\text{SiO}_2$  [4] over the range of  $0.43 \mu\text{m}$  to  $0.8 \mu\text{m}$

given by

$$n_{\text{TiO}_2}^2(\lambda) = 5.913 + \frac{0.2441}{\lambda^2 - 0.0803}, \quad (3)$$

and

$$n_{\text{SiO}_2}^2(\lambda) = 1 + \frac{0.6961663\lambda^2}{\lambda^2 - 0.0684043^2} + \frac{0.4079462\lambda^2}{\lambda^2 - 0.1162414^2} + \frac{0.8974794\lambda^2}{\lambda^2 - 9.896161^2}, \quad (4)$$

respectively. We note that  $\lambda$  in eqn. 3 and 4 is in the units of  $\mu\text{m}$ . We also introduce small losses in these materials through the imaginary parts of their refractive indices. The values used here, 0.00016 and 0.000034 for  $\text{TiO}_2$  and  $\text{SiO}_2$  respectively [5, 6]. Second semi-infinite medium is analyte and it is composed of air ( $n_A = 1$ )

### 3 Transfer matrix method

To express the optical response of structure, described in previous chapter, matrix method is used.

Since the whole medium is homogeneous in the  $z$  direction (i.e.,  $\partial n/\partial z = 0$ ), the electric field that satisfies Maxwell's equations has the form

$$E = E(x)e^{i(\omega t - \beta z)}, \quad (5)$$

where  $\beta$  is the  $z$  component of the wave vector and  $\omega$  is angular frequency. We assume that wave is propagating in the  $xz$  plane, and we further assume that the electric field is either  $s$  or  $p$  polarized. If we represent the amplitudes of  $E(x)$  as column vectors, the column vectors of different sides of  $j$ -th interface are related by

$$\begin{pmatrix} A_j \\ B_j \end{pmatrix} = \mathbf{D}_j^{-1} \mathbf{D}_{j+1} \begin{pmatrix} A_{j+1} \\ B_{j+1} \end{pmatrix}, \quad (6)$$

where  $\mathbf{D}_j$  are dynamical matrices given by

$$\mathbf{D}_j = \begin{cases} \begin{pmatrix} 1 & 1 \\ k_j & -k_j \end{pmatrix} \text{ for } s \text{ wave,} \\ \begin{pmatrix} 1 & 1 \\ \frac{k_j}{n_j^2} & -\frac{k_j}{n_j^2} \end{pmatrix} \text{ for } p \text{ wave,} \end{cases} \quad (7)$$

where

$$\beta = n_0 \frac{\omega}{c} \sin \theta \quad k_j = \left[ \left( n_j \frac{\omega}{c} \right)^2 - \beta^2 \right]^{1/2}. \quad (8)$$

Propagation through the bulk of the  $j$ -layer is described by the so-called propagation matrix  $\mathbf{P}_j$ , which is given by

$$\mathbf{P}_j = \begin{pmatrix} e^{ik_j t_j} & 0 \\ 0 & e^{-ik_j t_j} \end{pmatrix}, \quad (9)$$



where  $t_j$  is the thicknesses of  $j$ -th layer.

The relation between  $A_0$ ,  $B_0$  and  $A_a$ ,  $B_a$  can thus be written as

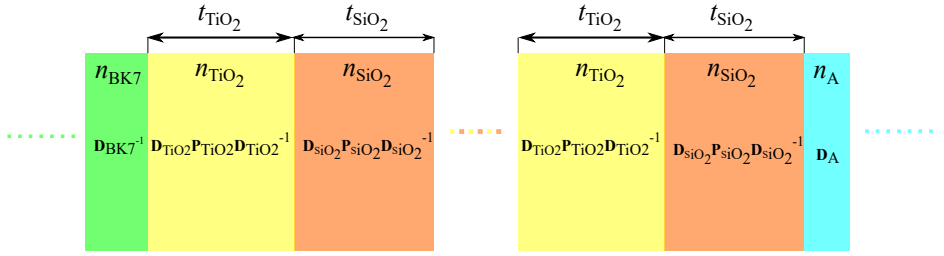
$$\begin{pmatrix} A_0 \\ B_0 \end{pmatrix} = \mathbf{D}_0^{-1} \left[ \prod_{j=1}^N \mathbf{D}_j \mathbf{P}_j \mathbf{D}_j^{-1} \right] \mathbf{D}_a \begin{pmatrix} A_a \\ B_a \end{pmatrix} = \mathbf{M}_{\text{tot}} \begin{pmatrix} A_a \\ B_a \end{pmatrix} \quad (10)$$

Here, we recall that  $N$  is the number of layers,  $A_0$ ,  $B_0$  and  $A_a$ ,  $B_a$  are the amplitudes of plane waves in incident semi-infinite medium and in final semi-infinite medium, respectively.

For our structure  $\mathbf{M}_{\text{tot}}$  can be written as

$$\mathbf{M}_{\text{tot}} = \mathbf{D}_{\text{BK7}}^{-1} \left( \mathbf{D}_{\text{TiO}_2} \mathbf{P}_{\text{TiO}_2} \mathbf{D}_{\text{TiO}_2}^{-1} \mathbf{D}_{\text{SiO}_2} \mathbf{P}_{\text{SiO}_2} \mathbf{D}_{\text{SiO}_2}^{-1} \right)^N \mathbf{D}_A, \quad (11)$$

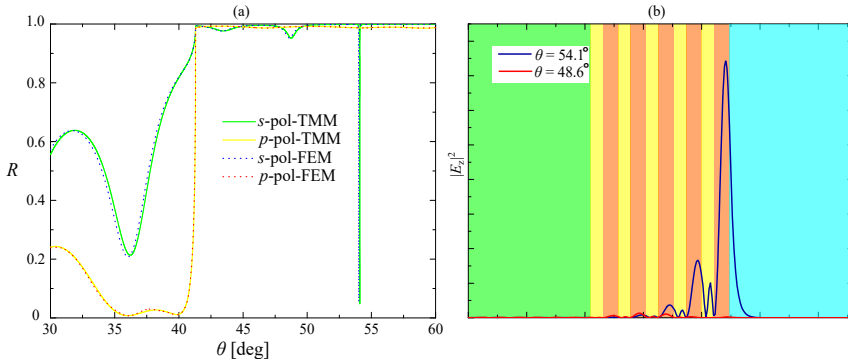
where  $N$  in Eq. 11 is number of bilayers,  $\mathbf{D}_{\text{TiO}_2}$ ,  $\mathbf{D}_{\text{SiO}_2}$ ,  $\mathbf{P}_{\text{TiO}_2}$ ,  $\mathbf{P}_{\text{SiO}_2}$  are dynamical and propagation matrices of  $\text{TiO}_2$  and  $\text{SiO}_2$  layers, respectively.



**Fig. 2.** Schematic representation of matrix method for considered structure.

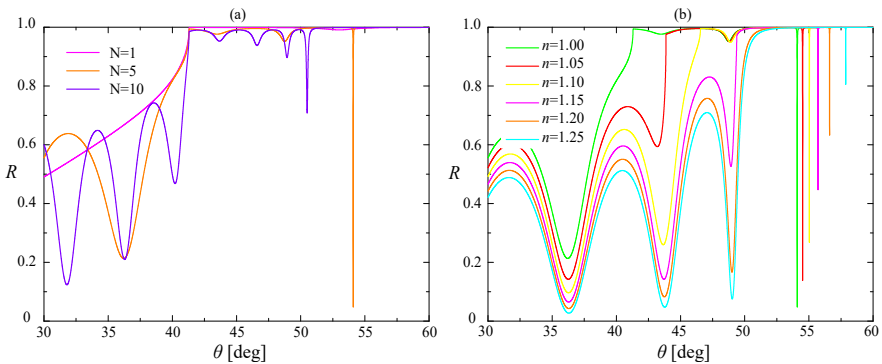
## 4 Theoretical results

Calculation was done by Transfer Matrix method (TMM) in MATLAB and by finite element method (FEM) in commercial software COMSOL Multiphysics. Figure shows dependence of reflectance  $R$  on angle on incident  $\theta$  for  $s$  and  $p$  polarized wave, respectively. As is obvious from Fig. 3 (a) good agreement between the two methods has been achieved. Dip in reflectivity about angle of  $54.1^\circ$  for  $s$  polarized wave indicated a surface mode resonance that is promising for sensing applications. The remaining dips are the due to the response of the multilayer system. To confirm that this is a surface mode, electric field distribution at mention resonance angle is shown in Fig. 3 (b). This figure clearly demonstrates optical field enhancement in the structure. Similarly, the normalized intensity distribution of guided mode field in the multilayer is demonstrated at a angle of incidence  $48.6^\circ$ . In both cases, an exponential tail in the analyte is obtained



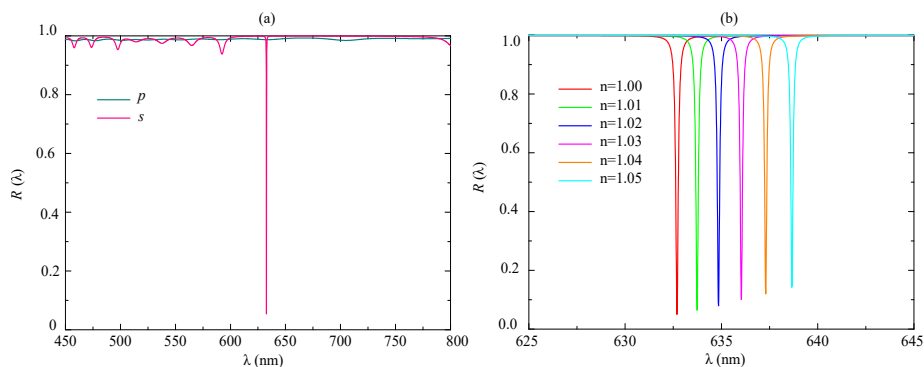
**Fig. 3.** (a) Theoretical dependence of reflectivity  $R$  on angle of incident  $\theta$  calculated by Transfer matrix method and by FEM for both polarizations. (b) Electric field distribution in the structure for  $s$  polarized wave.

with amplitude greater for the surface wave. Consequently, the structure is acceptable to be used as an optical sensor. For  $p$ -polarized wave non Bloch waves were excited as is clearly seen from Fig. 3 (a). Figure 4 (a) shows dependence of reflectivity  $R$  on angle of incident  $\theta$  for different number of bilayers  $N$ . It can be seen that for our case 5 bilayers is optimum for sensing application, because of for 5 bilayers the dip about resonance reaches minimum value. Figure 4 (b) shows dependence of reflectivity  $R$  on angle of incident  $\theta$  for different refractive indices of analyte  $n$ . From figure is clearly seen as the resonance shift towards grater angle with increasing refractive index of analyte. This shows ability of structure to work as a sensor. This type of sensor can work also in wavelength spectrum. Figure 5 shows spectral reflectivity for  $s$  and  $p$  polarized wave for angle



**Fig. 4.** Theoretical dependence of reflectivity  $R$  on angle of incident  $\theta$  for different number of bilayers  $N$  (a) and for different refractive indices of analyte  $n$  (b).

of incidence  $54.1^\circ$ . Again no surface waves are excited for  $p$  polarized wave. For  $s$  polarized wave Bloch surface waves occur about 630 nm. Spectral reflectance for different refractive indices of analyte is shown in Fig. 5 (b). We can see that with small change of refractive index of analyte, shift of resonance wavelength is observable.



**Fig. 5.** Spectral reflectances.

## Acknowledgments

This work was partially supported by the project SP 2019/26 funded by Ministry of Education, Youth and Sports of the Czech Republic.

## References

1. Y. Li et al: "Phase properties of Bloch surface waves and their sensing applications", *Applied Physics Letters* 103, 041116 (2013).
2. X. B. Kanga et al: "Design of guided Bloch surface wave resonance bio-sensors with high sensitivity", *Optics Communications* 383, 531-536 (2017).
3. J. R. Devore: "Refractive indices of Rutile and Sphalerite", *Journal of the Optical Society of America* 41, 416 (1951).
4. I. H. Malitson: "Interspecimen comparison of the refractive index of Fused Silica", *Journal of the Optical Society of America* 55, 1205 (1965).
5. S. Chao et al: "Low-loss dielectric mirror with ion-beam sputtered  $\text{TiO}_2$ - $\text{SiO}_2$  mixed films", *Journal of Applied Physics* 88, 4628 (2001).
6. C. C. Ting et al: "Structural evolution and optical properties of  $\text{TiO}_2$  thin films prepared by thermal oxidation of sputtered Ti films", *Applied Optics* 40, 2177 (2000).

## Publications

M. Gryga et al: "Surface electromagnetic wave sensor utilizing a one-dimensional photonic crystal", *Proc. SPIE* 2019, 11028 (2019)

# Observation of Magnetic Domains using the Magnetic Force Microscopy

Dmitry Markov, Jana Trojková, and Ondřej Životský

Department of Physics, FEECS,  
VŠB – Technical University of Ostrava, 17. listopadu 15,  
708 33 Ostrava – Poruba, Czech Republic  
dmitry.markov.st@vsb.cz

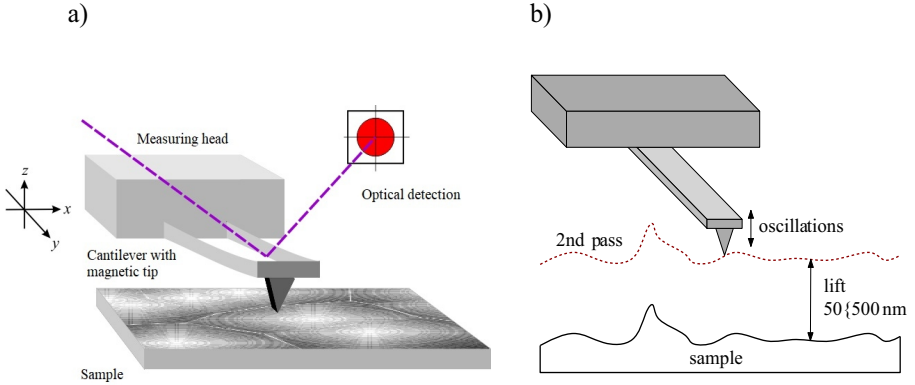
**Abstract.** Paper introduces magnetic force microscopy as a surface-sensitive technique suitable for observation of magnetic domains of different materials. Surface magnetic properties are investigated by Ntegra Prima NT-MDT microscope extended by external magnets for generation both in-plane and out-of-plane magnetic fields. As an example we present magnetic domain patterns measured on surfaces of materials that are potential candidates for applications in recording media, spintronics, and sensorics. We focus our attention to (i) transparent ferrite-garnet film prepared on gallium-gadolinium substrate, (ii) ingot  $\text{Co}_2\text{FeSi}$  Heusler alloy, and (iii) bilayered amorphous  $\text{FeSiB}/\text{FeNbSiB}$  ribbon.

**Keywords:** magnetic force microscopy, magnetic domains, thin film, ingot, ribbon

## 1 Introduction

Scanning Probe Microscopy (SPM) is a set of techniques that allow to analyze material surface with atomic resolution by using special probes. The construction of an image is done by moving in a raster scan, i. e. line by line in X-Y coordinates as shown in Fig. 1a. One of the SPM techniques is Atomic Force Microscopy (AFM) that was firstly introduced by Binnig, Quate, and Gerber in 1986 [1]. The idea is simple; the surface interacts with the tip of a cantilever by means of atomic forces, causing its deflection. Deviation of the probe is detected by optical method as shown in Fig. 1a. AFM is used for topography measurements of different types of materials like thin films, nanotubes, nanowires, organic materials, etc [2].

AFM has three basic measurement modes: contact, semi-contact, and non-contact. Selection of mode depends typically on type of measured sample. For example, semi-contact mode is often used for organic samples, because the tip does not have permanent interaction with brittle organic surface and the risk of damaging it is significantly lower. In contact mode the cantilever deflection under scanning reflects repulsive forces of surface (about  $\approx 10^{-7}\text{N}$ ) acting upon the tip. Semi-contact or tapping mode means something between contact and non-contact, where an amplitude modulation feedback is used to image the sample topography. The probe oscillates at a frequency close to its resonance and the



**Fig. 1.** (a) General scheme of AFM-MFM microscope. (b) Two-pass technique.

sample is imaged while the feedback adjusts the tip-sample separation to keep the oscillation amplitude at a fixed value [3]. In the non-contact mode the probe is far enough from the sample and does not touch its surface. In such a case only long-range forces are detected.

## 2 Magnetic Force Microscopy

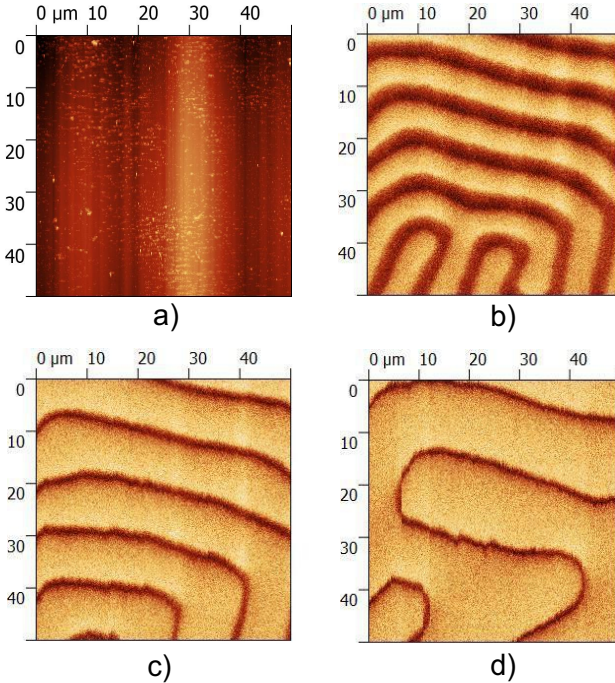
**Magnetic Force Microscopy (MFM)** is one of the AFM's modifications for studying magnetic properties of materials. The general concept is the detection of the magnetic force between the sample magnetic field and magnetic probe. MFM uses special tips with ferromagnetic thin film which is magnetized as one-domain system for the best measurement quality. Because not only magnetic forces act on the tip (the others could be capillary or van der Waals forces), it is necessary to separate them. There exist several methods, but the most common of them is so-called two-pass technique (see Fig. 1b). During the process of scanning, the surface topography image is determined by the contact or tapping mode (first pass). The probe is then lifted and the tip is forced to oscillate around the certain distance above the surface, the lift follows the trace of the surface pre-scanned in the first pass and predominantly long-range magnetic forces acting between the probe and surface are then recorded (second pass). The change of the phase shift is proportional to the gradient of the magnetic force

$$\Delta\varphi \approx \frac{Q F'_z}{k},$$

where  $Q$  is the quality factor of the cantilever,  $k$  its spring constant, and

$$F'_z = \mu_0 \int \mathbf{M}_T \cdot \frac{\partial^2 \mathbf{H}_S}{\partial z^2} dV_T$$

depends on the magnetization of the tip  $M_T$  and the field around the sample  $H_S$ .



**Fig. 2.** Topography (a) and MFM domain contrasts (b, c, d) observed on garnet film at different values of applied out-of-plane magnetic field (0 G, 300 G, 400 G).

## 2.1 Ntegra Prima

The AFM/MFM experiments were carried out in air at room temperature by Ntegra Prima microscope (NT-MDT, Russia). We used the MFM10 Co–Cr or HA\_FM Co–Fe coated cantilevers in semi-contact mode and two-pass method. The tips are magnetized perpendicularly to the sample surface and their coercivity is up to 16 kA/m. Maximum size of the analyzed area is  $100\ \mu\text{m} \times 100\ \mu\text{m}$ . The microscope is further extended by external magnets applying magnetic fields up to  $\pm 500$  Gauss out-of-plane and  $\pm 1000$  Gauss in-plane. This allows observation of magnetic domain patterns in dependence on external magnetic field.

## 3 Results and Discussion

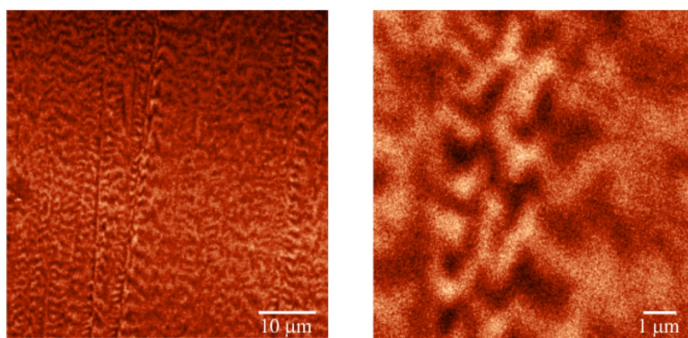
### 3.1 Magneto-optical $(\text{YSmLuCa})_3(\text{FeGe})_5\text{O}_{12}$ film

Fig. 2 shows examples of topography and magnetic domain contrasts measured on  $5\ \mu\text{m}$  thick magneto-optical film of  $(\text{YSmLuCa})_3(\text{FeGe})_5\text{O}_{12}$  prepared on the

substrate of gadolinium gallium garnet (GGG) –  $\text{Gd}_3\text{Ga}_5\text{O}_{12}$  – by isothermal liquid phase epitaxy (LPE). Produced films have smooth surface and are considered as optimal material for magnetic bubble memories due to strong induced perpendicular anisotropy. Therefore, applied positive external out-of-plane magnetic field (subplots c) and d)) leads to fast expanding of bright domains at the expense of dark ones. At magnetic field 500 Gauss (not presented) the magnetic contrast becomes completely bright and the film is in saturation state. Similar magnetization reversal is observed, when negative magnetic field is applied, only colours of magnetic domains are mutually interchanged [4].

### 3.2 $\text{Co}_2\text{FeSi}$ Heusler alloy

$\text{Co}_2\text{FeSi}$  Heusler alloys are due to their good optical and ferromagnetic properties mainly applied in spintronics. An ingot of corresponding composition was prepared by arc melting in the MAM-1 furnace, subsequently cut using spark erosion in deionised water into a disc of 20 mm in diameter and 500  $\mu\text{m}$  thick, and finally polished [5]. Because of large grains (up to hundreds of  $\mu\text{m}$ ) observed

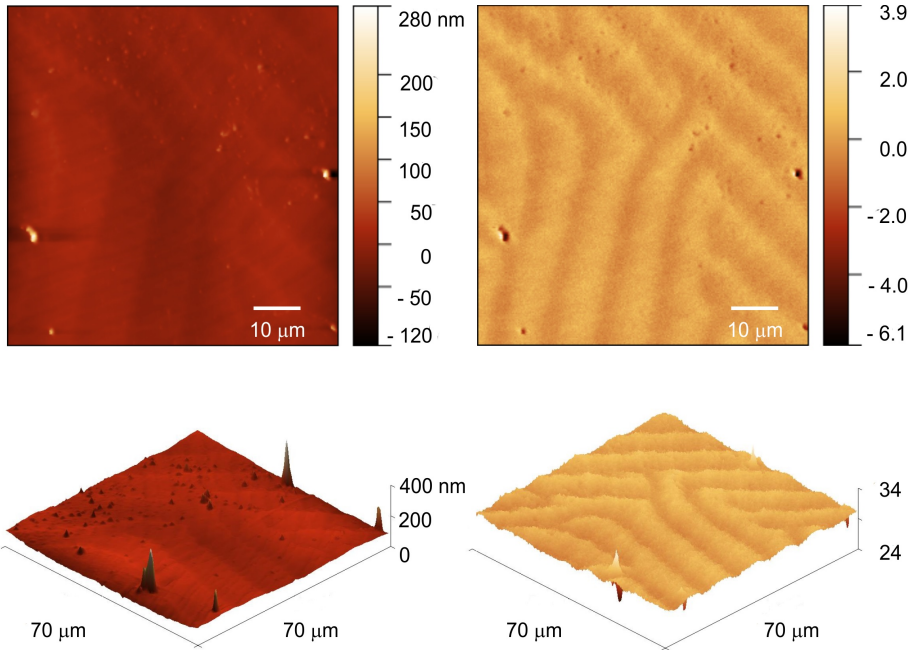


**Fig. 3.** MFM magnetic domains obtained inside the grain of  $\text{Co}_2\text{FeSi}$  ingot in bigger (left) and smaller (right) scanning area. No external magnetic field was applied.

using the scanning electron microscopy on the surface of  $\text{Co}_2\text{FeSi}$  alloy, magnetic domains presented in Fig. 3 were acquired from the inside of such grain. Typical fine fingerprint-like structure confirms again the presence of out-of-plane magnetic anisotropy that is easily detected by MFM due to almost perpendicular magnetization of the tip with respect to the sample surface.

### 3.3 Bilayered $\text{FeSiB}/\text{FeNbSiB}$ ribbons

The last material introduced is a bilayered  $\text{Fe}_{77.5}\text{Si}_{7.5}\text{B}_{15}/\text{Fe}_{74.5}\text{Nb}_3\text{Si}_{13.5}\text{B}_9$  ribbon prepared by planar flow casting (PFC) technique using crucible divided into two chambers. During the preparation process the  $\text{FeSiB}$  layer of the sample was in contact with surrounding atmosphere (air side), while the opposite



**Fig. 4.** The surface topographies (left) and their corresponding magnetic images (right) observed from the air side of FeSiB/FeNbSiB ribbon. 3D images are presented at lower subplots.

FeNbSiB layer was in contact with rotating wheel (wheel side). These amorphous soft magnetic materials are used mainly in sensor applications, like deflection or displacement sensors, as ferromagnetic shape-memory alloys and as alloys with enhanced magnetocaloric and giant magnetoimpedance effect [6]. Amorphous ribbons exhibit strongly inhomogeneous surface magnetic properties partly also due to higher surface roughness (typically tens-hundreds of  $\mu\text{m}$ ). Generally, the air ribbon side (see left subplot of Fig. 4) is a much more smoother than the wheel side, where mainly the air pockets and structure of rotating copper wheel influence the surface during preparation. MFM domain structure from the air sample side shown in right subplot of Fig. 4 consists of crossed stripe domains. In observed place the magnetization is oriented perpendicularly to the surface, but there exist other places, areas on the surface where practically no MFM contrast is obtained due to rotation of magnetization into the surface plane. It is also visible that topography image itself is slightly influenced by the magnetic forces depicted in the second pass magnetic contrast image. [6].

## 4 Conclusion

The paper is devoted to the introduction of AFM/MFM techniques that are presently widely used for studying topography and magnetic properties of mate-



rials. Non-destructiveness, high resolution up to tens of nanometers, and no need for special environment or sample treatment are considered as their main advantages. However, limitations of MFM are connected with the fact that the results depend on the tip magnetization, which may be unstable and its value is mostly unknown. Further, it provides only images of magnetic domains, no quantitative data or information on the direction of domains magnetization are obtained. Therefore, for better interpretation of results, MFM technique is often combined with the magneto-optical Kerr microscopy that has lower resolution due to used optical components, but magnetic domain contrast is obtained much faster and sensitivity to both in-plane and out-of-plane magnetization components can be achieved.

## Acknowledgments

This work was partially supported by the project SP 2019/26 funded by Ministry of Education, Youth and Sports of the Czech Republic.

## References

1. Binnig, G., Quate, C., and Gerber Ch.: Atomic Force Microscope. *Phys. Rev.* 56, 930 (1986)
2. Yalovenko, A.: AFM investigation of carbon nanotubes. *SPM-2003*, 171–173 (2003)
3. Garcia, R., San Paulo, A.: Attractive and repulsive tip-sample interaction regimes in tapping-mode atomic force microscopy. *Phys. Rev. B* 60, 4961 (1999)
4. Markov, D.: Imaging of Magnetic Domains by Magnetic Force Microscopy. Diploma Thesis, 1–59, Ostrava 2018
5. Titov, A., Životský, O., Hendrych, A., Janičkovič, D., Buršík, J., Jirásková, Y.: Co<sub>2</sub>FeSi Heusler Alloy Prepared by Arc Melting and Planar Flow Casting Methods: Microstructure and Magnetism. *Acta Physica Polonica Series A* 131, 654–656 (2017)
6. Trojková, J., Životský, O., Hendrych, A., Markov, D., Drobíková, K.: Magnetic domain patterns in bilayered ribbons studied by magnetic force microscopy and magneto-optical Kerr microscopy. *Scanning* 2018, 1–10 (2018)

# Vision Control of Industrial Processes

Lukasz Miszuda

Faculty of Electrical Engineering, Automatic Control and Informatics,  
Institute of Computer Science, Opole University of Technology,  
ul. Proszkowska 76, 45-758 Opole, Poland  
lukaszmiszuda@wp.pl

**Abstract.** The entire industry emphasizes ever-more efficient production machines; the only problem is man, who is unable to analyze what he sees very much. Control and analysis of current situations have been taken over by visual systems, which are not only able to draw conclusions from recorded images but also perform certain activities, such as determining position, identifying product defects, completeness, and controlling the robot in a given plane on their basis. Vision systems have already achieved such accuracy that they are increasingly used in machines' safety systems. Operating such devices is much more comprehensive than operating standard elements of the security system.

**Keywords:** vision technologies, vision security elements

## 1 Introduction

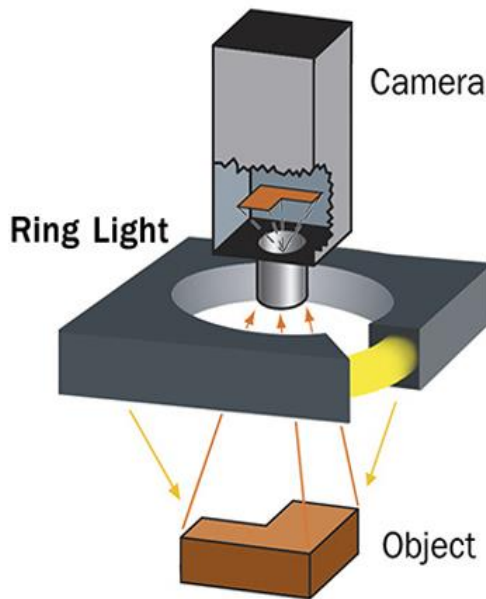
Nowadays, with omnipresent automation and desire to limit human factor in the production process, vision systems implemented in many production solutions have become a standard. Strict quality standards, process automation, error reduction and saving control results in databases - all that forces the use of technologies that guarantee full control over the quality of products. For this reason, the presence of vision systems at production lines is no longer a boon, but an absolute requirement. Vision technologies in the form of very complex systems, using programs analyzing given image and thanks to having used such systems for several years, have already appeared in security systems. Equipped with 2D/3D cameras, vision solutions allow manufacturers in the technology sector to reconcile both competitive and regulatory issues - the need for closer fault detection and quality assurance. Machine vision systems are often used to measure components, align assemblies, check print or surface quality and identify defective or missing components. All the processes implemented currently as part of the fourth industrial revolution are aimed at eliminating errors that can arise when the entire process is managed by man. Systems are more stable and presumably do not make mistakes. During the entire production process it is possible to choose the information that is of interest to the recipient. Continuous improvement

and new products introduced as part of Industry 4.0 development to some extent force continuous development of vision systems and the need to use them.

## 2 Vision systems

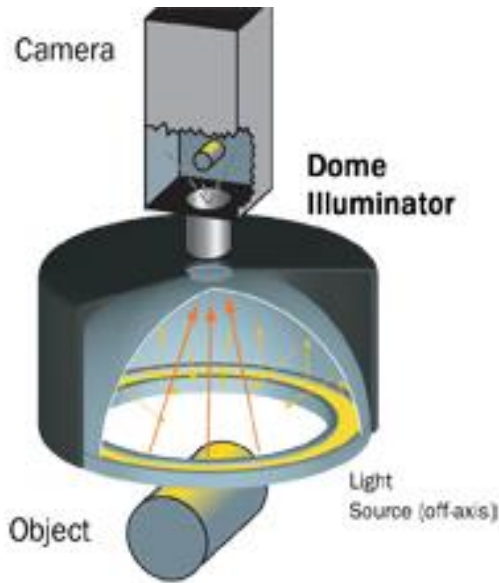
Industrial vision systems are systems of cooperating electronic devices. The function of an industrial vision system is automatic analysis of the environment, similar to that provided by sense of sight in people. Vision systems are devices that obtain information; devices for data acquisition and processing are part of the devices that help the vision system analyze the environment. These devices can consist in cameras of various types or camera systems, frame grabbers and other devices that can analyze data, i.e. processors or computers with software. The task of a vision system often consists in checking the physical characteristics of given objects - their dimensions, shapes, colors, etc. Thanks to the data acquired by that the device, we can easily make right decisions regarding e.g. the next stage of the manufacturing process.

The right selection of the element's lighting system, which determines how the image will be recorded by the camera, is crucial for the quality of the image obtained. The selection of illuminators should account for, among others, object geometry, its surface structure and characteristic features of the entire system. The lighting system should provide adequate contrast and minimize the recording of artifacts that can lead to erroneous conclusions in image analysis. Various models of illuminators are used, including systems in ring configuration (Fig. 1) or with rectangular matrix with LEDs.



**Fig. 1.** Ring illuminator[12]

For objects with convex shape and shiny surface, it is recommended to use dome-shaped illuminators (Fig. 2).



**Fig. 2.** Dome illuminators provide diffused illumination of the object, which reduces light flashes[12]

Another frequently used solution is to use the strobe effect. Illuminating a moving object with a flashing light gives the impression of stopping it. Difficulties associated with the implementation of such system may be associated with the need to synchronize light modulation with the movement of the object.

### 3 Intelligent camera

When considering cameras used in industrial vision, it is worth considering the definition of intelligent camera. Essentially, the camera referred to as intelligent, apart from an image recording circuit, is equipped with processor responsible for automatic selection of relevant information desired by the user from the recorded image. The selection is made without using external support modules.

The image obtained with the camera should be analyzed. For this purpose, dedicated software is most often used, which makes work significantly easier, faster and more efficient for designers and vision system operators. The vast majority of cameras used in vision systems in automation have a matrix smaller than 1/2" and can process no more than 64 frames / s. Of course, there are larger matrices which can reach up to 120 frames / sec. However, this is definitely a smaller group of devices in a wide range of products offered on the market. Cameras with larger matrices are also used by the maintenance department operating in the plant; with machines operating at very high speeds, there are sometimes situations when the machine stops and the

reason for stopping cannot be determined afterwards. By analyzing the image from such camera, we can see much more than human eye can see while watching the same situation.

It is also worth mentioning optical image recognition - the OCR algorithm ( Optical Character Recognition), which is perfect for reading serial numbers of given products. The algorithm ensures character differentiation and recognition. Another particularly interesting algorithm is the OCV algorithm ( Optical Character Verification), which allows for comparing printed texts with standard strings.

The most popular tasks implemented by industrial vision systems are:

2D:

- identifying parts, recognizing the position.
- measuring the position, distance and angles,
- managing the robot in the plane,
- central tool point programming, tool center point correction,
- palletisation on a plane,
- assembling (aligning) parts,
- recognizing defects on planes (surfaces),
- recognizing handwriting (OCR) and codes.

2.5 D:

- palletisation in 3D.

3D:

Determining the position of large objects in space (with 6 degrees of discretion) applicable to:

- sealing car bodies,
- car body varnishing,
- chassis sealing,
- assembly and dismantling,
- positioning of cranes,

3D stereo:

- measuring positions, distances and angles,
- determining coordinates, finding the edges,
- measuring seams, contours,
- managing the assembly,
- driving robots, vehicles,

- determining the position of the car body.

3D stereo multi:

- fitting windows on cars,
- assembling elements and components,
- assembling and dismantling the door,
- masking gaskets for car windows.

## **4      Vision security systems**

Among the many solutions available on the market in the scope of safety during production, vision systems are more and more often used to protect operator working within a given machine or station. This is due to the fact that machines introduced into production today are characterized by a very high degree of automation and complexity, however a given machine is still operated by man. With high technological advancement, safety barriers and safety sensors are not enough anymore. Vision systems used in the scope of security have the ability to specify not only in which area the system is to 'react' (it is an area that can be designated from the area that the camera 'sees'). If such a system is installed on a movable element, the designated area may change depending on the position of this element. It is mainly used in automatic trucks that move along a pre-determined route. The function of determining the response area is mainly used in places where the operator e.g. puts elements, parts on a conveyor belt or to another station. Vision security system ensures that the operator cannot enter while the station is in operation and that the station does not make any dangerous movements during operator's activities.

## **5      Conclusion**

Using vision systems provides a number of advantages - primarily in the industrial production process itself. A good vision system performs tasks with accuracy and consistency not possible to achieve with the work of human hands. This clearly translates into quality and production efficiency as well as the elimination of defective components, assembly control and tracking and capturing information at every stage of the process. Minimizing errors is also a guarantee of lowering production costs and increasing customer satisfaction. In addition, there are many benefits to eliminating direct contact between the inspected object and the components of quality control system. First of all, accidental destruction of the former and wear of the latter's components are avoided.

For several reasons, it is worth limiting the participation of men in the production process. For example, it allows to save space occupied by their positions, and when one vision system replaces many people at the same time, labor costs are significantly reduced.

In the case of production lines of some products, for example in the pharmaceutical and food industries, visual quality control without human intervention is necessary because of high requirements in the scope of hygiene. In others, it allows to keep employees away from dangerous factors, including ambient conditions, substances, machines. Vision control of robots also improves the quality of production and its flexibility, due to the fact that they can more easily adapt to the variability of the features of the details they operate.

The applications of vision systems can be divided into four categories of tasks. The first one includes targeting other devices at the object of their task.

## 6 References

1. *Charakterystyka systemów wizyjnych w przemyśle*, <http://poradnik.pkt.pl/inne/charakterystyka-systemow-wizyjnych-przemysle> [available: 10.06.2019]
2. *Rola i wdrożenie wizji maszynowej jako coraz ważniejszego aspektu Przemysłu 4.0* <http://www.systemywizyjne.pl/ps/nws/rola-i-wdrozenie-wizji-maszynowej-jako-coraz-wazniejszego-aspektu-przemyslu-4-0>, [available: 20.06.2019]
3. Bledowski K, *The internet of things: industrie 4.0 vs. the industrial internet*, 2015, <https://www.mapi.net/forecasts-data/internet-things-industrie-40-vs-industrial-internet>. [available: 14.12.2018].
4. *Systemy wizyjne wykorzystywane w przemyśle*, <https://proautomatic.pl> [available: 15.07.2019]
5. *Systemy wizyjne część I*, <https://automatykab2b.pl/temat-miesiaca/39536-systemy-wizyjne-czesc-i-podstawy-oswietlenie-i-objektywy> [available: 20.07.2019]
6. *Systemy wizyjne w zastosowaniach zrobotyzowanych*, <https://automatykaonline.pl>, [available: 18.07.2019]
7. *Systemy wizyjne – nieodzowny element nowoczesnej kontroli*, <https://automatykaonline.pl>, [available: 13.06.2019]
8. Mithe R., Indalkar S., Divekar N., *Optical Character Recognition*
9. Chevion D., Gilat I., Heilper A. *System and method for correction of optical character recognition with display of image segments according to character data*
10. Zbierajewska E, *Zastosowania systemów wizyjnych*
11. Halme R., Lanz M., *Review of vision-based safety systems for human-robot collaboration*
12. <https://www.microscan.com> [available: 10.07.2019]

# Assessment of the Effectiveness and Accuracy of Object Detection on the Example of a Power Line Insulator Detection System

Jakub Osuchowski

Faculty of Electrical Engineering, Automatic Control and Informatics,  
Institute of Computer Science, Opole University of Technology,  
ul. Proszkowska 76, 45-758 Opole, Poland  
jakub.osuchowski@gmail.com

**Abstract.** The purpose of the work is to outline the methods for object detectors assessment. The article describes the main evaluators i.e. Intersection over Union, precision, recall and average precision. With the use of those methods any object detector effectiveness and accuracy can be evaluate. As an example, the article uses a system that detects high voltage line insulators on digital images. In addition, the article describes the concept of detection, classification, localization and segmentation.

**Keywords:** Detection System, Power Line Isolator, Image Processing, Intersection over Union, Precision, Recall, Average Precision.

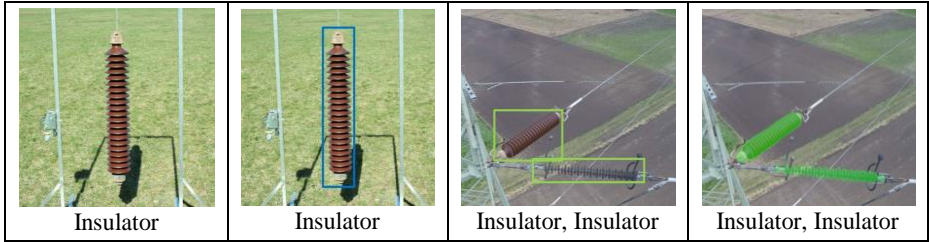
## 1 Introduction

Computer vision is an interdisciplinary field which has evolved quickly mostly thanks to deep learning methods. Researchers in this area have been experimenting many modern architectures and algorithms, which have influenced other fields as well. One of the main tasks in the field of deep learning is object detection. This task, together with other computer vision algorithms, is often and widely used, among others, in robotics and autonomous vehicles [1]–[3]. In addition to the concept of object detection there are other similar tasks such as image classification, localization and segmentation. The differences between these tasks are shown in Table 1.

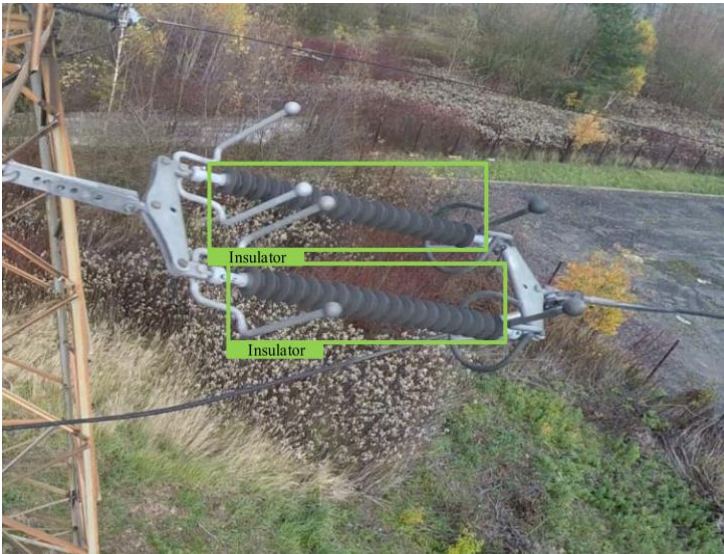
**Table 1.** The difference between classification, location, detection and segmentation

Single object		Multiple objects	
Classification	Classification + Localization	Detection	Segmentation





As presented in table 1, classification is about assigning an image with an object to one of the predefined classes. In turn, the task of localization is find where the object is and draw a bounding box around it. Object detection consists of classifying and locating but for all objects in the image. This means that each object will be assigned to object class, and a bounding box will be drawn around it (Fig. 1). Segmentation involves assigning each pixel to a specific class in such a way that each pixel is assigned to a specific instance of the object [4]–[9].



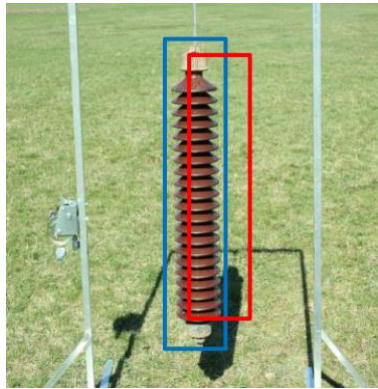
**Fig. 1.** An example of detection of long rod insulators on a digital image acquired during passage along a high-voltage line

Fig. 1 shows an example of prediction made by the detector on a digital image acquired during a passage along a high voltage line. In this particular case, the detection task was to assign classes to two objects simultaneously (classify) and draw bounding boxes around them (location).

## 2 Assessment of object detection accuracy

Detection accuracy for a specific data set is most often assessed on the basis of the intersection over union (IoU). Intersection over Union is an evaluation metric used to measure the accuracy of an object detector on a particular dataset. Intersection over Union is used typically to evaluate the performance feature detectors and descriptors and convolutional neural network detectors (i.e., R-CNN, Faster R-CNN, YOLO, etc.), but any algorithm that provides predicted bounding boxes as output can be evaluated using IoU. In order to assess the accuracy of the detector, it is necessary to have:

1. The ground-truth bounding boxes (i.e., the hand labeled bounding boxes from the testing set that specify where in the image object is).
2. The predicted bounding boxes from detector. (Fig. 2) [10].



**Fig. 2.** An example of an insulator detection. The predicted bounding box is drawn in red while the ground-truth bounding box is drawn in blue.

The intersection over union determines the difference in position and size between two areas marked in Fig. 2. This parameter is calculated using the formula:

$$IoU = \frac{A \cap B}{A \cup B}$$

where:

- A – predicted bounding box,
- B – ground-truth bounding box,
- $A \cap B$  – area of overlap,
- $A \cup B$  – area of union.

### 3 Assessment of object detection effectiveness

Another widely used measure of detection efficiency is the AP (average precision) parameter. This parameter is based on two other performance measures: precision and recall [11]. The precision parameter measures how accurate are the predictions. i.e. the percentage of the predictions are correct. This parameter is described by the following formula:

$$precision = \frac{TP}{TP + FP}$$

where:

TP – true positive – correct prediction,

FP – false positive – false prediction.

Parameter recall tells about how well the detector searches for objects, i.e. how many manually selected objects were found. The formula describing this parameter has the following form:

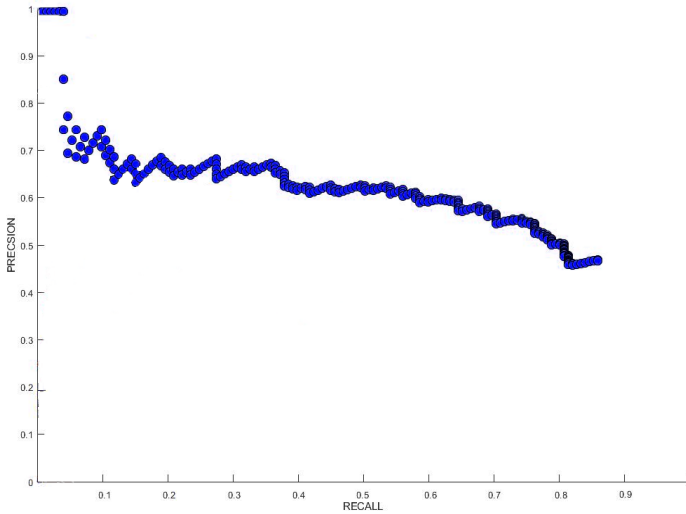
$$recall = \frac{TP}{TP + FN}$$

where:

TP – true positive – correct prediction,

FN – false negative – objects not found.

It should be noted that is necessary to determine when a given prediction is correct and when not. The IoU parameter described above is most often used for this task. Most often it is assumed that the given prediction is correct when the value of the IoU parameter is greater than 0.5 [11]–[15]. To determine the AP parameter, it is necessary to draw a precision (recall) curve. In the first step all the predictions are ranked in descending order according to the predicted confidence level. Next, the precision and recall parameters are calculated for each subsequent prediction and the point on the precision(recall) curve is marked. An example of a precision (recall) curve of insulator detection with the use of YOLO convolutional neural network is shown in Figure 3.



**Fig. 3.** An example of an precision(recall) curve of insulator detection with the use of YOLO convolutional neural network

Precision and recall are always between 0 and 1. Therefore, AP falls within 0 and 1 also. Before calculating AP for the object detection, the precision(recall) curve is often smooth out. Graphically, at each recall level, each precision value is replace with the maximum precision value to the right of that recall level. Finally, the IoU parameter is calculated using the following formula:

$$AP = \frac{1}{11} \sum_{r \in \{0.0, 0.1, \dots, 1.0\}} p(r)$$

where:

AP – average precision,

p –precision,

r –recall.

The mAP parameter (mean average precision) is also very often used. This is the arithmetic mean of all AP parameter values for all individual categories of objects from the data set [11]–[15].

## 4 Conclusion

The evaluation of detector performance is a very important task. The methods presented in the article allow to check if the detector is suitable for use in a particular case. Such a case may be e.g. detection of overhead

line insulators on digital images. Early detection of overhead line insulators failures is critical to avoid costly downtimes of whole high voltage power line. The presented methods can also be successfully used to evaluate training datasets under account of use during the process of supervised learning of any algorithm e.g., convolutional neural network.

## 5 References

1. E. Y. Chang and Y. F. Wang, "Toward building a robust and intelligent video surveillance system: A case study," 2004 IEEE Int. Conf. Multimed. Expo, vol. 2, pp. 1391–1394, 2004.
2. L. P. M. Sc, "Important features of a vision system for successful robot guidance applications."
3. D. DeMotte, "Visual Line Tracking Application Overview & Issues," Mach. Vis. Robot Guid. Work., 2004.
4. P. Sermanet, D. Eigen, X. Zhang, M. Mathieu, R. Fergus, and Y. LeCun, "OverFeat: Integrated Recognition, Localization and Detection using Convolutional Networks," 2013.
5. K. Bhure and J. D. Dhande, "Object Detection using SURF features," Int. Res. J. Eng. Technol., vol. 4, no. 7, pp. 1524–1526, 2017.
6. D. A. Lisin, "Image Classification with Bags of Local Features," no. May, 2006.
7. D. Garcia-Gasulla et al., "An Out-of-the-box Full-network Embedding for Convolutional Neural Networks," pp. 1–11, 2017.
8. K. Kawamura, "Localization of Insulators in Electric Distribution Systems by Using 3D Template Matching from Multiple Range Images," no. October, pp. 1534–1540, 1998.
9. Z. Zhao, N. Liu, and L. Wang, "Localization of multiple insulators by orientation angle detection and binary shape prior knowledge," IEEE Trans. Dielectr. Electr. Insul., vol. 22, no. 6, pp. 3421–3428, 2015.
10. D. Zhou et al., "IoU Loss for 2D/3D Object Detection," 2019.
11. P. Henderson and V. Ferrari, "End-to-end training of object class detectors for mean average precision," Lect. Notes Comput. Sci. (including Subser. Lect. Notes Artif. Intell. Lect. Notes Bioinformatics), vol. 10115 LNCS, pp. 198–213, 2017.
12. J. W. Yun, "Fructooligosaccharides - Occurrence, preparation, and application," Enzyme Microb. Technol., vol. 19, no. 2, pp. 107–117, 1996.
13. K. Oksuz, B. C. Cam, E. Akbas, and S. Kalkan, "Localization recall precision (LRP): A new performance metric for object detection," Lect. Notes Comput. Sci. (including Subser. Lect. Notes Artif. Intell. Lect. Notes Bioinformatics), vol. 11211 LNCS, pp. 521–537, 2018.
14. E. Hanna and M. Cardillo, "Faster R-CNN: Towards Real-Time Object Detection with Region Proposal Networks," Biol. Conserv., vol. 158, pp. 196–204, 2013.
15. K. He, G. Gkioxari, P. Dollár, and R. Girshick, "Mask R-CNN," Proc. IEEE Int. Conf. Comput. Vis., vol. 2017-October, pp. 2980–2988, 2017.

# Artificial Intelligence in the field of expressing human emotions – overview of available frameworks

Agnieszka Rozanska

Faculty of Electrical Engineering, Automatic Control and Informatics, Institute of Computer Science, Opole University of Technology, ul. Proszkowska 76, 45-758 Opole, Poland  
a.rozanska92@gmail.com

**Abstract.** In this paper author describe different approaches to artificial intelligence in field of expressing emotions by the machine. Different APIs, solutions and the most significant aspects of them were described, as well as recent research around the topic of showing human emotions by artificial intelligence.

**Keywords.** Artificial Intelligence, AI, Emotions

## 1. Introduction

Artificial intelligence, sometimes also called machine intelligence, is an intelligence shown by machines. The name is also used to describe a machine or computer that mimics human cognitive functions, such as learning or solving problems. In the IT field AI is dealing with intelligence whatsoever – creating models of intelligent behavior and computer applications that simulate these behaviors. The first steps towards artificial intelligence were taken in 1956 as academic research [1] and over the years it has been seen that progress in the work of artificial intelligence will be very slow and tedious. Fortunately, in recent years, accelerated progress has been noticed in field of artificial intelligence due to the advancement of current computing machines and its components.

One of the areas that have not yet been thoroughly studied in the field of artificial intelligence is area of human emotions. Currently used AI show emotions in a way it can be called as artificial, in which appropriate scripts are used to express emotions in appropriate situations and no AI is used in the general sense. Basic emotions such as anger, fear, joy and sadness are programmed in such a way as to respond with the right tone and words so that the person with whom the machine communicates think that these are the emotions expressed by the robot. However, it is rigid programming, written by the programmer, and these are not decisions made by AI.

Basic human emotions can be portrayed through artificial intelligence, but only when knowing what emotions are shown on the person that this AI interacts with.

This requires a specific library that will allow emotion recognition, such as OpenCV. Although it is not a AI framework, it is still worth mentioning, because it can be used in many different frameworks.

Open CV is a library that have more than 2500 algorithms [2] that enables many different options in computer vision field, such as face recognition, emotion recognition, object identification, motion tracking and augmented reality. It supports deep learning frameworks, such as PyTorch, TensorFlow and Caffe. OpenCV project was initially an Intel Research initiative. This library is cross-platform and can be used in Mac OS X, Windows and Linux. The library was created in the C language, but there are overlays that allow you to use it also in C ++, C #, Python, Java and JS. Its authors focus on image processing in real time.



**Fig. 1.** Screenshot of a working OpenCV library, written in Python language, executed on Linux Ubuntu [3].

This library can be easily used to detect faces and emotions and properly recognize them. It is open-source and can be easily compiled to work with different deep learning frameworks which is undoubtedly its advantage. Frameworks that can benefit from OpenCV library are described in later chapters of this paper.

### 3. TensorFlow

TensorFlow is an open source programming library written by the Google Brain Team [4]. It is used in machine learning and deep neural networks. The library consists of several modules. In its lowest layer there is a distributed execution engine, which has been implemented in the C++ programming language to improve performance. Above it are frontends written in several programming languages, including in Python and C++. Above is the API layer, which provides a simpler interface for commonly used layers in deep learning models. The next layer consists of high-level API, including Keras and Estimator API, which facilitate model creation and evaluation. Above this are ready-to-use models prepared by the library's creators.



*Fig. 2. Example of using TensorFlow as a foundation of application called DeepDream. Original photo (left) and neural style applied with TensorFlow (right) [5].*

### 4. Keras

Keras is an open-source neural-network library that is capable of running on top of TensorFlow [6], which is undoubtedly its advantage. It is designed to experiment with deep neural networks, being user friendly at the same time. From 2017, Keras is in TensorFlow's core library. It is not a standalone machine learning framework, it is rather an interface that offers more intuitive set of abstractions to make it much easier to develop deep learning models. It is written in Python, same as TensorFlow. It supports both recurrent networks and convolutional networks.

### 5. Caffe

Caffe (Convolutional Architecture for Fast Feature Embedding) is a deep learning framework made by BAIR [7]. It is open source under BSD (Berkeley Software Distribution) license. Stable release for this framework was released in April 2017. Its ad-



vantage over other deep-learning frameworks is its speed – it can process over 60 million images per day[6] with NVIDIA K40 GPU; that is 4ms per image for learning and 1ms per image for inference, though it supports many different types of learning architectures, but it is clearly seen, that this framework is geared towards image classification and segmentation. There is second version of Caffe, called Caffe2 that was announced by Facebook, although it was later merged into PyTorch project.

## 5. Comparison

There are several different elements that the author paid attention to when choosing frameworks: software availability, speed, open-source license, cross-platform, support for CUDA technology, and technical support for framework developers, i.e. is the project being developed and updated on a regular basis. CUDA technology is essential in future emotion recognition software development. All of these aspects are summarized in the table *Table 1*. below.

*Table 1. Deep-learning software comparison*

Name	Software availability	Open-source/ license	Platform	CUDA support	Last update
TensorFlow	Yes, on the website	Yes, Apache 2.0	Linux, macOS, Windows, Android	Yes	29-Aug-2019
Keras	Yes, on the website	Yes, MIT	Linux, macOS, Windows	Yes	22-Aug-2019
Caffe	Yes, on the website	Yes, BSD	Linux, macOS, Windows	Yes	02-Mar-2019

## 6. Conclusion

In this paper author described a brief analysis of different frameworks that potentially will be used as a AI with emotion recognition and being able to correctly show emotions itself.

The goal of author's research is to show different approaches to the artificial intelligence and different structures of frameworks that will potentially lead to future AI with emotions.

The future work involves a research on the field of human emotions and artificial intelligence. Current work is being completed towards learning AI to express basic emotions by itself.

## REFERENCES

1. Crevier D.: AI: The Tumultuous Search for Artificial Intelligence, New York, NY: BasicBooks, ISBN 0-465-02997-3
2. OpenCV: About (2019) <https://opencv.org/about/>
3. PyImageSearch: Ubuntu 16.04: How to install OpenCV. (2016) <https://www.pyimagesearch.com/2016/10/24/ubuntu-16-04-how-to-install-opencv/>
4. TensorFlow: Introduction to TensorFlow. (2019) <https://www.tensorflow.org/learn>
5. Wikimedia: TensorFlow. (2016) <https://commons.wikimedia.org/wiki/File:Toronto-MusicGarden10-TensorFlow2.jpg>
6. KerasL Keras documentation. (2019) <https://keras.io/#you-have-just-found-keras>
7. BAIR: Berkeley Artificial Intelligence Research. (2019) <https://bair.berkeley.edu/>

# Author Index

- Abolghasem, Mojgan, 482  
Alexa, Petr, 482  
Andrešič, David, 340  
Augustynek, Martin, 162
- Bača, Jakub, 48, 60  
Bailová, Michaela, 357  
Baroš, Jan, 114  
Běčák, Petr, 1  
Beháň, Ladislav, 452  
Béreš, Michal, 363  
Bielik, Martin, 285  
Blaheta, Radim, 363  
Blažek, Vojtěch, 7  
Borová, Monika, 120  
Brablík, Jindřich, 126  
Byrtus, Radek, 132
- Cigánková, Barbora, 340
- Damec, Vladislav, 108  
Danys, Lukas, 138  
Dedek, Jan, 144  
Dočekal, Tomáš, 150  
Dohnal, Jakub, 156  
Domesová, Simona, 369
- Fait, Michal, 291  
Fiedorová, Klára, 162  
Foltyn, Ladislav, 375
- Gaiová, Karolína, 168  
Gavlas, Antonín, 174  
Golembiovský, Matěj, 180  
Goňo, Radomír, 20
- Hájek, Lukáš, 464  
Hájovský, Radovan, 267  
Harach, Tomáš, 84  
Ho, Sang Dang, 54  
Horák, David, 387
- Chrástecký, Libor, 186
- Jahan, Ibrahim S., 14  
Jalowiczor, Jakub, 458  
Janečko, Tomáš, 298  
Jaroš, René, 192
- Kahánková, Radana, 198  
Klein, Tomáš, 90  
Kocman, Stanislav, 66, 72  
Kodytek, Pavel, 204  
Kolář, Jakub, 464  
Kolařík, Jakub, 210  
Konečný, Jaromír, 186, 273  
Kořený, Martin, 96  
Kotík, Vojtěch, 304  
Kotulla, Michal, 20  
Kouřil, Daniel, 48, 60  
Kozielová, Petra, 381  
Krátký, Michal, 351  
Krupa, Filip, 216  
Kružík, Jakub, 387  
Křestanová, Alice, 222  
Kudělka, Miloš, 310
- Ládrová, Martina, 228  
Látal, Jan, 464  
Lazecký, David, 26  
Litschmannová, Martina, 239  
Lukáš, Dalibor, 431
- Markov, Dmitry, 494  
Markovič, Ondřej, 393  
Martinek, Radek, 114, 126, 138, 192, 198, 210, 228  
Miszuda, Lukasz, 500  
Mišák, Stanislav, 7, 14, 41  
Mrovec, Martin, 397
- Němčík, Jakub, 233  
Novák, Martin, 470  
Novák, Tomáš, 1  
Nowak, Stanislav, 66
- Oczka, David, 239  
Ondraczka, Tomáš, 243  
Osuchowski, Jakub, 506  
Ožana, Štěpán, 267
- Pacholek, Jan, 403  
Paláček, Stanislav, 407  
Pečínka, Pavel, 72  
Pečínková, Vladana, 72  
Pecha, Marek, 413  
Penhaker, Marek, 222, 249, 279

Peterek, Ivo, 419  
Petružela, Michal, 33  
Pieš, Martin, 267  
Platoš, Jan, 285, 304, 334  
Plesník, Jakub, 310  
Praužek, Michal, 120, 168, 186, 273  
Przeczek, Samuel, 102

Raiman, Tom, 425  
Révay, Lukáš, 316  
Rozanska, Agnieszka, 512

Schmidt, Martin, 249  
Schneider, Miroslav, 255  
Sikora, Lubomír, 322  
Simkanič Radek, 328  
Sokanský, Karel, 1  
Stankuš, Martin, 186  
Straková, Erika, 431  
Strossa, Jan, 108  
Sun, Yujia, 334  
Šaloun, Petr, 340

Šoustek, Lukáš, 261

Tomaszek, Lukáš, 345  
Tran, Cuong Dinh, 78  
Trojková, Jana, 494

Ulčák, David, 436

Velička, Jan, 267  
Vitásek, Jan, 464  
Vitásek, Martin, 273  
Vondrák, Jaroslav, 279  
Vozňák, Miroslav, 458  
Vrtková, Adéla, 442  
Vysocký, Jan, 41

Zátopek, Lukáš, 351  
Závada, Jakub, 447

Žabka, Stanislav, 476  
Žídek, Jan, 144  
Životský, Ondřej, 494

Editors: Michal Krátký, Jiří Dvorský, Pavel Moravec  
Dept. of Computer Science  
VŠB – Technical University of Ostrava

Title: WOFEX 2019

Place, year, edition: Ostrava, 2019, 1<sup>st</sup>

Page count: 535

Edit: VŠB – Technical University of Ostrava,  
17. listopadu 15, 708 33 Ostrava-Poruba  
Czech Republic

Impression: 200

Not for sale.

ISBN 978-80-248-4333-9